The development and combination of electromagnetic non-destructive evaluation techniques for the assesment of cover concrete condition prior to corrosion

Raelize Loubser Du Plooy

l'université nantes angers le mans
PÔLE DE RECHERCHE ET D'ENSEIGNEMENT SUPÉRIEUR

UNIVERSITÉ DE NANTES

Thèse de Doctorat

Raelize LOUBSER DU PLOOY

Mémoire présenté en vue de l'obtention du
grade de Docteur de l'Université de Nantes
sous le label de l'Université de Nantes Angers Le Mans

Discipline : Automatique et informatique appliquée, Génie civil
Laboratoire : Institut Français des Sciences et Technologies des Transports, de l'Aménagement et des Réseaux (IFSTTAR)

Soutenue le 10 juin 2013

École doctorale : 503 (STIM)
Thèse n° : 000000000

The development and combination of electromagnetic non-destructive evaluation techniques for the assessment of cover concrete condition prior to corrosion

JURY

Rapporteurs :	**M. Andrea BENEDETTO**, Professeur des universités, Università degli Studi Roma Tre, Rome, Italie **M. Denys BREYSSE**, Professeur des universités, Université de Bordeaux, France **M. Eugen BRÜHWILER**, Professeur des universités, EPFL, Lausanne, Suisse
Examinateurs :	**M. Jean-Paul BALAYSSAC**, Professeur des universités, LMDC, Toulouse, France **M. Xavier DÉROBERT**, Ingénieur des travaux publics de l'état (HDR), IFSTTAR, Nantes, France **M. Ciaran MCNALLY**, Ingénieur de recherche, UCD, Dublin, Irelande **M. Franck SCHOEFS**, Professeur des universités, GeM, Université de Nantes, France **M^me^ Géraldine VILLAIN**, Ingénieur des travaux publics de l'état (HDR), IFSTTAR, Nantes, France
Invités :	**M. Gautier MOREAU**, Ingénieur de recherche, EDF, Chatou, France **M. Sergio PALMA LOPES**, Ingénieur des travaux publics de l'état, IFSTTAR, Nantes, France
Directeur de thèse :	**M. Xavier DÉROBERT**, Ingénieur des travaux publics de l'état (HDR), IFSTTAR, Nantes, France

Opgedra aan my liewe man vir al sy opofferings
om hierdie droom te laat waar word.

Mag ons nooit, ooit weer vir só lank van bed en tafel geskei wees nie!

Acknowledgements

I would firstly like to thank my PhD supervisors at IFSTTAR, Sergio PALMA LOPES, Géraldine VILLAIN and Xavier DÉROBERT for the guidance and support with which they provided me during the three years spanning this project. I especially appreciate their patience in helping me to cope with the challenges of being introduced to a new field of research and a new environment, very different to what I was used to. I would like to thank Ciaran McNALLY, leader of the TEAM project (Training in European Asset Management) of which this PhD formed part, who have managed the project and initiated several training weeks that were very useful. As external advisor of my work, he also provided me with indispensable guidance, especially during my secondment at University College Dublin. I would like thank Gautier MOREAU, who also acted as external advisor, for his valuable input and the evaluation of my annual progress.

I would like to thank my external reviewers, Professors Denys BREYSSE, Eugen BRÜHWILER and Andrea BENEDETTO who have agreed to take on the task of evaluating the work presented in this document. I also thank Professors Franck SCHOEFS and Jean-Paul BALAYSSAC for their interest in my work in having agreed to serve as part of the jury for my PhD defence.

Further, I appreciate all the technical assistance I received during the many experimental programs that was undertaken as part of this thesis. My thanks to Odile COFFEC, Anaëlle JOUBERT, Olivier BURBAN and Olivier DURAND at IFSTTAR, Azadeh ATTARI and Derek HOLMES at UCD, as well as Christelle LESTREHAN and Benoit THAUVIN of CETE de l'Ouest, St Brieuc.

Lastly I owe the work that was done here to the funding provided by the European Union through the Initial Training Network project TEAM, which also allowed me the opportunity to be exposed to research state of the art throughout Europe.

UNIVERSITÉ DE NANTES
membre de L'unam
L'Université Nantes Angers Le Mans
Division de la recherche et des écoles doctorales
Bureau des études doctorales & Coordination des écoles doctorales

ABSTRACT

THE DEVELOPMENT AND COMBINATION OF ELECTROMAGNETIC NON-DESTRUCTIVE EVALUATION TECHNIQUES FOR THE ASSESSMENT OF COVER CONCRETE CONDITION PRIOR TO CORROSION

Electromagnetic (EM) non-destructive evaluation techniques are sensitive to parameters related to the durability of concrete. This research project investigated the potential of electromagnetic investigation techniques to assess concrete durability and detect the presence of harmful agents (i.e. moisture and chlorides) in cover concrete. The combination of three in situ electromagnetic techniques to assess concrete condition was shown to have great potential in this context.

The first phase in this research project comprised a parametric study to assess the sensitivity of the different electromagnetic observables to concrete condition. Custom electromagnetic test equipment (an existing co-axial electromagnetic cell) and a multi-ring DC-resistivity cell (developed as part of this thesis) were employed. Multiple linear regression models were then developed for each EM observable (DC-resistivity and dielectric permittivity) as a function of degree of saturation, chloride content, porosity and chloride diffusivity.

During the second phase, EM evaluation techniques suitable for in situ measurements were used to assess the condition of homogeneous (unreinforced) concrete slabs. A multi-electrode DC-resistivity probe developed during this thesis enabling electrical resistivity tomography (ERT), a capacitive probe and ground penetrating radar (GPR) were employed. The techniques were combined to estimate the condition of each slab by the non-linear optimisation of the regression models developed in the previous phase.

Gradients in cover concrete were also investigated using these techniques and they all proved capable of identifying moisture and chloride gradients, with ERT showing particular potential.

Keywords : NDT, DC-resistivity, dielectric permittivity, concrete durability, chloride content, water content, porosity, diffusivity.

RÉSUMÉ

DÉVELOPPEMENT ET COMBINAISON DE TECHNIQUES ÉLECTROMAGNÉTIQUES NON DESTRUCTIVES POUR L'ÉVALUATION DU BÉTON D'ENROBAGE AVANT CORROSION

Sachant que les techniques d'auscultation électromagnétiques non destructives (EM) sont sensibles a de nombreux paramètres d'état des bétons, l'objectif de ce projet de recherche est d'étudier le potentiel de ces méthodes d'investigation EM pour évaluer la durabilité des bétons et détecter la présence d'agents agressifs.

Dans un premier temps, une cellule de mesure EM coaxiale-cylindrique et une cellule de résistivité multi-anneaux (mise au point conçue dans cette thèse) ont été utilisées pour une étude paramétrique. Des modèles de régression multi-linéaires ont été développés pour chaque observable EM (résistivité électrique et permittivité diélectrique) en fonction du degré de saturation, de la teneur en chlorures, de la porosité et du coefficient de diffusion de différentes formulations de bétons et mortiers.

Dans un deuxième temps, des techniques de mesure EM in-situ ont été utilisées sur des corps d'épreuve homogènes pour évaluer leur état : un capteur de résistivité multi-électrodes, développé dans le cadre de cette thèse, un capteur capacitif et un système radar. Ces techniques ont été combinées pour donner une estimation quantitative du taux de saturation, de la teneur en chlorures et de la porosité des mélanges par optimisation non-linéaire des modèles de régression, développés dans la phase précédente.

Enfin, l'aptitude de ces techniques in-situ a détecter des gradients a également été étudiée. Il a été constaté que la tomographie de résistivité électrique (TRE), utilisant le nouveau système multi-électrodes était particulièrement adapté a la détermination de gradients dans le béton d'enrobage.

Mots clés : END, résistivité électrique, permittivité diélectrique, durabilité du béton, teneur en chlorure, teneur en eau, porosité.

DU PLOOY Raelize
9 Rue Laënnec
44000 - Nantes

Visa du Directeur de thèse

Contents

List of Figures

List of Tables

Glossary

List of symbols

A	area	j	index (model parameters)
a	electrode spacing	K	coefficient of permeability
$\mathfrak{a}$	Archie's lithology exponent	k	iteration
$\boldsymbol{B}$	magnetic flux density	$\mathfrak{K}$	phase constant
$\mathcal{B}$	ionic product factor	L	length
b	binding capacity	m	mass
C	Logarithm of total chloride content	N	ionic transference number
$C\ell$	chloride content	n	number of measurements or observables
$\mathcal{C}$	capacitance	P	polarisability
C_v	coefficient of variation	$\mathcal{P}$	probability
c	concentration	p	degrees of freedom
$\boldsymbol{\mathcal{D}}$	electric flux density	$\mathfrak{p}$	pressure
D	diffusion coefficient	$\mathcal{Q}$	quality factor
d	distance	q	current density
$\boldsymbol{E}$	electrical field intensity	R	resistance
e	residual (error)	$\boldsymbol{r}$	spacial position x, y, z
$\mathfrak{e}$	void ratio	$\mathcal{R}$	resistance (in the sense of limit sate theory)
F	Faraday's constant	RH	relative humidity
$\mathcal{F}$	Archie's formation factor	S	degree of saturation
f	function() or frequency	t	time
G	geometric factor (Ohm's law)	T	temperature
G_c	geometric factor (capacitance)	U	universal gas constant
$\mathcal{G}_s$	specific gravity	V	electrical potential
I	current intensity	$\mathcal{V}$	volume
i	observation (index)	v	velocity
$\boldsymbol{J}$	current density	$\mathcal{W}$	load (in the sense of limit sate theory)
$\mathcal{J}$	flux	w	water content

x	x-distance or general variable
y	y-distance
Z	valence number
z	z-distance
α	attenuation constant
β	regression coefficient
χ	electric susceptibility
Υ	volumetric fraction
δ	difference
ϵ	regression error
η	viscocity
γ	density
Γ	tortuosity
κ	complex wave number
$\mathfrak{m}$	Archie's cementation exponent
$\mathfrak{n}$	Archie's saturation exponent
μ	magnetic permeability
ω	angular frequency
ϕ	porosity
π	3.1416
$\propto$	Lichtenecker-Rother mixing coefficient
ψ	Cole-Cole distribution parameter
ρ	electrical resistivity
ρ'	characteristic electrical resistivity
σ	electrical conductivity
τ	relaxation time
ç	speed of light
$\mathbf{J}$	Jacobian matrix
$\mathfrak{y}$	Jonscher dispersion parameter
ε	complex dielectric permittivity
ε_r'	dielectric constant
ε_r''	dielectric loss factor
ϱ	Tang-Nilsson migration constant
ϑ	flow velocity
$\wp$	temperature coefficient
ξ	activation energy

Acronyms and abbreviations

$\mathbb{C}$	calcium oxide
$\mathbb{S}$	silica
$\mathbb{A}$	alumina
$\mathbb{F}$	ferric oxide
$\mathbb{H}$	water
$\mathbb{C}$-$\mathbb{S}$-$\mathbb{H}$	calcium silicate hydrate
2D	two dimentional
3D	three dimentional
AC	alternating current
AFPC	Association Française pour la Construction
AFREM	L'Association Française de Recherches et d'Essais sur les Matériaux et les Constructions
CETE	Centre d'Etudes Techniques de l'Equipment
CIT	Cork Institute of Technology
DC	direct current
EM	electromagnetic
ERT	electrical resistivity tomography
FEM	finite element model
GGBS	ground granulated blast furnace slag
GPR	ground penetrating radar
HCP	hardened cement paste
IFSTTAR	Institut Français des Sciences et Technologies des Transports
LUNAM	L'Universit Nantes Angers Le Mans
MSE	mean squared error
NaCl	Sodium chloride (salt)
NDE	non-destructive evaluation
OLS	ordinary least squares
OPC	ordinary Portland cement
RCM	rapid chloride migration test
RCP	rapid chloride permeability test
REV	representative elemental volume
RSS	regression sum of squares
SHM	structural health monitoring

SS	sum of squares
SSE	sum of squared errors
TE	transverse magnetic
TEM	transverse electromagnetic
TM	tranverse electric
VNA	vector network analyser
W/B-ratio	water/binder-ratio
W/C-ratio	water/cement-ratio
WARR	wide angle reflection refraction

Chapter 1

Introduction

1.1 Background

Concrete is the most widely used man-made material today [77]. It has been used since ancient times for the construction of structures - often withstanding the test of time successfully proving its inherent durability. The reinforced concrete infrastructure that currently exists in the world represents a large economic and strategic asset that needs to be managed with great diligence. Yet many of the concrete structures built in the 20^{th} century are showing signs of deterioration, mainly due to problems related to the corrosion of the steel reinforcement. With the worldwide shift to sustainability and environmental consciousness, it has become a priority to maintain these structures as best as possible and to design new infrastructure to be durable in order to ensure their longevity.

Many authorities and owners of infrastructure have therefore introduced measures to address durability problems related to steel reinforcement. These measures usually combine two strategies: firstly, a performance based approach towards the design of new structures is adopted rather than the traditional prescriptive approach [42] [26]. This means that the service life of the structure is based on predictive models using durability criteria which are controlled during construction, instead of the traditional "deem-to-satisfy" approach based on concrete compressive strength. Secondly, structural health monitoring (SHM) is implemented to assess the condition of existing and new structures on a regular or continuous basis so that maintenance can be performed before serious damage is incurred. These approaches should improve the sustainability of the reinforced concrete infrastructural network, but in practice, efficient techniques are required to ensure that durability criteria are attained during construction and to monitor the performance of existing structures over their service life.

Traditional destructive testing techniques are in general time consuming and usually require cores to be drilled from the structures. They are thus neither optimal for regular, nor suitable for continuous monitoring. Various non-destructive evaluation (NDE) techniques have therefore been developed to enable more efficient assessment of concrete structures. The use of these techniques is of particular interest as they are faster, more cost efficient, can be performed in situ, do not require remedial action, and can therefore be performed over a large surface area on a regular basis. However, because concrete is a complex non-homogeneous material of which the properties and deterioration mechanisms are not yet completely understood, much work is still required to improve the reliability of these non-destructive techniques.

1.2 Problem Statement

Corrosion is a significant problem with regards to reinforced structural concrete and is mainly caused by the presence of water and chlorides in the vicinity of the steel reinforcement. In concretes of low quality or exposed to aggressive environments, the cover concrete that protects the steel is penetrated over time by chlorides which eventually leads to corrosion, degradation and loss of structural integrity. Various durability indicators have therefore been developed with the aim to assess the resistance of concrete to such degradation. However, they are usually time consuming to obtain in practice.

Electromagnetic (EM) non-intrusive prospecting is widely used in geophysical, medical and other applications [104] [211] [258] and have more recently been introduced to civil engineering for the non-destructive evaluation of concrete structures [172]. These EM non-destructive evaluation techniques are sensitive to the material properties of concrete and EM observables such as electrical resistivity have been suggested as indirect durability indicators [42]. Electromagnetic techniques are also sensitive to the presence of water and chloride and are therefore studied in order to assess the condition of concrete over time. Though a large amount of literature is available regarding the application of EM investigation techniques to concrete, most of these studies do not document results produced by several electromagnetic techniques on the same set of concretes for a wide range of conditions. There is thus still some uncertainty as to the exact nature of the relationships between electromagnetic observables and parameters indicative of concrete condition, as well as the influence of the interactions between these parameters on the electromagnetic response of concrete.

Also, when concrete is assessed in situ, there are many variables that have an influence on the electromagnetic response which are not necessarily related to the durability of the concrete as well as many other causes of uncertainty. These include external environmental

influences such as temperature, uncertainty due to the inherent variability of concrete as well as lack of accuracy and repeatability related to the measurement process [234]. When only one investigation technique is used, it is thus very difficult to quantitatively assess the durability of concrete or characterise its condition. The combination of EM and other non-destructive techniques have therefore become the focus of recent research in order to improve the reliability with which the durability and condition of concrete can be assessed in situ [50].

1.3 Objectives

The work that is presented in this thesis aims to advance the non-destructive durability assessment of cover concrete by improving and combining existing electromagnetic investigation techniques having different sensitivities to parameters related to the degradation of concrete. The main objectives were therefore as follows:

- To perform a rigorous parametric study to investigate the dependency of certain EM observables on a selection of important parameters related to concrete durability and condition;
- To use the findings of this study in order to combine the response of in situ EM non-destructive techniques to allow the evaluation of the condition of cover concrete to be performed more reliably;
- To develop certain EM test equipment and techniques required for the parametric study and the in situ testing of concrete as part of this thesis.

The work has several practical implications: Firstly, by improving the reliability with which the condition of in situ concrete can be quantified, the implementation of these techniques for quality control as part of a performance based approach in construction becomes a feasible option. Secondly, the combination of EM techniques can improve the non-destructive monitoring of degradation in concrete as part of a structural health monitoring strategy to serve as early warning of problem areas prior to corrosion. Thirdly, if the ingress of aggressive agents into cover concrete can be quantified more accurately, predictive service life models can be more easily updated.

1.4 Overview of the document

This document is divided into two parts. Part I deals with the fundamentals of concrete and electromagnetics and provides background as to the relevance of this theory in terms of this

thesis. Further, the electromagnetic techniques that are used as part of the experimental work presented here, and the principles on which they are based, are introduced. Part I is fundamental to the understanding and interpretation of the results in Part II.

Part II deals with the experimental work that was performed during this thesis. The development of two new devices for the measurement of electrical resistivity is presented, detailing their design, numerical modelling, validation and performance with regards to the variability of measurements. Thereafter the parametric study is presented during which master curves is produced to describe the sensitivity of electrical resistivity and dielectric permittivity to degree of saturation, chloride content, porosity and chloride diffusivity. Using these results, statistical analyses is performed and a regression model is developed for each EM observable. These models are then employed to combine the results from three in situ techniques (electrical resistivity, capacimetry and GPR) in order to estimate the condition of the concrete quantitatively.

Additional experimental work is also presented: A comparative study to compare the ability of the in situ EM techniques to identify water and chloride gradients in concrete slabs, as well as an in situ study on a 100 year old dismantled reinforced concrete bridge. The document is concluded with some final perspectives, future work and a list of publications realised during the thesis.

Part I

Theoretical background

Chapter 2

Concrete material properties and durability

2.1 Introduction

This chapter gives and overview of the the fundamentals of concrete material technology which will be referred to throughout the rest of this document. Firstly, an introduction is given to the composition of concrete and the basic properties and relationships that are used to define concrete condition. Then, important concepts regarding the durability of concrete are discussed including service life design, mechanisms causing deterioration and durability indicators related to corrosion. Lastly, the role that the electromagnetic non-destructive evaluation of concrete can play as part of durability design and assessment is introduced.

The chapter serves as background to the work presented in this thesis, as the electromagnetic response of concrete can only be interpreted if there is a fundamental understanding of the properties of concrete. Similarly, the relevance of electromagnetic investigation techniques can only be appreciated if it is presented in the context of concrete durability. The chapter therefore touches on the most important aspects of concrete properties, material technology and durability as relevant to the thesis, but for more details the reader is referred to some well-known textbooks [47] [202] [201].

2.2 Properties of concrete

2.2.1 Phase relationships in concrete

Concrete is a non-homogeneous composite material, mainly consisting of aggregates, binder (cementitious materials) and water. Phase relationships from soil mechanics [196] are used to define the relationship between the solid (aggregates and binder), liquid (pore solution) and gaseous (air) phases present in concrete. Figure 2.1 shows typical phase diagrams for the partially saturated, saturated and dry states of concrete indicating the different constituents in terms of mass m and volume $\mathcal{V}$.

Though the microstructure of concrete is known to be considerably more complex than represented by this simple model, the fundamental properties of concrete such as density, porosity and degree of saturation are defined using these phase relationships. These properties, as defined below, will be used throughout this document as indicative of concrete condition.[1]

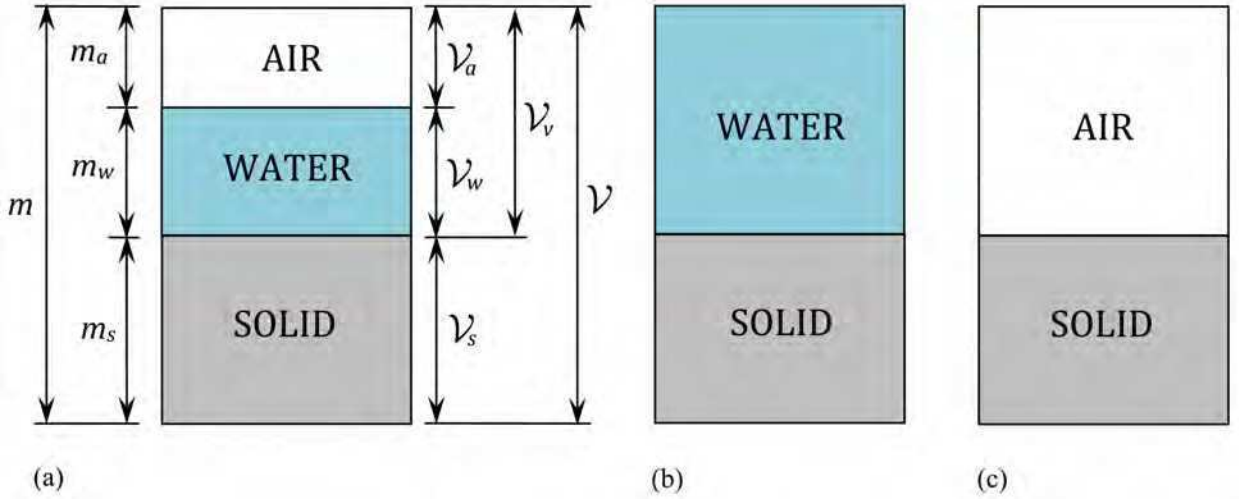

Figure 2.1: Simple model representing the solid, liquid and gaseous phases in concrete where (a) represents the partially saturated state, (b) the fully saturated state and (c) the dry state, after [196].

[1]Note that fractional parameters (which are dimensionless [-]) will often be expressed as percentages in the text and graphs to follow, but will always be used in fractional form as part of equations.

2.2.1.1 Density of concrete

For the general case as in Figure 2.1(a), density γ is expressed as the unit mass m per unit volume $\mathcal{V}$.

$$\gamma = \frac{m}{\mathcal{V}} \tag{2.1}$$

The dry density is an important property of concrete as it is strongly related to concrete durability and strength. In Equation (2.2), γ_{dry} [kg/m^3] is the dry density and m_s [kg] is the mass of the solid component for the dry state as per Figure 2.1(c).

$$\gamma_{dry} = \frac{m_s}{\mathcal{V}} \tag{2.2}$$

The saturated density includes the contribution of the water phase to density and is commonly used during mix design. In Equation (2.3), γ_{sat} [kg/m^3] is the saturated density and m_w [m^3] is the mass of the liquid component for the saturated case as per Figure 2.1(b).

$$\gamma_{sat} = \frac{m_s + m_w}{\mathcal{V}} \tag{2.3}$$

The specific gravity of concrete can be defined as the ratio of the density of the solid phase to the density of water:

$$\mathcal{G}_s = \frac{\gamma_{dry}}{\gamma_w} \tag{2.4}$$

where $\mathcal{G}_s$ [-] is the specific density and γ_w is the density of water (approximated as 1000 kg/m^3).

2.2.1.2 Porosity and void ratio

Porosity accessible to water, also referred to as capillary porosity, is defined as the ratio of the volume of voids to the total (bulk) volume of the material and is widely used as indicator of concrete quality and durability [42]. In Equation (2.5), ϕ [-] is the porosity and $\mathcal{V}_v$ [m^3] is the volume of the voids (thus the liquid and gas components as per Figure 2.1(a)).

$$\phi = \frac{\mathcal{V}_v}{\mathcal{V}} \tag{2.5}$$

The void ratio $\mathfrak{e}$ [-] expresses the volume of voids as a fraction of the volume of solids $\mathcal{V}_s$:

$$\mathfrak{e} = \frac{\mathcal{V}_v}{\mathcal{V}_s} \tag{2.6}$$

The relationship between porosity ϕ and void ratio $\mathfrak{e}$ is thus as follows:

$$\phi = \frac{\mathfrak{e}}{1+\mathfrak{e}} \tag{2.7}$$

and

$$\mathfrak{e} = \frac{\phi}{1-\phi} \tag{2.8}$$

2.2.1.3 Moisture condition of concrete

The degree of saturation S [-] indicates the fraction of the void volume that is filled with water and can range from 0 for dry to 1 for saturated conditions where $\mathcal{V}_w$ [m^3] is the volume of water (or pore solution):

$$S = \frac{\mathcal{V}_w}{\mathcal{V}_v} \tag{2.9}$$

The volumetric water content w [-] is defined as the fraction of the total volume that is filled by water:

$$w = \frac{\mathcal{V}_w}{\mathcal{V}} \tag{2.10}$$

By substituting Equations (2.5) and (2.9) in Equation (2.10) it can be seen that the volumetric water content and degree of saturation have a linear relationship governed by porosity:

$$w = \phi S \tag{2.11}$$

The gravimetric water content w_g [-] indicates the ratio of the mass of the water phase m_w to that of the solid phase m_s [kg] and can be expressed in terms of saturation, void ratio, porosity and specific gravity by substituting for Equations (2.4), (2.6) and (2.5):

$$w_g = \frac{m_w}{m_s} = \frac{\mathfrak{e}S}{G_s} = \frac{S\phi}{G_s(1-\phi)} \tag{2.12}$$

Another important parameter related to the moisture condition of concrete is relative humidity RH [%]:

$$RH = \frac{\mathfrak{p}_w}{\mathfrak{p}_w^*} \times 100 \tag{2.13}$$

where $\mathfrak{p}_w$ [kg/m^2] is the partial pressure of water vapour in the pore space and $\mathfrak{p}_w^*$ [kg/m^2] is the saturated vapour pressure of water at a given temperature.

Relative humidity is sometimes preferred to other indicators of the moisture condition of concrete as it can be easily related to the real climatic conditions to which the concrete is exposed. The volumetric water content of concrete can be expressed as a function of relative

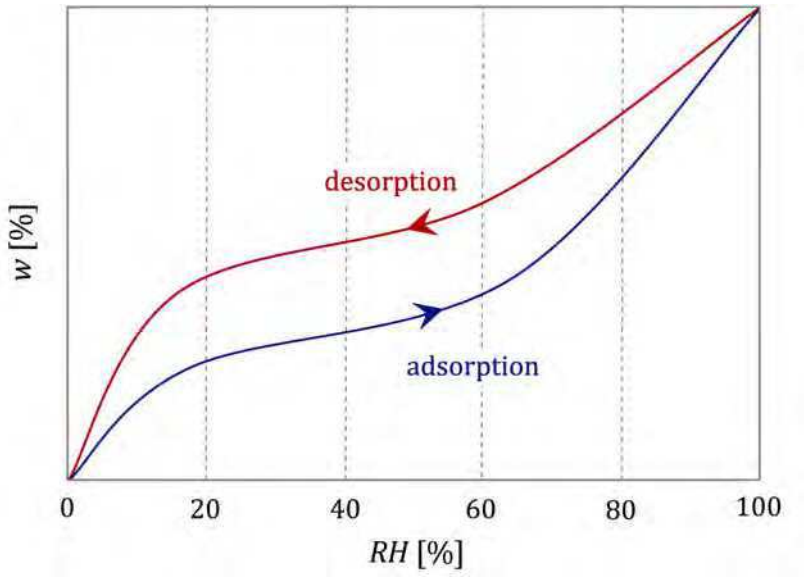

Figure 2.2: Water content as a function of relative humidity showing the hysteresis between the desportion and adsorption isotherms, after [40] and [32].

humidity $w = f(RH)$ which is referred to as the water vapour sorption isotherm [40] [32] as illustrated in Figure 2.2. The relationship is dependent on temperature and holds for conditions where the ambient relative humidity is in equilibrium with the relative humidity within the pores of the concrete. It is important to note that the relationship also depends on whether the relative humidity increases (adsorption isotherm) or decreases (desorption isotherm) and is thus marked by a strong hysteresis as is clear from Figure 2.2.

2.2.1.4 Practical determination of concrete condition

In order to determine the properties defined in the previous section in practice, they can be rewritten using the Archimedes principle which states that *the hydrostatic mass of an object equals its true mass minus the mass of displaced fluid*, where the "hydrostatic mass" refers to its mass in water. The properties most relevant to this thesis (dry density, porosity and degree of saturation) can therefore be expressed as below:

$$\gamma_{dry} = \frac{m_{dry}}{m_{sat} - m_h}\gamma_w \tag{2.14}$$

$$\phi = \frac{m_{sat} - m_{dry}}{m_{sat} - m_h}\gamma_w \tag{2.15}$$

$$S = \frac{m_x - m_{dry}}{m_{sat} - m_{dry}} \gamma_w \tag{2.16}$$

where m_h [kg] is the hydrostatic mass, $m_{sat} = m_s + m_w$ [kg] is the saturated mass, $m_{dry} = m_s$ [kg] is the dry mass (as per Figures 2.1(c) and 2.1(b)) and m_x [kg] is the unsaturated mass at a certain condition x.

For the purposes of this thesis density, porosity and degree of saturation are determined according to the test procedures recommended by AFPC-AFREM [5], using the aforementioned equations.

2.2.2 Chemical composition and microstructure of concrete

2.2.2.1 Hydration and pozzolanic reactions

The definitions in the previous section serve well as a rudimentary way of defining the quality and condition of concrete, especially since, in its fresh state, concrete is simply a mixture of water, cement, coarse and fine aggregates. However, it is important to realize that the microstructure of mature concrete is chemically very complex due to various reactions taking place during ageing. As a result of these reactions, of which hydration is the most important [200], hardened cement paste (HCP) is formed which binds the aggregates together into hydraulic concrete. The nature of the reactions and degree to which they take place govern to a large extent the final strength and density attained. The main chemical components taking part in the reactions to form hardened cement paste are usually simplified as follows [18]:

$\mathbb{C} = CaO$ (calcium oxide)

$\mathbb{S} = SiO_2$ (silica)

$\mathbb{A} = Al_2O_3$ (alumina)

$\mathbb{F} = Fe_2O_3$ (ferric oxide)

$\mathbb{H} = H_2O$ (water)

thus:

$\mathbb{C}_3\mathbb{S}$ = tricalcium silicate

$\mathbb{C}_2\mathbb{S}$ = dicalcium silicate

$\mathbb{C}_3\mathbb{A}$ = tricalcium aluminate

$\mathbb{C}_4\mathbb{A}\mathbb{F}$ = tetracalcium aluminoferrite

$\mathbb{C}\mathbb{H} = Ca(OH)_2$ (calcium hydrate)

$\mathbb{C}$-$\mathbb{S}$-$\mathbb{H} = \mathbb{C}_3\mathbb{S}_2\mathbb{H}_3$ (calcium silicate hydrate)

During the hydration of ordinary Portland cement (OPC), the calcium silicates in the cement react with water (Equations (2.17) and (2.18)) to form calcium silicate hydrate ($\mathbb{C}$-$\mathbb{S}$-$\mathbb{H}$) which is the main contributor to the strength of hardened cement paste. These two reactions also produce calcium hydrates ($\mathbb{C}\mathbb{H}$) which readily dissolve and saturate the pore water solution, causing the solution to be very alkaline. The alkalinity of the pore solution plays a critical role in protecting steel reinforcement against corrosion by preventing depassivation, as will be explained in Section 2.3. The calcium hydrates further react with the aluminas and aluminoferrites (as in Equations (2.19) and (2.20)) to form products which do not contribute significantly to strength, but help to reduce the porosity of the hardened cement paste [18].

$$2\mathbb{C}_3\mathbb{S} + 6\mathbb{H} \longrightarrow \mathbb{C}_3\mathbb{S}_2\mathbb{H}_3 + 3\mathbb{C}\mathbb{H} \tag{2.17}$$

$$2\mathbb{C}_2\mathbb{S} + 4\mathbb{H} \longrightarrow \mathbb{C}_3\mathbb{S}_2\mathbb{H}_3 + \mathbb{C}\mathbb{H} \tag{2.18}$$

$$\mathbb{C}_3\mathbb{A} + \mathbb{C}\mathbb{H} + 12\mathbb{H} \longrightarrow \mathbb{C}_4\mathbb{A}\mathbb{H}_{13} \tag{2.19}$$

$$\mathbb{C}_4\mathbb{A}\mathbb{F} + 4\mathbb{C}\mathbb{H} + 22\mathbb{H} \longrightarrow \mathbb{C}_4\mathbb{A}\mathbb{H}_{13} + \mathbb{C}_4\mathbb{F}\mathbb{H}_{13} \tag{2.20}$$

Additionally, pozzolanic reactions can play an important role in the formation of hardened cement paste. These reactions usually result from mineral admixtures that are used in combination with OPC in blended concretes, mainly for their lower heat of hydration and cost effectiveness [201]. Mineral admixtures can also improve the durability of the concrete, although this depends on the quality of the mineral addition and the mode of concrete degradation.

A commonly used mineral admixture is ground granulated blastfurnace slag (GGBS), which is a by-product from the iron and steel industry [202]. Cement mixtures containing GGBS first hydrate to form $\mathbb{C}$-$\mathbb{S}$-$\mathbb{H}$ as in Reaction (2.21). They then undergo a secondary pozzolanic reaction (Reaction (2.22)) with the dissolved calcium hydrate produced from Reactions (2.17) and (2.18) to form more $\mathbb{C}$-$\mathbb{S}$-$\mathbb{H}$, which further increases the strength and density of

the hardened cement paste. The porosity of concrete can therefore be significantly reduced by partially substituting OPC with GGBS [42].

Here ($\mathbb{C} + \mathbb{S}$) denotes GGBS and a and b are symbols to balance the reaction:

$$3(\mathbb{C} + \mathbb{S}) + 3\mathbb{H} \longrightarrow \mathbb{C}_3\mathbb{S}_2\mathbb{H}_3 + \mathbb{S} \tag{2.21}$$

$$(\mathrm{a} \times \mathbb{S}) + (\mathrm{b} \times \mathbb{CH}) + \text{other} \longrightarrow \mathbb{C}_3\mathbb{S}_2\mathbb{H}_3 + \mathbb{CA}\text{-products} \tag{2.22}$$

Other popular extenders such as fly ash, a by-product from coal combustion, and silica fume, from silicon and ferro-silicon alloy production, act as pure pozzolans and do not undergo hydration at all. They react with the calcium hydrate produced in Reactions (2.17) and (2.18) to produce $\mathbb{C}$-$\mathbb{S}$-$\mathbb{H}$ (Reaction (2.23)) and are particularly effective to reduce the porosity due to their small particle size.

$$2\mathbb{S} + 3\mathbb{CH} \longrightarrow \mathbb{C}_3\mathbb{S}_2\mathbb{H}_3 \tag{2.23}$$

2.2.2.2 Microstructure of concrete

Hardened cement paste therefore consists of the cement gel made up of unhydrated cement, the products of Reactions (2.17) to (2.23) and also gel pores and capillary pores (refer to Figure 2.3). The gel pores are formed inside the cement gel during the hydration and other reactions and are very small (around 2 nm in diameter) [202]. Even though typically a

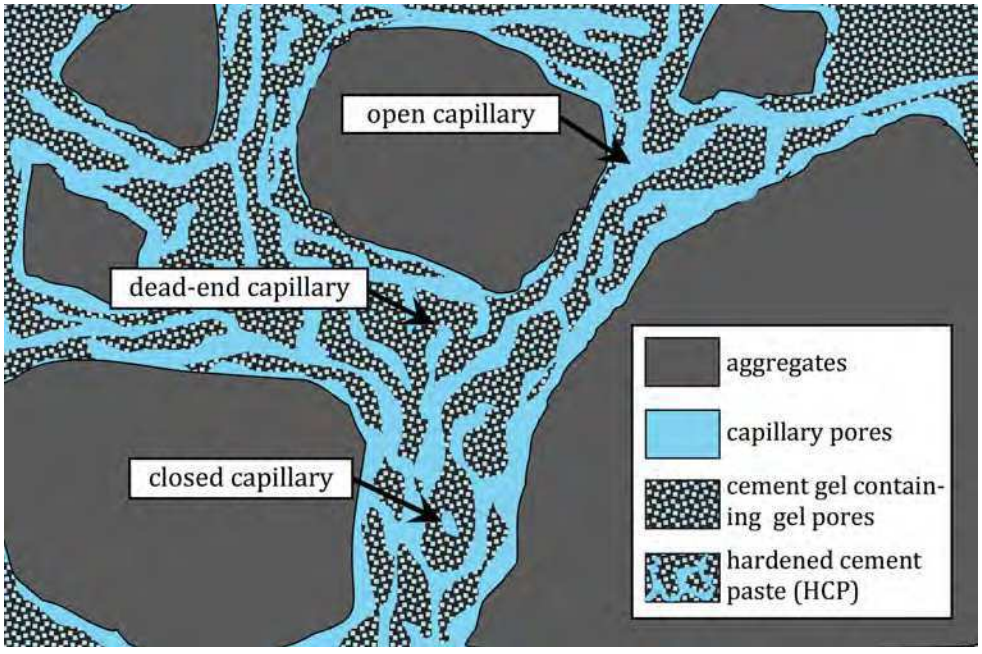

Figure 2.3: Schematic representation of the microstructure of concrete.

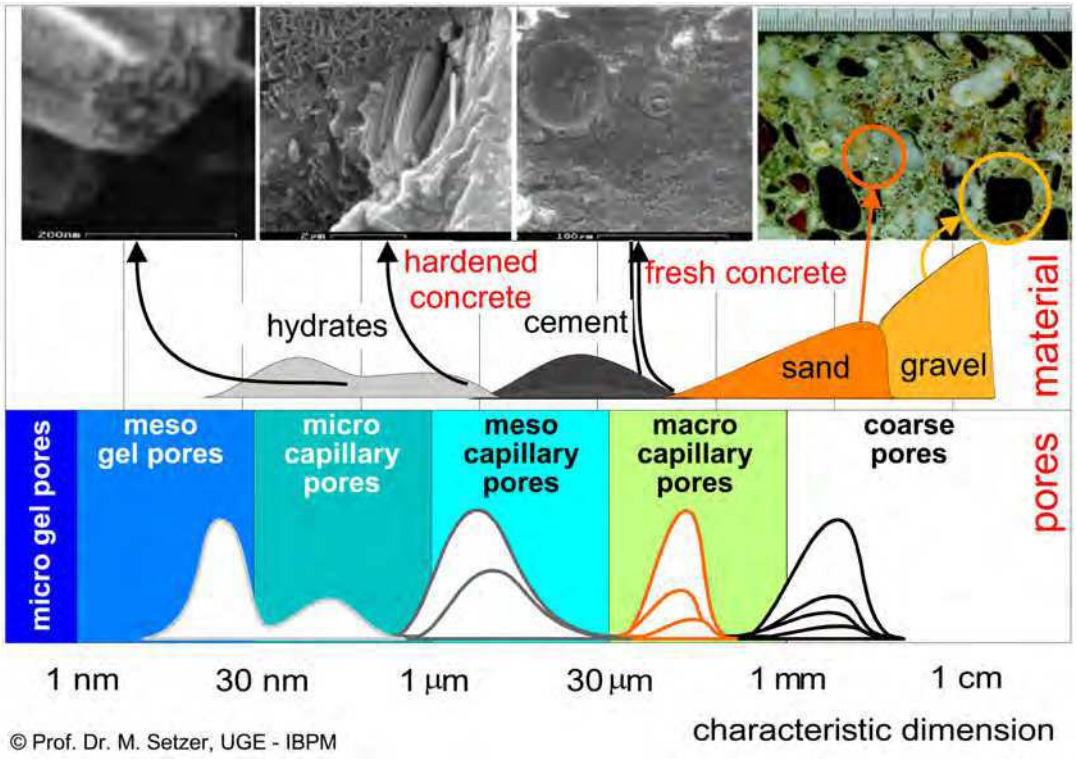

Figure 2.4: Characteristic dimensions of pores and materials found in concrete (©*Prof. M.J. Setzer, used with his consent*).

third of the cement gel consists of gel pores, the porosity of the cement gel is often considerably lower than that of most natural rocks [201]. Capillary pores are the residue of the original water-filled space in the fresh cement paste and are markedly larger than gel pores (around 1 micron in diameter) [202]. In fresh concrete these capillaries are a continuous interconnected system, containing mainly "open pores" [49]. However, as hydration proceeds, more capillaries are filled with cement gel and the number of "closed pores" and "dead-end pores" increases as per Figure 2.3. It is therefore mainly the size of the capillary pores that determines the porosity of concrete and their interconnectedness that determines its permeability. The characteristic dimensions of the pores found inside of components of mature concrete are shown in Figure 2.4.

The most important factor determining the porosity of the hardened cement paste is therefore the ratio of water to cement (W/C-ratio) or in the case where mineral admixtures are used, the water to binder ratio (W/B-ratio). This ratio governs the extent to which Reactions (2.17) to (2.23) can take place to fill the capillaries. Czernin [78] states that OPC cement with a W/C-ratio of approximately 0.4 will hydrate to a cement gel that will completely fill all of the pore space previously occupied by the fresh cement paste, resulting in no capillary pores. If the W/C-ratio is higher than this, the cement gel produced by full hydration will not fill all the space, resulting in open capillary pores allowing for ingress

of aggressive agents. For a water cement ratio below approximately 0.4, full hydration will be impossible due to the lack of capillary pore space and unhydrated cement will remain, reducing the strength of the concrete. Because the hydration reactions require more water than cementitious reagents, the addition of water during curing[2] is especially important for low W/C-ratio concretes. If the W/C-ratio is below a critical level (approximately 0.56 for OPC [18]) and curing is inadequate, the cement paste will not fully hydrate as the reaction will stop prematurely because of self-dessication. Because the W/C-ratio determines to what extent the capillaries are filled with gel solids after hydration, it governs the final porosity and the interconnectedness of pores of the hardened cement paste.

In the context of this thesis, the microstructure and condition of the outermost layer of concrete which protects the steel reinforcement from the environment (referred to as *cover concrete*), is very important. Cover concrete plays a crucial role in the durability of reinforced concrete structures as will be discussed in the next section.

2.3 Concrete durability

Durability, in terms of concrete structures, can be defined as the ability to maintain serviceability over a specified period of time without significant deterioration [26] [238]. The durability of concrete has been under much scrutiny in recent years [152] [186] [200], as many structures constructed in the 20^{th} century are showing signs of premature deterioration. The following extract was taken from a report by the American National Materials Advisory Board (ANMAB) dated 1987 [1], which brought about a turning point in concrete material sciences, as it focussed the attention on significant shortcomings in durability design throughout the United States and the world:

> *A problem exists with respect to inadequate durability of concrete in service. The reasons for the problem are both technical and institutional. The manifestation of the problem is premature distress and degradation of concrete in structures. Many different physical and chemical processes, including corrosion of steel reinforcement, sulphate attack, freezing and thawing, and alkali-aggregate reactions, interact to bring about premature deterioration.*

[2]The term "curing" refers to the process of ensuring that sufficient levels of moisture and heat are available after casting to facilitate concrete hardening.

The report estimated the replacement and repair costs of concrete infrastructure due to durability problems in the United States at "several hundred billion dollars" at the time. It underscored the urgency of the problem and stated that a better understanding of concrete material technology is required to improve durability design and standards. Subsequently concrete material science was established as a separate research discipline and the focus has shifted to performance based design and quality control to ensure durable concrete infrastructure. Durability is thus not an intrinsic property of concrete, but is rather associated with the performance of the material over a given design service life for a particular environmental exposure.

2.3.1 Performance based durability approach

Traditionally, concrete durability was addressed by a prescriptive "deem-to-satisfy" approach where mix specifications focussing on compressive strength (e.g. maximum W/C-ratios, minimum cement contents, percentage of entrained air) were prescribed according to the life span and exposure classification of the particular structure. Additionally, recommendations in terms of good construction practices were provided to ensure that proper placement, finishing and nominal cover were achieved during construction. These specifications were prescribed based on previous experience with the hope that the structure would attain the required service life. However, it has been shown that high compressive strength does not necessary give rise to durable concrete [187] [10], as durability is also a function of the transport properties of the concrete and not necessarily related to mechanical strength. Being a purely empirical approach, there was no means to explicitly relate the performance of the concrete to service life. This also implied that there was no means to evaluate the actual concrete quality achieved on site and whether that would in fact produce the durability required for the design life of the structure.

To address these shortcomings, there has been a worldwide shift towards a performance based approach [260] [7] [42] [26] where concrete durability is evaluated according to quantitative predictions relating degradation to environmental exposure and material parameters. This implies the development of reliable degradation and probabilistic models [10] using suitable durability indicators as input [27] [42] to estimate service life. Such models are now widely used during the design stage of new concrete structures and also to determine the residual life of existing structures, as most structures constructed in the 20^{th} century have not been designed with a performance based approach in mind.

Another important aspect of concrete durability is the implementation of structural health monitoring to evaluate the need for maintenance interventions. Good maintenance practices

can postpone premature deterioration and substantially increase service life.

The non-destructive evaluation (NDE) of concrete condition shows great potential in both serviceability life design and structural health monitoring [172] [50] [272]. In the first case, the indirect non-destructive estimation of parameters for input in the probabilistic models and quality control is a fast and inexpensive alternative to traditional destructive testing [7] [84]. In the second case, non-destructive testing lends itself to regular evaluation of concrete condition over a high spatial distribution which is ideal to facilitate timeous maintenance intervention [178] [39]. NDE techniques can also be used to evaluate the performance of repairs after maintenance interventions.

2.3.2 Service life design

The service life of a concrete structure is defined by the Eurocode 1 [3] as the period during which a structure will not require any specialist maintenance or major repairs. Service life design aims to ensure that the structure performs satisfactorily for a specified number of years, given a certain environmental exposure and concrete quality. The performance of the concrete therefore needs to be expressed by means of a limit state function which defines the border between a satisfactory and unsatisfactory condition. The limit state function includes loads $\mathcal{W}(t)$, usually related to exposure condition and cover concrete properties, as well as resistances $\mathcal{R}(t)$, related to the geometry of the reinforced system (e.g. cover thickness) [7]. Both load and resistance variables are time dependent. Thus at any given time, if the resistances exceed the load as in Equation 2.24, the structure meets the durability criteria. However, when the resistance becomes smaller than the load, the serviceability limit state is reached, indicating the end of the service life and thus a state of failure.

$$\mathcal{R}(t) - \mathcal{W}(t) > 0 \tag{2.24}$$

Because there is a large amount of uncertainty related to the change of the load and resistance variables over time, a probabilistic approach is adopted which takes into account the stochastic nature of these parameters. Equation (2.24) can be rewritten to define the probability of failure $\mathcal{P}_{f(SL)}$ over the service life of the structure [7]:

$$\mathcal{P}_{f(SL)} = 1 - \mathcal{P}\{\mathcal{R}(t) - \mathcal{W}(t)\} < 0 < \mathcal{P}_{target} \tag{2.25}$$

where t is time, $\mathcal{P}_{f(SL)}$ is the probability of failure within the intended service life SL and $\mathcal{P}_{target}$ is the accepted minimum value of failure probability. The concept of probabilistic service life design is demonstrated in Figure 2.5.

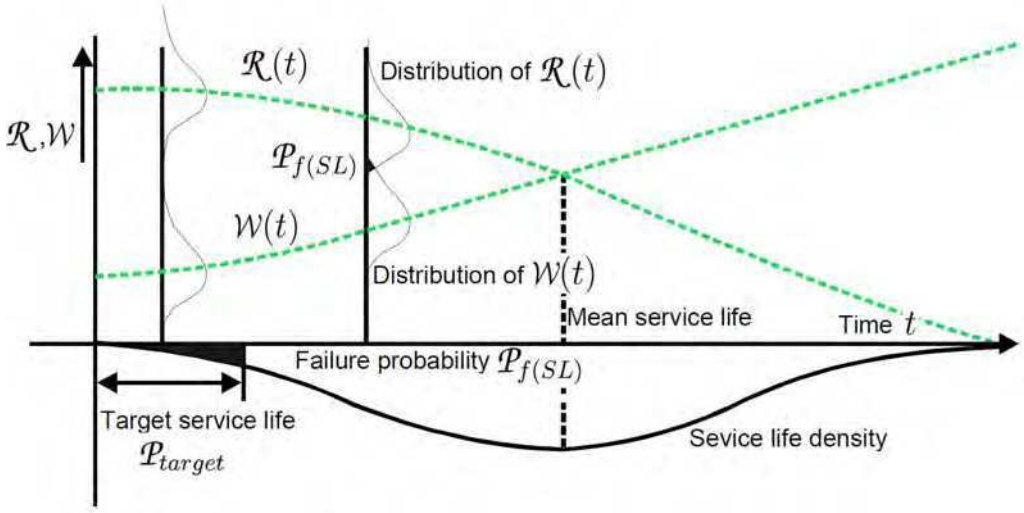

Figure 2.5: Failure probability and target service life after [7].

In order to perform a quantified service life design for new concrete structures, or a residual service life design for existing structures, the following elements are therefore required:

- Definition of the serviceability limit state beyond which the performance of the structure is compromised;
- Mathematical model relating the limit state to load and resistance variables;
- Input parameters for the model, having stochastic (random) characteristics which have been statistically determined;
- A target probability for which the performance is reliable throughout the designed service life.

Ideally, the performance of the structure is to be re-evaluated over its lifetime to update the original model and service life prediction. Regular inspection and testing forming part of the structural maintenance plan are therefore required to assess the time dependency of the model parameters and improve the performance based approach.

2.3.3 Concrete deterioration mechanisms

Designing for a specified service life requires knowledge of the parameters determining the ageing and deterioration of concrete structures. A good understanding of the mechanisms leading to concrete deterioration is therefore a prerequisite for any research dealing with concrete durability design. The main deterioration mechanisms associated with durability problems in concrete structures are reinforcement corrosion, alkali aggregate reaction, sul-

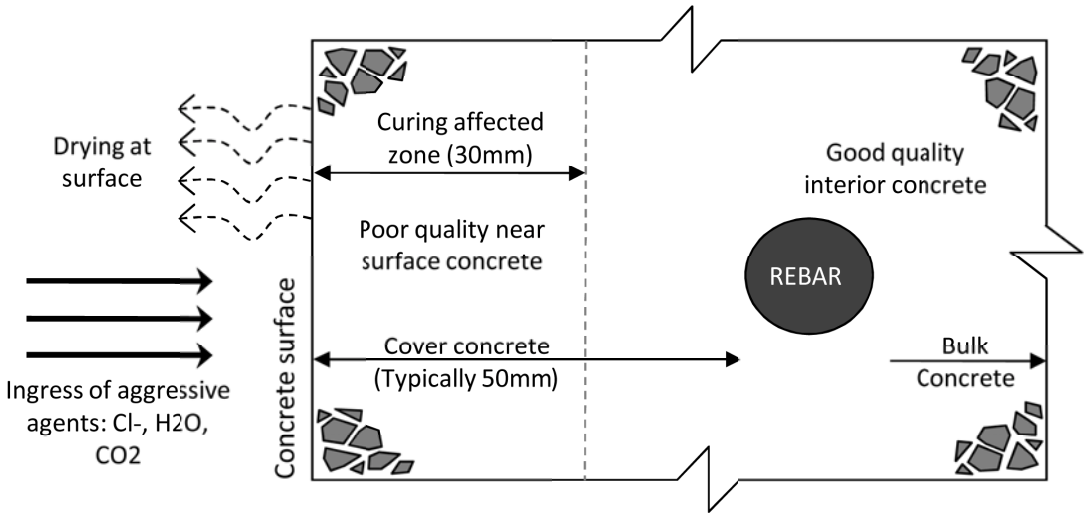

Figure 2.6: Schematic diagram of a reinforced concrete system, after [27].

phate attack, and frost action [7] [42]. Of these, the corrosion of the steel reinforcement is agreed to be the most significant [224] [7] [192] as it leads to major damage and loss of structural integrity and is a common occurrence throughout the world's ageing reinforced concrete network.

In a reinforced concrete system, the properties of the layer of cover concrete determine its resistance to the ingress of deleterious substances leading to the corrosion of reinforcement (refer to Figure 2.6). The steel reinforcement is protected by a film of oxides (Fe_2O_3) that forms due to the alkalinity of the pore solution as a result of the chemical nature of the cementituous constituents. When aggressive agents penetrate the cover concrete up to the level of the steel, this film becomes unstable or *depassivated*. The steel is then no longer protected and a galvanic reaction takes place which causes a reduction in the cross-section of the reinforcement and therefore the load carrying capacity of the structure. Additionally, an expansive reaction producing iron oxides (rust) can lead to spalling and degradation of the concrete.

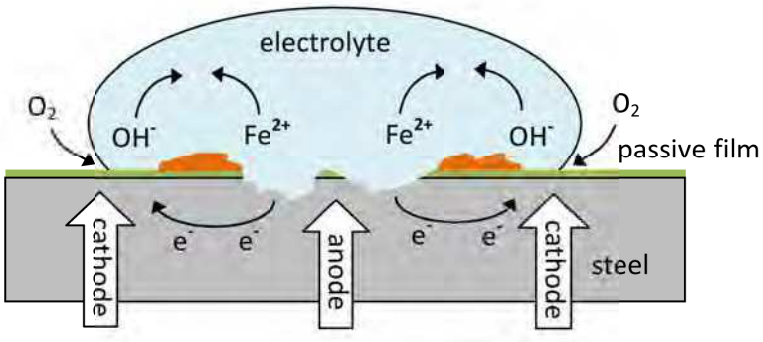

Figure 2.7: Simplified representation of the corrosion of steel.

The following four components are essential for the corrosion reaction to take place as demonstrated in Figure 2.7:

1. Anodic area where oxidation takes place and the iron dissolves, releasing electrons;

$$Fe \longrightarrow Fe^{2+} + 2e^{-} \tag{2.26}$$

2. Cathodic area where electrons are consumed through the reduction of oxygen;

$$O_2 + 2H_2O + 4e^{-} \longrightarrow 4OH^{-} \tag{2.27}$$

3. Metallic medium to conduct the electrons produced in Reaction (2.26);
4. Electrolytic medium to enable diffusion of the ions produced in Reaction (2.27).

Iron-oxide is then a result of the following reactions:

$$2Fe^{2+} + 4OH^{-} \longrightarrow Fe(OH)_2 \tag{2.28}$$

$$4Fe(OH)_2 + O_2 \longrightarrow 2Fe_2O_3.H_2O + H_2O \tag{2.29}$$

It is clear from the above reactions and Figure 2.6 that an ionic solution in contact with the steel is a prerequisite for corrosion. Such an environment is created by the presence of either chloride ions or the loss of alkalinity due to carbonation in the region of the reinforcement, with both cases requiring water to facilitate electrolytic conduction. The former leads to localised pitting corrosion and the latter to more general corrosion related problems.

Pitting corrosion is seen as especially harmful [123] [102] [42] as the cavities that form in the steel lead to rapid reduction of the cross-sectional area of the reinforcement and consequently the load carrying capacity of the structure. The severity of the pitting tends to vary logarithmically with the chloride concentration present in the pore solution [157]. The rapid deterioration of the passivation film and reinforcement in the presence of chloride ions have been attributed to various factors in literature, such as the increased solubility of metals due to the acidic nature of chloride anions [204], the presence of oxidising agents in an environment containing chloride and the small size of chloride anions [102].

During carbonation, carbon dioxide (CO_2) reacts with the hydration products, in particular calcium hydroxide ($Ca(OH)_2$) and calcium silicate hydrates, to form calcium carbonates ($CaCO_3$) and water. The reaction in itself is not harmful and leads to a decrease in the porosity due to the difference in molar volume between $CaCO_3$ and $Ca(OH)_2$ [259]. However, because alkalis are consumed during the reaction, the pH of the interstitial solution of the

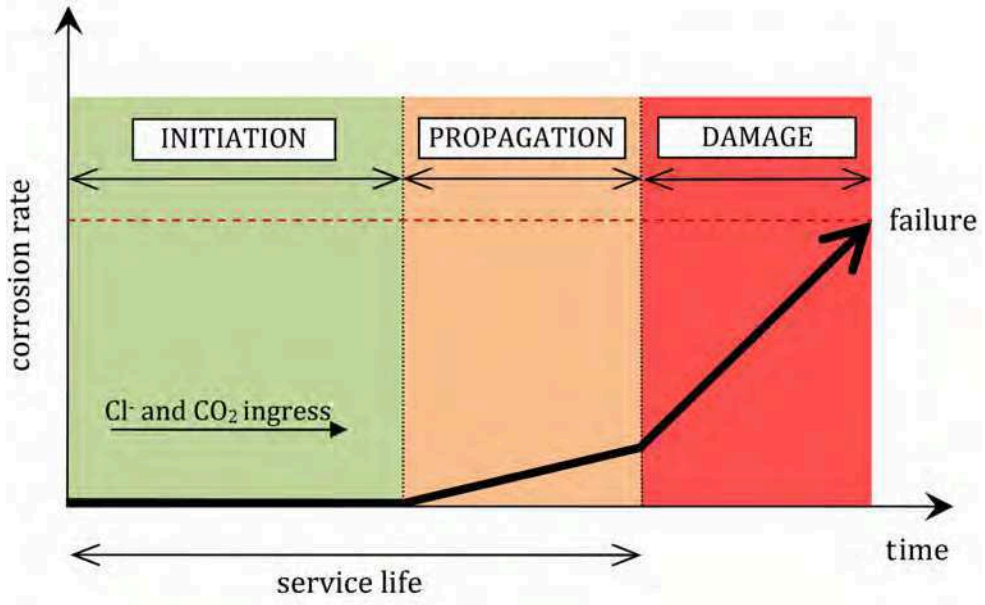

Figure 2.8: A conceptual model of the phases of corrosion in reinforced concrete, after [42].

concrete is reduced and the passive film becomes unstable. The water released by the reaction also aids in creating an environment favourable for corrosion to take place.

Because corrosion is such an important contributor to the degradation of reinforced structures, service life is often expressed in terms of the corrosion initiation and propagation phases as in Figure 2.8 [265] [7] [224]. During the initiation phase, aggressive agents such as chloride ions and carbon dioxide penetrate the outer cover concrete layer. Though there may be no noticeable deterioration during this stage, the chlorides or carbonation front eventually reaches the steel reinforcement. Subsequently depassivation of the steel takes place and the corrosion propagation stage commences, with corrosion taking place at a rate determined by the nature of the electrolytic pore solution and the amount of oxygen that is present. The serviceability limit of the structure is reached once damage starts occurring, such as spalling, cracking and loss of structural capacity due to the reduction in steel cross-section, leading to ultimate failure.

For corrosion related to chloride ingress, the propagation phase is often significantly shorter than the initiation phase. It can therefore be assumed that the service life of the structure is determined by the length of the initiation period [42] [7] which is then used as the serviceability limit state in probabilistic design of concrete structures. Tutti [265] states that the easiest way of increasing the service life of a structure is to extend the corrosion initiation period and thus delaying damage leading to collapse. Due to the significant contribution of corrosion to durability problems, much research has been done on the transport mechanisms facilitating corrosion [106]. This led to the development of so-called durability indicators or

indexes related to these mechanisms [265] [239] [27] [42] in order to predict and monitor the initiation of corrosion.

2.3.4 Transport mechanisms facilitating corrosion

Corrosion initiation and propagation are irrevocably linked to the ease with which fluids and ions move through the concrete matrix. The penetrability of the concrete is therefore of utmost importance when durability is considered [210]. The penetration of deleterious substances into concrete is usually described as diffusion, migration, permeation or capillary suction depending on the mechanism responsible for the ingress [206] [151]. The study of these mechanisms is vital to explain analytically and quantify and the perviousness of concrete in order to predict the onset of corrosion.

2.3.4.1 Permeation

When a pressure gradient exists within a cementitious medium, liquids will percolate through the capillary network. Darcy's law for steady state conditions [82] states that the flow rate will be directly proportionate to the hydraulic gradient and have been generalised for flow of a viscous liquid through a porous medium as in Equation (2.30).

$$\vartheta = -\frac{K}{\eta}\frac{d\mathfrak{p}}{dx} \tag{2.30}$$

where ϑ [m/s] is the flow velocity, K [m^2] is the intrinsic permeability of the medium, η [Ns/m^2] is the dynamic viscosity of the liquid and $d\mathfrak{p}$ [N/m^2] is the applied pressure difference over a flow distance dx [m].

2.3.4.2 Capillary suction

Fluids can be transported through a porous medium such as concrete even if there is no external pressure gradient present, due to surface tension that exists in the capillary pores. This capillary suction is determined by the porosity and the moisture condition of the medium [189] and can be measured through various methods relating the water intake to time [116]. It is especially associated with concrete exposed to wetting and drying cycles.

2.3.4.3 Diffusion

When the transport of ions through a media takes place due to a concentration gradient, it is referred to as diffusion. Fick's first law of diffusion for steady state conditions [99],

defines the flux per area over time as being proportional to the concentration gradient with the diffusion coefficient defined as per Equation (2.31) [76]:

$$\mathcal{J} = -D\frac{dc}{dx} \tag{2.31}$$

where $\mathcal{J}$ [mol/m$^2 s$] is the flux and c [mol/m^3] is the concentration, x [m] the distance and D [m^2/s] is the diffusion coefficient.

When non-steady state conditions are present, such as is usually the case in concrete, Fick's second law is used which describes the change in concentration per unit volume over time. The explicit solution for non-steady state conditions known as Crank's solution [76] (defined for simple geometries, constant boundary conditions and material properties), is widely used to determine the diffusion coefficient of concrete:

$$c(x,t) = c_0\left[1 - erf\left(\frac{x}{2\sqrt{Dt}}\right)\right] \tag{2.32}$$

where *erf* is the error function and the initial conditions for $t = 0$ are $c = 0$ for $x > 0$ and $c = c_0$ for $x = 0$.

2.3.4.4 Migration

Not all ions move with the same ease through a porous media. An electrical field can be generated if an imbalance in ions occurs due to the non-uniform transport of different ions. When a potential difference develops under such circumstances, the diffusion of ions is accelerated due to the resulting electrical current and is thus referred to as migration.

The Nernst-Planck equation expresses the flux of an ionic species as the sum of pure diffusion, electrical migration and convection[3] as in Equation (2.33) [31]:

$$\begin{array}{rcccccc} -\mathcal{J}_i & = & D_i\dfrac{\partial c_i(x)}{\partial x} & + & \dfrac{Z_i F}{UT}Dc_i\dfrac{\partial q(x)}{\partial x} & + & c_i q_i(x) \\ \text{flux} & = & \text{pure diffusion} & + & \text{electrical migration} & + & \text{convection} \end{array} \tag{2.33}$$

where $\mathcal{J}_i$ [mol/m$^2 s$] is the molar flux of the ionic species i (chloride in this case), D_i [m^2/s] is the diffusion coefficient of this species, $c_i(x)$ [mol/m^3] is the concentration of i as a function of its location x_i [m], Z is the valence number [-] of the species, F is Faraday's constant (96 485 C/mol), U is the universal gas constant (8.314 J/mol/K), T is the temperature

[3]The term "convection" here refers to flow due to both moisture and pressure gradients.

[K] , $V(x)$ [V] is the applied electrical potential as a function of x and $q_i(x)$ [m^2/s] is the convection velocity of i.

As pure diffusion is too slow to play a significant role in the accelerated process and convection can be discarded for saturated conditions, the flux can be said to depend only on the migration term [31]. Transport mechanisms related to the diffusion and migration of ions are particularly relevant with regards to corrosion induced by chlorides, as is discussed in the next section.

2.3.5 Durability indicators related to chloride ingress

Durability indicators aim to quantify the susceptibility of concrete to various pathologies [42] including the penetration of aggressive agents. The indicators related to the transport of gases, liquids and ions are key to the estimation of the time to corrosion initiation and also the rate of corrosion propagation. Durability indicators play an important role in various stages over the lifespan of a reinforced concrete structure:

- During the design phase as input for service life and probabilistic models to relate concrete durability to service life;
- During the construction phase as part of the quality assurance regime to ensure that the specified durability is in fact attained on site;
- During the service life of the structure for regular condition assessment as part of a structural health monitoring regime;
- For updating the service life models in order to reassess the estimated life of the structure due to the time-dependency of the durability indicators;
- For the determination of the residual life of existing structures that were not necessarily designed and built using a performance based approach and durability specifications.

In the context of this thesis, only durability indicators related to the ingress of chloride ions will be discussed. The transport of chloride ions is usually due to a complex combination of the transport mechanisms described in Section 2.3.4, with the dominating mechanism depending primarily on the environmental conditions to which the structure is exposed [8]. Below the water level, e.g. for submerged marine structures, the ingress of ions is generally governed by diffusion, as constant concentration boundary conditions exist. In the splash zone or tidal zones, capillary suction usually dominates, though there is also diffusion inwards and outwards as the concrete is exposed to alternating wetting and drying cycles. For road structures exposed to de-icing salts, a pressure gradient exists depending on the depth

of ponding, leading to ingress being a combination of diffusion, permeation and capillary suction. Migration plays a significant role during the propagation stage of corrosion, but is also typically used for accelerated chloride diffusion tests [6] [251].

The resistance of concrete against chloride diffusion is seen as one of the most important durability indicators [167], as it plays a major role in terms of chloride penetration under all conditions. This view is also supported by the fact that capillary suction rarely leads to chloride ingress up to the depth of the reinforcement and significant hydraulic gradients are not often present in concrete structures. There is no single generally accepted durability indicator for the evaluation of the resistance of concrete to chloride diffusion. Several test methods have been developed in recent years and can be classified as natural diffusion tests, migration tests and indirect tests based on electrical resistivity or conductivity [169].

2.3.5.1 Natural diffusion tests

Long term (natural) diffusion tests such as the salt ponding test (AASHTO T259 [9]) and the bulk diffusion test (NordTest 433 [4] or ASTM C1556) [14]) are probably the most realistic indicators of the diffusion properties of concrete. They yield either the *effective* or *apparent* diffusion coefficient depending on whether chemical binding of the chlorides are taken into account or not. When the diffusion of only the free chlorides is considered, the term effective diffusion coefficient $D_{n(eff)}$ [m^2/s] is used which is determined for the steady state condition using Equation (2.31). The diffusion coefficient taking the binding capacity b [-] of the concrete into account is referred to as the apparent diffusion coefficient $D_{n(app)}$ [m^2/s] and is determined for the non-steady state using Equation (2.32). The relationship between the effective and apparent diffusion coefficient can be expressed by Equation (2.34) [43]:

$$D_{n(eff)} = \phi(1+b)D_{n(app)} \tag{2.34}$$

Opinions differ as to whether the apparent or the effective diffusion coefficients represents the corrosion risk of concrete the best [42] [64] [109], i.e. whether it is the free or the total chlorides that needs to be taken into account in predicting the time to corrosion initiation and service life of a structure. It can be argued that corrosion initiation and corrosion propagation are respectively governed by the apparent and the effective chloride diffusion coefficient and that both coefficients are therefore important. Both $D_{n(app)}$ and $D_{n(eff)}$ are used as input for empirical and service life models, while $D_{n(eff)}$ is also used for predictive physical models of chloride ingress [42].

2.3.5.2 Migration diffusion tests

The penetration of concrete by chlorides is a slow process, making natural diffusion tests time consuming, expensive and impractical. Several accelerated tests have therefore been developed using electomigration as basis such as the rapid chloride permeability (RCP) test [11] [15], rapid chloride migration (RCM) test [6] and chloride conductivity test [27]. Most of these tests are based on the Nernst-Planck Equation (2.33) where only the term related to migration is retained. For non-steady state conditions, the *apparent* chloride diffusion coefficient for migration $D_{m(app)}$ [m^2/s] is determined by using the solution of Equation (2.33) by Tang and Nilsson [255] as per Equation (2.35), discarding the pure diffusion and convection terms:

$$D_{m(app)} = \frac{UT}{ZF}\frac{L}{\delta V}\frac{x_{C\ell} - \varrho\sqrt{x_{C\ell}}}{t} \tag{2.35}$$

where $Z = 1$ [-] for chloride ions, δV [V] is the potential drop over the specimen of length L [m], $x_{C\ell}$ [m] is the average chloride penetration depth, t [s] is the test duration and ϱ [-] is a constant that depends on the test conditions as defined by [256].

For steady state conditions, the Nernst-Einstein equation can be used when concrete is regarded as a "solid electrolyte" [167], relating the effective diffusion coefficient for migration $D_{m(eff)}$ [m^2/s] to bulk conductivity as per Equation (2.36):

$$D_{m(eff)} = \frac{UTN\sigma}{Z^2F^2c_{C\ell}} \tag{2.36}$$

where N [-] is the transference number of chloride ions relating to the current carried by the ions (assumed to be 1 by Lu [167]), $c_{C\ell}$ [mol/m^3] is the chloride concentration and σ [S/m] is the bulk conductivity.

The correspondence of the diffusion coefficient determined from migration techniques to those from natural diffusion has been the subject of several studies [169] [57] [6] [257]. From this it is often assumed that the effect of chloride binding becomes negligible for migration tests as the test duration is too short for strong binding to take place. This is confirmed by Baroghel-Bouny et al. [43] and it is therefore stated that $D_{m(eff)}$ can be determined from $D_{m(app)}$ by assuming the binding capacity $b = 0$ as in Equation (2.37) [43].

$$D_{m(eff)} = \phi D_{m(app)} \tag{2.37}$$

The relationship between the effective diffusion coefficients as determined by natural diffusion using Equation (2.34) and calculated from migration techniques using Equation (2.37) were compared by Baroghel-Bouny et al. [43] and acceptable results were obtained confirm-

ing that the effective diffusion coefficient for natural and migration techniques are comparable. It is therefore valid to assume the following relationship:

$$D_{d(eff)} = \phi(1+b)D_{d(app)} \approx D_{m(eff)} = \phi D_{m(app)} \tag{2.38}$$

2.3.5.3 Water permeability tests

Another parameter that is widely used as a durability indicator in terms of corrosion is the coefficient of water permeability K_w. Water permeability is important even in the context of chloride-induced reinforcement corrosion [43], as water acts as the carrier of chloride ions and the permeation of water into concrete is therefore of great interest. K_w is generally determined by applying Darcy's law (Equation (2.30)) in one of two ways [251]: either by measuring the rate of inflow and outflow over the specimen as per Equation (2.39) [151], or by measuring the depth of penetration in a given time using the Valenta equation (2.40). Several variations of these equations are used as the basis of various test methods [251] for example the CRD-C163 test method [2] and the Autoclam permeability test [44].

$$K_w = Q\frac{L}{A}\frac{1}{\delta h} \tag{2.39}$$

where K_w [m/s] is the coefficient of water permeability, Q [m^3/s] is volume of liquid flowing (discharge), L [m] is the thickness of the penetrated section, A [m^2] is the permeated section and δh [m] is the applied pressure head (corresponding to the height of a water column).

$$K_w = \phi\frac{L}{t}\frac{x_w}{\delta h} \tag{2.40}$$

where ϕ is the porosity and x_w [m] is the penetration depth of the water.

2.3.6 Electromagnetic assessment of durability

Most destructive tests for the durability assessment of concrete are cumbersome as they must be performed under controlled laboratory conditions and require lengthy pre-conditioning of the samples. Even so-called "accelerated" test methods, as described in Section 2.3.5.2, are time consuming and expensive to perform in the large quantities required for quality control or regular health monitoring. Also, durability indicators are significantly influenced by the ageing of concrete [151] and should ideally be re-assessed over time for updating of the service life models. There is thus a great need to develop alternative test methods that can be performed semi- or non-destructively to estimate concrete durability and monitor concrete condition [272] in order to supplement or even replace traditional test methods.

A promising alternative is the use of electromagnetic methods, because electromagnetic properties (electrical conductivity and dielectric permittivity) are sensitive to the condition of concrete in terms of water content, chloride content, porosity and can also be related to diffusion characteristics. The electromagnetic responses are usually quick and easy to obtain and can be determined for conditioned concrete specimens (semi-destructively) or for in situ concrete (non-destructively).

Semi-destructive electromagnetic techniques can be used during quality control for indirect assessment of durability indicators [118] [143], while non-destructive electromagnetic techniques are better suited for improved spacial coverage and frequent testing over time [178] [172]. Non-destructive techniques are not only advantageous in terms of time efficiency but also avoid the practical problems of core drilling, related to access and unnecessary damage as well as technical problems related to migration tests, such as heat production due to high applied voltages [251]. Being the main focus of this thesis, electromagnetic methods will be discussed extensively in Chapters 4 and 6. However, some work on durability assessment and health monitoring using electrical methods will be highlighted here.

2.3.6.1 Indirect durability indicators

Electrical conductivity (or its inverse electrical resistivity) has been suggested by various authors as indirect durability indicator to estimate chloride diffusivity [43] [31] [215] [118] [84] [143]. From the Nernst-Einstein Equation (2.36) it is clear that there is theoretically a linear relationship between the effective diffusion coefficient and bulk conductivity for constant temperatures and concentrations. This relationship can be redefined in terms of a product factor $\mathcal{B}$ as follows [31]:

$$\frac{D_0}{D_{r(eff)}} = \frac{\sigma_0}{\sigma} \tag{2.41}$$

with

$$D_{r(eff)} = \frac{D_0}{\sigma_0}\frac{1}{\rho'} = \frac{\mathcal{B}}{\rho'} \tag{2.42}$$

where σ_0 [S/m] is the conductivity of the interstitial solution, σ [S/m] is the bulk conductivity of the specimen, D_0 [m^2/s] is the free diffusion coefficient of chloride ions, $D_{r(eff)}$ [m^2/s] is the diffusion coefficient determined from resistivity, ρ' [Ω.m] is the characteristic (saturated) resistivity (with $\sigma = 1/\rho'$) and $\mathcal{B}$ [$m^3\Omega$/s] is the so called "product factor" which is dependent on the ionic concentration of the pore solution.

For the determination of the product factor in Equation (2.42) some assumptions are required. Baroghel-Bouny et al. [43] suggest that $\sigma_0 = 11.87$ S/m is a typical value for alkaline solutions as is found in concrete pores. However, the W/C-ratio and type of cement can significantly influence this value. D_0 is usually taken as 1.48×10^{-9} m^2/s being the

free diffusion coefficient for chloride ions in a 1 M solution at 25°C reported in literature. Andrade et al. [31] report that the slope of the relationship between $D_{r(eff)} \times 10^{-12}$ and σ' (the product factor $\mathcal{B}$) is relatively constant for different concretes at approximately 200. On the contrary, Baroghel-Bouny et al. [43] find that the product factor can range from 150 to 300 depending on the W/C-ratio of the concrete.

Many other studies have also been conducted in which the relationship between resistivity and the respective diffusion tests were determined empirically. Han [118] and De Rooij et al. [84] find a linear relationship between resistivity and the migration diffusion coefficient $D_{m(app)}$ and use this for Bayesian updating of probabilistic design models and on-site quality control. In a study spanning several years the Florida Department of Transportation (FDOT) tested the relationship between surface resistivity and the RCP test for a wide population of concretes of varying ages [143] [222] and decided to replace their RCP specifications by characteristic resistivity measurements due to good correlation found between the two methods (see Figure 2.9). This approach was also adopted by the Louisiana Department of Transportation (LDT) [229] [228].

There are still several issues that hamper the general use of resistivity as indirect durability indicator, both for core specimens and non-destructive in situ testing. Firstly, the most significant problem is that the degree of saturation of the in situ concrete is not necessarily known. Core specimens taken from site can be saturated easily enough and are often used for quality control purposes using resistivity instead of migration tests. However, for non-

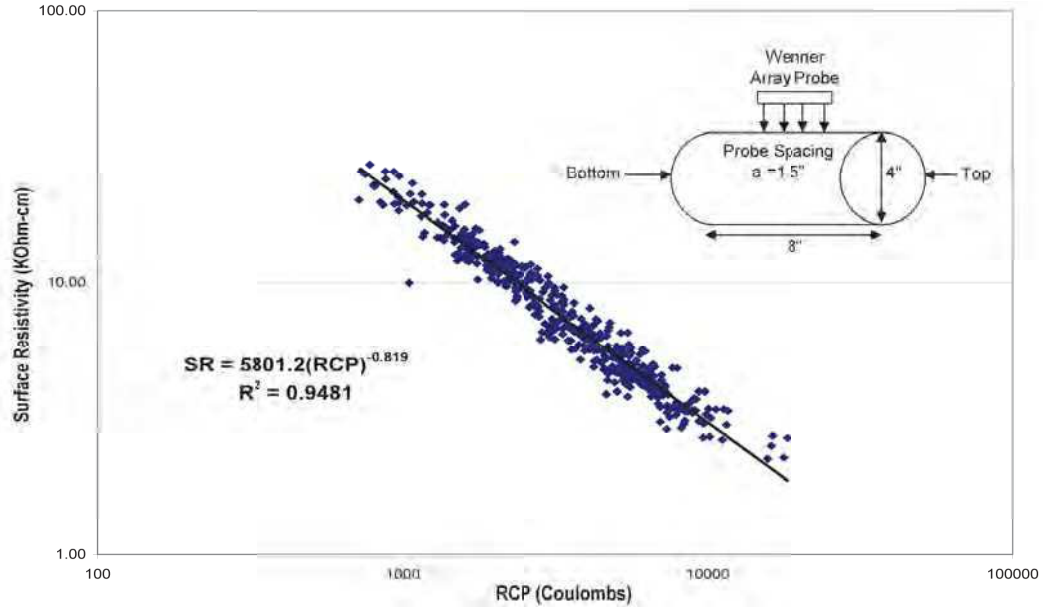

Figure 2.9: Relationship between rapid chloride permeability (RCP) test and surface resistivity for saturated conditions [143].

destructive in situ measurement, it is usually not possible to achieve saturated conditions on site unless the structure is submerged. Secondly, the extent of chloride contamination of the in situ concrete is not known. The application of theoretical models where there are assumptions regarding the conductivity of the interstitial solution, as required for Equation (2.42) or type of conducting ion, as required in Equation (2.36) could therefore be erroneous. Most empirical models are determined for concrete at saturated, uncontaminated and homogeneous conditions and can therefore only be used for in situ application if a calibration is performed to compensate for the on site saturation and chloride condition. Thirdly, theoretical models relate conductivity to effective diffusion, as it is dependent on the movement of free chlorides. In order to find the apparent diffusion coefficient (which is often the preferred input parameter in serviceability models) the porosity of the concrete must also be known, as per Equation (2.34). This can of course be determined from core specimens, but is a time consuming process.

Major causes of error related to the use of in situ conductivity (or resistivity) as indirect durability indicator, can therefore be listed as:

1. Uncertainty related to the saturation of the in situ concrete;
2. Uncertainty related to the concentration and type of conducting ions in the interstitial solution;
3. Uncertainty related to the porosity of the concrete, which influences the relationship between resistivity and diffusion coefficient.

Therefore, if the condition of concrete can be better characterised in terms of saturation, chloride content and porosity, diffusion characteristics of concrete could be more reliably estimated from resistivity measurements. Part of the focus of this thesis is thus to investigate the possibility of reducing these uncertainties by combining electromagnetic responses i.e. conductivity and frequency dependent permittivity.

2.3.6.2 Structural Health Monitoring

Not only are electromagnetic techniques useful for the indirect estimation of durability indicators, but also for structural health monitoring (SHM) of reinforced concrete structures. Structural health monitoring is usually related to characterisation and damage detection of engineering structures over their service life. Structural health monitoring implies the use of embedded or mobile sensors to assess the condition of existing structures on a regular, or continuous basis.

Resistivity has been suggested as a non-destructive investigation method for structural

Table 2.1: Concrete resistivity and risk of reinforcement corrosion at 20°C for OPC concrete [75].

Concrete Resistivity [Ω.m]	Risk of Corrosion
< 100	high
100-500	moderate
500-1000	low
> 1000	negligible

health monitoring as it is considered to be a good indication of corrosion risk. Table 2.1 relates corrosion risk of existing structures to resistivity values determined in situ [75]. Techniques related to permittivity have also been studied in this context [156] [236] [138], although often more in a qualitative sense to monitor change over time [271].

In the context of this thesis the focus is on the use of non-destructive electromagnetic techniques for the characterisation of cover concrete in terms of the ingress of aggressive agents. The use of electromagnetic investigation methods lends itself to the investigation of gradients over depth. This can either be achieved by mobile surface sensors, or embedded sensors that are fitted to the structures during construction. However, there is not a lot of literature available on this topic. Some studies have been conducted on the implementation of surface sensors [244] [86] and embedded sensors [180] [49] [67] for electrical or electromagnetic monitoring of water and chloride ingress in cover concrete, but more research in this domain is required.

2.4 Conclusion

The basic concepts regarding the properties of concrete have been presented in this chapter and the most important aspects related to its microstructure and chemical composition were discussed. It was emphasized that reinforced concrete infrastructure is a valuable asset that is to be designed and maintained by implementing an approach based on durability requirements. The durability of concrete is related to the inherent properties of the concrete associated with its pore structure and constituents, such as porosity, W/C-ratio and degree of hydration introduced in this chapter.

However, in order to predict the service life of concrete as part of a performance based approach towards durability, transport mechanisms such as diffusion and permeation, facilitating the transport of harmful agents into concrete, is also taken into account. As corrosion due to the penetration of agents such as chlorides and water is a major cause of durability problems in reinforced concrete structures, several durability indicators have been devised

to quantify the susceptibility of cover concrete to the transport of these agents. These durability indicators are usually determined by time consuming and expensive test methods which are not suitable for regular or continuous health monitoring of structures.

The role that electromagnetic non-destructive investigation techniques has to play in the assessment of concrete durability is thus of great interest as it is significantly faster and more cost efficient. The use of electromagnetic techniques have potential for practical application as part of quality control during construction and health monitoring over the service life of concrete infrastructure. The next chapters will discuss the fundamentals of electromagnetics and the respective electromagnetic investigation techniques relevant to this thesis.

Chapter 3

Electromagnetic fundamentals

3.1 Introduction

This chapter starts by reviewing the fundamentals of electromagnetic (EM) theory that form the basis of the techniques used to investigate concrete condition as part of this thesis. It then continues by discussing various models that have been proposed to describe the dielectric response of both pure and composite materials. Lastly, an overview is given of the influence of environmental conditions as well as mix constituents and their proportions on the electromagnetic behaviour of concrete in particular.

3.2 Fundamentals of electromagnetics

3.2.1 Maxwell's equations

Maxwell succeeded in the late nineteenth century to derive a set of relations from previously unrelated equations and observations in order to consistently describe the behaviour of electromagnetic fields. These equations are referred to as *Maxwell's equations* and form the basis of electromagnetic wave propagation and electric diffusion in materials. The fundamentals of electromagnetic theory are dealt with in numerous textbooks such as [252] [150] [38] [62] and only a general overview will be given here. The four time-domain differential equations proposed by Maxwell are presented as Equations (3.1) to (3.4).

Faraday's law of induction:

$$\nabla \times \boldsymbol{E}(\boldsymbol{r},t) = -\frac{\partial \boldsymbol{B}(\boldsymbol{r},t)}{\partial t} \tag{3.1}$$

Ampère's law with Maxwell's correction:

$$\nabla \times \boldsymbol{H}(\boldsymbol{r},t) = \frac{\partial \boldsymbol{\mathcal{D}}(\boldsymbol{r},t)}{\partial t} + \boldsymbol{J}_c(\boldsymbol{r},t) \tag{3.2}$$

Gauss's law:

$$\nabla \cdot \boldsymbol{\mathcal{D}}(\boldsymbol{r},t) = q(\boldsymbol{r},t) \tag{3.3}$$

Gauss's law for magnetism:

$$\nabla \cdot \boldsymbol{B}(\boldsymbol{r},t) = 0 \tag{3.4}$$

where the vectors $\boldsymbol{E}(\boldsymbol{r},t)$ [V/m] is the electrical field intensity, $\boldsymbol{B}(\boldsymbol{r},t)$ [T] is the magnetic flux density (magnetic induction), $\boldsymbol{H}(\boldsymbol{r},t)$ [A/m] is the magnetic field intensity, $\boldsymbol{\mathcal{D}}(\boldsymbol{r},t)$ [C/m] is the electric flux density (electric induction), $\boldsymbol{J}_c(\boldsymbol{r},t)$ [A/m^2] is the current density and $q(\boldsymbol{r},t)$ [C/m^3] is the scalar charge density; all of which are dependent on position in space $\boldsymbol{r}$ (x, y, z) [m] and time t [s] with ∇ being the vector differential operator $\left(\partial/\partial x, \partial/\partial y, \partial/\partial z\right)$.

Equation (3.1) relates to the work of Faraday and Henry who observed independently that an electrical current will be induced in a closed circuit by introducing a changing magnetic field. The inverse is also true as per Equation (3.2), which shows that a magnetic field can be induced by electrical current (Ampère's law) and by a changing electric field (Maxwell's correction). Equations (3.1) and (3.2) demonstrate the interdependence of electric and magnetic fields. These two *dynamic laws* are complemented by two *static laws* of which the first, Gauss's law (3.3), relates the total electric flux through a closed surface to the total enclosed charge. It implies that the divergence of the electrical flux density is equal to the density of electric charge. Gauss's law for magnetism (3.4) indicates that the total magnetic flux through a closed surface is always zero. This implies that punctual magnetic charge does not exist, the smallest possible magnetic source being a dipole.

These equations can be applied to any medium albeit non-linear, heterogeneous or anisotropic and therefore are fundamental to any work related to electromagnetics.

3.2.2 Constitutive equations

In order to relate the flux densities $\boldsymbol{J}_c(\boldsymbol{r},t)$, $\boldsymbol{B}(\boldsymbol{r},t)$ and $\boldsymbol{\mathcal{D}}(\boldsymbol{r},t)$ to electric and magnetic field intensities $\boldsymbol{E}(\boldsymbol{r},t)$ and $\boldsymbol{H}(\boldsymbol{r},t)$ certain constitutive equations are defined, the form of which depends on the medium in which the fields exist. To allow Maxwell's equations to be

applied in practice, the electromagnetic parameters for the linear isotropic case are defined as electrical conductivity σ, dielectric permittivity ε and magnetic permeability μ.

The constitutive relations (3.5), (3.6) and (3.7) describe the behaviour of charges at microscopic scale. The electromagnetic parameters σ [S/m] and ε [F/m] are related to the ability of a medium to transport electrical charge (conduction) and store electrical energy (polarisation) under an applied electric field, whilst μ [H/m] relates to the medium's ability to be magnetised under an applied magnetic field.

$$\boldsymbol{J}_c(\boldsymbol{r},t) = \sigma \boldsymbol{E}(\boldsymbol{r},t) \tag{3.5}$$

$$\boldsymbol{\mathcal{D}}(\boldsymbol{r},t) = \varepsilon \boldsymbol{E}(\boldsymbol{r},t) \tag{3.6}$$

$$\boldsymbol{B}(\boldsymbol{r},t) = \mu \boldsymbol{H}(\boldsymbol{r},t) \tag{3.7}$$

For an idealised medium where there is a clear distinction between free and bound charges, conduction and polarisation can be linked respectively to the movement of free and bounded charges. Under an applied electrical field, the movement of free charges produces a current density $\boldsymbol{J}_c(\boldsymbol{r},t)$ as a function of the number, charge and velocity of the charge carriers. These charge carriers can be either electrons (electronic conduction) or ions (electrolytic conduction).

In turn, bound charges will be displaced relative to their equilibrium positions under an applied electrical field leading to dielectric polarisation. For an electrically linear material, the polarisability $\boldsymbol{P}(\boldsymbol{r},t)$ [Cm^2/V] of a material varies proportionally to the electric field and is given by Equation (3.8):

$$\boldsymbol{P}(\boldsymbol{r},t) = \mathcal{D}(\boldsymbol{r},t) - \varepsilon_0 \boldsymbol{E}(\boldsymbol{r},t) \tag{3.8}$$

where $\varepsilon_0 \approx 8.854 \times 10^{-12}$ F/m is the dielectric permittivity of free space. The polarisability is also often described in terms of the electric susceptibility χ [-]:

$$\boldsymbol{P}(\boldsymbol{r},t) = \varepsilon_0 \chi \boldsymbol{E}(\boldsymbol{r},t) \tag{3.9}$$

where

$$\varepsilon = \varepsilon_0 (1 + \chi) \tag{3.10}$$

For real materials it is considerably more difficult to discern between the contributions of free and bound charge movement to polarisation and conduction. Polarisation can take several different forms depending on the material and frequency of the electric field (see Figure 3.1) of which atomic, electronic, molecular and interfacial polarisation is predominant in the radar frequency range.

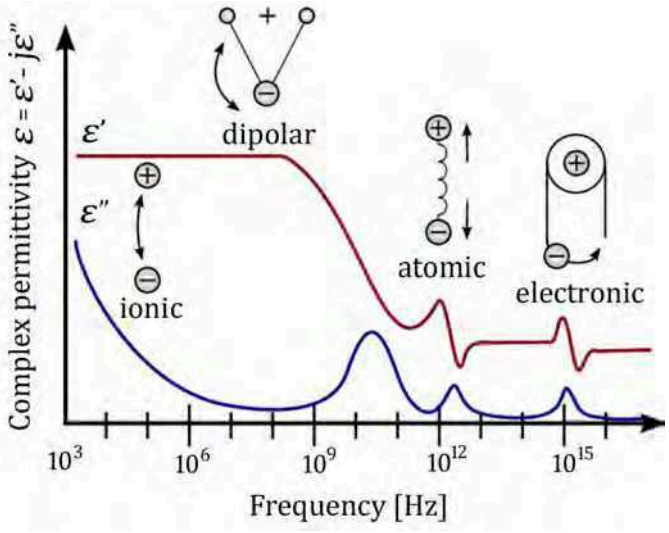

Figure 3.1: The dielectric spectrum (image from K.A. Mauritz via *Wikipedia*).

Polarisation due to bound charges includes atomic polarisation caused by the displacement of anions and cations in crystals relative to their normal positions, polarisation due to the distortion of the electron cloud of non-polar molecules referred to as electronic polarisation and molecular polarisation caused by the re-alignment (rotation) of polar molecules, such as water, to align themselves according to the applied electric field. When the electric field is removed, the displaced charge will take a certain time to return to their original positions. For atomic and electronic polarisation the reversal of the polarisation is complete. However, for molecular polarisation energy losses will occur due to friction and the inertia of the rotating molecules, leading to a decrease in the polarisation as the frequency increases. The time that it takes for charge to "relax" to a new equilibrium is referred to as the *relaxation time*.

For non-homogeneous materials free charge carriers such as ions can also lead to interfacial polarisation (known as the Maxwell-Wagner effect [119]) due to a surface charge build-up at interfaces between components with different dielectric properties. Thus, when an alternating electric field is applied, the losses will cause $\boldsymbol{J}_c(\boldsymbol{r}, t)$ and $\boldsymbol{E}(\boldsymbol{r}, t)$ to have both in-phase and out-of-phase components depending on the frequency of the field. The electrical conductivity and dielectric permittivity are thus treated as complex functions, with the real and imaginary parts denoted by single ($'$) and double ($''$) primes and j being the imaginary unit:

$$\sigma = \sigma' + j\sigma'' \tag{3.11}$$

$$\varepsilon = \varepsilon' - j\varepsilon'' \tag{3.12}$$

$$j^2 = -1 \tag{3.13}$$

Thus, at a microscopic scale, it can be said that the the real part of the conductivity of Equation (3.11) σ' represents the migration of free charges through ohmic conduction and the imaginary part σ'' the polarisation ability of the free charges due to interfacial polarisation. In Equation (3.12) the real part of the permittivity ε' relates to the polarisation ability due to atomic, electronic and molecular polarisation and the imaginary part ε'' corresponds to dielectric losses (relaxation) caused by the reorientation of polar molecules. The frequency where no more losses occur for a particular polarisation mechanism, is referred to as the relaxation frequency.

3.2.3 Effective permittivity

Electromagnetic investigation techniques operate at a macroscopic scale where it is not possible to discern between the in-phase and out-of-phase components of the electromagnetic properties. The measured effective electromagnetic response is therefore the result of the combination of both the real and imaginary part for conductivity and permittivity given in Equations (3.11) and (3.12). In order to combine these terms mathematically, Maxwell's equations (defined in the time domain in Section (3.2.1)) are transformed to the frequency domain by means of the Fourier transform for the case of harmonic time dependence:

$$\boldsymbol{E}(\boldsymbol{r},t) = \frac{1}{2\pi}\int_{-\infty}^{\infty} \boldsymbol{E}(\boldsymbol{r},\omega)e^{j\omega t}d\omega \tag{3.14}$$

where $\omega = 2\pi f$ [Hz] is the angular frequency of the changing electromagnetic field. The magnetic field can be transformed similarly.

The electric and magnetic fields therefore have a time dependency of $e^{j\omega t}$:

$$\boldsymbol{E}(\boldsymbol{r},t) = \boldsymbol{E}(\boldsymbol{r})e^{j\omega t} \tag{3.15}$$

$$\boldsymbol{H}(\boldsymbol{r},t) = \boldsymbol{H}(\boldsymbol{r})e^{j\omega t} \tag{3.16}$$

$$\boldsymbol{\mathcal{D}}(\boldsymbol{r},t) = \boldsymbol{\mathcal{D}}(\boldsymbol{r})e^{j\omega t} \tag{3.17}$$

$$\boldsymbol{J}_c(\boldsymbol{r},t) = \boldsymbol{J}_c(\boldsymbol{r})e^{j\omega t} \tag{3.18}$$

By substituting the partial time-derivative $\partial/\partial t$ in Equation (3.2) with the Fourier transform pair $j\omega$, it is rewritten for the frequency domain:

$$\nabla \times \boldsymbol{H}(\boldsymbol{r},\omega) = j\omega\boldsymbol{D}(\boldsymbol{r},\omega) + \boldsymbol{J}_c(\boldsymbol{r},\omega) \tag{3.19}$$

The total current density $\boldsymbol{J}_t(\boldsymbol{r},\omega)$ [A/m^2] observed in practice will therefore be a combination of conduction current $\boldsymbol{J}_c(\boldsymbol{r},\omega)$ due to movement of free charge and displacement current

$\boldsymbol{J}_d(\boldsymbol{r},\omega)$ due to dielectric losses:

$$\boldsymbol{J}_t(\boldsymbol{r},\omega) = \boldsymbol{J}_d(\boldsymbol{r},\omega) + \boldsymbol{J}_c(\boldsymbol{r},\omega) \tag{3.20}$$

Since conduction current can be written as $\boldsymbol{J}_c(\boldsymbol{r},\omega) = \sigma\boldsymbol{E}(\boldsymbol{r},\omega)$ and the displacement current as $\boldsymbol{J}_d(\boldsymbol{r},\omega) = j\omega\boldsymbol{\mathcal{D}}(\boldsymbol{r},\omega) = j\omega\varepsilon\boldsymbol{E}(\boldsymbol{r},\omega)$, the substitution of these into Equation (3.19) yields the expression for the total current density as in Equation (3.21):

$$\begin{aligned}\boldsymbol{J}_t(\boldsymbol{r},\omega) &= (j\omega\varepsilon + \sigma)\boldsymbol{E}(\boldsymbol{r},\omega)\\ &= j\omega(\varepsilon + \frac{\sigma}{j\omega})\boldsymbol{E}(\boldsymbol{r},\omega)\\ &= jw\varepsilon_e\boldsymbol{E}(\boldsymbol{r},\omega)\end{aligned} \tag{3.21}$$

The effective permittivity ε_e [F/m] is thus defined as a complex scalar that combines all the contributions of conductivity and permittivity:

$$\varepsilon_e = (\varepsilon + \frac{\sigma}{j\omega}) = (\varepsilon' + \frac{\sigma''}{\omega}) - j(\varepsilon'' + \frac{\sigma'}{\omega}) \tag{3.22}$$

with

$$\varepsilon'_e = \varepsilon' + \frac{\sigma''}{\omega} \tag{3.23}$$

$$\varepsilon''_e = \varepsilon'' + \frac{\sigma'}{\omega} \tag{3.24}$$

Effective permittivity is often expressed relative to the permittivity of free space. The relative effective permittivity ε_r [-] of a material is therefore defined as follows:

$$\varepsilon_r = \frac{\varepsilon'_e - j\varepsilon''_e}{\varepsilon_0} = \varepsilon'_r - j\varepsilon''_r \tag{3.25}$$

It can be said that on a macroscopic scale, the real part of the relative effective permittivity ε'_r [-] represents the capacity of the material to store electromagnetic energy as electrical polarisation. This is a real valued, dimensionless parameter generally referred to as the *dielectric constant*. The imaginary part of the effective relative permittivity ε''_r [-] represents the energy losses due to conduction and absorption and is often referred as the *loss factor*.

3.2.4 Electromagnetic wave propagation

The propagation of an electromagnetic wave in a dispersive (lossy) medium follows the laws of Maxwell as per Equations (3.1) to (3.4). In order to describe the wave propagation as a function of the electromagnetic properties defined in Section 3.2.2, the electromagnetic

field must be defined explicitly by substituting the constitutive equations (3.5) to (3.7) in Maxwell's equations (3.1) and (3.2). The wave equation (3.26) for the electric field can then be derived if the curl ($\nabla\times$) is taken of Equation (3.1) and Equations (3.2) and (3.4) are substituted in the result. Similarly the wave equation for the magnetic field can be determined by taking the curl of Equation (3.2). Equations (3.26) and (3.27) are also referred to as the Helmholtz Equations [38]. These two equations are identical for the electric and the magnetic fields, indicating that the two fields are in fact the components of the propagating electromagnetic wave.

$$\Delta \boldsymbol{E}(\boldsymbol{r},t) = \sigma\mu\frac{\partial \boldsymbol{E}(\boldsymbol{r},t)}{\partial t} + \varepsilon\mu\frac{\partial^2 \boldsymbol{E}(t)}{\partial t^2} \tag{3.26}$$

$$\Delta \boldsymbol{H}(\boldsymbol{r},t) = \sigma\mu\frac{\partial \boldsymbol{H}(\boldsymbol{r},t)}{\partial t} + \varepsilon\mu\frac{\partial^2 \boldsymbol{H}(t)}{\partial t^2} \tag{3.27}$$

where Δ is the Laplace operator and is equal to $\nabla^2 = \left(\partial^2/\partial x^2, \partial^2/\partial y^2, \partial^2/\partial z^2\right)$.

If Equation (3.26) is transformed to the frequency domain using the Fourier transform in Equation (3.14), Equation (3.28) is found (as this thesis focusses primarily on electrical phenomena only the solutions for the electric field are given here):

$$\Delta \boldsymbol{E}(\boldsymbol{r},\omega) = -\kappa^2 \boldsymbol{E}(\boldsymbol{r},\omega) \tag{3.28}$$

where

$$\kappa = \Re - j\alpha = \omega\sqrt{\mu\varepsilon_e} = \omega\sqrt{\mu\left(\frac{\sigma}{j\omega} - \varepsilon\right)} \tag{3.29}$$

κ [rad/m] is known as the complex wave number and $\Re$ [rad/m] and α [rad/m] are respectively referred to as the phase and attenuation constant.

For a planar wave propagating in the z-direction of which the electrical field is linearly polarised in the x-direction as in Figure 3.2, Equation (3.28) can be solved to find an explicit solution for the electric field component as follows:

$$\boldsymbol{E}_x(z,\omega) = \boldsymbol{E}(0,\omega)e^{-j\kappa z} = \boldsymbol{E}(0,\omega)e^{-\alpha z}e^{-j\Re z} \tag{3.30}$$

Subsequently α and $\Re$ can be expressed as functions of ε_e' and ε_e'':

$$\alpha = \omega\sqrt{\frac{\mu\varepsilon_e'}{2}\left[\sqrt{1+\left(\frac{\varepsilon_e''}{\varepsilon_e'}\right)^2} - 1\right]} \tag{3.31}$$

$$\Re = \omega \sqrt{\frac{\mu \varepsilon'_e}{2} \left[\sqrt{1 + \left(\frac{\varepsilon''_e}{\varepsilon'_e} \right)^2} + 1 \right]} \tag{3.32}$$

Equations (3.31) and (3.32) can then be solved for the real and imaginary parts of the effective permittivity as follows:

$$\varepsilon'_e(\omega) = \frac{\Re^2 - \alpha^2}{\mu \omega^2} \tag{3.33}$$

$$\varepsilon''_e(\omega) = \frac{2\alpha\Re}{\mu\omega^2} \tag{3.34}$$

The ratio of ε'_e to ε''_e is known as the quality factor $\mathcal{Q}$. The quality factor is often assumed to be constant but is in truth frequency dependent in dispersive media [132]:

$$\frac{1}{\mathcal{Q}} = \frac{\varepsilon'_e}{\varepsilon''_e} = \frac{\Re^2 - \alpha^2}{2\Re\alpha^2} \tag{3.35}$$

The relationships (3.31) to (3.34) are fundamental in determining the frequency dependent complex permittivity in a dispersive medium by means of electromagnetic investigation techniques.

In dielectric mediums where the energy losses are low ($\sigma << \omega\varepsilon$), the imaginary part of the wave number κ will be very small as the electromagnetic response is dominated by the polarisation. There is thus very little attenuation of the signal and the electromagnetic wave propagation can be described as "pure". For a very conductive medium the ohmic losses

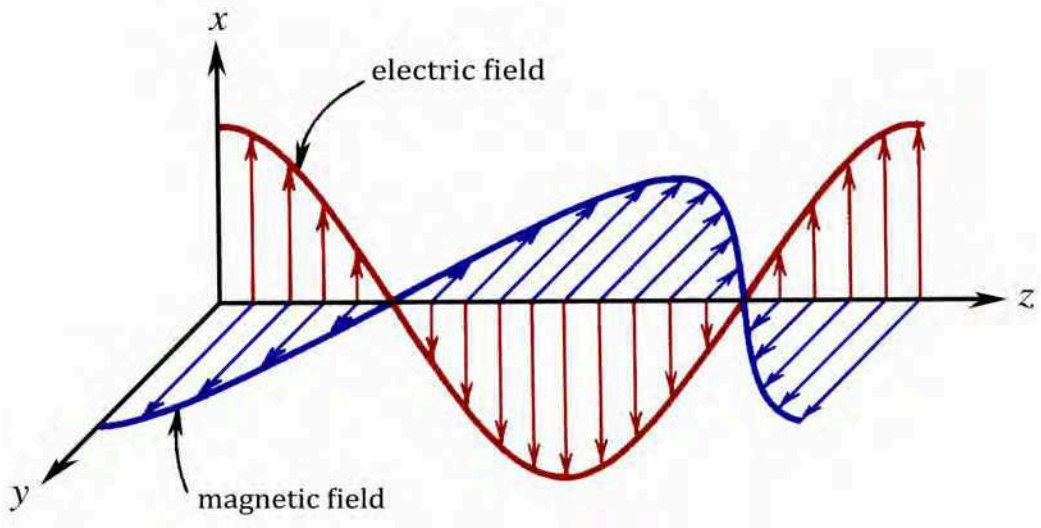

Figure 3.2: Electric and magnetic field components of a planar electromagnetic wave propagating in the z-direction and polarised in the x-direction, after [38].

are high and $\sigma >> \omega\varepsilon$. The term *diffusion* is then used to describe the electromagnetic response rather than *propagation*. According to Kraus and Carver [150], a medium can be classified to fall in one of the follow regions according to its electromagnetic properties as by the inequalities (3.36) to (3.38).

Dielectric region:

$$\frac{\sigma}{\omega\varepsilon} < \frac{1}{100} \tag{3.36}$$

Quasi-conducting region:

$$\frac{1}{100} < \frac{\sigma}{\omega\varepsilon} < 100 \tag{3.37}$$

Conducting region:

$$100 < \frac{\sigma}{\omega\varepsilon} \tag{3.38}$$

Whether a material behaves as a dielectric, quasi-conductor or conductor is dependent on the frequency of the electromagnetic field that is applied. Concrete behaves as a quasi-conductor in the radar wave frequency band with the extent of attenuation varying depending on its moisture and chloride content.

When a static electric field (or a field of very low frequency) is applied to concrete, it will act primarily as a conductor and Maxwell's equations can be simplified to the following:

$$\nabla \times \boldsymbol{E} = \boldsymbol{0} \tag{3.39}$$

$$\nabla \times \boldsymbol{H} = \boldsymbol{J} \tag{3.40}$$

$$\nabla \cdot \boldsymbol{E} = 0 \tag{3.41}$$

$$\nabla \cdot \boldsymbol{B} = 0 \tag{3.42}$$

3.2.5 Assumptions and conventions

As the work presented in this thesis deals with the electromagnetic response of hydraulic concrete, the electromagnetic theory presented in this section will be applied by making the following assumptions regarding the medium:

1. Linearity: It is assumed that the constitutive relations are not dependent on the size of the applied electric and magnetic field and are thus linear.
2. Homogeneity: Though concrete is non-homogeneous at a microscopic level, it can be regarded as homogeneous at a macroscopic level if the principles of homogenisation theory [232] [275] are complied with during the execution of electromagnetic test procedures. This implies that the electromagnetic parameters ε, σ and μ are deemed

to be representative of a homogeneous medium that is electromagnetically equivalent to the measured composite material. However, it must be noted that the assumed homogeneity is with regards to the composite nature of concrete and does not imply that gradients can not be present in terms of electromagnetic properties.

3. Isotropy: It is assumed that concrete is isotropic and that the electromagnetic parameters are not dependent on the direction of the electric and magnetic field vectors.

4. Non-magnetism: Concrete is assumed to be a non-magnetic material, thus having a magnetic permeability equal to that of free space ($\mu_0 \approx 1.257 \times 10^{-6}$ H/m). In practice this implies the presence of steel reinforcement must be avoided or compensated for when the electromagnetic measurements are made and that the concrete is not steel fibre reinforced.

5. Dispersiveness: Concrete can be regarded as a dispersive medium over the frequency range within which the EM testing techniques forming part of this thesis operate (approximately 30 - 3000 MHz). Dispersion is due to the polarisation response not being instantaneous when a time-varying electric field is applied and the electromagnetic parameters thus being frequency dependent. This frequency dependency manifests itself to a greater or lesser extent in concrete depending on its moisture condition and chloride content.

To avoid confusion in the chapters to follow, the *effective permittivity* will always refer to complex effective permittivity ε_e, whilst *complex permittivity* (or just *permittivity*) will refer to the complex relative effective permittivity $\varepsilon_r = \varepsilon_e/\varepsilon_0$ of which the ***dielectric constant*** is the real part ε_r' and the ***loss factor*** is the imaginary part ε_r''. The term ***conductivity*** σ will in general refer to direct current conductivity and will be a real number with ***resistivity*** ρ its inverse. With regards to composite materials such as concrete the electromagnetic properties may also be referred to as *bulk* properties, implying that they are representative of the macroscopic scale.

3.3 Models describing electromagnetic behaviour

The electromagnetic properties of materials vary over a wide range and it is therefore impossible to establish a representative model that suits all cases and conditions [220]. Conductivity is one of the physical properties with the largest range and can vary over approximately five orders of magnitude ($0.0001\ \mathrm{S/m} < \sigma < 1\ \mathrm{S/m}$) [184] [149] for engineering materials. Dielectric constants ε_r' also cover a considerable range, varying for simple materials from 1 for air to more than 80 for water [149].

Many mathematical models have been developed in an attempt to model the effective permittivity of various materials [149]. These models can be categorised as phenomenological models, composite material models and empirical or semi-empirical models. The performance of the models vary as to whether they aim to represent the frequency dependency of the electric response of simple dispersive materials (such as water) over a large frequency band, or whether they aim to estimate the electromagnetic response of a range of composite materials for a limited frequency band assuming non-dispersive behaviour.

3.3.1 Phenomenological models

Phenomenological models aim to describe the frequency dependent absorption-dispersion behaviour of materials based on the criteria of causality, thus using characteristic relaxation times. Simple materials such as water have a single, well defined polarisation mechanism for which the relaxation time τ [s] is known. The frequency dependent complex permittivity for such materials can therefore be modelled by the relationship proposed by Debye [85]:

$$\varepsilon_e = \varepsilon_\infty + \frac{\varepsilon_s - \varepsilon_\infty}{1 + j\omega\tau} \tag{3.43}$$

where ε_e is the effective permittivity, ε_s [F/m] is the dielectric permittivity for the static case and ε_∞ [F/m] is the dielectric permittivity at infinite frequencies. This model was adapted by Cole and Cole [73] for simple materials that have several polarisation mechanisms, having different relaxation times or relaxation time distributions:

$$\varepsilon_e = \varepsilon_\infty + \frac{\varepsilon_s - \varepsilon_\infty}{1 + (j\omega\tau)^{1-\psi}} \tag{3.44}$$

where ψ [-] is a distribution parameter ($0 < \psi < 1$) accounting for variation in relaxation times in the material.

These models are particularly suitable to describe the complex permittivity of materials for which the main form of polarisation is dipolar and for the frequency band surrounding the relaxation frequency. However, they are often not representative of more complex materials consisting of different phases. For these materials there is also polarisation due to interfacial and double layer effects as described in Section 3.2.2. A study by Hollender and Tillard [125] on geological materials compared modelled complex permittivities using Debye's model and its variants to experimental data and obtained significant differences, especially in terms of the imaginary part. An additional term containing the direct current conductivity σ_{DC} [S/m] is therefore added to Equation (3.44) to compensate for interfacial Maxwell-Wagner polarisation, forming what is known as the five parameter Cole-Cole model [223]:

$$\varepsilon_e = \varepsilon_\infty + \frac{\varepsilon_s - \varepsilon_\infty}{1 + (j\omega\tau)^{1-\psi}} - j\frac{\sigma_{DC}}{\omega\varepsilon_0} \tag{3.45}$$

Another approach is to discard the influence of relaxation time and thus loss peaks on the dielectric behaviour. The model of Jonscher [137], also called the universal dielectric response, is based on the assumption that all dielectric systems follow a frequency power law above their relaxation frequency. This model is more general than relaxation-time based models and can be applied to many different materials over a large frequency band:

$$\varepsilon_e = \varepsilon_0 \chi_r \left(\frac{\omega}{\omega_r}\right)^{n-1} \left[1 - jcot\left(\frac{\eta\pi}{2}\right)\right] + \varepsilon_\infty - j\frac{\sigma_{DC}}{\omega\varepsilon_0} \tag{3.46}$$

where χ_r is the relative real electric susceptibility at a reference frequency $f_r = \omega_r/2\pi$ [Hz] which have been chosen arbitrarily and η [-] is a dispersion parameter which can vary from 1 for a non-dispersive medium to 0 for a infinitely dispersive medium.

The Jonscher model was fitted to the electromagnetic response of concrete by Ihamouten et al. [133] [132] and was found to produce good results over a large frequency band (50 MHz to 850 MHz). This model will also be used as part of this thesis and it is discussed in more detail in Chapter 4 with respect to electromagnetic investigation techniques.

3.3.2 Composite material models

For composite materials such as soils and concrete, numerous mixing models and empirical models have been proposed over the past century [149] [245] [110]. Composite material models estimate the bulk electromagnetic properties as a function of the constituents of the material, where their respective electromagnetic properties, volume fractions and geometry are used as variables. These models can take the form of analytical mixing models or empirical models. Compared to phenomenological models, the input variables of composite material models are more easily related to saturation, porosity and interconnectedness of the pore system, which are indicators associated with the condition and quality of concrete (refer to Chapter 2.

In concrete, the solid components are usually non-conductive and have low, frequency-independent dielectric constants compared to that of the liquid phase. The pore solution therefore has the most important influence on conductivity, permittivity and its frequency dependency. For the application of mixing and empirical models to concrete it is therefore often defined as a two phase composite. The two phases are either taken as the aggregates and the hardened cement paste [191] or in the case of saturated conditions, the solid phase comprising the aggregates and cement gel and the liquid phase being the pore solution [223].

3.3.2.1 Maxwell's rule and variants

Simple two phase models to describe the electromagnetic response of composite materials as a function of its constituents date back to Maxwell. Maxwell's effective medium approximation for spherical inclusions immersed in a diluted solution (Maxwell's rule) is the starting point of most composite medium theories related to engineering materials [197] [245] [284]. The rule, also known as the Maxwell-Garnett theory, has been widely applied to materials consisting of solid inclusions suspended in a matrix phase as follows:

$$\varepsilon_e = \varepsilon_m + \frac{3\,\Upsilon\,\varepsilon_m(\varepsilon_i - \varepsilon_m)}{\varepsilon_i + 2\varepsilon_m - \Upsilon(\varepsilon_i - \varepsilon_m)} \tag{3.47}$$

where ε_e is the bulk effective permittivity of the composite material, ε_m and ε_i are the effective permittivities of respectively the host matrix and the inclusions and Υ [-] is the fraction of the inclusions. The effective permittivity was defined by Maxwell in terms of the direct current conductivity σ_{DC}, omitting the frequency dependent interfacial polarisation:

$$\varepsilon_e = \varepsilon'_e + j\left(\varepsilon''(\omega) + \frac{\sigma_{DC}}{\varepsilon_0\omega}\right) \tag{3.48}$$

Numerous models have been derived from Maxwell's rule aiming to accommodate more phases, the effects of grain shape, interfacial lamination, textural effects [103] [141] [110] or to simplify the model for static conditions [242].

The self similar model (SSM), also known as the differential effective medium model proposed by Sen et al. [242], aims to include environmental effects of spherical particle layers surrounding the solid inclusions to improve on Maxwell's rule:

$$\left(\frac{\varepsilon_e - \varepsilon_s}{\varepsilon_w - \varepsilon_s}\right)\left(\frac{\varepsilon_w}{\varepsilon_e}\right)^{\frac{1}{3}} = \phi \tag{3.49}$$

where ε_w is the permittivity of water, ε_s is the permittivity the solid phase and ϕ is the bulk porosity, thus the water fraction. The variant has been found particularly suited for saturated rocks and was also applied to saturated concrete by Robert [223] to determine its complex permittivity.

If it is assumed that the aggregates in concrete have a conductivity of zero, Maxwell's rule for conductivity at static conditions derived from Equation (3.47) can be simplified as follows:

$$\sigma_{DC} = \frac{2\,\sigma_m\,\Upsilon_m}{3 - \Upsilon_m} \tag{3.50}$$

where the σ_{DC} is the bulk conductivity, σ_m and Υ_m are respectively the conductivity and fractional volume of the hardened cement paste matrix.

Though these variants of Maxwell's rule have been widely used for different kinds of composites, the relationship is analytically defined for spherical inclusions of which the fraction is small compared to the matrix fraction. It is therefore in most cases not well suited for application on concrete composites [283], though it has been applied for mortars with evenly distributed particles and in saturated conditions with some success [284].

Monfore [191] proposed a model based on Equation (3.50) where the conductivity is a function of the effective path length L_e [m] in the direction of conduction:

$$\sigma = \frac{\sigma_m \, \Upsilon_m}{L_e} \tag{3.51}$$

where σ is the bulk conductivity for direct or alternating current. The tortuosity Γ [-], which is an indication of the interconnectedness of the pores in a composite material, can be related to the effective path length (actual path length) to the apparent path length L [m] (shortest linear distance in the direction of current flow):

$$\Gamma = \left(\frac{L_e}{L}\right)^2 \tag{3.52}$$

Monfore obtained good results for saturated mortar and concrete mixes. However, the disadvantage of this approach is that the effective path length and conductivity of the matrix phase are in general not practical parameters to determine.

3.3.2.2 Lichtenecker-Rother model and variants

To accommodate more phases, Lichtenecker and Rother [158] proposed the following relationship for the effective permittivity of multi-phase composites:

$$\varepsilon_e^{\propto} = \sum_{j=1}^{N} \Upsilon_j \varepsilon_j^{\propto} \tag{3.53}$$

where Υ_j is the volumetric fraction and ε_j is the effective permittivity of each phase j and $\propto$ is a mixing coefficient that depends on the layering of the components with respect to the direction of the applied electromagnetic field, ranging from -1 to 1.

The complex refraction index model (CRIM) [225] is a special case of the Lichtenecker-Rother model for isotropic materials where $\propto = 0.5$:

$$\sqrt{\varepsilon}_r = \sum_{j=1}^{N} \Upsilon_j \sqrt{\varepsilon}_j \tag{3.54}$$

Taking $\propto$ as 0.5 is substantiated by the square root relationship between the dielectric constant and wave velocity and can be derived theoretically from travel time calculations [225].

Equation (3.54) is referred to as the CRIM for complex permittivity and as the time propagation (TP) model for low loss mediums where $\varepsilon_r \approx \varepsilon_r'$ [149].

Though Equations (3.47), (3.49), (3.53) and (3.54) are defined for the frequency dependent permittivity, these composite material models can only approximate the permittivity at the frequency for which the input components are representative. These mixing models do not account for interfacial polarisation due to the Maxwell-Wagner effect (refer to Section 3.2.2) caused by surface charge build-up related to the ion content of the solution. They therefore in general fail to explain the dependence on salinity of the dielectric constant of materials at low frequencies [115] [223]. Mixing models therefore perform considerably better for low loss environments (where $\sigma < 0.01$ S/m) [175] and have been applied to concrete with some success [115] [96].

Attempts have been made to combine mixing models with the capability of phenomenological models to take dielectric losses of simple materials into account. This has been achieved by modelling the complex permittivity of the component that displays lossy behaviour e.g. the liquid phase, using the Debye's model (3.43), whilst assuming the non-lossy phases to have a constant permittivity. Robert [223] finds combining the SSM and CRIM models with the Cole-Cole model (Equation (3.45)) for saturated concrete underestimates the real part of the permittivity and overestimates the imaginary part at low frequencies but yields reasonable results.

3.3.2.3 Archie's law and variants

Another approach that is widely used pertaining to the conductivity of composite geological and engineering materials is the formation factor approach. This approach has been proposed by Archie [33] and is based on the relationship between the bulk conductivity of a porous material and the conductivity of the fluid with which it is saturated. The approach relates the measured bulk conductivity of the composite to its porosity as follows:

$$\mathcal{F} = \frac{\sigma_w}{\sigma_b} = \frac{\mathfrak{a}}{\phi^{\mathfrak{m}}} \tag{3.55}$$

where $\mathcal{F}$ [-] is Archie's formation factor, σ_w [S/m] is the conductivity of the pore solution, σ_b [S/m] is the saturated bulk conductivity, ϕ [-] is the porosity, $\mathfrak{m}$ [-] is the cementation exponent and $\mathfrak{a}$ [-] is the lithology factor.

The relationship is empirical with the exponents being estimated by linearising the relationship to a Log-Log scale:

$$Log(\mathcal{F}) = Log(\mathfrak{a}) - \mathfrak{m}Log(\phi) \tag{3.56}$$

The cementation exponent $\mathfrak{m}$ is related to the shape and distribution of the capillary pores and is therefore dependent on the permeability and the compaction of the composite material. Values for $\mathfrak{m}$ have been widely studied for geological materials and are estimated to range from approximately 1.3 to 2.2 for most rocks [240]. The lithology factor $\mathfrak{a}$ is meant to correct for variation in the microstructure of the composite. Studies on early age low W/C concretes (W/C = 0.5 to 0.8) by Whittington et al. [284], Morelli and Forde [194] and Hunkeler [131] found $\mathfrak{m}$-values to range from 1.2 to 1.96 and $\mathfrak{a}$-values in the order of 1. Tumidajski et al. [264] found that Archie's law applied well to hydrated cement pastes and mortars at 28 days with W/C-ratios equal to 0.35, finding $\mathfrak{m}$-values of 2.14 and 2.55 and $\mathfrak{a}$-values close to 1. Tumidajski et al. [264] also note the porosity dependence of $\mathfrak{m}$, therefore implying its mix dependency although in general $\mathfrak{m}$-values of 2 and $\mathfrak{a}$-values of 1 are assumed for concrete.

Archie's law also accommodates unsaturated conditions by means of a factor $S^{\mathfrak{n}}$ where S [-] is the degree of saturation and $\mathfrak{n}$ [-] is the saturation exponent. The saturation exponent is meant to take into account the influence of the coverage of the pore walls by pore solution on bulk conductivity. At lower saturations the interconnectedness of the pore solution coating the pore walls depends on the "oilyness" or wettability of the material. More isolated droplets will form in a material with low wettability which will therefore not contribute to the conductivity [89]. The higher the saturation, the less evident this influence becomes, leading to a non-linear increase in conductivity as a function of degree of saturation. The exponent $\mathfrak{n}$ was estimated as 2 for unconsolidated sands by Archie [33] and as not many studies have been conducted to determine $\mathfrak{n}$ for concrete specifically, a value of 2 is usually also assumed for concrete. Archie's law including the correction for saturation is defined as:

$$\sigma_b = \frac{1}{\mathfrak{a}} \sigma_w \phi^{\mathfrak{m}} S^{\mathfrak{n}} \tag{3.57}$$

Though Archie's law is seen as purely empirical [283], Sen et al. [242] have shown analytically that the self same model for the static limit derived from Equation (3.49), is equivalent to Archie's law for the saturated case where $\mathfrak{m} = 3/2$ and $\mathfrak{a} = 1$:

$$\sigma_{DC} = \sigma_w \phi^{\frac{3}{2}} \tag{3.58}$$

The analytical proof of Archie's law is also maintained by Glover [110], who finds that the cementation factor $\mathfrak{m}$ can be equated to the mixing coefficient $\propto$ in the Lichtenecker-Rother model (Equation (3.53)) for special cases. Glover thus expands Archie's law to more than one conducting phase [111], a model that has been successfully applied to high permeability concretes [198] [199].

A disadvantage of the application of Archie's law to concrete is the uncertainty related to the prediction of the conductivity of the pore solution [251]. Due to the chemical complexity

of hardened cement paste, the properties of the pore solution after saturation will not be the same as the external solution. This is due to various factors related to the cement content and type [131], binding of ions [251] (also refer to Chapter 7). Therefore several other aspects also influence bulk conductivity and permittivity of concrete to a greater or lesser extent that is not accounted for by the parameters in the laws discussed in this section. However, Archie's law remains widely applied to cementitious materials for the estimation of resistivity [106] [79] [277].

3.4 Influences on the electromagnetic properties of concrete

It is clear from the composite model theories discussed in Section 3.3.2 that conductivity and permittivity are functions of the electromagnetic properties of the pore solution and the concrete mix components, their fractional volumes and thus the condition of the concrete. Although these models have been applied to concrete (mostly pastes and mortars at saturated states), it is acknowledged that they perform less well for concrete than for rocks and soils, which are chemically simpler in general.

Many empirical studies have thus been conducted to relate the dielectric properties of concrete (usually expressed as bulk resistivity and bulk dielectric constant) to common engineering parameters associated with either the environment to which the concrete is exposed or the concrete mix components and proportions. The influence of moisture condition, chloride content, temperature as well as mix related factors such as aggregates, paste volume fraction, water cement ratio and cement type on the electromagnetic properties of concrete is therefore discussed in this section.

3.4.1 Influences related to environmental exposure

3.4.1.1 Moisture condition

The moisture condition of concrete can be either described in terms of degree of saturation S, water content w or relative humidity RH as discussed in Chapter 2.2.1.3. Empirical studies are therefore found based on all of these indicators, but in general degree of saturation is preferred.

Moisture condition has a particularly significant influence on the electromagnetic properties of concrete. Its influence on resistivity is due to the electrolytic nature of the conduction in

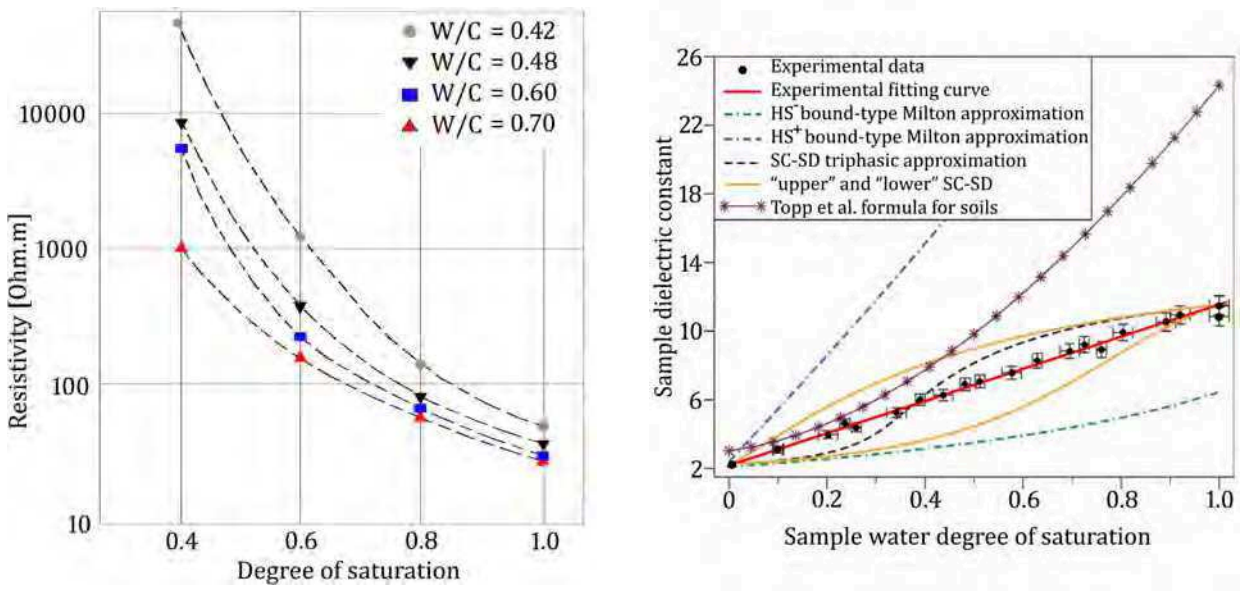

(a) (b)

Figure 3.3: The effect of degree of saturation on (a) DC-resistivity [108] for various concretes and (b) dielectric permittivity at 33 MHz [97] for soils (in red) also showing results from several models.

concrete [191], with the charge carriers being the ions present in the liquid phase. The presence of moisture also influences permittivity due to the high dielectric constant of water in comparison to that of the solid phases in concrete and also the interfacial polarisation caused by the charge build up between the solid and liquid phases as discussed in Section 3.3.2.

Research on the sensitivity of resistivity to concrete moisture condition yields varying results in terms of the reported relationship between the two parameters. The majority of studies [108] [166] [231] [154] [237] find a strong power-law increase in resistivity as the degree of saturation decreases (Figure 3.3(a)). This corresponds well to the power law dependency of conductivity to degree of saturation suggested by Archie in Equation (3.57). In contrast to Archie's law, Jacobs et al. [136] state a linear relationship between conductivity and water content for concretes over a range of W/C-ratios. This shows that there is still some uncertainty as to the form of the relationships between moisture condition and resistivity (or conductivity) for concrete.

Hunkeler [131] finds that the conductivity of concrete becomes effectively zero at relative humidities lower than approximately 40% and Larsen et al. [154] similarly show that the conductivities of a range of high performance concretes are reduced to zero at below 30% to 60% degree of saturation. This is in spite of the fact that there still remains a significant amount of water in the pore system at these moisture conditions. Whiting and Nagi [283] suggest that the remaining water becomes "non-conductive" because of surface forces

preventing ions from transporting current. Though Archie's law (Equation (3.57)) makes provision for the non-linear relationship between degree of saturation and resistivity through the saturation factor n, it does not account for the conductivity being zero at non-zero water contents.

Research relating the dielectric constant of concrete to moisture condition has not been so widely conducted as for resistivity, although many studies have been performed on other porous media. Villain et al. [274] [276] found a strong linear relationship between the degree of saturation and the dielectric constant at 33 MHz and 1 GHz for 9 different concretes. Fen et al. [97] also found a strong linear relationship for rocks in contrast with many empirical models developed for soils as shown in Figure 3.3(b). Similarly Bungey et al. [53] report a linear relationship at a frequency of 1 GHz for both low density and high density concretes. It therefore seems that there is general consensus that the dependency of the dielectric constant on degree of saturation is linear for concretes and rocks.

Very few studies are available on the effect of moisture on the loss factor related to concrete. Dérobert et al. [87] performed a parametric study on various concretes to assess the statistical significance of several parameters to the complex permittivity of concrete. A quadratic relationship between the loss factor and degree of saturation is suggested. The same study also highlights the strong frequency dependency of complex permittivity at low frequencies due to dielectric losses related to the presence of water in concrete, as can be seen in Figure 3.4(b) [87].

3.4.1.2 Chloride content

The presence of chlorides in concrete significantly increases the conductivity of the pore solution. An increase in the chloride content of the pore solution therefore leads to lower bulk resistivities. Studies by Hunkeler [131] and Sbartaï et al. [237] found the resistivity of concrete to be very sensitive to chloride content at lower concentrations (approximately 0 to 30 g/L NaCl) and less so at higher concentrations as can be seen in Figure 3.4(a). This corresponds to the linear relationship between conductivity and chloride content as described by Archie's law (3.57). On the other hand, Henry [122] and Polder [214] state that the influence of chloride on bulk resistivity is relatively small if compared to that of the other parameters such as moisture condition and parameters related to the pore structure. It is assumed that the relationship between chloride content and resistivity will change as the degree of saturation decreases and more chlorides precipitate. For low saturations, with little conducting ions remaining, the influence of chlorides on resistivity becomes negligible.

Chloride content also has a significant influence on permittivity, though not much work is

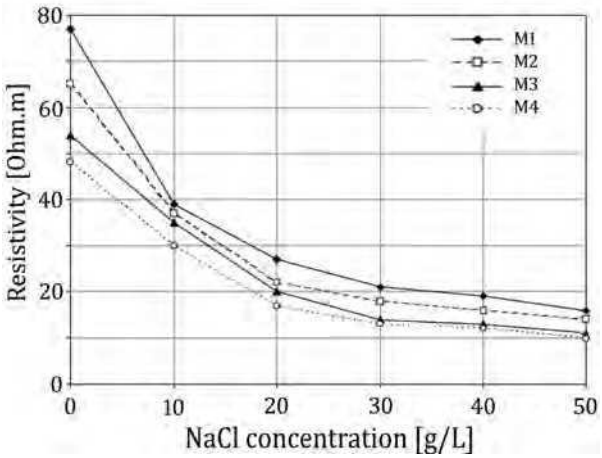

(a)

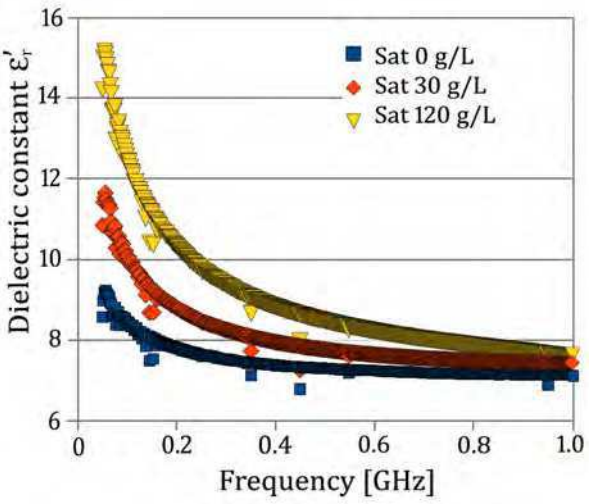

(b)

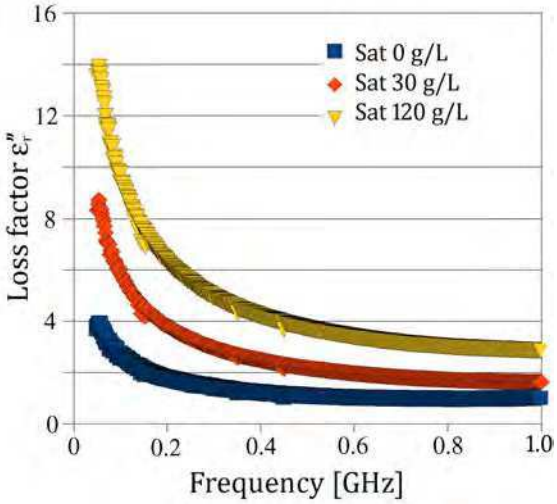

(c)

Figure 3.4: The effect of chloride content on saturated concrete for (a) DC-resistivity [237] for mixes M1, M2 M3 and M4 (W/C-ratios = 0.5, 0.6, 0.7 and 0.78) and complex permittivity over a frequency band from 50 MHz to 1 GHz for the (b) dielectric constant ε_r' and (c) loss factor ε_r'' at three different chloride concentrations (0 g/L, 30 g/L and 120 g/L) [87].

available on the exact nature of the relationship pertaining to concrete. Dérobert et al. [87] assume a linear relationship between chloride content and the dielectric constant and loss factor for saturated concrete. Similarly to resistivity the influence of chlorides also becomes negligible at dry conditions. The effect of chlorides on permittivity also shows strong frequency dependency and the effects of interfacial polarisation and dielectric losses at low frequencies lead to permittivity being far superior to that of uncontaminated pore solutions. This is even though the permittivity of saline water is comparable to that of pure water [175]. A study by Dérobert et al. [87] shows the marked increase in dielectric constant due to an increase in chloride content and also its significant frequency dependency 3.4(b).

The loss factor as in Figure 3.4(c) is especially sensitive to chloride content, approximately double that of the dielectic constant at low frequencies in this case.

3.4.1.3 Temperature

The electrical resistivity of concrete is influenced by temperature due to its effect on the behaviour of the ions in the pore solution. An increase in temperature leads to lower resistivity because of an increase in the mobility of the ions and thus their ability to transport current [214]. An increase in temperature also causes a decrease in the viscosity of the pore solution and to bound ions being released leading to changes in ionic concentrations [283] [209]. The approach often adopted to account for temperature changes is to standardise the measured resistivity to a reference temperature e.g. 20°C by applying a correction [181]:

$$\rho_T = \frac{\rho_{T(ref)}}{1 + \wp(T - T_{ref})} \tag{3.59}$$

where ρ_T [Ω.m] is the measured resistivity at temperature T, $\rho_{T(ref)}$ [Ω.m] is the resistivity at reference temperature T_{ref} and $\wp$ is the temperature coefficient for the material, with the temperatures and coefficient being either in Celsius or Kelvin. Values for $\wp$ [-] for saturated concrete are reported to be between 0.022 and 0.030 per °C [68]. This equation is however only applicable within a limited range of approximately ±5°C around the reference temperature.

The effect of temperature on materials can also be described by the Arrhenius equation [181] [283] which was proposed for resistivity by Rasch and Hinrichsen [218]:

$$\rho_T = \rho_{T(ref)} e^{\xi_a / U(\frac{1}{t} - \frac{1}{T_{ref}})} \tag{3.60}$$

where resistivities ρ_T and $\rho_{T(ref)}$ are at absolute temperatures T and T_{ref} [K], ξ_a [kJ/mol] is the activation energy for the conduction process, U is the gas constant (8.314 J/mol/K).

The activation energy ξ_a required for conductance in concrete has been widely studied [68] with values for saturated concrete varying from approximately 17 to 27 KJ/mol depending on water cement ratio, cement type, age, temperature range etc. Results from Hope et al. [127] for a range of concretes at saturated conditions are presented in Figure 3.5(a). The relationship conforms well to Equation (3.60) with ξ_a being equal to 24 KJ/mol. For convenience, the ratio ξ_a/U is often referred to as the activation constant [181] [49].

The degree of saturation and chloride content of concrete can cause the temperature dependency of resistivity to be more pronounced, especially at low saturations [136]. Due to the many influences affecting the temperature dependency of concrete resistivity, an empirical

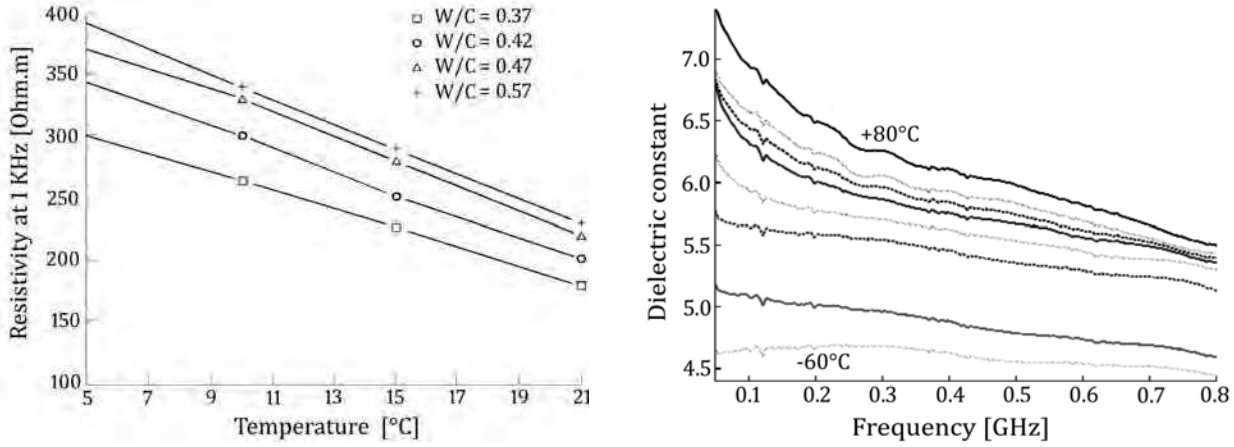

(a) (b)

Figure 3.5: The effect of temperature on concrete for (a) resistivity at 1 KHz for concretes with various W/C-ratios [127] and (b) dielectric permittivity from 45 MHz to 800 MHz (contours increasing from -60°C to +80°C) [145].

approach is often adopted whereby resistivity is corrected by 3% for saturated and 5% for dry concrete per degree temperature change [214] [49].

As temperature affects conductivity, it is implied that there should be some influence on the complex permittivity of concrete as well due to interfacial polarisation, particularly at low frequencies and for saturated conditions. The temperature dependency of the dielectric constant of water (water having a major influence on the permittivity in concrete) has been widely confirmed for large temperature variations [266]. However, the temperature dependency of the dielectric constant of concrete is in general assumed to be negligible [115] for the temperature variations experienced in practice.

Though not much research has been conducted on the temperature dependency of concrete permittivity, results from a study by Kim et al. [145] on concrete specimens from existing bridge decks are presented in Figure 3.5(b). The tests were performed for temperatures ranging from -60°C to +80°C and it was confirmed that the sensitivity of the dielectric constant is much greater at low frequencies than high frequencies. The variation in the dielectric constant over a more general range of temperatures from 0°C to +40°C was approximately 2% per degree at 100 MHz and 0.5% per degree at 800 MHz. A recent study by Saussol et al. [233] found values in the same range as Kim et al. [145] for various concretes at temperatures between 5°C and 50°C at frequencies of 33 MHz and 1GHz. This suggests that the effect of temperature on the dielectric constant of concrete may not be as insignificant as is generally assumed.

3.4.2 Concrete mix components and proportions

3.4.2.1 Properties of the aggregates

Rigorous specifications to ensure the quality of natural aggregates used in concrete related to soundness, density and water absorption [254] usually lead to their porosity and water content being low. Sound natural aggregates from igneous origin such as basalt, dolerite, granite, greywacke, quartzite, hornfels, flint and massive sandstones and limestones are generally used in concrete. The resistivity of these aggregates will differ according to their inherent porosities and ability to absorb water [191]. The resistivity of marbles and granites can exceed that of sandstones and limestone with between one and two orders of magnitude (refer to Table 3.1).

However, compared to the resistivity of the hardened cement paste phase containing the pore solution, the resistivity of the aggregates is essentially infinite [283]. It is therefore generally assumed that the effect of the type of aggregate on the bulk resistivity is negligible. An increase in the volume fraction of the aggregates will have a slight increase in the resistivity [130], but even for the densest possible aggregate packings the interconnectedness of the pore space will still be governed by the properties of the hardened cement paste rather than the aggregates.

On the contrary, the dielectric constant of the aggregates contributes greatly to the bulk permittivity of concrete [60] [87]. Though the permittivity of the aggregates are low as compared to that of the pore solution, the influence is significant due to the large aggregate volume fraction (generally between 60% and 80% in common concretes). This is especially evident for bulk dielectric constants at high frequencies and low saturations. Some values for the dielectric constants of dry and wet rock types used in concrete are presented in Table 3.2(a). Values for minerals that typically form part of these rocks are also listed in

Table 3.1: Approximate bulk resistivity of rocks commonly used in concrete with respect to their water absorption capacity [191].

Type	Absorption % by weight	Resistivity [Ω.cm] at 1000kHz
Sandstone	9.2	18 000
Limestone	6.0	30 000
Marble	0.9	290 000
Granite	0.34	880 000

Table 3.2: Typical dielectric permittivities of (a) aggregates and fluids found in concrete at 100 MHz as determined for different states by Davis and Annan [83] and Daniels [81] and (b) minerals found in concrete aggregates as determined by Olhoeft [208] adapted from [175].

(a) Material	Dielectric constant ε'_r	
	Davis and Annan [83]	Daniels [81]
Air	1	1
Fresh water	80	81
Sea water	80	
Fresh water ice	3 - 4	4
Sand (dry)	3 - 5	4 - 6
Sandstone (dry)		2 - 3
Sandstone (wet)		5 - 10
Limestone		
Limestone (dry)	4 - 8	7
Limestone (wet)		8
Granite	4 - 6	
Granite (dry)		5
Granite (wet)		7
Salt (dry)	5 - 6	4 - 7

(b) Mineral	Dielectric constant ε'_r
	Olhoeft [208]
Albite	7.0
Calcite	6.4
Olivine	7.2
Orthoclase	5.6
Pyroxene	8.5
Quartz	4.5
Halite	5.9
Ice	3.4

Table 3.2(b). It can be seen that the variations in the dielectric constants of these rocks are primarily determined by mineralogy and to a lesser extent by their moisture condition. Values vary between approximately 4 for quartzitic and 8 for calcitic rocks.

3.4.2.2 Mix parameters related to pore structure

In the following section the mix components and properties that determine the bulk porosity and the interconnectedness of the pore structure are shortly discussed. Of these the hardened cement paste and its volume fraction, water/cement-ratio, type of cement and degree of hydration are the most important. They are interrelated as the hardened cement paste volume governs the bulk amount of pores, whereas W/C-ratio and type of cement determine the size and the amount of pores within the hardened cement paste. The W/C-ratio and type of cement also determines the rate of hydration [201] and the extent to which hydration is completed [200] [18]. The pore structure is of particular interest in terms of the electromagnetic properties of concrete, as it plays a major role in the moisture content and transport properties of the concrete.

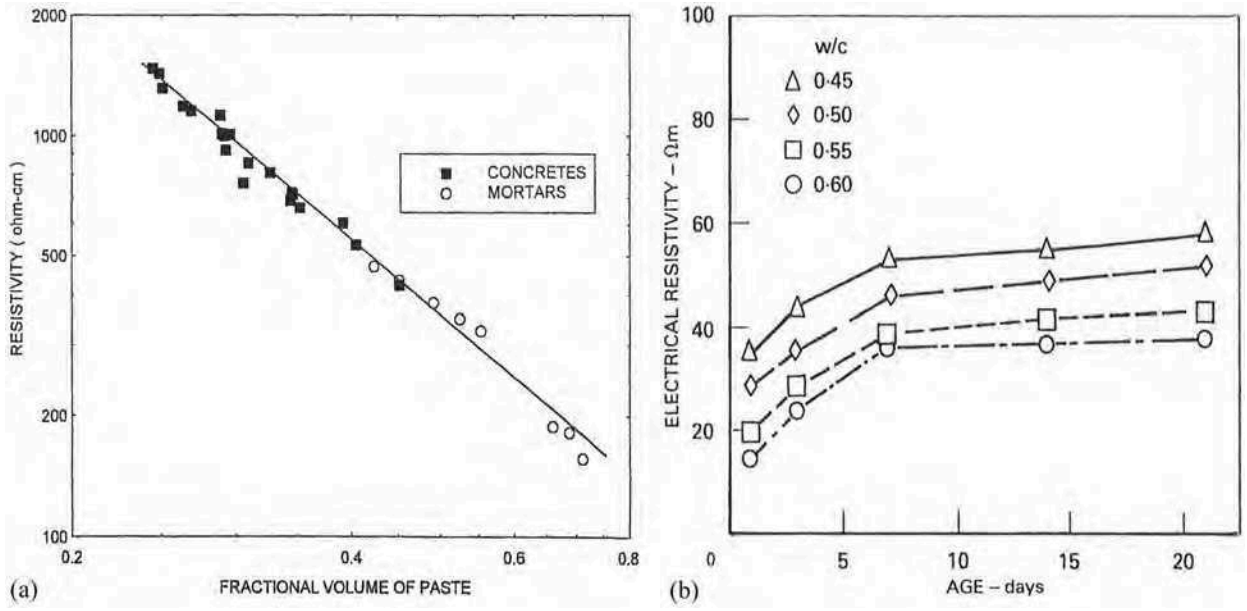

Figure 3.6: Results from two studies on saturated concretes and mortars showing the effect or (a) cement paste fraction [179] and (b) ageing, i.e. hydration [130], on resistivity.

3.4.2.2.1 Hardened cement paste fraction

The hardened cement paste (HCP) consists of the cement gel and the capillary pores as described in Chapter 2.2.2. The cement gel itself has a high resistivity in the same range as that of the aggregates and a relatively low dielectric constant in the order of 10 [254] [96]. This is in spite of the presence of the gel water, which is mostly bound, preventing ionic conduction and molecular polarisation. The dielectric constant of bound water is estimated at approximately 4 instead of the 80 for free water [219]. The unhydrated cement also has a high resistivity and dielectric constant in the order of that of quartz.

Because the pore solution in the hardened cement paste facilitates conduction and leads to the majority of the polarisation, the fraction of hardened cement paste in the concrete has a significant influence on its dielectric properties. McCarter [179] finds bulk resistivity is to a large extent governed by the fractional volume of the cement paste. His results show a strong linear relationship for saturated mortars and concretes at a constant W/C-ratio, as shown in Figure 3.6(a). In terms of permittivity, little research could be found that exclusively studies its dependency of the paste volume, although the relationship is evident due to the link between paste volume and porosity (and therefore moisture condition).

3.4.2.2.2 Water/cement-ratio

Water/cement-ratio (W/C-ratio) is a fundamental mix parameter which governs the microstructure of the hardened cement paste and the properties of its interstitial solution [283] [201]. As the W/C-ratio increases, the porosity of the hardened cement paste, the average pore radii and pore connectivity increase and the gel density decreases [131].

It has been shown by numerous studies [191] [253] [130] that the resistivity of hardened cement paste decreases with increasing W/C-ratio ratio as can be seen in the results in Figures 3.4(a), 3.3(a) and 3.5. It is also noted that the influence of W/C-ratio on resistivity is dependent on the degree of saturation [108]. At high saturations resistivity is significantly less sensitive to W/C-ratio than at low saturations as can be seen in Figure 3.3(a).

Permittivity is also sensitive to W/C-ratio due to its influence on the hardened cement paste's porosity. Dérobert et al. [87], as part of the statistical analysis of the influence of various parameters on complex permittivity, suggest a linear relationship between W/C-ratio and the dielectric constant. However, a quadratic relationship is suggested for the loss factor and it is also noted that there is a significant interaction between W/C-ratio and degree of saturation.

3.4.2.2.3 Degree of hydration and mineral admixtures

There are several other factors that also contribute the reduction of porosity and permeability of the hardened cement paste. As concrete ages hydration takes place and the capillary pores are gradually filled with cement gel as described in Section 2.2.2.2. The resistivity of young concrete will therefore increase [130] (Figure 3.6(b)) and the permittivity will decrease [223] and finally stabilise after a time which is dependent on the W/C-ratio. Though the EM response of the mature concrete is governed by the W/C-ratio, it is also significantly influenced by the type of cement (i.e. if it is a blend of OPC and mineral additions or not). The addition of GGBS and fly-ash will lead to a denser hardened cement paste as explained in Chapter 2.2.2.1, and thus higher resistivity and lower permittivity than regular OPC concretes.

Mineral admixtures also have a major influence on the rate of hardening of the concrete paste. For OPC concrete most of the hydration will take place during the first 28 days [98] [181]. Though GGBS and fly-ash may slow down initial hardening of the concrete, the reduction of the pore size will continue long after that of OPC concretes due to secondary hydration and pozzolanic reactions. This will also lead to lower ion concentrations [42]. It is generally accepted that the effect of chemical admixtures such as water reducers, set

retarders and accelerators on the electromagnetic properties are small in comparison to those of mineral admixtures [283].

3.5 Conclusion

In this chapter the fundamentals of electromagnetics were presented as related to concrete in the context of this thesis. The two electromagnetic properties that are relevant to concrete are complex permittivity and conductivity (usually expressed as its inverse resistivity). Various approaches to the modelling of these electromagnetic properties, and the success of these models pertaining to concrete, were also discussed. Lastly literature on empirical studies that had been conducted to assess the influence of concrete condition, constituents and mix parameters on its electromagnetic response was reviewed.

From this chapter it is clear that the complexity of the electromagnetic response of materials and the ease with which it can be interpreted increase with the complexity of the material. Both analytical and empirical models developed to describe electromagnetic behaviour have limitations when applied to concrete due to the chemical complexity of its constituents and the interactions between them. However, there is no denying that the electromagnetic response of concrete is dependent on its moisture and chloride condition as well as parameters related to its inherent properties, though there is not always consensus as to the form of the respective dependencies.

The electromagnetic evaluation of concrete is therefore of much interest in terms of concrete durability and health assessment making additional research to improve the reliability of models and the interpretation of results essential. During the experimental work presented in the second part of the thesis the relationships between DC-resistivity, the dielectric constant and loss factor and parameters linked to concrete condition and quality will be further investigated. The influence on the electromagnetic response due to interactions between the different indicators will also be studied, an aspect that has not often been explicitly addressed in literature.

Chapter 4

EM measurement techniques

4.1 Introduction

The principles of electromagnetics have been used in geophysical exploration since the early 1900's. A wide range of methods have been developed and are discussed in several textbooks [211] [88] [258]. The techniques are traditionally classified as either electrical or electromagnetic methods, depending on whether the response is obtained by direct application of current or by induced wave propagation in the medium. As problems with concrete durability became evident, some of these methods have also been adapted for the investigation of concrete structures. The electrical and electromagnetic properties of concrete were studied for the first time during the 1950's and 1960's [117] [262] [205] [122] [191] when field techniques from geophysics were used for the investigation of bridge decks, with wider application on concrete structures following soon after in the 1970's and 1980's [29] [267] [173].

In the following sections an overview is given of the electromagnetic techniques available to determine the resistivity and permittivity of concrete, as is relevant to this thesis. Semi-destructive techniques for concrete specimens in controlled laboratory conditions and related surface techniques for non-destructive testing on site are discussed as both form part of the scope of this thesis.

4.2 Electrical resistivity investigation techniques

Techniques to evaluate the electrical resistivity ρ of concrete (preferred to its inverse conductivity, $\sigma = 1/\rho$) have been widely applied to concrete as part of durability assessment

regimes. Direct current (DC)-resistivity (or low frequency alternating current resistivity) is commonly used due to its simplicity and reliability. Though it is possible to determine frequency dependent resistivity of concrete over the entire spectrum using impedance spectroscopy [282] [248], it is difficult to implement in situ [176] and is therefore not included in the techniques presented here.

The term DC-resistivity in the context of this thesis will usually in truth refer to low alternating current resistivity for reasons explained in Section 4.2.1.3. The following sections will discuss the principles of methods pertaining to DC-resistivity which are used as part of this thesis and the factors that influence measurement accuracy. The techniques presented here are also developed further as part of the experimental work and which will be discussed in detail in Chapter 6.

4.2.1 Laboratory investigation

4.2.1.1 Principles

For direct current applications, i.e. static electrical field, the conditions as described in Equations (3.39) to (3.42) are applicable. The constitutive relationship for resistivity (Equation (3.5)) also known as Ohm's law in vector form, can therefore be written as follows in terms of resistivity ρ [Ω.m]:

$$\boldsymbol{J}_c = \sigma \boldsymbol{E} = \frac{1}{\rho}\boldsymbol{E} \tag{4.1}$$

The resistivity of concrete can be easily determined for specimens of simple geometries (with constant cross-sections over their length) if the current is regarded as uniform, given the assumptions in terms of linearity, homogeneity etc. hold, as presented in Section 3.2.5. The electric field can be expressed as the gradient of a scalar potential V from Equation (3.39) [258]:

$$\boldsymbol{E} = -\nabla V \tag{4.2}$$

The substitution of (4.1) in (4.2) yields:

$$\boldsymbol{J}_c = -\frac{\nabla V}{\rho} \tag{4.3}$$

By assuming that the specimen has a uniform cross-section and that a uniform electric field is applied at each end, the current lines thus being parallel to the length of the specimen, Equation (4.3) can be integrated over the length of the specimen to yield Equation (4.4).

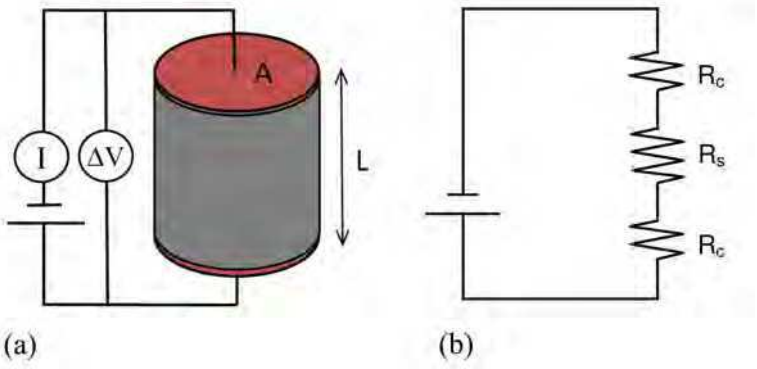

Figure 4.1: 2-electrode resistivity measurement showing a diagram of (a) the application of Ohm's law for specimens of uniform cross-section and (b) contact and specimen resistance.

$$\boldsymbol{J}_c = \frac{I}{A} = \frac{\delta V}{\rho L} \tag{4.4}$$

where I [A] is the current applied over the cross-sectional area A [m^2], L [m] is the length of the specimen and δV [V] is the potential difference as shown in Figure 4.1(a).

Solving for ρ gives:

$$\rho = \frac{A}{L}\frac{\delta V}{I} \tag{4.5}$$

with

$$\rho = G\frac{\delta V}{I} = GR \tag{4.6}$$

where G is defined as the geometric factor (also referred to as the cell constant) specific to a particular geometry and electrode configuration and R [Ω] is the electrical resistance.

This approach has been widely applied in laboratory conditions for the determination of bulk resistivity of homogeneous concrete cubes and cores [181] [214] [203] [118] [250] and is referred to as the end-to-end two point electrode method using Ohm's law. The method will be henceforth referred to as the *2-electrode method* implying that current is applied and potential difference is measured by electrodes located at the same position at the extremities of the specimen.

4.2.1.2 Contact resistance

When current is injected through electrodes placed directly in contact with the semiconductor such as concrete, a contact resistance is produced at the electrode-specimen interface [65]. This contact resistance is a function of the area of the electrode, the surface texture and moisture condition of the specimen. The contact resistance will thus increase as the

contact area of the electrode decreases [69] and can significantly interfere with measurement or render it impossible [155].

For the 2-electrode method as described above, the measured resistance R includes both the resistance of the specimen R_s and the contact resistances R_c (as in Figure 4.1(b), assuming the same contact resistance at both electrodes) thus giving:

$$R = R_s + 2R_c \tag{4.7}$$

In order for the measurements to be reliable, the contact resistance must be sufficiently low when compared to the specimen resistance [190] [195]. Several approaches have been suggested to improve the contact between metal electrodes and concrete such as covering the contact area with graphite or mortar pastes [191] [284], electrolytic solutions [121] [203], conductive gels [172], conductive paints [154] or water impregnated sponges [154] [250]. Newlands et al. [203] found in a study on sponge contacts that the contact resistance is also dependent on the conductivity of the contact solution and on the pressure exerted on the contact.

The presence of an unknown contact resistance resulting from the varying efficacy of the different contacts can therefore lead to significant uncertainty in terms of the final bulk resistivity. Larsen et al. [154] compared two different contact conditions (conductive paint and lead electrodes with wetted sponges) and report that although the results for saturated conditions compare well, the scatter increases as the bulk resistivity of the specimen increases as in Figure 4.2. Newlands et al. therefore highlight the need to standardise the 2-electrode resistivity method in terms of contact conditions but as far as could be determined, this has not yet been achieved.

4.2.1.3 Electrode polarisation

Polarisation of the electrode-specimen interface is another phenomenon that can lead to measurement errors, especially at direct current conditions. This polarisation should not be confused with the polarisation within the concrete which is associated with its permittivity, i.e. its ability of storing electric energy. In this case it is mainly a boundary effect of electrochemical origin known as a "double layer capacitance" [55] that is caused by the differences in ability of charge to be transported by the electrode (metallic conduction) or by the pore fluid (electrolytic conduction). This leads to the development of a counter voltage which is a function of the surface area of the electrode in contact with the specimen and the amount of current applied [190]. Monfore [191] proposes to determine this "counter voltage" due to polarisation for static conditions by applying two respective voltages of

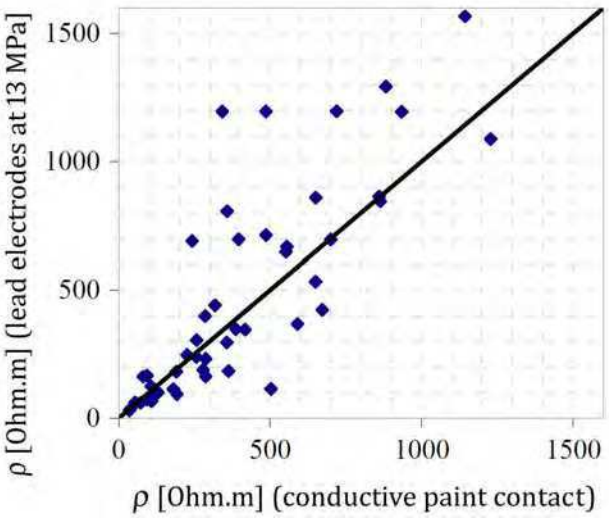

Figure 4.2: Comparison of 2-electrode resistivity [Ω.m] measured with two different contact conditions [154], i.e. conductive paint and lead electrodes.

different magnitudes and measuring the resulting currents (assuming that the voltage due to polarisation is constant over the range of applied voltages):

$$I_1 = \frac{V_1 - V_p}{R} \tag{4.8}$$

$$I_2 = \frac{V_2 - V_p}{R} \tag{4.9}$$

where V_1 [V] and V_2 [V] are two applied voltages of different magnitudes, I_1 [A] and I_2 [A] are the measured currents, V_p [V] is the polarisation voltage and R [Ω.m] is the resistance of the specimen.

V_p and R can then be solved for from Equations (4.8) and (4.9):

$$V_p = \frac{V_2 I_1 - V_1 I_2}{I_2 - I_1} \tag{4.10}$$

and

$$R = \frac{V_2 - V_1}{I_2 - I_1} \tag{4.11}$$

Monfore found good results for saturated concrete. However, after a voltage is applied some time is required for polarisation to take effect and the current to stabilise. Hansson and Hansson [120] address the problem of polarisation in concrete by determining current as a function of the applied potential and then taking the slope of the relationship as the DC-resistance of the specimen. This is also a time-consuming solution.

These approaches are laborious when many measurements are required or if there are time constraints. Most researchers thus rather attempt to avoid polarisation effects than to compensate for them as suggested by Monfore. This is achieved by applying low frequency alternating current (AC) instead of direct current. This approach, proposed by Hammond and Robson [117], is now commonly used as it is widely reported that resistivity is not significantly frequency dependent at the low frequencies [185]. It is suggested that AC currents at a frequency of less than 1000 Hz approximate DC-resistivity [209], although this frequency is dependent on the specimen dimensions and the electrode configuration.

4.2.1.4 Variability

Research that has been done on the variability of 2-electrode resistivity testing of concrete by Newlands et al. [203] found the percentage difference of results obtained by two laboratories for the resistivity of the same saturated concrete specimens to be less than 10%. The variability of 2-electrode bulk resistivity was also assessed in an extensive round-robin testing program as part of a joint transportation research program of the Indiana Department of Transport [250] according to the specifications of ASTM C802-09a [13]. Saturated specimens were fitted with plate electrodes and sponge contacts wetted with a standard solution at a standard pressure to minimise variation due to contact resistance. An AC current of 13 Hz was used to minimise polarisation effects. The coefficient of variation for laboratory testing was found to be between 3% and 5% and for multi-laboratory between 7% and 14%. It should however be noted that results on specimens of unsaturated condition can display significantly higher with variation of between 30% or 40% being acceptable [154].

4.2.2 In situ investigation

4.2.2.1 Homogeneous conditions

For in situ measurement of resistivity the application of Ohm's law used for laboratory investigation described in Section 4.2.1 is not practical. Surface investigation methods using point electrodes are more suitable. This approach has been employed in geophysics for many years [258] by using Ohm's law for a single point current source C_1 applied to the surface of a homogeneous isotropic halfspace (subsurface) as in Figure 4.3(a), assuming the return electrode C_2 is at an infinite distance. In this case, the current flows radially away from the source, and the potential varies inversely with distance from the current source.

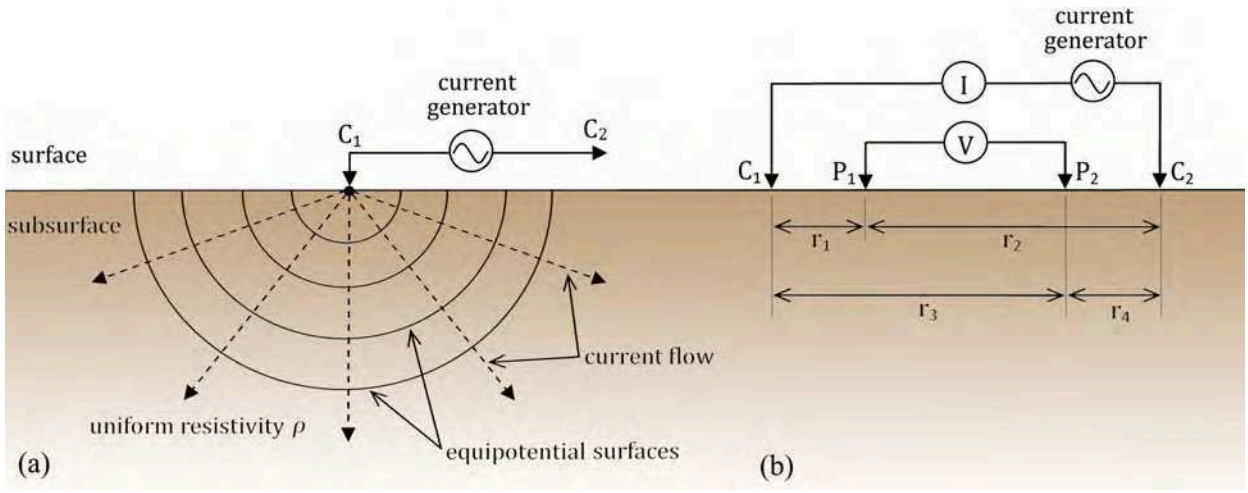

Figure 4.3: Representation of (a) a single current source with current lines and equipotential distribution and (b) a 4-point measurement configuration for a homogeneous halfspace, after [258].

The potential at a point in the subsurface can be expressed as follows:

$$V(r) = \left(\frac{I\rho}{2\pi}\right)\frac{1}{r} \tag{4.12}$$

where r [m] is the distance from the source.

In practice at least two current injection electrodes are used creating a potential symmetrical distribution in the subsurface described by Equation (4.13):

$$V = \frac{I\rho}{2\pi}\left(\frac{1}{r_1} - \frac{1}{r_2}\right) \tag{4.13}$$

where r_1 [m] and r_2 [m] are the distances of the point in the subsurface for which the potential V is determined from current injection point C_1 and C_2 respectively.

Most often though, four points are used where current is injected through two electrodes (C_1 and C_2) and the potential difference δV [V] is measured between the two remaining electrodes (P_1 and P_2) with r_1 to r_4 [m] defined as in Figure 4.3(b):

$$\delta V = \frac{I\rho}{2\pi}\left[\left(\frac{1}{r_1} - \frac{1}{r_2}\right) - \left(\frac{1}{r_3} - \frac{1}{r_4}\right)\right] \tag{4.14}$$

Various versions of the 4-point method have been used in geophysics, but for application on concrete the Wenner-configuration [281] is almost exclusively used. For this configuration the electrodes are arranged in a line and spaced at a constant distance a [m]. Current is then injected at the outer electrodes and potential difference measured over the inner electrodes. Equation (4.15) can therefore be rewritten as follows analogous to Equation (4.5):

$$\rho = 2\pi a\frac{\delta V}{I} \tag{4.15}$$

where $2\pi a$ is the geometric factor G for a Wenner configuration.

The measured potential difference is a response to the electric properties of a certain volume of the subsurface that is affected by the applied electric field. The contribution of these properties to the measured response decreases gradually over what is referred to as the *influence depth* until it becomes negligible. Various conventions have been adopted to approximate a depth that can be associated with the surface response, with an approach based on the Fréchet derivative for the homogeneous halfspace being the most widely accepted [163].

The Fréchet derivative is a sensitivity function that indicates the degree to which a change in resistivity at a point in the subsurface will influence the potential measured on the surface [182]. Thus, the higher the value of the sensitivity function, the greater the influence of that particular region of the subsurface on the potential reading. For the one-dimensional case, the sensitivity of surface potential between two points P_1 and P_2 spaced a [m] apart can be expressed as a function of the depth z [m]. This function is known as the "depth investigation characteristic" [226] and is shown in Figure 4.4 for the Wenner configuration:

$$F_{1D}(z) = \frac{2}{\pi} \frac{z}{(a^2 + 4z^2)^{1.5}} \tag{4.16}$$

In Figure 4.4 both the investigation depth associated with the maximum value of sensitivity and the median of the sensitivity function are indicated. Though the maximum value has been used by some authors as representative of the depth of investigation of an array, the use of the median depth of investigation proposed by Edwards [95] has been shown to be the most robust approach. For the homogeneous halfspace the median depth of investigation z_e of a Wenner array was determined by Edwards [95] as $0.519a$, thus being approximately half of the electrode spacing a.

Wenner measurements as per Equation (4.15) are widely used in situ as a non-destructive method to assess corrosion risk [214] [30] [230] [217] [162], as described in Section 2.3.6.2, even though in situ concrete often does not conform to the criteria of the homogeneous infinite halfspace for which the relationship is defined. Polder [214] proposes to compensate for local inhomogeneities by taking enough measurements to have a representative data-set (recommending at least five measurements). Wenner measurements have also been used for quality control on concrete specimens as an alternative to conventional diffusion tests as described in Section 2.3.6.1 [195] [162]. In this case a new geometric factor is calculated to account for the boundary effects of the specimens, an approach which will be explained in detail in Chapter 6.

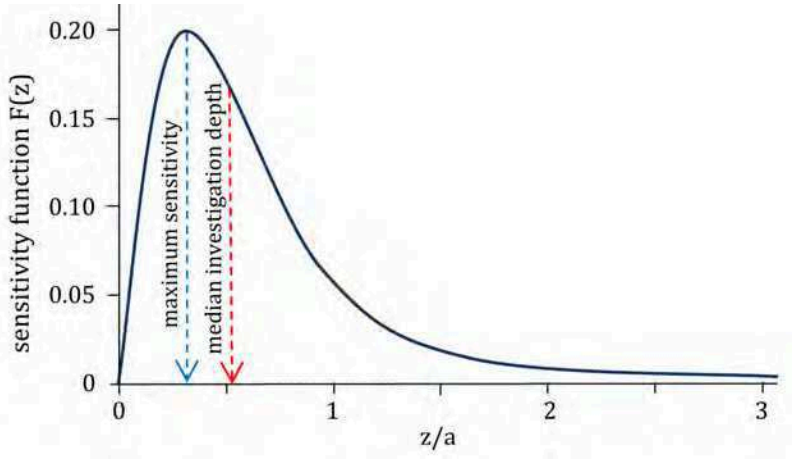

Figure 4.4: The one dimensional Fréchet sensitivity function for the Wenner configuration as function of depth over electrode spacing z/a [163].

4.2.2.2 Non-homogeneous conditions

Property gradients are often present in the subsurface, as is the case with in situ concrete due to the presence of moisture, chloride etc. In order to characterise the concrete in terms of these gradients, multiple resistivity measurements at various electrode spacings are required. If the theory and conventions for the homogeneous halfspace (Equations (4.12) to (4.16)) are applied for non-homogeneous conditions such as this, the measured surface resistivities are referred to as *apparent* resistivities and their associated median depths of investigation as the *pseudodepths* [163]. These apparent resitivities are a qualitative indication of the true subsurface resistivity as they are responses to an investigated volume of unknown properties and size. In order to obtain a representative model of the non-homogeneous subsurface resistivity an inversion process is required.

Geophysical inversion is thus used to approximate subsurface resistivity from a set of surface measurements. The goal is to find a mathematical model of which the synthesised responses will approximate the actual observed data. Firstly, the mathematical relationship between the electrical properties of the model (*model parameters*) and its synthetic responses (*model responses*) must be found. This is referred to as the forward problem and can be either a continuous or a discretised function. In geophysical inversion the model is usually discretised into a grid with resistivity values assigned to each cell serving as the model parameters [163]. The model responses are then derived from the model parameters using a finite element or finite difference procedure [246].

Because the forward problem is usually non-linear, a non-linear inversion protocol has to be applied. Amongst various available options, the most popular with regards to geophysical

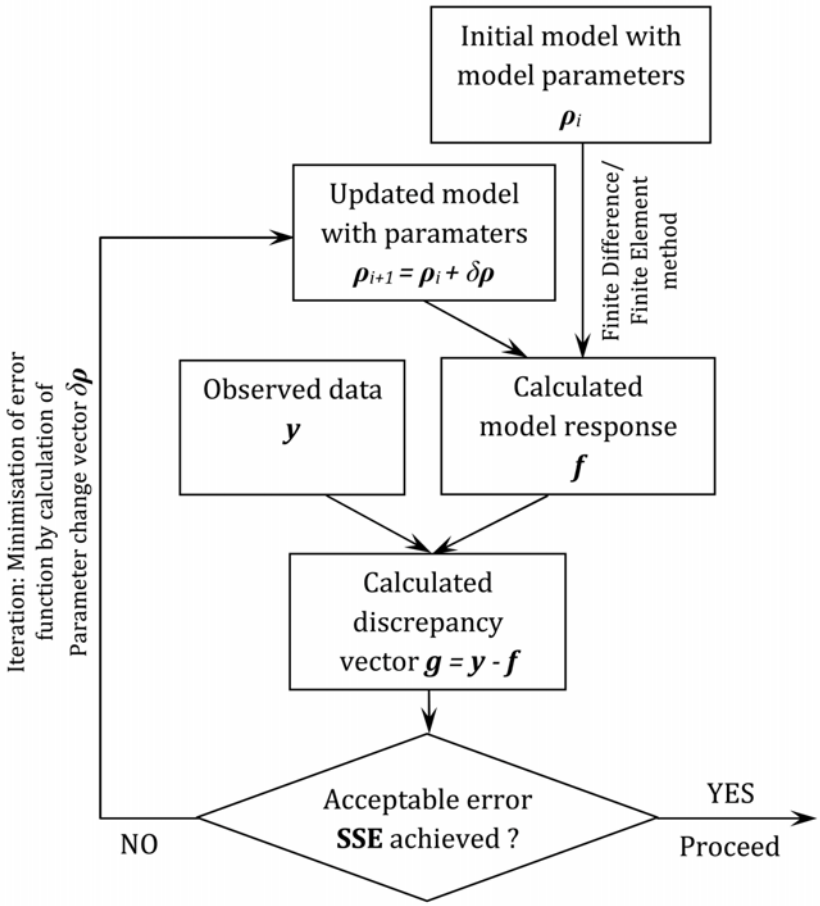

Figure 4.5: Diagram detailing the inversion process to obtain a representative subsurface model from observed apparent resistivity data.

inversion is the minimisation of a linearised damped least squares objective function [164]. This implies an iterative procedure where the errors between the model responses and observed apparent resistivity data are minimised by adjusting the model parameters as demonstrated in Figure 4.5.

This is usually achieved by starting from an initial model and using least squares optimisation to obtain model responses that are within acceptable limits from the observed data. This approach can be expressed using matrix algebra as follows [163]:

$$\begin{array}{lll} \textit{Observed data}: & \textit{Model responses}: & \textit{Model parameters}: \\ \boldsymbol{y} = \begin{bmatrix} y_1 \\ y_2 \\ \vdots \\ y_n \end{bmatrix} & \boldsymbol{f} = \begin{bmatrix} f_1 \\ f_2 \\ \vdots \\ f_n \end{bmatrix} & \boldsymbol{\rho} = \begin{bmatrix} \rho_1 \\ \rho_2 \\ \vdots \\ \rho_p \end{bmatrix} \end{array}$$

where n is the number of measurements and p is the number of model parameters.

The difference between the observed data $\boldsymbol{y}$ and the model response $\boldsymbol{f}$ is given by the discrepancy vector $\boldsymbol{g}$.

$$\boldsymbol{g} = \boldsymbol{y} - \boldsymbol{f} \tag{4.17}$$

The sum of squares error SSE is then determined by the following equation:

$$SSE = \boldsymbol{g}^T\boldsymbol{g} = \sum_{i=1}^{n} g_i^2 \tag{4.18}$$

To optimise the model, the sum of squares error is minimised by adapting the model parameters in an iterative process using the Gauss-Newton least squares equation [161] as in Equation (4.19) where $\delta\boldsymbol{\rho}$ is the model parameter change vector:

$$\mathbf{J}^T\mathbf{J}\delta\boldsymbol{\rho}_i = \mathbf{J}\boldsymbol{g} \tag{4.19}$$

where $\mathbf{J}$ is the $m \times n$ Jacobian matrix of first order partial derivatives that describes the change in the model responses due to a change in each model parameter:

$$\mathbf{J} = \begin{bmatrix} \frac{\partial f_1}{\partial \rho_1} & \frac{\partial f_1}{\partial \rho_2} & \cdots & \frac{\partial f_1}{\partial \rho_p} \\ \frac{\partial f_2}{\partial \rho_1} & \frac{\partial f_2}{\partial \rho_2} & \cdots & \frac{\partial f_2}{\partial \rho_p} \\ \vdots & \vdots & \ddots & \vdots \\ \frac{\partial f_n}{\partial \rho_1} & \frac{\partial f_n}{\partial \rho_2} & \cdots & \frac{\partial f_n}{\partial \rho_p} \end{bmatrix} \tag{4.20}$$

The model is then adjusted by means of the calculated model parameter change vector for the next iteration $k+1$:

$$\boldsymbol{\rho}_{k+1} = \boldsymbol{\rho}_k + \delta\boldsymbol{\rho}_k \tag{4.21}$$

The least squares optimisation is often an "ill-posed" inverse problem [261], but this can be overcome partially by using a dampening factor that minimises the "roughness" of the model, usually by constraining the range of model parameter change vector [188].

The visual representation of inverted resistivities as a two dimensional (2D) or three dimensional (3D) image, is referred to as electrical resistivity tomography (ERT). ERT has been successfully applied in various fields of which geophysical investigation, industrial process tomography and medical imaging are examples. However, it has been rarely applied to concrete and then mainly for the detection of mechanical defects [80] [128] and reinforcement [139] [244]. ERT will be employed as part of this thesis to investigate property gradients in concrete, particularly in terms of moisture and chloride content (refer to Chapter 9.3).

4.3 Dielectric permittivity investigation techniques

Background on the techniques used to determine relative permittivity as part of this thesis will be given in this section. Laboratory techniques are capable of determining the frequency dependent complex permittivity of concrete over a wide frequency range. By using different in situ techniques the dielectric constant of concrete can also be determined at different frequencies on site. The frequency dependence of the electromagnetic behaviour of contaminated concrete can thus be exploited to assess its condition. Progress has also been made to determine the complex permittivity of in situ concrete by Ihamouten et al. [134] [132], and this work is implemented as part of this thesis.

4.3.1 Laboratory investigation

4.3.1.1 Coaxial electromagnetic cell

A popular method for the determination of the frequency dependent complex permittivity of concrete specimens with simple geometries is the co-axial transmission line technique [63] [74] [23] [221]. This technique can cover a wide frequency range up to several GHz, but usually requires specimens to be carefully machined and prepared and is therefore only suited for use in controlled laboratory conditions.

A cylindrical closed-ended coaxial transmission/reflection line (hereafter referred to as the *EM-cell*) is used as part of this thesis for the investigation of concrete specimens in the laboratory. This EM-cell was developed by IFSTTAR as part of a research program from 2002 to 2005 by Adous et al. [20] [19]. It is suited for determining the complex permittivity of cylindrical specimens and cores of dimension 75 mm dia.$\times$70 mm and with a maximum aggregate size of 20 mm, over a frequency band of 50 MHz to approximately 1.6 GHz. It therefore accommodates most common concretes over a frequency band where the permittivity of concrete displays dispersive behaviour if it contains water and chlorides.

The EM-cell makes use of a vector network analyser (VNA), connected to a coaxial conical transition and cylindrical coaxial line which consists of two concentric conductors separated by air. The coaxial line is in turn linked to a cylindrical waveguide containing the specimen as illustrated in Figure 4.6(a) and (b). The device operates on the principle that the reflection coefficient of the propagating wave due to the interface between the coaxial line and the specimen can be related to the complex permittivity of the material.

The principal mode of electromagnetic wave propagation in a coaxial line is the transverse electromagnetic (TEM) mode. When the wave reaches the interface of the specimen, a part

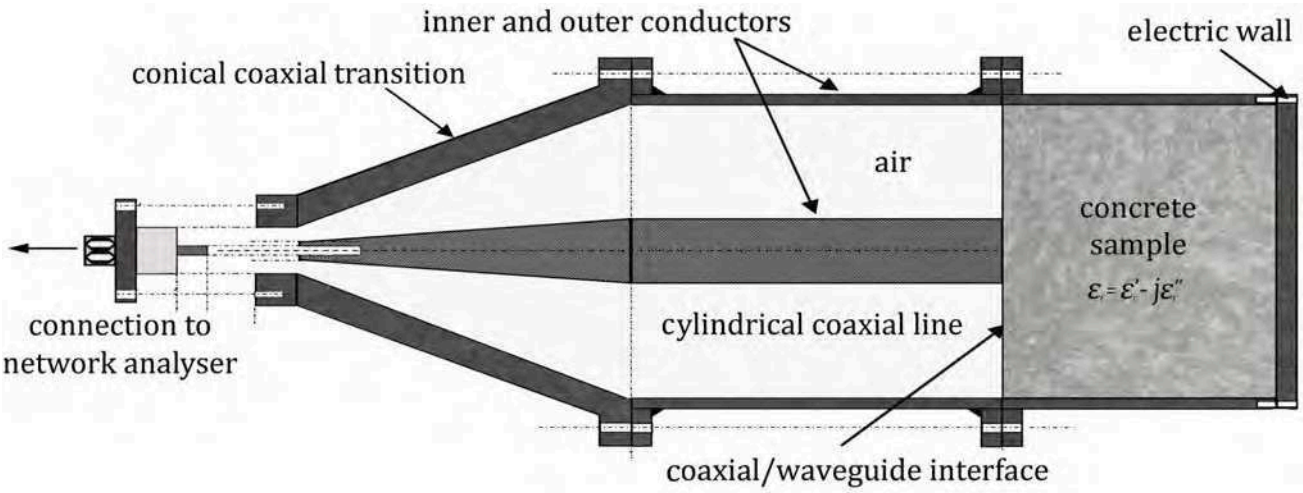

(a)

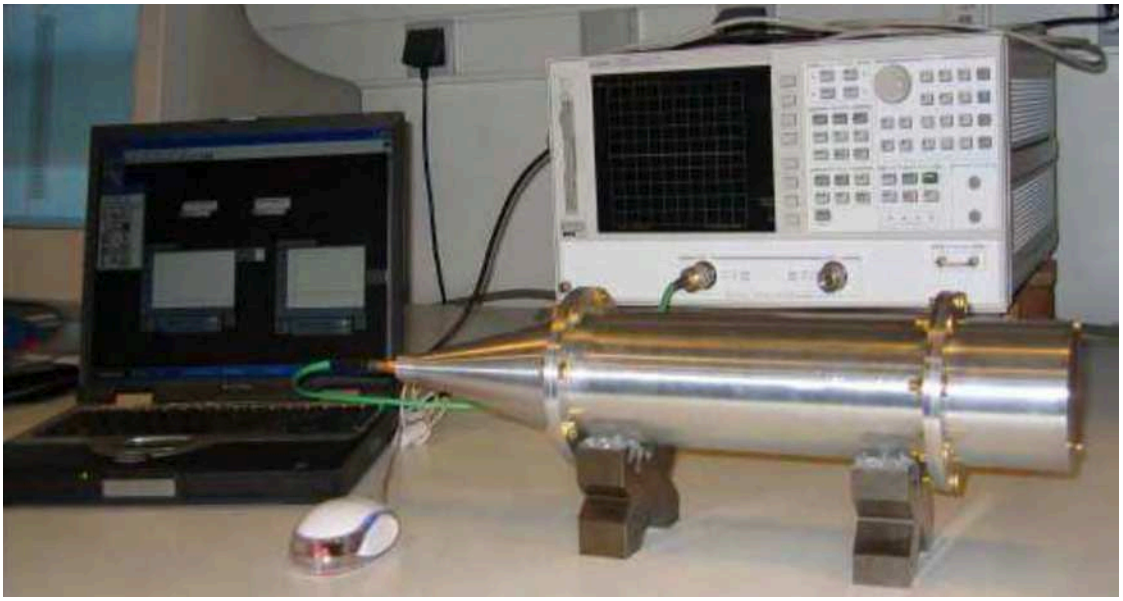

(b)

Figure 4.6: (a) Schematic showing the section of the conical coaxial transition and cylindrical coaxial line and (b) the complete setup for the EM-cell showing the vector network analyser and software tools, after [20].

of the energy is reflected back in the form of a TEM fundamental propagating mode and the other part is localized at the discontinuity in the form of higher transverse magnetic (TM) evanescent modes. To determine the reflection coefficients of the TEM and TM modes Adous et al. [20] [19] use a mode-matching technique based on the EM field continuity equations, the total reflection condition at the waveguide metallic wall termination and orthogonality properties of modes in both the coaxial and waveguide regions. As the reflection coefficient cannot be related analytically to the complex permittivity due to the complexity of the electromagnetic analysis, an inversion process is implemented using numerical optimisation based on the iterative Newton-Raphson approach [216].

Before measurement starts, the device is calibrated by creating three different conditions (short circuit, open and load) at the coaxial/waveguide interface for which metallic plate, empty specimen holder and Teflon specimens are used respectively. The EM-cell has been used successfully in several studies [87] [133] [132], and yields good results if care is taken with the preparation of the specimens in terms of homogeneity and geometry and if good contact at the interface is ensured. Ihamouten et al. [133] have however shown that the operational upper frequency limit (which depends on the specimen size and the real part of its permittivity) can be considerably less than 1.6 GHz and can be as low as 550 MHz for highly water and chloride contaminated specimens. They ascribe this to a resonance phenomenon that adversely influences the measurements causing them to be numerically unstable above this limit. Care was therefore taken as part of this thesis to avoid the inclusion of unstable results at higher frequencies. It was however observed that the frequency dependency of the dielectric properties of concrete are usually limited to a range below the operational limit of the EM-cell.

4.3.2 In situ investigation

4.3.2.1 Capacitive probe

The permittivity of a material can also be determined by using the parallel plate capacitor technique [22] for simple geometries at low frequencies. When a uniform electric field is applied over a specimen of uniform cross-section, capacitance can be expressed by the following analytical expression derived from the constitutive equation (3.6) as follows:

$$\mathcal{C} = \frac{A}{d}\varepsilon_0\varepsilon_r' \tag{4.22}$$

where $\mathcal{C}$ [F] is the capacitance, A [m^2] is the surface area of the parallel electrodes and d [m] is the distance between the electrodes.

Due to its simplicity, the two-plate capacitive method has been adapted for surface measurement for in situ applications [263] [287], where the plates are located side by side. The analytical solution in Equation (4.22) is therefore no longer applicable, but a geometric factor G_c [-] related to the size and spacing of the plates can be determined by numerical modelling on materials of known permittivity:

$$\mathcal{C} = G_c \varepsilon_0 \varepsilon_r' \tag{4.23}$$

The capacitive probe system used as part of this thesis [86] is based on a system that was developed by LCP (*Laboratoire de Ponts et Chaussées*) in France in the 1970's for the investigation of cover concrete [263]. Similar systems have also been used for the measurement of water content in concrete [144].

The capacitive probe measurements are made by determining the resonance frequency of an oscillating circuit, where an alternating voltage (30-35 MHz) is applied over the electrodes placed on the investigated material as in Figure 4.7(a) and (b). The capacitance can be theoretically related to the resonance frequency as follows:

$$f_{osc} = \frac{1}{2\pi\sqrt{\mathcal{L}\mathcal{C}}} \tag{4.24}$$

where f_{osc} [Hz] is the resonance frequency and $\mathcal{L}$ [H] is the inductance.

However, the measured capacitance is not only dependent on the dielectric properties of the investigated material $\mathcal{C}_{mat}$ [F] but is also influenced by the ambient conditions $\mathcal{C}_{amb}$ [F]

Figure 4.7: (a) Capacitive probe used as part of this thesis with plate-electrodes of three different sizes: small, medium and large (b) illustration of the placement of the plate electrodes and their influence depths.

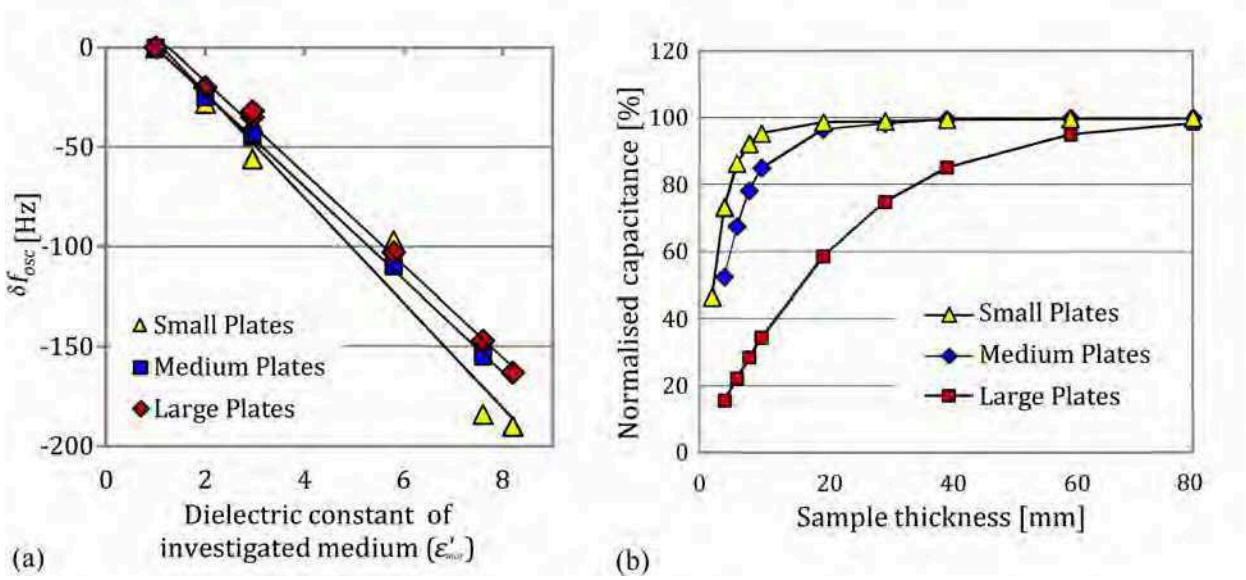

Figure 4.8: (a) Calibration curves for the three plate electrode sets of the capacitive probe and (b) the influence depth of each plate size [86].

(e.g. temperature, humidity properties of the probe) and can be written as:

$$\mathcal{C} = \mathcal{C}_{amb} + \mathcal{C}_{mat} \tag{4.25}$$

Substituting Equations (4.23) and (4.25) in Equation (4.24) and assuming that $\mathcal{C}_{mat} \ll \mathcal{C}_{amb}$, which is true for most engineering materials, the relationship between ε_{mat} and f_{osc} is written as follows:

$$f_{osc} = \frac{1}{2\pi}\sqrt{\frac{\varepsilon'_{amb}}{G_c \mathcal{L} \varepsilon_0}}\left(1 - \frac{\varepsilon'_{mat}}{2\varepsilon'_{amb}}\right) \tag{4.26}$$

where ε'_{amb} [-] is a virtual dielectric constant corresponding to the influence of the ambient conditions and ε'_{mat} [-] is the relative permittivity of the investigated material.

In practice, the measured resonance frequency is related directly to the dielectric constant my means of calibration on materials of known permittivity. This calibration process accounts for prevalent ambient conditions by not using an measures but rather the difference between the resonance frequency measured in air and on the material δf_{osc} [Hz]. The relationship between the measured resonance frequency shift δf_{osc} and the dielectric constant ε'_{mat} is assumed to be linear over the permittivity range of concrete as can be seen in Figure 4.8(a). The coefficients a and b are therefore experimentally fitted as per Equation (4.27).

$$\delta f_{osc} = a + b\varepsilon'_{mat} \tag{4.27}$$

The capacitive probe has three interchangeable sets of plate electrodes (small, medium and large) that enable measurement over increasing depth as demonstrated in Figure 4.7(c). Results from numerical modelling performed with the *Femlab* software package (Figure 4.8(b)) show the influence of the thickness of the investigated element on the measured capacitance (normalised with respect to the modelled capacitance of the element). It is therefore clear that the investigated depth increases as the size of the electrodes increase, as was also found in various other studies [86] [24].

Although an inversion process to quantitatively relate measured dielectric constants of a non-homogeneous concrete to depth has not yet been developed for the capacitive method, Figure 4.8(b) shows that the subsurface depth influencing the measurement for the respective plate electrodes vary from approximately 9 mm to 80 mm depending on the size of the electrodes. Boundaries located closer than this to the electrodes will therefore affect the measurement. Although these boundary effects can be corrected for, the experiments in this thesis are conducted on the basis that the specimens are large enough to avoid any influence from the boundaries.

4.3.2.2 Ground penetrating radar

The use of ground penetrating radar (GPR) for inspection of structural concrete has become well established over the last twenty years due to significant advances in acquisition capabilities of equipment and the ease and speed with which radar can be used on site [249]. Radar is a non-destructive surface technique that functions on the principle that electromagnetic wave pulses are transmitted through the investigated medium and the received signal is then analysed in terms of propagation velocity or amplitude.

The ground coupled GPR system consists of two bi-static antennae (dissociated transmitter and receiver) which are applied to the surface of the investigated medium. The antennae can either remain at a fixed offset to perform a GPR scan as in Figure 4.9(a), or for multi-offset measurements where the receiver is moved with respect to the transmitter (i.e. the wide angle reflection refraction (WARR) technique as in Figure 4.9(b)). The range of radar frequencies is usually between 0.1 and 3 GHz, with deeper penetration possible at lower frequencies but better resolution at high frequencies. For the investigation of concrete, antennae with central frequencies of 1.5 or 2.6 GHz are usually a good compromise [147].

Traditionally radar is used in reflection mode [52], where the transmitted EM signal is reflected from any interface where a strong contrast in dielectric properties occurs. This configuration has been widely used for characterisation of the geometric properties of concrete, such as element thickness, reinforcement location and void detection [71] [54] [171].

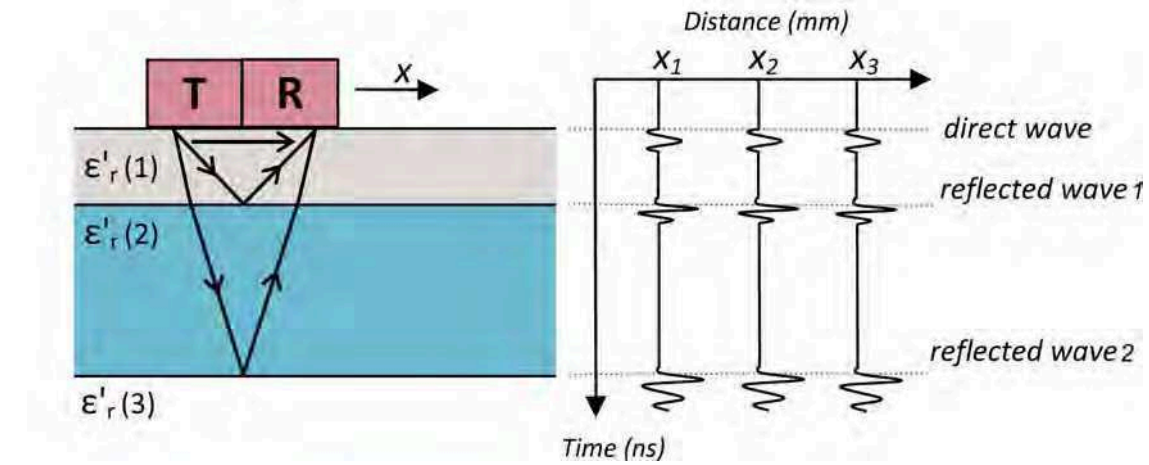

(a)

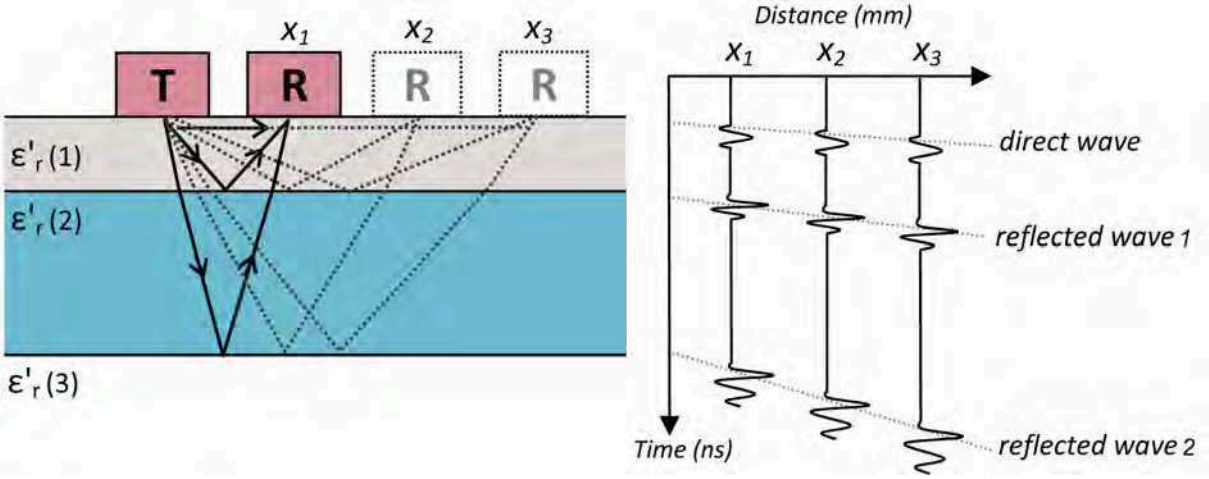

(b)

Figure 4.9: Schematic of GPR measurements with ground-coupled bi-static antennae on a medium with strong contrasting interfaces using (a) the fixed offset configuration and corresponding received signals for the direct and reflected waves and (b) a multi-offset (WARR) configuration and the signals for the direct and reflected waves, indicating the arrival time t as a function of the distance x between the antennae (T-R offset).

However, the velocity at which the wave travels in the medium and the extent to which the wave form is modified during propagation is also linked to the electromagnetic properties of the material. More recent studies have therefore focussed on using GPR for the evaluation of the condition of concrete in terms of water and chloride content [156] [236] [129] [273].

Though analysis of the reflected wave can be useful to determine concrete properties, it requires the presence of a reflector at a known depth. As this is not always the case, use of the direct wave (travelling from the transmitter to the receiver at the air/material interface as in Figure 4.9) to determine concrete properties in the absence of a reflector, has also

been investigated [237] [147]. The velocity of the direct wave is influenced by the properties of the upper part of the subsurface [148] and it has been theoretically proven to travel up to a depth approximately equal to one wave length [147]. This makes the direct wave particularly suited for investigation of the permittivity of cover concrete, an attribute that will be exploited as part of this thesis. The propagation velocity of the direct wave will therefore be used to determined the permittivity of concrete from GPR measurements in the chapters to follow.

The group velocity v_g of an electromagnetic pulse (the velocity of the pulse's *envelope* or overall shape) can be expressed as a function of the dielectric constant ε'_r and loss factor ε''_r, where $ç \approx 300$ m/s is the EM wave velocity in free space [86]:

$$v_g = \frac{ç\sqrt{2}}{\sqrt{\sqrt{\varepsilon_r'^2 + \varepsilon_r''^2} + \varepsilon'_r}} \tag{4.28}$$

In a medium where losses are low ($\rho > 100$ Ω.m [175]), as is usually the case for concrete in the range of radar frequencies, this equation can be simplified to:

$$v_g \approx \frac{ç}{\sqrt{\varepsilon'_r}} \approx \frac{x}{t} \tag{4.29}$$

where x [mm] is the propagation distance of the wave in the material between the transmitter and receiver and t [ns] is the propagation time.

For a low loss (non-dispersive) medium the estimation of the dielectric constant from the group velocity yields good results, especially if a multi-offset configuration is used [114]. However, when the medium has a high water and chloride content and is dispersive, the waveform of the signal is affected by dielectric losses. The wave envelope tends to "spread out" as the propagation distance increases due to the frequency dependency of the electromagnetic response. Errors may therefore occur because the exact arrival times of the signals can not be accurately determined by evaluating the amplitude peaks. This is demonstrated on synthetic data from Ihamouten [132] in Figure 4.10(a) to (d) where the group velocity estimated from the arrival times (Equation (4.29)) is compared to the phase velocity (velocity of an individual wave phase, e.g. the crest or trough). The phase velocity is determined by Jonscher's model (Equation (3.46)) which takes into account dispersion. The correspondence between the group and phase velocity is good for a low loss environment as in Figure 4.10(a) and (b) (where the dispersion parameter is high $\eta = 0.94$), but is poorer for a high loss medium ($\eta = 0.60$), where a significant discrepancy is observed between the two data sets (Figure 4.10(d)).

Instead of the using group velocity for dispersive media, the phase velocity is preferred [132], from which the frequency dependent permittivity can be determined using more elaborate

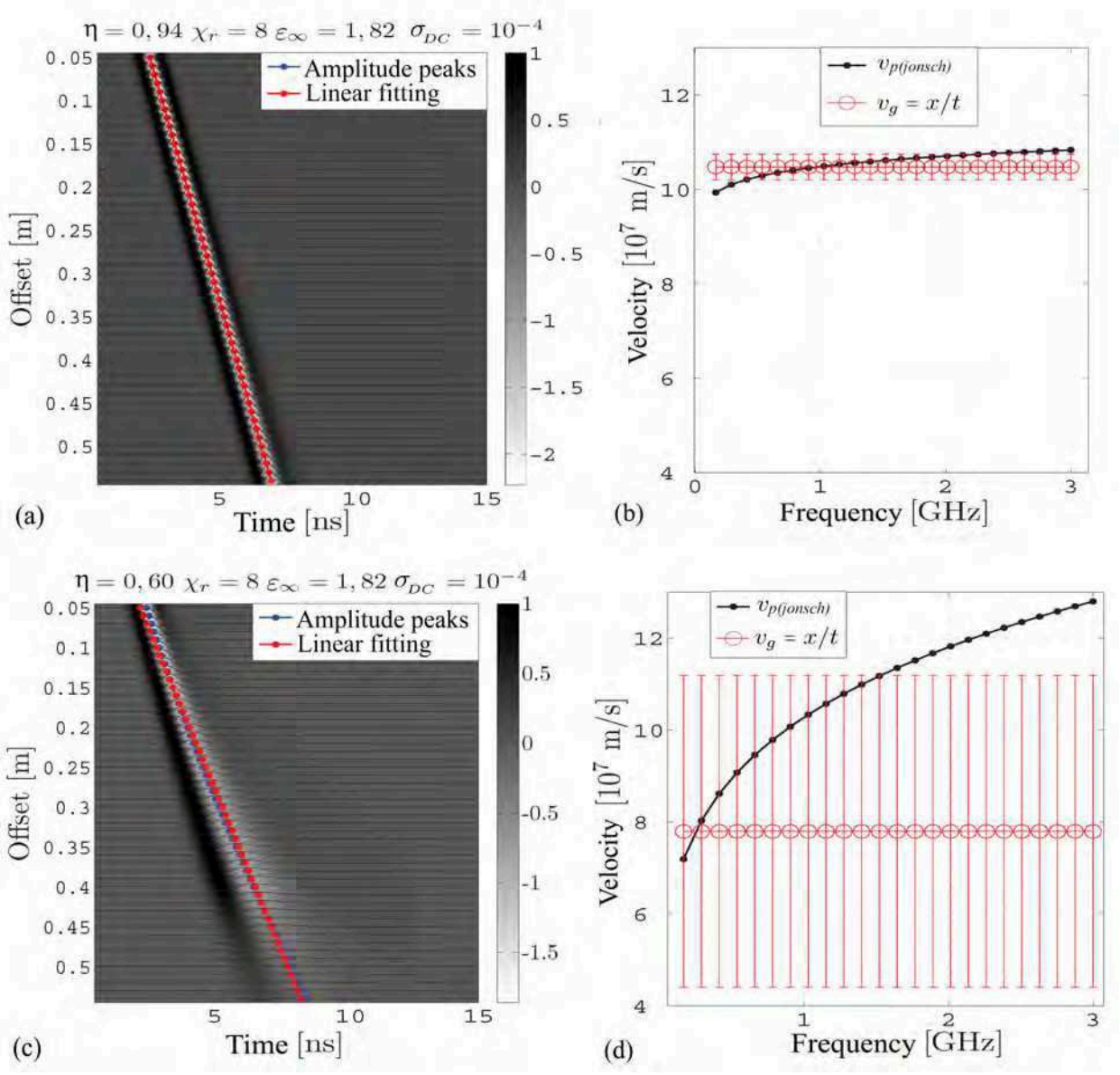

Figure 4.10: Synthetic radargrams (WARR configuration) for (a) a non-dispersive medium and (c) a dispersive medium, indicating the error between group velocity v_g estimated from the arrival time of the amplitude peaks and phase velocity $v_{p(jonsch)}$ determined by Jonscher's model for (b) the non-dispersive case (with dispersion parameter $\eta = 0.94$) and (d) the dispersive case with $\eta = 0.60$ [132].

methods. The "inter-coupling method" developed by Ihamouten et al. [134] [132] to determine frequency dependent complex permittivity from WARR (Figure 4.9) measurements is used as part of this thesis. The method is detailed in [132] and involves the transformation of the filtered direct wave signals (Figure 4.11(a)) from the time to the frequency domain by using a modified version of the two dimensional Fourier transform (referred to as the "$f - \beta$ transform") [28]. A dispersion curve (Figure 4.11(b)) is then generated which is a

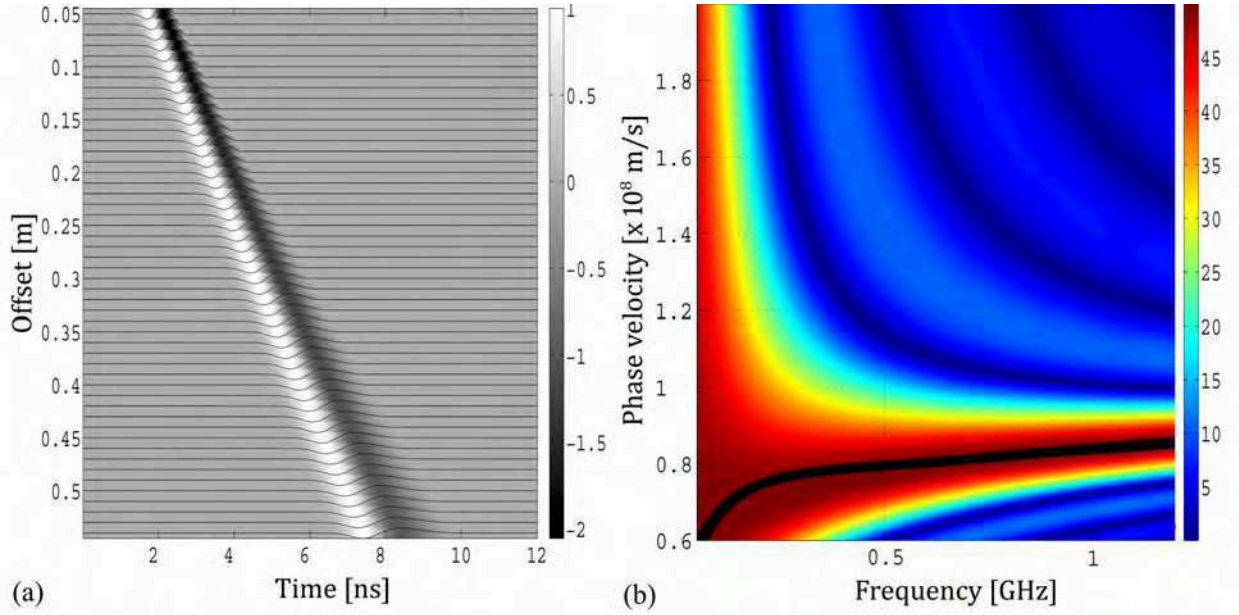

Figure 4.11: (a) A synthetic radargram demonstrating multi-offset (WARR) data in the time domain and (b) the corresponding dispersion curve showing the phase velocity as a function of frequency [132].

visual representation of the phase velocity v_p as a function of frequency, where the maximum amplitudes, defined by a colormap, represent the modes of the propagating wave [34] [35] [269].

The phase velocity is then used to find the frequency dependent phase constant β and attenuation constant α (refer to Equations (3.31) and (3.32)), which is required to determine the complex permittivity. The phase constant can be related to phase velocity by the following equation:

$$v_p = \frac{2\pi f}{\beta} \tag{4.30}$$

The attenuation constant is found by first determining the quality factor $\mathcal{Q}$ (refer to Chapter 3.2.4) through an inversion process where the Jonscher model (Equation (3.46)) is optimised with respect to the phase velocity determined by the $f - \beta$ transform. The estimated attenuation constant can then be calculated according to Equation (3.35). Once the phase constant and the attenuation constant have been determined, the complex permittivity can be calculated from Equations (3.33) and (3.34). It is important to note that the accuracy with which the quality factor is determined can have a significant influence on the results for the loss factor, due to the important role that the attenuation plays in Equation (3.34) [132].

Ihamouten [132] also developed a method to estimate depth of a layer of contrasting per-

mittivity based on EM waveguide theory [270] from multi-offset measurements on concrete. This method is also exploited as part of this thesis. It aims to estimate the depth of a boundary of contrasting permittivity within the concrete by using the multi-modal response of the reflected electromagnetic energy. Since the analysis of needs to be performed in the frequency domain, multi-offset measurements are also required here, as for the inter-coupling method. A synthetic model is optimised to conform to the true electromagnetic response after transformation of the measured data to the frequency domain. The model parameters are defined by assigning the depth of the boundary and the permittivity of the upper and lower layers (with the assumption that the permittivities are known from analyses of the direct wave). The model is then manually optimised by changing the depth and comparing the synthesised output to that of the actual results. The theory will not be discussed in detail here and for more details the reader is referred to [132].

An important practical aspect of these multi-offset WARR techniques is that the quality of the analysis dependent greatly on the number of offsets at which measurements are made. In a numerical parametric study over frequency range 500 MHz to 1200 MHz, Ihamouten [132] found that an insufficient number of offsets significantly influenced the calculated average phase velocity, due to a lack of resolution. He also found that the size of the increments was not so important, but noting that in practice the measurement error would be higher for smaller increments. Ihamouten therefore suggests using increments of 5 mm for at least 20 offsets to obtain good results from the inversion protocol. This rule was adhered to as far as possible for WARR measurements made as part of this thesis.

4.4 Conclusion

In this chapter the electromagnetic principles and techniques were discussed that was used in the experimental work presented in the following chapters. For laboratory measurements, the existing resistivity techniques based on Ohm's law (Section 4.2.1.1) will form the basis of the development of a new resistivity cell in Chapter 6. The frequency dependent complex permittivity will be determined by means of the existing EM-cell (Section 4.3.1.1).

In terms of in situ investigation techniques, a new resistivity probe is developed in Chapter 6 to determine the resistivity of non-homogeneous concrete by means of ERT, based on the principles presented in Section 4.2.2.2. The in situ techniques related to permittivity will be the capacitive probe for investigation at low frequencies (Section 4.3.2.1) and GPR at high frequencies (Section 4.3.2.2). Either a fixed offset or multi-offset (WARR) GPR configuration (or both) is used depending on the objectives of the study and the test conditions, as will be discussed for each case in the chapters to follow.

Part II

Experimental work

Chapter 5

Overview of experimental work

5.1 Introduction

Part II of this document is dedicated to the experimental programs, data analysis and interpretation of results that were performed as part of this thesis. The main focus of the experimental work was to determine the relationships between the electromagnetic properties of concrete (electric resistivity and dielectric permittivity) and parameters related to concrete condition and durability in a rigorous fashion. These relationships were then used for the non-destructive characterisation of concrete by means of in situ EM investigation techniques.

The majority of the experimental work was performed under controlled laboratory conditions. Therefore, a distinction should be made between the testing of *concrete cores* with laboratory techniques (using the resistivity- and EM-cell), the testing of *concrete slabs* with in situ techniques and actual *in situ testing*. The laboratory techniques were used to determine the EM properties of a wide range of concrete specimens as accurately as possible in the shortest possible amount of time. Thereafter the in situ techniques were applied to conditioned slabs in order to create a controlled, ideal environment before they were applied to more challenging in situ conditions. It should also be noted that homogeneous, unreinforced concrete was mainly used for the experimental campaigns, although studies on concrete slabs containing property gradients and in situ concrete containing steel reinforcement were also conducted.

This chapter will give an overview and the motivation for the experimental programs that were undertaken. It also lists the concrete mix formulations that were used. It is therefore meant to serve as introduction and reference for the work presented in Part II of this document.

5.2 Chapter overview

The chapters forming part of Part II are as follows:

Chapter 6: Development of resistivity equipment

Chapter 6 details the development and validation of innovative new resistivity measurement devices, a multi-ring resistivity cell and two versions of a multi-electrode resistivity probe. These new devices had to be developed for the measurement of electrical resistivity as part of the thesis before the main experimental work could commence. The resistivity cell was required for the laboratory investigation on concrete cores in Chapter 7 and a resistivity probe, for the laboratory investigation of concrete slabs in Chapters 8 and 9 and the in situ measurements in Chapter 9.

Chapter 7: The dependency of EM properties on concrete condition

Chapter 7 presents the bulk of the work that has been conducted as part of this thesis. Firstly, a parametric study on which the interpretation of most of the results in the following chapters is based, is discussed. This study aimed to determine the relationship between EM observables and parameters related to concrete condition including degree of saturation, chloride content, porosity and chloride diffusivity. Testing was conducted on homogeneous, conditioned concrete cores of various mix formulations using laboratory investigation techniques.
Secondly, the results were used to evaluate the performance of two well known composite material models, Archie's law and the CRIM model, over a range of concrete conditions and formulations. Lastly, multiple linear regression models were developed for each of the EM observables as a function of the condition parameters for which the parametric study was conducted. Regression analysis is performed to evaluate the significance of the respective parameters and the interactions between them.

Chapter 8: Use of in situ EM techniques to estimate concrete condition

Chapter 8 focusses on a study that was conducted on homogeneous conditioned concrete slabs using in situ investigation techniques. The slabs were of the same mix formulation as the concrete used for the parametric study in Chapter 7, and therefore allowed for the results of the in situ and laboratory techniques to be compared. Further, the multiple linear regression models are combined to estimate the condition of the concrete slabs from the EM observables by means of non-linear optimisation.

Chapter 9: Collaborative experimental work

The last chapter in Part II presents three studies that were conducted in collaboration with other research institutions:

- A study on the influence of mineral admixtures and hydration on concrete resistivity and chloride diffusivity, in collaboration with *University College Dublin* (UCD), Ireland;
- A study of the ingress of chloride contaminated solutions into concrete using in situ EM techniques, in collaboration with *CETE de l'Ouest, Saint-Brieuc, France*;
- The characterisation of a 100 year old concrete bridge using in situ EM techniques, in collaboration with UCD and the *Cork Institute of Technology* (CIT), Ireland.

5.3 Concrete mix formulations

Several mix formulations were used as part of the experimental work. All of the mix formulations are listed in this section as some of them were used in more than one study. This section will therefore serve as reference for the next four chapters in terms of mix design. A short explanation is given as to the role of the respective formulations in the thesis, but a more in-depth discussion on the choice of mix and details of the mix properties are given in the Chapters to follow.

5.3.1 Mix set 1

The concrete selected for the main body of experimental work presented in Chapters 7 and 8 was designed as part of a previous internal research project [275] at IFSTTAR and is presented in Table 5.1. The references of B2 to B6 are retained for the sake of consistency with previous experimental campaigns where the same mix designs were used. Mix B2 is indicated in blue as it is only used here as part of the validation of the resistivity devices in Chapter 6. The formulations were chosen to cover a range of concrete conditions in terms of durability as required for the parametric study. The motivation for their selection is discussed in more detail in Chapter 7.

Table 5.1: Mix formulations B3 to B6 used for the parametric study on cores (Chapter 7) and in situ techniques on homogeneous slabs in Chapter 8 (Mix B2 is only used in Chapter 6 for the validation of resistivity equipment).

Constituents [kg/m^3]	**Origin**	**Mix**				
		B2	**B3**	**B4**	**B5**	**B6**
Aggregate (10/20)	Pontreaux, gneiss	474	0	0	0	0
Aggregate (6/10)	Pontreaux, gneiss	317	773	785	0	0
Sand (0/2)	Pontreaux, gneiss	452	428	449	601	652
Sand (0,4)	Pilier, alluvial	453	417	445	597	649
Cement (CEM I 52.5)	Lafarge (St Pierre La Cour)	344	519	341	757	492
Water		236	188	235	262	332
Glénium 27 plasticiser	BASF	0	13	0	19	0
Fresh Density		2275	2338	2256	2236	2124
W/C-ratio		0.68	0.36	0.69	0.35	0.67

5.3.2 Mix set 2

The collaborative study with the University College Dublin was undertaken with the main aim to study the influence of admixtures on resistivity and the chloride diffusion properties of concrete over time (Chapter 9). Three mixes with varying ground granulated blast furnace slag (GGBS) contents were studied as per Table 5.2. The mix design, casting and determination of chloride diffusion coefficients were conducted by UCD. A secondary goal of this experimental program was to validate the resistivity measurement devices that were developed as discussed in Chapter 6.

5.3.3 Mix SB

The mix formulation presented in Table 5.3 was used for experimental work in collaboration with CETE, Saint-Brieuc to study the ingress of various electrolytic solutions into concrete by means of in situ EM non-destructive techniques. The mix was designed to be representative of common concretes used in France, with the relatively high W/C-ratio facilitating quick ingress of moisture. The mix design, casting, conditioning and destructive characterisation of the concrete were performed by CETE, Saint-Brieuc.

Table 5.2: Mix formulations D1 to D3 used in collaboration with UCD for the validation of new resistivity devices (Chapter 6) and the study of the influence of GGBS on resistivity and chloride diffusion coefficient (Chapter 9).

Constituents [kg/m^3]	**Origin**	**Mix**		
		D1 (0% GGBS)	**D2** (50% GGBS)	**D3** (70% GGBS)
Aggregates (10/20)	Belgard, Limestone	625	625	625
Aggregates (6/10)	Belgard, Limestone	312	312	312
Sand	Offaly, Glacial	935	935	935
Cement (CEM II/A-L)	Irish Cement	307	154	92
GGBS	ECOCEM	0	154	215
Total cementitious content		307	307	307
Water		172	172	172
Fresh Density		2397	2384	2382
W/C-ratio		0.56	0.56	0.56

Table 5.3: Mix formulation SB used in the collaborative experimental study with CETE, Saint-Brieuc.

Constituents [kg/m^3]	**Origin**	**Mix SB**
Aggregates (10/20)	Croix Gibat, gneiss	621
Aggregates (6.3/16)	Croix Gibat, gneiss	425
Sand (0/4)	Fréhel, arkosic	567
Sand (0/4)	Mauron, alluvial	332
Cement (CEMII/A LL 42.5 R)	Lafarge (St Pierre La Cour)	267
Water		169
Plasticiser (Chrysoplast 760 (SPHRE))	CHRYSO	1.6
Fresh Density		2374
W/C-ratio		0.63 (0.58)*

* Effective W/C-ratio taking into account the water absorption of the aggregates.

Chapter 6

Development of resistivity devices

6.1 Objectives

This chapter details the steps in the development and validation of new resistivity devices that were required for the experimental work performed as part of this thesis. As mentioned previously, the principle focus of the experimental work was to study the EM properties of concrete in a parametric study (Chapter 7) and then to apply the results to in situ EM techniques. Equipment for the laboratory and in situ investigation of permittivity was already available within IFSTTAR, i.e. the cylindrical EM-cell described in Chapter 4.3.1.1 and the capacitive probe presented in Chapter 4.3.2.1. A commercial SIR-3000 GPR system from Geophysical Survey Systems, Inc. (GSSI), capable of performing multi-offset measurements, connected to transmitting and receiving antennae of 1500 MHz central frequency, was also available. However, for resistivity measurements, new electrode outlet ports were required for both laboratory and in situ investigation. A resistivity cell was therefore developed to enable resistivity measurements on core specimens during the parametric study, as well as two versions of a resistivity probe for surface resistivity measurements during the other experimental programs.

Though the measurement of concrete resistivity is well documented in literature (as is clear from Chapter 3.4) and in situ techniques are commonly applied in practice using commercial resistivity probes [228], these devices are novel as they were customised for the purpose of this thesis and contain some original aspects that have not been previously described in literature. Notably, the resistivity cell and probes are designed with the ability to detect the presence of resistivity gradients in concrete over depth. This functionality was of particular importance during the experimental work, as it was crucial to verify the homogeneity of the specimens for the parametric study (Chapter 7) in order to obtain

reliable results. Furthermore, the capability of the equipment to assess gradients can also be employed to assess the ingress of aggressive agents into concrete, which is of particular value for the study of diffusion characteristics and the durability of cover concrete. Geometry was important for the design of the resistivity cell, as it had to accommodate specimens of dimensions equivalent to the existing cylindrical EM-cell in order to enable the measurement of permittivity and resistivity on the same core specimens.

The resistivity devices that were developed and validated as part of the work presented in this chapter are therefore:

1. A multi-ring resistivity cell for the characterisation of concrete cores;
2. Multi-electrode probes for the characterisation of in situ concrete:
   (a) Mobile surface probe;
   (b) Embedded probe.

The most important aspects of the development of the resistivity devices as described in this chapter are:

→ The configuration and design of the various devices;

→ Numerical modelling to determine the appropriate geometric factors for the particular electrode configurations of each device taking into account the influence of the boundaries of the investigated specimen;

→ The evaluation of the reliability of resistivity measurements on conditioned concrete cores and slabs.

The resistivity devices presented in this chapter were used in conjunction with a commercial multichannel resistivity meter (Syscal Pro 48 Switch, Iris Instruments®). The Syscal Pro has numerous sophisticated functionalities and is normally used for geophysical investigations. In terms of this thesis, it was preferred for over simpler equipment such as multimeters, because customised sequences could be programmed for multi-electrode measurements. Multiple measurements could therefore be conducted in an automated fashion saving a considerable amount of time.

The Syscal Pro is capable of injecting very low-frequency alternating current (range of 0.125 Hz to 4 Hz) which produces results equivalent to that of direct current. It can inject current intensities as high as 2.5 A with an accuracy of 0.2% (also with a low current option for small specimens) and can receive potentials as high as 15 V. It also performs automatic polarisation compensation with linear drift correction using digital filtering, which compensates to a great extent for the effects of electrode polarisation. For the purposes of

this thesis, a frequency of 4 Hz was used and the injected current was varied as not to exceed the range of the receiver in terms of potential difference.

6.2 Development of a multi-ring resistivity cell

The multi-ring electrode, electrical resistivity cell developed as part of this thesis is presented in this section and will be referred to as the ***resistivity cell*** hereafter. The term "cell" refers to the device in which the concrete specimen is placed to be tested. The cell is in turn connected to the Syscal Pro resistivity meter, as described in the previous section.

6.2.1 Principle

The multi-ring resistivity cell operates on the principle of the direct application of Ohm's law as presented in Chapter 4.2.1.1. As a reminder, the direct application of Ohm's law is suited for specimens of simple geometry (uniform cross-section A and length L) such as cylinders, where the resistivity is analytically determined by Equation (4.5), repeated here for convenience:

$$\rho = \frac{A}{L}R = GR \tag{6.1}$$

It is therefore appropriate for semi-destructive measurements on cores in a controlled laboratory environment. Instead of the *2-electrode* method which is usually associated with the direct application of Ohm's law [283], a *4-electrode* measurement configuration is developed here. Thus, the current injection and potential measurement electrodes are separated in contrast with the 2-electrode method where both injection and measurement take place via the same electrodes. For the direct application of Ohm's law it is assumed that the specimens are homogeneous and isotropic. If the specimens are non-homogeneous, the resistivity determined by this method may be significantly different from local resistivities. It is therefore more correct to refer to *apparent* resistivity when property gradients are present.

6.2.2 Configuration

The resistivity cell (Figure 6.1(a)) consists of two insulating half-cylinder PVC casings that clamp around a concrete core specimen with a diameter of 75 mm and height of 70 mm (equivalent to the size of the cylindrical EM-cell). Five ring-electrodes with a width of 2 mm each are equally spaced over the height of the cell at intervals of 70/6 mm = 11.7 mm. The electrodes are from abrasion resistant metallised foam to ensure uniform contact between the electrodes and the specimen with low surface resistance. The metallised sponge also

(a)

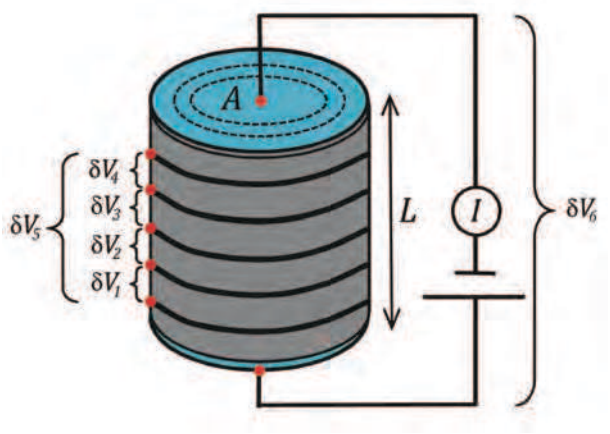

(b)

Figure 6.1: Multi-ring resistivity cell developed for the investigation of concrete cores with (a) showing the cell with various sizes of current injecting electrodes and (b) a diagram indicating the measurement positions of potential differences: δV_1, δV_2, δV_3, δV_4, δV_5 for 4-electrode measurements and δV_6 for the 2-electrode method.

reduces the need to moisten the electrodes, which is undesirable as it may alter the condition of the specimen and influence the measurements. Current is injected through two stainless steel plate-electrodes at the top and bottom of the specimen with damp sponges separating the metal from the concrete surface to improve contact resistance and mitigate polarisation effects. The resulting potential difference is then measured between any two of the ring-electrodes (Figure 6.1(b)). The ring-electrodes allow for the potential difference to be determined at intervals over the height of the specimen ($\delta V1$ to $\delta V4$) enabling the homogeneity of the specimen to be assessed in the vertical direction.

It has been reported in literature [113] that a 4-electrode approach (usually with reference to a Wenner configuration) yields more reliable results than the 2-electrode method due to it being less sensitive to errors caused by contact resistance and electrode polarisation. This assumption was further investigated here in terms of the multi-ring resistivity cell by assessing the performance of a 4-electrode and 2-electrode configuration for a range of contact conditions (refer to Section 6.2.4). To achieve this, contact resistance and electrode polarisation were varied by changing the contact area of the current injection electrodes. The diameter of the plate-electrodes could therefore be adapted to various sizes (4 mm, 10 mm, 20 mm, 30 mm and 75 mm) with the use of insulating PVC disks as in Figure 6.1(a).

6.2.3 Numerical modelling of geometric factors

6.2.3.1 Modelling approach

The analytical geometric factor derived from Ohm's law (Equation (6.1)) is not applicable to electrode sizes smaller than the cross-sectional area of the specimen unless the height of the specimen significantly exceeds its diameter. This section details the numerical modelling that was performed to find geometric factors for each plate and ring-electrode configuration using the commercial finite element software package COMSOL Multiphysics® in conjunction with MATLAB®. The sensitivity of the modelled geometric factors to the fineness of the model mesh, and the width and conductivity of the ring-electrodes were also studied. These modelled geometric factors compensate for the diameter of the current injection electrodes, the spacing of the ring-electrodes and the geometry of the specimens.

In order to model a geometric factor for each electrode combination, the approach proposed by Marescot et al. [174] was used as per Equations (6.2) and (6.3).

$$\rho_s = G\frac{\delta V_s}{I_s} = GR_s \tag{6.2}$$

$$\rho_m = G\frac{\delta V_m}{I_m} = GR_m \tag{6.3}$$

where ρ_s [Ω.m], δV_s [V], I_s [A] and R_s [Ω] are the resistivity, potential difference, current intensity and resistance determined by measurement of the concrete specimen and ρ_m [Ω.m], δV_m [V], I_m [A] and R_m [Ω] are the resistivity, potential difference, current intensity and resulting resistance for a model that is geometrically identical to the specimen. By substituting Equation (6.3) into Equation (6.2), the resistivity of the specimen can be determined as follows:

$$\rho_s = \frac{\rho_m}{R_m}R_s \quad \text{where} \quad G = \frac{\rho_m}{R_m} \tag{6.4}$$

A finite element model with geometry and electrode configuration identical to that of the multi-ring resistivity cell was therefore generated having an assigned resistivity of $\rho_m = 1$ Ω.m and an assigned current of $I_m = 1$ A, as is presented in Figure 6.2(a). The resistivity of the ring-electrodes were modelled as having a resistivity of 0.001 Ω.m which corresponds to the published resistivity of the metallised sponges from which they are manufactured [153]. Substituting the assigned model parameters in Equation (6.3) gives the modelled geometric factor:

$$G_m = 1/\delta V_m. \tag{6.5}$$

where G_m [m] is the modelled geometric factor and δV_m is the modelled potential difference for each electrode configuration, the model having an assigned resistivity of 1 Ω.m and with a current of $I_m = 1$ A being injected.

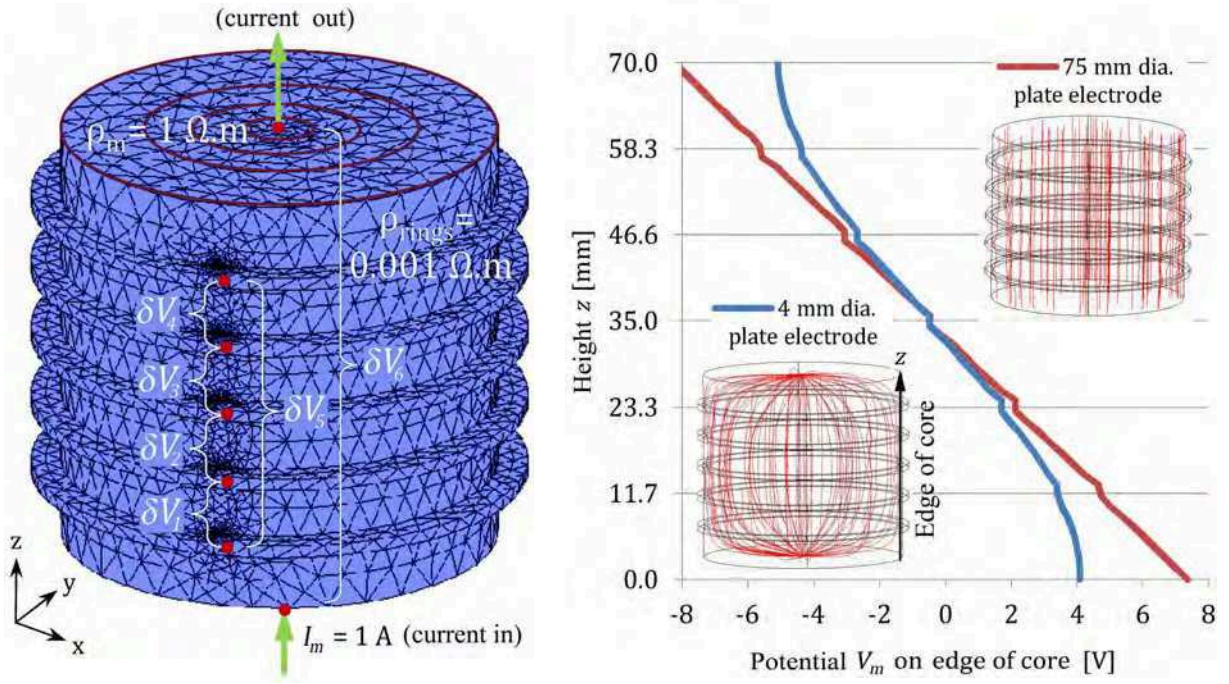

(a) (b)

Figure 6.2: Numerical modelling of the multi-ring resistivity cell, (a) indicating the properties of the finite element model and the positions of the modelled potential differences and (b) showing the modelled potential over the height of a specimen (on its "edge") for a current injection electrode diameter of 4 mm and 75 mm. The modelled electrical field line distributions for the 4 mm and 75 mm plate-electrode case are also shown (in red).

It can be seen in Figure 6.2(b) that the modelled potential on the "edge" of the core is significantly influenced by the diameter of the current injection (plate) electrodes. The electrical field for plate-electrodes smaller than 75 mm is not uniform and leads to the modelled geometric factors varying from the analytical geometric factor $G = A/L$. It is therefore clear that the direct application of Ohm's law will yield significant errors for current injection electrodes smaller than the cross-sectional area of the specimen, especially between the rings located closest to the plate-electrodes.

6.2.3.2 Sensitivity to fineness of mesh and modelled ring width

The sensitivity of the modelled geometric factors to the fineness of the mesh of the FEM model was investigated for each plate-electrode diameter as is presented in Figure 6.3(a). It can be seen that the geometric factors stabilise at approximately $3{\times}10^5$ mesh nodes as is shown in for measurement position δV_5. Geometric factors calculated from a numerical model are therefore sensitive to the fineness of the mesh. However, for this case the sen-

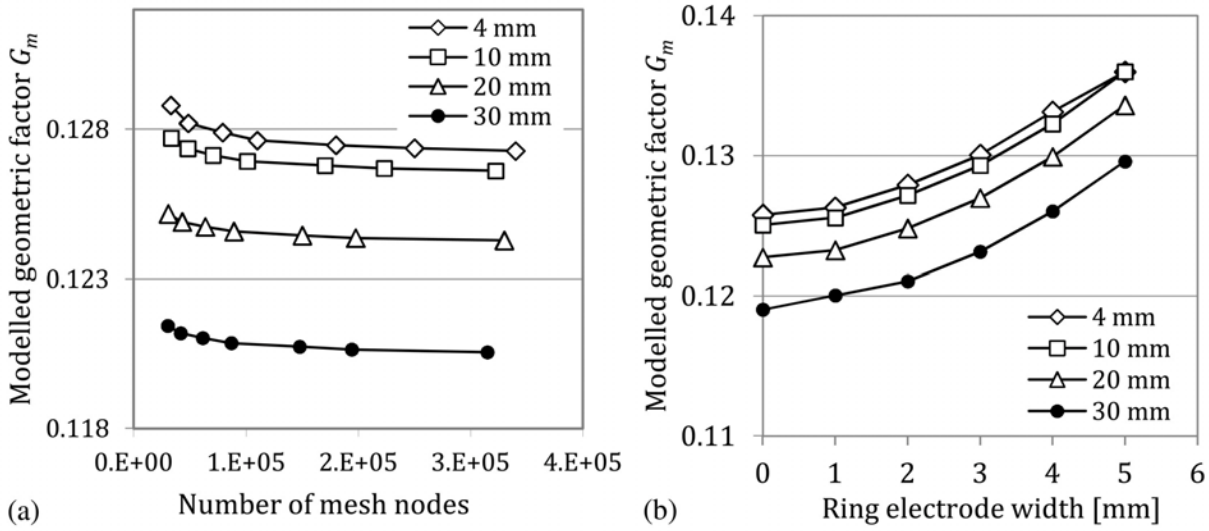

Figure 6.3: The sensitivity of modelled geometric factors for the resistivity cell to (a) the number of mesh nodes in the model and (b) the width of the ring-electrodes, for measurement position δV_5 (refer to Figure 6.1(b)) with 4 mm, 10 mm, 20 mm and 30 mm diameter plate-electrodes.

sitivity is not very significant, as the total percentage change in the geometric factor over the number of nodes that were studied (0.3×10^5 to 3.4×10^5) does not exceed 1.2%, even for the worst case being the 4 mm electrode. It needs to be emphasised that the sensitivity of the modelled geometric factors to the number of mesh nodes is model specific and must therefore be re-evaluated for a model with a different geometry or electrode configuration.

The influence of the width of the ring-electrodes on the modelled geometric factors was also investigated (with the number of mesh nodes $> 3\times10^5$) as shown in Figure 6.3(b). It is observed that the geometric factor for all the plate-electrode sizes increases quadratically with electrode width. The ring-electrode width of 2 mm causes an increase in the modelled geometric factor of approximately 2% with respect to the case with no rings (width = 0 mm). Due to practical considerations a ring width of 2 mm was viewed as a good choice (i.e. ensuring low contact resistance, while still being thin enough for local measurements).

It should be noted that results for the 75 mm diameter plate-electrodes are not indicated on Figures 6.3(a) and (b) as they fell in a different range to those for the other electrodes, making visual representation on the same graph difficult. However, they showed the same trends as the other electrodes.

A minimum of 3×10^5 mesh nodes and 2 mm ring widths were used to calculate the geometric factors for each injection electrode size and ring-electrode position as presented in Table 6.1. The percentage difference of the modelled geometric factors for the 75 mm diameter disk electrode $G_{m(75mm)}$ (which corresponds to the diameter of the specimen) was compared

Table 6.1: Final modelled geometric factors for each injection electrode size and potential measurement position.

Plate-electrode diameter	**Modelled geometric factor [m]**					
	δV1	δV2	δV3	δV4	δV5	δV6
		(4-electrode method)				(2-electrode method)
4 mm	0.574	0.451	0.451	0.574	0.129	0.0037
10 mm	0.570	0.449	0.449	0.570	0.127	0.0095
20 mm	0.556	0.443	0.443	0.556	0.125	0.0199
30 mm	0.534	0.433	0.433	0.534	0.121	0.0305
75 mm	0.386	0.385	0.385	0.386	0.096	0.0635

Table 6.2: Modelled and analytical geometric factors (G_m and G_a) for the 75 mm plate-electrode as well as the percentage difference between the two due to the influence of the 2 mm wide ring-electrodes and numerical errors.

Geometric factor [m]	**Measurement position**					
	δV1	δV2	δV3	δV4	δV5	δV6
$G_{m(75mm)}$	0.386	0.385	0.385	0.386	0.096	0.0635
$G_{a(75mm)}$	0.379	0.379	0.379	0.379	0.095	0.0630
%difference $\left(\frac{G_{m(75mm)}}{G_{a(75mm)}} - 1\right)$	1.850%	1.583%	1.583%	1.850%	1.053%	0.7937%

to the analytical geometric factors $G_{a(75mm)}$ calculated from Equation (4.6), as per Table 6.2. The percentage difference was found to be between 1% and 2% which corresponded to the influence of the ring-electrodes and numerical errors. It was therefore verified that the modelled factors converged to the correct geometric factors.

6.2.3.3 Use of modelled geometric factors for non-homogeneous conditions

The geometric factors as per Table 6.1 are calculated for homogeneous conditions. When these factors are applied to non-homogeneous conditions, the resulting resistivity is not the true resistivity of the specimen, but an apparent resistivity related to the homogeneous case. It was therefore investigated whether these *apparent* resistivities were comparable to the true resistivity halfway between two ring-electrodes for non-homogeneous models.

To achieve this, two non-homogeneous models were generated with a conductivity gradient over the height z of the modelled specimen: the first with a linear conductivity gradient

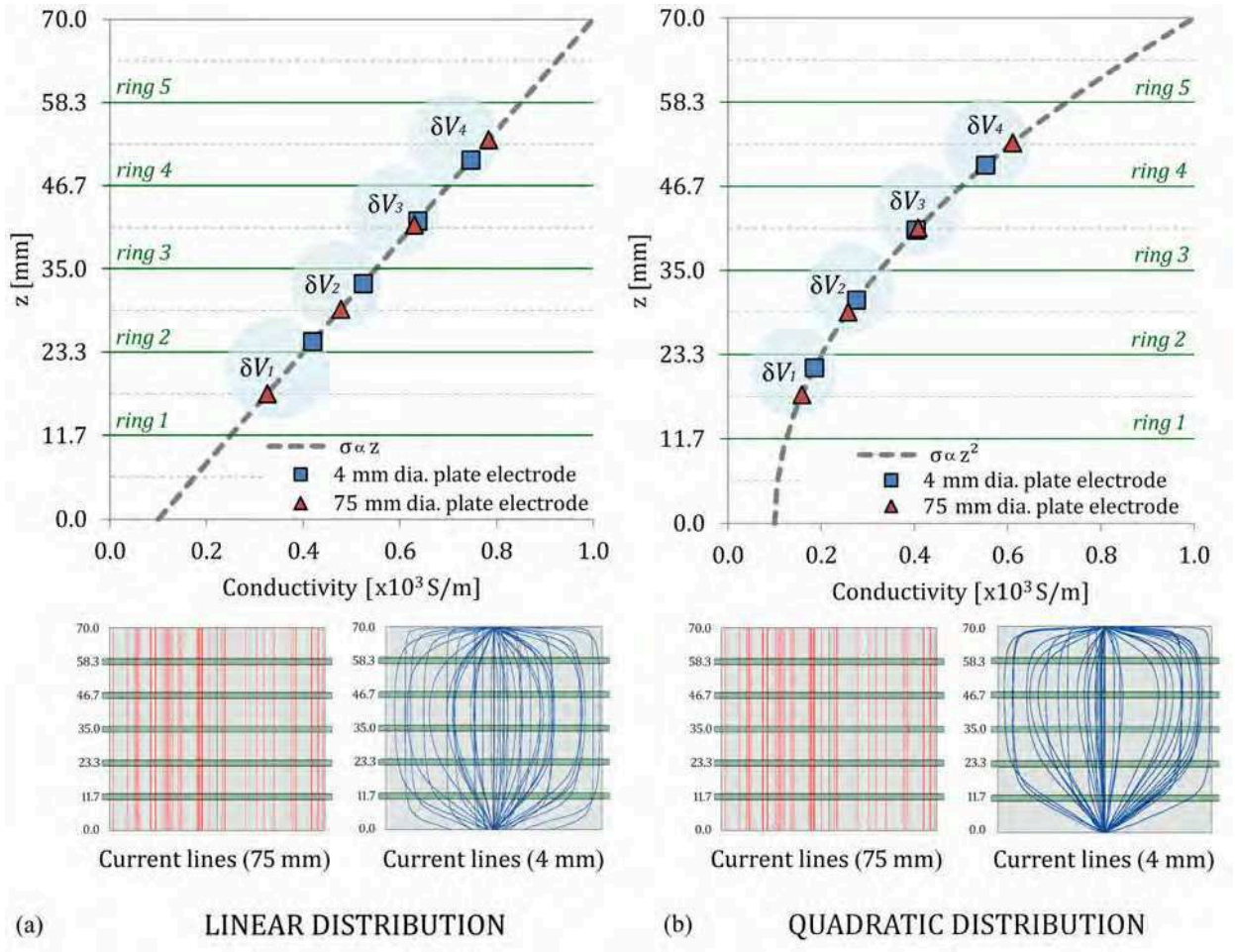

Figure 6.4: Investigation of pseudo-positions for apparent conductivities for electrode pairs δV_1 to δV_4 determined from modelled geometric factors for two non-homogeneous models having respectively (a) linear and (b) quadratic conductivity distributions over the height of the model. The modelled current lines for each case are also indicated.

$\sigma \propto z$, and the second with a quadratic change in conductivity $\sigma \propto z^2$ (where conductivity $\sigma = 1/\rho$). In Figures 6.4(a) and (b) the modelled conductivity gradients are indicated for the linear and quadratic case by a dashed grey line. In order to assess whether the modelled geometric factors (Table 6.1) would yield resistivities that were halfway between the ring-electrodes for the non-homogeneous case, the geometric factors from Table 6.1 for the *homogeneous* case were applied to the modelled potential differences for the *non-homogeneous* case for positions δV_1 to δV_4.

The resulting calculated conductivities were plotted on the modelled conductivity line to see where they were positioned with respect to the ring-electrodes. It can be seen in Figures 6.4(a) and (b) that values for the 75 mm plate-electrode are located approximately in the middle between each ring-electrode pair, irrespective of whether the conductivity is a linear

or quadratic function of z. However, for the 4 mm electrode this is not the case due to the electrical field line distribution being distorted. The current lines for each case are also indicated in Figures 6.4(a) and (b) from which it is clear that they are asymmetrical over the height of the model when the 4 mm plate-electrodes are used, whereas current lines for the 75 mm plate-electrodes are always parallel.

It is thus concluded that apparent resistivities obtained for the 75 mm injection plate-electrodes represent the local resistivity at the z-position halfway between the ring-electrodes, whereas the location of apparent resistivity determined using injection electrodes with an area smaller than the cross-sectional area of the specimen, is not so easily defined. The modelled geometric factors, as obtained in Table 6.1, were subsequently used to evaluate the performance of the 2-electrode and 4-electrode method on homogeneous, saturated concrete specimens.

6.2.4 Comparison of the 2-electrode and 4-electrode methods

High contact resistances and electrode polarisation are the two most significant causes of error in resistivity measurement as explained in Chapter 4.2.1.1 [113] [268]. Due to the complexity of these two phenomena they were not simulated during the numerical modellisation described in the previous sections, but their influence was investigated on concrete core specimens by comparing results from a 2-electrode and a 4-electrode configuration.

For 2-electrode resistivity measurements, the bulk resistance R is measured between the two injecting electrodes and therefore includes the contact resistance as per Equation (4.7) and Figure 4.1. If the contact resistance is high relative to the resistance of the specimen, the calculated resistivity will not reflect the true resistivity of the specimen. For 4-electrode measurements, current is injected through two electrodes and potential difference is measured over the remaining two electrodes. The assumption is that the influence of contact resistance and polarisation will be partially avoided by this approach.

This assumption was investigated by comparing results from the resistivity cell for a 2-electrode ($\delta V6$) and a 4-electrode ($\delta V5$) configuration as indicated in Figure 6.1(b). As both contact resistance and polarisation are dependent on the injection electrode size, all the different plate-electrode sizes were used to vary the contact resistance an polarisation and study the resulting effect on the resistivities that are obtained. Testing was conducted on a water saturated, homogeneous mortar (Mix B5, Table 5.1) with three measurements taken for each plate-electrode size. The resistivity was then obtained by applying the geometric factors from Table 6.1 to correct for electrode size and configuration. The difference between results from the 2-electrode and 4-electrode methods would therefore only be due to the

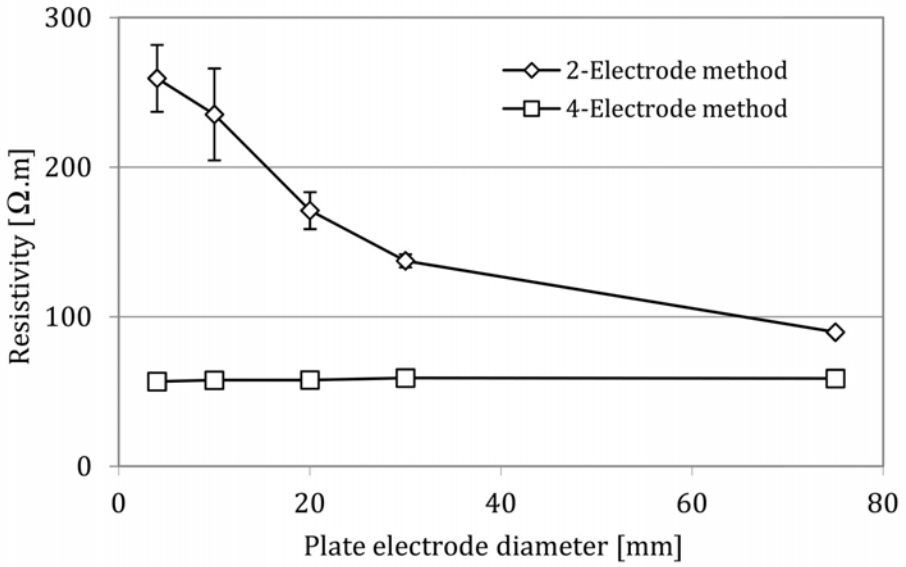

Figure 6.5: Measured resistivities determined with the 2-electrode and 4-electrode methods for current injection electrodes of varying diameter on homogeneous core B5-4, with a estimated resistivity of 62 Ω.m.

influence of contact resistance and electrode polarisation. The actual resistivity of the specimen was estimated by means of Archie's law (Equation 3.57) at approximately 62 Ω.m (the variables were approximated as $\phi = 0.19$ (Table 7.3), $\rho_w = 1/\sigma_w = 18$ Ω.m [159], $\mathfrak{a} = 1$, $\mathfrak{m} = 2$ [264] and $S = 1$).

Results for both methods are given in Figure 6.5. Resistivities determined by 2-electrode measurements are significantly higher than the expected resistivity value of 62 Ω.m and increase as the injection electrode size decreases. The 2-electrode configuration also shows more variability as the electrode size decreases, with the standard deviation indicated by the error bars. In contrast, results for the 4-electrode method are stable irrespective of electrode size with an average of 57.9±0.7 Ω.m, corresponding well to the estimated value. Although the effect of contact resistance and electrode polarisation cannot be separated using this investigation method, it is clear that their combined influence on the reliability of 2-electrode measurements is considerable. On the other hand, the 4-electrode method does not seem to be significantly affected by contact resistance and electrode polarisation.

The 4-electrode method was therefore exclusively used during the experimental work conducted as part of this thesis. However, despite using four electrodes, high contact resistances at the current injection electrodes can still produce erroneous results if the potential difference over the ring-electrodes exceeds the range of the measurement equipment. For very resistive specimens, a current attenuation box in conjunction with the Syscal Pro resistivity meter was therefore required in order to keep measurements within acceptable limits.

Though a 75 mm diameter plate-electrode was mainly used during for experimental work (Chapter 7), it was observed that using the smaller plate-electrodes could significantly reduce the measured potential difference over the ring-electrodes and thus reduce the need for current attenuation. This finding was especially useful when testing specimens at low degrees of saturation. In terms of electrode polarisation, it was assumed that the 4-electrode method together with the capability of the Syscal Pro to correct for polarisation effects were sufficient to obtain accurate resistivity results.

6.2.5 Summary

The design and modelling of the multi-ring resistivity cell was discussed in this section. Geometric factors which are applied to measured resistance values in order to correct for the configuration of the electrodes and the geometry of the investigated specimen, were determined by means of numeric modelling. It was found that the modelled geometric factors are influenced by the number of nodes in the model as well as the width of the ring-electrodes. It was also established that for the 75mm plate-electrodes, the application of these geometric factors to a non-homogeneous medium will yield apparent resistivities that are equivalent to the true resistivities midway between the ring-electrodes. However, the same is not true for electrodes smaller than the cross-sectional area of the specimen. Further it was confirmed that 4-electrode measurements successfully mitigate the effects of polarisation and contact resistance and are therefore superior to 2-electrode measurements.

6.3 Development of multi-electrode resistivity probes

In this section two versions of a new multi-electrode resistivity probe are presented, the difference between the two being mainly their application. The first version is a mobile surface probe that is aimed at the in situ assessment of concrete condition at *ad hoc* positions. The second is an embedded probe aimed at monitoring the change in concrete properties at a fixed position. The two devices will be referred to respectively as the ***surface probe*** and the ***embedded probe*** in this section. As for the resistivity cell, these devices were used in conjunction with the Syscal Pro resistivity meter.

Multi-electrode measurements over a range of electrode spacings enable the resistivity of a medium to be estimated as a function of investigation depth by means of geophysical inversion (Chapter 4.2.2.2). The development of the resistivity probes were therefore undertaken to assess the resistivity and homogeneity of the slabs during the experimental work in Chapter 8 and for the collaborative experimental work on the ingress of water and chlorides into

concrete.

6.3.1 Principles

For the non-destructive evaluation of in situ concrete elements of arbitrary shape, the use of parallel plate injection electrodes (as in Section 6.2) is not practical and surface measurements using point-electrodes are thus often used (refer to Chapter 4.2.2). The 4-point Wenner configuration (electrode spacing a at equal intervals) is commonly used in practice as a non-destructive corrosion risk investigation tool [243] [107]. Usually these evaluations are based on *apparent* resistivities obtained for a single electrode spacing using the geometric factor $G = 2\pi a$ as defined for the homogeneous infinite halfspace (see Equation 4.15) [30]. The measurements are thus a very general indication of the resistivity of the cover concrete. When property gradients are present, these apparent resistivities cannot be related to a specific depth in the subsurface accurately as they are representative of an unknown influence volume as explained in Chapter 4.2.2.2.

Because the investigation of resistivity gradients in cover concrete can be related to the ingress of aggressive agents, multi-electrode measurements that can be inverted to obtain a representative model of subsurface resistivity over depth are potentially very valuable. There has been very limited research on the use of multi-electrode resistivity measurements and ERT for concrete structures and then usually with the aim to detect defects rather than property gradients [66] [17].

Though numerous array types are used in geophysics for subsurface investigation, the Wenner array (refer to Chapter 4.2.2) was selected here for the modelling and validation of the probes in this section. The Wenner configuration is preferred due to its sensitivity to variations over depth in the subsurface [163], being appropriate for concrete experiencing ingress of aggressive agents from the surface. The Wenner configuration is also advantageous due to its good signal to noise ratio, which is important for the investigation of very resistive materials such as concrete.

The multi-electrode probes presented in this section enable the mapping of subsurface resistivities of arbitarily shaped concrete elements by implementing the steps as demonstrated in Figure 6.6. Firstly, multiple 4-point Wenner surface measurements are obtained for all possible electrode spacings and combinations (Figure 6.6(i)). Because in situ concrete elements are often not massive enough to avoid boundary effects, the application of geometric factors defined for the infinitely deep halfspace ($2\pi a$) can yield misleading results, especially for measurements at larger electrode spacings. New geometric factors are therefore determined by means of numerical modelling (Figure 6.6(ii)) that takes into account the boundaries of

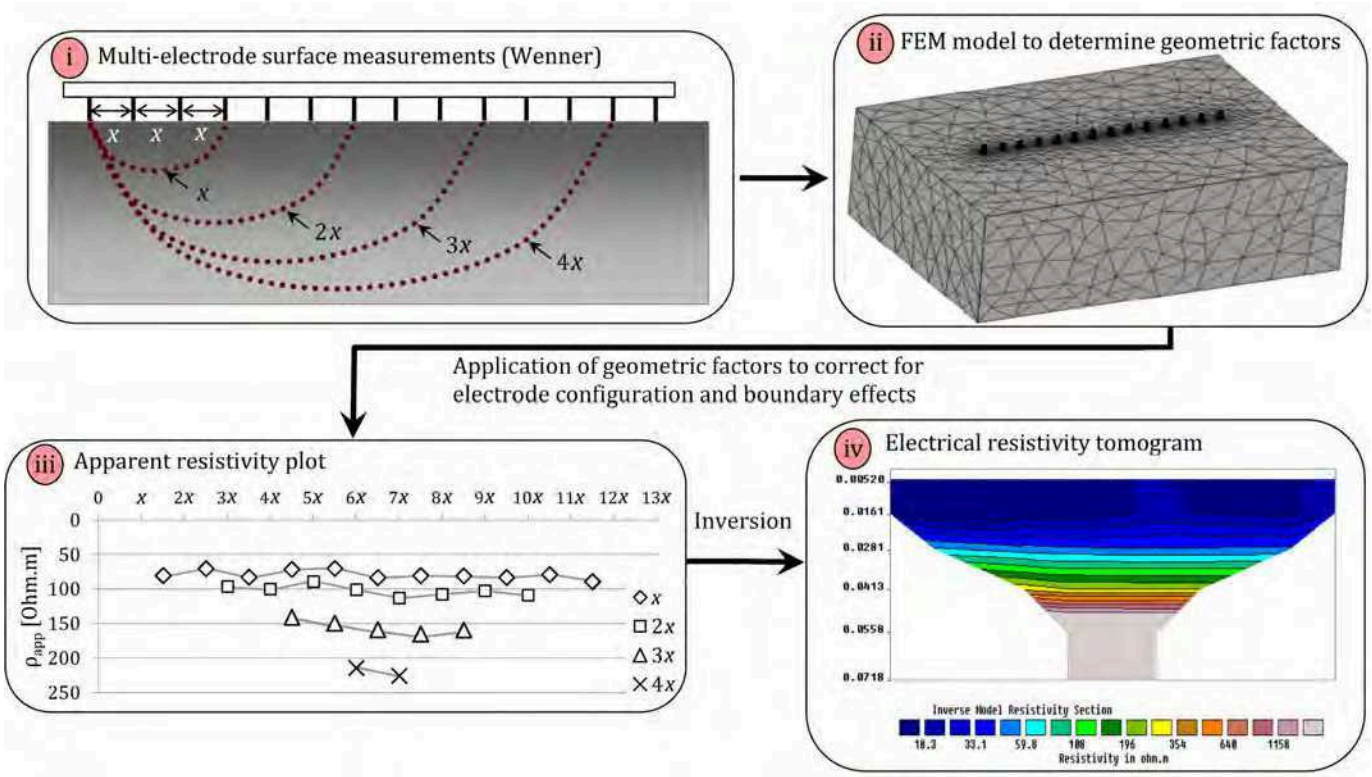

Figure 6.6: Steps in data treatment for resistivity measures with (i) indicating multi-electrode 4-point surface measurements showing the increase in investigation depth as the electrode offset increases, (ii) geometric correction by numerical modeling, (iii) calculated apparent resistivities for the Wenner configurations for each level of investigation and (iv) inverted resistivities over depth using the inversion software *Res2Dinv* [164].

the concrete element. Apparent resistivities can then be calculated to give a *pseudosection* of the subsurface (Figure 6.6(iii)). For concrete that does not have significant gradients, these apparent resistivities should approach the true resistivity of the concrete. However, when the concrete is not homogeneous the measurements have to be inverted as described in Chapter 4.2.2.2 to obtain a model (tomogram) of the "true" resistivity distribution of the subsurface as in Figure 6.6(iv).

6.3.2 Configuration

The two versions of the multi-electrode resistivity probe were designed to be identical in terms of electrode arrangement, the only difference being that the one is a mobile hand-held probe and the other is embedded flush with the concrete surface during casting. However, it was anticipated that there may be a difference in the reliability of their results due to a difference in electrode contact conditions. Their almost identical nature therefore enabled

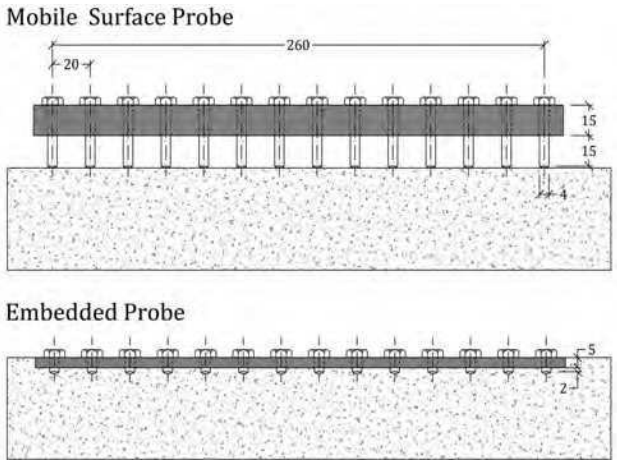

(a)

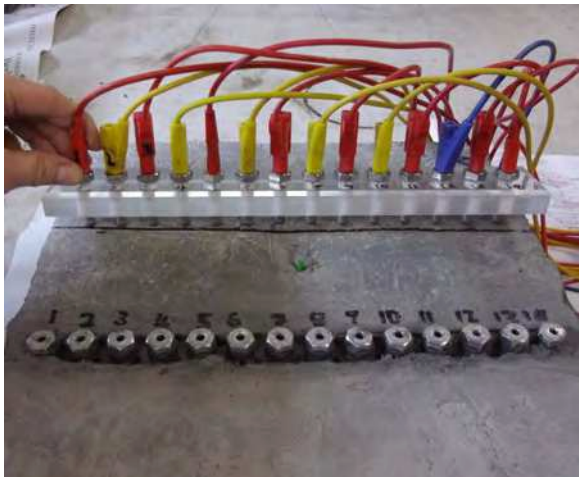

(b)

Figure 6.7: Multi-electrode resistivity probes developed for the investigation of concrete slabs with (a) showing the mobile surface probe and the embedded probe and (b) demonstrating their implementation on concrete slabs.

the comparison of their performance in terms of the consistency of results and contact resistance.

Each probe consists of a linear array of 14 point-electrodes spaced at 20 mm intervals which amounts to a lateral coverage of 260 mm as shown in Figure 6.1(a). According to the recommendations of Gowers and Millard [113], this configuration only allows for a maximum nominal aggregate size of up to 13 mm used in the concrete mix. However, it was deemed to be optimal as the number of 14 electrodes allows for a tomogram to be obtained for an adequate depth and resolution, without causing the probe to be impractically long. For a Wenner array, 26 measurements can be obtained at four pseudodepth levels reaching a maximum inverted investigation depth of approximately 80 mm as shown in Figure 6.6(i), (iii) and (iv). The probes are also compact enough to fit onto relatively small concrete elements and avoid significant influence of steel reinforcement. Though no reinforcement was used during the main experimental programs forming part of this thesis, the probes are suitable for in situ measurement of reinforced concrete having a mesh spacing of up to 200 mm if they are placed diagonally to the steel grid (refer to Chapter 9.4).

The 14 point-electrodes consist of hollow screws with an inner diameter of 4 mm that are fitted with metallised foam tips to improve contact. The electrodes are connected to the commercial Syscal Pro by means of banana connectors that are plugged into the electrodes which act as sockets. Because the electrodes are hollow, the contact resistance of the embedded probe can be reduced by inserting a small amount of water in the electrodes prior to measurement. The plate on which the electrodes are mounted is made from transparent

PVC in order to be able to verify that there is no air trapped underneath the embedded probe during installation.

6.3.3 Numerical modelling of geometric factors

When surface resistivity techniques are applied in situ on concrete, the elements are seldom massive enough for the boundaries not to affect the measurements. The presence of boundaries can cause apparent resistivities calculated from analytical geometric factors defined for the infinite halfspace (e.g. Equation (4.15)) to be significantly different from the true resistivity - even for homogeneous materials. Gowers and Millard [113] found large errors for resistivities calculated from 4-point Wenner measurements ($G_a = 2\pi a$) on thin concrete members or near the edges of concrete elements. Gowers and Millard therefore recommend measurements to be carried out in the centre of concrete elements and with an electrode spacing small enough to avoid a significant influence of the bottom boundary. They suggest that the proportion of element thickness to electrode spacing should exceed approximately 4 [113].

6.3.3.1 Influence of boundaries of the investigated medium on geometric factors

In this thesis, the approach is to account for the influence of the boundaries, rather than to avoid it. In order to evaluate when the need for such a correction exists for a 4-point Wenner array, the sensitivity of modelled geometric factors to boundaries parallel (x-direction), perpendicular (y-direction) and below (z-direction) the electrode contact points were investigated by numerical modelling in COMSOL Multiphysics®. Figure 6.8 shows the modelled geometric factors G_m relative to the analytical geometric factor $G_a = 2\pi a$ as a function of the respective boundary offsets (d_x, d_y and d_z), normalised with respect to the distance between the electrodes a. The offset from the outermost electrode to each boundary was increased incrementally, whilst the other two boundaries were kept at an essentially infinite distance. In Figure 6.8 it can be seen that the offset to the z-boundary has the most significant influence, followed by the x- and then the y-boundaries. The modelled geometric factor G_m approaches the analytical geometric factor ($G_m/G_a > 0.99\%$) when $d_z/a > 4.5$, $d_x/a > 3.25$ and $d_y/a > 2.75$. It is therefore concluded that all boundary effects become negligible at d/a-ratios of above 4.5, which corresponds well with the value suggested by Gowers and Millard [113].

With the maximum electrode spacing of the resistivity probes being 80 mm, it was certain that it would often be impossible to avoid boundary effects for measurement on concrete

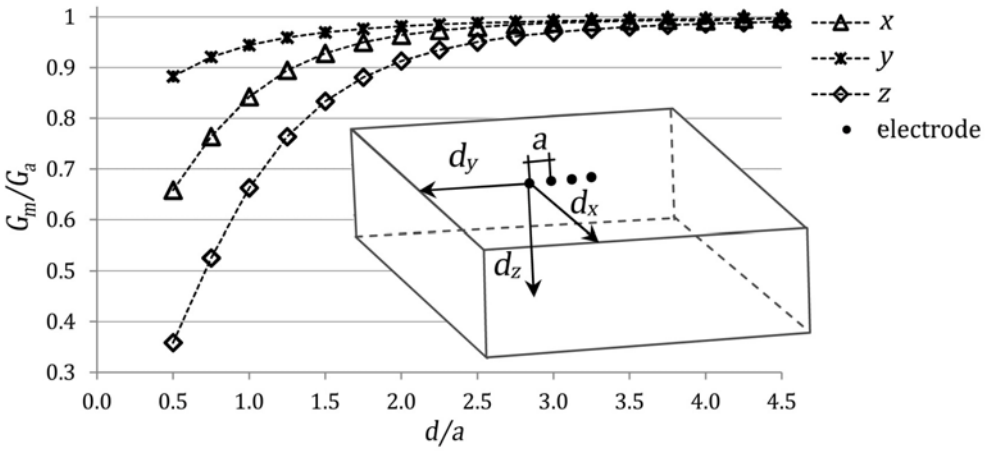

Figure 6.8: Impact of boundaries on modelled Wenner geometric factors relative to analytical Wenner geometric factors (i.e. no boundaries).

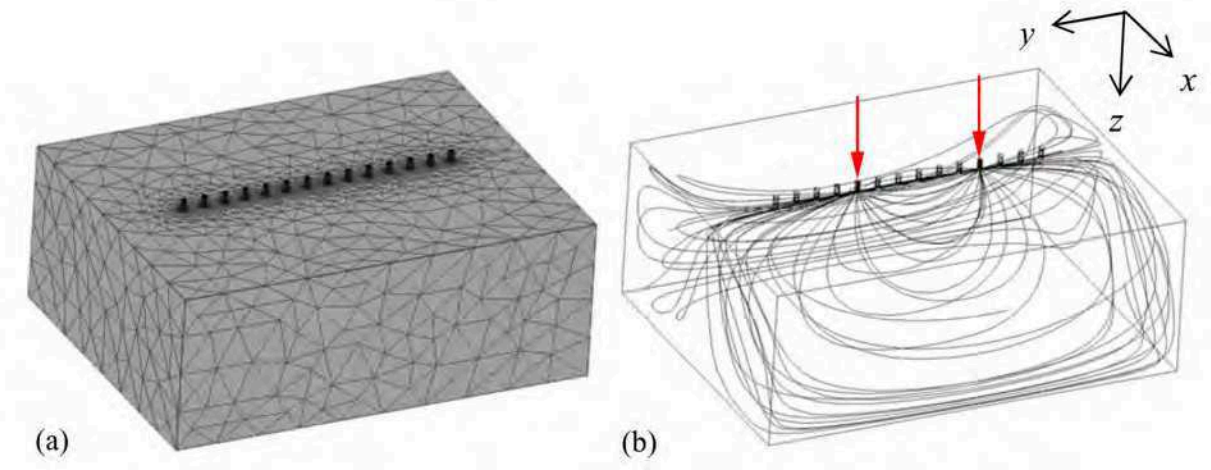

Figure 6.9: Numerical modelling to determine geometric factors for finite geometries assessed with the surface probe with (a) the FEM mesh for a slab and (b) the influence of the boundaries on the electric field distribution for a particular pair of injecting electrodes.

elements (an element depth of more than 360 mm being required). Therefore, new geometric factors were calculated using the approach described in Section 6.2.3 by means of Equation (6.5). A finite element model (FEM) was therefore generated for both the surface and embedded versions, assuming insulated boundary conditions.

The model for the surface probe is shown in Figure 6.9(a) for a simple concrete slab. The models can be adapted easily to the relevant dimensions of the investigated element in order to calculate geometric factors for each electrode combination. Figure 6.9(b) demonstrates the influence of the boundaries on the electric field distribution and therefore on the geometric factor that must be applied to measured resistances.

6.3.3.2 Influence of embedding on geometric factors

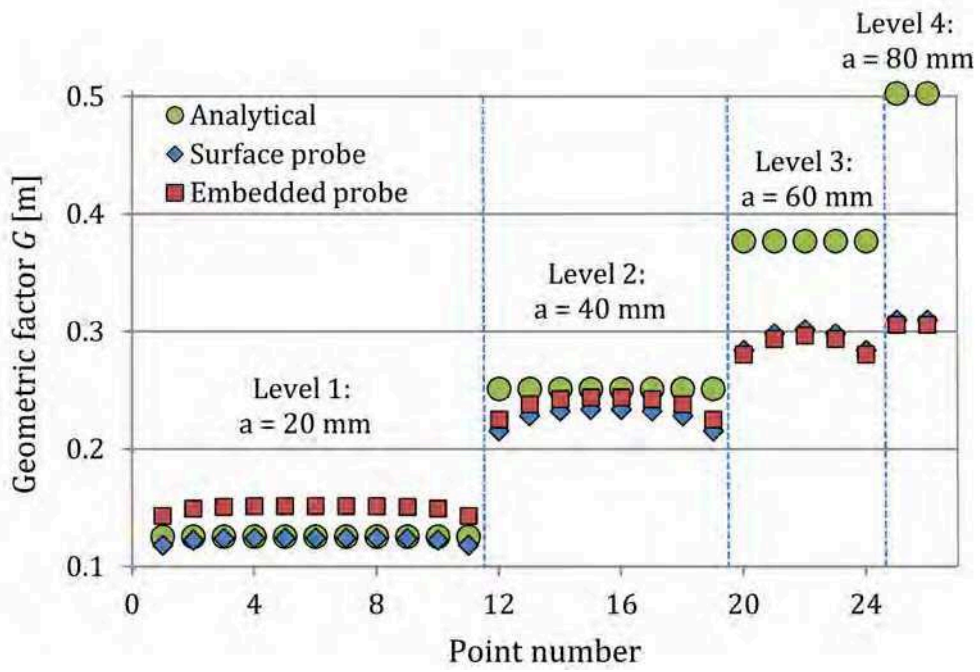

Figure 6.10: Modelled geometric factors for the surface probe and the embedded probe for a homogeneous slab element, showing each of the 26 electrode combinations (points) possible for a Wenner configuration and the corresponding analytical geometric factors for an infinite homogeneous halfspace ($G_a = 2\pi a$).

Although the configuration of the embedded resistivity probe is identical to that of the surface probe, the position of the electrodes is not the same with respect to the surface of the concrete element after installation as per Figure 6.7(a). Figure 6.10 shows the geometric factors for the surface and embedded probes of a modelled homogeneous slab element of dimensions 300×300×120 mm. The modelled geometric factors are indicated for each of the 26 electrode combinations (measurement points) possible for an array of 14 electrodes using the Wenner configuration (refer to Figure 6.6(i)). It can be seen that the geometric factors for the surface and embedded probe differ significantly for $a = 20$ mm (approx. 21%) where the investigation depth of the measurements are small. However, this difference decreases as the investigation depth increases and becomes negligible for $a = 80$ mm (approx. 1%).

Figure 6.10 also illustrates the influence of the boundaries of the medium on the geometric factors. The analytical Wenner geometric factor for an infinite homogeneous halfspace ($G_a = 2\pi a$) does not take into account boundaries. The influence of the boundary in the z-direction is clear from the large discrepancy between the analytical and modelled geometric factors at $a = 80$ mm (approx. 62%). The influence of the y-direction is also evident in the modelled values being lower for the first and last values of each investigation level

(corresponding to the points closest to the sides of the slab element).

The influence of the diameter of the electrode sizes on the geometric factors was also studied and it was found that there was no significant difference between the geometric factors for point-electrodes and those of the 4 mm diameter sponge electrodes (for an electrode spacing of 20 mm).

6.3.4 Summary

The design and modelling of the surface and embedded multi-electrode resistivity probes were discussed in this section. It was verified that the analytical geometric factors that are often applied to Wenner probe measurements on concrete can cause significant errors due to the presence of boundaries. A FEM model was created for both the surface and the embedded probe which can be customised to the dimensions of the concrete element, in order to model the correct geometric factor for each electrode combination. It was also observed that there is a significant difference between the modelled geometric factors of the surface and embedded probes for small investigation depths.

6.4 Validation of resistivity cell and probes

The functioning of the resistivity measurement equipment and the accuracy of the modelled geometric factors were investigated as part of the work presented in this section. Firstly a "calibration" procedure was undertaken on solutions of known resistivity and secondly a "cross verification" was conducted on concrete cores and slabs to compare the performance of the respective devices.

6.4.1 Calibration on aqueous solutions

The accuracy of results from the three resistivity devices was initially evaluated on homogeneous aqueous solutions of varying resistivity, as it was assumed that very low contact resistances would be present and that the electrode polarisation would be corrected for by the Syscal Pro resistivity meter. The solutions created nearly ideal conditions to verify that the geometric factors did indeed yield the correct resistivity results for both the cell and probes.

The experimental set-up is illustrated in Figure 6.11 with testing conducted at a controlled temperature of 20°C. The resistivity of solutions over a range equivalent to that of concrete

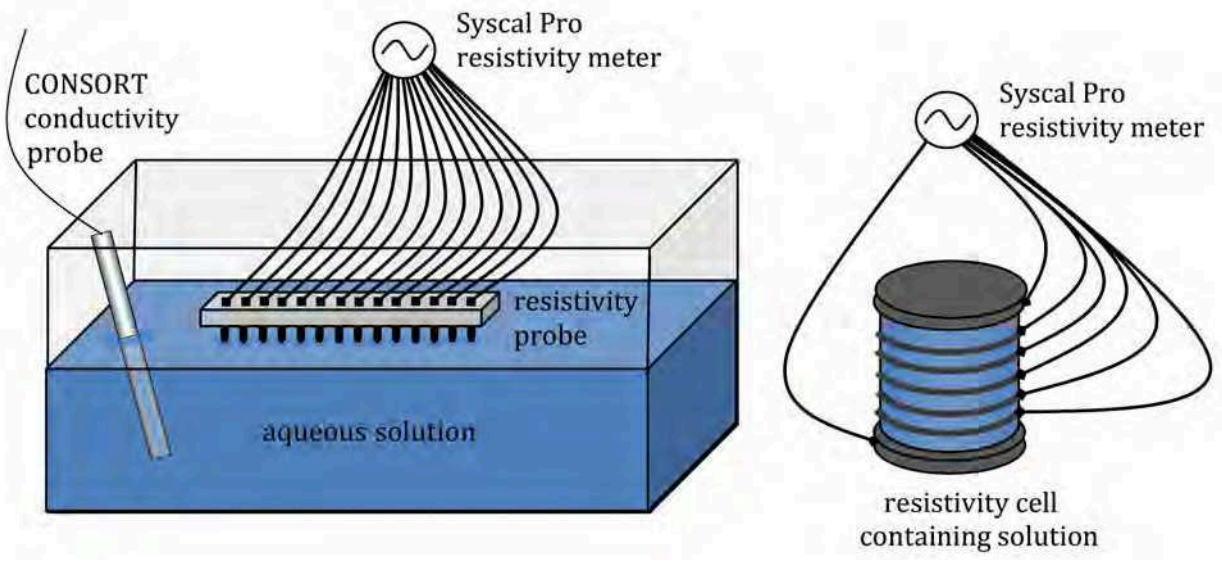

Figure 6.11: Experimental set-up for testing of the surface probe and resistivity cell on solutions of known resistivity.

(± 20 to 1000 Ω.m) was measured. To attain this, distilled water was used to which tap water was added incrementally to reduce its resistivity. Firstly, the solution was placed in a container of 400×300×200 mm and measurements were taken with the surface probe of which the electrodes just touched the surface of the water. Measurements were then taken of the same solution in the resistivity cell after it had been made watertight with silicone. A calibrated commercial conductivity probe (CONSORT C561) was used to determine the true resistivity of the solution (being the inverse of the measured conductivity). The process was repeated six times for six different solutions. The embedded probe was not yet available for testing at the time, but it was expected that its performance would be comparable to that of the surface probe due to their similar configuration.

The potential difference was measured for each of the electrode combinations possible with a Wenner array for the surface probe (26 measurement points). For the resistivity cell, measurements were made between each consecutive ring-electrode (4 measurement points) using the 75 mm diameter plate-electrodes. Geometric factors modelled in COMSOL Multiphysics® were applied to each measurement to obtain resistivities (Equation (4.6)), corrected for the boundary effects of the container and the cell. The average resistivity for each solution was then calculated for the probe (from the 26 measurement points) and for the cell (from 4 measurement points) respectively. The mean resistivity and standard deviation obtained for the commercial probe, surface probe and the resistivity cell are shown in Figure 6.12 and Table 6.3.

Figure 6.12 shows that values for the resistivity cell and probe compare well with results

Figure 6.12: Resistivity probe and cell results against resistivities calculated from a commercial CONSORT probe measurements.

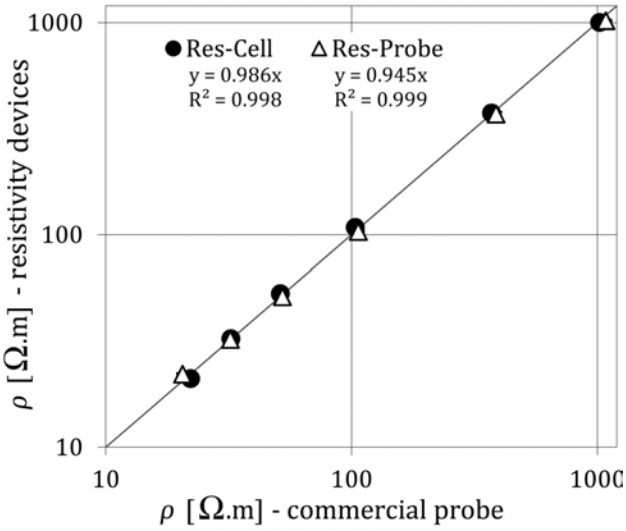

Table 6.3: Resistivity probe and cell results against resistivities calculated from a commercial CONSORT probe measurements.

Test	Measured Resistivity [Ω.m]		
	Consort probe	Resistivity probe	Resistivity cell
1	1020.4	1081.6±9.5	1002.0±16.3
2	370.4	386.7±8.0	374.6±6.3
3	103.4	106.5±0.8	108.2±1.1
4	51.3	52.3±0.9	53.0±0.7
5	32.3	32.1±0.4	32.5±0.5
6	22.1	20.5±0.2	21.1±0.3

calculated from the commercial conductivity probe. It was therefore concluded that the application of modelled geometric factors yields reliable results for the ideal case of a aqueous solution which is assumed to be homogeneous and has low contact resistance. However, results of the resistivity cell and probes had to be validated further on real concrete, as will be discussed in the next section. It is also observed in Table 6.3 that the standard deviations increase as the means of the measured resistivity increase. In order to compare the error for results from different concretes the *coefficient of variation* C_v (standard deviation divided by the mean) is therefore used in the subsequent assessment of the devices on concrete.

6.4.2 Assessment on concrete specimens

The performance of all three devices was evaluated extensively during an experimental program in collaboration with University College Dublin (being a secondary goal of the study which will be discussed in more detail in Chapter 9.2). Mixes D1, D2, and D3 as listed in Table 5.2 were used having varying ground granulated blast furnace slag (GGBS) contents (0%, 50% and 70%). The concrete was tested at different ages enabling data to be obtained for a range of resistivities. Two slabs were cast for each mix of which the first was to be tested with the resistivity probes and the second from which three cores were drilled for testing with the resistivity cell as indicated in Figure 6.13. The cores were trimmed on both ends to a height of 70 mm in order to avoid variability associated with the surface layer of concrete. Only two probes manufactured for embedding were available at the time

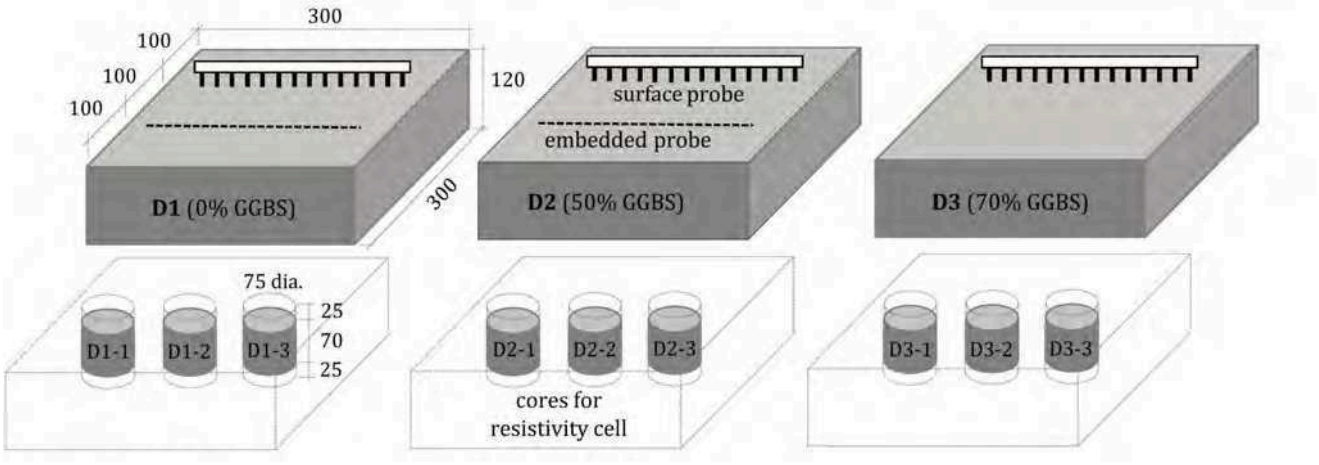

Figure 6.13: Preparation of specimens for testing of Mix D1, D2 and D3 with the resistivity cell and probes.

of casting and thus only slab D1 and D2 were fitted with an embedded probe each.

6.4.2.1 Variability of repeated measurements

An investigation of how consistent results were when repeated was carried out on the cores and slabs from Mixes D1 and D2 (saturated and assumed homogeneous), 14 days after casting. The variability was assessed by leaving the resistivity devices ***in place*** between measurements. This variability is referred to here as "Type A" variability and is associated with the inherent variability of the measured resistivity determined by Equation (4.6), thus including the variability due to the devices themselves, but excluding spacial variability of the material and variability due to contact condition.

For the resistivity cell 8 measurements were taken between each of the consecutive ring-electrodes (position δV_1 to δV_4 as indicated in Figure 6.1(b)) for each core specimen, using the 75 mm diameter plate-electrodes. No significant degradation of the results during testing was observed as could have been caused by drying of the concrete and increase in contact resistance. The geometric factors calculated in Table 6.1 for δV_1 to δV_4 were then applied to obtain the resistivities between each ring-electrode. The Type A variability of resistivity cell measurements was found to be good with coefficients of variation C_v varying from 0.1% to 1% as listed in Table 6.4 for core D1-1 (0% GGBS) and D2-1 (50% GGBS).

For the surface probe and the embedded probe 8 measurements were taken per electrode combination (26 Wenner measurement points) and the geometric factors as per Figure 6.10 were then applied to obtain the resistivity of each point. The coefficient of variation for each of the 26 measurement points is presented in Figure 6.14 for Mix D2. The coefficients

Table 6.4: Type A variability results for measurement points δV_1 to δV_4 of the resistivity cell, for Core D1-1 and Core D2-1.

Core D1-1	Resistivity [Ω.m]		
	Mean	Stdev	C_v
δV_1	34.7	0.3	0.9%
δV_2	35.7	0.3	0.8%
δV_3	32.7	0.3	1.0%
δV_4	34.7	0.3	0.9%
Core D2-1	Mean	Stdev	C_v
δV_1	157.6	0.3	0.2%
δV_2	135.1	0.2	0.1%
δV_3	144.2	0.2	0.1%
δV_4	148.9	0.2	0.1%

Figure 6.14: "Type A" variability results of the surface probe and embedded probe showing the coefficient of variation C_v of each of the 26 Wenner measurement points (Mix D2).

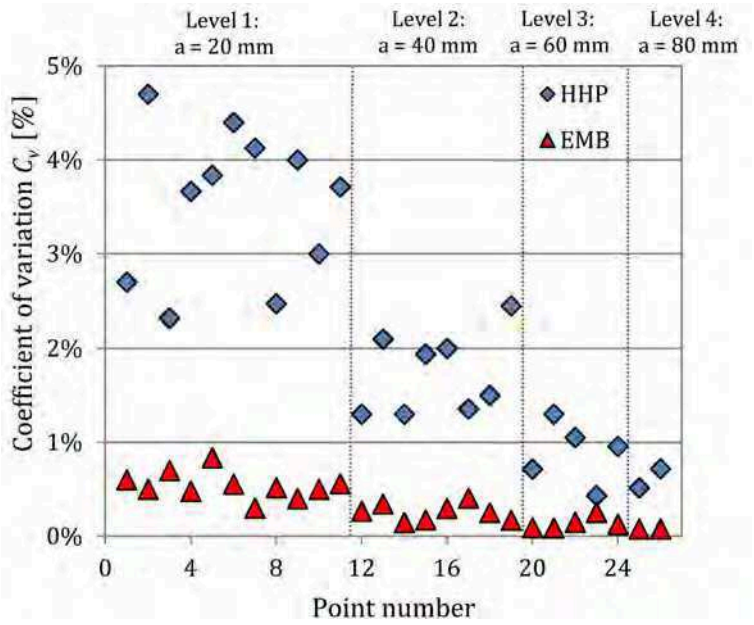

of variation determined for the surface probe vary from 0.5% to 4.5% and for the embedded probe from 0.1% to 1%. It is observed that the coefficient of variation is higher for surface measurements than for embedded measurements. However, there is a decrease in variability as the electrode spacing increases, with the C_v for both the surface and embedded probe being less than 1% for the maximum electrode spacing of 80 mm.

It was anticipated that one of the main advantages of the embedded probe over the surface probe would be improved contact resistance. Resistivities for each of the 26 measurement points of the surface and embedded probes are plotted against the contact resistance measured between the current injection electrodes in Figure 6.16 for both Mix D1 and D2. However, the average resistivity of the 26 measurement points for both probes is almost identical in spite of the large difference in contact resistance. It therefore seems that contact resistance may not be as important as literature suggests [177] [155] - that is if it is within reasonable limits (i.e. not causing measurements to be outside of the range of the equipment). This supports the finding in Section 6.2.4 that the 4-electrode measurement approach mitigates the impact of contact resistance successfully.

6.4.2.2 Variability of re-applied measurements

An investigation of the consistency of measurements when the devices were *removed and re-applied* was also carried out on the cores and slabs from Mixes D1 and D2, 14 days after casting. This variability is referred to here as Type B variability and is associated with the variation due to spacial variability and different contact conditions between each measurement application. The Type B variability of the resistivity cell and surface probe were evaluated by taking 8 measurements per point, as for the Type A variability, but by moving the electrodes to a position close to that of the previous measurement. (Type B variability as defined here does therefore not apply to the embedded probe and it was therefore excluded from this study.)

The coefficients of variation for the Type B variability of resistivity cell measurements varied from 0.8% to 10.5%. Coefficients of variation for the surface probe was between 4% and 8% and was found to be dependent on the electrode spacing, similar to that of the Type A variability. Figure 6.15 shows that the coefficient of variation decreases with the number of measurements taken. It is observed that the coefficients of variation stabilise after approximately six measurements. The coefficients of variability are higher for smaller electrode spacings a, corresponding to a smaller investigation depth, which indicates that localised surface conditions and anomalies have a greater influence on measurements closer to the surface.

The range of the coefficients of variation that was obtained for Type B variability is similar to those reported by Morris [195] (4% to 11%) for 20 measurements with a surface Wenner probe ($a = 25.4$ mm) on concrete cores with a maximum aggregate size of 19 mm at 100% relative humidity. According to Andrade et al. [30] a coefficient of variation of 10% is good and 20% is acceptable for controlled conditions while up to 30% is normal for on-site conditions. It is therefore concluded that all three devices yield results within an acceptable range of variability.

6.4.3 Cross verification of resistivity cell and probe

In this section results from the resistivity cell and the two probes are compared for Mixes D1, D2 and D3 over a period of six months after casting. The specimens were kept submerged in water at a constant temperature of 20°C and tested weekly for the first month after casting and thereafter monthly up to an age of 24 weeks. The only influence on resistivity measurements was therefore the change in the concrete pore structure over time due to hydration.

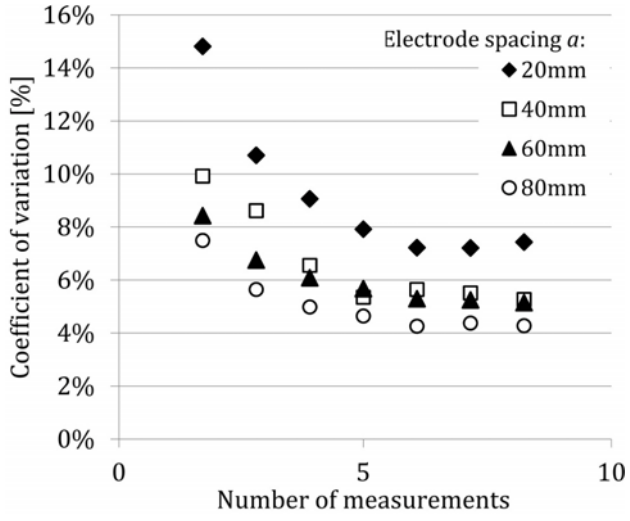

Figure 6.15: Type A variability of the surface resistivity probe showing the decrease in coefficient of variation as the number of measurements and the electrode spacing increase (Mix D2).

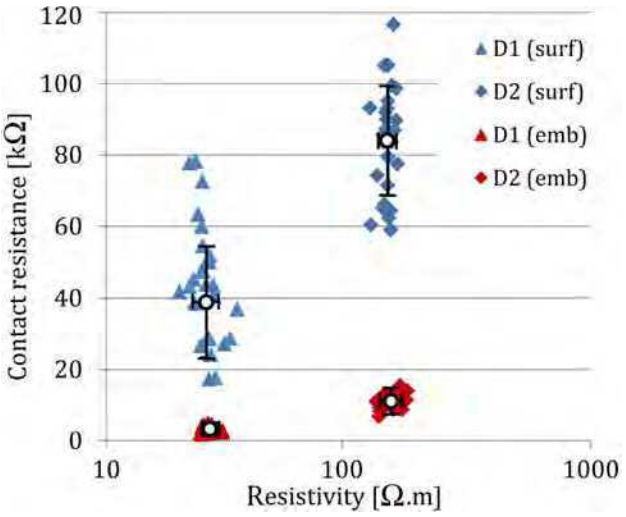

Figure 6.16: Contact resistance against apparent resistivity for the 26 measurement points of the surface and embedded probes (Mixes D1 and D2).

6.4.3.1 Homogeneity assessment

In order to compare the results from the resistivity devices reliably, the homogeneity of each of the specimens was first assessed. This was done by studying resistivities at the different measurement points (corresponding to different depths and lateral displacements) for each specimen at an age of 14 days. For the concrete cores, resistivities over the height of the specimens (measurement points δV_1 to δV_4) were used. For the slab specimens, resistivities obtained for electrode spacings of $a = 40$ mm and larger (measurement points 12 to 26 as per Figure 6.10, corresponding to investigation levels two, three and four) were used, as determined with the surface probe. It was decided to use only these measurement points in order to avoid the variability associated with measurements for small investigation depths. It also meant that the investigated volume would correspond better to that of the cores from which the outer 25 mm layer had been removed (refer to Figure 6.13).

Figure 6.4.3.1 and Table 6.5 show results for each mix for a set of the core specimens (D1-1, D2-1 and D3-1). The resistivities are unchanged over the height of the specimens (δV_1 to δV_4). It can also be seen that the percentage difference from the mean for all the specimens is below 8.6%, which is less than the reported error for Type B variability (Section 6.4.2.2). The results for the slab specimens are shown in Figure 6.18 and Table 6.6 and are also similar irrespective of the level of investigation or lateral shift of the measurement point. The percentage difference from the mean is less than 8.3% with the difference being random. It is therefore concluded that there were no significant resistivity gradients present in either

Table 6.5: % Difference in resistivity from the mean for resistivity results of core specimens D1-1, D2-1 and D3-1.

Core	D1-1	D2-1	D3-1
Point	% Difference from mean		
δV_1	0.7%	7.6%	4.5%
δV_2	3.7%	-7.8%	-2.2%
δV_3	-5.1%	-1.5%	-8.6%
δV_4	0.7%	1.7%	6.3%
	Mean resistivity [Ω.m]		
	34.5	146.5	242.2

Figure 6.17: Resistivity results for measurement points δV_1 to δV_4.

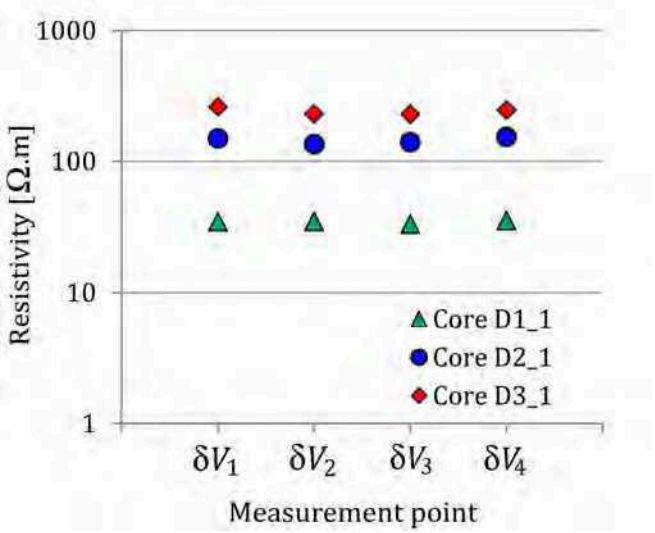

the cores or the slabs which confirms the assumption that the specimens are homogeneous. It can thus be said that the resistivity results are representative of the true bulk resistivity of the specimens and are not apparent resistivities, as would be the case for non-homogeneous specimens.

6.4.3.2 Comparison of resistivity results

Mean resistivities and standard deviations for all three of the devices, on all three mixes, over the 24 week investigation period are presented in Figure 6.19(a). Results from the different resistivity devices compare very well. The results for the resistivity cell, surface probe and embedded probe are very similar for Mixes D2 and D3. For Mix D1 the resistivities from the cell are slightly higher, with the discrepancy increasing with age. As this is not the case for the other two mixes, it is suggested that the discrepancy should not be attributed to the measurement device, but rather to an inherent difference in the properties of the core and slab specimens of Mix D1.

The coefficients of variation between the devices were determined per mix for the entire duration of the test program and were found to range from approximately 0.2% to 10% (refer to Figure 6.19(b)). It is observed that the variability increases as the concrete ages and that it is different for the three mixes, Mix D1 having the highest variability (due to reasons suggested above) and Mix D3 having the lowest. However, variability is within reasonable limits for controlled conditions (less than approximately 20% [30]).

It can therefore be concluded that the resistivity cell, surface probe and embedded probe

Table 6.6: % Difference in resistivity from the mean for resistivity results of slab specimens for Mixes D1, D2 and D3.

	Slab	D1-1	D2-1	D3-1
	Point	% Difference from mean		
Level 2	12	3.1%	-0.2%	4.2%
	13	-5.8%	8.6%	-8.3%
	14	-5.6%	4.4%	-6.1%
	15	2.7%	-4.9%	1.9%
	16	6.3%	-4.7%	-1.4%
	17	6.8%	3.0%	-0.7%
	18	-0.1%	5.5%	7.3%
	19	-7.0%	-4.6%	5.5%
Level 3	20	-8.2%	3.5%	-6.1%
	21	-7.5%	-1.5%	-3.9%
	22	3.9%	-4.9%	-3.2%
	23	5.3%	-1.4%	5.0%
	24	0.9%	3.8%	4.2%
Level 4	25	2.6%	-2.6%	-1.2%
	26	2.5%	-0.9%	2.9%
		Mean resistivity [Ω.m]		
		31.2	149.3	263.4

Figure 6.18: Resistivity results for measurement points 12 to 26 corresponding to investigation levels 2 to 4.

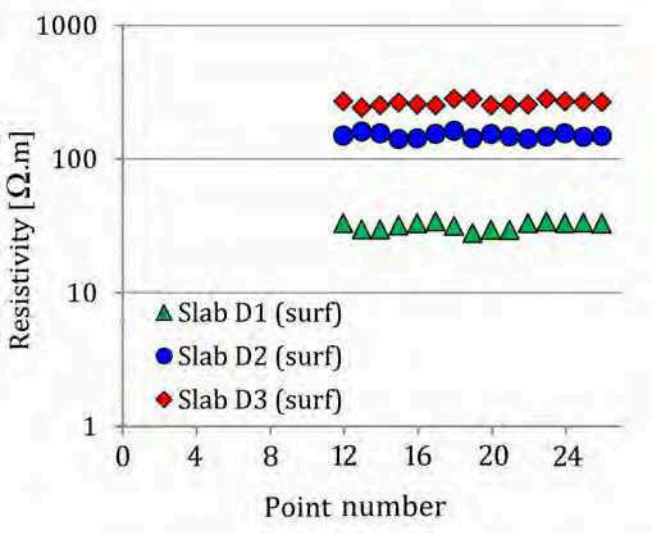

yield similar results within the measurement uncertainty of approximately 10% (for controlled conditions), irrespective of the properties of the concrete mix.

6.4.4 Influence of aggregate size on measurements

In this section another important aspect that influences resistivity measurements on concrete is addressed: the size of the aggregates used in the concrete mix. This investigation was conducted on Mixes B2, B4 and B6 as in Table 5.1, using specimens that formed part of the experimental work presented in the next chapter. The mixes respectively contained nominal maximum aggregate sizes of 4 mm, 10 mm and 20 mm.

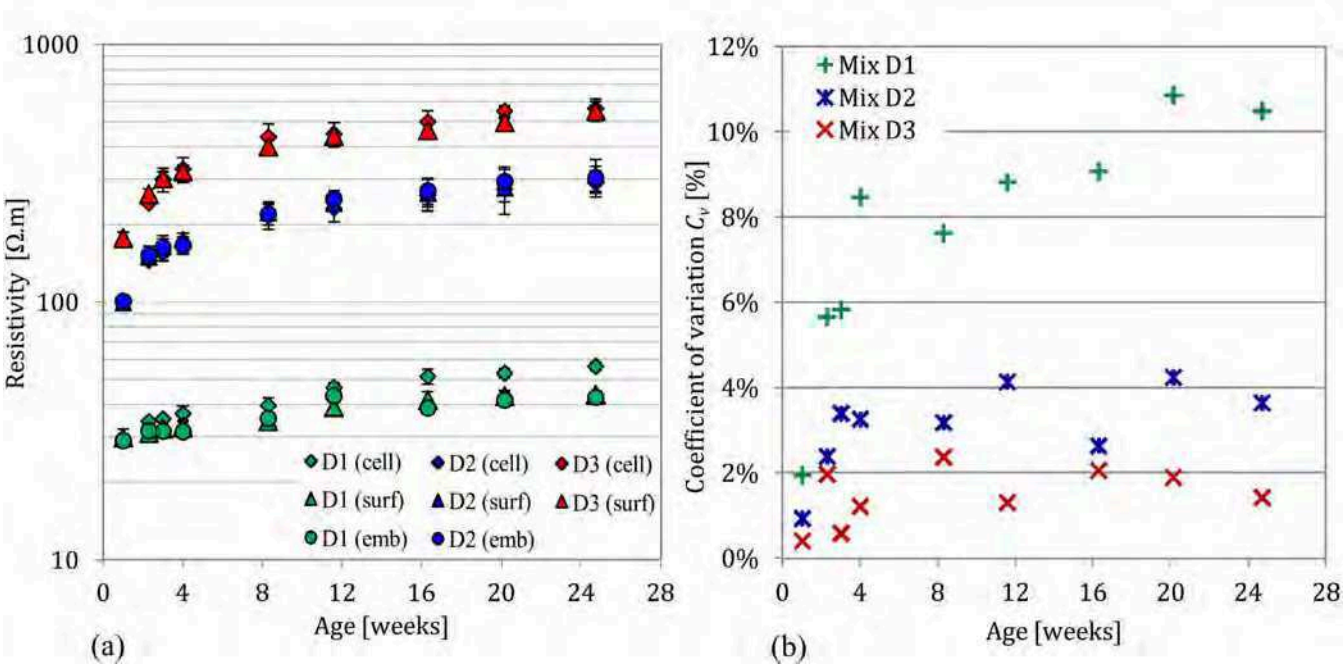

Figure 6.19: (a) Results for Mixes D1, D2 and D3 for the resistivity cell, surface probe and embedded probe tested from an age of 1 week to 24 weeks and (b) the corresponding coefficients of variation calculated between the three devices.

6.4.4.1 Principles

In homogenisation theory [232], representative elementary volume (REV) is defined as the minimum volume of a heterogeneous material for which the measurement results become independent of the size of the investigated volume (refer to Chapter 3.2.5). This is not to be confused with non-homogeneity due to property gradients as dealt with in Sections 6.2.3.3 and 6.4.3.1, but relates to the inherent non-homogeneous nature of concrete at microscopic level (as explained in 6.2.3). For example, Bungey and Millard [53] recommend that cores for the measurement of mechanical properties of concrete mixes containing aggregates of 20 mm, should have a diameter of at least 75 mm. Villain et al. [275] state that the EM-cell (testing cores of diameter 75 mm) presented in Chapter 4.3.1.1 can accommodate mixes with aggregate sizes of up to 20 mm. Gowers and Millard [113] find that 4-point Wenner resistivity measurements do not exceed a coefficient of variation of 5% if the spacing between the inner electrodes is greater than 1.5 times the aggregate maximum particle size. It is therefore clear that the investigated concrete volume can only be regarded as macroscopically homogeneous if the influence of the maximum aggregate size on the measured bulk property (e.g. resistivity in this case) is not significant.

6.4.4.2 Sensitivity of the resistivity cell to aggregate size

For the resistivity cell the spacing between the ring-electrodes has been chosen as 11.7 mm, while the nominal maximum aggregate size used in common concretes ranges up to 20 mm. The ratio of 1.5 suggested by Gowers and Millard [113] would therefore only be valid for concretes containing aggregates of a nominal size less than 8 mm. Though Gowers and Millard's recommendation is related to Wenner point-electrode measurements and not ring-electrodes, it was necessary to investigate the effect of maximum aggregate size on the resistivity cell measurements.

The investigation was achieved by assuming the potential difference measured between the two outermost rings with a spacing of 58.3 mm (δV_5) would yield resistivity results that are not influenced by aggregate size and would therefore be accurate. The sum of the potential differences measured over the intermediary rings (δV_1 to δV_4), should theoretically equate to δV_5. However, if the potential measurements δV_1 to δV_4 are disturbed by the presence of the aggregates (which are infinitely resistive compared to the cement paste), their sum would be higher than δV_5. The percentage error associated with the presence of the aggregates was therefore determined as per Equation (6.6).

$$\frac{\delta V1 + \delta V_2 + \delta V_3 + \delta V_4}{\delta V_5} - 1 = \%Error \tag{6.6}$$

Three saturated concrete cores (Mixes B2, B4 and B6) were tested by measuring $\delta V1$, $\delta V2$, $\delta V3$, $\delta V4$ and $\delta V5$ ten times per specimen with a constant applied current. The percentage error for each of the ten measures was then calculated as per Equation (6.6). The results are indicated in Figure 6.20 with the error bars signifying the standard deviation of the calculated percentage errors. The average percentage error increases from 0.04% for 4 mm aggregates to 0.24% for 20 mm aggregates and is regarded as low compared to errors reported in terms of variability.

6.4.4.3 Sensitivity of the surface probe to aggregate size

A similar strategy was followed to investigate the influence of aggregate size on the resistivity probes as the electrode spacing of 20 mm did not conform to the recommendations of Gowers and Millard for nominal stone sizes above 13 mm. It was assumed that measurements for the largest electrode spacing $a = 80$ mm would be free from any influence of the aggregates. The error of measurements for $a = 20$ mm was therefore calculated by the following equation:

$$\frac{\bar{\rho}_{20mm}}{\bar{\rho}_{80mm}} - 1 = \%Error \tag{6.7}$$

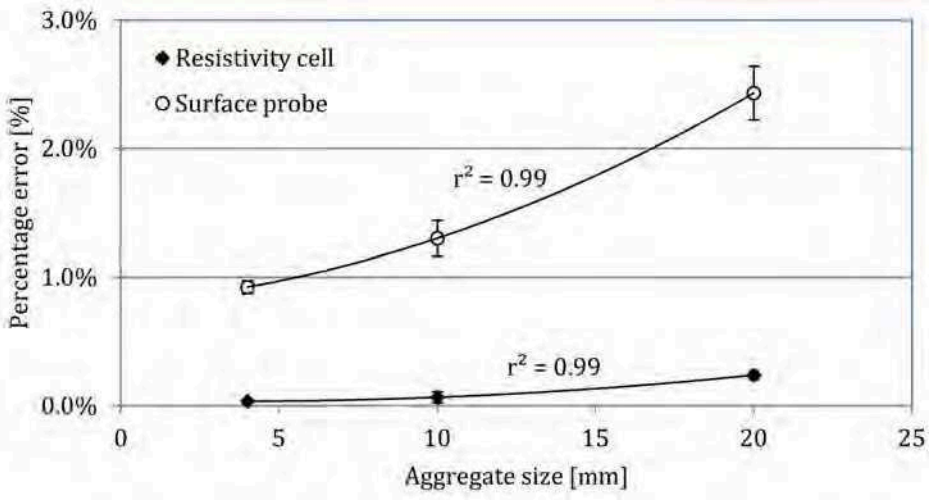

Figure 6.20: Percentage error in potential difference caused by an increase in nominal maximum aggregate size for the multi-ring cell and the surface probe.

The results are shown in Figure 6.20 and display the same trend as for the resistivity cell. The average percentage error increases from 0.9% for 4 mm aggregates to 2.4% for 20 mm aggregates.

The percentage errors for the surface probe are significantly higher than for the resistivity cell, although the errors for both devices are regarded as low for controlled conditions [195]. The difference between results for the two devices highlights the advantage of using ring-electrodes as opposed to point-electrodes, where the influence of the aggregates on measurement is more significant due to their small contact area [113]. It is concluded that the spacing of the ring-electrodes of the resistivity cell at 11.7 mm is sufficient to study concretes where the aggregate size is less than 20 mm and would probably accommodate far larger aggregate sizes without significant measurement error. Errors for the resistivity probe are also far below reported values for Wenner measurements [30] and are therefore regarded as acceptable to investigate concrete containing aggregates up to at least 20 mm nominal size.

6.5 Conclusion

In this chapter new devices for the measurement of concrete resistivity were presented: a multi-ring resistivity cell for laboratory application, and two versions of a multi-electrode resistivity probe for in situ application. The multi-electrode configuration of each of these devices enables resistivity to be assessed over the depth of the investigated concrete. It also enables many measurements to be made in a relatively short time, from which a reliable

average resistivity can be determined for a homogeneous concrete specimen.

It was found that boundary effects can be corrected for by geometric factors determined from a finite element model of the same geometry as the investigated medium. For homogeneous concrete the application of these factors will yield resistivities similar to the true bulk resistivity. For non-homogeneous concrete it will yield apparent resistivities, however the true resistivities as a function of depth can be approximated by means of geophysical inversion (this is further explored in Chapter 9).

For the resistivity cell, it was found that the use of a plate-electrode size corresponding to the cross-sectional area of the specimen yields resistivities approximately halfway between the ring-electrodes, even for non-homogeneous specimens. This is therefore a special case where the apparent resistivities can in fact be associated with a specific depth. It was also confirmed that the 4-electrode method performs better than the 2-electrode method, successfully mitigating the effects of contact resistance and electrode polarisation.

The consistency of the results in term of variability for the three resistivity devices on saturated homogeneous concrete was found to be good. Resistivities determined by each of the devices for a wide range of concrete conditions (in terms of mix and age) compared very well. The homogeneity of concrete cores and slabs were also successfully evaluated by exploiting the multi-electrode functionality of the devices.

The capability of the resistivity cell and probes to determine the bulk resistivity of concrete, assess its homogeneity, and relate gradients to investigation depth will be used extensively in the experimental work presented in the following chapters.

Chapter 7

Investigation of the dependency of EM properties on concrete condition

7.1 Objectives

In this chapter the main experimental work that was conducted as part of this thesis is presented. The chapter focusses on the investigation, evaluation and modelling of the dependency of electromagnetic (EM) observables on concrete condition in a controlled laboratory environment. Results from this chapter are implemented in Chapter 8 to characterise concrete slabs from EM observables obtained using techniques suitable for in situ testing.

In Section 7.2 a parametric study, with the aim to produce master curves for EM properties as a function of a selection of condition parameters is presented. Firstly, a short introduction on the principles of the Design of Experiments (DOE) is given, whereafter the selection of the EM observables and condition parameters forming part of the parametric study are discussed. Next, the criteria that were followed to select the appropriate concrete mixes and the experimental schedule to condition and test the specimens are detailed. Lastly the results of the parametric study are presented and the dependency of each EM response on the respective condition parameters is evaluated.

In Section 7.3 the capacity of two well-known composite material models to simulate the experimental results is investigated. In Section 7.4 multiple linear regression is introduced as a method to obtain a more representative model for the electromagnetic response of concrete. The contribution of the respective condition parameters and their interactions to the EM responses is thus evaluated by means of statistical analysis.

7.2 A parametric study in controlled conditions

In this section an introduction is given to the Design of Experiments, which plays an important role in the parametric study presented later in this chapter. The reasoning and methodology that were followed to select appropriate parameters, to prepare the specimens, conduct the test campaign and analyse the results are also given. The main goal of the parametric study was to obtain master curves for the studied EM observables as a function of the most important condition parameters in order to use these relationships as part of the regression modelling in Section 7.4.

7.2.1 Design of Experiments

7.2.1.1 Overview

The "Design of Experiments" (DOE) is an important field of study which should be considered during the planning of any experimental program where the influence of various variables on a response is studied. The methodology for the design of experiments (hereafter referred to as *experimental design*) was first proposed by Fisher [100] [101], who detailed a systematic and statistical approach to compare the influences of various factors on a response in the most efficient way. The goals of experimental design are listed by Goupy and Creighton [112] as follows:

- *Quickly arrive at the best possible results*
- *Omit unnecessary trials*
- *Give results with the best possible precision*
- *Progress without failure*
- *Establish a model for the studied phenomenon*
- *Discover the optimal solution*

The advantages of a well designed experiment are therefore substantial. Experimental design has been applied in many fields and is the topic of several textbooks [193] [112] [48]. Only the most basic fundamentals will therefore be highlighted here.

In the design of experiments the influence of certain parameters (*factors*) on the experimental result (*response*) is expressed as a function as in Equation (7.1).

$$y = f(x_1, x_2, x_3, ..., x_p) \tag{7.1}$$

where the response y is a function of the factors $x_1, x_2, ..., x_p$, with p the number of factors.

Experimental design is based on the assumption that an empirical model, where the response is approximated by a polynomial function, can accurately predict results for a well defined experimental domain [168]. The model to be investigated as part of the experimental program is "designed" by selecting the *levels* at which each factor is to be tested. The number of levels of a factor is associated with the *degree* of its relationship with the response. For example, a 2-level factor enables the evaluation of a linear relationship and a 3-level factor the evaluation of a quadratic relationship and so forth. The complexity of the polynomial function in Equation 7.1 is therefore governed by the relationships that are assumed between each of the factors and the response. Factors are restricted to lie between a lower level and a upper level which defines the *factor domain*. The respective factors are often centred and scaled (i.e. normalised) to lie between the same minimum and maximum of -1 and 1 and are then referred to as *coded factors* [112].

A common type of designed experiment is the full factorial model where all the interactions between the factors are included in the polynomial function. Equation (7.2) is an example of a full factorial model for three factors with two levels each.

$$y = \beta_0 + \beta_1 x_1 + \beta_2 x_2 + \beta_3 x_3 + \beta_{12} x_1 x_2 + \beta_{13} x_1 x_3 + \beta_{23} x_2 x_3 + \beta_{123} x_1 x_2 x_3 \tag{7.2}$$

where y is the response, x_1, x_2, x_3 are the factors and the $\beta_1, \beta_2, \beta_3, ..., a_{123}$ are the coefficients of the polynomial.

In order to solve the model coefficients in this example, 8 tests are required i.e. the product of the levels of all the factors, thus 2×2×2. This 2^3 experiment (with coded factors) is represented graphically in Figure 7.1(a), with the design matrix containing the levels at which the factors are to be tested for each test-point indicated in Figure 7.1(b). The coefficients are then obtained through some form of optimisation. If the factors are coded, the coefficients can be compared to assess the importance of the respective factors and their interactions. Using this approach, terms that do not significantly contribute to the response can be removed from the model, whereafter adjusted coefficients for a new, simplified model can be determined.

7.2.1.2 Implementation

Classically, the design of an experiment starts with the selection of the response and the factors whose influence on the response is to be evaluated. Thereafter appropriate levels

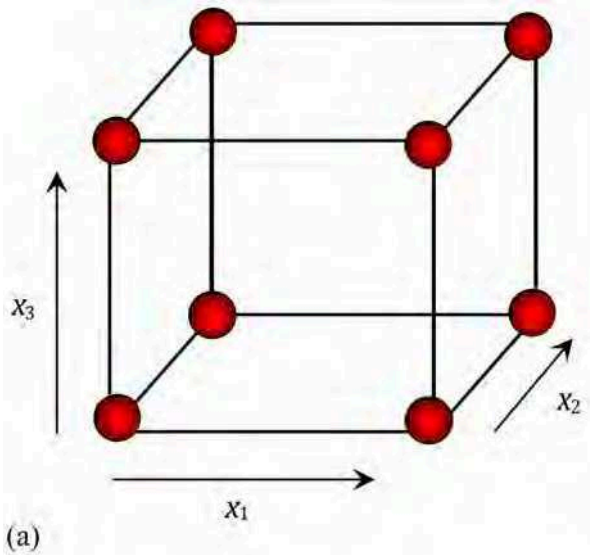

Test	Factor X_1	Factor X_2	Factor X_3
1	−1	−1	−1
2	1	−1	−1
3	−1	1	−1
4	1	1	−1
5	−1	−1	1
6	1	−1	1
7	−1	1	1
8	1	1	1

(b)

Figure 7.1: Representation of a 2^3 full factorial designed experiment with (a) a graphical representation of the p-dimensional space of factors ($p = 3$ in this example) (b) the design matrix showing the coded test levels required for each test.

are assigned to each factor in accordance to the assumed relationship between the response and each factor. In the context of the work presented in this thesis the *EM observables* represent the *response* and the parameters related to *concrete condition* represent the *factors*. However, the principles of experimental design were not implemented rigorously from the start of the experimental phase because of uncertainty as to the minimum number of levels that were required for each factor in order to produce a realistic model. This was due to the inconsistent findings reported in literature regarding the nature of the dependency of EM properties on the state of concrete (refer to Chapter 3.4).

It was thus decided rather to perform a parametric study, covering a range of levels for the most important condition parameters, in order to produce master curves from which the relationships between the EM observables and condition parameters could be evaluated individually. Nevertheless the principles of experimental design were used as a guide to shape the experimental program and was then super-imposed on the experimental data to statistically evaluate the significance of the interactions between the various factors as presented in Section 7.4.

The following sections explain the reasoning and methodology on which the selection of the EM observables, condition parameters and levels for the parametric study were based.

7.2.2 Selection of EM observables

The EM observables selected for the parametric study were governed by the response that could be obtained from the in situ techniques discussed in Chapter 4.2.2 and the frequencies at which they operate. As a reminder, these techniques and their capabilities are summarised below:

- The ***surface resistivity probe*** measures apparent resistivity and operates at very low frequencies yielding results equivalent to that of direct current. From this apparent resistivities can be obtained which equate the true resistivity of a concrete element for homogeneous conditions. For non-homogeneous conditions true resistivities can be estimated by means of inversion of the measured resistivities as discussed in Chapters 4.3.1.1 and 4.2.2.2.
- The ***capacitive probe*** measures the resonance frequency shift at low frequencies of approximately 33 MHz, from which the dielectric constant is calculated using a set of calibration curves.
- ***Ground penetrating radar*** (GPR) using antennae with a central frequency 1500 MHz is employed in different configurations yielding different observables:
  - The *fixed offset* GPR configuration enables the calculation of an approximated dielectric constant from the velocity of the propagating material wave. The actual central frequency of the material wave in concrete is approximately 900 MHz for 1500 MHz antennae, but may vary for concrete with different properties [132].
  - The *multi-offset* (WARR) GPR configuration enables the frequency dependent complex permittivity to be determined from an inversion protocol that was adapted by Ihamouten [132] for concrete. However, the reliability of the results for the loss factor is less than that for the dielectric constant and decreases as the frequency decreases. The loss factor at low frequencies (equivalent to the capacimetry range) cannot be reliably determined with this method at this stage.

The parametric study was conducted under controlled laboratory conditions on concrete core specimens by employing the new resistivity cell presented in Chapter 6.2 and the EM-cell described in Chapter 4.3.1.1. This test campaign was to produce experimental data from which EM observables corresponding to those of the in situ techniques could be obtained.

The first EM observable to be used as part of the parametric study was ***DC-resistivity*** (ρ). The actual parameter used for the purpose of the master curves was the logarithm of resistivity $Log(\rho)$, due to various reasons. Firstly, the use of $Log(\rho)$ corresponds with common practice [234], due to the wide range of resistivity values that are possible for concrete.

Secondly, the use of the logarithm is advantageous when regression analysis is performed, because the Log-transformation causes the variance of resistivity measurements (which increases with as the mean increases, Figure 4.2) to be stabilised. Results from the resistivity cell could be used as EM observables for the purposes of the parametric study as they were representative of results from in situ techniques, as was confirmed in Chapter 6.4.3.

The EM-cell enabled the measurement of the frequency dependent complex permittivity over a large bandwidth (approximately 50 MHz to 1000 MHz) from which values corresponding to the responses of the in situ techniques could be obtained to generate the appropriate master curves. The ***dielectric constant at 33 MHz*** (ε_1') was selected as the second EM observable in order to correspond to the frequency at which the capacitive probe operates. Values at 33 MHz, which are out of the range of the EM-cell, were obtained by fitting the experimental results from the cell to Jonscher's model [137] and extrapolating the optimised model to 33 MHz as proposed by Ihamouten et al. [133]. This methodology is also detailed in the thesis of Ihamouten [132] and by Villain et al. [274] and will not be further elaborated on here.

The third EM parameter for which master curves were determined was the ***dielectric constant at 900 MHz*** (ε_2'). Data at this frequency could be easily extracted from the experimental results produced by the EM-cell. The dielectric constant at 900 MHz was deemed to be adequately representative of the dielectric constant determined from fixed offset GPR data (1500 MHz antennae) in spite of some variation in the true central frequency of the in situ response. This is motivated by the fact that the dielectric constant at high frequencies is not particularly frequency dependent and is therefore not sensitive to limited variation in frequency.

Master curves were also produced for the ***loss factors at 33*** and ***900 MHz*** (ε_1'' and ε_2'') for the sake of completeness, though the determination of the loss factors with in situ techniques is less reliable at present [132] as mentioned above. The data for the master curves of ε_1'' and ε_2'' were obtained from EM-cell data in the same manner as the respective dielectric constants.

Figure 7.2 shows the frequencies at which the different EM observables related to complex permittivity are obtained from experimental data from the EM-cell. The optimised fitting of Jonscher's model to the experimental data and its extrapolation to 33 MHz are indicated in red and blue for the dielectric constant and loss factor respectively. Table 7.1 summarises the details of the selected EM observables, the symbols by which they will be referred to from here onwards, how they were obtained and to which in situ technique they relate.

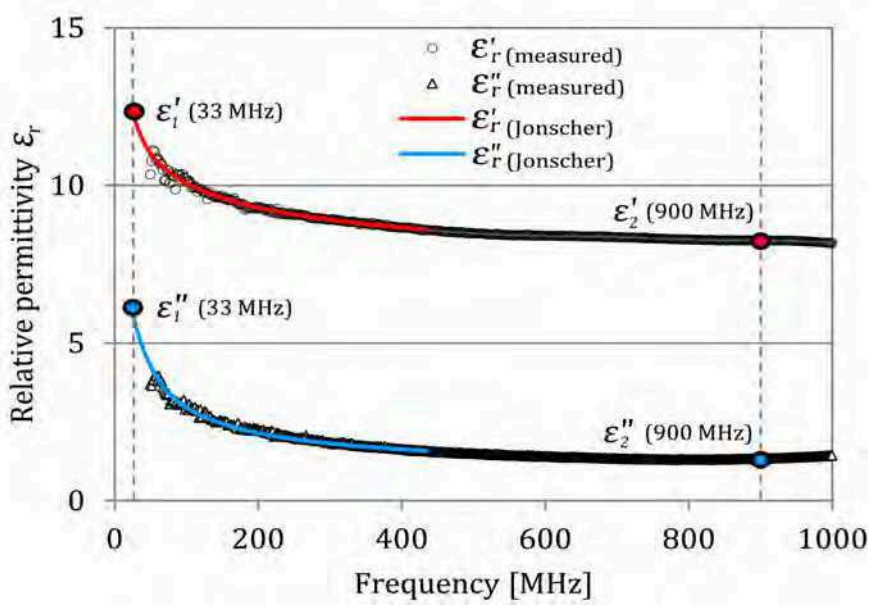

Figure 7.2: Extraction of EM observables related to permittivity at low and high frequencies from experimental data obtained from the EM-cell (Mix B3-1, $S = 80\%$, $C = 0$ g/L).

Table 7.1: Electromagnetic observables selected for the parametric study.

EM observable	Frequency	Symbol	Unit	Laboratory device	In situ device
DC-resistivity	-	$Log(\rho)$	-	resistivity cell	resistivity probe
Dielectric constant	33 MHz	ε'_1	-	EM-cell	capacimeter
Dielectric constant	900 MHz	ε'_2	-	EM-cell	GPR (1.5 GHz)
Loss factor	33 MHz	ε''_1	-	EM-cell	-
Loss factor	900 MHz	ε''_2	-	EM-cell	GPR (1.5 GHz)

7.2.3 Selection of concrete condition parameters

The selection of the parameters related to concrete condition for the parametric study is discussed in this section. Before introducing these parameters some clarification is needed as to what the term "condition parameters" signifies. The parameters that influence the electromagnetic properties of concrete can be categorised into two groups [283]: parameters related to concrete condition in terms of the environmental exposure and parameters related to the concrete durability in terms of to the inherent material properties of the concrete. The former depends on the location of the concrete an the climatic conditions and includes parameters that can vary significantly over time, such as moisture content, chloride content, the ambient temperature etc. (refer to Chapter 3.4.1). The latter depends on the concrete

mix formulation and construction practices (refer to Chapter 3.4.2) and can be quantified by parameters such as porosity, W/C-ratio, permeability, diffusivity and many more.

With regard to service life design (Chapter 2.3.2), parameters related to material properties are used as input for predictive models, whereas parameters from both categories are used in structural health monitoring. Parameters related to environmental exposure are usually referred to in terms of environmental class [26] or exposure class [8], whereas those related to material properties are referred to as durability indicators [41] or durability indexes [26]. In this thesis, for the purpose of modelling the electromagnetic properties of concrete, the term ***condition parameters*** is therefore introduced as a general description referring to all these parameters. The models and empirical studies discussed in Chapter 3.3 were used as the basis for the selection of the appropriate condition parameters for the parametric study. The parameters used in composite material models such as Archie's law and the CRIM model (discussed in Chapter 3) have been widely used in literature to model the influence of concrete condition on resistivity and permittivity. These models demonstrate the influence of the presence of water, the ionic content of the pore solution and bulk porosity on resistivity and permittivity. The findings of the empirical studies, as presented in Chapter 3.4, also confirm that all the EM observables selected in Section 7.2.2 are significantly sensitive to these three variables.

Degree of saturation (S) was chosen as the condition parameter to represent the hydric state of the concrete, as it is independent from porosity, unlike water content. The conductivity of the pore solution is largely dependent on the presence of chloride ions [47]. The condition parameter chosen to represent the ion content of the pore solution was therefore chosen as ***total chloride content*** ($C\ell_t$) by weight of cement, as this is the standard measure for chloride content used in practice [16] [12] [202]. It should be noted that chloride content expressed as "percentage by weight of concrete" may be more appropriate, as the vacuum saturation procedure could result in chlorides penetrating the aggregates. However, "percentage by weight of cement" was retained as unit due to it being the standard convention. Also, in literature the *free* chloride content is more often related to the EM properties of concrete [43] than total chloride content, however, it is difficult to determine in practice (refer to Section 7.2.5.5). Therefore, because the proportion of free to total chlorides is governed by the inherent properties of the concrete [135], it was assumed here that parameters related to material properties would compensate for the use of total chlorides.

Porosity accessible to water (ϕ) was chosen as the first condition parameter to represent the concrete material properties in terms of pore structure. The dependency of resistivity on the interconnectedness of the pore structure is also often cited in literature [43]. The interconnectedness of the pore structure can be expressed by parameters such as tortuosity (Chapter 3.3.2.1) and indirectly by diffusivity (Chapter 2.3.4.3) and permeability (Chapter 2.3.4.1) and more. The dependency of resistivity on the interconnectedness of the pores is confirmed by the Nernst-Einstein relationship between diffusion and conductivity (Equa-

Table 7.2: Condition parameters selected for the parametric study.

State parameters	Symbol	Unit	Test method
Degree of saturation	S	%*	AFPC-AFREM protocol [5]
Total chloride content	$C\ell_t$	%bwc**	Potentiometric-AFREM protocol***
Porosity	ϕ	%*	AFPC-AFREM protocol [5]
Chloride diffusivity	D	$\times 10^{-12}$ m^2/s	Rapid chloride migration, Nordtest 492 [6]

*percentage is used in the text and graphs, though all equations are based on fractions

**percentage by weight of cement

***new protocol proposed for the purposes of this thesis

tion (2.36)) and the presence of the lithology factor $\mathfrak{a}$ in Archie's law (which is meant to account for the interconnectedness of the pores [33]). These parameters are all related to the ease with which concrete is penetrated by various substances. As they are all correlated [21] [25], it was not of critical importance which one was selected as condition parameter representative of the interconnectedness of the pore structure for this study - any parameter related to the penetrability of the concrete would suffice. However, a parameter related to ***chloride diffusivity*** (D) was deemed the most appropriate, as the penetrability of concrete in terms of conductive ions such as chloride was of particular interest in terms of this thesis.

To summarise, the selected parameters can be categorised as those related to environmental condition, being degree of saturation and chloride content, and those related to concrete material properties, being porosity and chloride diffusivity. The condition parameters are listed in Table 7.2, also indicating the test protocols according to which they were determined (which will be further detailed in Section 7.2.5.4).

Three important influences on the EM observables were not included in the parametric study, namely temperature, the nature of the aggregates and cement type. These variables were kept constant throughout the experimental campaign as not to influence the results. It was felt that their exclusion would not prevent the master curves from being used for in situ application. The influence of temperature is mainly important in terms of resistivity measurement and can be corrected for to a large extent, as described in Chapter 3.4.1.3. The influence of the nature of the aggregates is more important for the determination of complex permittivity, especially at GPR frequencies and dry states [87]. However, when some information of the investigated concrete is known, e.g. whether the aggregates are primarily of siliceous or calcareous origin, a correction for the nature of the aggregates is possible [87] [274]. Lastly, the type of cement has an influence on the microstructure of the concrete and the properties of the pore solution [47]. Although it was assumed that this

influence would manifest itself in the parameters that form part of the study in any case i.e. porosity and diffusivity, only ordinary Portland cement (OPC) mixes were used to avoid unnecessary variability.

7.2.4 Concrete mix design

The concrete mixes to form part of the parametric study were carefully selected and the main considerations that were taken into account are listed below:

1. *Concrete property range:* the concrete had to represent a range of porosities and diffusivities to enable the influence of these condition parameters on the EM observables to be studied. The concretes also had to be representative of common concretes used in practice in order for the master curves to be applicable outside of this study.
2. *Age of the concrete:* it was important to perform the study on concrete of which the pore structure would remain unchanged for the duration of the experimental program. Mature concrete of which the hydration had stabilised was therefore required in order to obtain good results.
3. *Ability to be easily conditioned:* as the concrete was to be tested at several different levels of degree of saturation and chloride content, the concrete specimens had to be of a size and mix that could be easily saturated, homogenised and dried yielding results within reasonable time.

With these criteria in mind, four mature concretes representing four concrete mix designs (B3, B4, B5 and B6) were selected, as indicated in Chapter 5, Table 5.1. The concrete had been cast in 2007, three years before the start of the work presented here. It formed part of two preceding PhD theses [61] [132] and an internal IFSTTAR project [272] on the dependency of electromagnetic and ultrasound observables on water content. The mix designs were carried out using the software package BétonlabPro ©LCPC [241]. As part of the thesis of Ihamouten [132] six slabs of dimensions 600×600×120 mm were cast per mix, five of which were homogenised at various states of relative humidity for EM testing with in situ techniques. A portion of the sixth slab was cored to obtain specimens which were tested in the EM-cell and witness cores to confirm the homogeneity of the slabs through gammadensimetry [278]. The remainder of the sixth slab (a portion of approximately 400×600×120 mm) was subsequently stored in saturated conditions. Additional cylindrical specimens had also been manufactured at the same time as the slabs from which the properties of each mix were determined by means of destructive testing and chemical characterisation.

The research presented in this chapter differs from previous work by Ihamouten et al. [132] on the EM response of concrete, as here DC-resistivity was included as observable and chloride content was studied in addition to water content. Since there was some overlap between the respective experimental programs, it was envisaged that raw data from Ihamouten's work could supplement this parametric study. However, it was subsequently found that very little of the data was useful for this study, as testing had been conducted at relatively low saturations (below 64%) due to the experimental protocol that was followed. Because corrosion risk becomes significant at resistivities below approximately 100 Ω.m, which correspond to degrees of saturation above approximately 60% [46], data at higher saturations was required for the parametric study presented here.

7.2.4.1 Properties of selected concrete mixes

The selected mixes comprised two concretes (B3 and B4) and two mortars (B5 and B6) which were representative of a range of concretes in terms of durability [275]. The most important properties of the selected mixes are shown in Table 7.3, which should be read in conjunction with Table 5.1 in Chapter 5. The characteristic compressive strength was determined in 2007 at an age of 28 days and the porosity accessible to water at 90 days. The porosity was re-evaluated in 2011 for the purposes of the work presented here. The chloride diffusion coefficient was determined in 2012 specifically for this study using the migration test method NordTest 492 [6] (refer to Appendix A.2).

The pore structure of each of the four mixes is represented schematically in Figure 7.3(a) to demonstrate the relationship between the mix properties W/C-ratio and paste volume and

Table 7.3: Properties of the selected mixes forming part of the parametric study.

Mix properties	Unit	B3	B4	B5	B6
W/C-ratio	-	0.36	0.69	0.35	0.67
Paste volume fraction	-	0.37	0.36	0.54	0.51
Maximum nominal aggregate size	mm	10	10	4	4
Slump	mm	10	11	22	62
Entrained air	%	2.9	3.8	2.7	2.7
Compressive strength (28 days, 2007)	MPa	67.5	37.1	66.6	34.0
Porosity accessible to H_2O (90 days, 2007)	%	13.5±0.3	17.5±0.6	19.5±0.3	26.4±0.5
Porosity accessible to H_2O (4 yrs, 2011)	%	12.9±0.2	18.2±0.4	19.1±0.3	26.9±0.5
Dry density (4 yrs, 2011)	kg/m^3	2253	2129	2101	1892
Chloride diffusivity (5 yrs, 2012)	$\times 10^{-12}$ m^2/s	4.1	55.4	6.5	62.1

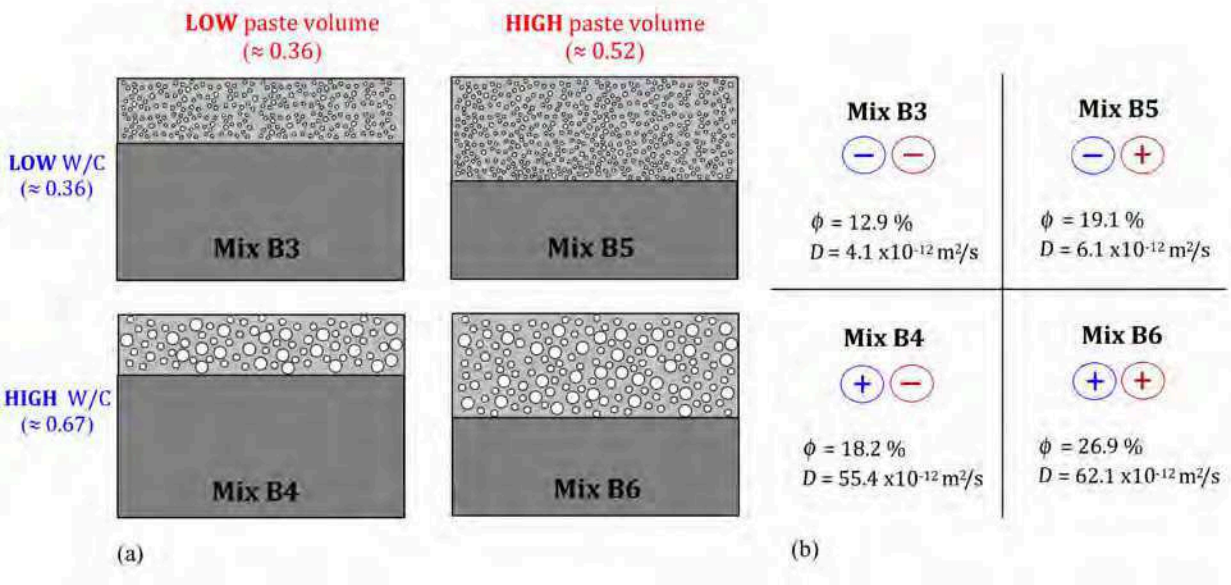

Figure 7.3: Representation of Mixes B3, B4, B5 and B6 selected for the parametric study showing (a) their composition and (b) the combinations of minimum and maximum W/C-ratios (blue) and paste volumes (red), with the porosities (4 yrs) and chloride diffusion coefficients (5 yrs) indicated.

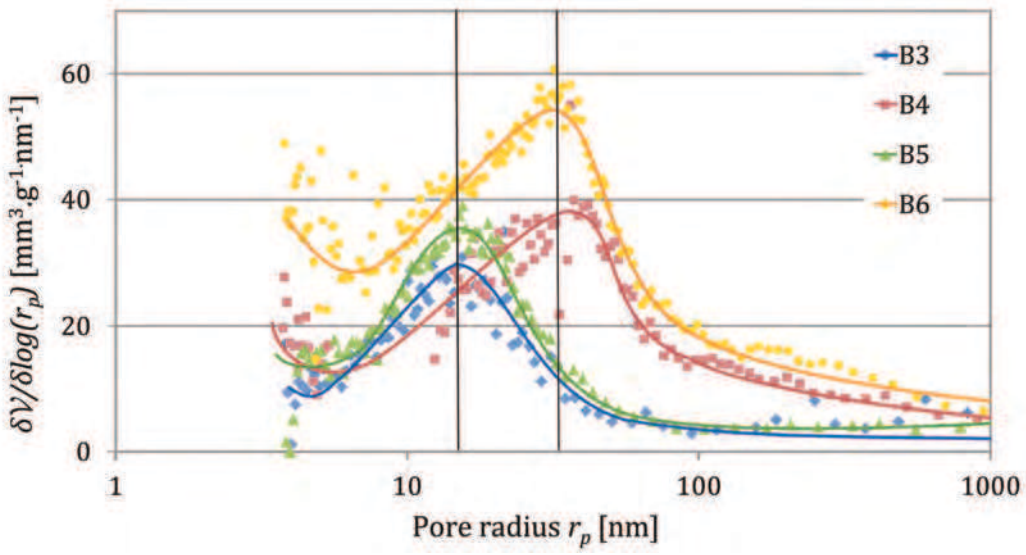

Figure 7.4: Pore size distribution of Mixes B3, B4, B5 and B6 (trendlines added manually).

the condition parameters porosity and diffusivity for each mix. The schematic for each mix is divided into the aggregate and hardened cement paste components, reflecting the paste volume fraction of each mix. The hardened cement paste contains the pores of which the size is determined by the W/C-ratio.

The mixes had been designed to cover all combinations of the lower (−) and upper (+) limit of W/C-ratio and paste volume, similar to a 2^2 experimental design as indicated in Figure 7.3(b). These combinations resulted in low porosity and low diffusivity for the (−)(−) case (Mix B3) and in high porosity and high diffusivity for the (+)(+) case (Mix B6).

The two intermediate cases (+)(−) and (−)(+), corresponding to Mixes B4 and B5, yielded similar bulk porosities but diffusivities that were significantly different. This highlights that concrete with similar porosities can have very different pore structures. It therefore enabled the comparison of the dependency of the EM observables on two mixes with different pore structures but similar bulk porosities.

The difference in pore structure of the mixes is also illustrated by the pore radius distributions in Figure 7.4. The results were obtained from mercury intrusion porosimetry [5] as part of the work of Ihamouten [132]. It can be seen that pore radii for Mixes B3 and B5 are lower than that of Mixes B4 and B6. This corresponds to the difference in diffusivity between the low W/C-ratio mixes (B3 and B5) and the high W/C-ratio mixes (B4 and B6). Further it is observed that the the peak of each distribution (corresponding to the maximum volume of pores) is correlated to the porosity, increasing from Mixes B3 to B6.

7.2.4.2 Age of the concrete

It was confirmed that the hydration of the mixes had stabilised by comparing the porosities of the mixes determined in 2011 to the original values obtained in 2007. The protocol proposed by AFPC-AFREM [5] was adopted to determine the porosity by implementing Equation (2.15). In accordance with the protocol, a core specimen of each mix was vacuum saturated to determine its saturated and hydrostatic mass and subsequently dried at 105°C until mass stabilisation to determine its dry mass. In Figure 7.5 it can be seen that there was no significant reduction in porosity from 2007 to 2011 and it was therefore assumed that the concretes were completely stable in terms of pore structure.

7.2.4.3 Ease of conditioning

Knowledge about the ease with which the respective concrete mixes could be conditioned was available from the previous experimental program of Ihamouten [132]. In fact, the

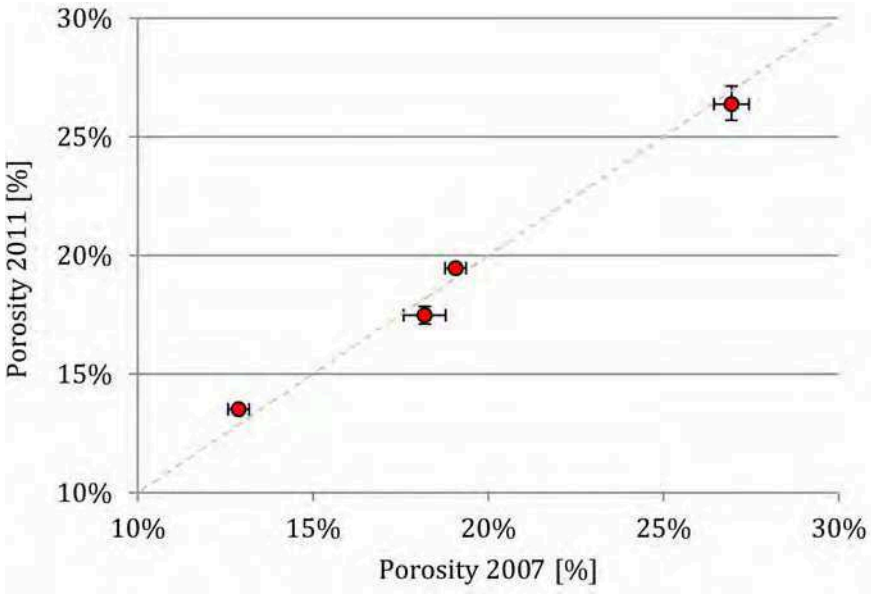

Figure 7.5: Results for the porosity of Mixes B3, B4, B5 and B6 measured in 2011 against results from 2007, demonstrating that the mixes are mature.

exclusion of Mixes B1 and B2 from this parametric study, was because it took significantly longer to condition these mixes during the previous study due to the larger aggregates they contained. As there were stringent time constraints for the preparation of concrete specimens, only Mixes B3, B4, B5 and B6 which had previously proved to condition within reasonable time, were selected.

Concrete cores of 75 dia.×70 mm were used to obtain the master curves, as they were suitable for testing in the resistivity- and EM-cell. These relatively small cores were much easier to condition, to homogenise and to manoeuvre than concrete slab specimens and therefore saved considerable amounts of time. Three specimens could therefore be prepared per test-point leading to more reliable results. This approach ensured that the maximum amount of information could be obtained to the best precision in the least amount of time.

7.2.5 Experimental program

7.2.5.1 Test overview

The experimental program was scheduled to start at the beginning of 2011, after the development of the resistivity devices presented in Chapter 5. It was a priority to test as wide range of condition parameters related to the environment (degree of saturation and chloride content) as the time permitted for each of the four selected mixes. The resistivity

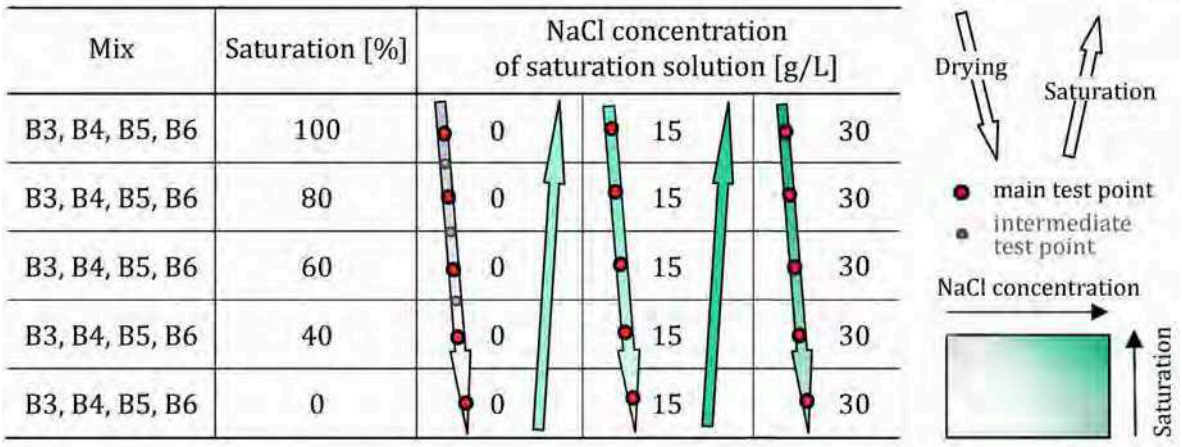

Figure 7.6: Test schedule indicating test-points at each degree of saturation and chloride concentration for the parametric study.

and permittivity of the four mixes were tested over the range of degrees of saturation and chloride concentrations as indicated in Figure 7.6. Special interest was taken in the influence of degree of saturation on the various EM observables, as it was regarded as a particularly significant variable in the literature related to the EM response of concrete (discussed in Chapter 3). To condition the specimens, a drying protocol was followed with the main measurement points at 100%, 80%, 60%, 40% and 0% saturations for three states of NaCl conditioning (0, 15 and 30 g/L NaCl). Intermediate measurement points at 90%, 70% and 50% saturation were also included for the initial, uncontaminated state.

7.2.5.2 Concrete conditioning

Testing for the parametric study commenced at a water saturated state (0 g/L NaCl) after the specimens were saturated under vacuum with tap water according to the protocol recommended by AFPC-AFREM [5]. The specimens were then dried at a temperature of 70°C until they reached the mass associated with the required degree of saturation as calculated by means of Equation (2.16). The porosities determined in 2007 were used to calculate these masses as the new porosities were not yet available at this stage. The temperature of 70°C was selected as it was regarded as low enough to prevent bound water to be released during drying, thus avoiding a change in the chemical structure of the concrete [5].

The specimens were then wrapped in aluminium foil ensuring that they were airtight and homogenised at 70°C for a minimum of two weeks. After the test-point at 40% saturation and 0 g/L NaCl, the specimens were dried until their mass stabilised. They were then subsequently saturated with a saline solution of 15 g/L NaCl to obtain the second level in terms of chloride content. The third chloride level was obtained by drying the specimens

Table 7.4: Details of the test specimens used in the parametric study.

		No*	Dimensions	Purpose
EM	**testing**	**BX-1**	**75 dia.×70 mm**	**EM testing: specimen 1**
		BX-2	**75 dia.×70 mm**	**EM testing: specimen 2**
		BX-3	**75 dia.×70 mm**	**EM testing: specimen 3**
Property	verification	BX-4	75 dia.×70 mm	Verification of porosity (2011)
		BX-5	75 dia.×70 mm	Chloride content: 0 g/L witness core
		BX-6	75 mm dia. 75 dia.×70 mm	Chloride content: 15 g/L witness core
		BX-7	75 mm dia. 75 dia.×70 mm	Chloride content: 30 g/L witness core
		BX-10	100 dia.×100 mm	Verification of homogeneity
Diffusion	testing	BX-11	100 dia.×50 mm	Chloride diffusivity: specimen 1
		BX-12	100 dia.×50 mm	Chloride diffusivity: specimen 2**
		BX-12	100 dia.×50 mm	Chloride diffusivity: specimen 3**

*"X" refers to 3, 4, 5 and 6

**specimens from the campaign of Ihamouten [132]

contaminated with 15 g/L NaCl after they were tested at 40% saturation and then saturating them again with a 15 g/L NaCl solution. It was assumed that the cumulative effect of the two saturations would correspond to a NaCl concentration of approximately 30 g/L, which is equivalent to that of sea water.

The complete testing program spanned a period of approximately one and a half years.

7.2.5.3 Test specimens

The specimens for each mix were sourced from the remainder of the sixth slab that had been cast during the thesis of Ihamouten [132] (refer to Section 7.2.4). The core specimens that were drilled from these slabs were to serve various purposes: Three specimens per mix were drilled to be tested in the EM and resistivity cell as part of the parametric study. One additional core specimen per chloride state was to be conditioned with the test specimens to serve as witness core for the destructive determination of the true chloride content for each mix. Witness cores were also required to verify that adequate homogenisation was achieved for each degree of saturation by means of gammadensimetry. Furthermore, additional specimens were required to verify the porosity as was discussed in Section 7.2.4.2 and to establish the chloride diffusion properties of each mix. Table 7.4 lists the cores that were extracted, their dimensions and the purpose for which they were used.

7.2.5.4 Test protocols

Testing was conducted under controlled laboratory conditions at a temperature of 70°C. Test specimens were left to cool for a minimum of 24 hours after they were removed from the oven and weighed before testing commenced. Cooling took place while the specimens were still wrapped in aluminium foil to prevent any moisture loss and de-homogenisation.

Measurements for each test-point were conducted firstly in the EM-cell and then in the resistivity cell to avoid moisture from the resistivity cell's plate-sponge electrodes influencing the permittivity measurements. For the saturated states the specimens were towel dried before testing. Both complex permittivity and resistivity were tested in two opposing directions by turning the specimens around top-to-bottom in the cell. The averaged value was then taken as representative of the EM observable of each specimen. For the final results each EM observable was calculated as the average of the specimens (BX-1, BX-2 and BX-3) for each test point. The corresponding experimental uncertainty was estimated by the standard deviation. Test results at 0% saturation were only obtained for permittivity as measurements with the resistivity cell were not possible at dry conditions (due to resistivity being essentially infinite and thus outside of the range of the equipment).

The multi-ring functionality of the resistivity cell described in Chapter 6.2 was employed to verify the homogeneity of the test specimen at each test-point. Additionally gammadensimetry tests [278] were performed on witness cores at two test points ($S = 60\%$ and $S = 40\%$ for 0 g/L NaCl). The results from the resistivity cell and gammadensimetry were found to compare well and thus only the resistivity cell was used for the remainder of the campaign to assess homogeneity (as demonstrated in Chapter 6.4.3.1).

After the testing was completed, the degree of saturation of each test-point was adjusted to correspond to the porosity obtained in 2011, seeing that it was initially based on the 2007 porosity values.

7.2.5.5 Determination of chloride content

It needs to be noted that the chloride concentration of specimens after saturation is not necessarily the same as that of the external solution. The actual achieved chloride content inside the specimens can vary significantly for the respective mixes depending on their mix characteristics.

This can be ascribed to various factors of which the most important are listed below:

- Chemical binding of the chloride-ions with the cement particles can lead to the conductivity of the pore solution (which is mainly determined by the free chlorides) being less than the conductivity of the external solution [170].
- The chemical binding capacity of the respective mixes varies according to their W/C-ratio and diffusion characteristics [170] [135].
- The mobility of chloride ions through a porous medium is less than that of water. During an accelerated saturation process where there is limited time for diffusion, the concrete may be saturated before chloride ions have reached all the pores accessible to water [93]. This can lead to lower chloride concentrations achieved in the denser mixes.
- Ions already present in the pores before the saturation can lead to the ionic concentration in the pore solution after saturation being different from that of the external solution [131] [135].

The true total chloride content therefore had to be determined for the purposes of the master curves and regression modelling. Interest was also taken in the free chloride content, as the conductivity of the pore solution was in actual fact determined by the mobile chlorides that are not chemically bound. The destructive testing protocol performed on the witness cores is therefore described in this section.

As a novel method to determine the total and free chloride content in a shorter time than is required by traditional methods, the combination of two existing test methods was investigated during this thesis. The first method on which the new test protocol was based was the potentiometric method for the determination of total chloride content by internal calibration proposed by Clemeña and Apusen [72]. The potentiometric method entails the grinding and subsequent cold digestion of concrete specimens by means of acetic acid. The potential of the digested solution is then measured with a chloride-ion selective electrode before and after two precise additions of a small amount of standard 1 mol NaCl solution. From these three measurements the chloride content can then be determined by means of the following equation based on the Nernst equation:

$$\frac{V_{in} - V_{in+s}}{V_{in} - V_{in+2s}} = \frac{Log(c_{in}) - Log(c_{in} + c_s)}{Log(c_{in)} - Log(c_{in} + 2c_s)} \tag{7.3}$$

where V_{in} [V] is the initial potential of the digested solution, c_{in} [g/L] is the initial chloride concentration of the digested solution, V_{in+s} [V] and V_{in+2s} [V] are the measured potentials after each addition of the standard 1 mol solution c_s [g/L] of NaCl. The only unknown is

therefore the initial chloride concentration c_{in} [g/L] which can be solved iteratively. The total chloride content is then expressed in terms of percentage by weight of cement [%bwc]:

$$C\ell_t = \frac{c_{in}\mathcal{V}}{\Upsilon_{cem}} \tag{7.4}$$

where $C\ell_t$ [%bwc] is the total chloride content percentage by weight of cement and $\mathcal{V}$ [L] is the volume of the digested solution and Υ_{cem} is the fraction of cement per concrete by weight.

The potentiometric method is much quicker to perform than standard methods based on titration and the loss in accuracy has been reported as negligible [72] [183].

The second method of which elements were included in the test method developed here, was the AFREM test procedure [59] to determine free chloride content. The AFREM protocol proposes to separate the free chlorides from the bound chlorides by limiting the contact period allowed for dissolution. The method is based on research that has shown that the exposure of concrete dust to water for approximately three minutes will cause only the free chlorides to dissolve [123]. After three minutes of exposure the solution is stabilised with a nitric acid solution and filtered to remove the undissolved impurities. The chloride ion content is then determined by means of silver nitrate titration. As titration is a time consuming process, it was proposed for the purposes of this thesis that the potentiometric method be employed to determine the free chloride content instead of titration.

For the purposes of this thesis, the potentiometric method and AFREM protocol were therefore combined to determinate the total and free chlorides in a more time efficient way. The protocol followed for this combined potentiometric-AFREM method is detailed in Appendix A.1.

7.2.5.5.1 Proposal for a combined potentiometric-AFREM method to determine total and free chloride content

The integrity of the proposed combined potentiometric-AFREM method (Appendix A.1) to determine total and free chloride content is evaluated in this section based on the results that were obtained for Mixes B3, B4, B5 and B6. The measured total and free chloride contents for each mix and their standard deviations are shown in Table 7.5 and in Figure 7.7(a) and 7.7(c) in terms of percentage by weight of cement [%bwc].

Firstly, in order to assess whether the results for total chloride content were realistic, the salinities achieved within the concrete after saturation ("internal" NaCl concentration) were compared to the external salinities of 0 g/L, 15 g/L and 30 g/L (15 + 15 g/L) NaCl. The total achieved NaCl concentration $c_{t(NaC\ell)}$ was calculated from the measured total chloride

Table 7.5: Total and free chloride contents of Mixes B3, B4, B5 and B6 measured by the combined potentiometric-AFREM method.

Mix	External NaCl concentr. [g/L]	Total chorides ($C\ell_t$) [% bwc*]		Free chorides ($C\ell_f$) [% bwc*]		Free Cl fraction $C\ell_f / C\ell_t$	Total NaCl concentr. achieved $c_{t(NaC\ell)}$ [g/L]
		Mean	Std Dev	Mean	Std Dev		
B3	0	0.06%	0.02%	0.01%	0.00%	0.22	2.52
B4	0	0.15%	0.04%	0.04%	0.02%	0.29	2.65
B5	0	0.05%	0.01%	0.02%	0.00%	0.31	2.05
B6	0	0.11%	0.04%	0.03%	0.01%	0.29	2.03
B3	15	0.30%	0.06%	0.10%	0.01%	0.32	11.65
B4	15	0.71%	0.08%	0.26%	0.01%	0.36	12.80
B5	15	0.25%	0.04%	0.06%	0.01%	0.24	10.00
B6	15	0.77%	0.06%	0.19%	0.01%	0.25	13.79
B3	30**	0.53%	0.05%	0.13%	0.04%	0.24	21.70
B4	30	1.51%	0.08%	0.52%	0.10%	0.34	27.05
B5	30	0.49%	0.04%	0.16%	0.02%	0.32	19.79
B6	30	1.37%	0.19%	0.50%	0.08%	0.37	24.46

* by weight of cement
** 15 + 15 g/L NaCl (refer to Section 7.2.5.2)

content $C\ell_t$ by means of Equation (7.5), taking into account the difference in molar mass between Cl and NaCl and thus obtaining the total NaCl content per pore space volume in g/L. These estimated NaCl concentrations could then be compared with the concentration of the external solutions.

$$c_{t(NaC\ell)} = \frac{58.4}{35.5} c_{t(C\ell)} = \frac{1.65}{1000} \frac{\gamma_{dry} C\ell_t \Upsilon_{cem}}{\phi} \tag{7.5}$$

where $c_{t(NaC\ell)}$ [g/L] is the achieved total NaCl concentration per pore space volume, $c_{t(C\ell)}$ [g/L] is the achieved total chloride concentration per pore space volume, $C\ell_t$ [%bwc] is the total chloride content by weight of cement, γ_{dry} is the dry density of the concrete $[kg/m^3]$, Υ_{cem} fraction of cement per unit mass concrete and ϕ is the porosity.

The calculated values for external NaCl concentration and the achieved internal NaCl concentration are also listed in Table 7.5 and shown in Figure 7.7(b). The values for external and achieved NaCl concentration correspond well, though the achieved concentrations are slightly lower than the concentrations of the external solutions. The reason suggested for

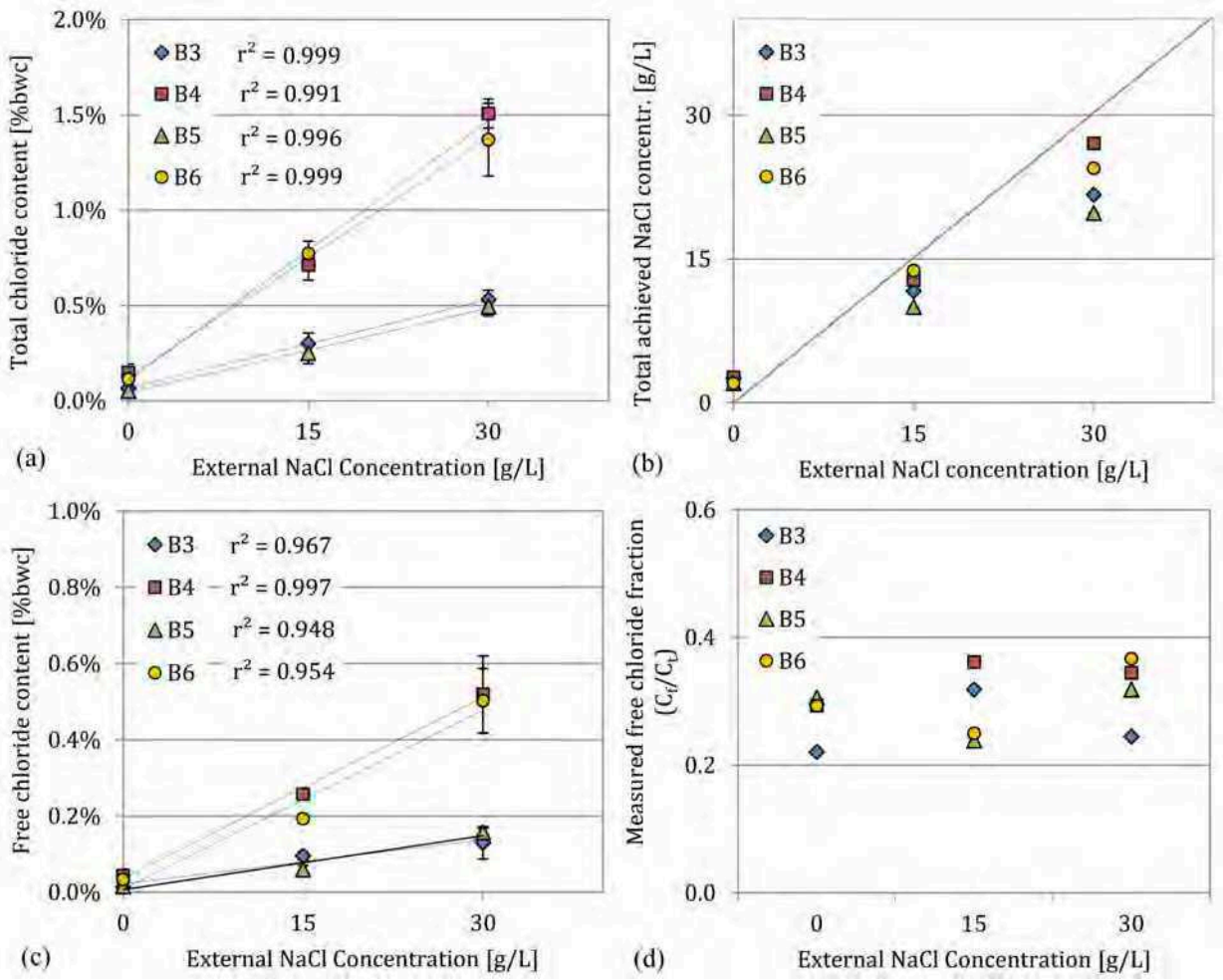

Figure 7.7: Results for Mixes B3, B4, B5 and B6 from the combined potentiometric-AFREM method showing the measured (a) total chloride content, (b) the estimated achieved total NaCl concentration, (c) free chloride content and (d) the free chloride content fraction.

this is that the chloride ions are less mobile than the water and may not have reached all the pores during the saturation process, thus leading to the lower achieved concentrations. This theory is supported by results in Chapter 9.3.4.3, which demonstrate that chloride ions penetrate concrete more slowly than water. The linear nature of the results in Figure 7.7(b) also proves that the protocol of saturating the same specimens twice with 15 g/L NaCl did indeed approximate a final concentration of 15 + 15 $\approx$ 30 g/L NaCl as assumed in Section 7.2.5.2.

Due to the good correspondence between the known external and the determined internal concentrations, with the variation accounted for, it is concluded that the combined potentiometric-AFREM method suggested in Section 7.2.5.5 yields accurate results for total chloride content.

Mixes with high W/C-ratios such as B4 and B6 were expected to have a lower binding capacity than the low W/C-ratio Mixes B3 and B5 as is well documented in literature [170] [285]. The ratios of free chloride content to total chloride content $C\ell_f/C\ell_t$ are listed in Table 7.5 and are also shown against the external solution in Figure 7.7(d). Values are scattered between 22% and 37% and do not show any visible difference for the respective mixes, contrary to the expectation. In general, the obtained free chloride fractions are somewhat lower than is reported in literature for mature OPC concretes [170].

The results for total and free chloride contents in Table 7.5 were used to estimate the conductivity of the pore solution, which was required to evaluate the performance of Archie's law for resistivity as discussed in Section 7.3. However, the accuracy of the potentiometric-AFREM combination method for the determination of total and free chlorides could not be verified by means of traditional titration methods [59] during the course of this thesis due to time constraints. It therefore remains to be further validated.

Lastly, some interesting observations can be made from these results. In Figure 7.8(a) it can be seen that the total and free chloride contents correlate very well with the diffusivity of the respective mixes, thus being markedly higher for the diffusive mixes (B4 and B6) than for the denser mixes (B3 and B5). This demonstrates the effect of pore size and interconnectedness on the penetration of chloride ions under pressure gradient during the saturation process. It is also interesting to note the correlation between the total chloride and free chloride contents as in Figure 7.8(b). This implies that for the purpose of the regression modelling presented in Section 7.4, it is irrelevant whether total or free chlorides are used.

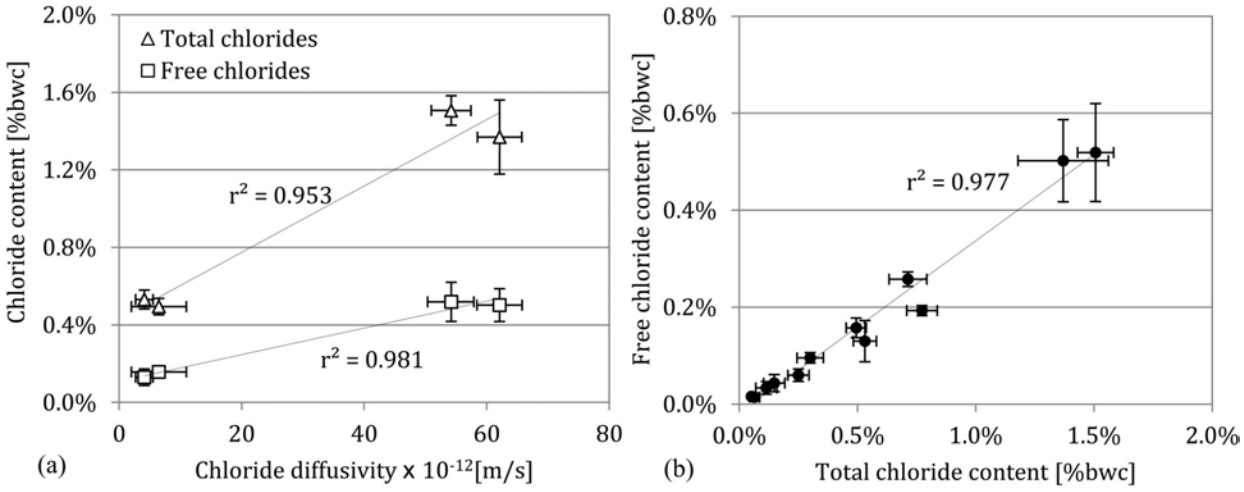

Figure 7.8: (a) Correlation between total and free chloride contents and chloride diffusivity and (b) free chloride against total chloride content.

7.2.6 Parametric study: results and discussion

The influence of the degree of saturation, chloride concentration and content as well as porosity and chloride diffusivity of each mix on the respective EM observables are discussed in detail in the following sections.

7.2.6.1 Dependency of EM observables on degree of saturation

The influence of degree of saturation on the EM observables $Log(\rho)$, ε_1', ε_2', ε_1'' and ε_2'' is presented in Figure 7.9 for the 0 g/L NaCl case. Some scatter is observed with regards to the degree of saturation, i.e. the values do not correspond exactly to the values envisaged as part of the test schedule in Figure 7.6. This is due to the fact that there was some moisture loss during the homogenisation process in spite of the best efforts to seal the specimens in an airtight manner. Also, because the degree of saturation was initially calculated using the 2007 porosities and then later corrected for the porosities as determined in 2011, there was an additional shift in degree of saturation from the planned values.

The following sections deal with both the dependency of the EM observables on saturation and on parameters related to concrete quality i.e. porosity and chloride diffusivity. This is because it was observed that the relationship of the EM observables with porosity and chloride diffusivity is dependent on the degree of saturation as will be explained below.

7.2.6.1.1 DC-resistivity

It is clear from Figure 7.9(a) that the relationship between the degree of saturation and the logarithm of resistivity $Log(\rho)$ is not linear. This is in line with the majority of results in literature as discussed in Chapter 3.4.1.1. A second order polynomial relationship gives a good fit to the experimental data with r^2-values greater than 0.95 for all mixes. This quadratic relationship corresponds to the suggestion of Whiting and Nagi [283] mentioned in Chapter 3.4.1.1, that the increasing change in resistivity at lower saturations is because of the presence of "non-conducting" moisture due to loss in the interconnectivity of the pore solution.

When the resistivity values for the different mixes are compared, the highest resistivities are observed for Mix B3 and the lowest for Mix B6, which correspond to their durability being respectively good and poor. The resistivity of the "high W/C" mixes (B3 and B5) is more sensitive to decrease in degree of saturation than that of the "low W/C" mixes (B4 and B6) which can be related to quicker loss of connectivity of the pore solution for denser

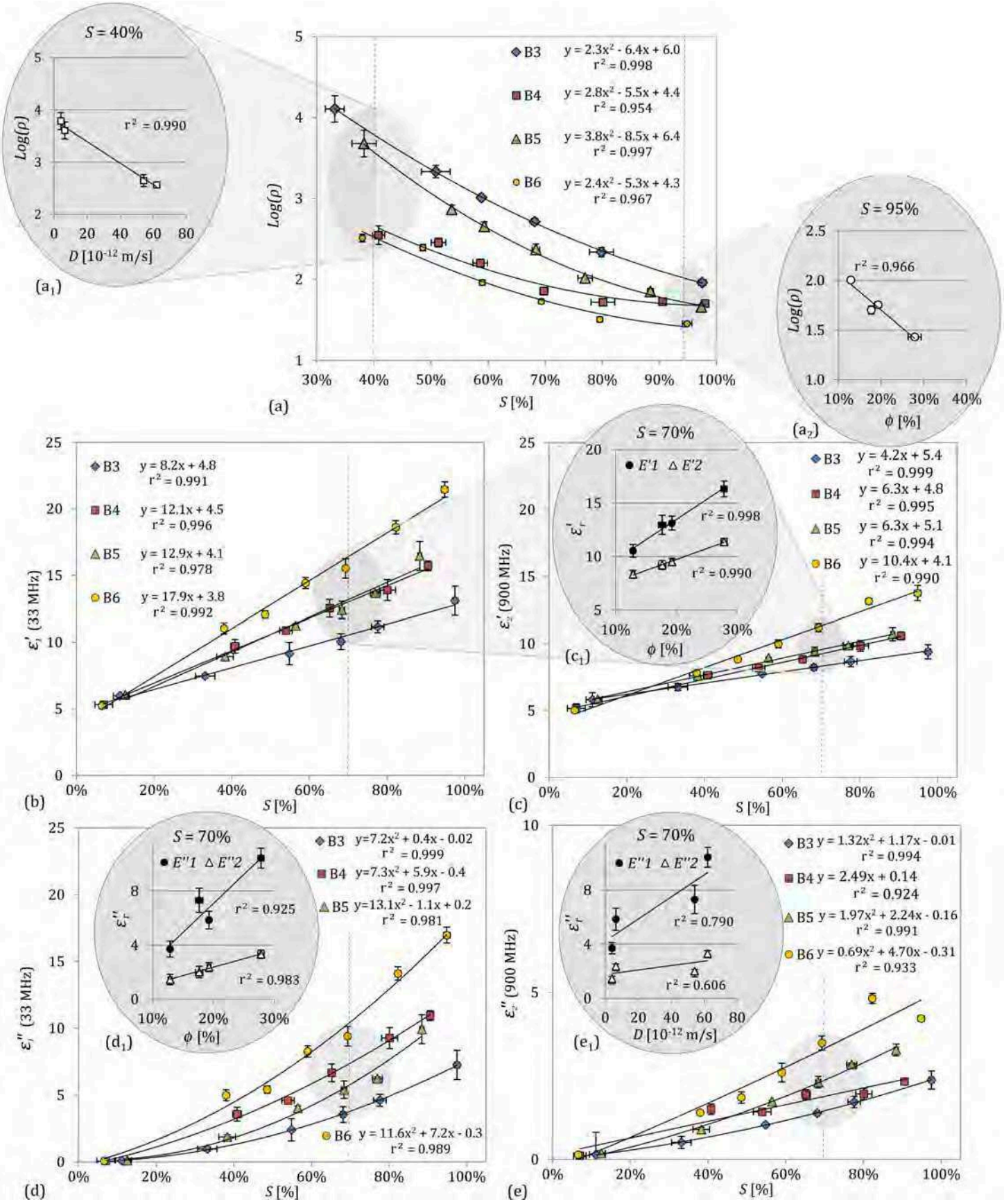

Figure 7.9: EM observables as a function of degree of saturation for (a) the logarithm of resistivity $Log(\rho)$, (b) dielectric constant at 33 MHz ε'_1, (c) dielectric constant at 900 MHz ε'_2, (d) loss factor at 33 MHz ε''_1 and (e) loss factor at 900 MHz ε''_2.

concretes.

An important observation is that $Log(\rho)$ is approximately directly proportional to porosity at near saturated conditions ($S = 95\%$) as in Figure 7.9(a_2), whereas it is directly proportional to chloride diffusivity at low saturations ($S = 40\%$) as can be seen in Figure 7.9(a_1). This trend is very clear when Mixes B4 and B5 are compared. These two mixes have similar porosities (18.2% and 19.1% respectively) and have almost identical resistivities at saturated conditions. However, the diffusion properties of Mixes B4 and B5 are very different (55.4 and 6.5×10^{-12}m^2/s) which correlate with the results for $Log(\rho)$ at low saturations. This suggests that porosity is the governing parameter related to concrete durability determining resistivity at high degrees of saturation and that chloride diffusivity is more important at low saturations. Put differently, at near saturated conditions $Log(\rho)$ is proportional to the water content as $w = \phi S$ (with $S = 1$), whereas at unsaturated conditions $Log(\rho)$ is proportional to the interconnectedness of the pores, of which chloride diffusivity is a measure.

7.2.6.1.2 Complex permittivity

The dielectric constants at 33 MHz ε'_1 and 900 MHz ε'_2 show a strong linear relationship with degree of saturation as can be seen in Figures 7.9(b) and 7.9(c). The linear relationship proves that the dielectric constants are correlated to the volumetric water content and does not significantly depend on the interconnectedness of the pores. This is deduced because the porosity ϕ of each mix is a constant, and therefore $\varepsilon' \propto w$, where $w = \phi S$. The increase in loss of interconnectedness of the pore solution with a decrease in saturation, manifests as a non-linear dependency of the EM observable on degree of saturation if it is sensitive to the interconnectedness of the pores, as for resistivity. The linear dependency of the dielectric constants was therefore expected, as polarisation is a result of the storage of electric charge and does not significantly depend on the flow of charge as for resistivity (refer to Chapter 3.2.2). When the different mixes are compared, the dielectric constants at both low and high frequencies are linearly related to porosity with Mix B6 having the highest dielectric constants and Mix B3 the lowest as can be seen in Figure 7.9(c_1) ($S = 70\%$ was chosen to present the data, but it can be seen that the relationship remains unchanged irrespective of the saturation). Mixes B4 and B5 yield very similar results and it is therefore suggested that porosity is the governing material property determining the dielectric constants, irrespective of the saturation. The diffusion characteristics of the concrete is therefore of little importance in terms of the dielectric constant.

The loss factors show a quadratic relationship with degree of saturation as can be seen in Figures 7.9(d) and (e). This non-linear behaviour is particularly strong at low frequencies as can be seen for ε''_1 at 33 MHz in Figure 7.9(d). This can be ascribed to the EM losses that are

due to ohmic conduction as explained in Chapter 3.2.2 which leads to the dependency of the loss factors on the interconnectedness of the pore solution, similar to resistivity. However, losses are also partially due to other phenomena, i.e. frictional dielectric relaxation and it is therefore difficult to relate the behaviour of the different mixes to porosity or chloride diffusivity exclusively. It can therefore be seen in Figures 7.9(d_1) and 7.9(e_1) for $S = 70\%$, that neither porosity nor chloride diffusivity correlates perfectly with the loss factors. This demonstrates that the loss factors are influenced by a combination of both these parameters.

When Figures 7.9(b) and 7.9(d) are compared with Figures 7.9(c) and 7.9(e), it seems that the complex permittivity at 33 MHz (ε_1' and ε_1'') is more sensitive to degree of saturation than the complex permittivity at 900 MHz (ε_2' and ε_2''). This frequency dependency of the sensitivity of permittivity to degree of saturation is due to the dispersive nature of saturated concrete as explained in Chapter 3.4.1.1. It appears as if the loss factor at 33 MHz has the highest sensitivity to degree of saturation when looking at the gradient of the fitted curves. To compare the sensitivity of the dielectric constants and loss factors, the observables measured at each saturation condition were expressed as a percentage difference of their values at 30% degree of saturation, which is a realistic minimum saturation for concrete in a natural environment. Figure 7.10 shows the percentage difference for each observable related to permittivity (for Mix B3) over the measured saturation range included in the parametric study. The observations stated above are therefore confirmed as it is clear that the loss factors are significantly more sensitive to degree of saturation than the dielectric

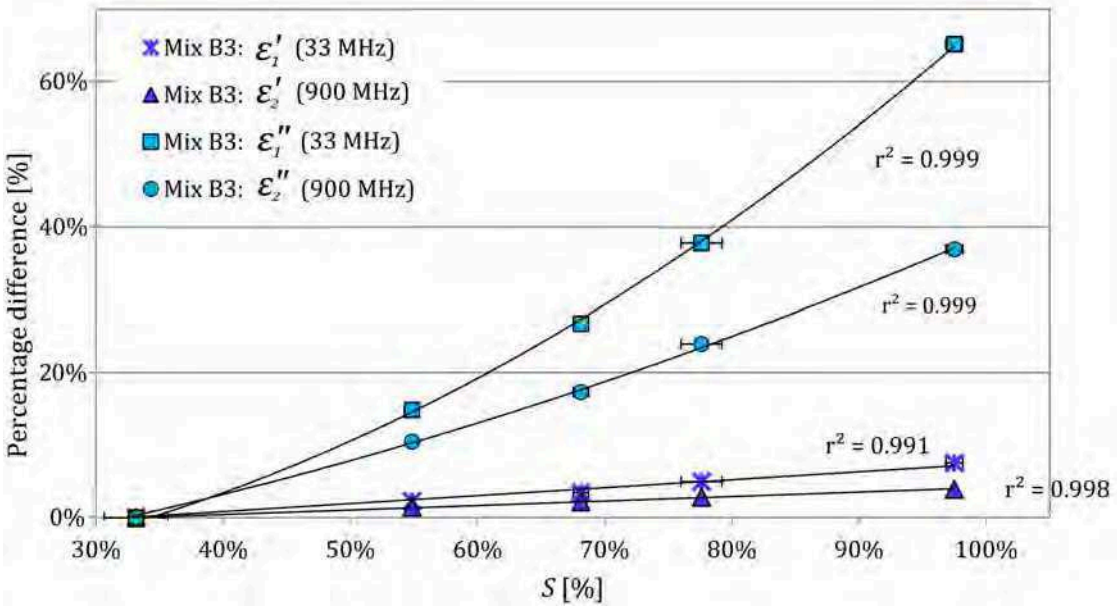

Figure 7.10: The sensitivity of dielectric constants and loss factors to degree of saturation for Mix B3.

constants. The sensitivity of the various EM observables to degree of saturation will be compared in more detail as part of the regression modelling presented in Section 7.4.

7.2.6.2 Dependency of EM observables on salinity and chloride content

It needs to be reiterated here that the salinity (and thus the conductivity) of the external solution does not necessarily correspond to the conductivity of the pore solution after saturation. The relationship between the EM observables and the actual chloride content may therefore not be the same as that of the salinity (NaCl concentration) of the external solution used for saturation (i.e. 0, 15 and 30 g/L NaCl). For this reason the dependency of the EM observables on both these parameters related to chloride content is discussed.

7.2.6.2.1 Dependency of EM observables on salinity of external solution

The first step in assessing the chloride dependency of the EM observables was simply to look at the results in terms of the salinity (NaCl concentration) of the external solution used for saturation. The results for the saturated case are shown in Figure 7.11. In order to compare the EM observables at a constant degree of saturation, values were calculated at exactly 100% saturation from the relationships obtained for degree of saturation at each external NaCl concentration level (as presented for the 0 g/L case in Figure 7.9).

Resistivity decreases with an increase in salinity of the external solution, as is to be expected. When the different mixes are compared it is observed that $Log(\rho)$ is correlated to the porosity at 0 g/L (Figure 7.11(a_1)), but is better correlated to chloride diffusivity at 15 and 30 g/L NaCl (Figure 7.11(a_2)). Although the reason for this is not confirmed, it is suggested here that chloride-ions are less mobile in the mixes with a smaller average pore size (B3 and B5) than in the mixes with larger pores (B4 and B6). This would explain why the resistivity of mixes with smaller pores are less sensitive to the salinity of the external solution.

Both the dielectric constant and loss factor at 33 MHz (ε'_1 and ε''_1) shown in Figures 7.11(b) and 7.11(d) display a significant increase as the salinity of the external solution increases. The loss factor seems to be significantly more sensitive to chloride concentration than the dielectric constant. It also is noted that results for the different mixes are once again distributed linearly with the porosity, with Mixes B4 and B5 yielding very similar results. The dielectric constant at 900 Hz ε'_2 (Figure 7.11(c)) shows very little sensitivity to the salinity of the external solution with the graphs being nearly horizontal. In contrast, the loss factor at 900 MHz ε''_2 is quite sensitive to salinity and displays a significant relative increase from 0 to 30 g/L NaCl (Figure 7.11(e)). The sensitivity of the loss factors to salinity can be attributed, as with degree of saturation, to interfacial polarisation and related phenomena

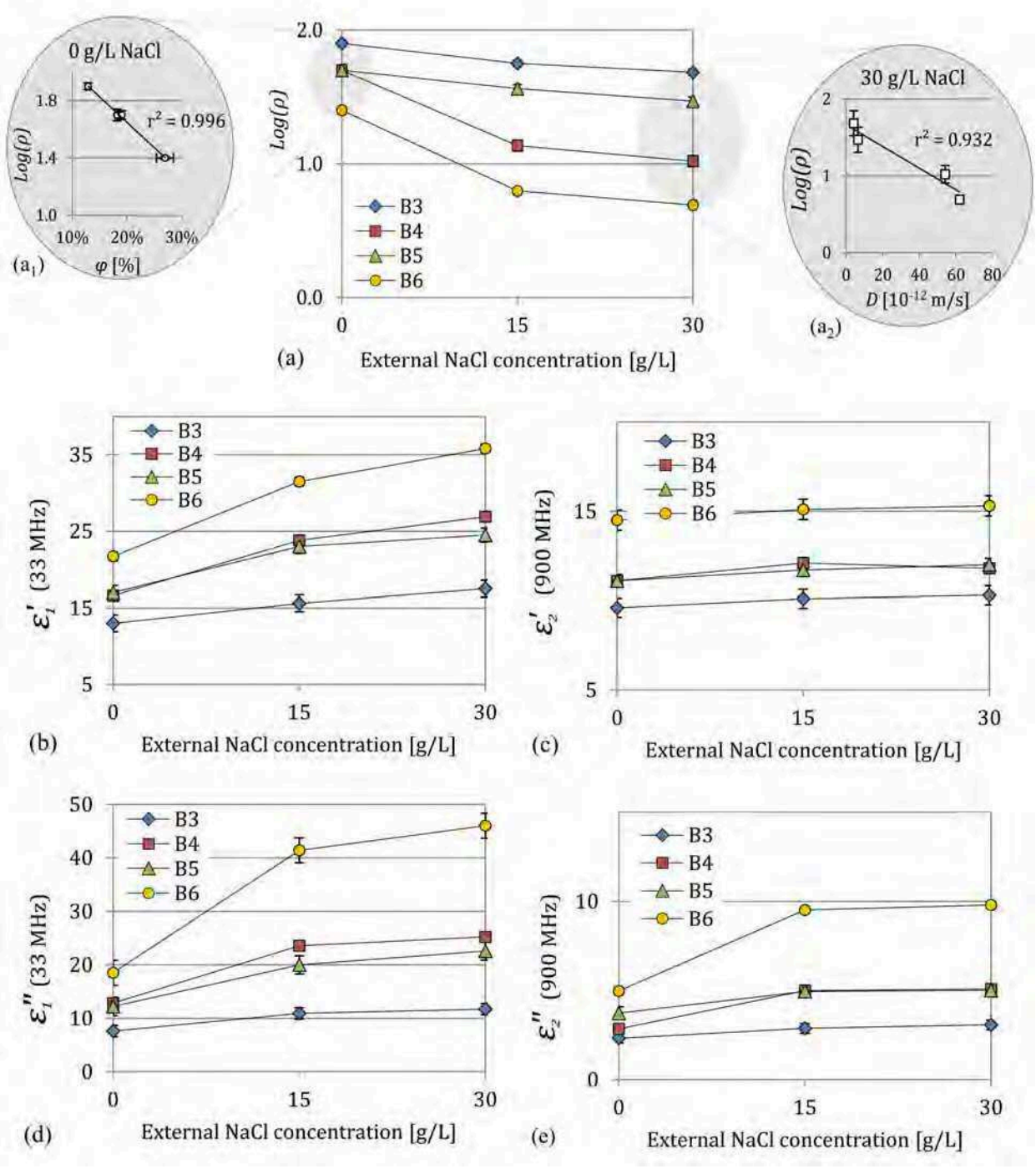

Figure 7.11: EM observables as functions of the salinity (NaCl concentration) of the external solution extrapolated to saturated conditions respectively for (a) the logarithm of resistivity $Log(\rho)$, (b) the dielectric constant at 33 MHz ε'_1, (c) the dielectric constant at 900 MHz ε'_2, (d) the loss factor at 33 MHz ε''_1 and (e) the loss factor at 900 MHz ε''_2.

which are further intensified by the presence of chloride ions. The sensitivity of the different EM observables to the presence of chloride will be further explored in Section 7.4.

7.2.6.2.2 Dependency of EM observables on total chloride content

The EM observables are shown as a function of total chloride for the saturated case in Figure 7.13. The trends of the relationship between the EM observables and total chloride content are similar to that of the external NaCl concentration in Figure 7.11. The relationship between all the EM observables and total chloride content is logarithmic, with the chloride dependency of all the EM observables decreasing as chloride content increases. Though it is accepted in literature that the electromagnetic properties of concrete are influenced by the presence of chloride (refer to Chapter 3.4.1.2), the actual nature of these relationships has not been widely studied. However, if the results from the literature presented in Chapter 3.4.1.2 are closely studied, non-linear relationships are evident. In Figure 7.12 data extracted from literature (Figures 3.4(a) and (b)) are shown, and it can be seen that $Log(\rho)$, ε_1' and ε_1'' also display non-linear trends in these two studies.

Unlike the external concentrations in Figure 7.11, the true levels of chloride contamination of Mixes B3 and B5 differ considerably from that of Mixes B4 and B6 for the three test points of 0, 15 and 30 g/L NaCl. This can be attributed to the different material properties of the concrete mixes. Firstly, a higher porosity will lead to more pore space containing contaminated solution and therefore a higher bulk chloride content. Secondly, in a diffusive

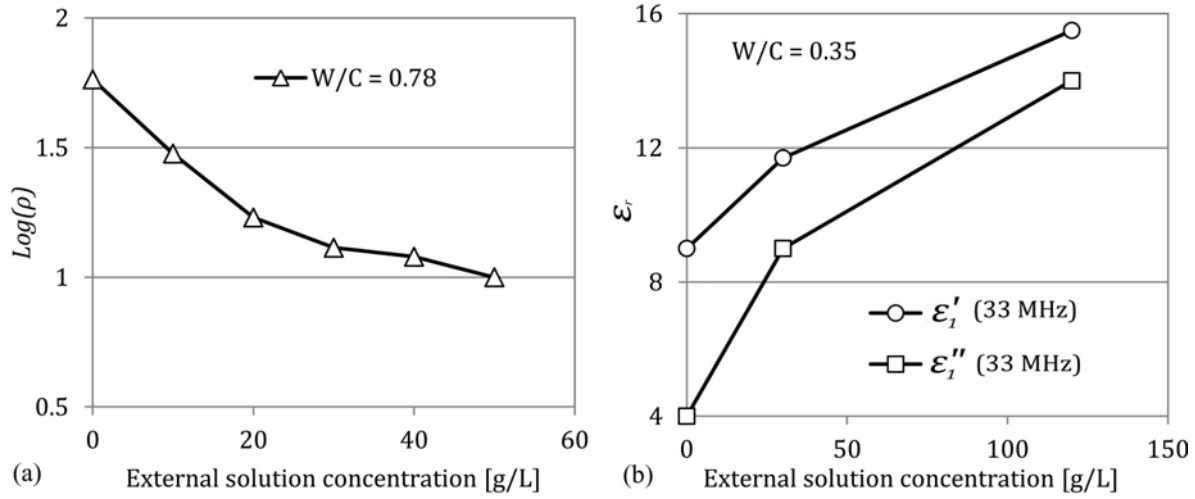

Figure 7.12: Results for saturated concrete extracted from literature for the sensitivity of (a) the logarithm of resistivity $Log(\rho)$ [237] and (b) the dielectric constant ε_1' and loss factor ε_1'' at 33 MHz [87] to the NaCl concentration of the external solution.

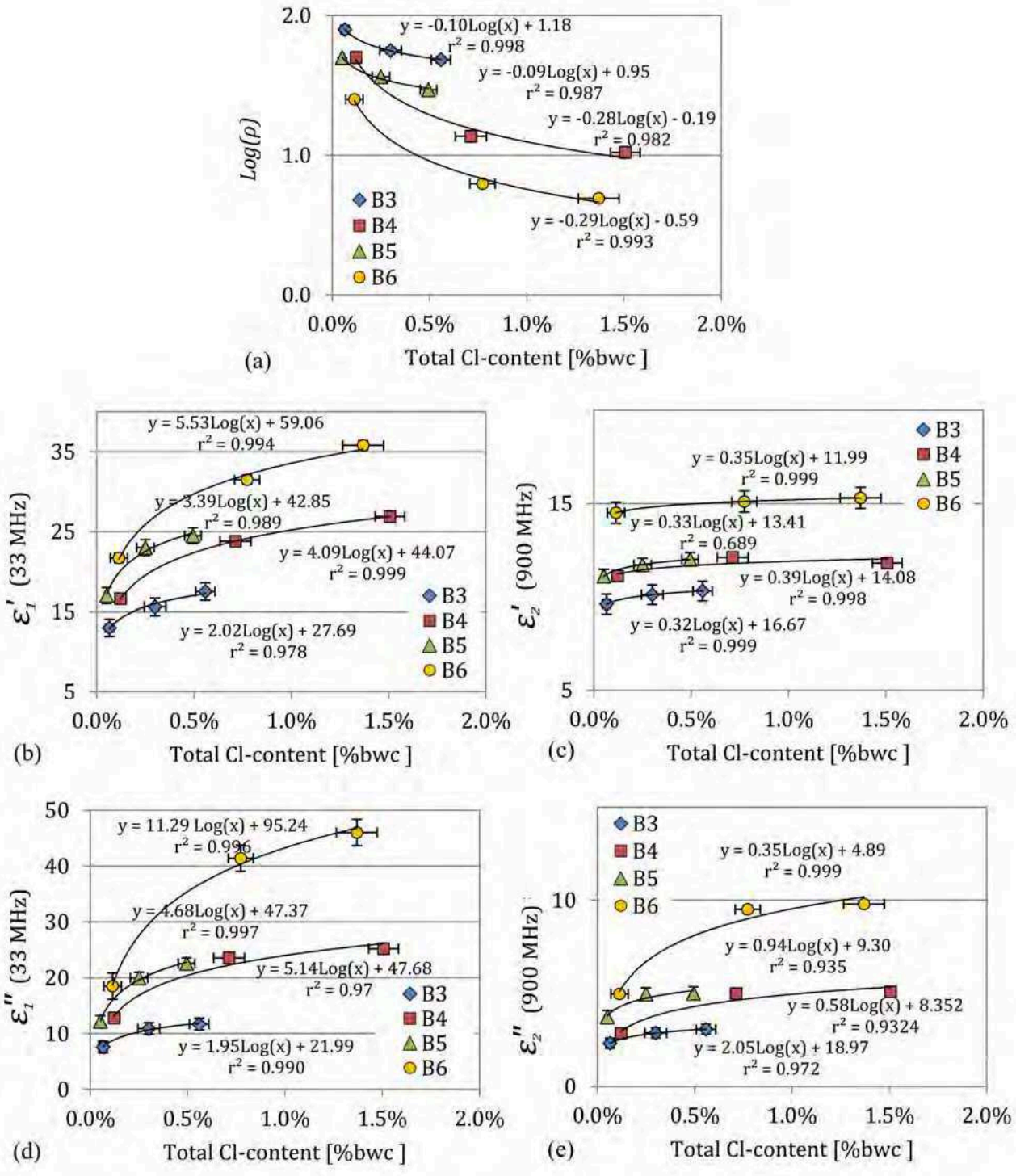

Figure 7.13: EM observables as functions of total chloride content by weight of cement for (a) the logarithm of resistivity $Log(\rho)$, (b) the dielectric constant at 33 MHz ε'_1, (c) the dielectric constant at 900 MHz ε'_2, (d) the loss factor at 33 MHz ε''_1 and (e) the loss factor at 900 MHz ε''_2 for saturated conditions.

concrete the chlorides will more easily reach all the pores leading to a higher chloride content in the pores. The total chloride contents of Mixes B4 and B6 are approximately three times higher that that of Mixes B3 and B5. The fact that there is such a large difference between results for Mixes B4 and B5 (having similar porosities) implies that the achieved chloride content after saturation is to a large extent governed by chloride diffusivity rather than porosity.

When the coefficients of the fitted logarithmic curves of the different observables for permittivity are compared, it seems that the loss factor at 33 MHz ε_1'' is the most sensitive to chloride content followed by the dielectric constant at 33 MHz ε_1' and the loss factor at 900 MHz ε_2''. In contrast, the dielectric constant at 900 MHz ε_2' is the least sensitive and displays almost no sensitivity to chloride content. This corresponds to findings from Dérobert et al. [87] related to Figures 3.4(b) and (c) in Chapter 3.

7.2.7 Summary

The most noteworthy observations as a result of this parametric study are listed below:

- The logarithm of resistivity has a quadratic dependency on degree of saturation which is correlated to porosity at high degrees of saturation and to chloride diffusivity at low degrees of saturation. There is also a strong logarithmic relationship between $Log(\rho)$ and total chloride content.
- Dielectric constants at both low and high frequencies have a linear dependency on degree of saturation and a logarithmic relationship with total chloride content. Results for the different mixes show a linear relationship with porosity and it is concluded that chloride diffusivity plays a negligible role where the dielectric constant is concerned. Dielectric constants at 33 MHz are more sensitive to saturation and chloride content than those at 900 MHz.
- Loss factors at both low and high frequencies have a quadratic relationship to saturation and logarithmic relationship to chloride content. Though the master curves developed for the loss factors may have limited application in practice with the current techniques available, they could have great potential once techniques to determine in situ loss factors of concrete are more mature. The significant sensitivity of the loss factor at low frequencies to degree saturation and chloride content could prove especially useful if methods to determine this observable in situ are improved.

Before embarking on the development of new models based on the relationships found in this section, the experimental data was first used to investigate the performance of existing

models as discussed in the next section.

7.3 Application of existing models to measured data

In this section two composite theory models presented in Chapter 3.3.2 are applied to the experimental data that was obtained as a result of the parametric study. It was decided to test the performance of the two composite material models that are the most commonly encountered in literature, being Archie's law (Chapter 3.3.2.3) and the CRIM model (Chapter 3.3.2.2).

7.3.1 Application of Archie's law for conductivity

The capability of Archie's law to accurately describe the resistivity of concretes over the range of mixes, saturations and chloride concentrations forming part of the experimental campaign, is investigated in this section. Archie's law (Equation (3.57)) is discussed in Chapter 3.3.2 and is restated here for the sake of convenience. The first variant of Archie's law is for the saturated case:

$$\sigma_b = \frac{1}{\mathfrak{a}}\sigma_w \phi^{\mathfrak{m}} \tag{7.6}$$

where σ_b [S/m] is the saturated bulk conductivity, σ_w [S/m] is the conductivity of the pore solution, ϕ [-] is the porosity, $\mathfrak{m}$ [-] is the cementation exponent and $\mathfrak{a}$ [-] is the lithology factor.

In order to fit the coefficients $\mathfrak{a}$ and $\mathfrak{m}$, Archie's formation factor $\mathcal{F}$ [-] is defined as σ_w/σ_b to obtain the following relationship:

$$Log(\mathcal{F}) = Log(\mathfrak{a}) - \mathfrak{m} Log(\phi) \tag{7.7}$$

It should be noted here that the use of the resistivity "formation factor" $\mathcal{F}$ has been expanded since the formulation of Archie's law, to describe the microstructure of concrete in general [140]. The formation factor is therefore used here in its original sense [33] and should not be confused with its definition in terms diffusion [43] which is often used to estimate the tortuosity of concrete [79] [21].

The second version of Achie's law makes provision for variation in degree of saturation S, with the saturation exponent $\mathfrak{n}$ accounting for the non-linear dependency of resistivity on degree of saturation:

$$\sigma_b = \frac{1}{\mathfrak{a}}\sigma_w \phi^{\mathfrak{m}} S^{\mathfrak{n}} \tag{7.8}$$

To evaluate the performance of Archie's law for the complete dataset produced by the parametric study, the parameters $\mathfrak{a}$ and $\mathfrak{m}$ were firstly fitted by means of Equation (7.7) using data for the saturated state. The modelled bulk conductivities were then determined for each data point by means of Equation (7.8), with the saturation exponent $\mathfrak{n}$ taken as 2 [33].

Since porosity and degree of saturation were known parameters, the only unknown parameter was the conductivity of the pore solution for saturated conditions. The estimation of this parameter for input into Archie's model is therefore discussed next.

7.3.1.1 Estimation of the conductivity of the pore solution

The conductivities of each of the external solutions used for the saturation of the specimens (0, 15 and 30 g/L NaCl) were rigorously noted during the experimental campaign using the commercial CONSORT probe (Table 7.6). However, it is acknowledged (as explained in the previous section 7.2.5.5 and stated in literature [131]) that the properties of the pore solution after saturation is not necessarily the same as that of the external solution.

Though methods exist to determine the conductivity of pore solution after saturation (i.e. by the extraction of pore fluid from concrete specimens by means of the application of very high pressure [165]), they require specialised equipment and are usually only suitable for mortars [59] or concrete with low W/C-ratios [43]. It was therefore opted to estimate the conductivity of the pore solution indirectly from the chloride contents as determined for each mix in Table 7.5. It was assumed that the chloride ions were the principle carriers of current and that the contribution of other conducting ions were negligible for the chloride contaminated states (15 and 30 g/L NaCl).

The concentration of free chlorides in the saturated pore solution was therefore determined by means of the following equation:

$$c_{f(C\ell)} = \frac{C\ell_f}{C\ell_t} c_{t(C\ell)} \tag{7.9}$$

where $c_{f(C\ell)}$ [g/L] is the free chloride concentration, $C\ell_f/C\ell_t$ is the free chloride fraction and $c_{t(C\ell)}$ [g/L] is the total chloride concentration as listed in Table 7.5.

The relationship between the free chloride concentration and conductivity was taken from literature [279] [51], but was also confirmed experimentally during the study as the following:

$$\sigma_w = 0.31 c_{f(C\ell)} \tag{7.10}$$

where σ_w [S/m] is the estimated conductivity of the pore solution.

Table 7.6: Estimated conductivities of the pore solutions for Mixes B3, B4, B5 and B6 after saturation with solutions containing 0, 15 and 30 g/L NaCl, also indicated the measured conductivity of the external solutions before saturation.

Mix	External NaCl concentr. [g/L]	Measured conductivity of the external solution [S/m]	Estimated pore solution conduct. σ_w [S/m]
B3	0	0.05	0.10
B4	0	0.05	0.15
B5	0	0.05	0.12
B6	0	0.05	0.11
.....	.....	.....	.....
B3	15	2.09	0.69
B4	15	2.09	0.87
B5	15	2.09	0.45
B6	15	2.09	0.64
.....	.....	.....	.....
B3	30*	4.19*	0.99
B4	30*	4.19*	1.74
B5	30*	4.19*	1.18
B6	30*	4.19*	1.68

*15 + 15 g/L NaCl ≡ 2.09 + 2.1 S/m

The resulting estimated conductivities of the pore solutions for each mix are shown in Table 7.6. It can be seen that the estimated conductivity of the pore solution after saturation with water (0 g/L NaCl) is higher than the measured conductivity of the water. This is due to the ions that are already present in the pores of the concrete before saturation and corresponds to conductivities reported by Hunkeler [131]. In contrast, the conductivity of the pore solution is lower than the measured external conductivity for the 15 and 30 g/L NaCl cases. This can be related to chloride binding [170] [135]. The estimated conductivities were therefore regarded as acceptably accurate.

7.3.1.2 Results and discussion

By using the estimated conductivity values, Archie's parameters $\mathfrak{m}$ and $\mathfrak{a}$ were determined according to Equation (7.7) as being respectively 2.42 and 0.38 (Figure 7.14(a)). These values did not give a good fit for modelled conductivity versus the measured conductivity with an r^2-value of 0.72 as in Figure 7.14(b). This shows that Archie's law does not perform

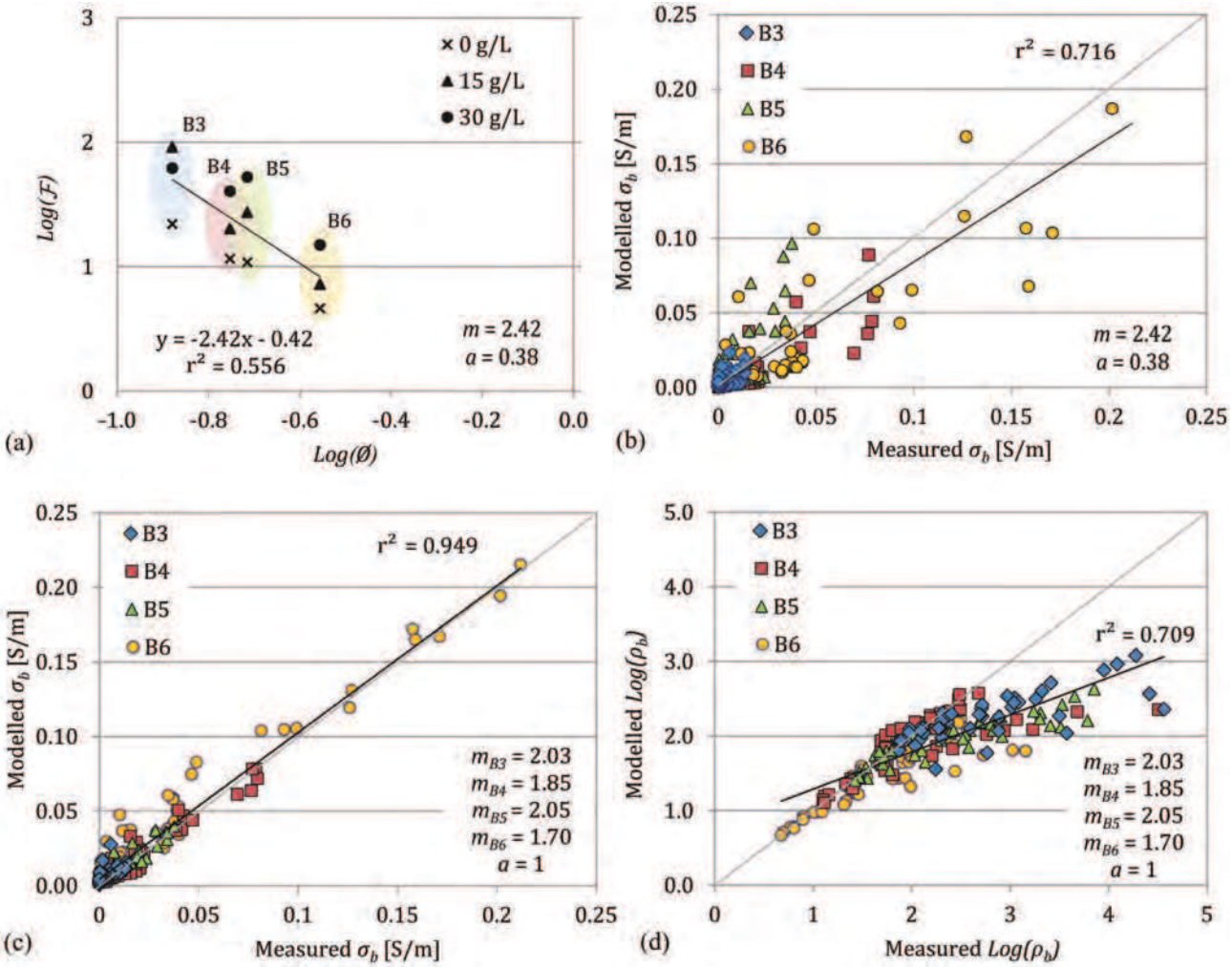

Figure 7.14: Application of Archie's law by (a) data fitting of the logarithm of Archie's formation factor $Log(\mathcal{F})$ and logarithm of porosity $Log(\phi)$ to determine average $\mathfrak{m}$ and $\mathfrak{a}$ values, (b) modelled conductivity versus measured bulk conductivity σ_b for average parameters $\mathfrak{m} = 2.42$ and $\mathfrak{a} = 0.38$, (c) modelled conductivity versus measured bulk conductivity σ_b for mix specific parameters $\mathfrak{m}$ with $\mathfrak{a} = 1$ and (d) modelled logarithm of resistivity $Log(\rho_b) = Log(1/\sigma_b)$ versus the measured values for mix specific parameters $\mathfrak{m}$ with $\mathfrak{a} = 1$.

well when general $\mathfrak{m}$ and $\mathfrak{a}$-values are fitted for mixes of varying properties and therefore requires individually fitted parameters for each mix to allow for their different behaviour. By setting $\mathfrak{a} = 1$, mix-specific $\mathfrak{m}$-values were calculated which yielded a much better fit as shown in Figure 7.14(c) with $\mathfrak{m}$-values for Mixes B3, B4, B5 and B6 calculated as respectively 2.03, 1.85, 2.05 and 1.70.

The high r^2-value of 0.95 in Figure 7.14(c) masks the poorer performance of Archie's law at lower conductivities. This can be clearly seen in Figure 7.14(d) where the modelled logarithm of resistivity $Log(\rho_b) = Log(1\backslash\sigma_b)$ is presented versus the measured logarithm of

resistivity . Though the model fits well for values corresponding to saturated conditions for each mix ($Log(\rho_b) \approx 1$ to 2), there is a significant discrepancy between the modelled and measured data for higher values of $Log(\rho_b)$. Results for saturated conditions are thus well modelled by Archie's law if the properties of the respective mixes are taken into account by the $\mathfrak{m}$-values, but performs poorly for unsaturated conditions. This is because Archie's law is defined to go through the origin with zero conductivity reached only when the material is completely dry. For concrete, this is not the case, as high quality mixes can become practically unconductive at saturations as high as 40% to 60%. This is confirmed widely in literature [283] [154] and can also be seen in Figure 7.9(a) were resistivities for Mixes B3 and B5 approach 10 000 Ω.m at 40% saturation (being equal to a conductivity of 0.0001 S/m which could be regarded as negligible). The poor fitting of Archie's law at lower saturations also reflects the observation that resistivity is dependent on the interconnectedness of the pore solution rather than porosity at lower saturations, as made in Section 7.2.6.1.

It is concluded that Archie's law describes the behaviour of concrete well for high saturations when mix specific $\mathfrak{m}$-values are used. However, generalised parameters cannot be applied to a range of mixes and the model also does not perform well at lower saturations.

7.3.2 The CRIM model for dielectric permittivity

A recent study by Fares [96] investigated the use of the Maxwell-Garnet, Bruggeman, CRIM and Lichtenecker-Rother models for the estimation of the dielectric constant on the same set of mixes as used here for the parametric study. The CRIM model was found to perform the best. The models were only applied to water contaminated concrete and at a frequency of 750 MHz. For the purposes of this thesis, particular interest was taken in the performance of the model at different states of chloride content and different frequencies i.e. 33 and 900 MHz. The CRIM model (3.54) is discussed in Chapter 3 and is rewritten here in terms of the condition parameters to estimate the EM observables ε'_1 and ε'_2 at 33 or 900 MHz.

$$\sqrt{\varepsilon'} = \Upsilon_{p1}\sqrt{\varepsilon'_{p1}} + \Upsilon_{p2}\sqrt{\varepsilon'_{p2}} + \Upsilon_c\sqrt{\varepsilon'_c} + \phi S\sqrt{\varepsilon'_w} + \phi(1-S)\sqrt{\varepsilon'_a} \tag{7.11}$$

where Υ_{p1}, Υ_{p2} and Υ_c are the volumetric fractions of the solid constituents as listed in Table 7.7, with ε'_{p1}, ε'_{p2} and ε'_c their dielectric constants for the chosen frequency and ε'_w and ε'_a are the dielectric constants of the liquid and air phase respectively.

The dielectric constants of the mix constituents were previously determined during the study by Fares and are listed in Table 7.7. The results of the modelled dielectric constants ε'_1 versus the measured values for ε'_1 (at 33 MHz) are presented in Figure 7.15(a) and for

Table 7.7: Volumetric fractions and dielectric constants of mix constituents.

	Aggr.1 (Pontreau)	**Aggr.2 (Pillier)**	**Cement gel**	**Pore solution**	**Air**
Mix	Volumetric fraction				
	Υ_{p1}	Υ_{p2}	Υ_c	$\Upsilon_w = \phi S$	$\Upsilon_a = \phi(1-S)$
B3	0.46	0.16	0.25	$0.13S$	$0.87S$
B4	0.47	0.17	0.19	$0.18S$	$0.82S$
B5	0.46	0.16	0.25	$0.19S$	$0.81S$
B6	0.47	0.17	0.19	$0.27S$	$0.63S$
Freq.	Dielectric constant per constituent				
	ε'_{p1}	ε'_{p2}	ε'_c	ε'_w	ε'_a
33 MHz	5.7	5.1	11.8	81	1
900 MHz	5.7	5.1	10.9	80	1

ε'_2 (at 900 MHz) in Figure 7.15(b). The r^2-values at 33 MHz and 900 MHz are 0.67 and 0.82 respectively, indicating a fit that is better at high frequencies than low frequencies, but nevertheless relatively poor for both. For both frequencies the discrepancy between the modelled and the measured values increases as the dielectric constant increases, which can be associated with an increase in degree of saturation.

At 33 MHz the measured dielectric constants are higher than the modelled values for high dielectric constants. This can be attributed to interfacial polarisation (Maxwell-Wagner effect) in concrete containing conductive liquid which is especially significant at low frequencies. This effect cannot be accounted for by the combination of the dielectric constants of a material's constituents as for a volume-averaging model such as the CRIM model. A significant difference in fit between the mixes for the 0, 15 and 30 g/L NaCl external solutions is observed. The performance of the model decreases as the chloride concentration increases which is consistent with the increase in interfacial polarisation that is associated with a more conductive pore solution.

At 900 MHz, there is not a noticeable difference between the goodness of fit of the mixes saturated with 0, 15 and 30 g/L NaCl solutions. This implies that interfacial polarisation does not play a substantial role at high frequencies, consistent with literature [286]. However, there is still a discrepancy between the measured and modelled values with the former being lower than the latter for high dielectric constants - contrary to results for 33 MHz. The CRIM model does not account for the increase in dielectric losses with degree of saturation. The actual measured dielectric constants are therefore lower than the modelled values due

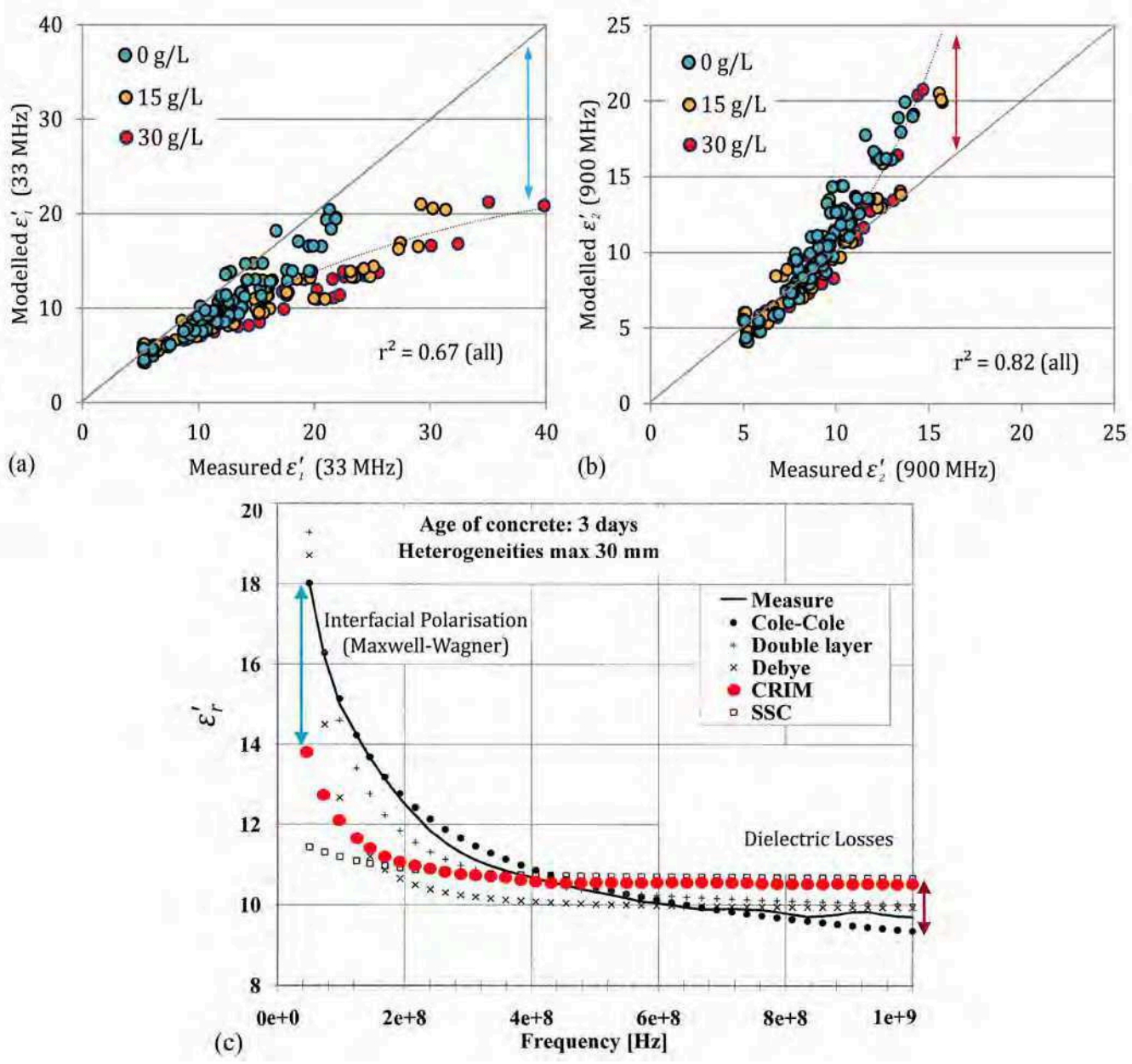

Figure 7.15: Results for the CRIM model showing (a) modelled dielectric constants ε'_1 against measured dielectric constants ε'_1 at 33 MHz, (b) modelled dielectric constants ε'_2 against measured dielectric constants ε'_2 at 900 MHz and (c) results from a previous study by Robert [223] showing the performance of various phenomenological and composite theory models from 0 to 1000 MHz.

the occurrence of these losses as can be seen in Figure 7.15(b).

These conclusions correspond to findings from a study on water saturated concrete specimens of Robert [223] presented in Figure 7.15(c). These results also found the CRIM model (in red) to under-estimate the dielectric constant at low frequencies (blue arrows) and over-estimate the dielectric constant at high frequencies (red arrows), similar to results found here. Robert noted in his study that the phenomenological Cole-Cole model is much better suited to estimate the frequency dependent permittivity of concrete.

7.3.2.1 Summary

It is concluded here that composite theory models such as Archie's law and the CRIM model have significant shortcomings when the EM observables of different concretes are modelled over a range of saturations, chloride contents and frequencies. While Archie's law performs well at saturated conditions its performance is inadequate at unsaturated conditions and for mixes of varying properties. The CRIM model performs well at low saturations but yields unsatisfactory results for conditions associated with high saturations and chloride contamination.

The more complex phenomenological models as discussed in Chapter 3 do indeed perform better than the simple composite theory models according to literature [223] [132]. In recent work by Revil [220] a "unified model" is proposed to explain the electromagnetic response of porous materials over a wide range of frequencies (1 mHz to 1 GHz). This model combines aspects from phenomenological models, Archie's law and volume-averaging models (of which the CRIM model is an example) and succeeds to model the EM response for a wide range of data sets. However, it is difficult to relate all of the parameters on which this approach is based to the parameters associated with concrete condition as defined in Section 7.2.3.

7.4 Multiple linear regression analysis

7.4.1 Principles

It is clear from the previous section that it is not a simple task to define a general relationship between the condition of concrete and its EM responses for the wide range of states forming part of the parametric study. A different approach is therefore introduced here: Regression analysis can be a very useful tool when the dependency of a response on a set of independent variables is difficult to describe analytically, as is the case for concrete. Regression does not require the exact physics of the phenomenon to be known in order to evaluate the

relationship between the dependent and independent variables. It also forms the basis of experimental design, as discussed in Section 7.2.1. Therefore, multiple linear regression analysis was chosen as tool to evaluate the combined influence of the condition parameters on the EM observables in this thesis.

The general equation for multiple linear regression is presented in Equation (7.12).

$$y_i = \beta_0 + \beta_1 x_{i1} + \beta_2 x_{i2} + ... + \beta_p x_{ip} + e_i = \hat{y}_i + e_i \tag{7.12}$$

$i = 1, 2, ..., n$

where y_i is the response for the i^{th} observation, $x_{i1}, x_{i2}, ..., x_{ip}$ are the variables, $\beta_0, \beta_1, ..., \beta_p$ are the regression coefficients, $\hat{y}_i$ is the modelled (predicted) value and e_i is the estimated error (residual). Also, n is the number of observations and p is the number of degrees of freedom. (Note that although no interaction terms (refer to Section 7.2.1) are shown here for simplicity's sake, it does not mean interactions cannot be included in the model).

When the problem is overdetermined for n observations, i.e. $n > p$, the regression coefficients can be determined by means of ordinary least squares (OLS). The least squares method minimises the sum of squared errors (SSE) by finding the optimum of the second order norm (Equation (7.13)), therefore setting the derivative function (Equation (7.14)) to zero (Equation (7.15)), where $j = 1, 2, ..., p$).

$$\text{SSE} = \sum_{i=1}^{n} (y_i - \hat{y}_i)^2 = \sum_{i=1}^{n} e_i^2 \tag{7.13}$$

$$\frac{\partial(\text{SSE})}{\partial \beta_i} = 2 \sum_{i=1}^{n} e_i \frac{\partial e_i}{\partial \beta_j} \tag{7.14}$$

$$-2 \sum_{i=1}^{n} e_i \frac{\partial \hat{y}_i}{\partial \beta_j} = 0 \tag{7.15}$$

This is expressed in matrix notation in Equation (7.16) and was used for all optimisation performed in this section in order to determine regression coefficients:

$$\hat{\beta} = (\boldsymbol{X}^T \boldsymbol{X})^{-1} \boldsymbol{X}^T \mathbf{Y} \tag{7.16}$$

where the vector matrix $\hat{\boldsymbol{\beta}}$ of length p contains the estimated regression coefficients, the $n \times p$ matrix $\boldsymbol{X}$ contains the variables and the vector matrix $\boldsymbol{Y}$ of length n contains the response for each observation.

In regression analysis the goodness of fit and the significance of the respective variables can be evaluated by calculating the statistics as listed below. These statistics form the basis

of the regression analysis presented in this section. First the total, regression and residual sum of squares must be defined:

$$\mathrm{SS} = \sum_{i=1}^{n} (y_i - \bar{y})^2 \tag{7.17}$$

where SS is the total sum of squares.

$$\mathrm{RSS} = \sum_{i=1}^{n} (\hat{y}_i - \bar{y})^2 \tag{7.18}$$

where RSS is the regression sum of squares.

$$\mathrm{SSE} = \sum_{i=1}^{n} (y_i - \hat{y}_i)^2 = \sum_{i=1}^{n} (e_i)^2 \tag{7.19}$$

where SSE is the sum of squared errors also known as the residual sum of squares.

$$\bar{y} = \frac{1}{n} \sum_{i=1}^{n} y_i \tag{7.20}$$

The coefficient of determination r^2 can then be calculated to evaluate the goodness of fit of the regression models. In general r^2-values of below 0.95 are viewed as unacceptable for the purposes of this thesis.

$$\mathrm{r}^2 = 1 - \frac{\sum_i (y_i - \hat{y})^2}{\sum_i (y_i - \bar{y})^2} = 1 - \frac{\mathrm{SSE}}{\mathrm{SS}} \tag{7.21}$$

where r^2 is the coefficient of determination.

The mean squared error MSE is a measure of the average size of the residuals and is usually used in conjunction with the coefficient of variation to evaluate goodness of fit. It is calculated as follows:

$$\mathrm{MSE} = \sqrt{\frac{\mathrm{SSE}}{n - p - 1}} \tag{7.22}$$

where MSE is the mean square error, n is the number of observations and p the degrees of freedom.

To evaluate the significance of the regression coefficients, hypothesis testing is used. In multiple linear regression, the coefficient of determination r^2 often increases as more variables are added to the model, even though the additional variables do not necessarily improve the model. The partial F-test is therefore used to evaluate whether the change in r^2 due to additional variables is statistically significant. The partial F-test uses the null hypothesis that all the regression coefficients are zero, thus $\mathrm{H}_0 : \beta_1 = \beta_2 = ... = \beta_p = 0$. The r^2-value of a restricted model, of which the number of variables is successively increased, is then

compared to that of the full unrestricted model by calculating the partial F-statistic for each case as follows:

$$F = \frac{(\mathrm{r}_{\mathrm{r}}^2 - \mathrm{r}_{ur}^2)/q}{\mathrm{r}_{ur}^2/(n-p-1)} = \frac{(RSS_{ur} - RSS_r)/q}{MSE_{ur}} \tag{7.23}$$

where $\mathrm{r}_{\mathrm{r}}^2$ and r_{ur}^2 are the coefficients of determination of the restricted and unrestricted regression model and q is the difference in the number of variables that are being tested between the unrestricted and restricted model, i.e. $q = p_r - p_{ur}$.

The F-statistic follows the F-distribution and is compared to a critical value which is associated with a chosen level of confidence to assess whether each term significantly contributes to the response. If the F-statistic is greater than the F-critical value, the null hypothesis fails and the term is significant. A confidence level of 95% is usually assumed, which implies that the probability of the F-statistic to be more than the critical value must be more than $\alpha = 0.05$ for the term not to be significant. Using this approach the terms that are found not to be significant can then be removed to simplify the regression model without compromising its predictive capability.

Finally, when multiple linear regression analysis is performed, certain assumptions are made regarding the population and the residual term (consisting of the residuals e for each observation) [124]. Of these assumptions the most relevant are:

1. *Representativeness*: The variables x and response y in the sample constitute a good representation of X and Y of the population.
2. *Homoscedasticity*: The variance of the residual term is constant for all combinations of the variables, i.e. e is not related to the value of Y.
3. *Collinearity*: No perfect collinearity exists between any of the variables X, i.e. it is not possible to express any of the variables as a linear combination of the others.
4. *Measurement error*: The measurement errors for all of the variables are negligible.
5. *Linearity*: The response Y is a linear combination of the variables X, but needs not be linear *in* the variables (i.e. $y = \beta_0 + \beta_1 x + \beta_2 x^2 + ...$ is still a linear combination)
6. *Distribution of residual term*: The residual term is a random variable which is normally distributed and has a mean equal to zero and a constant variance.

The assumptions of multiple linear regression are often not strictly met in practice, or cannot be verified due to a lack of a sufficient number of observations. However, this does not necessarily mean that regression analysis cannot yield good results if the assumptions are complied with to a reasonable extent, as was found in previous experimental studies on concrete by Dérobert et al. [87] and Villain et al. [273]. These assumptions also form the

basis of experimental design as discussed in the Section 7.2.1, as multiple linear regression plays a fundamental role in experimental design.

For the regression analysis performed here, the assumptions are tested and adherence justified in Section 7.4.2.2.

7.4.2 Application of regression analysis to experimental data

In this section the development of multiple linear regression models to estimate the respective EM observables from the condition parameters, as defined in the parametric study in Section 7.2, are presented. The models are evaluated using the statistical tools as discussed in Section 7.4.1.

It is important to remember here that the experimental work was aimed at the estimation of the condition parameters from the EM response by the combination of the respective in situ techniques (as will be detailed in Chapter 8). This was to be achieved by solving the simultaneous multiple systems equation consisting of the regression models presented in this section. Thus, in order solve an evenly defined problem, the number of equations for the EM observables ("knowns") had to be equal to the number of condition parameters ("unknowns") as is demonstrated for a four parameter system in Equation (7.24).

$$\begin{bmatrix} EM_1 \\ EM_2 \\ EM_3 \\ EM_4 \end{bmatrix} = \begin{bmatrix} a_0 & a_1 & a_2 & a_3 & a_4 \\ b_0 & b_1 & b_2 & b_3 & b_4 \\ c_0 & c_1 & c_2 & c_3 & c_4 \\ d_0 & d_1 & d_2 & d_3 & d_4 \end{bmatrix} \begin{bmatrix} 1 \\ P_1 \\ P_2 \\ P_3 \\ P_4 \end{bmatrix} \tag{7.24}$$

where EM_1, EM_2, ... denote known EM observables measured in situ, the subscript 0 denoting the coefficients for the constant terms and where a_i, b_i, c_i and d_i (with i = 0, 1, ..., 4) are the known coefficients determined for each condition parameter P_1, P_2, ... as part of the regression modelling presented in this section.

For a simple case without interactions between the condition parameters the vector matrix $\mathbf{P}$ can be solved through inversion using Equation (7.16). For systems containing interactions, the inverse problem is not so easily solved and an iterative approach is used to find $\mathbf{P}$ by assigning appropriate constraints as is further discussed in Chapter 8.

For the purposes of this thesis, with the available EM techniques as listed in Table 7.1, the EM observables that could be easily and reliably measured in situ were DC-resistivity and the dielectric constants at respectively 33 and 900 MHz. The loss factor at 900 MHz could

also be determined, but with the procedure being more time consuming and yielding less reliable results (refer to Chapter 4.3.2.2). An in situ technique to determine the loss factor at 33 MHz was not yet available. It was therefore decided to develop two systems of equations: Firstly, a system of equations consisting of regression models for *three* EM observables based on *three* condition parameters and secondly, a system of models for *four* EM observables containing *four* the condition parameters were developed. The first system was expected to be easier to implement in practice, whilst the second was expected to perform better over a wide range of concretes.

For the first system of regression models, the three condition parameters to which resistivity and the dielectric constants ε_1' and ε_2' were the most sensitive were selected. Degree of saturation S and total chloride content $C\ell_t$ were chosen as variables associated with concrete condition. Porosity ϕ was chosen as parameter representing the properties of the concrete as all three the selected EM observables displayed a dependency on porosity during the parametric study (unlike chloride diffusivity which only seemed to influence resistivity). The second set of regression models additionally included chloride diffusivity as condition parameter and the loss factor at 900 MHz ε_2'' as EM observable.

7.4.2.1 Dependencies and ranges of parameters

The relationships assumed between the EM observables and the condition parameters were based on those observed as a result of the parametric study. A quadratic relationship was assumed between the EM observables and degree of saturation as was found to exist between $Log(\rho)$ and S (Figure 7.9(a)). Though a linear dependency was observed for most of the EM observables related to permittivity, a quadratic relationship was adopted for all models, with the anticipation that the models that in truth had linear dependencies would be simplified during the hypothesis testing mentioned in Section 7.4.1. A logarithmic relationship between chloride content and all the EM observables was assumed as supported by the findings in Section 7.2.6.2.

The relationship between porosity and the various EM observables was taken as linear, corresponding to saturated conditions as can be seen in Figure 7.9. This linear relationship was less valid for unsaturated conditions where resistivity was concerned and it was thus anticipated that modelled resistivity values at unsaturated conditions would yield poorer results for the 3-parameter resistivity model than for the 4-parameter model. It was thus to be seen if the inclusion of diffusivity as part of the four parameter study (Section 7.4.2.4) would improve the results. The dependency of the EM observables on diffusivity was taken as linear.

Table 7.8: (a) Ranges of the condition parameters used for multiple linear regression with (a) the ranges of the condition parameters indicating their assumed relationship with all of the EM observables and (b) the resulting ranges for the EM observables.

(a)

	State parameter		Relation with
No	Symbol	Range	EM observables
1	S	0.30 to 1 [-]	quadratic
2	C^*	-3.29 to -1.87 [-]	logarithmic
3	ϕ	0.13 to 0.27 [-]	linear
4	D	4.1 to 62.1×10^{-12} m^2/s	linear

(b)

	EM observable	
No	Symbol	Range
1	$Log(\rho)$	0.68 to 4.49 [-]
2	ε_1'	7.35 to 37.42 [-]
3	ε_2'	6.75 to 15.64 [-]
4	ε_2''	0.48 to 10.00 [-]

$^*C = Log(C\ell_t)$

The relationship assumed for each condition parameter in terms of all the EM observables are listed in Table 7.8(a).

The ranges of the respective condition parameters included in the models corresponded to the measurements made during the parametric study and were also realistic for in situ conditions. The range for each condition parameter is shown in Table 7.8(a). The corresponding ranges of the EM observables that were included in the models are indicated Table 7.8(b).

7.4.2.2 Adherence to assumptions for regression analysis

It is not always easy to verify that the general assumptions for linear regression hold - normally due to a lack of data. Regression is therefore often implemented without considering the assumptions rigorously. This was also the case here, although adherence to the assumptions are justified as best as possible.

Representativeness: For the purposes of this study it was assumed that the condition parameters and the EM observables were representative of the population. This assumption was based on the fact that the measurements were representative of the specimen, when the conditions of homogenisation theory were met as discussed in Chapter 3.2.5. Also, at least three specimens were tested per conditioning level in order to ensure results were representative of the mix.

Homoscedasticity was also adhered to, though as a fortunate consequence of circumstances as will be explained. A variable is homoscedastic when the variance stays constant over the whole range of the parameter. Though this is true for most of the EM observables and

condition parameters used here, the variance of resistivity ρ and chloride content $C\ell_t$ increase significantly with an increase in their values, as is clear from Figures 4.2 and 7.8. In literature homoscedasticity is usually addressed by transformation of the data to its logarithm or inverse [124]. Because it was decided to use $Log(\rho)$ for the regression analysis (due to this being common practice) and $Log(C\ell_t)$ (because it better represents the dependency of the observables on the condition parameters), the effects of non-homoscedastic behaviour were largely dealt with.

Collinearity: For a designed experiment, multi-collinearity should not be present, because the combination of test levels (as illustrated by Figure 7.1) makes correlation between the factors impossible. However, because the test procedure followed as part of the parametric study was not in strict accordance with experimental design, collinearity was nonetheless verified by calculating the variance inflation factor (VIF) [124] for each of the condition parameters:

$$\mathrm{VIF}_j = \frac{1}{1 - \mathrm{r}_j^2} \tag{7.25}$$

where r_j^2 is the coefficient of determination from the regression of the j^{th} parameter on the remaining $p - 1$ parameters.

The VIF is commonly used to assess collinearity and it is usually assumed that a VIF greater than 10 indicates multicollinearity and that a VIF of 1 indicates no collinearity [124]. Results for the four condition parameters degree of saturation S, total chloride content $C\ell_t$, porosity ϕ and diffusivity D were respectively 1.16, 1.05, 1.99 and 2.2 indicating that there was no significant multicollinearity.

Measurement error: In terms of measurement error, it was assumed that the use of laboratory equipment in controlled conditions yielded results as accurate possible. However, to ensure no erroneous results were included in the regression analysis, data was cleaned by removing outliers with a residual e_i larger than the $mean \pm 3(\mathrm{MSE})$, while ensuring that values still accounted for all the levels required by experimental design.

Assumptions regarding linearity and the distribution of the residual term are addressed as part of Sections 7.4.2.3.1 and 7.4.2.4, where results from residual analysis for each model are presented. It was therefore accepted for the purposes of the work presented here, that all the assumptions are adhered to within an acceptable margin.

7.4.2.3 Results for a system of three multiple regression models

7.4.2.3.1 Full factorial regression

The multiple regression models based on three condition parameters presented here are similar to a 3×2^2 full factorial experiment as explained in Section 7.2.1. This enabled the evaluation of all the interactions between the condition parameters and gave a twelve term function for each EM observable as in Equations (7.26) to (7.28):

$$Log(\rho)_i = \mathrm{a}_0 + \mathrm{a}_1 S_{i1} + \mathrm{a}_2 S_{i2}^2 + \mathrm{a}_3 C_{i3} + \mathrm{a}_4 \phi_{i4} + \mathrm{a}_5 S_{i5} C_{i5} + ... + \mathrm{a}_{11} S_{i11}^2 C_{i11} \phi_{i11} + e_{\mathrm{a}i} \quad (7.26)$$

$$\varepsilon'_{1i} = \mathrm{b}_0 + \mathrm{b}_1 S_{i1} + \mathrm{b}_2 S_{i2}^2 + \mathrm{b}_3 C_{i3} + \mathrm{b}_4 \phi_{i4} + \mathrm{b}_5 S_{i5} C_{i5} + ... + \mathrm{b}_{11} S_{i11}^2 C_{i11} \phi_{i11} + e_{\mathrm{b}i} \quad (7.27)$$

$$\varepsilon'_{2i} = \mathrm{c}_0 + \mathrm{c}_1 S_{i1} + \mathrm{c}_2 S_{i2}^2 + \mathrm{c}_3 \mathrm{C}_{i3} + \mathrm{c}_4 \phi_{i4} + \mathrm{c}_5 S_{i5} \mathrm{C}_{i5} + ... + \mathrm{c}_{11} S_{i11}^2 \mathrm{C}_{i11} \phi_{i11} + e_{\mathrm{c}i} \quad (7.28)$$

where a_0, ..., a_j,..., a_{11}, b_0, ..., b_j,..., b_{11} and c_0, ... c_j,..., c_{11} are the regression coefficients for each term of the respective regression models (thus j = 0, 1, ..., 11) for $Log(\rho)$, ε'_1 and ε'_2, S_{ij}, C_{ij} and ϕ_{ij} are the condition parameters for the i^{th} observation, and the $(j+1)^{th}$ term of the polynomial and $e_{\mathrm{a}i}$, $e_{\mathrm{b}i}$, $e_{\mathrm{c}i}$ are the residuals for the i^{th} observation of each model.

More data levels than were required for a traditional 3×2^2 full factorial program were included in the model, as all results corresponding to the selected ranges in Table 7.8 from the parametric study were used. This was deemed to add to the accuracy of the model. The regression coefficients were determined by means of OLS as per Equation (7.16).

The three resulting regression models including all interactions are presented in Figure 7.16, with the modelled values displayed against the measured values for each EM observable. The four concrete mixes are shown in different colours in order to study the performance of the model for each mix. The linear fitting and coefficients of determination r^2 are indicated separately for each mix as well as the combined r^2 and mean squared error MSE (in the right bottom corner of each figure). All the modelled results display a linear relationship with the measured data, thus conforming to the assumption of linearity (Section 7.4.2.2).

As anticipated, the regression model for $Log(\rho)$ does not perform as well as the other two models with the r^2-value of 0.939 being markedly lower than those for ε'_1 and ε'_2. It is suggested that this is due to the influence of the diffusion properties on the resistivity response at lower saturations. In Figure 7.16(a) it is clear that the modelled values for the two mixes with similar porosities (B4 and B5) show the largest discrepancy from the measured values, which increases with an increase in resistivity. This reflects what has been observed as part of the parametric study, i.e. that porosity is not the only mix property affecting the response. The two models for the low and high frequency dielectric constants yield better results with r^2-values close to 0.98. Results for Mixes B4 and B5 are similar

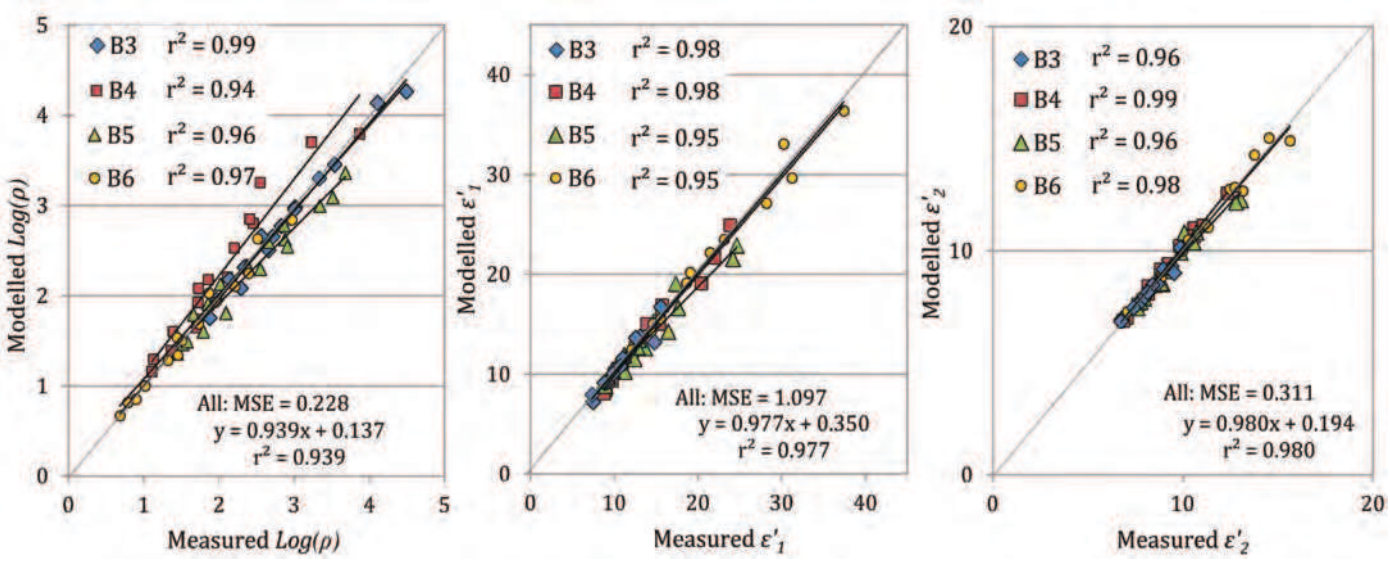

Figure 7.16: Modelled results for 3-parameter multiple regression including ***all interactions***, against measured values for (a) the logarithm of resistivity $Log(\rho)$, (b) the dielectric constant at 33 MHz ε'_1 and (c) the dielectric constant at 900 MHz ε'_2.

to those of the other two mixes, supporting the assumption that the dielectric constant is largely dependent on porosity in terms of microstructure.

To see whether the interaction terms play a role in the goodness of fit, the regression analysis was also performed without the interaction terms as in Figures 7.17(a), (c) and (e). Analysis of the residuals was conducted for each EM observable and the results are plotted in the adjacent Figures 7.17(b), (d) and (f). It can be seen that the performance of resistivity model is not significantly affected by the removal of the interaction terms as the MSE and r^2-values do not differ much from the full model. When Figure 7.17(b) is studied, it is observed that the residuals are randomly scattered and no particular trend in the error values can be identified. This conforms to the criteria for regression analysis as mentioned in Section 7.4.1 where the distribution of the errors are assumed to be random.

In contrast, results for the low frequency dielectric constant ε'_1 (Figure 7.17(c)) undergo a major reduction in r^2 and an increase in the MSE when the interactions are removed. The residuals in Figure 7.17(d) display a clear parabolic trend which is indicative of the fact that there are influences of some interactions that cause a non-random divergence from the linear relationship. The same trend is observed for the high frequency dielectric constant ε'_2 in Figures 7.17(e) and 7.17(f). The removal of the interaction terms therefore causes the models not to conform to the assumptions of regression listed in Section 7.4.1.

This implies that there are interactions between the condition parameters that cannot be disregarded for ε'_1 and ε'_2 if the assumption regarding distribution of the residuals are to be

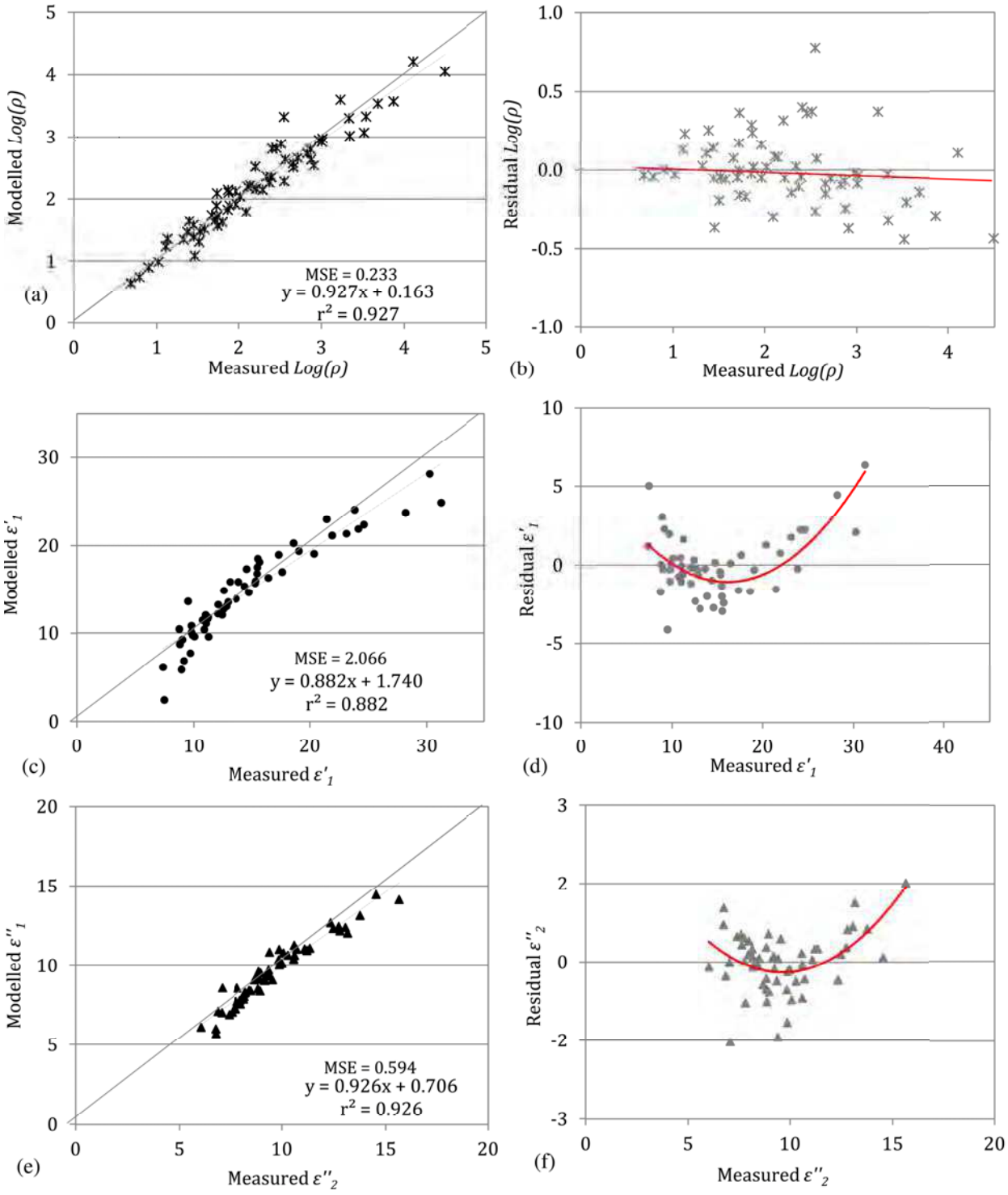

Figure 7.17: Modelled results for 3-parameter multiple regression including ***no interactions***, against measured values for (a) the logarithm of resistivity $Log(\rho)$ (b) and its residual plot, (c) the dielectric constant at 33 MHz ε_1' (d) and its residual plot and (e) the dielectric constant at 900 MHz ε_2' (f) and its residual plot.

complied with. The importance of the respective interactions is therefore investigated in the next section to assess how much the models can be simplified whilst still conforming to the assumptions of regression.

7.4.2.3.2 Simplification of the 3-parameter regression models

Before the coefficients of the models were evaluated statistically by means of the partial F-test as described in Section 7.4.1, three operations were performed on the experimental data. The operations enabled direct comparison of the magnitudes of the coefficients to evaluate their relative importance and were as follows:

1. Each level of the condition parameters was coded to fall between the lower and upper limits of -1 and 1 by means of the equation $\mathrm{P}_{i(coded)} = 2(\mathrm{P}_i - \mathrm{P}_{min})/(\mathrm{P}_{max} - \mathrm{P}_{min}) - 1$. The magnitude (absolute value) of the coefficients could then be compared to assess the importance of each term relative to the other terms in the specific model.

2. The second order term for degree of saturation was linearised by using the equation $S_2 = S_1^2 - 2/3$ [160], where S_1 is the coded degree of saturation and S_2 is the linearised quadratic term.

3. The EM observables were expressed as a percentage difference of the minimum value recorded in the parametric study for the ranges as in Table 7.8. The relationship of $\mathrm{Log}(\rho)$ was also converted to be positive with S, C and ϕ. In this way the coefficients could be evaluated on an inter-model basis to see how the sensitivity of the EM observables compared for each condition parameter.

The partial F-test with a confidence level of 95% was then conducted for each model to assess the significance of each regression coefficient statistically. Table 7.9 shows the coefficients for the normalised parameters and the probability that the null hypothesis is true ($\mathcal{P} > F$). The coefficients for which the F-statistic has a probability of above 95% to be non-zero are marked in yellow ($\alpha < 0.05$). The "yellow terms" therefore play a statistically significant role in the regression model.

When the results for $Log(\rho)$ are studied as per Table 7.9, it is observed that there are no significant interactions between the condition parameters for a confidence level of 95%, as was implied by the residual analysis in Figure 7.17(b). The coefficient of the quadratic term S_2 is clearly significant according to the F-test. When the magnitudes of the coefficients are compared, the degree of saturation is found to be the most important parameter with the porosity, chloride content and the quadratic term of saturation S_2 having smaller contributions to the modelled value.

Table 7.9: Coefficients for the normalised parameters for the full factorial three model system, their significances as determined by the partial F-test and the adjusted coefficients for the simplified model (coefficients having a probability of less the 5% to be zero are marked in yellow).

EM obs. / Cond. param.	*Log(ρ)*			ε'_1			ε'_2		
	$a_{(norm)}$	$\mathcal{P} > F$	$a_{adj(norm)}$	$b_{(norm)}$	$\mathcal{P} > F$	$b_{adj(norm)}$	$c_{(norm)}$	$\mathcal{P} > F$	$c_{adj(norm)}$
1	3.60		3.62	2.07		2.09	1.44		1.45
S_1	1.65	< 0.0001	1.71	1.02	< 0.0001	1.04	0.44	< 0.0001	0.43
S_2	-0.73	< 0.0001	-0.80	0.08	0.052	-	0.03	0.067	-
C	0.48	0.000	0.39	0.51	< 0.0001	0.49	0.06	0.001	0.05
ϕ	0.67	< 0.0001	0.71	0.49	< 0.0001	0.45	0.18	< 0.0001	0.18
$S_1 C$	0.22	0.072	-	0.44	< 0.0001	0.42	0.04	0.053	-
$S_2 C$	-0.22	0.292	-	-0.11	0.870	-	-0.03	0.260	-
$S_1 \phi$	-0.27	0.053	-	0.31	< 0.0001	0.33	0.16	< 0.0001	0.17
$S_2 \phi$	0.04	0.881	-	-0.08	0.552	-	0.00	0.751	-
ϕC	0.07	0.344	-	0.30	< 0.0001	0.42	-0.01	0.088	-
$S_1 C \phi$	0.08	0.646	-	0.21	0.027	-	-0.05	0.072	-
$S_2 C \phi$	0.01	0.971	-	-0.24	0.107	-	-0.05	0.287	-
r^2		0.939			0.979			0.986	
r^2(adjusted)		0.927			0.970			0.979	

When results for the dielectric constant at 33 MHz ε'_1 are studied, it is observed that the quadratic term of degree of saturation is not significant, as was also suggested as part of the parametric study. Several of the second order interactions are however significant, as was anticipated from the residual analysis in Figure 7.17. These are the interactions of degree of saturation with porosity, degree of saturation with chloride content, as well as porosity with chloride content. It is suggested that these interactions are a result of the complex nature of the electromagnetic phenomena that are linked to dispersion at low frequencies. These phenomena (such as the Maxwell-Wagner effect, double layer polarisation and the Debye effect [223]) are all related to the interaction between the interfaces of the particles, water and ions and can therefore be intuitively linked to the interaction between saturation, porosity and chloride content displayed by the regression analysis. For the dielectric constant at 900 MHz ε'_2, the quadratic term of degree of saturation is also not significant, in line with previous observations. Less interaction terms are significant at 900 MHz than at 33 MHz. There is no interaction between degree of saturation and chloride content, which corresponds to the fact that dielectric behaviour is less dispersive at this frequency and not sensitive to chloride as discussed in Chapter 3.4.

The regression analysis was repeated by only retaining the terms that were found to be significant. The adjusted normalised regression coefficients are indicated in Table 7.9 as

well as the full factorial and adjusted coefficients of determination r^2 and r^2(adjusted). It can be seen that even though the models have been significantly simplified, there is no major decrease in their coefficients of determination. This confirms that the EM observables are not significantly dependent on the terms that have been removed. A systems equation (Equation 7.24) consisting of the three simplified models as a resulting from the regression analysis is used in the following chapter to estimate the condition parameters from EM observables.

7.4.2.4 Results for a system of four multiple regression models

7.4.2.4.1 Full factorial regression

Equations (7.26) to (7.28) in the previous section were expanded to incorporate chloride diffusivity as condition parameter and a fourth regression model for the loss factor at 900 MHz ε_2'' was added to obtain the system of equations containing four regression models. The new 3×2^3 full factorial problem thus gave a 24 term regression model for each EM observable as per Equations (7.29) to (7.32).

$$Log(\rho)_i = \mathrm{a}_0 + \mathrm{a}_1 S_{i1} + \mathrm{a}_2 S_{i2}^2 + \mathrm{a}_3 C_{i3} + \mathrm{a}_4 \phi_{i4} + \mathrm{a}_5 D_{i5} + ... + \mathrm{a}_{23} S_{i23}^2 C_{i23} \phi_{i23} D_{i23} + e_{\mathrm{a}i} \quad (7.29)$$

$$\varepsilon'_{1i} = \mathrm{b}_0 + \mathrm{b}_1 S_{i1} + \mathrm{b}_2 S_{i2}^2 + a_3 C_{i3} + \mathrm{b}_4 \phi_{i4} + \mathrm{b}_5 D_{i5} + ... + \mathrm{b}_{23} S_{i23}^2 C_{i23} \phi_{i23} D_{i23} + e_{\mathrm{b}i} \quad (7.30)$$

$$\varepsilon'_{2i} = \mathrm{c}_0 + \mathrm{c}_1 S_{i1} + \mathrm{c}_2 S_{i2}^2 + \mathrm{c}_3 \mathrm{c}_{i3} + \mathrm{c}_4 \phi_{i4} + \mathrm{c}_5 D_{i5} + ... + \mathrm{c}_{23} S_{i23}^2 C_{i23} \phi_{i23} D_{i23} + e_{\mathrm{c}i} \quad (7.31)$$

$$\varepsilon''_{2i} = \mathrm{d}_0 + \mathrm{d}_1 S_{i1} + \mathrm{d}_2 S_{i2}^2 + \mathrm{d}_3 C_{i3} + \mathrm{d}_4 \phi_{i4} + \mathrm{d}_5 D_{i5} + ... + \mathrm{d}_{23} S_{i23}^2 C_{i23} \phi_{i23} D_{i23} + e_{\mathrm{d}i} \quad (7.32)$$

where the variables are defined as per Equations (7.26) to (7.28) with the addition of the EM observable ε''_{2i} and the condition parameter chloride diffusivity D and coefficients d_j with j = 0, 1, ..., 23.

The measurements taken as part of the parametric study were sufficient to serve for all the required combinations of factors as required by traditional experimental design for a 3×2^3 full factorial. The results for the full factorial regression of each EM observable are shown in Figure 7.18. When the results are compared to Figure 7.17(a), it is observed that the r^2-value for $Log(\rho)$ has improved significantly from 0.939 to 0.991 due to the inclusion of diffusivity as condition parameter. The mean squared error is also reduced from 0.228 to 0.085. MSE-values for ε'_1 and ε'_2 are very similar to values for the 3-parameter models and the results for ε''_2 also show a good fit with a coefficient of determination of 0.986.

Figures 7.19(a), (c), (e) and (g) show results for the 4-parameter models when all the interaction terms are removed. The residual plots are also indicated in Figures 7.19(b), (d) (f) and (h). If these are compared to Figure 7.17 for the 3-parameter models, it is

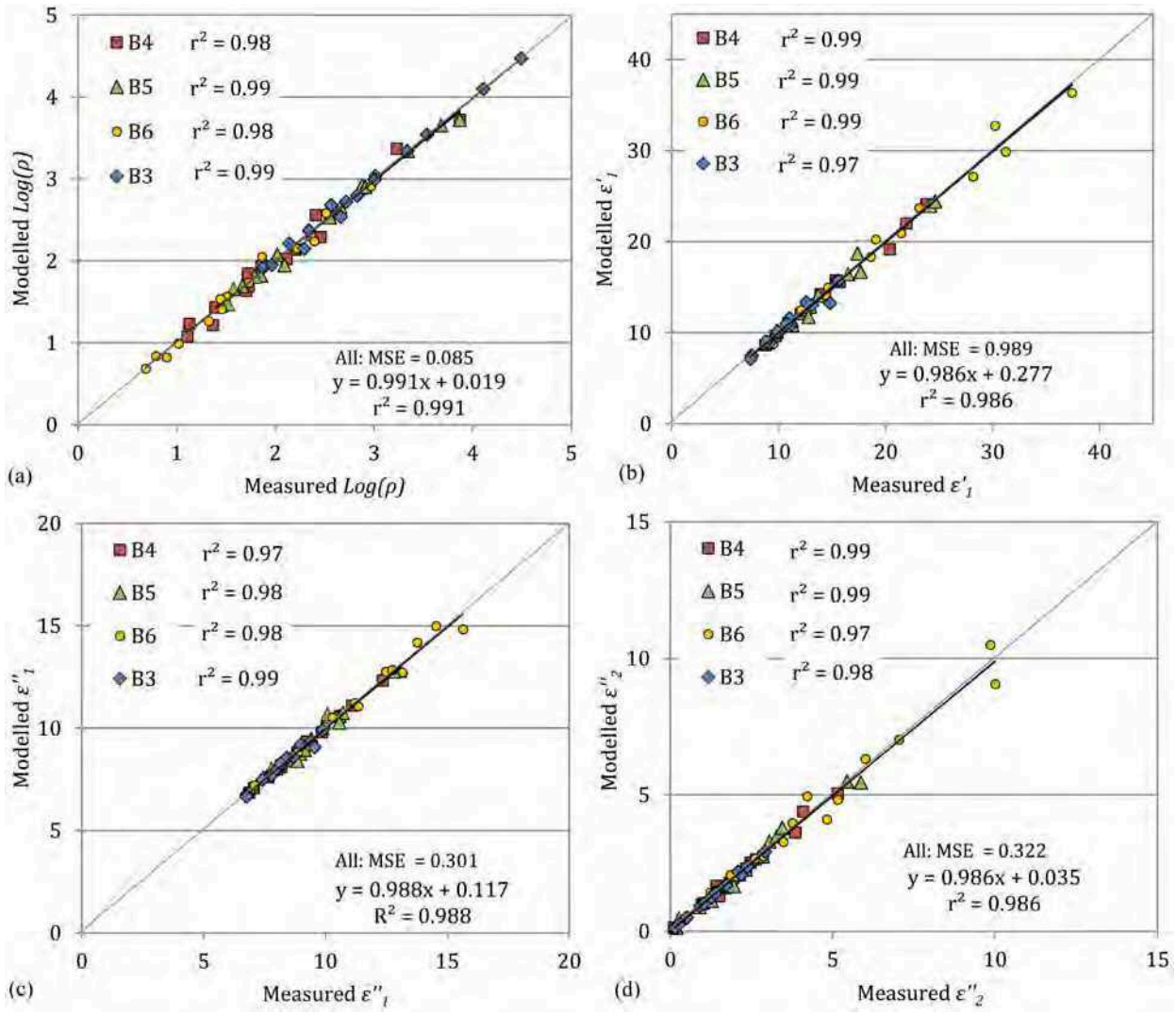

Figure 7.18: Modelled results from 4-parameter multiple regression including ***all interactions***, against measured values for (a) the logarithm of resistivity $Log(\rho)$, (b) the dielectric constant at 33 MHz ε'_1, (c) the dielectric constant at 900 MHz ε'_2 and (d) the loss factor at 900 MHz ε''_2.

observed that although $Log(\rho)$ has a better fitting, it seems that the residuals are not randomly distributed anymore. The results for ε'_1 and ε'_2 are almost identical to that of the 3-parameter case, suggesting that the addition of the influence of diffusivity is not significant on these two parameters. In Figures 7.19(g) and (h) it can be seen that the model of the loss factor ε''_2 is very much influenced by the removal of the interactions. The r^2-value decreases from 0.986 to 0.863 and the MSE-value increases from 0.322 to 0.995, thus illustrating a strong dependency on the interaction terms.

The significance of the interactions for the 4-parameter models were therefore statistically assessed and the results are presented in the next section.

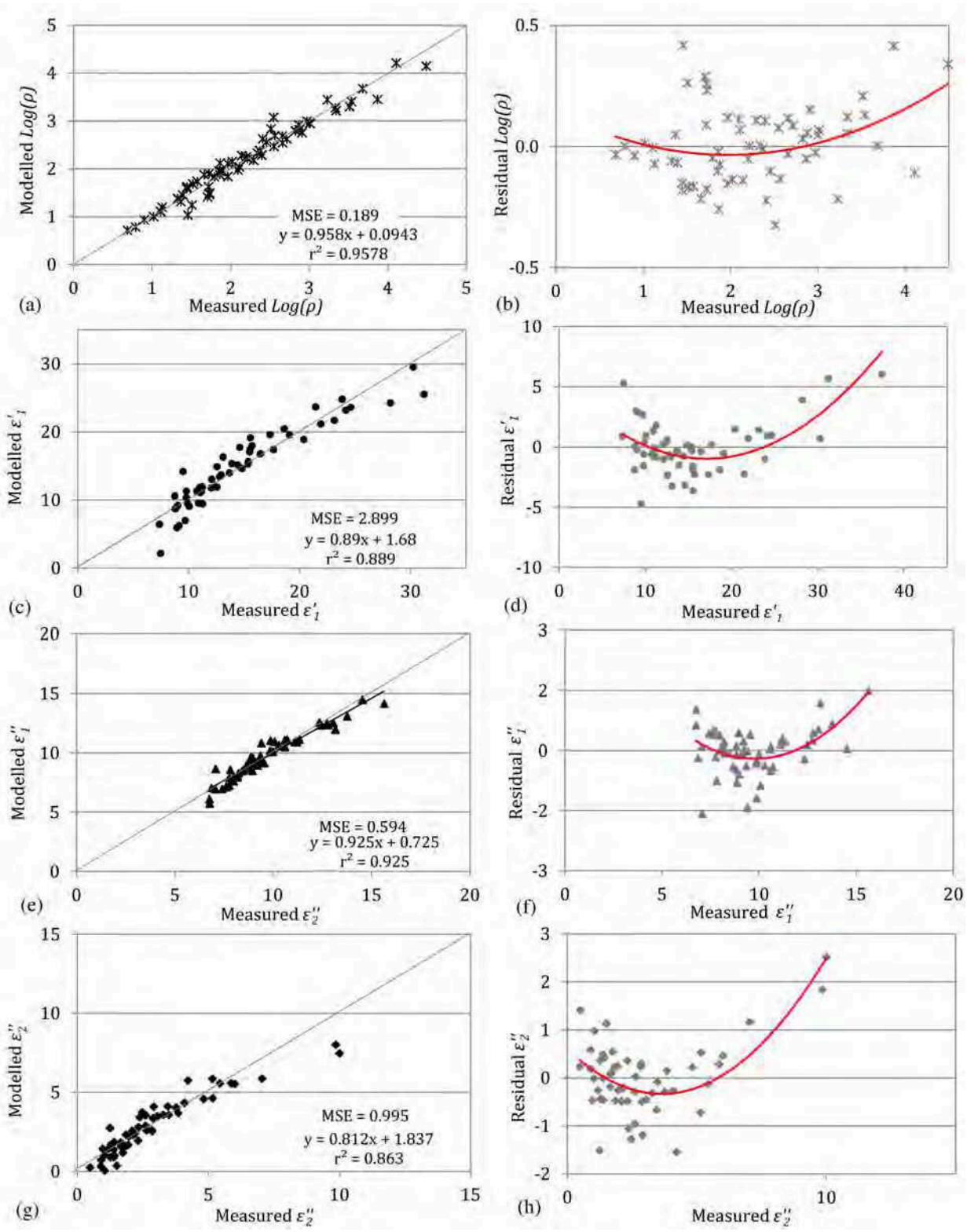

Figure 7.19: Modelled results for 4-parameter multiple regression including ***no interactions***, against measured values for (a) the logarithm of resistivity $Log(\rho)$ (b) and its residual plot, (c) the dielectric constant at 33 MHz ε_1' (d) and its residual plot, (e) the dielectric constant at 900 MHz ε_2' (f) and its residual plot and (g) the loss factor at 900 MHz ε_2'' (g) and its residual plot.

Table 7.10: Coefficients (after normalisation) for the full factorial 4-parameter models indicating the significance of each coefficient as determined by the partial F-test, with coefficients having a probability of less than 1% to be zero marked in yellow. The regression coefficients for the simplified models are also shown.

EM obs. / Cond par.	$Log(\rho)$			ε_1'			ε_2'			ε_2''		
	$a_{(norm)}$	$\mathcal{P}>F$	$a_{adj(norm)}$	$b_{(norm)}$	$\mathcal{P}>F$	$b_{adj(norm)}$	$c_{(norm)}$	$\mathcal{P}>F$	$c_{adj(norm)}$	$d_{(norm)}$	$\mathcal{P}>F$	$d_{adj(norm)}$
1	3.59			2.03		2.09	1.41		1.445	2.57		2.763
S_1	1.626	< 0.0001	1.732	1.048	< 0.0001	1.038	0.426	< 0.0001	0.433	2.153	< 0.0001	2.300
S_2	-0.658	< 0.0001	-0.845	0.230	0.014	-	0.117	0.041	-	0.788	< 0.0001	0.324
C	0.275	< 0.0001	0.297	0.438	< 0.0001	0.491	0.046	0.001	0.050	0.602	< 0.0001	0.900
ϕ	0.310	< 0.0001	0.394	0.431	< 0.0001	0.452	0.176	< 0.0001	0.184	1.009	< 0.0001	1.271
D	0.376	< 0.0001	0.349	0.048	0.014	-	0.058	0.029	-	0.113	0.000	-0.156
S_1C	0.413	0.000	-0.015	0.442	< 0.0001	0.415	0.072	0.035	-	0.905	< 0.0001	1.027
S_2C	-0.217	0.029	-	0.032	0.717	-	0.058	0.243	-	0.643	0.051	-
$S_1\phi$	0.183	0.000	0.043	0.478	< 0.0001	0.328	0.190	< 0.0001	0.168	1.357	< 0.0001	1.440
$S_2\phi$	0.079	0.351	-	0.213	0.491	-	0.098	0.700	-	0.668	0.080	-
S_1D	-0.441	< 0.0001	-0.247	-0.166	0.015	-	-0.018	0.181	-	-0.481	< 0.0001	-0.561
S_2D	0.059	0.655	-	-0.257	0.172	-	-0.088	0.341	-	-0.738	0.036	-
$C\phi$	-0.080	0.035	-	0.113	< 0.0001	0.415	-0.071	0.039	-	-0.031	< 0.0001	0.560
CD	0.156	0.228	-	0.179	0.025	-	0.057	0.334	-	0.482	0.042	-
ϕD	-0.029	0.013	-	0.031	0.141	-	0.042	0.778	-	0.227	0.938	-
$S_1C\phi$	-0.114	0.324	-	0.165	0.013	-	-0.016	0.034	-	0.215	0.003	0.608
$S_2C\phi$	0.470	-	-	0.013	-	-	0.135	0.193	-	0.963	-	-
$S_1\phi D$	0.259	0.331	-	-0.166	0.088	-	0.009	0.570	-	0.112	0.831	-
$S_2\phi D$	-0.166	-	-	-0.257	-	-	-0.137	0.043	-	-0.707	-	-
S_1CD	0.279	0.013	-	0.087	0.712	-	-0.018	0.812	-	0.378	0.137	-
S_2CD	-0.324	-	-	-0.158	-	-	-0.143	0.114	-	-0.574	-	-
$C\phi D$	0.470	0.015	-	0.133	0.265	-	-0.055	0.602	-	0.063	0.339	-
$S_1C\phi D$	-0.145	-	-	0.057	-	-	-0.055	0.275	-	0.063	-	-
$S_2C\phi D$	-0.285	-	-	-0.239	-	-	-0.091	0.281	-	-0.267	-	-
r^2		0.991			0.986			0.988			0.986	
r^2 (adjusted)		0.972			0.970			0.979			0.978	

7.4.2.4.2 Simplification of the 4-parameter regression models

To evaluate the contribution of the condition parameters and their interactions, a higher confidence level was used than for the 3-parameter models. A confidence level of 99% was selected as it was expected that the addition of diffusivity would improve the reliability of the fitted coefficients and therefore justify assessing their significance to a higher confidence. The normalised regression coefficients that are significant according the partial F-test ($\alpha = 0.01$) are indicated in yellow in Table 7.10.

The probabilities for the partial F-test confirm what was observed during the parametric study. It shows that diffusivity plays an important role in terms of resistivity as can be seen by the significance of the coefficient for D in Table 7.10. The magnitude of the coefficient for diffusivity (0.376) is in the same range as that of porosity (0.310), indicating that resistivity is dependent on both these condition parameters. There are four additional significant coefficients for the resistivity model when compared to that of the 3-parameter model, being the values for D, S_1C, $S_1\phi$ and S_1D. Although the 3-parameter model suggested no interactions between the condition parameters, the 4-parameter model show significant interactions between saturation and chloride, porosity and diffusivity respectively. It is suggested that the significance of the S_1C and $S_1\phi$-interactions were masked in the 3-parameter model due to the poorer fit of the data. It does however seem intuitive that there should be some interaction between these parameters, as is implied by the difference in rate of change of the fitted curves for the respective mixes in Figure 7.9(a) as the saturation decreases and also by the residual plot (Figure 7.19(b)).

When the coefficients for ε_1' and ε_2' are studied, the significant terms are found to be exactly the same as those for the 3-parameter model. This indicates that the inclusion of diffusivity does not improve these models and therefore confirms that the dielectric constant has little or no dependency on the diffusive properties of concrete. However, when the coefficients of ε_2'' are studied, it can be seen that the diffusivity plays an important role in terms of the loss factor. The loss factor at 900 MHz has the most significant interactions of all the EM observables. The interactions that are significant for resistivity are also significant for the loss factor with the addition of the $C\phi$-interaction and the second order interaction $S_1C\phi$. This illustrates the intricate nature of the EM response for the loss factor as suggested in Section 7.2.6.1.2.

The coefficients of determination for the full factorial models r^2 and the simplified models r^2(adjusted) are indicated in Table 7.10 and it is observed that there is not a major reduction in the fit with all the adjusted r^2-values being above 0.97.

7.4.2.4.3 Comparison of the sensitivity the EM observables to condition parameters

From these results the sensitivity of the EM observables and condition parameters can be quantitatively compared. When Figure 7.20(a) for the 3-parameter models is studied, it can be seen that all the EM observables display the greatest sensitivity to degree of saturation, followed by porosity and then chloride content. The logarithm of resistivity is the most sensitive to degree of saturation and porosity, while the dielectric constant at 900 MHz ε_2' is the least sensitive to all the condition parameters. ε_2' shows almost no sensitivity to chloride

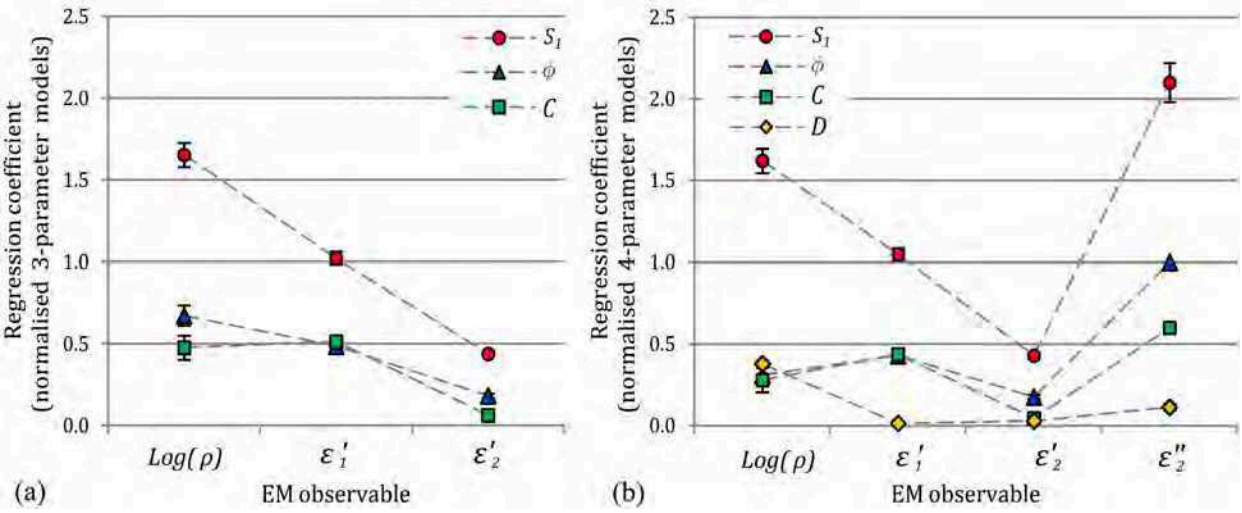

Figure 7.20: Comparison of normalised regression coefficients for each EM observable for regression models based on (a) three condition parameters and (b) four condition parameters.

content, which corresponds to what is reported in literature [87].

The coefficients for the models based on four condition parameters are plotted in Figure 7.20(b). When the values for resistivity are studied, it can be seen that the coefficient for porosity has decreased due to the addition of diffusivity. The influence on resistivity in terms of concrete quality is now shared between these two condition parameters. Values for ε_1' and ε_2' are unchanged from the 3-parameter models, with practically no influence from diffusivity as expected. When the coefficients of the loss factor at 900 MHz ε_2'' are studied, it is surprising to note that ε_2'' is particularly sensitive to degree of saturation, porosity and chloride content compared to the other observables. This is interesting as results at high frequencies are usually associated with low sensitivity to concrete state. However, this is clearly not the case for the loss factor at 900 MHz and implies that the sensitivity of the loss factor at 33 MHz would be even more significant. This highlights the potential of the loss factor as EM observable to assess concrete condition that could be useful in future once the techniques to determine in situ loss factors are more advanced.

7.4.3 Summary

The regression analysis presented in this section confirmed many of the observations made as part of the parametric study in Section 7.2. It was confirmed that the logarithm of resistivity $Log(\rho)$ and loss factor ε_2'' are not only dependent on saturation, chloride and porosity, but also on the diffusivity of the concrete. Likewise, it was confirmed that the dielectric constants ε_1' and ε_2' do not share this dependence on diffusivity. Further it was confirmed that the dependency of $Log(\rho)$ and ε_2'' on degree of saturation is quadratic whilst

that of ε_1' and ε_2' is linear.

All the EM observables display great sensitivity to degree of saturation, with the loss factor ε_2'' being the most sensitive followed by the resistivity and then the dielectric constants at 33 and 900 MHz. ε_2'' at 900 MHz is also the most sensitive to chloride content, followed by resistivity and ε_1', with the dielectric constant at 900 MHz ε_2' showing almost no sensitivity to chloride content.

The regression models were significantly simplified from the full factorial problem whilst still retaining a good fit to the data ($r^2 > 0.97$). Interactions that were found to be significant were mainly first order interactions between degree of saturation and each of the other condition parameters.

7.5 Conclusion

In this chapter the methodology and results from a parametric study on the dependency of EM observables on the condition of concrete, was presented. An introduction was given to experimental design and the motivation for the selection of particular EM observables and condition parameters was discussed. Technical aspects regarding the experimental work were then dealt with, such as the selection of appropriate mix designs, the test program and procedures for the conditioning and testing the specimens.

The results for the parametric study showed very different dependencies for the logarithm of resistivity and complex permittivity (at low and high frequencies) with regard to degree of saturation, porosity and diffusivity. Resistivity and the loss factors were found to be dependent on all three these condition parameters, whereas dielectric constants only showed sensitivity to degree of saturation and porosity. Total chloride content was found to relate logarithmically to all the EM observables.

Results from the parametric study were used to test two composite theory models, Archie's law for conductivity and the CRIM model for the dielectric constant at low and high frequency. Archie's model gave acceptable results for saturated conditions but failed at lower saturations. On the contrary, the CRIM model gave acceptable results for low saturations, but large discrepancies for high saturations.

Lastly, multiple linear regression modelling was performed to statistically assess the contribution of the respective condition parameters and their interactions on the EM observables. Two systems, the first consisting of 3-parameter models and the second of 4-parameter models were studied. The observations regarding the difference in sensitivity of the EM observables on the condition parameters was confirmed and compared statistically. The re-

sulting simplified system of equations for the 3-parameter models is used in the next chapter to characterise concrete from EM observables obtained from in situ testing techniques.

Chapter 8

Combination of in situ EM techniques to estimate concrete condition

8.1 Introduction

When non-destructive evaluation is conducted in situ there are many uncertainties that can influence the quality of the assessment. Of these the most notable are related to the testing method, the influence of the environment, uncertainty due to the intrinsic variability of the concrete, human factors and data interpretation. In order to improve the reliability of the in situ assessment of concrete condition, the combination of NDE techniques have attracted much interest in recent years [50]. The combination of techniques can be approached in various different ways depending on the objective of the non-destructive assessment [50]. Methods range from the qualitative comparison of trends in measurements between two or more NDE techniques [247] [92], to much more sophisticated strategies such as possibilistic data-fusion [213] and data mining [234]. However, it is acknowledged that more research is required on the combination of non-destructive techniques to exploit its full potential in terms of the quantitative assessment of in situ concrete.

The experimental work presented in this chapter is a continuation of the work presented in Chapter 7. The relationships established in the previous chapter are here applied to the in situ techniques. The methodology that was adopted to combine results from the various in situ techniques was based on work by Villain et al. [276] as part of the SENSO project (a French initiative which focussed on the combination of NDE techniques). A very similar approach was followed, i.e. to combine the results of three EM in situ techniques to obtain the degree of saturation, chloride content and water content by means of the multiple solution of the system of equations.

However, the experimental program presented here differed from the previous study in terms of the following:

- Resistivity replaced ultrasound (impact echo) [56] as investigation technique used in conjunction with capacimetry and GPR - resistivity is more sensitive to chloride content than impact echo (which is mainly sensitive to the mechanical properties of the mix [276]);
- Instead of using linear relationships between the condition parameters and EM observables, the models produced as part of the previous section were implemented;
- Testing with in situ techniques was performed in a controlled laboratory environment and the uncertainties related to the environment were therefore minimised.
- Testing was conducted on the same mixes as were used to establish the regression models in Chapter 7.4.2 and no calibration was therefore required, contrary to the previous study [276].

In the first section the experimental work in terms of the preparation and testing of the concrete specimens is discussed. In the following sections, the approach that was used to combine the regression models is described and the results for the estimation of the condition parameters are presented.

8.2 Preparatory work and testing of concrete

The concrete mixes that were used as part of the work presented here were the same as for the parametric study as indicated in Table 5.1. The advantage of this was that the concrete was already mature and that the mix properties known, thus minimising additional destructive testing to determine the true state of the concrete. The intention was to test the slabs at different homogeneous states (in terms of saturation and chloride content) using the EM techniques suited for in situ assessment. The techniques to be employed were surface resistivity measurements, the capacitive method and ground penetrating radar, as presented in Chapter 4. Testing was to be conducted under controlled laboratory conditions, thus creating a "best case" scenario in order to investigate whether the condition parameters could be accurately estimated from the EM observables.

It was of critical importance that the slabs were conditioned in as short a time as possible due to the time constraints associated with the thesis. The same protocol was therefore adopted as with the core specimens in Chapter 7, i.e. saturation under vacuum and subsequent oven drying and homogenisation. This protocol limited the size of the slabs to the maximum size that could fit in the vacuum tank and oven. Two slabs of 300×220×100 mm were cut

per mix from the original 600×600×120 mm slabs used as part of the experimental work of Ihamouten [132] (as explained in Chapter 7.2.4). These slabs were previously tested at different relative humidities and were therefore uncontaminated by chloride. They were stored in unsaturated conditions inside a workshop following the end of the experimental work of Ihamouten. To remove any traces of carbonation that might have occurred since their casting, the thickness of each slab was reduced to 100 mm by sawing a 10 mm slice off the top and bottom. This would ensure that the reduction in porosity caused by carbonation [277] would not affect surface measurements.

8.2.1 Concrete conditioning

The protocol that was followed to obtain the different levels of degree of saturation and chloride content are described in this section. Figure 8.1 illustrates the test program and Table 8.1 lists the saturations and chloride concentrations of the four conditionings at which tests were performed.

The slabs were saturated under vacuum with tap water and left in the solution for two weeks to ensure complete saturation. It was confirmed that they were completely saturated by calculating their target saturated mass from their known porosity (as determined in 2011) and dry density as per Table 7.3 and estimated volume by substituting $m_{dry} = \gamma_{dry}\mathcal{V}$ into Equation (2.16) as follows, where $S = 1$:

$$m_{target} = \mathcal{V}(\gamma_{dry} + \phi\gamma_w) \tag{8.1}$$

where m_{target} [kg] is the target saturated mass, $\mathcal{V}$ [m^3] is the volume calculated from the

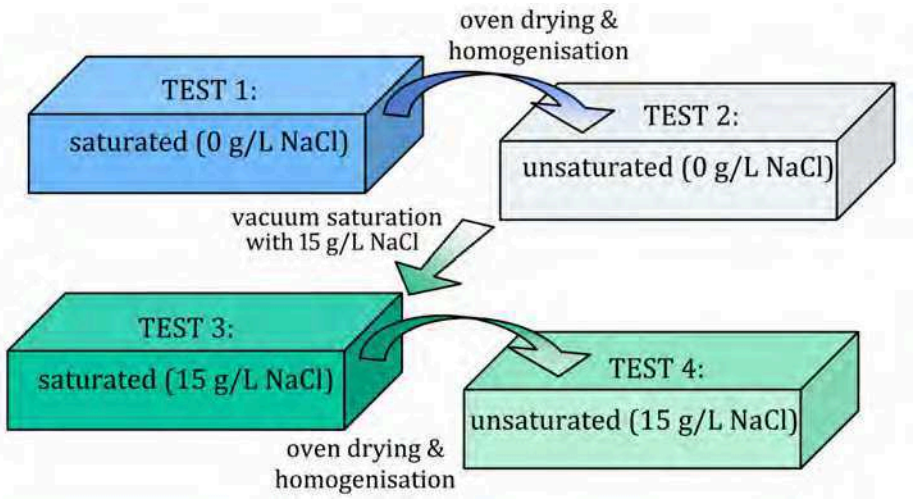

Figure 8.1: Schematic to illustrate the protocol that was followed to condition the slabs to four different states (performed for one slab per mix).

Table 8.1: Conditioned states of concrete slabs for testing with in situ techniques.

Slab (mix)	**Uncontaminated**			**NaCl contaminated**		
	Degree of saturation [%]		Chloride	Degree of saturation [%]		Chloride
	Test 1	Test 2	[%bwc]	Test 3	Test 4	[%bwc]
B3	100	64.7	0.06	100	87.0	0.36
B4	100	51.4	0.12	100	78.7	0.79
B5	100	59.7	0.05	100	90.7	0.25
B6	100	42.5	0.11	100	75.2	0.67

measured dimensions of the slab, γ_{dry} [kg/m^3] is the dry density and ϕ is the porosity (2011) and γ_w [kg/m^3] is the density of water.

The first measurements (Test 1) were taken at the saturated, uncontaminated state. Afterwards the slabs were dried for one month at 70°C to allow testing at an unsaturated, uncontaminated state. The degree of saturation that was reached after drying varied for each slab and was calculated from their mass by means of Equation (2.16). The slabs were sealed in an airtight manner with aluminium foil and homogenised at 70°C for two months before testing. Testing at the second state (Test 2) was then performed and afterwards the slabs were dried for three months up to a near dried state. They were then saturated with a NaCl solution of 15 g/L together with one witness core per mix to determine the actual total chloride content by means of the potentiometric-AFREM method as described in Chapter 7.2.5.5. The chloride contaminated slabs were tested at a saturated state (Test 3) and at an unsaturated state (Test 4) after one month of drying and two months of homogenisation.

8.2.2 Testing protocol

The relatively small size of the slabs was convenient in terms of conditioning, but it was anticipated that it would adversely affect results - especially in terms of ground penetration radar. Calculations based on estimated propagation speeds before the slabs were cut, indicated that the multi-offset (WARR) measurements would be significantly distorted by boundary reflections. The number of offsets required for good results from the inversion process (approximately 20 [132]) would lead to measurements too close to the sides of the slabs. This was confirmed by preliminary testing on Slab B3 as can be seen in Figure 8.2(a) where the distortion of the signals for the multi-offset configuration is clearly visible.

An approximated dielectric constant could still be determined from the velocity of the direct

wave by means of the fixed offset configuration. Figure 8.2(b) shows that measurements in the centre of the slabs were unaffected by the boundary reflections for this configuration. No problem was envisaged for resistivity measurements, as the results could be corrected for boundary effects. The capacitive method would not be affected by the size of the slabs, as the influence from the side boundaries could be avoided by taking measurements more than 50 mm away from the sides [24] [275]. The depth of the slabs also exceeded the influence depth of even the large electrode set. The techniques that were therefore employed were surface resistivity, capacimetry and GPR from which the EM observables, the logarithm of resistivity $Log(\rho)$ and the dielectric constants at approximately 33 MHz ε_1' and 900 MHz ε_2', were obtained. Unfortunately the loss factor ε_2'' could not be determined as the WARR configuration did not produce acceptable results. Testing was conducted at a controlled temperature of 20°C.

The multi-electrode resistivity probe was used in Wenner configuration and allowed for the homogeneity of the slabs to be confirmed due to its ability to measure apparent resistivity for increasing influence depths. The slabs were placed on a non-conducting surface and the probe was placed close to the centre of the upper face as demonstrated in Figures 8.3(a) and (b). Three measurements (a 26-point sequence) were taken per slab and the result for each measurement point was averaged. Each of these was then corrected for boundary effects by applying a geometric factor as per Equation (4.6) that was modelled using finite element analysis as explained in Chapter 6.3.3.

For the capacitive sensor, the large plate electrode set was used in order to obtain results for the largest possible influence depth and with the least variability. Eight measurements were taken in the vicinity of the centre of the slabs in order to avoid influence of the side boundaries as shown in Figures 8.2(c) and (d). The corresponding dielectric constants were then determined from Equation (4.27) by applying the coefficients fitted to the calibration curves presented in Figure 4.8(a).

The fixed offset GPR configuration using antennae with a central frequency of 1500 MHz was used as described in Chapter 4.3.2.2 and demonstrated in Figure 8.3(e) and (f). The antennae were positioned near the centre of the slab to avoid distortion from reflected waves. They were then moved laterally over a 100 mm distance and measurements were taken at increments of 10 mm. The propagation speed of the direct wave was determined from the arrival time of the signal for each measurement and was obtained from the radargrams using the software package REFLEXW. The dielectric constant was then determined for each increment by applying Equation (4.29) and averaged for the final result.

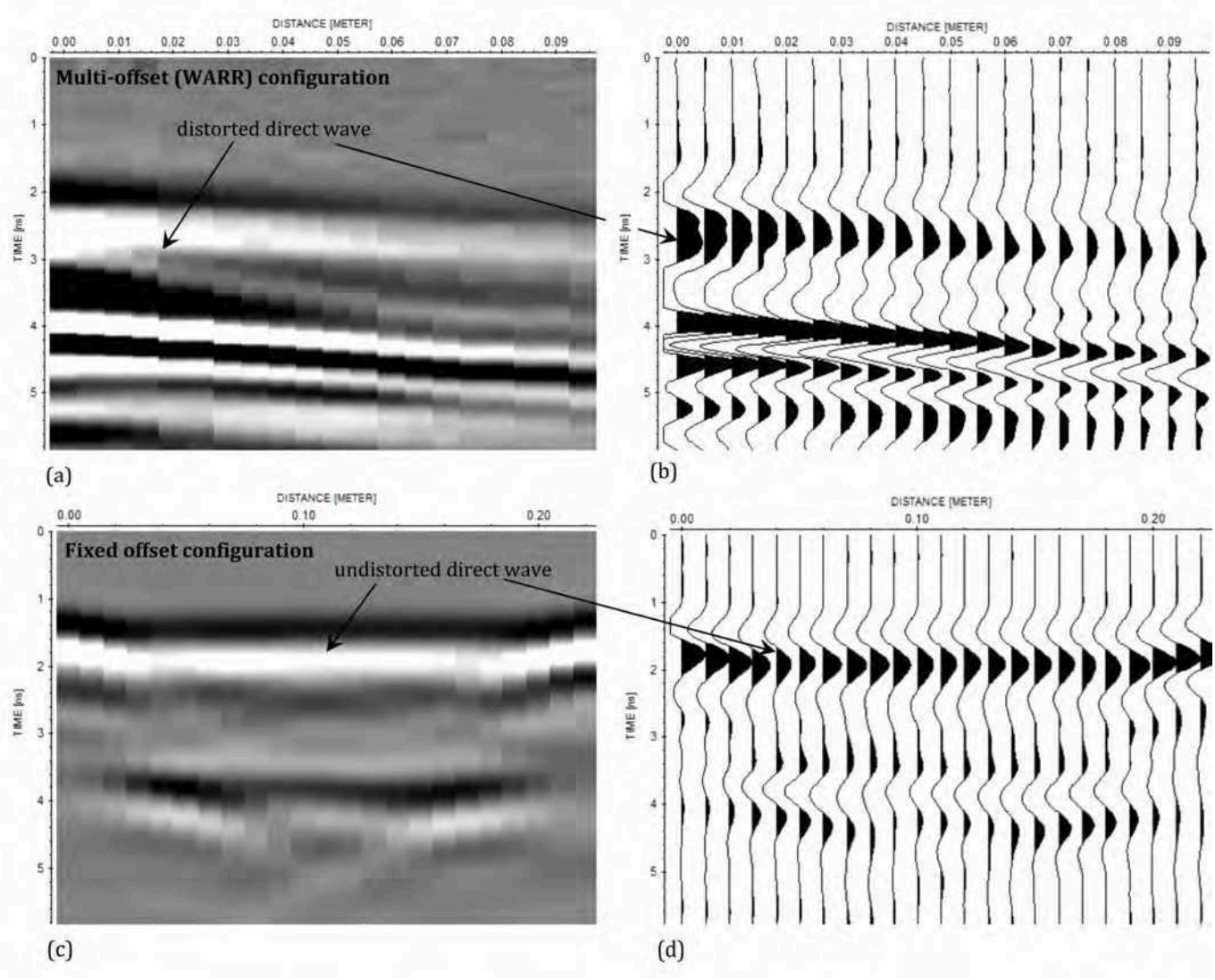

Figure 8.2: Radargrams for Slab B3 under water-saturated conditions showing (a) the multi-offset (WARR) configuration with distortion of the direct wave due to reflections from the side boundaries and (b) the fixed offset configuration with a clear undistorted direct wave.

8.3 Results and discussion

8.3.1 Evaluation of homogeneity

The multi-electrode resistivity probe was used to evaluate the homogeneity of the slabs. Their homogeneity could be assessed both horizontally and over depth by looking at the variation of the point measures laterally and between each investigation depth (corresponding to electrode spacings $a = 20$ mm to 80 mm).

(a)

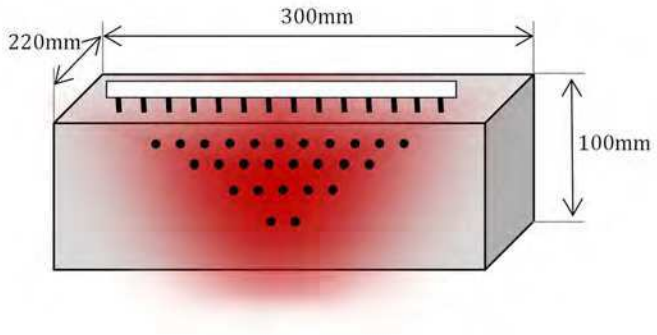

(b)

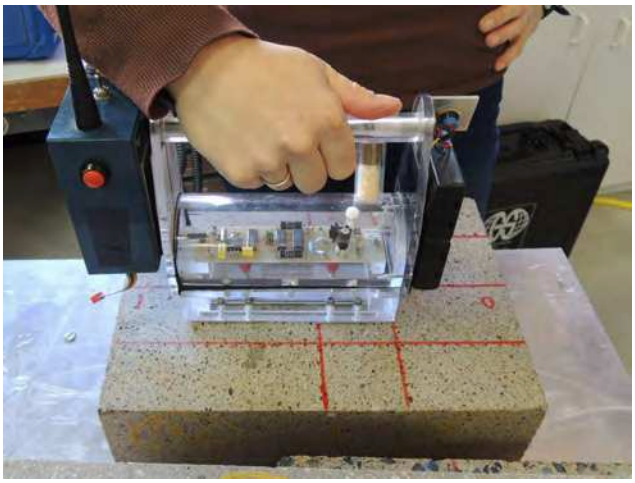

(c)

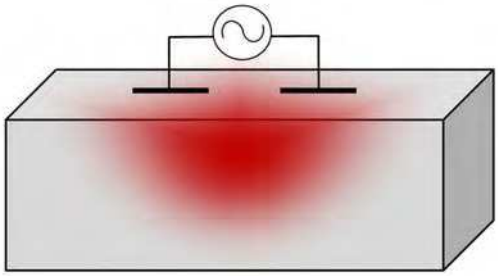

(d)

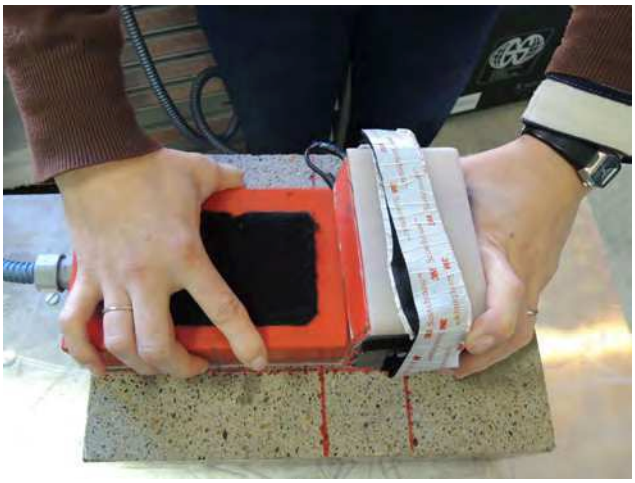

(e)

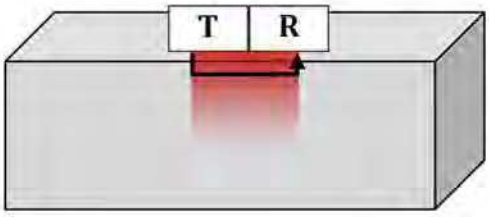

(f)

Figure 8.3: The in situ EM techniques used during the experiment and an illustration of their application with (a) the resistivity probe with (b) its configuration (with pseudodepths of 26 measurement points), (c) the capacitive probe with (d) its configuration and (e) fixed offset ground penetrating radar using the direct wave with (f) its configuration.

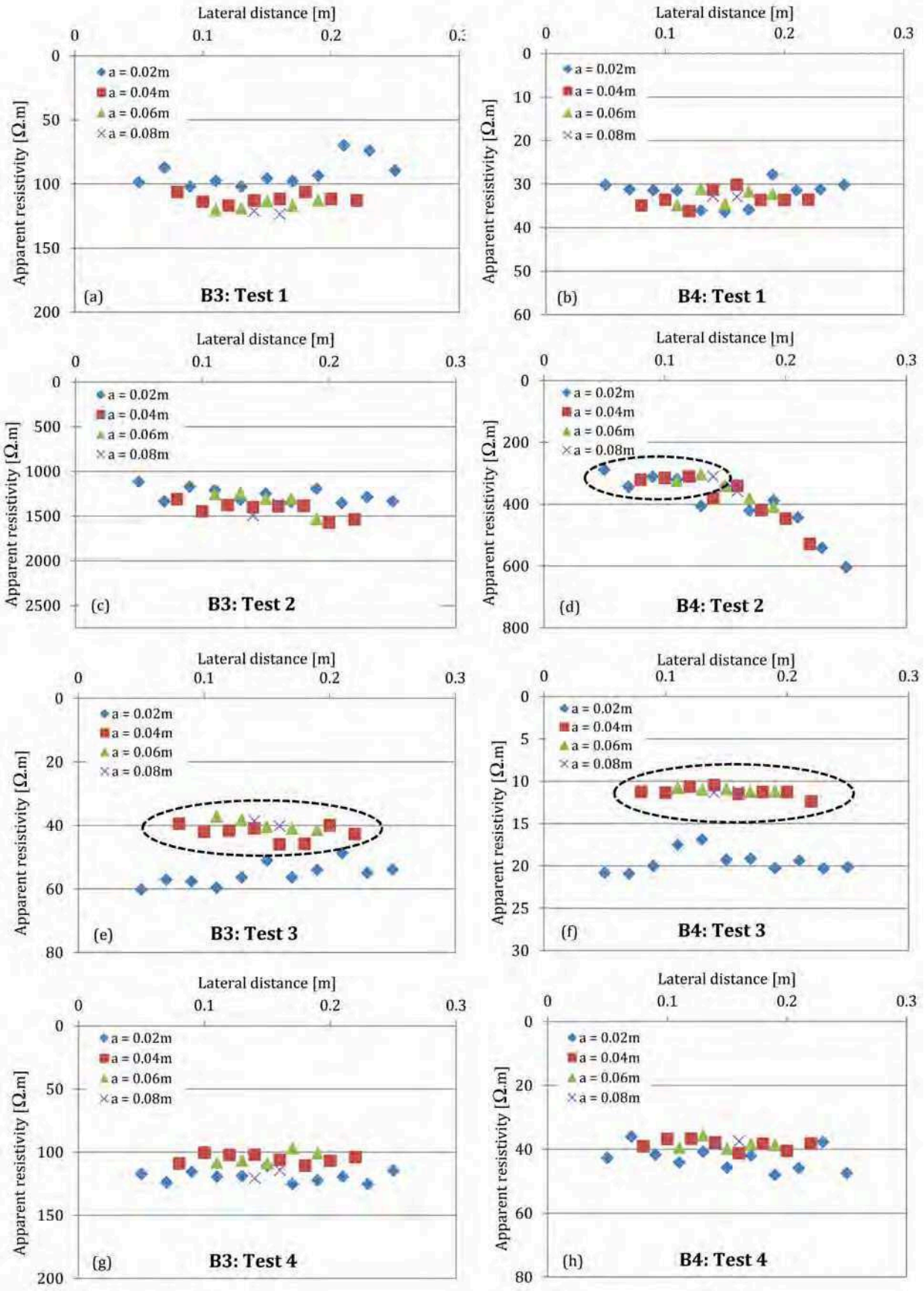

Figure 8.4: Apparent resistivities for Slabs B3 and B4 obtained from the multi-electrode resistivity probe for Tests 1 to 4, with the ellipses indicating the measurement points included in the final results.

Resistivity results for Tests 1, 2, 3 and 4 (Table 8.1) are presented in Figure 8.4. Only the results for Slabs B3 and B4 are shown, as the two mortars B5 and B6 showed similar or better results in terms of homogeneity. Slab B3 represented the "worst case"-scenario as it had the lowest porosity and was therefore the most difficult to homogenise. However, it can be seen in Figure 8.4(a), (b) and (c) that apparent resistivities are quite uniform for each test, both laterally and over depth. The measurements representing an influence depth closest to the surface ($a = 20$ mm), show significantly more variability than the other three levels, corresponding to the findings from the preliminary work presented in Chapter 6.4.2.1. Only results for the second, third and fourth level of investigation, corresponding to electrode spacings of 40 mm, 60 mm and 80 mm, were therefore used as part of the final results.

Two interesting observations are made when Figure 8.4(d) and Figures 8.4(e) and (f) are studied respectively. Firstly, it can be seen that results for Slab B4 (Test 2) are clearly not homogeneous in the lateral sense. The apparent resistivities increase substantially from the left to the right of the slab. As to the reason for this, it can only be speculated that the slab was not properly sealed during homogenisation. Though great care was taken to ensure that the aluminium wrapping was airtight, it is possible that the wrapping sustained damage which could account for the non-homogeneous condition. In any case, it was decided not to completely discard the measurements, but to use only those to the left of the slab as circled in Figure 8.4(d).

The second interesting observation is the difference between the first level of measurement and the other levels for the saturated, chloride contaminated state (Test 3) in Figures 8.4(e) and (f). It is unsure what caused the resistivity close to the surface to be so much higher than for the deeper levels. It is suggested that surface drying can explain this phenomenon as there was a delay (approximately two hours) between the radar and the resistivity measurements for this particular test, which could have caused some drying of the outermost skin of the concrete. By only including the deeper investigation levels in the final results (as circled in Figures 8.4(e) and (f)), this effect was largely eliminated. The coefficient of variation C_v for each slab calculated using these values was less than 15% for each of the states and rarely exceeded 10%. This corresponds to errors that have been reported in literature for surface measurement on homogeneous concrete in laboratory conditions [195] [30] and to those found in Chapter 6.4.2.1.

For interest's sake, the geometrically corrected apparent resistivities were also inverted using the software package *Res2Dinv* [164], as explained in Chapter 6.3.1. Theoretically, the apparent resistivities should be similar to the true inverted resistivities when the slabs are homogeneous. In Figure 8.5 it can be seen that this is indeed the case with the inverted

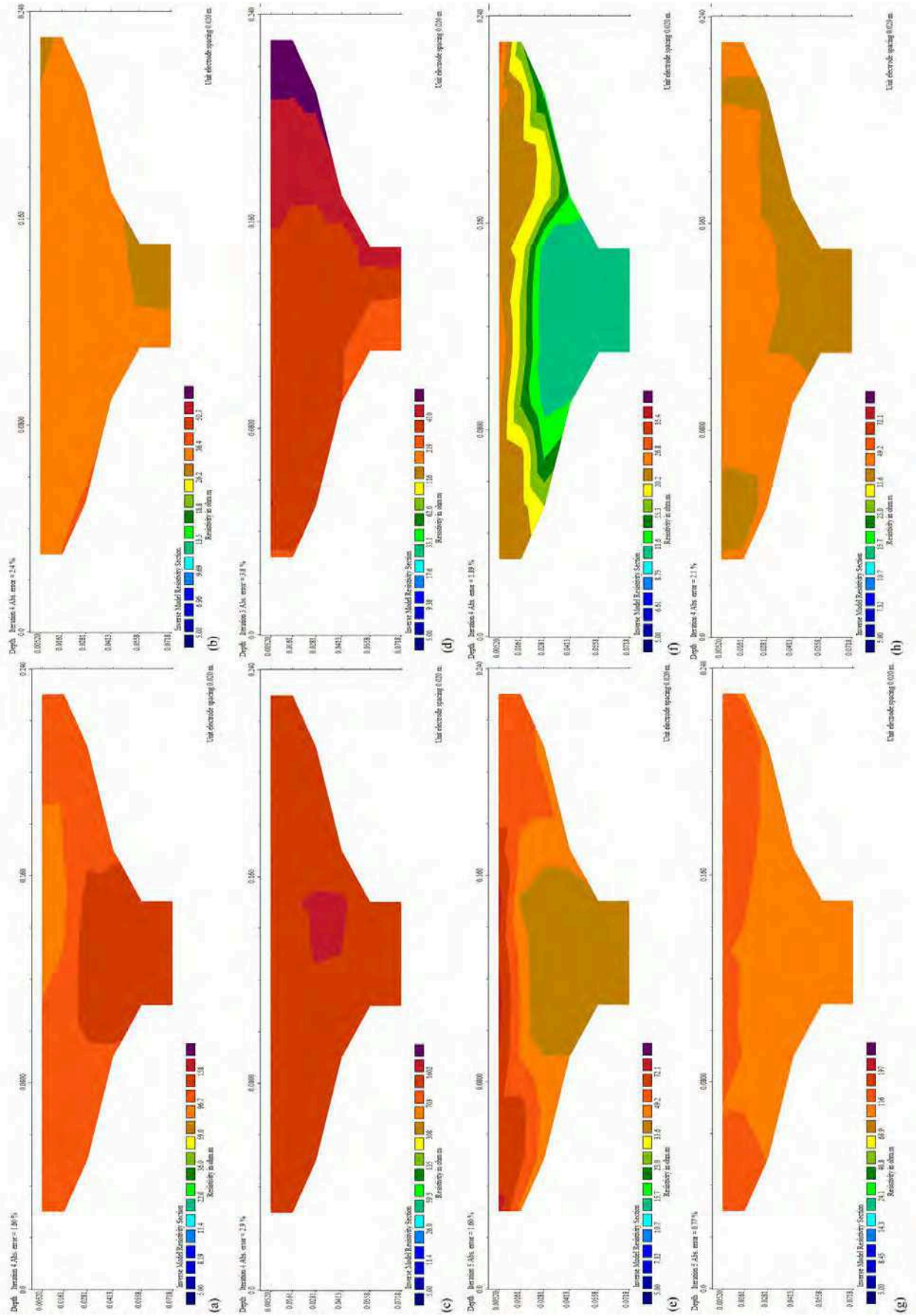

Figure 8.5: Inverted resistivity results for Slabs B3 (a), (c), (e) and (g) and Slab B4 (b), (d), (f) and (h) obtained from the multi-electrode resistivity probe for Tests 1 to 4.

resistivities being very similar to those plotted in Figure 8.4.

The value of the multi-electrode probe for verification of homogeneity is therefore clearly demonstrated here. As a result of this homogenisation assessment only measurements to the left of Slab 4 were used to calculate final average values for the EM observables. It was assumed that the effects of surface variability would be mitigated by only using resistivity measurements for larger spacings and the plate electrode with the largest influence depth for the capacitive method. For GPR, results for Test 3 were compared for the direct wave and the reflected wave (having a larger influence depth). No significant difference was found, suggesting that results for the direct wave is representative of the slabs.

8.3.2 Discussion of results for the three in situ techniques

The final, averaged results for the resistivity probe, capacitive sensor and ground penetrating radar are shown in Figure 8.6. For this study, it would be more correct to refer to *apparent* resistivity and dielectic permittivity, as some of the slabs were found to be not strictly homogeneous. However, these values approached the true EM properties of the slabs due to the selective use of data as demonstrated in Section 8.3.1.

The EM observables for each slab are plotted against degree of saturation and total chloride content in Figures 8.6(a), (c) and (e). The data is presented as a planar surface for each slab for purposes of display, though it should be noted that this is not strictly correct as some the EM observables have non-linear relationships with degree of saturation and total chloride content as discussed in Chapter 7.2.6. Nevertheless, the trends can be clearly observed, with a strong decrease in $Log(\rho)$ and an increase in the dielectric constants as the degree of saturation and chloride content increase.

In Figures 8.6(b), (d) and (f) the measured results for the in situ test techniques are plotted against predicted values as calculated using the regression models developed in Chapter 7.4. The errorbars indicate the standard deviation for each final measurement. The results from the slabs correspond relatively well to that of the estimated values with r^2-values of 0.943, 0.945 and 0.972 for the resistivity, capacimetry and GPR respectively. This is acceptable if it is taken into account that there are multiple uncertainties that played a roll during the testing of the slabs as well as the development of the regression models. The inherent random variation of the observables and condition parameters, uncertainties related to homogenisation, the test techniques, test operator etc., all lead to the accumulation of error, even when conditions are controlled. A coefficient of determination in the order of 0.95 is therefore regarded as good for the purpose of this study.

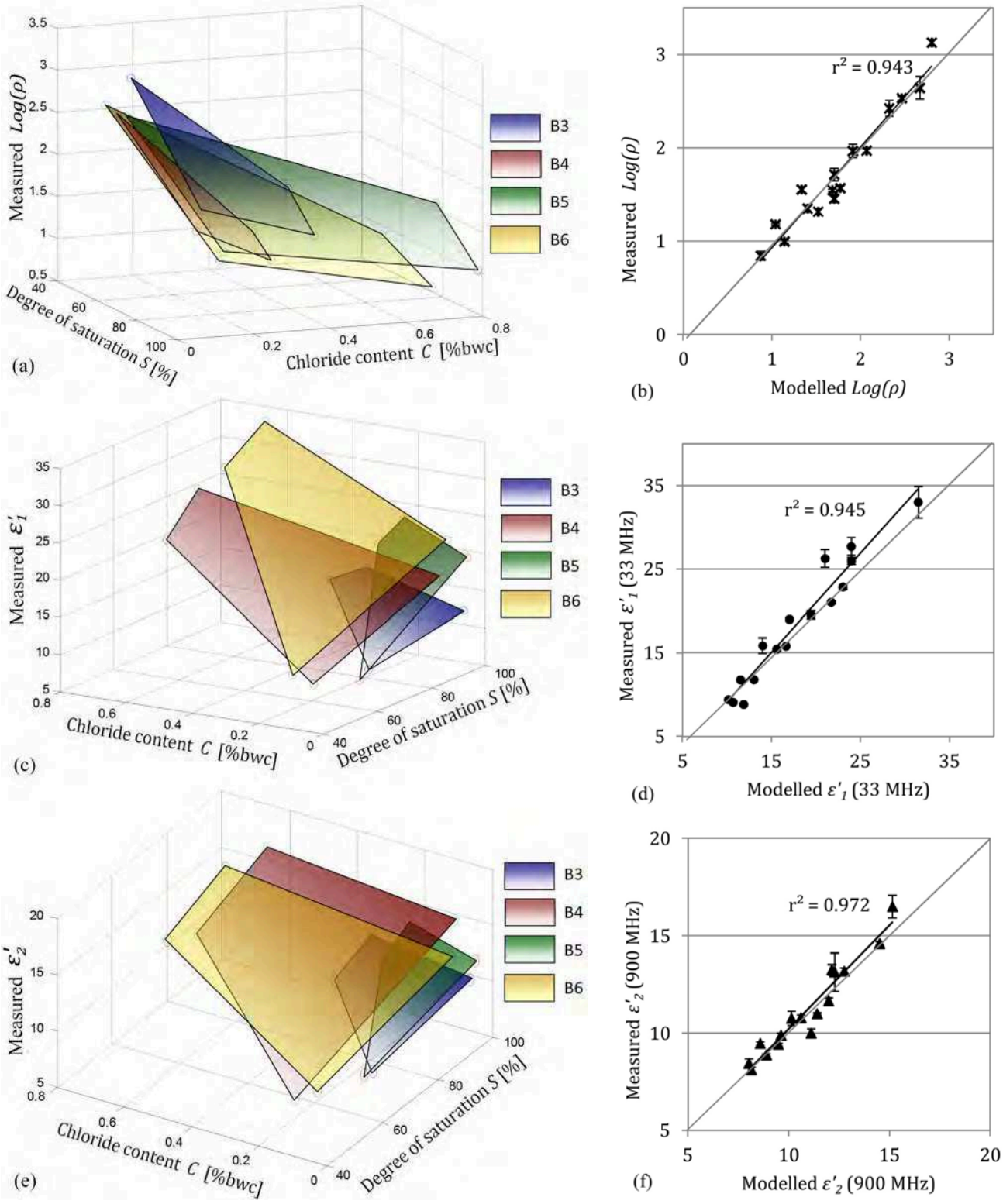

Figure 8.6: EM observables for in situ EM techniques on conditioned slabs plotted (left) as a function of saturation and chloride content and (right) against the modelled values for (a)-(b) logarithm of resistivity (c)-(d) dielectric constant at ≈ 33 MHz and (e)-(f) dielectric constant at ≈ 900 MHz.

8.3.3 Estimation of condition parameters from EM observables

8.3.3.1 Methodology

The objective of the experimental work presented in this Chapter, was to estimate the condition parameters of the slabs for each test condition from the multiple linear regression models developed in Chapter 7.4. The three observables that were obtained from the experimental work allowed for the 3-parameters simultaneous system of equations as defined in Chapter 7.4.2.3.1 to be solved. The system of equations (7.26) to (7.28) was simplified according to the findings of the regression analysis and rearranged, as shown in Equations (8.2) to (8.4):

$$0 = Log(\rho) - (\mathrm{a}_0 + \mathrm{a}_s S + \mathrm{a}_{s_2} S^2 + \mathrm{a}_c C + \mathrm{a}_\phi \phi + \mathrm{a}_{s\phi} S\phi + \mathrm{a}_{sc} SC) + e_{Log(\rho)} \tag{8.2}$$

$$0 = \varepsilon'_1 - (\mathrm{b}_0 + \mathrm{b}_s S + \mathrm{b}_c C + \mathrm{b}_\phi \phi + \mathrm{b}_{s\phi} S\phi + \mathrm{b}_{sc} SC + \mathrm{b}_{c\phi} C\phi) + e_{\varepsilon'_1} \tag{8.3}$$

$$0 = \varepsilon'_2 - (\mathrm{c}_0 + \mathrm{c}_s S + \mathrm{c}_c C + \mathrm{c}_\phi \phi + \mathrm{c}_{s\phi} S\phi) + e_{\varepsilon'_2} \tag{8.4}$$

where $Log(\rho)$, ε'_1 and ε'_2 are the average measured values for the logarithm of resistivity, dielectric constants at 33 MHz and at 900 MHz, $\mathrm{a}_{...}$, $\mathrm{b}_{...}$ and $\mathrm{c}_{...}$ are the regression coefficients for each condition parameter as calculated as part of the regression analysis shown in Table 8.2. The two interaction terms a_{sc} and $a_{s\phi}$ were added to the simplified regression

Table 8.2: Final regression coefficients for the 3-parameter models for the EM observables $Log(\rho)$, ε'_1 and ε'_2 corresponding to the adjusted normalised coefficients in Table 7.9, with interactions SC and $S\phi$ added for $Log(\rho)$.

EM obs. / State par.	$Log(\rho)$	ε'_1	ε'_2
	a	b	c
1	7.995	-17.632	7.571
S_1	-11.033	31.176	-0.634
S_2	3.865	0	0
C	-0.014	-8.679	0.383
ϕ	-11.385	63.748	-9.858
S_1C	-0.543	11.341	0
$S_1\phi$	7.100	93.605	42.223
$C\phi$	0	30.655	0
r^2	0.936	0.970	0.979

model of $Log(\rho)$, as they were found to be significant in the 4-parameter regression analysis as presented in the previous chapter (Table 7.10).

The EM observables were now the "knowns" and the condition parameters the "unknowns", in contrast with the linear regression problem in Chapter 7.4. The problem now became a non-linear inversion problem. For non-linear systems the use of least squares optimisation does not necessarily yield a closed solution [207]. This means that local minima can exist, and finding the global or appropriate minimum can be quite difficult. For this reason so-called "open methods" are used where initial values are chosen for the parameters that must be solved and they are then refined by means of successive approximation to obtain the solution. Of these methods the Newton-Raphson method is probably the most widely used [58].

Numerical methods and optimisation theory were not the main focus of this study and are therefore not discussed at length, as several textbooks detail their application to engineering problems [142] [58] [146]. The application of the Newton-Raphson method is therefore only demonstrated briefly here in terms of the parameters used for this study. The method finds the solution of a non-linear function $F(x) = 0$, where $F(x)$ is the residual term, by extending the tangent from the initial guess of the parameter x_k to the x-axes as in Figure 8.7. This usually results in an improved estimate of the parameter and the solution is therefore approximated by means of iteration.

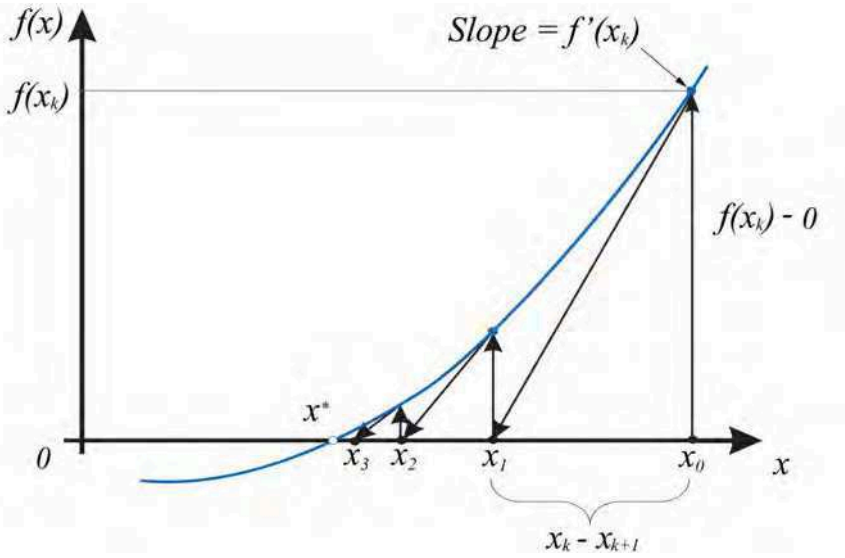

Figure 8.7: Graphical depiction of the Newton-Raphson method. A tangent to the function of x_k (i.e. $f'(x)$) is extrapolated down to the x-axis to provide an estimate of the root at x_{k+1}, after [58].

The method can be derived by expansion of the Taylor series [58], or by geometrical interpretation using Figure 8.7 as follows:

$$F'(x_k) = \frac{F(x_k) - 0}{x_k - x_{k+1}} \tag{8.5}$$

thus

$$x_{k+1} = x_k - \frac{F(x_k)}{F'(x_k)} \tag{8.6}$$

which is known as the *Newton-Raphson formula* [58] where $F'(x_k)$ is the derivative of $F(x_k)$ for the k^{th} iteration.

In terms of the work presented here, the system of equations (8.2) to (8.4), the function $\boldsymbol{F}(\boldsymbol{x})$ to be solved was defined as follows:

$$\boldsymbol{F}(\boldsymbol{x}) = \mathbf{0} = \begin{bmatrix} f_1(\boldsymbol{x}) \\ f_2(\boldsymbol{x}) \\ f_3(\boldsymbol{x}) \end{bmatrix} = \begin{bmatrix} Log(\rho) \\ \varepsilon_1' \\ \varepsilon_2' \end{bmatrix} - \begin{bmatrix} Log\hat{\rho}(\boldsymbol{x}) \\ \hat{\varepsilon}_1'(\boldsymbol{x}) \\ \hat{\varepsilon}_2'(\boldsymbol{x}) \end{bmatrix} \tag{8.7}$$

where $\boldsymbol{x}$ is a vector consisting of the condition parameters:

$$\boldsymbol{x} = \begin{bmatrix} S \\ C \\ \phi \end{bmatrix} \tag{8.8}$$

$Log(\rho)$, ε_1' and ε_2' are the measured values and $Log\hat{\rho}(\boldsymbol{x})$, $\hat{\varepsilon}_1'(\boldsymbol{x})$ and $\hat{\varepsilon}_2'(\boldsymbol{x})$ are the predicted values of the EM observables using the regression coefficients as in Table 8.2. For the initial guess of the condition parameters $\boldsymbol{x}_k$ values closer to the solution is found by implementing the Newton-Raphson method (8.6) as follows:

$$\begin{bmatrix} f_1(\boldsymbol{x}_k + d\boldsymbol{x}) \\ f_2(\boldsymbol{x}_k + d\boldsymbol{x}) \\ f_3(\boldsymbol{x}_k + d\boldsymbol{x}) \end{bmatrix} = \begin{bmatrix} f_1(\boldsymbol{x}_k) \\ f_2(\boldsymbol{x}_k) \\ f_3(\boldsymbol{x}_k) \end{bmatrix} + \begin{bmatrix} \frac{\partial f_1}{\partial S} & \frac{\partial f_1}{\partial C} & \frac{\partial f_1}{\partial \phi} \\ \frac{\partial f_2}{\partial S} & \frac{\partial f_2}{\partial C} & \frac{\partial f_2}{\partial \phi} \\ \frac{\partial f_3}{\partial S} & \frac{\partial f_3}{\partial C} & \frac{\partial f_3}{\partial \phi} \end{bmatrix}_{\boldsymbol{x}_k} \begin{bmatrix} dS \\ dC \\ d\phi \end{bmatrix} \tag{8.9}$$

thus

$$\boldsymbol{F}(\boldsymbol{x}_k + d\boldsymbol{x}) = \boldsymbol{F}(\boldsymbol{x}_k) + \mathbf{J}d\boldsymbol{x} \tag{8.10}$$

where the partial derivatives are evaluated at $\boldsymbol{x} = \boldsymbol{x}_k$ and $\mathbf{J}$ is the Jacobian matrix. To find the new vector $\boldsymbol{x}_{k+1} = \boldsymbol{x}_k + d\boldsymbol{x}$ for the next iteration, $F(\boldsymbol{x}_{k+1})$ is set to 0 which simplifies (8.10) to the following:

$$-\boldsymbol{F}(\boldsymbol{x}_k) = \mathbf{J}d\boldsymbol{x} \tag{8.11}$$

The procedure is repeated until a value for $\boldsymbol{F}(\boldsymbol{x})$ is reached that is "sufficiently close" to zero. Various ways are used to assess whether $\boldsymbol{F}(\boldsymbol{x})$ is adequately close to zero, such

as evaluating the norm (Equation (8.12)), setting a predefined tolerance $f_i(\boldsymbol{x})$ (Equation (8.13)) or constraints for each function (Equation (8.14)).

$$\|\boldsymbol{F}(\boldsymbol{x})\|_p = \left(\sum_i \mid f(\boldsymbol{x}_i)^p \mid \right)^{1/p} \tag{8.12}$$

where p is the order of the norm, with the second order norm usually used.

$$\frac{\|\boldsymbol{F}(\boldsymbol{x}_k)\|}{\|\boldsymbol{F}(\boldsymbol{x})_0\|} < tol \tag{8.13}$$

where $\|\boldsymbol{F}(\boldsymbol{x}_0)\|_p$ is the norm for the initial guess and $\|\boldsymbol{F}(\boldsymbol{x}_k)\|_p$ the norm for the evaluated iteration.

$$\text{Max}\{\mid f(\boldsymbol{x}_1) \mid, \mid f(\boldsymbol{x}_2) \mid, \mid f(\boldsymbol{x}_3) \mid, ...\} < tol \tag{8.14}$$

As part of this thesis existing optimisation software tools (Microsoft Excel™ Solver using the simplex, generalized reduced gradient, and branch and bound methods based on the Newton-Raphson method [105]), were employed to find the optimised solution of each condition parameter. It is important to stress that the optimisation of a non-linear problem as discussed above did not necessarily converge to the correct solution. Due to the uncertainties related to the models and measurement used here, the solution tended to be a local minimum rather than the global minimum. It was therefore important to set appropriate constraints and provide a realistic initial guess from which the iteration process was started. It was decided to evaluate the functions by evaluating both Equation (8.13) and (8.14). A general tolerance was set (being quite high at 15%), whereas a maximum error value was assigned to each function separately. In this way the different sensitivities of the respective EM observables to the condition parameters (as in Figure 7.20) could be accounted for by for example setting a smaller error for $Log(\rho)$ than for ε_2'. This was a crude way of weighting the respective functions according to their importance.

In order to obtain results within realistic bounds, the range of each condition parameter was also constrained. The selected ranges were [0.2 to 1.1] for saturation, [0.1 to 0.3] for porosity and [-4 to -1.5] for the logarithm of chloride content. These ranges corresponded to those for which the models were developed, being appropriate for concrete, and were additionally widened to compensate for the regression errors of each condition parameter obtained during the regression modelling in Chapter 7.4. The initial guess of each condition parameter was taken as the median of the ranges as defined above. However, in practice these guesses could be improved if some *a priori* information regarding the condition of the concrete were known (which was assumed not to be the case for the purposes of this study).

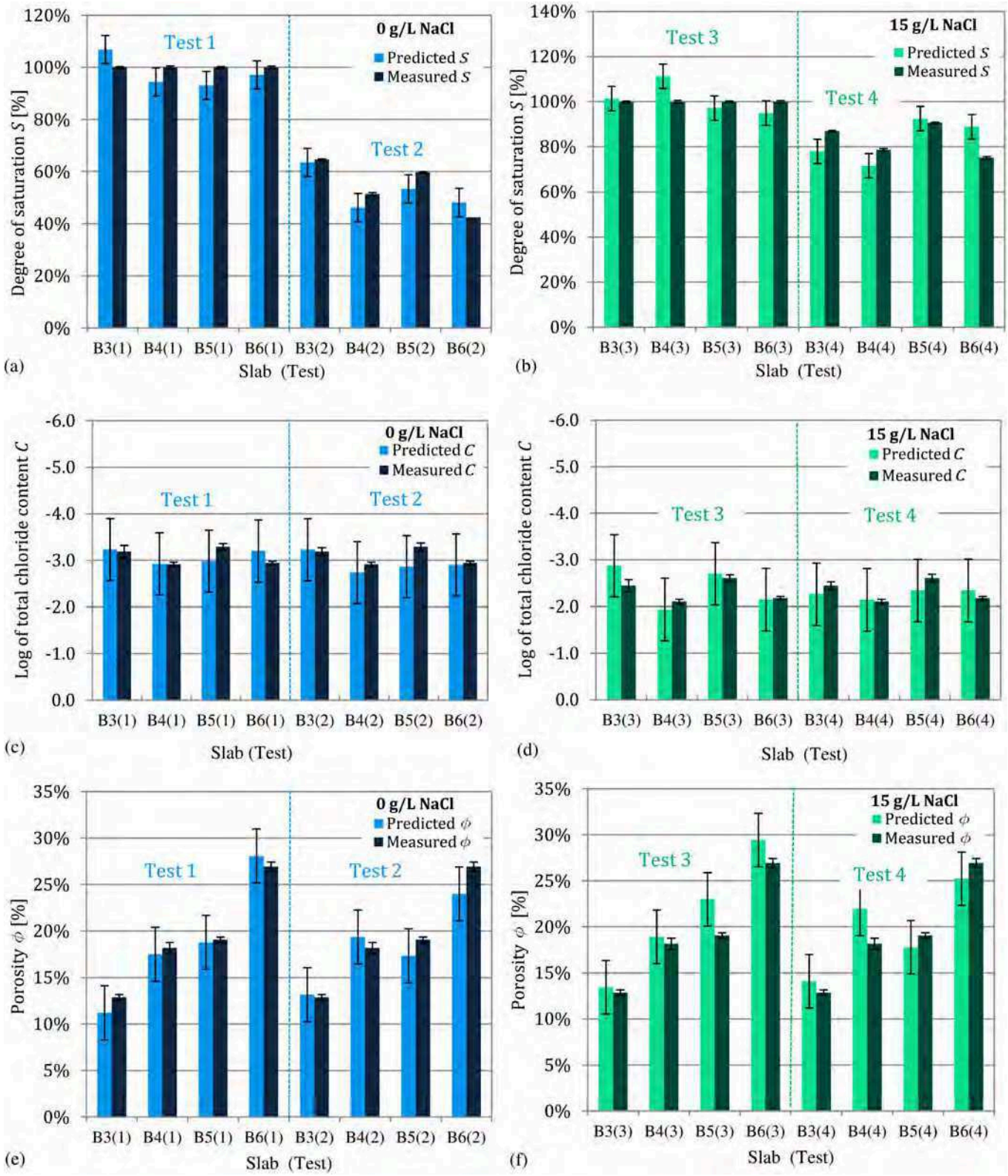

Figure 8.8: Predicted and measured values for (a) degree of saturation at 0 g/L NaCl (Tests 1 and 2) and (b) at 15 g/L NaCl (Tests 3 and 4), (c) the logarithm of total chloride content at 0 g/L NaCl (Tests 1 and 2) and (c) at 15 g/L NaCl (Tests 3 and 4) and (e) porosity at 0 g/L NaCl (Tests 1 and 2) and (f) at 15 g/L NaCl (Tests 3 and 4).

8.3.3.2 Results and discussion

The results for the respective condition parameters are indicated for each slab and each test in Figure 8.8. The *predicted values* refer to the condition parameters as determined from the measured EM observables using the optimisation as described above, while the *measured values* are the values that were directly determined as in Table 8.1. The error bars for the predicted values are the mean squared errors (MSE) for each condition parameter determined during the regression analysis in Chapter 7.4. The error bars for the measured values are commonly accepted standard deviations from literature for saturation and porosity, and the measurement error for the logarithm of chloride content as determined from 3 tests (as in Appendix A.1). When Figure 8.8 is studied it is observed that the results obtained from the optimisation process are quite good, with the predicted values of the condition parameters not far off from the actual measured values.

In order to study the effect of multiple minima on the results an approach similar to Villain et al. [276] was followed. The chloride content of Slab B3 (Test 1) was thus plotted as a function of the regression model of each EM observable, by fixing the degree of saturation or porosity respectively at the measured (actual) values of 100% and 12.9%. To Equations (8.2) to (8.4) were therefore rearranged to obtain Equations (8.15) to (8.17) solving for C:

$$C = \frac{Log(\rho) - (\mathrm{a}_0 + \mathrm{a}_s S + \mathrm{a}_{s_2} S^2 + \mathrm{a}_\phi \phi + \mathrm{a}_{s\phi} S\phi)}{\mathrm{a}_c + \mathrm{a}_{sc} S} \tag{8.15}$$

$$C = \frac{\varepsilon_1' - (\mathrm{b}_0 + \mathrm{b}_s S + \mathrm{b}_\phi \phi + \mathrm{b}_{s\phi} S\phi)}{\mathrm{b}_c + \mathrm{b}_{sc} S + \mathrm{b}_{c\phi} \phi} \tag{8.16}$$

$$C = \frac{\varepsilon_2' - (\mathrm{c}_0 + \mathrm{c}_s S + \mathrm{c}_\phi \phi + \mathrm{c}_{s\phi} S\phi)}{\mathrm{c}_c} \tag{8.17}$$

where $Log(\rho)$, ε_1' and ε_2' are the measured EM observables (thus known) and the coefficients $a_{...}$, $b_{...}$ and $c_{...}$ are as in Table 8.2. S was fixed at 100 % and C was calculated for $\phi = 0.05 : 0.002 : 0.3$ to obtain C as function of porosity. Then ϕ was fixed at 12.9% and C was calculated for $S = 0.2 : 0.002 : 1.2$ to obtain C as function of the degree of saturation.

The same procedure was followed for each EM observable. Results are shown in Figure 8.9(a) and (b) with the greyed areas indicating the regions that fall outside of the ranges as defined for the optimisation of the condition parameters. It can be seen that there is only one solution for the logarithm of chloride content in Figure 8.9(a) at $C = Log(C\ell_t) \approx$ -3 and $\phi \approx 12\%$, corresponding well to the measured values of -3.19 and 12.9%. However, in Figure 8.9(b) it can be seen that there are multiple solutions, but that only one of these falls within the defined ranges for the condition parameters. This solution corresponds to good approximations of $C \approx$ -3 and $S \approx 100\%$.

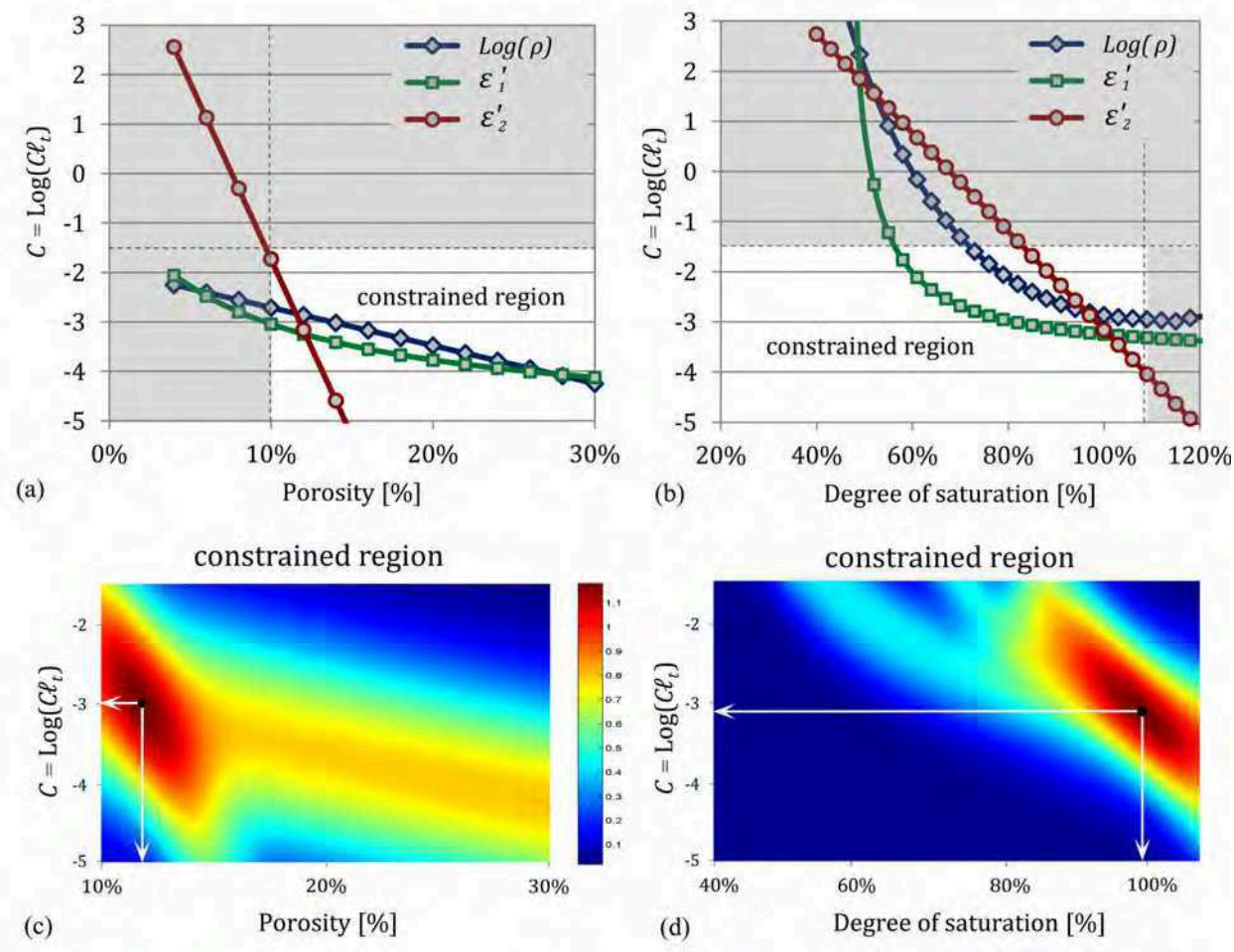

Figure 8.9: Results for Slab B3 showing plotted curves for each EM observable with (a) the degree of saturation fixed at 100% and (b) the porosity fixed at 12.8% and (c) and (d) showing only the constrained regions with the maximums yielded by merging the probability density functions for each EM observable (scale of which is indicated by the colour bar).

The absolute percentage errors of the predicted values relative to the measured values are indicated in Table 8.3 and Figure 8.10. It can be seen that the absolute percentage errors of the condition parameters for the 0 g/L NaCl case (Tests 1 and 2) are good, being less than 15%. However, it seems that the variability is higher for the 15 g/L NaCl case (Tests 3 and 4) with the absolute percentage errors being only less that 20%. It is suggested that the reason for this decrease in reliability with increase in chloride content may be the fact that the chloride content is the condition parameter to which $Log(\rho)$ and ε'_1 are the least sensitive and to which ε'_2 is not sensitive at all.

The various graphs do not cross exactly at a common point, thus there is a zone were the solution is possible, called the "predition zone" by Sbartaï et al. [234]. In order to estimate more precisely the solutions for the condition parameters, the graphs for each

Table 8.3: Absolute percentage errors of the predicted values for the condition parameters degree of saturation, logarithm of total chloride content and porosity with respect to the measured values.

	Absolute percentage error [%] $\mid pred./meas. - 1 \mid$					
0 g/L	**Test 1**			**Test 2**		
	S	$C = Log(C\ell_t)$	ϕ	S	$C = Log(C\ell_t)$	ϕ
B3	6.9%	1.3%	12.9%	1.7%	1.2%	2.3%
B4	5.6%	0.4%	3.7%	10.1%	6.1%	6.5%
B5	6.9%	9.4%	1.5%	10.6%	13.0%	9.0%
B6	2.8%	8.8%	4.3%	13.4%	1.4%	10.9%
15 g/L	**Test 3**			**Test 4**		
	S	$C = Log(C\ell_t)$	ϕ	S	$C = Log(C\ell_t)$	ϕ
B3	1.4%	17.5%	4.5%	10.4%	7.5%	9.5%
B4	11.3%	7.9%	4.1%	9.0%	2.0%	20.8%
B5	2.8%	3.5%	20.6%	2.0%	10.1%	6.6%
B6	5.0%	1.3%	9.3%	18.3%	7.8%	6.3%

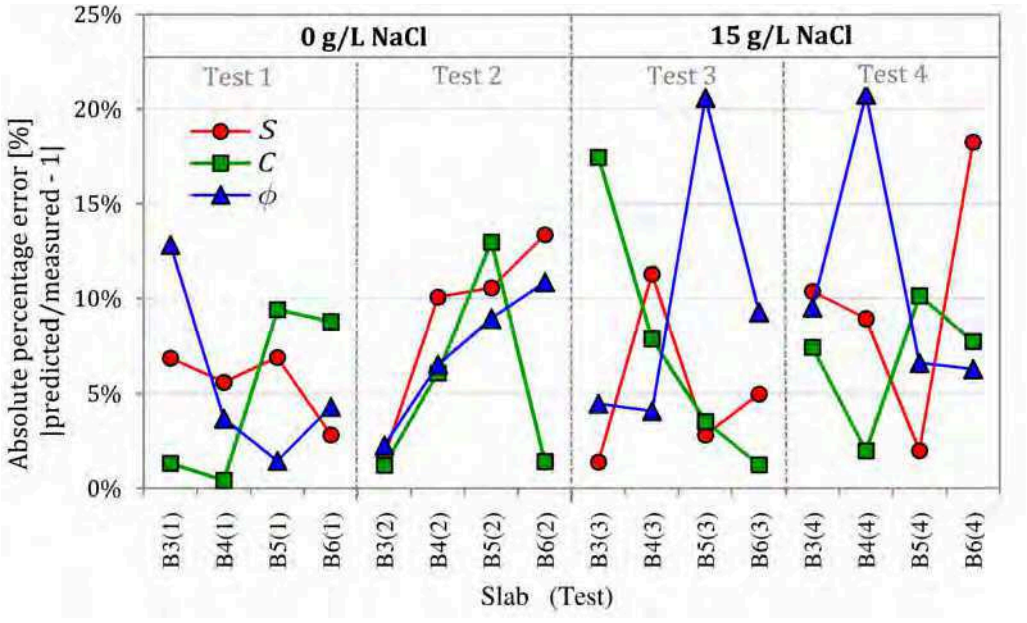

Figure 8.10: Plot of absolute percentage errors of the predicted values for the condition parameters degree of saturation, logarithm of total chloride content and porosity with respect to the measured values.

Figure were merged in Matlab® to obtain a maximum as per Figure 8.9(c) and (d). This was accomplished by first fitting a relationship to the curves in Figures 8.9 (a) and (b) and then assigning a normal distribution to each of the fitted functions with a standard deviation equal to the MSE of porosity and degree of saturation respectively. The obtained probability density function for each curve were then summed together using a three dimensional mesh grid to obtain the final fused graphs. A more precise value could thus be determined for the respective condition parameters. This procedure is especially useful if some *a priori* information is available, for instance one of the condition parameters, or if many NDT observables are used [234] [235] resulting in a large prediction zone.

8.3.4 Practical application of the combination of EM techniques

The non-destructive characterisation of concrete in terms of saturation, chloride content and porosity as presented above, is very relevant in terms of the health monitoring of existing concrete infrastructure (refer to Chapter 2.3.6.2) where regular testing is required over time. Non-destructive testing allows for much faster and cheaper testing when results are required on a regular basis and avoids the damage incurred by the cores required for destructive testing.

In practice, when non-destructive testing is employed for the health monitoring of mature concrete, it is feasible to determine porosity (and diffusivity) once off by means of the standard destructive test methods. It can then be assumed that these parameters related to concrete microstructure will remain unchanged and that the variation in the EM observables over time will be due to the variation in degree of saturation and chloride content. Assuming this, the reliability of the solution of the non-linear system presented in Section 8.3.3 can be improved by including the known *a priori* information e.g. porosity in this case.

Another application of non-destructive testing is that of quality control of newly constructed structures described in Chapter 2.3.6. This is highly relevant in terms of a performance based approach to concrete durability which has been widely adopted for concrete works in recent times. Resistivity is often used as indirect durability indicator for this purpose [7] [42], but because the characteristic resistivity is required (i.e. the saturated resistivity) concrete cores are usually extracted from the structures and then saturated and tested in a laboratory environment. Direct surface resistivity measurements on the structure are thus not used to determine the characteristic resistivity as in situ concrete is rarely at a saturated state. Here the combination of non-destructive EM techniques to estimate the state of in situ concrete can be very advantageous. For new concrete, it can be assumed that there is no chloride contamination and that the actual total chloride content is fixed

Table 8.4: Predicted characteristic (saturated) resistivity values (logarithm of resistivity $Log(\rho'_p)$ and corresponding resistivity ρ'_p) and corresponding measured characteristic values (logarithm of resistivity $Log(\rho')$ and corresponding resistivity ρ') for the purposes of quality control at saturated uncontaminated conditions.

Slab	Predicted values		Measured values		% error
	$Log(\rho'_p)$	ρ'_p [Ω.m]	$Log(\rho')$	ρ' [Ω.m]	$\mid (\rho'_p - \rho')/\rho' \mid$
B3	2.06	115.66	2.01	102.81	12.50%
B4	1.52	33.35	1.50	31.73	5.10%
B5	1.68	47.93	1.76	57.59	16.77%
B6	1.42	26.11	1.40	24.84	5.12%

at trace amounts. As the degree of saturation and porosity can be estimated quite reliably by the solution of the system of equations as presented in Section 8.3.3.2, the characteristic (saturated) resistivity required for quality control can then be back-calculated using the regression model developed for $Log(\rho)$.

This approach was followed to estimate the characteristic resistivity of Slabs B3, B4, B5 and B6 from the predicted results obtained for the unsaturated, uncontaminated case (Test 2). The porosity and chloride content (corresponding to that of uncontaminated concrete) were therefore known and were plugged into Equation (8.2) together with $S = 1$ to estimate the characteristic resistivity. Results for the predicted resistivities and the measured resistivities for the saturated, uncontaminated state (Test 1) are shown in Table 8.4. The predicted characteristic resistivity ρ'_p differs from the measured resistivity ρ' with a percentage error of less than 20%. The results are regarded as quite good when it is taken into account that the percentage error is in the same range as the reported coefficient of variation for surface resistivity measurements.

8.4 Conclusion

The experimental work presented in this chapter focussed on the use of in situ techniques to characterise concrete in different homogeneous states. Results for the respective EM observables obtained on slabs at four conditionings compared well with those of the cell measurements in the previous chapter. These results were combined to estimate the condition parameters (degree of saturation, chloride content and porosity) of the slabs for the different states. This was achieved by solving the non-linear system of equations developed in Chapter 7.4.2, using an iterative numerical optimisation procedure.

The condition parameters were estimated quite well for the water contaminated states (less than 15% percentage error), and somewhat less well for the chloride contaminated states (less than 20%). It is suggested that the inclusion of a fourth technique, which is sensitive to chloride content, as discussed in Chapter 7.4.2.4, can improve the results and also allow for the estimation of diffusivity as condition parameter. The combination of the regression models when no *a priori* information is available therefore delivers acceptable results for measurements in a controlled laboratory environment. As some information is often available regarding the investigated medium in practice, it would be possible to improve the reliability with which the condition parameters are estimated for in situ concrete, where the variability of the concrete is usually higher.

The combination of EM techniques by solving of a system of equations as presented in this chapter has several applications in practice, such as the health monitoring of existing structures or as part of a performance based approached for quality control of newly built structures. However, much work is still needed to improve the numerical optimisation procedure and treatment of cumulative errors, which is especially significant for the analysis of in situ measurements.

Chapter 9

Collaborative experimental work

9.1 Introduction

In this chapter supplementary experimental work is presented that was performed in collaboration with various institutions as part of the thesis. Three experimental campaigns were undertaken in parallel with the main experimental work presented in the previous three chapters:

1. In collaboration with *University College Dublin* (UCD), Ireland: A study on the influence of mineral admixtures and hydration on concrete resistivity and chloride diffusivity;
2. In collaboration with *CETE de l'Ouest, Saint-Brieuc, France*: A study of the ingress of chloride contaminated solutions into concrete using in situ EM techniques;
3. In collaboration with UCD and the *Cork Institute of Technology* (CIT), Ireland: The characterisation of a 100 year old concrete bridge using in situ EM techniques.

The first study is discussed in short in Section 9.2, while the second and third are addressed by the inclusion of two articles preceded by a short introduction. These studies were complimentary to the main experimental work presented in the previous chapters, as they addressed issues related to the EM non-destructive evaluation that were only briefly mentioned in the previous chapters. The first study investigates the influence of ground granulated blastfurnace slag, a mineral admixture, on the properties of concrete. The resistivity and chloride diffusivity of the concrete were studied over time, also creating the opportunity to study the relationship between these two parameters.

The second study focussed in the investigation of property gradient in concrete, which is an important aspect that has not been addressed in the previous chapters where only homogeneous specimens were used. All the in situ EM techniques discussed in Chapter 4 were employed and their capability to identify the ingress of saline solutions into concrete was evaluated. Lastly, a study is presented where the in situ techniques were used to assess the condition of elements from a bridge that had been exposed to severe conditions. Although the techniques were not combined as proposed in Chapter 8, the correlation between the EM observables were studied in order to assess the concrete qualitatively. This is also a form of combination that is commonly implemented in practice [50].

9.2 Study on the influence of mineral admixtures and hydration on concrete resistivity and chloride diffusion coefficient

9.2.1 Objectives

In this section a collaborative study that was undertaken in partnership with University College Dublin (UCD), Ireland is presented. This study, conducted on young concrete, was partially focussed on the development and testing of the resistivity measurement equipment as discussed in Chapter 6, but also aimed to investigate certain aspects that were not addressed during the parametric study in Chapter 7.

Firstly, the test campaign aimed to investigate the dependency of the resistivity on the type of cement used and the degree of hydration thereof. Several studies [117] [126] [45] indicate that resistivity is sensitive to mineral admixtures such as ground granulated blastfurnace slag (GGBS), fly-ash and silica fume due the changes they cause in the microstructure and the properties of the pore solution of concrete. Resistivity has been suggested as an indirect measure of hydration rate by some authors [191] [130] and was thus also used in this study to assess the evolution of the pore structure over time for early age concrete.

In conjunction with resistivity, the effect of the admixtures and hydration on chloride diffusivity was studied. As a result, the relationship between resistivity and chloride diffusion coefficient could be investigated in more depth than was possible during the parametric study in Chapter 7.2.

The opportunity was also used to compare the relationship between resistivity and diffusivity obtained in the parametric study to that for concrete of a vastly different nature in terms of constituents. It could therefore be assessed whether chloride diffusivity could serve as a

Figure 9.1: Testing of Mix D1, D2 and D3 with the resistivity cell (cores) and the surface resistivity probe (slabs).

parameter indicative of concrete quality (as suggested in Chapter 7.2.3) for a wide range of concrete compositions, states of hydration and origins of the constituents.

9.2.2 Mix design and testing

The three mixes that were studied are listed in Table 5.2 as part of the introduction to Part 2 of this document. They contained different quantities of ground granulated blast furnace slag (GGBS) partly substituting the ordinary Portland cement (OPC) as binder (the term *binder* is used here rather than *cement* to indicate that a blend was used). Mix D1 contained no GGBS (0% OPC replacement), in Mix D2 50% of the OPC was replaced by GGBS and in Mix D3 70%. All other constituents were identical for the three mixes, allowing for the influence of only the GGBS to be studied. It was expected that the GGBS would alter the concrete microstructure and the properties of the pore solution [47], which would be reflected by the resistivity response, diffusion coefficient and hydration rate.

After casting, the concrete specimens were kept in a saturated state at 20°C and only removed from the water for testing. Testing was conducted on a monthly basis over a period of six months to determine the resistivity of each mix. The resistivity was determined

on both slabs and witness cores using the multi-ring resistivity cell and the multi-electrode surface probe as in Figure 9.1. Measurements were taken on three cores per mix between each ring electrode of the resistivity cell, taking two measurements by turning the cores upside down. Three 26-measurement sequences were run on the slabs for each test time. The probe was placed approximately in the middle of the slab and was moved slightly between each sequence. After measurement the geometric factors as determined in Chapter 6, Sections 6.2.3 and 6.3.3 were applied to calculate the apparent resistivity of each measurement point. The specimens were regarded as homogeneous, as discussed in Chapter 6.4.3.1 and it could thus be said the the calculated apparent resistivities approximated the true resistivity of each specimen. The final resistivity of each mix for each test time was thus determined by averaging all the results from the resistivity cell and probe.

The chloride diffusion coefficients for each of the concrete mixes had been previously determined as part of another PhD project [37] on the a different set of specimens for the same time intervals. Three core specimens were tested per mix of which the top and bottom 20 mm were trimmed to remove the more variable surface concrete. The diffusion coefficients were determined according to the Nord Test 492 [6], a the rapid chloride migration test that was also used in the parametric study (included in Appendix A.2). Unfortunately the porosity of the specimens could only be determined after the completion of the testing at an age of six months and not during the course of the experimentation.

9.2.3 Results and discussion

9.2.3.1 Effect of GGBS and time on resistivity and chloride diffusivity

Average results for resistivity and chloride diffusivity over time are shown in Figures 9.2(a) and (b). Note that the logarithm is not used here in order to compare the change over time between the mixes more easily. Both the resistivity and chloride diffusion coefficient are time dependent. The change over time can be linked to the hydration and the densification of the concrete microstructure leading to a subsequent increase in resistivity and decrease in diffusivity. The change is much more rapid in the first weeks after casting and tends to stabilise towards the end of the six month (24 week) testing period as the hydration slows down. This corresponds to the general trends reported for early age concrete in literature [181].

There is a marked difference between the results for the respective mixes. Mix D1 containing no GGBS has a significantly lower resistivity and higher diffusion coefficient than Mixes D2 and D3. These observations correspond to the known influence of GGBS on concrete density

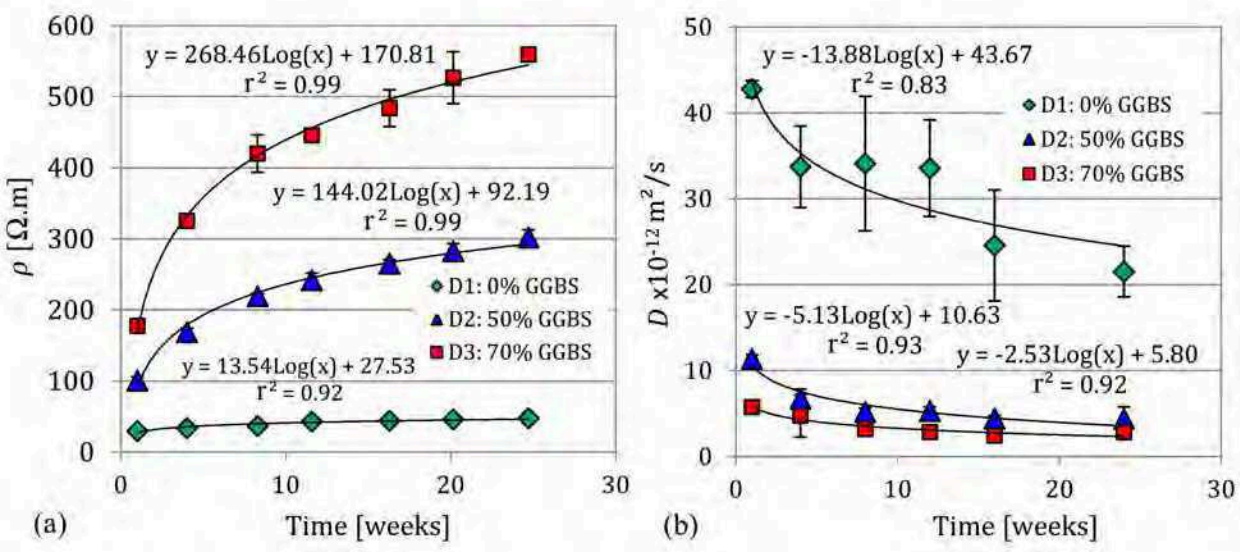

Figure 9.2: Average results for (a) the resistivity and (b) the chloride diffusivity for Mix D1 containing no GGBS, Mix D2 with 50% GGBS and Mix D3 with 70% GGBS tested monthly over a period of 24 weeks at a saturated state.

and hydration rate as explained in Chapter 2.2.2. The proportional change of the resistivity for Mix D1 over time, as represented by the slope of the logarithm of the fitted curves in Figure 9.2(a), is lower than that of the other two mixes implying that hydration took place more slowly in the OPC concrete than in concretes containing slag. This is interesting, as it is normally assumed that GGBS initially retards the setting process [280]. However, it is also reported that the refinement of the concrete pores due to the presence of GGBS may start as early as a few days after casting [47]. This would explain the higher proportional change in resistivity for the mixes containing GGBS where hydration continues long after that of OPC concretes. After a six month period the hydration of the OPC mix had therefore been completed, while the hydration for the GGBS mixes was still continuing.

Results for the diffusion coefficient in Figure 9.2(b) show the same trends in the inverse direction to that of resistivity. These results are considerably more variable than the resistivity results, especially for the OPC mix. Unfortunately the reason for this is hard to judge as the diffusion coefficients were determined outside of this study.

9.2.3.2 Relationship between resistivity and chloride diffusion coefficient

The results for the logarithms of resistivity and diffusivity of the saturated specimens are plotted against one another in Figure 9.3. It was anticipated that there would be a linear relationship for each of the respective mixes between the two properties, because the chloride diffusion coefficient was determined by migration (refer to Chapter 2.3.4.4), i.e. diffusion

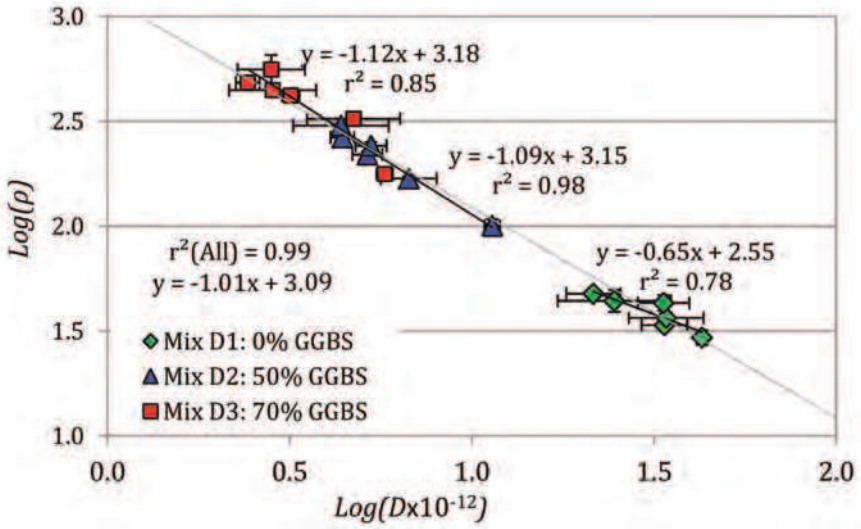

Figure 9.3: Results from Mix D1 containing no GGBS, Mix D2 with 50% GGBS and Mix D3 with 70% GGBS for the logarithm of resistivity against the logarithm of chloride diffusion coefficient.

accelerated by an electrical current. It is therefore logical that the results for chloride diffusivity would inherently be related to the electrical resistivity of the concrete as implied by Nersnt-Einstein Equation (2.36). When the relationship between resistivity and diffusivity for the respective mixes is studied in Figure 9.3, the linear relationships for the respective mixes are not so evident due to the high variability of the results for diffusivity. However, they can still clearly be observed.

It was anticipated that there would be a difference in the slope and intercept of fitted lines of the different mixes due to a reduction in the ion content of the pore solution caused by the presence of GGBS [47]. This was expected because of the dependency of resistivity on the properties of the pore solution existing in the specimens [33] [43], while the rapid chloride migration test is not [43]. However, it is clear from Figure 9.3 that the relationship between resistivity and diffusivity is not significantly sensitive to the difference in GGBS content between the three mixes. The slopes of Mix D2 and D3 are almost identical (-1.09 and -1.12), whilst the difference in slope of Mix D1 (-0.65) is probably due to the variability of the results as it clear from Figure 9.2. This is demonstrated by the strong overall linear correlation between the mixes with the combined coefficient of determination being 0.99 as in Figure 9.3. It is thus suggested that the alteration of the pore solution due to the presence of GGBS is completely overshadowed by the change in pore structure caused by its presence. It is concluded that the relationship between resistivity and the chloride diffusion coefficient (determined by migration) is not significantly affected by mineral admixtures such as GGBS.

Lastly, the results were compared to those obtained in the parametric study in Chapter 7 to see if the relationship is comparable between two completely different mix sets. The mixes for the experimental work conducted during this study is referred to as *Mix Set 2* and those for the parametric study as *Mix Set 1* as introduced in Chapter 5. Figure 9.4(a) shows results for both campaigns at a saturated state. It was concluded in the parametric study in Chapter 7.2 that resistivity is dependent on porosity at high saturations and on diffusivity at low saturations. Though this hypothesis could not be rigorously explored during this study, some interesting deductions can nonetheless be made.

Results for Mix Set 2 and Mix Set 1 are shown in Figure 9.4(a) for saturated conditions. As the results for both mix sets are at saturated conditions, it could well be asked why the Mix Set 2 shows a strong linear relationship between Log(ρ) and Log(D) and Mix Set 1 does not. It is suggested that the discrepancy between the results of the two studies can be linked to difference in water/binder (W/B)-ratio (and thus porosity) of the respective mixes which is constant for Mix Set 2 (W/B ≈ 0.56, $\phi_{6mths} \approx 15\%$), but varies significantly for Mix Set 1 as per Table 7.3.

It was stated in Chapter 2.3.6.1 [43] that the Nernst-Einstein Equation (2.36) can be used to express the relationship between the characteristic (saturated) resistivity and the *effective* diffusion coefficient (Equation (2.42) repeated here for convenience):

$$D_{eff} = \frac{\mathcal{B}}{\rho'} \tag{9.1}$$

where D_{eff} [$\times 10^{-12}$m^2/s] is the effective diffusion coefficient, ρ' [Ω.m] is the characteristic resistivity and $\mathcal{B}$ [$\times 10^{-12}$ $\Omega.m^3/s$] is a factor which is dependent on the ionic strength of the pore solution, which is in turn significantly dependent on the W/B-ratio of the concrete [43].

The lower the W/B-ratio, the higher the reported values for $\mathcal{B}$ [43]. Though the diffusion coefficient used in this study is the *apparent* diffusion coefficient instead of the *effective* diffusion coefficient, a similar dependency on W/B-ratio for the slopes of the fitted lines in Figure 9.4(a) is assumed. In that case, if the results for Mix Set 1 and Mix Set 2 are normalised with respect to their W/B-ratios of approximately 0.36 (B4 and B5), 0.68 (B4 and B6) and 0.56 (D1-D3), they will shift in the directions as indicated by the arrows in Figure 9.4(a). This is demonstrated in Figure 9.4(b) where the ratio $\frac{Log(\rho)}{W/B}$ is plotted against the logarithm of the diffusion coefficient. The agreement between the mix sets is considerably improved as a result. If it is considered that the W/B-ratio largely determines the porosity of hardened cement paste [47], the conclusion that resistivity is highly dependent on porosity at saturated conditions reached in Chapter 7.2, corresponds to the findings here and to the reported dependency of $\mathcal{B}$ on W/B-ratio by Baroghel-Bouny et al. [43].

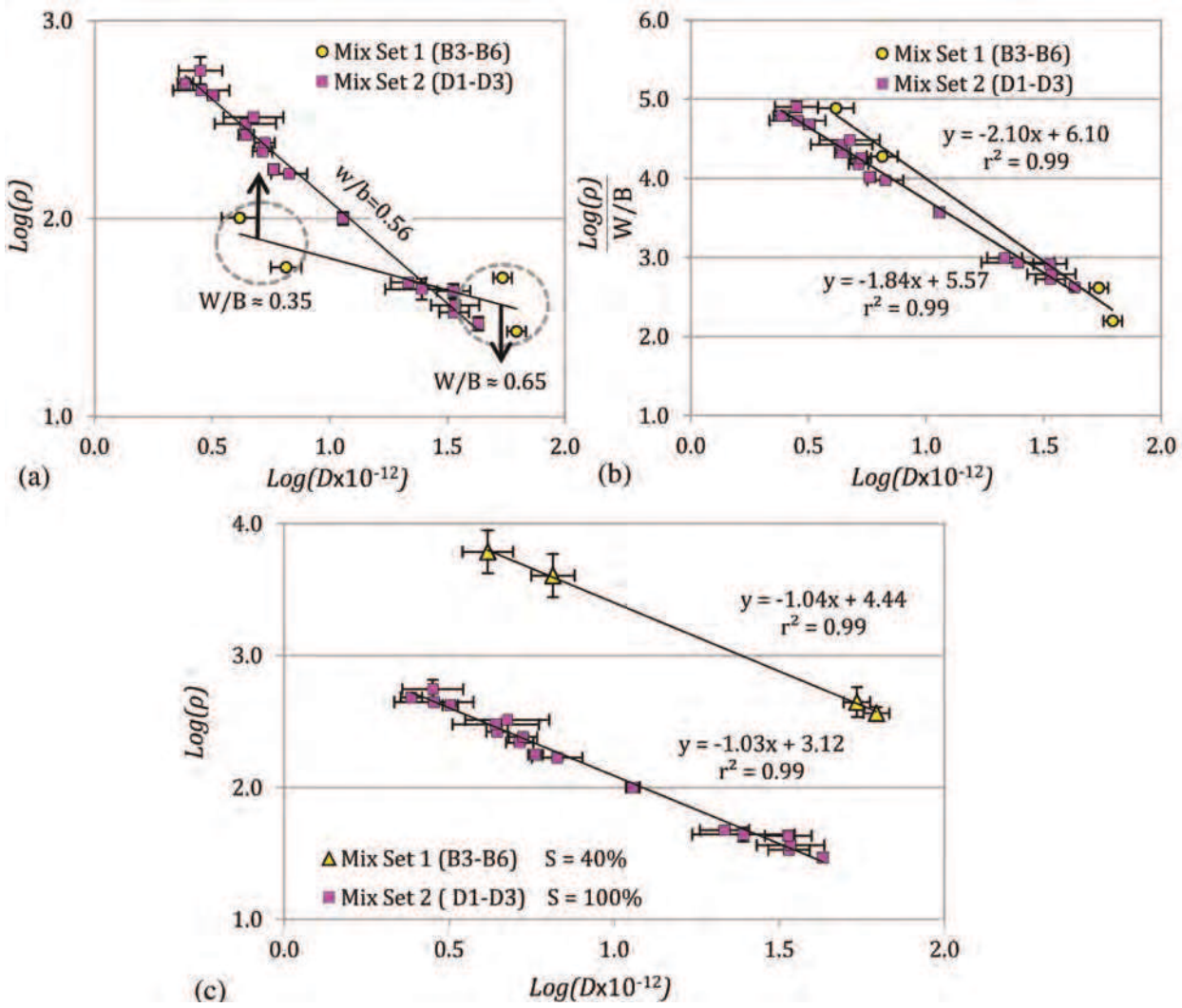

Figure 9.4: Results for Mix Sets 1 and 2 for (a) the logarithm of resistivity against the logarithm of chloride diffusion coefficient (b) the same results normalised for W/B-ratio and (c) Mix Set 2 at 100% saturation and Mix Set 1 at 40 % saturation.

In Figure 9.4(c) the unsaturated condition of Mix Set 1 ($S = 40\%$) from the parametric study as per Figure 7.9 is compared to Mix 2 at saturated conditions ($S = 100\%$). The results are quite interesting as Mix Set 1 displays a slope (-1.04) that is almost identical to that of Mix Set 2 (-1.03). It is suggested that the shift between the two Mix Sets is only due to the difference in degree of saturation. This confirms earlier conclusions in Chapter 7.2.6.1 that the relationship between resistivity and diffusivity is not significantly dependent on the porosity at lower saturations. This is an interesting finding as resistivity at *saturated* conditions is almost always used in literature to estimate diffusion characteristics indirectly (in spite of the known influence of W/B-ratio and porosity on the relationship).

9.2.4 Summary

It is confirmed that resistivity at the saturated state is very sensitive to the changes in the pore structure of early age concrete and that this enables the effects of the type of cement used to be studied indirectly. It was also found that the changes caused by the amount of GGBS and hydration to the pore solution are not significant enough to influence the relationship between resistivity and the apparent chloride diffusion coefficient. The diffusion coefficient is therefore a good parameter to include in the Combined EM Approach as presented in Chapter 7.4.2.4 as is represents several aspects related to the quality of the concrete, i.e. interconnectedness of the pores, type of cement and degree of hydration.

However, although resistivity is almost exclusively related to the diffusion properties of the concrete at conditions of low saturation, it was reasserted that resistivity at saturated conditions is also influenced by the W/B-ratio and thus the porosity of the concrete. The findings from Chapter 7.2 suggesting that it is better to include both porosity and diffusivity in the regression model for resistivity in order to represent the durability of the concrete over a wide saturation range, is therefore confirmed.

. . . . . .

9.3 Study of the ingress of chloride contaminated solutions into concrete using in situ EM techniques

An important aspect of the non-destructive EM techniques used as part of this thesis is that they have the potential to detect property gradients that are present in the investigated material. In this section a study was performed to compare the ability of EM in situ techniques (electrical resistivity tomography, capacimetry and ground penetrating radar) to monitor the ingress of water and chloride into concrete. The study was conducted in collaboration with *CETE de l'Ouest, Ouvrages d'art et maritimes, Saint-Brieuc, France* who was responsible for the casting and conditioning of the concrete, destructive testing and fixed-offset radar measurements. The subsequent article that is currently under review for publication in *Materials and Structures* is presented in this section.

ELECTROMAGNETIC NON-DESTRUCTIVE EVALUATION TECHNIQUES FOR THE MONITORING OF WATER AND CHLORIDE INGRESS INTO CONCRETE: A COMPARATIVE STUDY

R. du Plooy[1], G. Villain[1], S. Palma Lopes[1], A. Ihamouten[2], X. Dérobert[1], B. Thauvin[3]

[1]*LUNAM Université, IFSTTAR, MACS, F*-44340, *Bouguenais, France*
[2]*CETE de l'Ouest, DLRCA, Méthodes Physique Advancées, ERA*17, *Angers, France*
[3]*CETE de l'Ouest, Ouvrages d'Art et Maritimes, Saint-Brieuc, France*

9.3.1 Abstract

One of the main causes of the deterioration in reinforced concrete structures is damage resulting from steel corrosion. During the service life of the structure, aggressive agents, particularly chlorides, are transported through the protective cover concrete layer. Once the reinforcement is reached, the steel is depassivated and corrosion propagation and loss of structural capacity follow. Non-destructive electromagnetic evaluation techniques can be used to assess concrete condition. This paper demonstrates the potential of these methods to monitor the ingress of water and chlorides into cover concrete. The electromagnetic parameters that are studied here are electrical resistivity and dielectric permittivity, material properties that are both sensitive to volumetric water content and chloride content. Results from an experimental study conducted on concrete slabs in a controlled laboratory environment are presented and the capacity of three in-situ electromagnetic techniques to assess the ingress of electrolytes and discern between their salinity is compared.

KEYWORDS: *non-destructive testing, resistivity, permittivity, water and chloride content*

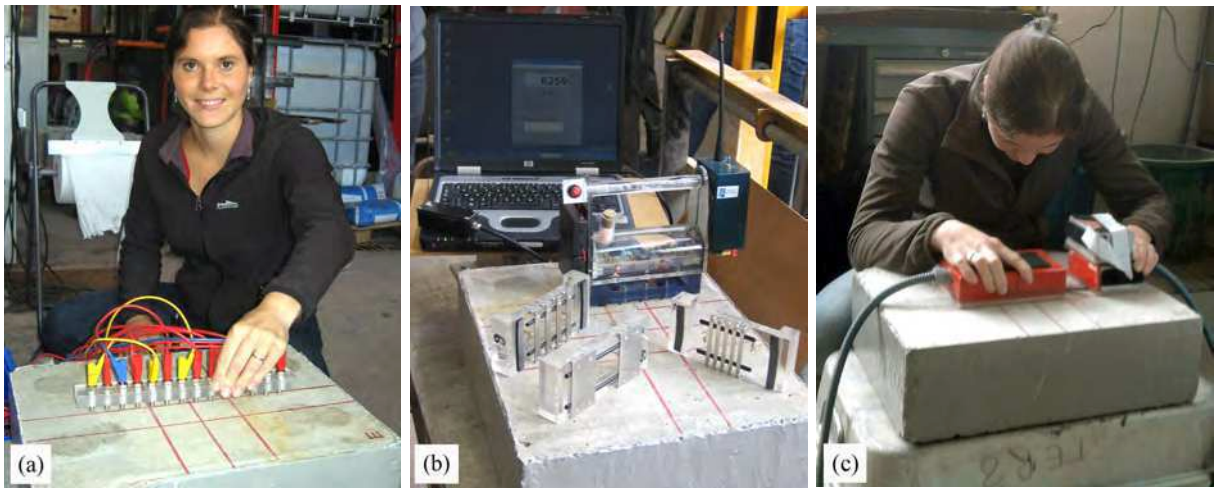

Figure 9.5: EM non-destructive testing techniques used to assess gradients in concrete, with (a) the multi-electrode resistivity probe, (b) the capacitive probe and (c) the ground penetrating radar (GPR) here in the (WARR) configuration (Method 2).

Figure 9.6: Conditioning of concrete slabs and witness cores (for gammadensimetry) for Slabs 1 (0 g/L NaCl), 2 (15 g/L NaCl) and 3 (30 g/L NaCl) , temp. 20°C and RH 80%.

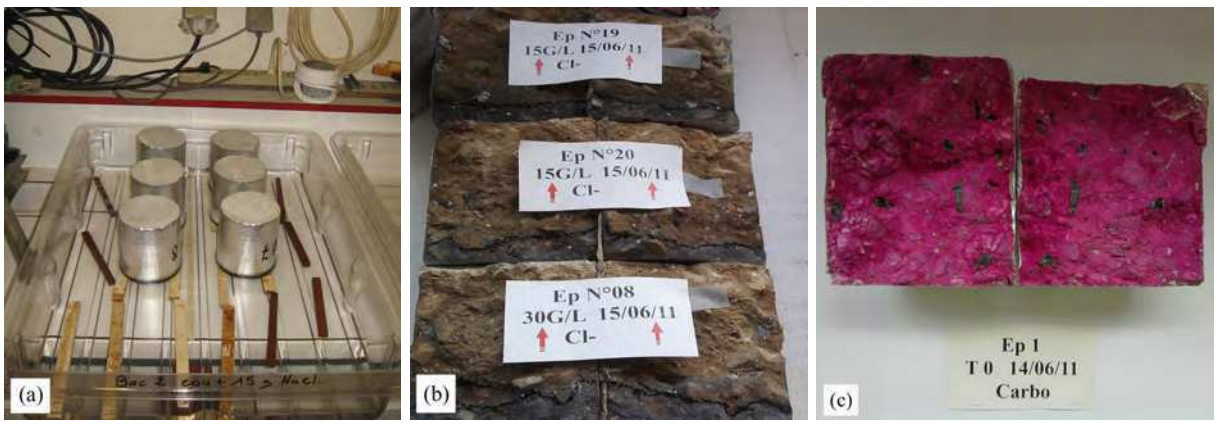

Figure 9.7: Destructive testing of witness cores with (a) conditioning for chloride ingress, (b) cloride ingress by means of $AgNO_3$ and (c) carbonisation by means of phenolphthalein.

9.3.2 Introduction

The principal cause of deterioration in reinforced concrete bridge structures is damage resulting from steel corrosion [7] [192] [224] [42]. The corrosion process is usually divided into two stages, namely initiation and propagation [265]. During the corrosion initiation stage aggressive agents, particularly chlorides, are transported through the protective cover concrete layer by means of various mechanisms such as diffusion, permeation, sorption and migration [206] [151]. The corrosion propagation stage commences when these aggressive agents have reached the reinforcement and caused the depassivation of the steel. This leads to an electrochemical oxidation reaction that reduces the area of the reinforcing and yields products of increased molecular volume, causing the weakening of the steel and spalling of the concrete. The presence of chlorides is linked to a particularly aggressive form of corrosion known as pitting corrosion [102]. The severity of the pitting increases logarithmically with an increase in the concentration of chlorides present in the pore solution [157].

Non-destructive electromagnetic evaluation techniques are sensitive to the presence of water and chlorides in concrete [191] [87] and have many advantages when compared to conventional destructive testing techniques as they are easier, quicker and cheaper to perform and do not damage the structure [178]. These techniques can therefore be used for continuous health monitoring of concrete structures in order to identify problem areas and enable remedial actions to be taken before the corrosion propagation stage commences and damage is incurred.

The focus of this paper is to evaluate cover concrete condition in terms of water and chloride content during the corrosion initiation stage using electromagnetic (EM) evaluation techniques. The three in situ electromagnetic techniques as part of the work presented here are Electrical Resistivity Tomography (ERT), Capacimetry and Ground Penetrating radar (GPR). The respective electromagnetic observables obtained from these techniques are direct current (DC) resistivity, low frequency relative permittivity and high frequency relative permittivity. These are material properties that are sensitive to chloride and volumetric water content to various extents. The EM observables can also be related to concrete durability indicators [264] [276] as the presence of water and chlorides is highly dependent on the porosity of the concrete.

The various EM techniques are capable of obtaining the electromagnetic properties of concrete over depth. An experimental study was conducted during which water and chloride ingress into unreinforced concrete was investigated and the results from the respective techniques are presented in this paper.

9.3.3 Electromagnetic properties and their sensitivity to water and chloride content[1]

9.3.3.1 Direct current (DC) electrical resistivity

In this section the theoretical background of electrical resistivity (refer to Chapter 4.2.1.1) and the sensitivity of resistivity to concrete condition (refer to Chapter 3.4) are discussed. Electrical resistivity tomography (ERT) is also presented as in situ technique for the purposes of this study for which can be referred to Chapters 4.2.2.2 (inversion of apparent resistivity) and 6.3.1 (developement of the multi-electrode resistivity probe).

9.3.3.2 Relative permittivity

In this section the theoretical background of dielectric permittivity (refer to Chapter 3.2.3) and the its sensitivity to concrete condition (refer to Chapter 3.4) are discussed. The EM in situ techniques related to permittivity used as part of the study are also presented being capacimetry (refer to Chapter 4.3.2.1), fixed off-set ground penetrating radar (GPR) and multi-offset GPR (refer to Chapter 4.3.2.2).

9.3.4 Experimental Program

An experimental study was undertaken to investigate the ingress of water and chloride into concrete through capillary action. The experimental protocol was inspired by a study of Ihamouten [132], where a hydrical characterization of a wide range of concrete was conducted. Subsequently, electromagnetic observables of the concrete were monitored with the non-destructive electromagnetic evaluation techniques suitable for in situ application as described in the previous section. The main aim of the study was to compare the ability of the respective methods to detect the ingress of electrolytes into concrete, as well as to discern between electrolytes of different chloride contents. Various semi-destructive and destructive tests were also performed for comparative purposes (see Section 9.3.4.1).

[1] *As the principles of electromagnetics and the description of the in situ electromagnetic techniques have already been discussed in this document, it will not be repeated. Reference is therefore made to the appropriate sections as is relevant to this part of the article.*

9.3.4.1 Concrete mix parameters

The mix design used for the experimental program is presented in Table 9.1:

The effective water cement ratio (taking the absorption of the respective aggregates into account) was calculated as 0.58. This relatively high W/C ratio was chosen to enable the rapid ingress of the solutions into the concrete so that monitoring over a relatively short time is required.

Three identical concrete slabs of 450×50×130 mm were cast for the assessment of water and chloride ingress over time (Figure 9.6). Numerous smaller cylindrical specimens were also fabricated as witness cores and for destructive testing. The mix was characterised in terms of durability by means of core tests as in Table 9.2.

The slabs were cured for 28 days and then dried for two months at 60°C and one month at 85°C until a constant mass was reached. Each slab was then partially submerged up to 20

Table 9.1: Mix design as used for the experimental program.

Constituents	Origin	Dry Weight [kg/m3]	Coefficient of Absorption [%]
Coarse Aggr. (10/20)	Croix Gibat	621	1.0%
Coarse Aggr. (6.3/16)	Croix Gibat	425	1.6%
Sand (0/4)	Fréhel	567	8.1%
Sand (0/4)	Mauron	332	5.2%
Cement	Lafarge	267	-
(CEMII/A LL 42.5 R)	*(Saint Pierre La Cour)*		
Water		169	-
Admixture	CHRYSO 760 (SPHRE)	1.6	-

Table 9.2: Characterisation of mix in terms of durability.

Durability Indicator as determined by the protocols of AFPC-AFREM [5]	Unit	Symbol	Result	Durability class [42]
Chloride diffusion coefficient	10^{-12} m^2/s	$D_{m(app)}$	25.4	Poor
Characteristic electrical resistivity	Ω.m	ρ_c	54	Poor
Water permeability	$kg/(m^2h^{0.5})$	K_w	2.2	-
Porosity accessible to water	%	ϕ	15.7	Poor
Gas permeability	10^{-18} m^2	K_{gas}	509	Poor

Table 9.3: Table of testing times for non-destructive and destructive investigation techniques.

Test	Time of immersion	Non-destructive testing on slabs				Semi-destructive and destructive testing on witness cores		
	[days]*	Resistivity	Capacimetry	GPR (1) fixed offset	GPR (2) WARR	Gamma-densimetry	Colorimetry	Chloride profiles
T0	0	-	×	×	×	×	-	-
T1	0.1	×	×	×	×	×	×	×
T2	0.3 (0.4)	×	×	×	×	×	×	×
T3	0.9 (1.1)	×	×	×	×	×	×	×
T4	1.1 (1.4)	×	×	×	×	×	×	-
T5	1.6 (2.1)	×	×	×	×	×	×	-
T6	6.2	-	-	-	-	×	×	-
T7	23.2	×	×	-	×	×	-	×

*Time of immersion for semi-destructive and destructive testing in brackets where different.

mm in a solution of different chloride content (Slab 1: 0 g/L, Slab 2: 15 g/L and Slab 3: 30 g/L NaCl). The corners of the slabs were placed on wooden blocks to enable ingress from the bottom face, whilst their sides were coated with epoxy resin to prevent lateral ingress. The EM properties of the slabs were subsequently tested over a period of three days (T0 to T5) to monitor the ingress of the electrolytes, after 6 days (T6) and finally at 23 days (T7) when the slabs were presumed to be saturated as indicated in Table 9.3. The slabs were kept under controlled conditions of 20°C and relative humidity of 80% for the duration of the experimental program.

The EM techniques were implemented as follows (refer to Figure 9.8) for each concrete slab:

(a) DC-resistivity was determined from multi-electrode measurements at 4 Hz on the wet face of the concrete. A numerically modelled geometric factor was then applied to each measurement point to correct for electrode spacing and boundary effects yielding the apparent resistivities (Chapter 6.3.1). The measured apparent resistivities were inverted using the commercial inversion software package *Res2Dinv* [164] using a "robust" model constraint to optimise the results for sharp transitions.

(b) Dielectric constants were determined at approximately 33 MHz by means of the capacitive method for the small, medium and large plate electrodes and testing was conducted on the wet face of the concrete.

(c) GPR method 1: Fixed offset GPR measurements in reflection mode were used to esti-

mate the ingress depth of the solutions over time (refer to 4.3.2.2). Measurements at a central frequency of 2600 MHz were taken on the dry face of the slabs, assuming that the dry part of the concrete was non-dispersive. The group velocity of the EM wave could be determined for the dry state (T0) as the depth of the reflecting surface (bottom of the slab) was known. The depth of the saturation front was subsequently calculated using the arrival times of the wave reflected from the saturation front and the known velocity for the dry state. The amplitude of the direct wave was also evaluated as a function of time and chloride concentration.

(d) GPR method 2: The GPR WARR configuration (Chapter 4.3.2.2) with a central frequency of 1500 MHz was applied on the dry face of the concrete slabs. This enabled the determination of the dielectric constants of the homogeneous dry ε_{r1} and saturated ε_{r2} states by means of the wave guide inversion procedure [132]. Moreover, that allows the estimation of ingress depth of the solutions over time. The dispersion curves for all the transverse electrical (TE) modes of the propagating wave were then determined by means of the wave field transform f-β of the real observed data. A weighted permittivity calculated from the known values for ε_{r1}, ε_{r2} and a chosen ingress depth h_1 ($h_2 = 130\text{mm} - h_1$) was then assigned to a numerical model to produce synthetic dispersion curves for each mode. By manually optimising h_1 until it matched the dispersion curves obtained for the real data, the ingress depth of the solution for each test time was determined. For more detailed information on this technique refer to [132].

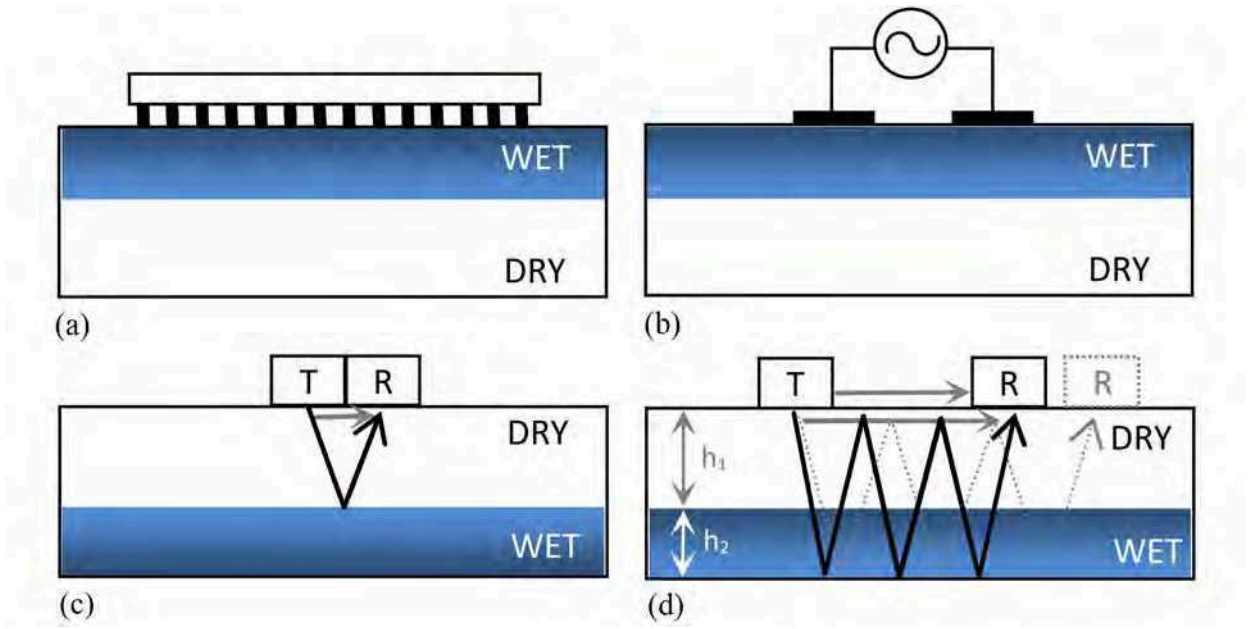

Figure 9.8: Schematic representation of the four EM configurations used to monitor the ingress of the solutions into concrete slabs with (a) representing the ERT method, (b) the capacitive method, (c) GPR Method 1 and (d) GPR Method 2.

Destructive and semi-destructive tests were also performed on witness specimens placed in the respective solutions to verify non-destructive results:

(e) Gammadensimetry was performed to assess the depth of the water ingress front for test times T0 to T7. This method measures the gamma ray absorption of the specimen over height increments of 5 mm and is particularly effective in determining water content relative to the dry or saturated state due to the high gamma-ray absorption coefficient of water. The technique is not sensitive to the presence of chlorides because of the similarity in the absorption coefficients of chloride and those of aggregates and hydrated cement paste. Full details on the technique are available in [278].

(f) Chloride ingress was assessed with colorimetry [42] by spraying silver nitrate on vertically split witness specimens for chloride contaminated solutions for each test time (Figure 9.7(b)).

(g) Chloride concentrations were determined by means of chloride profiling [36] at test times T1, T2, T3 and T7.

A summary of the testing times and the tests that were conducted is presented in Table 9.3.

9.3.4.2 Results and discussion

9.3.4.2.1 DC-Resistivity

Extracts from the tomograms for each slab at test times T1 to T5 and T7 obtained from inversion the *Res2Dinv* software package [164] are presented in Figure 9.9(a). A sharp transition from low resistivity (moisture/chloride contaminated region) to high resistivity (dry region) can be observed for each condition. This transition represents the penetration depth of the respective solutions and moves deeper with time until the slabs reach a homogeneous, saturated condition at T7 (23 days).

Average resistivity values for each depth increment calculated from the inversion results are plotted in Figure 9.9(a). For the slab containing no chlorides (Slab 1) the resistivity for the saturated state was found to be approximately 60 Ω.m (indicated by the dashed line). The depth of the saturation front for Slab 1 at test times T1 to T5 is estimated to be where the respective curves break away from the saturated curve (T7). For Slabs 2 and 3 the depth of the saturation ingress front, for each test time is taken at the point where the respective curves cross the 60 Ω.m-line. The assumed hypothesis is therefore that the water penetrates more quickly than the chloride ions and that a resistivity equal to that of water saturated concrete marks the ingress front even for the chloride contaminated slabs. Following this procedure the rate of ingress in all three slabs are found to be very similar. The depth of

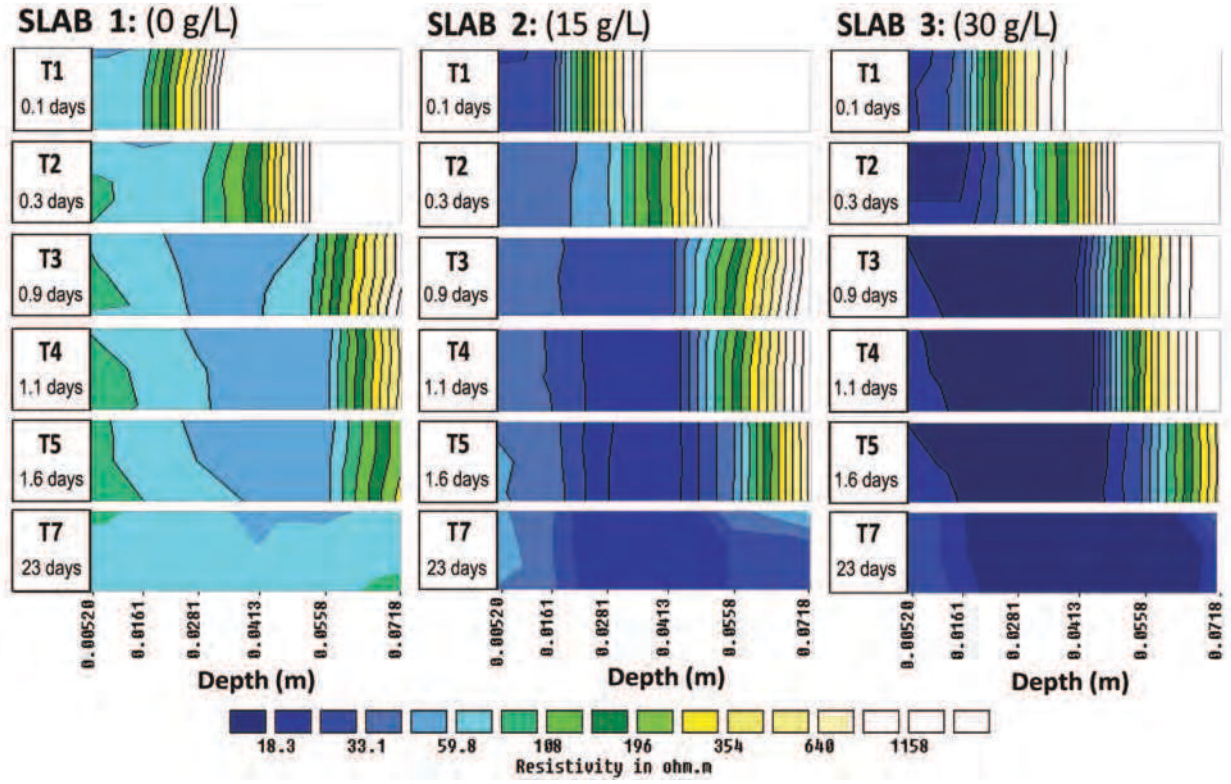

(a)

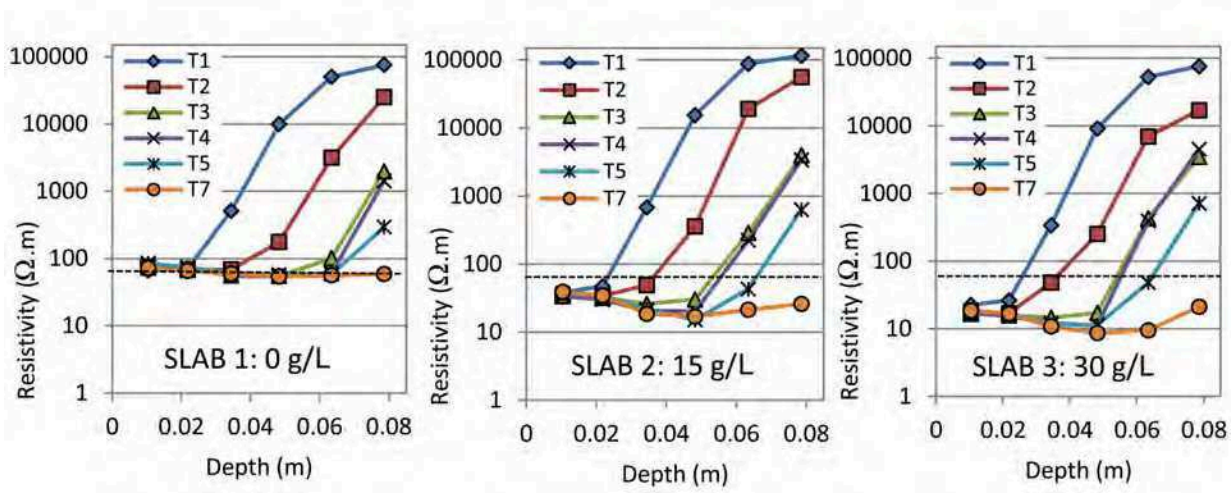

(b)

Figure 9.9: Resistivity inversion results for Slab 1 (0 g/L NaCl), Slab 2 (15 g/L NaCl) and Slab 3 (30 g/L NaCl) from test time T1 to T5 and T7 showing (a) extracts from electrical resistivity tomograms and (b) average horisontal resistivity calculated from ERT over depth.

the ingress front shifts from approximately 20 mm for the initial state at T1 to a completely saturated state at T7.

Curves for the chloride contaminated slabs in Figure 9.9(b) break away more gradually from the final curve at T7 indicating that there is a chloride concentration gradient within the saturated zone behind the ingress front. This is consistent with results from destructive testing presented in Figure 9.13 which will be discussed later.

The average resistivity reached after 23 days varies significantly for the three slabs showing the ability of resistivity to discern between the different chloride concentrations: approximately 60 Ω.m for Slab 1, 26 Ω.m for Slab 2 and 18 Ω.m for Slab 3. The saturated value for Slab 1 compares well with the characteristic resistivity value obtained in Table 9.1 with the percentage error of 11% corresponding to that reported in literature [30].

A limitation of the multi-electrode resistivity technique is that the minimum electrode spacing (20 mm in this case) determines the resolution of the results obtained by the inversion (i.e. the inverted depth increments). Due to the resolution associated with this particular electrode configuration the position of the saturation front can only be determined to approximately the nearest 10mm. The ERT resolution power decreases intrinsically as the distance to the electrodes increases as does the number of data points that are obtained. This causes results to have a higher uncertainty and lower resolution at greater depths.

Additionally, for this specific study the inversion process was challenged by the great contrast in resistivity between the saturated areas and the dry areas where resistivity is essentially infinite. This caused difficulty for the optimisation algorithms to resolve and is possibly the reason why the ingress front measured by the gammadensimetry in Figure 9.13 is considerably steeper than that obtained from the inverted resistivity results in Figure 9.9(a). The shape of the ingress front as obtained by ERT should therefore be regarded with some caution in this particular case.

9.3.4.2.2 Capacitive method

Permittivities calculated by means of the capacitive method for the small, medium and large electrode sets are presented in Figure 9.10(a), (b) and (c). As discussed in Chapter 4.3.2.1, the respective electrodes investigate different volumes of the concrete subsurface. The constant state that is reached when the curves flatten out is representative of a homogeneous, saturated condition having been reached over the subsurface volume for which the sensor is sensitive. Curve flattening occurs later as the influence depth of the electrode sets increases and can therefore be associated with the ingress of the electrolytes. If looked closely, it can be seen that the uncontaminated Slab 1 achieves a constant state more quickly than the

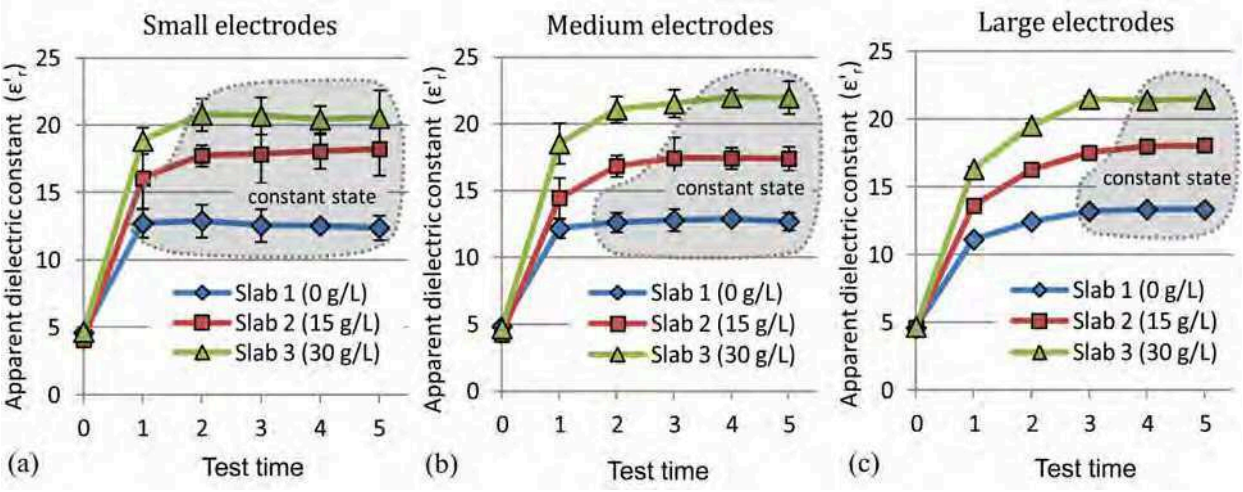

Figure 9.10: Permittivities for each slab (chloride contaminating solution) per test time as determined with the different capacitive electrode sets of sizes (a) small with an influence depth of 9 mm, (b) medium with an influence depth of 20 mm and (c) large with an influence depth of 80 mm.

contaminated slabs. This corresponds to the observation regarding resistivity that there is a chloride gradient behind the saturation front.

The sensitivity of the capacitive method to chloride content can be seen as there is a significant increase in relative permittivity with an increase in chloride content. Values reached for a homogeneous state are approximately 13.3 for Slab 1, 18.1 for Slab 2 and 21.5 for Slab 3. An inversion protocol for this technique is planned for the near future to enable the mapping of permittivity over depth, similar to that for resistivity.

9.3.4.2.3 Ground penetrating radar (GPR)

Method 1:

Extracts from radargrams for the fixed offset GPR configuration in reflection mode (antenna central frequency 2600 MHz) are presented in Figure 9.11(a). As the tests were conducted from the dry side of the concrete slab (refer to Figure 9.8), the direction of ingress is from the bottom up. The wave reflected from the saturation front can be clearly discerned and is indicated with an arrow for each test time.

The ingress rate of the saturation front for the three slabs was found to be similar, supporting results from the resistivity measurements. However, there was a significant difference in the amplitude of the direct wave showing the influence of the salinity of the respective solutions on the wave form as can be seen in Figure 9.11(b). The amplitude of the direct wave also diminished significantly as the ingress progressed and the chloride content increased.

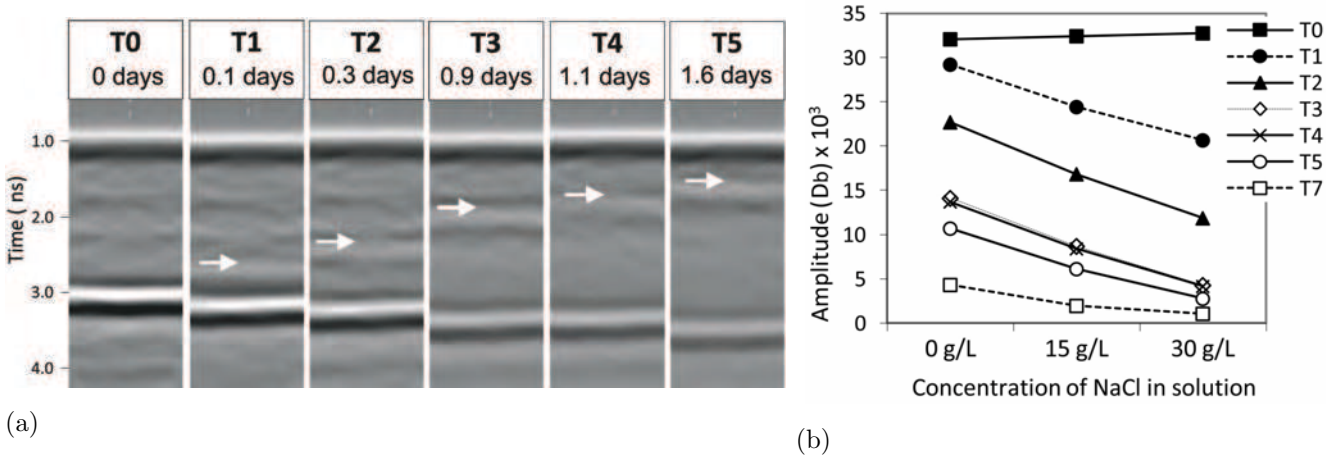

Figure 9.11: GPR method 1: Fixed offset measurements in reflection mode (a) extracts from the radargrams for Slab 1 indicating reflected wave from ingress front, (b) difference in the amplitude of the direct wave for the respective solutions.

Method 2:

GPR measurements with the WARR configuration (antenna central frequency 1500 MHz) yielded relative permittivities of Slab 1, 2 and 3 determined from the direct wave as approximately 4.7 for the dried state ε_{r1} and 8.7, 9.4 and 9.8 for the saturated states ε_{r2}.

It was verified that the signals obtained for the TE modes had penetrated through the ingress front and were mainly from the bottom of the slab, in contrast with method 1, where signals reflected from the ingress front could be clearly discerned. The ingress depths were thus determined by using the approach described in Section 9.3.4.1 [132] where the dispersion curves for each test time were matched to manually optimise synthetic data as presented in Figure 9.12. The results compared well with those obtained from the fixed offset GPR results (Figure 9.11). They demonstrate the wave guide approach to estimate ingress depth of solutions into concrete. It also indicates that the evolution of the ingress front can be estimated by using the reflected wave from the bottom of the concrete element when the ingress boundary is not sufficiently strong to produce a reflection.

9.3.4.3 Comparison of EM techniques

In this section, the results from the various non-destructive techniques will be compared to those obtained from the semi-destructive and destructive testing on witness cores. The capability of the various non-destructive methods to monitor the evolution of the saturation ingress front as well as to discern between the different chloride concentrations of the solutions is also discussed.

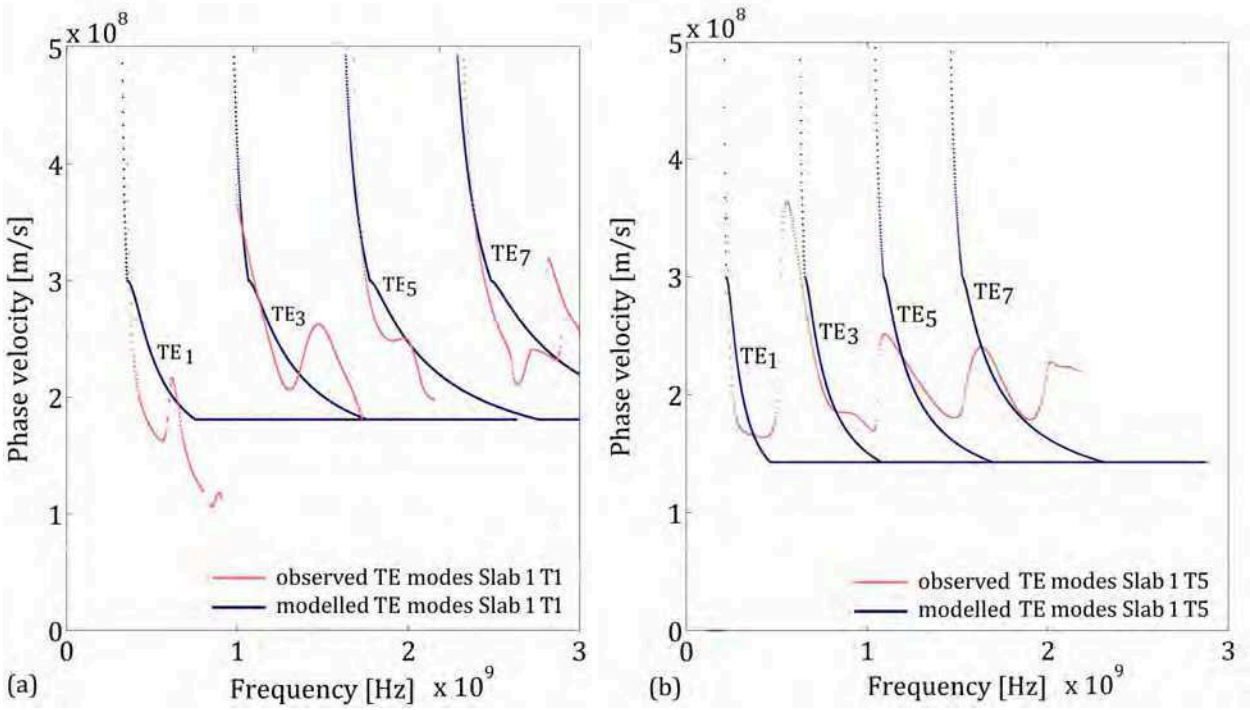

Figure 9.12: GPR Method 2: Real (observed) and synthesised (modelled) TE modes for Slab 1 at test times (a) T1 (optimised ingress depth of 20mm) and (b) T5 (optimised ingress depth of 80mm). The axis of the phase velocity extends to the physically impossible value of 5×10^8 in order to better observe the asymptotes.

9.3.4.3.1 Evaluation of the ingress of the saturation front

All non-destructive methods employed as part of the experimental campaign succeeded to some extent to follow the progress of the saturation ingress front over time for the various slabs. Resistivity and GPR results showed that the rate of ingress for the respective slabs was very similar. It was confirmed by means of gammadensimetry on witness cores that there was indeed little difference between the rates of water ingress in the respective slabs. In terms of gammadensimetry, the water ingress front is defined as lying between the "saturated" and "dry" limits defined by the intercepts indicated in Figure 9.13(a). Gamma-intercept 1 will be referred to here as the saturation ingress front and gamma-intercept 2 will be referred to as the water ingress front.

Figure 9.13(b) presents average water contents calculated from gammadensimetry results witness cores showing the variation of water content over the depth of the cores for each test time. Figure 9.13(c) plots the saturation and water ingress front with the chloride ingress front as obtained from colorimetry. It can be seen that the penetration of chloride ions takes place more slowly than the penetration of water. Figure 9.13(d) shows chloride profiling results for witness cores containing 30 g/L chloride tested at T1, T2 and T3 and T7. A

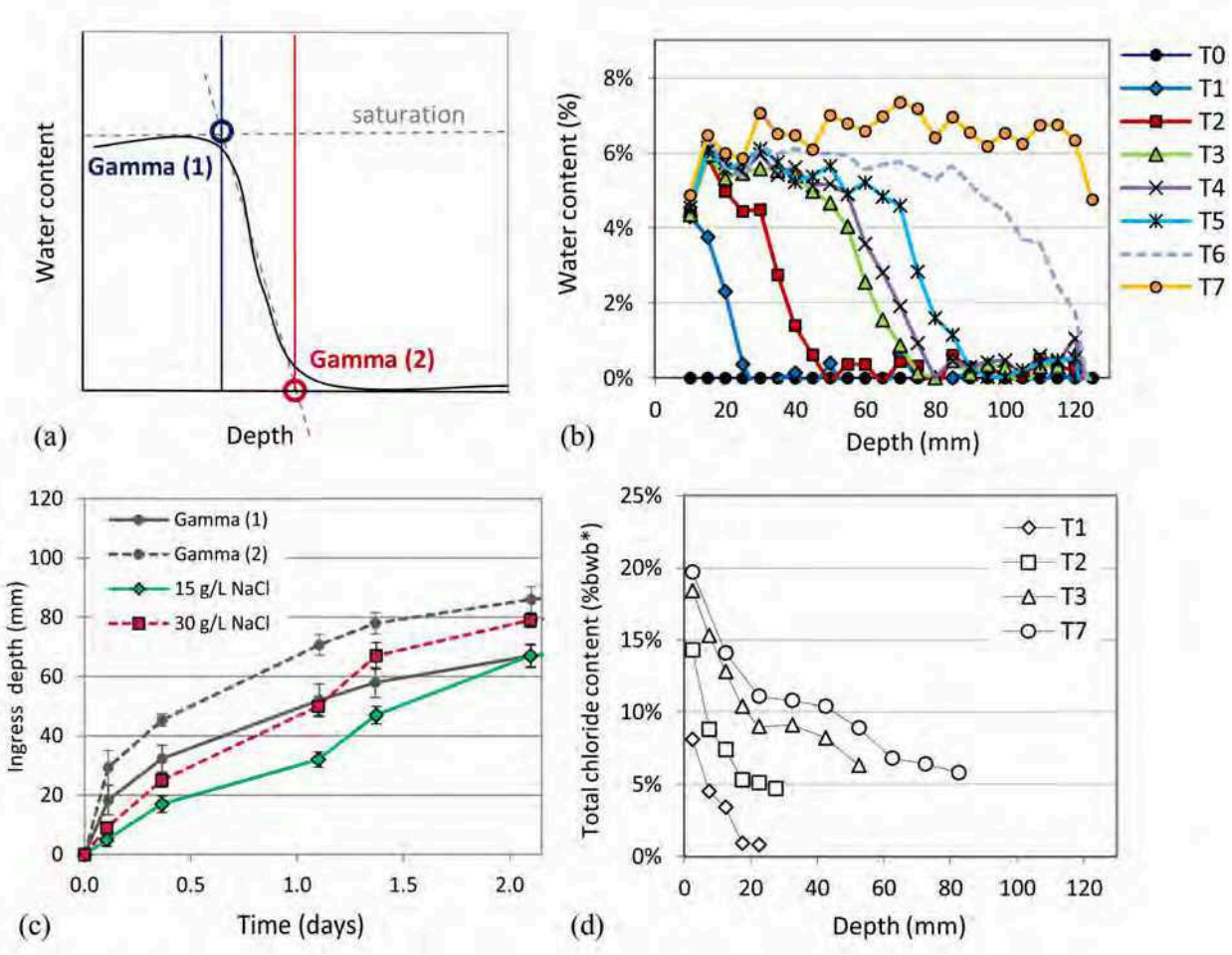

Figure 9.13: Destructive test results on witness specimens (a) schematically showing intercept 1 and intercept 2 used to define the limits of the water ingress front in terms of gammadensimetry, (b) gammadensimetry results for witness cores showing the penetration of the water ingress for each test time, (c) the penetration of the water ingress front (gammadensimetry) and the chloride front (colorimetry) for 15 g/L and 30 g/L witness specimens over time and (d) total chloride concentration measured by chloride profiling for the 30 g/L case (*by weight of concrete).

significant gradient in the total chloride concentration is observed between the surface and the chloride ingress front. It is therefore concluded that the assumption made in terms of resistivity measurements that the saturation ingress front can be associated with a resistivity close to that of water saturated concrete, even for the contaminated slabs, is valid.

There is a very good correlation between the rate of water penetration as estimated from the non-destructive measurements and the semi-destructive gammadensimetry results. Figure 9.14 shows the ingress depth over time determined by resistivity (ERT), fixed offset (GPR 1) and multi-offset (GPR 2) radar data and gammadensimetry. A difference can be noticed between the results from ERT and the GPR data. This is most probably due to the experimental protocol that was followed, where resistivity measurements were made from the wet

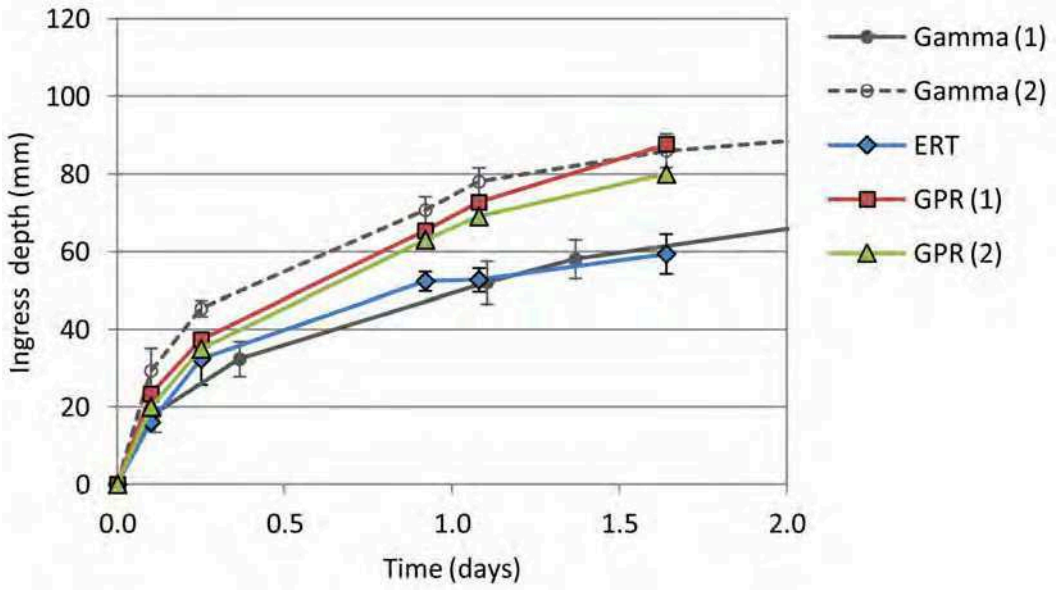

Figure 9.14: Estimation of water penetration as determined non-destructively by resistivity, fixed offset radar (GPR 1) and multi-offset radar (GPR 2) measurements as well as gammadensimetry results for the saturation ingress front (Gamma 1) and water ingress front (Gamma 2).

face of the slabs and the ingress front was determined at the position corresponding to the resistivity of saturated concrete. The ingress front estimated by ERT therefore corresponds to that of the saturation ingress front (Gamma 1) as can be seen in Figure 9.14. GPR measurements were taken from the dry face of the slabs and the estimated ingress depths lie closer to the water ingress front (Gamma 2). The propagation of the electromagnetic waves was therefore primarily influenced by the position of the water ingress front. As the inversion process for capacimetry is still under development, it is not yet possible to plot the position of the ingress front over depth as estimated by capacimetry.

9.3.4.3.2 Sensitivity to chloride content

Values for resistivity (ERT), low frequency permittivity (capacimetry), direct wave amplitudes (GPR 1) and high frequency permittivity (GPR 2) displayed very different sensitivities to the presence of chloride in the specimens. The results from the three methods where normalized with respect to Slab 1, containing no NaCl, to assess the sensitivity of the various methods to chloride. The relative difference for each of the methods with respect to Slab 1 is presented in Figure 9.15 for the saturated condition (T7). Figure 9.15 shows that the amplitude of the direct wave at 2600 MHz is the most sensitive to chloride content. This is due to the significant attenuation of the wave that is caused by the presence of chlorides. Results from ERT are sensitive to the presence of chlorides to a lesser extent, followed by permittivity determined from capacimetry at 33 MHz and the permittivity determined

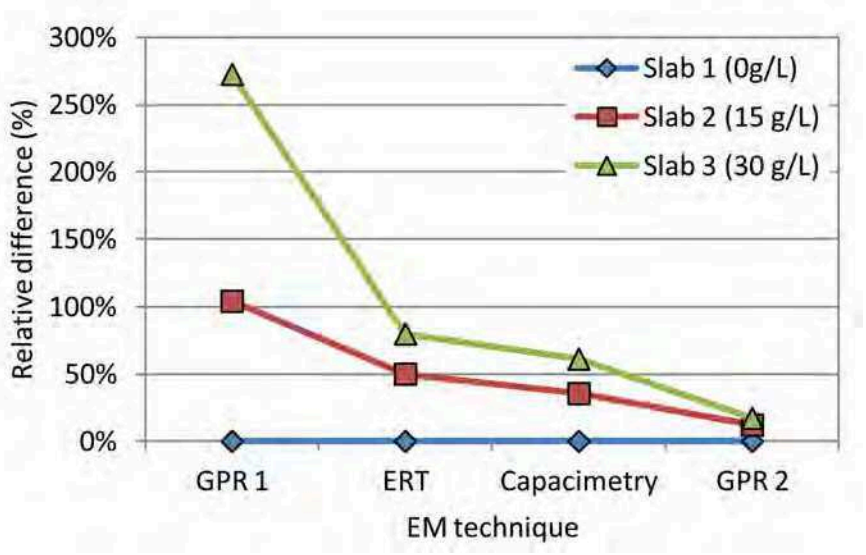

Figure 9.15: Sensitivity of EM methods to chloride content.

at 1500 MHz. This difference in sensitivity of the various methods has great potential in terms of further work on the combination of electromagnetic methods to estimate water and chloride content in concrete.

9.3.5 Summary

An experimental study was conducted to compare the capability of three electromagnetic NDE techniques to monitor the condition of concrete slabs. Three slabs were placed in solutions of 0 g/L, 15 g/L and 30 g/L NaCl respectively and the ingress of the electrolytes was monitored over a period of three days and again measured at 23 days. The techniques used were ERT, capacimetry and GPR (two configurations). The conclusions of the study are as follows:

1. Electrical resistivity tomography is a useful tool to track the ingress of electrolytes in concrete. A 14 electrode probe and an inversion protocol adapted to concrete were developed in order to obtain the resistivity profiles presented here. The profiles correlate well with the water content profiles determined by gammadensimetry tests conducted on cores of identical conditioning. The technique also clearly indicates a decrease in resistivity as the NaCl content in the concrete increases.

2. Capacimetry show promise to monitor property gradients in concrete as measurement over different depths of influence is possible using different electrode configurations. However, an inversion protocol is still required to enable permittivity over depth to be obtained. Capacimetry results clearly discern between the different concentrations

of chloride in the slabs and are quite sensitive to variations in chloride due to the low frequency at which it operates.

3. Results from the fixed offset GPR in the reflection mode (2600 MHz) show good capability of tracking the water ingress front. It is however limited by the fact that a clear boundary of contrasting permittivity is required for the technique to be successful. It would therefore probably not be possible to identify a more gradual transition in concrete condition. The amplitudes obtained for the saturated state shows a significant sensitivity to chloride content.

4. The use of the multi-offset (WARR) configuration (1500 MHz) enabled the estimation of the water ingress front by treating the slabs as a wave guide. This method is particularly useful if the electromagnetic wave is not reflected from the ingress front, but penetrates this barrier and is reflected from the bottom of the concrete element. The sensitivity of permittivity determined by GPR to chloride content for saturated conditions was much less than for the other methods due to the higher frequencies at which GPR is used for concrete applications.

The in situ techniques show varying capacity to provide quantitative and qualitative information on the condition of concrete and to identify the presence of property gradients. All techniques show promise for the future non-destructive characterisation of concrete and research on the combination of these methods to quantitatively estimate water and chloride content is in progress.

Acknowlegdements

We want to thank O. Coffec and A. Joubert of IFSTTAR *(Institut Français des Sciences et Technologies des Transports, de l'Aménagement et des Réseaux)*, Nantes, France and C. Lestréhan and S. Roux of CETE *(Centre d'Etudes Techniques de l'Equipment) de L'Ouest, Ouvrages d'Art et Maritimes*, Saint-Brieuc, France for the technical support they provided. This research was funded by the European Union as part of the Marie Curie Initial Training Network Framework 7 Project TEAM (Training in European Asset Management) and the *Ministère de l'Ecologie, du Développement durable et de l'Energie* of France.

9.4 Characterisation of a 100 year old concrete bridge using in situ EM techniques

The following section is dedicated to the non-destructive and destructive investigation of elements from the original Mizen Head footbridge (Ireland) in collaboration with University College Dublin (UCD) and the Cork Institute of Technology (CIT).

The Mizen Head footbridge was constructed in the beginning of the twentieth century at the south-western tip of Ireland to provide access to a light house on Cloghan Island. The bridge was of particular interest as it was one of the first reinforced concrete bridges constructed in Ireland and also the concrete arch bridge with the longest span in Europe (52 m) at the time of its completion in 1909. Due its extreme location 45 m above a deep sea inlet, it was exposed to particularly harsh environmental conditions through-out its service life. It was decommissioned in 2009 and a replica was constructed in its place in an award winning project to preserve the heritage of this iconic bridge. The original bridge was thus

Figure 9.16: The newly constructed replica of the Mizen head bridge, county Cork Ireland and an insert of the original bridge constructed in 1909, (main photo from *http://apresidentsblogbypjrudden.blogspot.fr* and insert by ©C.W. Glynn, licensed for reuse under the Creative Commons Licence).

dismantled and several concrete elements were kept at the Cork Institute of Technology for the purpose of research.

Though the non-destructive testing was not technically performed "in situ", it was performed in uncontrolled conditions on parts of an actual structure. It was thus a good opportunity to assess the performance of the in situ EM techniques on concrete posing particularly challenging circumstances. These challenges were mainly related to the age, construction methods and the long history of maintenance of the bridge, as listed below:

- The bridge was constructed using a proprietary steel reinforced system that consisted of round bars, rectangular bars and corrugated steel sheets. As the EM techniques are sensitive to the presence of reinforcement, the bars had to be avoided or their effects had to be corrected for during the investigation.
- As it was a footbridge and not carrying high loads, the concrete members were quite slender and their geometry had to be considered to avoid or correct for boundary effects.
- The composition and properties of the concrete displayed significant spacial variability due to the construction methods that were used at the time of construction. Aggregates from various sources were used and even some chloride contaminated beach sand, which probably contributed to the deterioration of the structure. The structure was also partially built in situ and partially built from precast elements.
- The bridge was covered with a bitumen impregnated fibre glass membrane and coated with masonry paint in the early 1970's. This served to protect the structure from further chloride attack, but also locked in the existing chlorides leading to anaerobic corrosion of the steel.

It was therefore of interest to study whether the EM techniques could produce results consistent with the destructive testing that was performed as part of this campaign and during previous investigations. Several reports containing a range of destructive results were also available for reference. It was subsequently found that the non-destructive and destructive measurements followed similar trends, though the combination of the methods as per Chapter 8 was not attempted due to the variability of the results and the uncertain origin of the concrete aggregates (on which permittivity is dependent).

The work presented here form part of the proceedings of the *International Conference on Durable Structures: from construction to rehabilitation* (ICDS12) held 31 May to 1 June 2012 in Lisbon, Portugal [90].

(a) (b)

(c) (d)

Figure 9.17: Testing of concrete elements from the dismantled Mizen Head footbridge with showing (a) WARR GPR measurements on a slab element, (b) capacitive probe measurements of a hanger, (c) a hanger where the protective paint and bituminous coating had been removed for resistivity testing and (d) a slab element from which core specimens had been taken for non-destructive testing (chloride diffusion coefficient).

NON-DESTRUCTIVE AND DESTRUCTIVE CONDITION ASSESSMENT OF A 100 YEAR OLD CONCRETE BRIDGE

Raelize du Plooy[a], Azadeh Attari[b], Ciaran McNally[b], Mark Richardson[b], Sergio Palma Lopes[a], Géraldine Villain[a], Xavier Dérobert[a]

[a]*LUNAM Université, IFSTTAR, MACS, F*-44340, *Bouguenais, France*
[b]*University College Dublin, Dublin, Republic of Ireland*

9.4.1 Abstract

The durability of cover concrete is the controlling factor in determining the rate at which corrosion initiation takes place within steel reinforced concrete structures. Various destructive and non-destructive techniques are available to assess corrosion risk and to monitor the ingress of aggressive agents such as chlorides. This paper presents results from a concrete condition assessment of a 100 year old bridge suffering from severe corrosion using electrical resistivity, capacimetry, radar (non-destructive), iodide migration and electron microscopy (destructive) techniques.

KEYWORDS: *Concrete durability, corrosion, non-destructive testing*

9.4.2 Introduction

Corrosion is a major cause of deterioration in reinforced concrete structures. The ingress rate of aggressive agents such as chlorides depends on the durability of the concrete and the severity of the environment to which the structure is exposed. Both destructive and non-destructive evaluation (NDE) techniques have been suggested as indicators for chloride penetration resistance of concrete [251]. For this study a selection of assessment techniques were used to evaluate the condition of dismantled elements from the Mizen Head footbridge (Ireland).

The original Mizen Head bridge was completed in 1909 to provide access to Cloghán island and is seen as an early example of precast reinforced concrete construction [227]. The bridge was subject to harsh environmental conditions including sea spray, prevalent wet fog and salt carrying winds. It was covered with a protective coating in 1972 due to signs of steel corrosion and was dismantled in 2010 as it was suffering from severe corrosion related deterioration such as spalling, cracking and delamination.

Table 9.4: Summary of previous condition assessments.

Report	**Strength** [N/mm^2]	**Density** [kg/m^3]	**Cl-content** [% bwc*]	**Carbonation depth** [mm]
QUANTAB,1986	-	-	1.1 - 4.5	-
Mac Craith,1989	46 - 73	2160 - 2425	-	10 - 35
Ruane et al, 2004 [227]	26 - 51	-	1.9 - 4.1	1
MATTEST, 2011	27 - 70	2150 - 2330	1.9 - 3.9	-

*percentage by weight of cement

Various condition assessments had been conducted over the past 30 years of which the results are summarised in Table 9.4. The results display great variability in terms of strength, density and chloride content, but are consistent for the respective assessments. The high chloride contents are also noteworthy.

9.4.3 Assessment methods

After dismantling, sections of the bridge were stored for further analysis; this included a range of destructive and non-destructive assessment methods.

9.4.3.1 Non-destructive techniques[2]

9.4.3.1.1 Electrical resistivity tomography (ERT)

Electrical resistivity is linked to corrosion risk in concrete due to its sensitivity to porosity, pore connectivity, water and chloride content. For this study ERT was conducted by means of a multi-electrode resistivity probe developed by IFSTTAR in 2011 [91] (refer to Chapter 6.3). ERT refers to the mapping of subsurface resistivities through the inversion of electrical responses from measurements taken at increasing electrode spacing and lateral offsets, for which *Res2Dinv* [163] software was used as part of this study.

[2] *Although this section is largely a repetition of statements found elsewhere in this document, the text was retained as in the original article, with reference to the appropriate Chapters added for a more detailed reference.*

9.4.3.1.2 Capacimetry

Capacimetry can be used to indirectly determine the apparent dielectric constant of non-homogeneous in situ concrete. The term *apparent* is used here because these results are surface values representing a certain volume of investigation and are not inverted to obtain the true dielectric constant over depth. The capacitive probe used for this study was assembled in 2006 by IFSTTAR [87]. It operates at a low frequency (33 MHz) where dielectric permittivity is very sensitive to concrete water and chloride content. The device has 4 interchangeable plate-electrode sets (small, medium, medium+[3] and large) enabling measurement at increasing influence depths from approximately 9 mm to 80 mm [87].

9.4.3.1.3 Ground penetrating radar (GPR)

The velocity at which electromagnetic waves propagate through concrete is influenced by the presence of moisture and chlorides. For this study GPR was used at a central frequency of 1.5 GHz with a bi-static (WARR) antenna configuration, where the transmitter and receiver were dissociated to enable multi-offset measurements [86]. The received signal for the direct wave was inverted using the "inter-coupling method" [132] to obtain the frequency dependent real and imaginary parts of permittivity, as described in Chapter 4.3.2.2. It has been shown that the more dispersive the medium, the more frequency dependent the permittivity [87].

9.4.3.2 Destructive techniques

9.4.3.2.1 Rapid iodide migration (RIM)

The diffusion coefficient of concrete is a key parameter in corrosion initiation. Accelerated methods such as rapid chloride migration (RCM) test are now commonly used for determining diffusion coefficient in concrete, but few are available for concrete that contain external chlorides [6]. One possible method is the RIM test [8], a modification of the RCM, where iodide ions replace chlorides. Iodide is similar to chloride in size, binding and transport behaviour and unlikely to be pre-existing in a concrete structure.

[3] *This electrode set is not mentioned in the previous work as it was not employed, however it has an influence depth between that of the medium and large electrode sets.*

9.4.3.2.2 Scanning electron microscopy (SEM)

Analysis of images obtained from SEM has been previously used for characterizing the microstructure of concrete and cement paste [9]. In this imaging method, a high energy electron beam is scanned across the surface and the signal intensity resulting from interaction of electrons and the specimen is measured. This intensity is used to produce a monochromatic image, with grey colour levels representing the difference in the flux of electrons, revealing the presence of different phases in the specimens. X-ray signals can also be produced, in order to identify the elements present in the specimens.

9.4.4 Results and discussion

9.4.4.1 Non-destructive evaluation

The selected NDE techniques required concrete elements large enough to minimise border effects and avoid reinforcement. Elements that conformed reasonably to these criteria were mainly from the deck slab and hangers as indicated in Figure 9.18. The geometry of each element and the position of the steel reinforcement was also carefully noted in order to calculate corresponding geometric factors for the correction of resistivity data.

Testing was performed on the upper face of deck slab sections; it was later discovered that the deck was covered with a granolithic wearing course during construction varying from 20 to 60 mm, which presence could also be identified by the results. Results for the deck were consistent for all the elements tested, as were those of the hangers, giving confidence in the reliability of the results.

Modelled resistivity over depth obtained by ERT are shown in Figure 9.19 and the apparent dielectric constants from capacimetry are shown in Figure 9.20(b) for Slab 3 and Hanger 3.

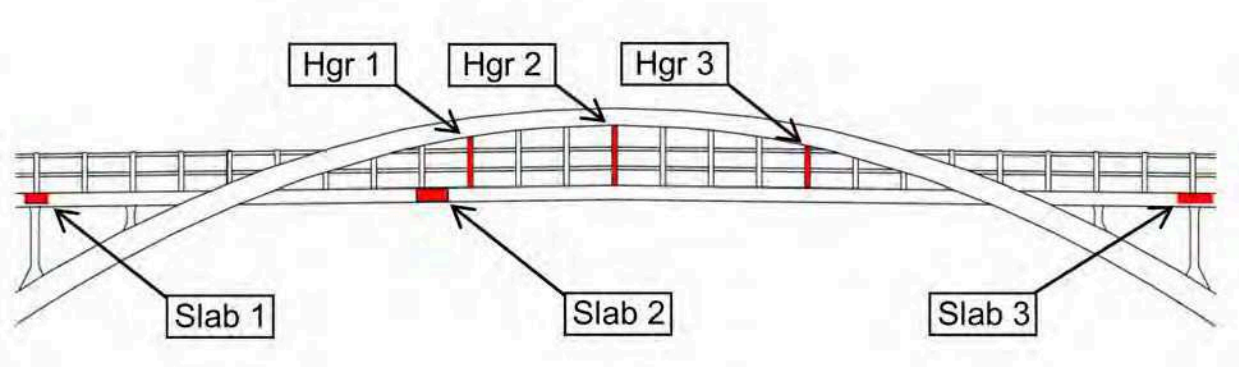

Figure 9.18: Test location diagram (northern elevation).

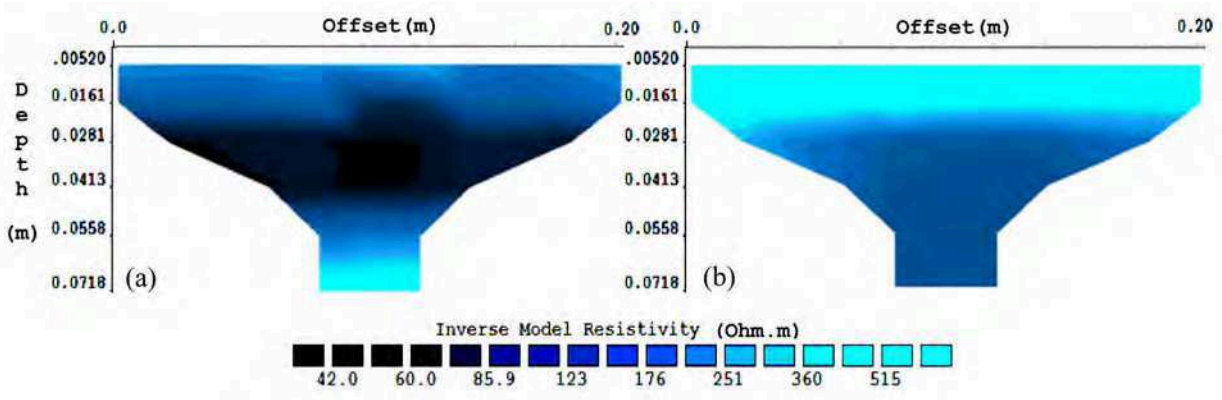

Figure 9.19: ERT mappings showing the inverted 2-dimensional resistivity for (a) Slab 3 and (b) Hanger 3, up to a depth of approximately 70 mm.

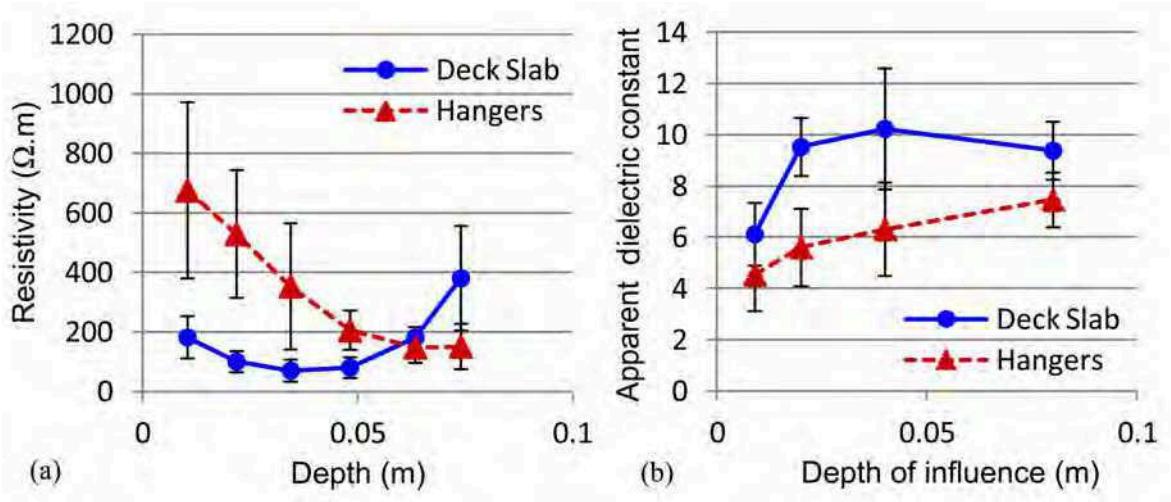

Figure 9.20: Average (a) inverted resistivities from ERT over depth and (b) apparent dielectric constants from capacimetry for each influence depth for Slab 3 and Hanger 3.

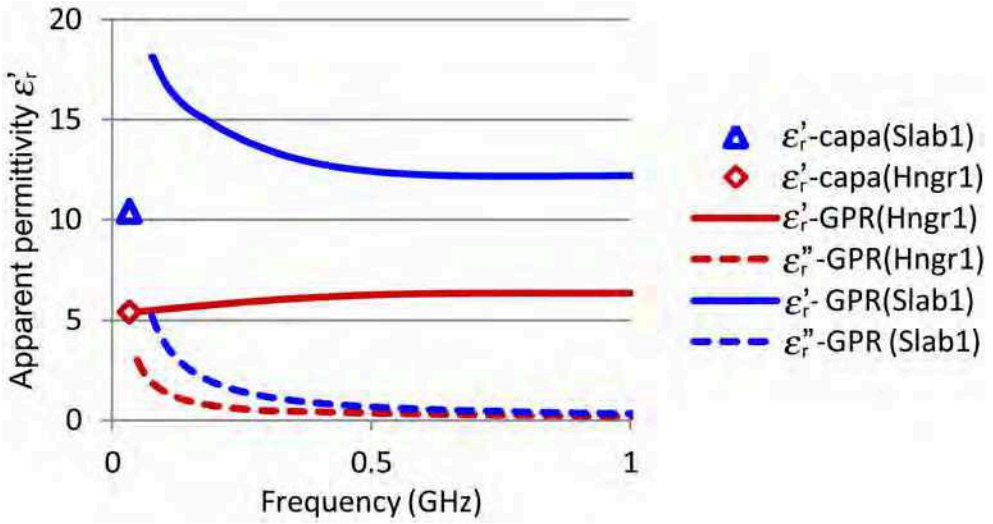

Figure 9.21: Apparent permittivities from multi-offset GPR measurements and capacimetry (medium electrode set) for Slab 1 and Hanger 1.

The results are seen as representative of all the elements that were tested. When results for the deck slab and hanger are compared, very different trends are observed. All slabs displayed low resistivity at a depth of 20 to 40 mm (Figure 9.19(a), coinciding with the bottom of the wearing course. It is suggested that salt water ponding on the deck, of which evidence was found, may have infiltrated over time leading to low resistivities (Figure 9.20(a)) and associated high dielectric constants (Figure 9.20(b)) in the vicinity of the joint for the slabs. The hangers show a strong decrease in resistivity moving inwards from the surface. The high resistivities close to the surface are unexpected and may be due to carbonation which can lead to reduced porosity [42]. Average resistivities for the hangers are generally higher than for the deck (Figure 9.20(a)), whilst capacimetry shows lower dielectric constants for the hangers than for the deck slab (Figure 9.20(b)). These results are consistent with there being lower chloride contents in the hangers than in the deck slab.

In Figure 9.21 it can be seen that the apparent complex permittivities obtained from multi-offset GPR data (ε_r' and ε_r'') are higher for the deck than for the hangers and show more frequency dependency, corresponding to a dispersive medium. The apparent dielectric constants obtained from capacimetry data (for the medium pate electrode) corresponds well to GPR results for the hangers, but less so for the deck slab. This is most likely because the direct wave was contained within the wearing coarse layer, whereas the capacimetry results were also influenced by the deeper substructure.

9.4.4.2 Destructive evaluation

Six specimens were taken from the deck slab and one from the hangers for RIM testing. It was only possible to obtain 1 specimen from the hangers due to irregular steel distribution within these members. The results for these tests are provided in Table 9.5. The comparison of these values with the criteria presented in the literature [94], indicate high permeability and suggest a poor quality concrete, particularly in the deck slab.

Specimens were also taken for SEM analysis and attempts made to characterise their porosity as an indicator of concrete durability [70]. The specimen preparation method impacts greatly on the quality of the images; the preparation method adopted here has been de-

Table 9.5: Diffusion Coefficient obtained using the RIM test method

Specimen ID	Slab 1			Slab 2		Hanger
	1-A	1-B	1-C	2-A	2-B	3-A
D_{eff} ($\times 10^{-12}$m^2/s)	18.2	15.1	39.7	5.4	40.0	5.2

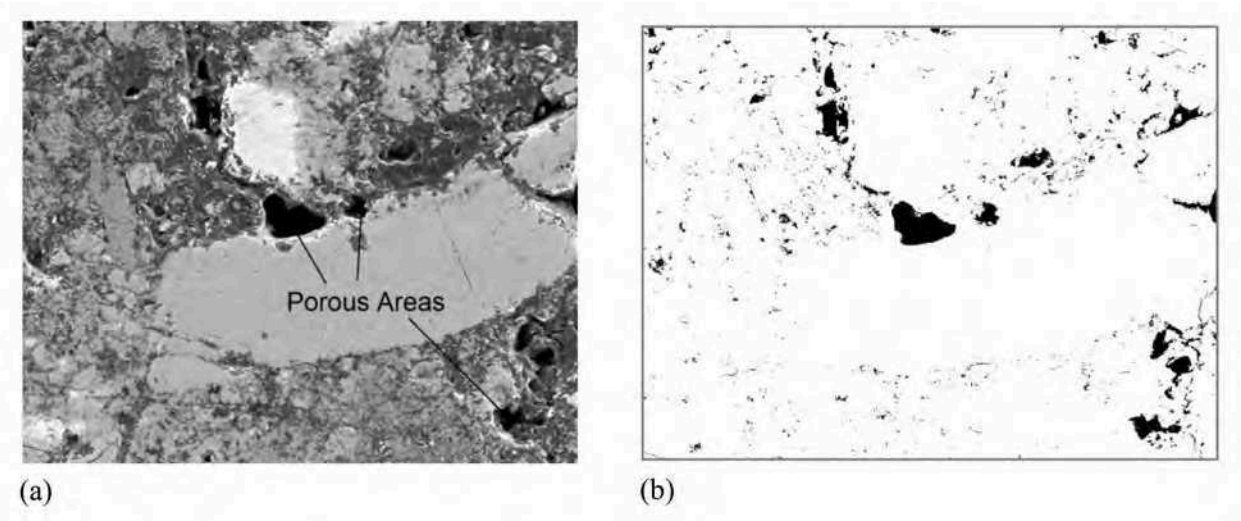

Figure 9.22: (a) SEM image of specimen 1 (Slab 1) and (b) the corresponding binary image.

scribed elsewhere [37]. This leads to pores, voids and cracks appearing as the darkest phase in the SEM images (Figure 9.22(a)). Thresholds were defined to separate out these phases and produce a binary image. Specimen porosity was then determined as the area fraction of the relevant phases on the binary image (Figure 9.22(b)). Area fractions are measured by pixel count, and results are provided in Table 9.6. Again it can be seen that there is a lot of variety within the specimens and that the average porosity of specimens taken from the hanger is less than those obtained from slabs.

However, care should be taken in interpreting these results. Although automated image analyses are frequently employed and thresholding methods identified for separating out various phases and features of concrete [288], the grey colour levels pertaining to these phases are not fixed and depend greatly on the image acquisition system, among other parameters.

Table 9.6: Porosity of specimens estimated by SEM image analysis (in % area)

Specimen ID	Slab 1	Slab 2	Hanger
1	18.91	10.29	5.81
2	14.06	8.82	11.65
3	9.63	7.59	7.17
4	10.10	7.08	-
5	9.33	-	-
6	8.86	-	-
Average	**11.81**	**8.62**	**8.21**

9.4.5 Summary

A range of test methods not typically used in bridge assessment have been applied to the dismantled Mizen Head footbridge. These included destructive and non-destructive methods and were applied to both hanger and deck slab sections. All testing methodologies indicated a large amount of variation in the concrete quality, consistent with the results of previous bridge inspections. In addition, all methods correctly identified the quality of the concrete in the hangers to be superior to that used in the slabs. While at the moment these results are largely qualitative, work is continuing to develop these testing methodologies to allow their use in future bridge assessment and in concrete deterioration models.

Acknowledgements

The TEAM project is a Marie Curie Initial Training Network and is funded by the EC 7th Framework Programme (PITN-GA-2009-238648). Our thanks to James Morgan (Cork Institute of Technology) and Ana´elle Joubert (IFSTTAR) who were involved in the non-destructive testing campaign.

9.5 Conclusion

This section demonstrates that the use of EM non-destructive testing has potential for various applications. The first study demonstrates that there is a strong relationship between resistivity and chloride diffusion coefficient determined by migration. It was also found that this relationship is independent of the addition of mineral admixtures such as GGBS for this case, but is less valid when the W/B-ratio and porosity of the concretes vary - especially at saturated conditions. However, most interestingly, it seems that resistivity is dependent on only diffusivity at low saturations. The relationship between resistivity and the chloride diffusion coefficient is of particular interest in terms of serviceability life modelling and quality control as the chloride diffusion coefficient is widely used as part of a performance based approach to durability [42] [26], but is time consuming to determine, unlike resistivity [251]. This study also shows that in order to develop a regression model for concrete resistivity that is valid over a wide range of saturations (as in Chapter 7.4.2), it is advisable to include both diffusivity and porosity (or W/B-ratio) as input parameters.

During the second study it was demonstrated that the in situ EM techniques ERT, capacimetry and GPR have potential to identify the presence of water and chloride gradients within concrete. Resistivity tomography, using the multi-electrode probe that was developed as part of the work presented here, proved particularly capable in this context. By using ERT it was also possible to quantify the degree of saturation by applying the calibration curves that had been developed as part of the parametric study presented in Chapter 7.2. These results are encouraging as they demonstrate the possibility of estimating the rate of chloride ingress into cover concrete by using non-destructive techniques, which could be very useful in terms of structural health monitoring.

Lastly, a non-destructive evaluation was conducted using the aforementioned in situ methods on elements from a decommissioned bridge. The aim was to assess the potential of the methods under challenging uncontrolled conditions. The results from the non-destructive investigation displayed the same trends as to those of destructive testing that was done as part of the same and earlier experimental programs.

Though there is admittedly still a long way to go and much refinement of the methods required to obtain a reliable, quantitative results, it is clear from these studies that the non-destructive electromagnetic evaluation of concrete infrastructure is a valuable way to assess the durability of structures in a efficient and cost effective way.

Chapter 10

Conclusion, future work and publications

10.1 Conclusion

Reinforced concrete infrastructure forms an integral and indispensable part of modern society. In order to ensure the construction of durable concrete structures and to maintain them as best as possible over their service lives, monitoring of the condition of the concrete is essential. Many of the traditional destructive test procedures to assess concrete durability are expensive and time consuming. The non-destructive evaluation (NDE) of concrete structures is therefore adopted by an increasing number of authorities to supplement or even replace these destructive techniques.

Electromagnetic (EM) non-destructive investigation techniques are particularly suited for the assessment of concrete condition, as they are sensitive to parameters associated with corrosion, which is arguably the most significant problem with regards to ageing reinforced concrete structures. However, the inherent variability of concrete, as well as other influences on these techniques associated with in situ testing, are such that the use of a single technique often does not yield reliable results. The combination of several non-destructive techniques has therefore become the subject of much interest in the NDE research community in recent years in order to improve the reliability and interpretation of results.

This thesis focused on the combination of EM evaluation techniques as a way to assess the durability and condition of cover concrete during the corrosion initiation stage. Though a large amount research is available on the dependency of the EM observables on various aspects of concrete condition and durability, most studies do not document the response of several EM techniques on the same concrete. In order to achieve this, two new devices for

the measurement of electrical resistivity were developed in order to assess both the resistivity and dielectric permittivity of the same specimens. A parametric study was then conducted to evaluate the EM response of a range of concrete mixes and conditionings in a controlled laboratory environment.

A significant contributor the uncertainty of EM measurements is the inhomogeneity of the concrete due to variation in water content, chloride content and porosity. The resistivity devices were therefore designed to be capable of detecting the presence of gradients in the concrete under investigation. This enabled the homogeneity of the specimens to be confirmed, or data affected by gradients to be discarded for the parametric study, ensuring reliable results. As a result of the parametric study, a regression model was developed for each EM observable which could be determined with the available in situ techniques (resistivity, capacimetry and GPR). These techniques were combined in order to estimate the degree of saturation, chloride content and porosity of concrete slabs by the solution of a system of equations consisting of the regression models.

The capacity of EM investigation techniques to detect the presence of gradients in concrete is also of much value in practice, especially for the continuous health monitoring of cover concrete. The ability of the three in situ techniques to monitor the ingress of water and chlorides into concrete was therefore also studied in a collaborative experimental campaign. Other collaborative work that was conducted includes the study of the relationship between resistivity and chloride diffusion coefficient as well as an in situ study using EM investigation techniques.

The main tasks performed as part of the research presented in this thesis can therefore be summarised as follows:

I. A multi-ring resistivity cell for the testing of concrete cores and a multi-electrode resistivity probe for in situ applications were developed, both capable of identifying property gradients due to the variation in water and chloride contents;

II. A parametric study was conducted during which master curves were produced to describe the dependency of the EM observables electrical resistivity, dielectric constant and loss factor (at high and low frequencies) on condition and durability parameters, i.e. water content, total chloride content, porosity and chloride diffusion coefficient. Statistical analysis of the data was then performed to produce a regression model for each EM observable;

III. The regression models were used to combine the results of three in situ EM investigation techniques (ERT, capacimetry and GPR) to estimate the condition of concrete under controlled conditions. This was conducted on slabs of known condition by the

simultaneous solution of the system of equations considering of these models using numerical optimisation. The reliability of the models and estimation procedure could therefore be validated;

IV. The relationship between electrical resistivity and chloride diffusion coefficient was investigated as a function of cement type and degree of hydration. Results agreed with finding in literature as to the strong linear relationship between the two parameters and also found it to be independent of cement type. As the diffusion coefficient is an important durability indicator which serve as input parameter for many predictive service life models, this finding is significant;

V. The three in situ EM techniques were compared as to their ability to detect the ingress of saline solutions into concrete. It was found that all of the techniques could assess the presence of gradients in concrete and also discern between the concentration in chloride, with ERT being particularly capable of assessing both these;

VI. An in situ study was conducted to assess the performance of the in situ EM techniques in challenging uncontrolled conditions by using EM techniques and the trends for the non-destrutive assessment corresponded well those from destructive testing.

The findings of these studies demonstrate the potential of electromagnetic non-destructive techniques to estimate the condition of concrete non-destructively and to monitor the evolution of parameters related to corrosion over time. The combination of these techniques is an indispensable tool to reduce the uncertainty that is associated with in situ results. It is therefore feasible to employ electromagnetic non-destructive evaluation techniques as part of the management strategy of reinforce concrete infrastructure to ensure the sustainability of this asset in the long term.

10.2 Future work

The success of the combination of the EM techniques as described above is partly due to the results being mainly for controlled laboratory conditions. For the actual evaluation of concrete on site using the models and approach developed as part of this document much further work is required. Some of the important issues that was not fully addressed during this thesis and which are the topic of current research are the following:

I. Though the concrete used as part of this thesis varied greatly in durability, they were not nearly representative of all the types of concrete found in practice. All sorts of mineral and chemical admixtures, accelerators and retarders are used in concrete. Though the models developed here should be applicable to most of these if they only

influence the porosity and diffusion characteristics of the concrete, further work is required to assess the sensitivity of EM observables to these additives. A lack in literature in on this subject exists especially for dielectric permittivity, since it has been studied far less frequently than resistivity.

II. The models developed here for dielectric permittivity does not take into account the influence of the aggregate type used in the concrete, which is well known to be significant. Even though it is accepted that a difference in aggregate type will only cause a "shift" in the model which could be corrected for by calibration, more work is required in this regard.

III. As the experimental work was for the most part conducted on unreinforced concrete, more research is required on the influence of the presence of steel on the electromagnetic responses. Though the geometric correction of resistivity data for the reinforced concrete (Chapter 9.4) was investigated, it was not included in this document for lack of time. In literature, most studies avoid the influence of reinforcement by measuring in-between the rebars, however this is not always possible and more research on this topic is thus required.

IV. The inversion of results for non-homogeneous concrete to estimate the true EM properties over depth was only conducted for resistivity. As these inversion algorithms are technically composed for an infinite halfspace, it still remains to be validated that the application of a geometric factor before inversion (as was done in this thesis) will always yield accurate results. An inversion process is also possible for results from the capacitive probe and the development of this procedure is currently studied at IFSTTAR.

V. The variability of measurements conducted in situ is significantly higher than from the specimens used in this thesis. Therefore, the more NDE techniques employed, the better the trends in results can be interpreted and the reliability of the results ensured. In practice, it is a thus far more complex task to optimise results in order to characterise in situ concrete qualitatively. Current research adopts more sophisticated approaches for the combination of NDE techniques than employed in this thesis. Statistical modelling using the theory of possibility [212] or the fuzzy neural network [234] [235] are for example used in ongoing research to optimise the results from several NDE techniques to estimate concrete condition.

VI. The work presented here will also be further pursued by combining EM techniques to assess water content and chloride content gradients in concrete independently.

10.3 Publications

The publications that were authored and co-authored as a results of the work presented here are as follows:

10.3.1 International journal publications

R. du Plooy, S. Palma Lopes, G. Villain and X. Dérobert, Development of a multi-ring resistivity cell and multi-electrode resistivity probe for investigation of cover concrete condition, *NDT & E international*, 54:27-36, 2013.

R. du Plooy, G. Villain, S. Palma Lopes, A. Ihamouten, X. Dérobert, B. Thauvin, Electromagnetic non-destructive evaluation techniques for the monitoring of water and chloride ingress into concrete: a comparative study, *Materials and Structures* (under review), 2013.

10.3.2 Publications in the proceedings of conferences

R du Plooy, 2011, The non-destructive electromagnetic characterisation of cover concrete, *Proceedings of Marie Curie Researchers Symposium, "SCIENCE - Passion, Mission, Responsibilities"*, Polish Presidency of the EU Council, Warsaw, Poland, 25-27 September 2011.

R. du Plooy, S. Palma Lopes, G. Villain, X. Dérobert, B. Thauvin and C. Lestréhan, 2012, Comparison of electromagnetic non-destructive evaluation techniques for the monitoring of chloride ingress in cover concrete, *Proceedings of the* 6^{th} *International Conference on Bridge Maintenance, Safety and Management* (IABMAS), Lake Como, Italy, July 8-12 2012.

R. du Plooy, A. Attari, C. McNally, M. Richardson, S. Palma Lopes, G. Villain and X. Dérobert, Destructive and non-destructive condition assessment of a 100 year old concrete bridge, proceedings of ICDS12-International Conference Durable Structures: from construction to rehabilitation, Lisbon, Portugal, 31 May-1 June 2012.

R. du Plooy, S. Palma Lopes, G. Villain, X. Dérobert, The Combination of Electromagnetic Non-Destructive Evaluation Techniques for the Determination of Effective Diffusion Coefficient, First International Conference on Concrete Sustainability, Tokyo, Japan, 27-29 May 2013.

G. Villain, R. du Plooy, A. Ihamouten, S. Palma Lopes, B. Thauvin, X. Dérobert, Use of electromagnetic non-destructive techniques for monitoring the chloride ingress into concrete,

Proceedings of the 7th International Workshop on Advanced Ground Penetrating Radar (IWAGGPR 2013), Nantes, France, July 2-5, 2013.

T. Lecieux, Y. Lecieux, F. Schoefs, R. Du Plooy, S. Palma Lopes, S. Bonnet, M. Roche, Dveloppement d'un capteur intégré pour la mesure de résistivité dans le béton, *Proceedings of the 6ème Colloque Interdisciplinaire en Instrumentation*, Lyon, Franc, 29-30 January 2013.

Bibliography

[1] Concrete Durability: A Multibillion-Dollar Opportunity. Technical report, National Materials Advisory Board, National Research Council, Report NMAB 437, National Academic Press, 1987.

[2] CRD – C Standard 163 : *Test Method for Water Permeability of Concrete Using Triaxial Cell*. United States Army Corps of Engineers, `http://www.wbdg.org/ccb`, 1992.

[3] European Standard EN 1991 – 1 : *European Standard: Eurocode 1: Actions on Structures Part 1 - Basis of Design*. European Committee for Standardisation, 1994.

[4] Nordtest Method NT Build 433 : *Concrete, hardened: Accelerated chloride penetration*. NORDTEST, Espoo, Finland, 1995.

[5] *AFPC-AFREM Durabilité des Bétons: Méthodes recommandées pour la mesure des grandeurs associées à la durabilité*. Laboratoire Matériaux et Durabilité des Constructions, INSA Génie Civil, Toulouse, France, 1997.

[6] Nordtest Method NT Build 492 : *Chloride migration coefficient from non-steady-state migration experiments*. NORDTEST, Espoo, Finland, 1999.

[7] *General Guidelines for Durability Design and Redesign*. Project No. BE 95-1347, DuraCrete: Probabilistic Performance based Durability Design of Concrete Structures, The European Union - Brite EuRam III, 2000.

[8] European Standard EN 206 – 1 : *Concrete - Part 1: Specification, performance, production and conformity*. AFNOR, 2000.

[9] AASHTO Standard T259 : *Standard Method of Test for Resistance of Concrete to Chloride Ion Penetration*. AASHTO: American Association of State Highway and Transportation Officials, 2002.

[10] FIB Model Code for Service Life Design. *Bulletin 34, FIB, EPFL, Lausanne*, pages 1–116, 2006.

[11] AASHTO Standard T277 – 07 : *Electrical Indication of Concrete's Ability to Resist Chloride Ion Penetration*. AASHTO: American Association of State Highway and Transportation Officials, 2007.

[12] ASTM Standard $C1218_C1218M - 99$: *Standard Test Method for Water-Soluble Chloride in Mortar and Concrete*. ASTM International, West Conshohocken, PA, DOI : $10.1520/C1218_C1218M - 99R08$, `http://www.astm.org`, 2008.

[13] ASTM Standard C802 – 09a : *Standard practice for conducting an interlaboratory test program to determine the precision of test methods for construction materials.* ASTM International, West Conshohocken, PA, DOI: 10.1520/C0033-03A, `http://www.astm.org`, 2009.

[14] ASTM Standard C1556 – 11a : *Standard Test Method for Determining the Apparent Chloride Diffusion Coefficient of Cementitious Mixtures by Bulk Diffusion.* ASTM International, West Conshohocken, PA, DOI: 10.1520/C1556-11A , `http://www.astm.org`, 2011.

[15] ASTM Standard C1202 – 12 : *Standard Test Method for Electrical Indication of Concretes Ability to Resist Chloride Ion Penetration.* ASTM International, West Conshohocken, PA, DOI: 10.1520/C1202-12, `http://www.astm.org`, Philadelphia, 2012.

[16] ACI Committee 318. *Building code requirements for structural concrete : (ACI 318-95).* Farmington Hills, MI : American Concrete Institute, 1995.

[17] N. Abu-Zeid, D. Botteon, G. Cocco, and G. Santarato. Non-invasive characterisation of ancient foundations in Venice using the electrical resistivity imaging technique. *NDT & E International*, 39(1):67 – 75, 2006.

[18] B. Addis and G. Owens, editors. *Fultons Concrete Technology.* Cement & Concrete Institute of South Africa, Midrand, 8 edition, 2001.

[19] M. Adous. *Caractérisation électromagnétique des matériaux traités de génie civil dans la bande de fréquences 50 MHz - 13 GHz.* PhD thesis, l'Université de Nantes, IFSTTAR, 2006.

[20] M. Adous, P. Quéffélec, and L. Laguerre. Coaxial/cylindrical transition line for broadband permittivity measurement of civil engineering materials. *Measurement Science and Technology*, 17:2241–2246, 2006.

[21] S. Ahmad, A.K. Azad, and K.F. Loughlin. A study of permeability and tortuosity of concrete. *30th Conference on Our World in Concrete & Structures: 23 - 24 August 2005, Singapore*, 2005.

[22] I.L. Al-Qadi, O.A. Hazim, W. Su, and S.M. Riad. Dielectric properties of Portland cement concrete at low radio frequencies. *International Journal of Rock Mechanics and Mining Sciences and Geomechanics Abstracts*, 33:160A–160A(1), 1996.

[23] I.L. Al-Qadi, S.M. Riad, R. Mostaf, and W. Su. Design and evaluation of a coaxial transmission line fixture to characterize portland cement concrete. *Construction and Building Materials*, 11(3):163 – 173, 1997.

[24] M. Al Shamaa. Caractérisation hydrique de bétons d'ouvrages par méthode capacitive. Master's thesis, Masters dissertation, Université de Nantes-Saint-Nazaire, 2009.

[25] K.K. Al-Tarawneh, O. Buzzi, K. Krabbenhft, A.V. Lyamin, and S.W. Sloan. An Indirect Approach for Correlation of Permeability and Diffusion Coefficients. *Defect and Diffusion Forum, Trans Tech Publications, Switzerland*, 283-286:504–514, 2009.

[26] M.G Alexander and H. Beushausen. Performance-based durability testing, design and specification in South Africa: latest developments. *Proceedings of The International Conference on Concrete Construction*, Kingston University, London, UK, 9-10 September, 2009.

[27] M.G. Alexander, J. R. Machkechnie, and Y. Ballim. Guide to the use of durability indexes for achieving durability in concrete structures. Technical report, Research Monograph 2, Department of Civil Engineering, University of Cape Town, 1999.

[28] D. Alleyne and P. Cawley. A two-dimensional Fourier transform method for the measurement of propagating multimode signals. *Journal of the Acoustical Society of America*, 89:1159–1168, 1991.

[29] A.V. Alongi, T.R. Cantor, C.P. Kneeter, and Jr. A. Alongi. *Concrete Evaluation by Radar Theoretical Analysis.* Transportation Research Board Record No. 853, 1982.

[30] C. Andrade, R. Polder, and M. Basheer. Chapter 5. Non-Destructive Methods to Measure Ion Migration, RILEM Report 040, Non-Destructive Evaluation of the Penetrability and Thickness of Concrete Cover. *RILEM TC 189-NEC: State of the Art Report*, pages 91–112, 2007.

[31] C. Andrade, M.A. Sanjuan, A. Recuero, and O. Rio. Calculation of chloride diffusivity in concrete from migration experiments, in non steady-state conditions. *Cement and Concrete Research*, 24:1214–1228, 1994.

[32] C. Andrade, J. Sarría, and C. Alonso. Relative humidity in the interior of concrete exposed to natural and artificial weathering. *Cement and Concrete Research*, 29:1249–1259, 1999.

[33] G.E. Archie. The Electrical Resistivity Log as an Aid in Determining Some Reservoir Characteristics. *Transactions of the AIME*, pages 54–62, 1942.

[34] S.A. Arcone. Field observations of electromagnetic pulse propagation in dielectric slabs. *Geophysics*, 49:1763–1773, 1984.

[35] S.A. Arcone, P.R. Peapplesz, and L. Liu. Propagation of a ground-penetrating radar (GPR) pulse in a thin-surface waveguide. *GEOPHYSICS*, 68:1922–1933, 2003.

[36] G. Arliguie and H. Hornain. GranDuBé - Grandeurs associées à la Durabilité des Bétons AFGC-RGCU. *Presses de l'ENPC, Paris*, 2007.

[37] A. Attari, C. McNally, and M.G. Richardson. Evaluation of chloride ingress parameters in concrete using backscattered electron (BSE) imaging to assess degree of hydration - A proposal. In *Proceedings of Bridge & Concrete Research in Ireland*, Dublin, 2012.

[38] C.A. Balanis. *Advanced Engineering Electromagnetics.* John Wiley and Sons (WIE), 1989.

[39] J.P. Balayssac, S. Laurens, G. Arliguie, M.A. Ploix, D. Breysse, X. Dérobert, and B. Piwakowski. Evaluation of concrete structures by combining non-destructive testing methods (SENSO project). *Proceedings of NDTCE09, Non-Destructive Testing in Civil Engineering*, Nantes, France, 30 June-3 July, 2009.

[40] V. Baroghel-Bouny. Concrete: From material to structure,. *Proceedings of the International RILEM Conference, Arles, France, September 11-12*, pages 144–165, 1996.

[41] V. Baroghel-Bouny, C. Andrade, R. Torrent, and K. Scrivener. *Proceedings of the International RILEM Workshop on Performance Based Evaluation and Indicators for Concrete Durability (pro047)*, 2007.

[42] V. Baroghel-Bouny et al. *Concrete Design for a Given Structure Service Life.* AFGC, 2007.

[43] V. Baroghel-Bouny, K. Kinomura, M. Thiery, and S. Moscardelli. Easy assessment of durability indicators for service life prediction or quality control of concretes with high volumes of supplementary cementitious materials. *Cement & Concrete Composites*, 33:832–847, 2011.

[44] P.A.M. Basheer, A.E. Long, and F.R. Montgomery. The Autoclam - a new test for permeability. Concrete. *Journal of the Concrete Society*, pages 27–29, 1994.

[45] D. Baweja, H. Roper, and V. Sirivivatnanon. Corrosion of Steel in Marine Concrete: Long-Term Half-Cell Potential and Resistivity Data. *Proceedings of the Third CANMET/ACI International Conference on Concrete in Marine Environment (SP-163)*, pages 89–110, New Brunswick, Canada, 4-9 August, 1996.

[46] A. Bentur, S. Diamond, and N.S. Berke. *Steel Corrosion in Concrete: Fundamentals and Civil Engineering Practice*. Chapman & Hall, London, UK, 1997.

[47] L. Bertolini, B. Elsener, P. Pedeferri, and R.B. Polder. *Corrosion of steel in concrete*. WILEY-VCH Verlag, 2004.

[48] G.P.E. Box, J.S. Hunter, and W.G. Hunter. *Statistics for Experimenter: Design Innovation and Discovery*. John Wiley and Sons, New Jersey, 2005.

[49] W. Brameshuber, M. Raupach, P. Schröder, and C. Dauberschmidt. Non-destructive Determination of the Water-Content in the Concrete Cover using the Multiring-Electrode. *Non-Destructive Testing in Civil Engineering, International Symposium (NDT-CE 2003)*, 2003.

[50] D. Breysse, editor. *Non-Destructive Assessment of Concrete Structures: Reliability and Limits of Single and Combined Techniques: State-Of-the-Art Report of the RILEM Technical Committee 207-INR*. Springer, Technology & Engineering, 2012.

[51] United Kingdom Broads Authority. *Guide to the relationship between salinity measures*, `http://www.broads-authority.gov.uk/broads/live/managing/rivers-and-broads/broads-water-quality-partnership/`.

[52] J.H. Bungey. Sub-surface radar testing of concrete: a review. *Construction and Building Materials*, 18(1):1 – 8, 2004.

[53] J.H. Bungey, S.G. Millard, B.A. Austin, C. Thomas, and M.R. Shaw. *Permittivity and Conductivity of concrete structures at radar frequencies. in:Concrete in the Service of Mankind: Concrete repair, rehabilitation and protection*. E. & F. N. Spon, 1996.

[54] O. Buyukozturk and H.C. Rhim. Detection of delaminations in concrete using a wideband radar. *Structural Materials Technology. An NDT Conference*, pages 55–60, 1996.

[55] M. Cabeza, P. Merino, A. Miranda, X.R. Nóvoa, and I. Sanchez. Impedance spectroscopy study of hardened Portland cement paste. *Cement and Concrete Research*, 32(6):881 – 891, 2002.

[56] N.J. Carino. The impact echo method: an overview. *Proceedings of the Structures Congress & Exposition, American Society of Civil Engineers*, page 18, Washington, D.C., United States, May 21-23, 2001.

[57] M. Castellote and C. Andrade. Round-Robin Test on methods for determining chloride transport parameters in concrete. *Materials and Structures*, 39:955–990, 2006.

[58] S.C. Chapra and R.P. Canale. *Numerical Methods for Engineers, 4th Edition*. McGraw-Hill, 2001.

[59] T. Chaussadent and G. Arliguie. AFREM test procedures concerning chlorides in concrete: Extraction and titration methods. *Materials and Structures*, 32:230–234, 1999. 10.1007/BF02481520.

[60] J. Chazelas, V. Baltazart, L. Laguerre, X. Dérobert, and G. Villain. Étude des propriétés diélectriques des bétons. Technical report, Laboratoire Central des Ponts et Chaussées, 2005.

[61] M. Chekroun. *Charactérisation mécanique de premiers centimètres du _'eton avec des ondes de surface.* PhD thesis, PhD dissertation, Ecole Doctorale des Sciences pour l'Ingénieur Géosciences Architechture, Nantes, 2008, 176p.

[62] D.K. Cheng. *Field and Wave Electromagnetics.* Addison-Wesley, 1992.

[63] W.C. Chew. Design and calibration of a large broadband dielectric measurement cell. *Geoscience and Remote Sensing, IEEE Transactions on*, 29:42–47, 1991.

[64] D.H. Chisholm and N.P. Lee. Actual and Effective Diffusion Coefficients for Concrete in Marine Environments. *Proceedings of the 20th Biennal Conference of the Concrete Institute of Australia*, Perth, Australia, 11-14 September, 2001.

[65] W.A. Chisholm and A. Phillips. Contact and geometric resistivitance of wire frame electrodes. *IX International Symposium on Lightning Protection*, 2007.

[66] M. Chouteau, S. Vallières, and E. Toe. A multi-dipole mobile array for the non-destructive evaluation of pavement and concrete infrastructures: a feasability study. *BAM International Symposium (NDT-CE 2003) Non-Destructive Testing in Civil Engineering*, 2003.

[67] T.M. Chrisp, W.J. McCarter, G. Starrs, P.A.M. Basheer, and J. Blewett. Depth-related variation in conductivity to study cover-zone concrete during wetting and drying. *Cement & Concrete Composites 24*, pages 415–426, 2002.

[68] T.M. Chrisp, G. Starrs, W.J. McCarter, E. Rouchotas, and J. Blewett. Temperature-conductivity relationships for concrete: An activation energy approach. *Journal of Materials Science Letters*, 20:1085–1087, 2001. 10.1023/A:1010926426753.

[69] D.D.L. Chung. *Applied Materials Science: Applications of Engineering Materials in Structural, Thermal, and Other Industries.* CRC Press, Florida, 2001.

[70] P.A. Claisse, J.G. Cabrera, and D.N. Hunt. Measurement of porosity as a predictor of the performance of concrete with and without silica fume. *Advances in Cement Research*, 13:165–174, 2001.

[71] G.G. Clemeña. *CRC handbook of NDT of concrete.* Boca Raton, FL: CRC Press, 1991.

[72] G.G. Clemeña and C.M. Apusen. An alternative potentiometric method for determining chloride content in concrete samples from reinforced concrete bridges. Technical report, Virginia Transportation Research Council, 2002.

[73] K.S. Cole and R.H. Cole. Dispersion and Absorption in Dielectrics I. Alternating Current Characteristics. *Journal of Chemical Physics*, 9, 1941.

[74] C. Courtney, J. Lehr, D. Mason, B. Motil, and A. Lovesee. Measurement and Characterization of the Electromagnetic Properties of Materials. Technical report, Voss Scientific Technical Report No. VS-603, Albuquerque, 1996.

[75] R.N. Cox, R. Cigna, Ø. Vennesland, and T. Valente. COST 509, Corrosion and protection of metals in contact with concrete, Final Report. *EUR 17608 EN, 1997:148, Brussels*, 1997.

[76] J. Crank. *Mathematics of diffusion, 2nd Edition.* Clarendon Press, Oxford, 1975.

[77] J.M. Crow. The concrete conundrum. *Chemistry World*, 62, 2008.

[78] W. Czernin. *Cement chemistry and physics for civil engineers.* Chemical Pub. Co., New York, 1962.

[79] J.F. Daïan. Coefficients de stransfert: application des modèles et compraison avec les mesures. Technical report, Transferts dans les Bétons et Durabilités des Ouvrages (OA9). LTHE and LCPC, 1999.

[80] W. Daily, A. Ramirez, A. Binley, and S.Daily1994 Henry-Poulter. Electrical resistance tomography of concrete structures, ECAPT94: 3rd European concerted action meeting on process tomography, Lisbon (Portugal), 24-27 Mar 1994. 1994.

[81] D. J. Daniels. *Surface-penetrating radar - IEE Radar, Sonar, Navigation and Avionics Series 6*. London, The Institue of Electrical Engineers, 1996.

[82] H. Darcy. *Les Fontaines Publiques de la Ville de Dijon*. Dalmont, Paris, 1865.

[83] J.L. Davis and A.P. Annan. Ground-penetrating radar for high-resolution mapping of soil and rock stratigraphy. *Geophysical Prospecting*, 37:531–551, 1989.

[84] M.R. De Rooij, R.B. Polder, and H.H. Van Oosten. Validation of service life performance of in situ concrete by TEM and RCM measurements. *HERON*, 52:225–238, 2007.

[85] P. Debye. Polar Molecules. *Chemical Catalogue Company*, 1929.

[86] X. Dérobert, J. Iaquinta, G. Klysz, and J.-P. Balayssac. Use of capacitive and GPR techniques for the non-destructive evaluation of cover concrete. *NDT & E International*, 41(1):44 – 52, 2008.

[87] X. Dérobert, G. Villain, R. Cortas, and J.-L. Chazelas. EM characterization of hydraulic concretes in the GPR frequency band using a quadratic experimental design. *Proceedings of NDTCE09, Non-Destructive Testing in Civil Engineering*, Nantes, France, 30 June-3 July, 2009.

[88] M.B. Dobrin and C.H. Savit. *Introduction To Geophysical Prospecting*. McGraw-Hill International Editions, 1988.

[89] E.C. Donaldson and T.K. Siddiqui. Relationship Between the Archie Saturation Exponent and Wettability. *SPE Formation Evaluation*, 4:359–362, 1989.

[90] R. Du Plooy, A. Attari, C. McNally, M. Richardson, S. Palma Lopes, G. Villain, and X. Dérobert. Destructive and non-destructive condition assessment of a 100 year old concrete bridge. *Proceedings of DURABLE STRUCTURES: from construction to rehabilitation (ICDS12)*, pages 1–8, Lisbon Portugal, 31 May - 1 June, 2012.

[91] R. Du Plooy, S. Palma Lopes, G Villain, and X. Dérobert. Development of a multi-ring resistivity cell and multielectrode resistivity probe for investigation of cover concrete condition. *NDT & E International*, 54:27–36, 2013.

[92] R. Du Plooy, S. Palma Lopes, G. Villain, and X. Dérobert. Comparison of electromagnetic non-destructive evaluation techniques for the monitoring of chloride ingress in cover concrete. *Proceedings of the Sixth International IABMAS Conference*, pages 1–8, Stresa, Lake Maggiore, Italy, 8-12 July, 2012.

[93] R. Du Plooy, G. Villain, S. Palma Lopes, A. Ihamouten, X. Dérobert, and B. Thauvin. Electromagnetic non-destructive evaluation techniques for the monitoring of water and chloride ingress into concrete: a comparative study. *Materials and Structures (In Press)*, 2013.

[94] C. Edvardsen and M.T. Jepsen. Chloride migration coefficient from non-steady state migration. *Proceedings of the 2nd International RILEM Workshop, Testing and Modelling Chloride Ingress into Concrete (pro019)*, pages 203 – 209, Paris, France, 11-12 September, 2000.

[95] L.S. Edwards. A modified pseudosection for resistivity and induced-polarization. *Geophysics*, 42:1020–1036, 1977.

[96] M. Fares. Etude de modèles d'homogénéisation appliqués aux mesures non destructives électromagnétiques des constituants du béton en vue d'en déduire la teneur en eau. Master's thesis, Ecole Central, Université de Nantes, IFSTTAR, France, 2012.

[97] T. Fen-Chong, A. Fabbri, J.-P. Guilbaud, and O. Coussy. Determination of liquid water content and dielectric constant in porous media by the capacitive method. *C. R. Mecanique*, 332:639–645, 2004.

[98] R.M. Ferreira and S. Jalali. NDT measurements for the prediction of 28-day compressive strength. *NDT & E International*, 43(2):55 – 61, 2010.

[99] A. Fick. Poggendorffs Annalen. *Philosophical Magazine*, 10:30–39, 1855.

[100] R.A. Fisher. The Arrangement of Field Experiments. *Journal of the Ministry of Agriculture of Great Britain*, 33:503–513, 1926.

[101] R.A. Fisher. *The design of experiments*. Oliver and Boyd, 1935.

[102] G. Frankel. *ASM Handbook, Volume 13A, Corrosion: Fundamentals, Testing, and Protection*. ASM International, 10 edition, 2003.

[103] H. Fricke. The Electric Conductivity and Capacity of Disperse Systems. *Physics*, 1:106, 1933.

[104] B.D. Fuller and S.H. Ward. Linear System Description of the Electrical Parameters of Rocks. *IEEE Transactions on Geoscience Electronics*, 8:7–18, 1970.

[105] D. Fylstra, L. Lasdon, J. Watson, and A. Warren. Design and Use of the Microsoft Excel Solver. *INTERFACES*, 28:29–55.

[106] E.J. Garboczi. Permeability, diffusivity and microstructural parameters, a critical review. *Cement and Concrete Composites*, 20:591–601, 1990.

[107] O.E. Gjørv. *Durability Design of Concrete Structures in Severe Environments*. Taylor & Francis Group, 2009.

[108] O.E. Gjørv, Ø. Vennesland, and A.H.S. El-Busiady. Electrical Resistivity of Concrete in the Oceans. *9th Annual Offshore Technology Conference, Houston, Texas*, pages 581–588, 1977.

[109] G.K. Glass, B. Reddy, and N.R. Buenfeld. The participation of bound chloride in passive in breakdown on steel in concrete. *Corrosion Science*, 42:2013–2021, 2000.

[110] P.W.J. Glover. A generalized Archies law for n phases. *Geophysics*, 75:247–265, 2010.

[111] P.W.J. Glover, M.J. Hole, and J. Pous. A modified Archie's law for two conducting phases. *Earth and Planetary Science*, 180:369 to 383, 2000.

[112] J. Goupy and L. Creighton. *Introduction to Design of Experiments*. SAS Institute Inc, 2007.

[113] K.R. Gowers and S.G. Millard. Measurement of Concrete Resistivity for Assessment of Corrosion Severity of Steel Using Wenner Technique. *ACI Materials Journal*, 96:536–542, 1999.

[114] R. Greaves. Velocity variations and water content estimated from multi-offset, ground-penetrating radar. *Geophysics*, 61:83–695, 1996.

[115] U.B. Halabe, K. Maser, and E. Kausel. Propagation characteristics of electromagnetic waves in concrete. Technical report, U.S. Army Office, 1988.

[116] C. Hall. Water sorptivity of mortars and concrete - a review. *Magazine of Concrete Research*, 41:51–61, 1989.

[117] E. Hammond and T.D. Robson. Comparison of Electrical Properties of Various Cements and Concretes. *The Engineer*, 199:78–80, 1955.

[118] N. Han. Role of NDE in quality control during construction of concrete infrastructures on the basis of service life design. *Construction and Building Materials*, 18:163–172, 2004.

[119] T. Hanai. Theory of the dielectric dispersion due to the interfacial polarization and its application to emulsions. *Colloid & Polymer Science*, 171:23–31, 1960. 10.1007/BF01520320.

[120] I.L.H. Hansson and C.M. Hansson. Electrical Resistivity Measurements of Portland Cement Based Materials. *Cement and Concrete Research*, 13:675–683, 1983.

[121] C.J. Hauck. *The Effect of Curing Temperature and Silica Fume on Chloride Migration and Pore Structure of High Strength Concrete*. PhD thesis, Doctoral Dissertation, Norges Tekniske Hgskole (NTH), University of Trondheim, Norway, 1993.

[122] R.L. Henry. Water vapour transmission and electrical resistivity of concrete. *Final Report, U.S. Naval Civil Engineering Laboratory, Port Hueneme, California*, 1964.

[123] P.C. Hewlett. *LEA's Chemistry of Cement and Concrete, 4th Ed.* Elsevier Science & Technology Books, 2004.

[124] J.P. Hoffmann. *Linear Regression Analysis: Applications and Assumptions*. Department of Sociology Brigham Young University, 2010.

[125] F. Hollender and S. Tillard. Modelling GPR wave propagation and reflection with Jonscher parametrization. *Geophysics*, 63, 1998.

[126] B.B. Hope and A.K. Ip. Corrosion of Steel in Concrete Made with Slag Cement. *ACI Materials Journal*, 84:525–531, 1987.

[127] B.B. Hope, A.K. Ip, and D.G. Manning. Corrosion and electrical impedance in concrete. *Cement and Concrete Research*, 15(3):525–534, 1985.

[128] T.-C. Hou and J.P. Lynch. Tomographic imaging of crack damage in cementitious structural components. *4th International conference on earthquake engineering, Taipei, Taiwan, 12-13 October*, 2006.

[129] J. Hugenschmidt and R. Loser. Detection of chlorides and moisture in concrete structures with ground penetrating radar. *Materials and Structures*, 41:785–792, 2008.

[130] B.P. Hughes, A.K.O. Soleit, and R.W. Brierly. New Technique for Determining the Electrical Resistivity of Concrete. *Magazine of Concrete Research*, 37:243–248, 1985.

[131] F. Hunkeler. The resistivity of pore water solution - a decisive parameter of rebar corrosion and repair methods. *Construction and Building Materials*, 10(5):381–389, 1996. Durability of Reinforced Concrete Structures.

[132] A. Ihamouten. *Caractrisation physique et hydrique de btons d'ouvrage par propagation d'ondes lectromagnetique*. PhD thesis, Universit de Nantes, Ecole Doctorale Science et Technologies de I'information et Mathmatiques., 2011.

[133] A. Ihamouten, K. Chahine, V. Baltazart, G. Villain, and X. Dérobert. On variants of the frequency power law for the electromagnetic characterization of hydraulic concrete. *Instrumentation and Measurement, IEEE Transactions on*, 60:3658–3668, 2011.

[134] A. Ihamouten, X. Dérobert, and G. Villain. Extraction of the frequency variation of the complex permittivity using GPR. *6th International Workshop on Advanced, Ground-Penetrating Radar (GPR), Aachen, Germany*, pages 144–149, 2011.

[135] T. Ishida, S. Miyahara, and T. Maruya. Chloride binding capacity of mortars made with various portland cements and mineral admixture. *Journal of Advanced Concrete Technology*, 6:287–301, 2008.

[136] F. Jacobs, M. Basheer, and C. Andrade. Chapter 6: Effect of Moisture and Temperature on Non-Destructive Penetrability Tests. *Non-Destructive Evaluation of the Penetrability and Thickness of Concrete Cover; RILEM TC 189-NEC: State of the Art Report*, 2007.

[137] A. Jonscher. The 'universal' dielectric response. *Nature*, 267:673–679.

[138] A. Kalogeropoulos, J. Van der Kruk, J. Hugenschmidt, S. Busch, and K. Merz. Chlorides and moisture assessment in concrete by GPR full waveform inversion. *Near Surface Geophysics*, 9:277–285, 2011.

[139] K. Karhunen, A. Seppänen, A. Lehikoinen, and J.P. Kaipio. Locating reinforcing bars in concrete with Electrical Resistance Tomography. *Concrete Repair, Rehabilitation and Retrofitting II - Alexander et al (eds), Taylor & Francis Group, London, ISBN 978-0-415-46850-3*, 2009.

[140] T.J. Katsube. Review of formation resistivity factor equations related to new pore structure concepts. *Geological survay of Canada: Current research*, page 9 p., 2010.

[141] G.V. Keller. *Handbook of Physical Properties of Rocks, Vol. I.* CRC Press, Boca Raton, Florida, 1982.

[142] C.T. Kelley. *Iterative Methods for Linear and Nonlinear Equations*. Society for Industrial and Applied Mathematics, Philadelphia, 1995.

[143] R.J. Kessler, R.G. Powers, E. Vivas, M.A. Paredes, and Y.P. Virmani. Surface resistivity as an indicator of concrete chloride penetration resistance. Technical report, Florida Department of Transportation, 2008.

[144] A. Khelidj, G. Bastian, V. Baroghel-Bouny, and G. Villain. Experimental study of the evolution of heat and moisture transfer parameters of a concrete slab. *Magazine of Concrete Research*, 59:377–386, 2007.

[145] S. Kim, J. Surek, and J. Baker-Jarvis. Electromagnetic Metrology on Concrete and Corrosion. *Journal of Research of the National Institute of Standards and Technology*, 116:655–669, 2011.

[146] J. Kiusalaas. *Numerical Methods in Engineering with Matlab™*. Cambridge University Press, 2005.

[147] G. Klysz and J.-P. Balayssac. Determination of volumetric water content of concrete using ground-penetrating radar. *Cement and Concrete Research*, 37:1164–1171, 2007.

[148] G. Klysz, X. Ferrieres, J.P. Balayssac, and S. Laurens. Simulation of direct wave propagation by numerical FDTD for a GPR coupled antenna. *NDT & E International*, 39(4):338 – 347, 2006.

[149] M.D. Knoll. *A petrophysical basis for ground penetrating radar and early time electromagnetics: Electrical properties of sand-clay mixtures*. PhD thesis, University of British Columbia, 1996.

[150] J.D. Kraus and K.R. Carver. *Electromagnetics*. McGraw-Hill, 1973.

[151] J. Kropp and M. Alexander. Non-Destructive Evaluation of the Penetrability and Thickness of Concrete Cover Chapter 2: Transport Mechanisms and Reference Tests, RILEM Report 040. *RILEM TC 189-NEC: State of the Art Report*, pages 13–34, 2007.

[152] J. Kropp and H. Hilsdorf. *Performance Criteria for Concrete Durability, RILEM Report No. 12*. F&N Spon, London, 1995.

[153] Laird Technologies, `www.lairdtech.com`. *Product Brochure: Metallized Conductive Products*.

[154] C.K. Larsen, E.J. Sellevold, F. Askeland, J.-M. Østvik, and Ø. Vennesland. Electrical resistivity of concrete Part II: Influence of moisture content and temperature. *2nd International Symposium on Advances in Concrete through Science and Engineering 11-13 September 2006, Quebec City, Canada*, 2006.

[155] J.F. Lataste, C. Sirieix, D. Breysse, and M. Frappa. Improvement of electrical resistivity measurement for non destructive evaluation of concrete structures. *Life Prediction and Aging Management of Concrete Structures*, 2004.

[156] S. Laurens, J. Balayssac, J. Rhazi, and G. Arliguie. Influence of concrete relative humidity on the amplitude of Ground-Penetrating radar (GPR) signal. *Materials and Structures*, 35(4):198–203, 2002.

[157] H.P. Leckie and H.H. Uhlig. Environmental Factors Affecting the Critical Potential for Pitting in 18 - 8 Stainless Steel. *Journal of The Electrochemical Society*, 113:1262–1267, 1966.

[158] K. Lichtenecker and K. Rother. Die Herlritung Des Logarithmischen Mischungsgesetzes aus Allgemeinen Prinzipien der Stationaren Stromung. *Physics Zeitschrift*, 39:255–260, 1931.

[159] T.S. Light, S. Licht, A.C. Bevilacqua, and K.R. Morashc. Fundamental Conductivity and Resistivity of Water. *Electrochemical and Solid-State Letters*, 8:E16–E19, 2005.

[160] R. Linder. *Les Plans D'Expériences: Un outil indispensable á l'expérimentateur*. Presses de l'école national des ponts et chasses, 2005.

[161] L.R. Lines and S. Treitel. Tutorial : A review of least-squares inversion and its application to geophysical problems. *Geophysical Prospecting*, 32:159–186., 1984.

[162] Y. Liu, A. Suarez, and F.J. Presuel-Moreno. Characterization of New and Old Concrete Structures Using Surface Resistivity Measurements. page 263, 2010.

[163] M.H. Loke. *Tutorial : 2-D and 3-D electrical imaging surveys*. Geotomo Software, 27th January 2010.

[164] M.H. Loke and R.D; Barker. Rapid least-squares inversion of apparent resistivity pseudosections by a quasi-Newton method. *Geophysical Prospecting*, 44:131–152, 1996.

[165] P. Longuet, L. Burglen, and A. Zelwer. La phase liquide du ciment hydraté. *Revue des Matériaux de Construction et des Travaux Publics*, Publication CERILH No 219, 676:35–41, 1973.

[166] W. Lopez and J.A. Gonzalez. Influence of the degree of pore saturation on the resistivity of concrete and the corrosion rate of steel reinforcement. *Cement and Concrete Research*, 23(2):368–376, 1993.

[167] X. Lu. Application of the Nernst-Einstein equation to concrete. *Cement and Concrete Research*, 27(2):293–302, 1997.

[168] T. Lundstedt, E. Seifert, L. Abramo, B. Thelin, A. Nyström, J. Pettersen, and R. Bergman. Experimental design and optimization. *Chemometrics and Intelligent Laboratory Systems*, 42:3–40, 1998.

[169] T. Luping. Chlortest - Guideline for the practical use of methods for testing the resistance of concrete to chloride ingress. Technical report, EU Funded research project under 5FP GROWTH Programme, 2005.

[170] T. Luping and L. Nilsson. Chloride binding capacity and binding isotherms of OPC pastes and mortars. *Cement and Concrete Research*, 23(2):247 – 253, 1993.

[171] C. Maierhofer and S. Leipold. Radar investigation of masonry structures. *NDT & E International*, 34(2):139 – 147, 2001.

[172] V.M. Malhotra and N.J. Carino. *Handbook on Nondestructive Testing of Concrete*. CRC Press, 2004.

[173] D.G. Manning and F.B. Holt. Detecting Deterioration in Asphalt-Covered Bridge Decks. *Transportation Research Board Record No. 899*, 1984.

[174] L. Marescot, S. Rigobert, S. Palma Lopes, R. Lagabrielle, and D. Chapellier. A general approach for DC apparent resistivity evaluation on arbitrarily shaped 3D structures. *Journal of Applied Geophysics*, 60(1):55–67, September 2006.

[175] A. Martinez and A.P. Byrnes. Modeling Dielectric-constant values of Geologic Materials: An Aid to Ground-Penetrating Radar Data Collection and Interpretation. *Current Research in Earth Sciences, Bulletin 247*, 2001.

[176] T.O. Mason, S.J. Ford, J.D. Shane, J.-H. Hwang, and D.D. Edwards. Experimental limitations in impedance spectroscopy of cement-based materials. *Advances in Cement Research*, 10:143–150, 1998.

[177] G.C. Mays. *Durability of Concrete Structures: Investigation, repair, protection*. E & FN Spon, London, 1992.

[178] D.M. McCann and M.C. Forde. Review of NDT methods in the assessment of concrete and masonry structures. *NDT & E International*, 34(2):71–84, 2001.

[179] W.J. McCarter. A parametric study of the impedance characteristics of cement-aggregate systems during early hydration. *Cement & Concrete Composites*, 24:1097–1110, 1994.

[180] W.J. McCarter, T.M. Chrisp, A. Butler, and P.A.M. Basheer. Near-surface sensors for condition monitoring of cover-zone concrete. *Construction and Building Materials*, 15(2-3):115 – 124, 2001.

[181] W.J. McCarter, M.C. Forde, and H. W. Whittington. Resistivity characteristics of concrete. *Proc. Inst. Civ. Engs.*, Part 2:107–117, 1981.

[182] P.R. McGillivray and D.W. Oldenburg. Methods for calculating Frechet derivatives and sensitivities for the non-linear inverse problem : A comparative study. *Geophysical Prospecting*, 38:499–524, 1990.

[183] C. McNally, M. Richardson, C. Evans, and T. Callanan. Chloride diffusion coeficient determination for specifications. *Proceedings of the 6^{th} International Congress on Global Construction*, Dundee, Scotland, UK, 5-7 July, 2005.

[184] J.D. McNeill. Electrical Conductivity of Soils and Rocks, Technical Note TN-5. Technical report, Geonics Ltd., Mississauga, Ontario, Canada, 1980., 1980.

[185] J.D. McNeill. Electrical Conductivity of Soils and Rocks, Technical Note TN-5. *Geonics Ltd., Mississauga, Ontario, Canada*, 1980.

[186] P.K. Mehta. Durability - critical issues for the future. *Concrete International*, pages 27–33, 1997.

[187] P.K. Mehta and R.W. Burrows. Building durable structures in the 21st century. *Concrete International*, 23:57–63, 2001.

[188] W. Menke. *Geophysical Data Analysis: Discrete Inverse Theory*. Academic Press, London, 1989.

[189] L.B. Mercer. Permeability of concrete - 1: theoretical considerations, laboratory methods, details of experimental work with new apparatus. *The Common Wealth Engineer*, pages 349–57, 1945.

[190] S. G. Millard. Discussion on Paper 9674: Reinforced concrete resistivity measurement techniques. *Proc. Instn Civ. Engrs*, Part 2:895–898, 1991.

[191] G.E. Monfore. The Electrical Resisitivity of Concrete. *Journal of the PCA Research and Development Laboratories*, 10:35–48, 1968.

[192] H.F. Montemor, A.M.P. Simoes, and M.G.S. Ferreira. Chloride-induced corrosion on reinforcing steel: from the fundamentals to the monitoring techniques. *Cement & Concrete Composites*, 25:491–502, 2003.

[193] D.C. Montgomery. *Design and Analysis of Experiments*. Wiley, 2000.

[194] R. Morelli and M.C. Forde. Electrical Conduction Through Concrete Using Formation Factor Theories. *Proceedings of the International Conference on Structural Faults and Repair*, pages 411–422, London, 7-9 July, 1987.

[195] W. Morris, E.I. Moreno, and A.A. Sagüès. Practical evaluation of resistivity of concrete in test cylinders using a Wenner array probe. *Cement and Concrete Research*, 26(12):1779 – 1787, 1996.

[196] V.N.S. Murphy. *Geotechnical Engineering: Principles and Practices of Soil Mechanics and Foundation Engineering*. Marcel Dekker, New York, 2002.

[197] M.N. Nabighian. *Electromagnetic Methods Vol.1: Theory (Investigations in Geophysics Series No. 3)*. Society Of Exploration Geophysicists, 1988.

[198] Weiss J Olek J. Neithalath, N. Characterizing Enhanced Porosity Concrete using Electrical Impedance to Predict Acoustic and Hydraulic Performance. *Cement and Concrete Research*, in press, 2006.

[199] Weiss J. Olek J. Neithalath, N. Predicting the Permeability of Pervious Concrete (Enhanced Porosity Concrete) from Non-Destructive Electrical Measurements. 2011.

[200] A. Neville. Maintenance and durability of structures. *Concrete International*, pages 52–56, 2001.

[201] A.M. Neville. *Properties of Concrete*. Pearson Education Ltd., Harlow, 5th edition edition, 2011.

[202] A.M Neville and J.J. Brooks. *Concrete Technology (Second Edition)*. Pearson Education Ltd., Harlow, 2010.

[203] M. Newlands, M. Jones, S. Kandasami, and T. Harrison. Sensitivity of electrode contact solutions and contact pressure in assessing electrical resistivity of concrete. *Materials and Structures*, 41:621–632, 2008. 10.1617/s11527-007-9257-6.

[204] R. Newman. Pitting Corrosion of Metals. *The Electrochemical Society Interface*, pages 33–38, 2010.

[205] P. Nikkanen. On the Electrical Properties of Concrete and Their Applications. *Vaftion Tebsilliren Tutkirndaitos, Tiedotus, Sarja III, Rakennus*, 60:75, 1962.

[206] L.O. Nilsson, E. Poulsen, P. Sandberg, H.E. Sørensen, and O. Klinghoffer. Chloride penetration into concrete, State-of-the-art, transport processes, corrosion initiation, test methods and prediction models, The Report No. 53. Technical report, HETEK, Road Directorate, Copenhagen, 1996.

[207] http://www.itl.nist.gov/div898/handbook/ NIST/SEMATECH e-Handbook of Statistical Methods, editor. *The Engineering Statistics Handbook*. 2003.

[208] G.R. Olhoeft. Electrical Properties of Rocks. *In, Physical Properties of Rocks and Minerals, Y. S. Touloukian, W. R. Judd, and R. F. Roy, eds.: New York, New York, Hemisphere Publishing Corporation*, pages 257–329, 1989.

[209] J.-M. Østvik, C.K. Larsen, Ø. Vennesland, E.J. Sellevold, and M.C. Andrade. Electrical resistivity of concrete - Part I: Frequency dependence at various moisture contents and temperatures. *2nd International Symposium on Advances in Concrete through Science and Engineering, Quebec City, Canada, September 11-13*, 2006.

[210] M. Otieno, M. Alexander, and H. Beushausen. Transport mechanisms in concrete, Corrosion of steel in concrete, Assessment of corrosion. 2010.

[211] D.S. Parasnis. *Principles of Applied Geophysics*. Chapman & Hall, London, New York, 1986.

[212] M.A. Ploix, V. Garnier, D. Breysse, and J. Moysan. NDE data fusion to improve the elvaluation of concrete structures. *NDT & E International*, 44:442–448, 2011.

[213] M.A. Ploix, V. Garnier, D. Breysse, and J. Moysan. Possibilistic NDT data fusion for evaluating concrete structures. *Proceedings of NDTCE09, Non-Destructive Testing in Civil Engineering*, Nantes, France, 30 June-3 July, 2009.

[214] R.B. Polder. Test methods for on site measurement of resistivity of concrete - a RILEM TC-154 technical recommendation. *Construction and Building Materials*, 15(2-3):125–131, March 2001.

[215] R.B. Polder. Chloride diffusion and resistivity testing of five concrete mixes for marine environment. *Proceedings of the 1st RILEM workshop on Chloride Penetration into Concrete*, St Rémy lès Chevreuse, France, 15-18 October, 1995.

[216] W.H. Press, B.P. Flanner, S.A. Teukolsky, and W.T. Vetterling. *Numerical Recipes: The Art of Scientific Computing (3rd Ed.)*. Cambridge University Press, Cambridge, 2007.

[217] F. Presuel-Moreno and W.H. Hartt. Protection of reinforced concrete bridge substructures using submerged bulk anodes. Technical report, Florida Departmetn of Transportation, 2009.

[218] E. Rasch and F.W. Hinrichsen. Uber eine Beziehung zwischen Elektrischer Leitfahigkeit und Temperatur. *Zeitschrift fur Electrochemie*, 14:41–48, 1908.

[219] Report rep031 : Advanced Testing of Cement-Based Materials during Setting and Hardening Final Report of RILEM TC 185-ATC. Reinhardt, H.W. and Grosse, C.U. ed. Technical report, RILEM, 2005.

[220] A. Revil. Effective conductivity and permittivity of unsaturated porous materials in the frequency range 1 mHz - 1GHz. *Water Resources Research*, 49:1–22, 2013.

[221] H.C. Rhim and O. Buyukozturk. Electromagnetic Properties of Concrete at Microwave Frequency Range. *Materials Journal*, 95:262–271, 1998.

[222] K.A. Riding, J.L. Poole, A.K. Schindler, M.C.G. Juenger, and K.J. Folliard. Simplified Concrete Resistivity and Rapid Chloride Permeability Test Method. *ACI Materials Journal*, pages 390–394, 2008.

[223] A. Robert. Dielectric permittivity of concrete between 50 MHz and 1 GHz and GPR measurements for building materials evaluation. *Journal of Applied Geophysics*, 40(1-3):89–94, 1998.

[224] S. Rostam. Service life design of concrete structures - a challenge to designers as well as to owners. *Asian Journal of Civil Engineering (Building and Housing)*, 6:423–445, 2005.

[225] K. Roth, R. Schulin, H. Fluhler, and W. Attinger. Calibration of time domain reflectometry for water content measurement using a composite dielectric approach. *Water Resources Research*, 26:2267–2273, 1990.

[226] A. Roy and A. Apparao. Depth of investigation in direct current methods. *Geophysics*, 36:943–959, 1971.

[227] K. Ruane and A. Healy. Assessment testing Mizen Head footbridge. *Bridge Engineering*, BE3:117–122, 2004.

[228] T. Rupnow and P. Icenogle. Surface Resistivity Measurements for Quality Assurance Pave the Way to Savings in Louisiana. *TR NEWS*, 279:46–47, 2012.

[229] T.D. Rupnow and P. Icenogle. Evaluation of surface resistivity measurements as an alternative to the rapid chloride permeability test for quality assurance and acceptance, Baton Rouge, LA, 2011, pp. 68. Technical report, Louisiana Department of Transportation, 2011.

[230] A.A. Sagüès and K. Lau. Corrosion Evaluation with bridges with epoxy coated rebar. Contract no BD544-23, Final Report. Technical report, Florida Department of Transportation, 2009.

[231] M. Saleem, M. Shameem, S.E. Hussain, and M. Maslehuddin. Effect of moisture, chloride and sulphate contamination on the electrical resistivity of Portland cement concrete. *Construction and Building Materials*, 10(3):209 – 214, 1996.

[232] E. Sanchez-Palencia. *Non-Homogeneous Media and Vibration Theory: Lecture Notes in Physics, Volume 127.* Springer-Verlag, 1980.

[233] J.L. Saussol, S. Chataigner, X. Dérobert, G Villain, and C. Aubagnac. Influence de la temprature sur les mesures lectromagntiques de la teneur en eau du bton. *Internal report IFSTTAR, Paris*, pages 1–14, 2013.

[234] Z.-M. Sbartaï, D. Breysse, M. Larget, and J.-P. Balayssac. Combining NDT techniques for improved evaluation of concrete properties. *Cement & Concrete Composites*, 34:725–733, 2012.

[235] Z.M. Sbartaï and V. Garnier. Decision making for concrete evaluation usig fusion of NDT techniques. *Proceedings of DURABLE STRUCTURES: from construction to rehabilitation (ICDS12)*, pages 1–6, Lisbon Portugal, 31 May-1 June, 2012.

[236] Z.M. Sbartaï, S. Laurens, J.-P. Balayssac, G. Arliguie, and G. Ballivy. Ability of the direct wave of radar ground-coupled antenna for NDT of concrete structures. *NDT & E International*, 39(5):400–407, 2006.

[237] Z.M. Sbartaï, S. Laurens, J. Rhazi, J.P. Balayssac, and G. Arliguie. Using radar direct wave for concrete condition assessment: Correlation with electrical resistivity. *Journal of Applied Geophysics*, 62(4):361–374, 2007.

[238] P. Schiessl. *Corrosion of steel in concrete, report of RILEM report Technical Committee 60-CSC.* Chapman & Hall, London, 1988.

[239] P. Schiessl. New approach to service life design of concrete structure. *Asian Journal of Civil Engineering (Building and Housing)*, 6, 2005.

[240] J.H. Schon. *The Electrical Properties of Rocks, In: Physical Properties of Rocks: Fundamentals and Principles of Petrophysics*. Pergamon Pr, 1996.

[241] T. Sedran and F. deLarrard. BétonlabPro, software for concrete mix design. `IFSTTAR,http://www.lcpc.fr/betonlabpro/.` 2000.

[242] P.N. Sen, C. Scala, and M.H. Cohen. A self-similar model for sedimentary rocks with application to the dielectric constant of fused glass beads. *Geophysics*, 46:781–795, 1981.

[243] 0. Sengul and O.E. Gjørv. Electrical Resistivity Measurements for Quality Control During Concrete Construction. *Materials Journal*, 105:541–547, 2008.

[244] A. Seppänen. Electrical Resistance Tomography Imaging of Concrete. *Concrete Repair, Rehabilitation and Retrofitting II Alexander et al (eds), Taylor & Francis Group, London, ISBN 978-0-415-46850-3*, 2009.

[245] A. Sihvola. *Electromagnetic Mixing Formulas and Applications*. London, U.K.: IEE, 1999.

[246] P.P. Silvester and R.L. Ferrari. *Finite elements for electrical engineers*. Cambridge University Press, 1990.

[247] C. Sirieix, J.-F. Lataste, D. Breysse, S. Naar, and X. Dérobert. Comparison of nondestructive testing: Infrared thermography, electrical resisitivity and capacity methods for assessing a reinforced concrete structure. *Journal of Building Appraisal*, 3:77–88, 2007.

[248] K.A. Snyder, C. Ferraris, N.S. Martys, and Garboczi E.J. Using Impedance Spectroscopy to Assess the Viability of the Rapid Chloride Test for Determining Concrete Conductivity. *Journal of Research of the National Institute of Standards and Technology*, 105:497–509, 2000.

[249] M.N. Soutsos, J.H. Bungey, S.G. Millard, M.R. Shaw, and A. Patterson. Dielectric properties of concrete and their influence on radar testing. *NDT & E International*, 34(6):419 – 425, 2001.

[250] R.P. Spragg, J. Castro, T.E. Nantung, M. Paredes, and W.J. Weiss. Variability Analysis of the Bulk Resistivity Measured Using Concrete Cylinders. Technical report, Publication FHWA/IN/JTRP-2011/21. Joint Transportation Research Program, Indiana Department of Transportation and Purdue University, West Lafayette, Indiana, 2011. doi: 10.5703/1288284314646, 2011.

[251] K. Stanish, R.D. Hooton, and M.D.A. Thomas. Testing the Chloride Penetration Resistance of Concrete: A Literature Review. *Department of Civil Engineering University of Toronto, Ontario, Canada. FHWA Contract DTFH61-97-R 00022*, 1997.

[252] J.A. Stratton. *Electromagnetic Theory*. Mcgraw-Hill College, 1941.

[253] J.-K. Su, C.-C. Yang, W.-B. Wu, and R. Huang. Effect of moisture content on concrete resistivity measurement. *Journal of the Chinese Institute of Engineers*, 25:117–122, 2002.

[254] D.M. Suchorski. *Aggregates for Concrete*. ACI Education Bulletin E1-07, American Concrete Institute, 2007.

[255] L. Tang and L.O. Nilsson. Chloride diffusivity in high strength concrete at different ages. *Nordic Concrete Research*, 11:162–170, 1992.

[256] L. Tang and L.O. Nilsson. Rapid determination of the chloride diffusivity in concrete by applying an electrical field. *ACI Materials Journal*, 89:49–53, 1992.

[257] L. Tang and L.O. Nilsson. Ionic migration and its relation to diffusion. *In: Hooton RD, Thomas MDA, Marchand J, Beaudoin JJ, editors. Skalny JP, series editor. Materials science of concrete, special vol.: Ion and mass transport in cementbased materials. Am Ceram Soc, Westerville*, pages 81–96, 2001.

[258] W.M. Telford, L.P. Geldart, and R.E. Sheriff. *Applied Geophysics.* Cambridge University Press, 1990.

[259] M. Thiéry. *Modélisation de la carbonatation atmosphérique des matériaux cimentaires - Prise en compte des effets cinétiques et des modifications microstructurales et hydrique.* PhD thesis, Doctoral thesis ENPC, LCPC, Paris, 2005, 333p.

[260] M.D.A. Thomas and M.R. Jone. *A critical review of service life modelling of concretes exposed to chlorides, Concrete in service of mankind: Radical Concrete Technology.* F.N Spon, London, 1996.

[261] A.N. Tikhonov and V.Y. Arsenin. *Solutions of ill-posed problems.* Washington: Winston and Sons, 1977.

[262] J.M. Tobio. A Study of the Setting Process. Dielectric Behaviour of Several Spanish Cements. *Silicates Industrials*, 24:30–35, 1959.

[263] N. Tran and R. Ambrosino. Mésure de la teneur en eau des sols et des matriaux par une mthode capacitive: 3 - applications de la méthode capacitive de mesure de la teneur en eau. *Bulletin des Ponts et Chausses*, 60:173–175, 1972.

[264] P.J. Tumidajski, A.S. Schumacher, S. Perron, P. Gu, and J.J. Beaudoin. On the relationship between porosity and electrical resistivity in cementitious systems. *Cement and Concrete Research*, 26(4):539 – 544, 1996.

[265] K. Tutti. Corrosion of steel in Concrete. *Research Report 4.82, Swedish Cement and. Concrete Research Institute, Stockholm*, 1982.

[266] M. Uematso and E.U. Franck. Static Dielectric Constant of Water and Steam. *Journal of Physical and Chemical Reference Data*, 9:1291–1305, 1980.

[267] C.P. Ulricksen. *Application of Impulse Radar to Civil Engineering.* PhD thesis, Doctoral Thesis, Lund University, Dept. of Engineering Geology, Sweden, 1982.

[268] B. van de Steen, B. Wuytens, A. Vervoort, and D. van Gemert. Evaluation of mineral building materials: Problems related to resistivity methods. *Materials and Structures/Matériaux et Constructions*, 31:126–132, 1998.

[269] J. Van der Kruk. Fundamental and Higher Mode Inversion of Dispersed GPR Waves Propagating in an Ice Layer. *IEEE Transactions on Geoscience and Remote Sensing*, 45, 2007.

[270] J. Van der Kruk, R. Streich, and A. Green. Properties of surface waveguides derived from separate and joint inversion of dispersive TE and TM GPR data. *Geophysics*, 71:K19–K29, 2006.

[271] G. Villain. Résultats de mesures non destructives réalisés sur des poutres réparés et exposées á un marnage naturel, Rapport No. 10 V0, Projet FUI-MAREO. pages 1–19.

[272] G. Villain. *Vers une évaluation des indicateurs de durabilité du béton pour le suivi de ses dégradations en laboratoire et sur ouvrage.* Ouvrages d'art OA 70, IFSTTAR, Paris, 2012.

[273] G. Villain, X. Dérobert, Z.M. Sbartaï, and J.-P. Balayssac. Evaluation of concrete water content and other durability indicators by electromagnetic measurements. *Proceedings of the 13th International Conference on Ground Penetrating Radar (GPR)*, Lecce, Italy, 21-25 June, 2010.

[274] G. Villain, A. Ihamouten, and X. Drobert. Use of Frequency Power Law to Link the Results of Two EM Testing Methods for the Characterization of Humid Concrete. *In: 6th International Workshop on Advanced Ground Penetrating Radar (IWAGPR), 22-24 June 2011, Aachen, Germany*, pages 1 – 5, 2011.

[275] G. Villain, A. Ihamouten, X. Drobert, T. Sedran, O. Burban, O. Coffec, M. Dauvergne, J. Alexandre, L.M. Cottineau, L. Le Marrec, and M. Thiéry. Adapted mix design and characterisation for non destructive assessment of concrete. *In: Prodeecings of the 2nd International Conference Marine Environment Damage to Coastal and Historical Structures (MEDACHS), 28-30 April 2010, La Rochelle, France*, 2010.

[276] G. Villain, Z. Sbartaï, X. Dérobert, V. Garnier, and J.-P. Balayssac. Durability diagnosis of a concrete structure in a tidal zone by combining NDT methods: laboratory tests and case study. *Construction and Building Materials*, 37:893–903, 2012.

[277] G. Villain and M. Thiéry. Impact of carbonation on microstructure and transport properties of concrete. *Proceedings of the 10^{th} international conference on Durability of Building Materials and Components*, pages 1–8, Lyon, France, 17-20 May, 2005.

[278] G. Villain and T. Thiery. Gammadensimetry: A method to determine drying and carbonation profiles in concrete. *NDT & E International*, 39:328–337, 2006.

[279] R.J. Wagner, R.W. Boulger Jr, C.J. Oblinger, and B.A. Smith. *Guidelines and Standard Procedures for Continuous Water-Quality Monitors: Station Operation, Record Computation, and Data Reporting.* U.S. Department of the Interior, U.S. Geological Survey, 2006.

[280] P.J. Wainwright and H. Ait-Aider. The influence of cement source and slag additions on the bleeding of concrete. *Cement and Concrete Research*, 25:1445–1456, 1995.

[281] F. Wenner. A method for measuring earth resistivity. *Bureau of Standards*, 12:469–478, 1915.

[282] R. Weydert and C. Gehlen. *Electrolytic Resistivity of Cover Concrete, Relevance, Measurement and Interpretation.* Proceedings of 8th Conference on Service Life and Durability of Materials and Components, Vancouver, Canada, 30 May-3 June, 1999.

[283] D.A. Whiting and M.A. Nagi. Electrical resistivity of concrete - literature review. *Portland Cement Association, R & D Serial no. 2457*, page 57, 2003.

[284] H.W. Whittington, J. McCarter, and M.C. Ford. The conduction of electricity through concrete. *Magazine of Concrete Research*, 33:114, 1981.

[285] Y. Xi and Z.P. Bazant. Modeling chloride penetration in saturated concrete. *Journal Of Materials in Civil Engineering*, 58, 1999.

[286] H. Yang and H. Wong. Microstructure and Electromagnetic Properties of $SrTiO_3/Ni_{0.8}Zn_{0.2}Fe_2O_4$ Composites by Hybrid Process. *POE composites for RF applications, http://www.paper.edu.cn/index.php/default/en_releasepaper/downPaper/200906-503*, pages 1–11, 2009.

[287] J.J. Yoho. Design and Calibration of a RF Capacitance Probe for Non-Destructive Evaluation of Civil Structures. Master's thesis, Virginia Polytechnic Institute and State University, 1998.

[288] H. Zhao and D. Darwin. Quantitative backscattered electron analysis of cement paste. *Cement and Concrete Research*, 22:695–706, 1992.

Appendix A

Test methods for chloride content and chloride diffusion coefficient

A.1 Proposed potentiometric-AFREM method to determine the free and total chloride content of concrete

1. Scope

The method detailed here is a combination of the potentiometric method to determine total chloride content using internal calibration proposed by Clemeña and Apusen [72] and the AFREM procedure [59] to determine free and total chlorides.

2. Reagents

2.1 Distilled water.

2.2 Standard 1 M NaCl solution.

2.3 53% nitric acid solution.

2.4 Ionic strength adjuster (5 M sodium nitrate solution).

3. Apparatus

3.1 pH/mV meter, with accuracy of ±0.1 mV and resolution of 0.1 mV.

3.2 Combination chloride-ion selective electrode and temperature compensation probe, compatible with the pH/mV meter.

3.3 Scale sensitive to 0.0001 gram with a minimum capacity of 100 grams.

3.4 An adjustable-volume digital pipette, with a range of 0.200 to 1.000 mL.

3.5 Glassware: 250 mL beakers, 2.5 mL and 50 mL graduated cylinders and 100 mm funnels.

3.6 Mechanical stirrer.

3.7 Magnetic stirrer.

3.8 Filter paper

4. Procedure: Free chloride content

4.1 Grind and sieve the concrete to be tested to a grain size of less than 0.2 mm.

4.2 Weigh to the nearest milligram a 2.5 g sample of the powdered concrete.

4.3 Transfer the sample quantitatively into a 250 mL beaker.

4.4 Add 100 mL of distilled water and agitate the solution for 3 minutes at 20°C with the mechanical stirrer.

4.5 Stabilise with 1 mL of the 53% nitric acid solution.

4.6 Filter into a clean 250 mL beaker by placing filter paper into the 100 mm funnel and slowly adding the solution.

4.7 Record the final volume of the solution.

4.8 Place a stirring bar in the beaker containing the filtered solution and add 2 mL of ionic-strength adjuster while gently stirring with the magnetic stirrer.

4.9 Immerse the tips of the combination chloride-ion electrode in the solution. Record the new potential reading as V_in. Keep the solution continuously stirred.

4.10 Add 0.25 mL of the standard 1 M NaCl solution with a digital pipette, and record the new potential as V_{in+s}.

4.11 Add a second 0.25 mL of the standard 1 M NaCl solution and record the final potential reading as V_{in+2s}.

4.12 Stop the stirring of the solution.

4.13 Calculate the chloride content of sample with the spreadsheet as per Table A.1.

5. Procedure: Total chloride content

5.1 Grind and sieve the concrete to be tested to a grain size of less than 0.2 mm.

5.2 Weigh to the nearest milligram a 5 g sample of the powdered concrete.

5.3 Transfer the sample quantitatively into a 250 mL beaker.

5.4 Add 50 mL of distilled water and agitate the solution for 2 minutes at 20°C with the mechanical stirrer.

5.5 Add 80 mL of distilled water and 20 mL of 53% nitric acid solution and stir anew for 30 minutes.

5.6 Filter into a clean 250 mL beaker by placing filter paper into the 100 mm funnel and slowly adding the solution.

5.7 Record the final volume of the solution.

5.8 Place a stirring bar in the beaker containing the filtered solution and add 2 mL of ionic-strength adjuster while gently stirring with the magnetic stirrer.

5.9 Immerse the tips of the combination chloride-ion electrode in the solution. Record the new potential reading as V_{in}. Keep the solution continuously stirred.

5.10 Add 0.5 mL of the standard 1 M NaCl solution with a digital pipette, and record the new potential as V_{in+s}.

5.11 Add a second 0.5 mL of the standard 1 M NaCl solution and record the final potential reading asV_{in+2s}.

5.12 Stop the stirring of the solution.

5.13 Calculate the chloride content of the sample with the spreadsheet as Table A.1.

	A	B	C	D	E	F	G	H	I	J	K
1											
2	This portion is for entry of the mass of each sample used and the measured potentials, before and after each addition of a 0.50 mL portion of a standard										
3											
4	**Sample**	**Mass [Cl-] in S [g]**	**Sample mass [g]**	**Solution volume [L]**	**ISA volume [L]**	**S volume [L]**	V_{in} [mV]	V_{in+S} [mV]	V_{in+2S} [mV]		
5	1	=35.453*0.0005	5	0.1	0.002	0.0005					
6	2										
7	3										
8	4										
9	5										
10											
11	This portion performs the iterative calculation to arrive at the find the Cl content of the sample:										
12											
13	**Iteration**	**Mass [Cl-] in S [g]**	**Voltage slope (R1)**	**Concentration Slope (R2)**						**(R1-R2)**	**Cl content [%bwc]**
14	1	0.0001	=($G3-$H3)/($G3-$I3)	=(LOG(B13/SUM(D$3:E$3)+LOG((B13+B$3)/(SUM(D$3:E$3)+F$3)))/(LOG(B13/SUM(D$3:E$3))-LOG((B13+2*B$3)/(SUM(D$3:E$3)+2*F$3)))						=C13-D13	=B13/(C3*γ_C)
15	2	0.0002	=($G3-$H3)/($G3-$I3)	=(LOG(B14/SUM(D$3:E$3)+LOG((B14+B$3)/(SUM(D$3:E$3)+F$3)))/(LOG(B14/SUM(D$3:E$3))-LOG((B14+2*B$3)/(SUM(D$3:E$3)+2*F$3)))						=C14-D14	=B14/(C3*γ_C)
16	3	0.0003	=($G3-$H3)/($G3-$I3)	=(LOG(B15/SUM(D$3:E$3)+LOG((B15+B$3)/(SUM(D$3:E$3)+F$3)))/(LOG(B15/SUM(D$3:E$3))-LOG((B15+2*B$3)/(SUM(D$3:E$3)+2*F$3)))						=C15-D15	=B15/(C3*γ_C)
17	4	0.0004	=($G3-$H3)/($G3-$I3)	=(LOG(B16/SUM(D$3:E$3)+LOG((B16+B$3)/(SUM(D$3:E$3)+F$3)))/(LOG(B16/SUM(D$3:E$3))-LOG((B16+2*B$3)/(SUM(D$3:E$3)+2*F$3)))						=C16-D16	=B16/(C3*γ_C)
18	5	0.0005	=($G3-$H3)/($G3-$I3)	=(LOG(B17/SUM(D$3:E$3)+LOG((B17+B$3)/(SUM(D$3:E$3)+F$3)))/(LOG(B17/SUM(D$3:E$3))-LOG((B17+2*B$3)/(SUM(D$3:E$3)+2*F$3)))						=C17-D17	=B17/(C3*γ_C)
19	etc.	etc.	etc.	etc.						etc.	etc.
20											
21	Notes										
22	1	The example is for total chloride content and the quantities should therefore be adjusted for free chloride content as per the indicated procedure.									
23	2	S refers to the standard 1 M NaCl solution, ISA refers to ionic strength adjuster.									
24	3	The formula in cell B1 calculates the amount of chloride ions present in 0.50 mL of 1.000M NaCl solution by mass (35.49*0.0005 = 0.01773 g).									
25	5	γ_C refers to the percentage of cement by mass of concrete constituents, thus (kg/m^3)/kg/m3), and is used to calculate the percentage of chloride by weight of cement [%bwc].									
26											
27											

Table A.1: Example spreadsheet for the calculation of chloride content using internal calibration.

A.2 Nordtest Method 492: determination of non-steady state chloride diffusion coefficient by migration

nordtest method

NT BUILD 492

Approved 1999–11

1(8)

CONCRETE, MORTAR AND CEMENT-BASED REPAIR MATERIALS:
CHLORIDE MIGRATION COEFFICIENT FROM NON-STEADY-STATE MIGRATION EXPERIMENTS

UDC 691.32/691.53/691.54

Key words: Chlorides, concrete, diffusion, mortar, repair materials, migration, test method

1 SCOPE

This procedure is for determination of the chloride migration coefficient in concrete, mortar or cement-based repair materials from non-steady-state migration experiments.

2 FIELD OF APPLICATION

The method is applicable to hardened specimens cast in the laboratory or drilled from field structures. The chloride migration coefficient determined by the method is a measure of the resistance of the tested material to chloride penetration. This non-steady-state migration coefficient cannot be directly compared with chloride diffusion coefficients obtained from the other test methods, such as the non-steady-state immersion test or the steady-state migration test.

3 REFERENCES

/1/ NT BUILD 201, "Concrete: Making and curing of moulded test specimens for strength tests", 2nd ed., Approved 1984-05.

/2/ NT BUILD 202, "Concrete, hardened: Sampling and treatment of cores for strength tests", 2nd ed., Approved 1984-05.

/3/ NT BUILD 208, "Concrete, hardened: Chloride content", 2nd ed., Approved 1984-05.

/4/ Tang, L and Sørensen, H.E., "Evaluation of the Rapid Test Methods for Chloride Diffusion Coefficient of Concrete, NORDTEST Project No. 1388-98", SP Report 1998:42, SP Swedish National Testing and Research Institute, Borås, Sweden, 1998.

4 DEFINITIONS

Migration: The movement of ions under the action of an external electrical field.

Diffusion: The movement of molecules or ions under a concentration gradient or, more strictly, chemical potential, from a high concentration zone to a low concentration zone.

5 SAMPLING

The method requires cylindrical specimens with a diamete 100 mm and a thickness of 50 mm, sliced from cast cylinc or drilled cores with a minimum length of 100 mm. cylinders and cores should meet the requirements descri in NT BUILD 201 and NT BUILD 202 respectively. Th specimens should be used in the test.

6 TEST METHOD

6.1 Principle

An external electrical potential is applied axially across specimen and forces the chloride ions outside to migrate the specimen. After a certain test duration, the specime axially split and a silver nitrate solution is sprayed on to of the freshly split sections. The chloride penetration de can then be measured from the visible white silver chlo precipitation, after which the chloride migration coefficient be calculated from this penetration depth.

6.2 Reagents and apparatus

6.2.1 Reagents

- Distilled or de-ionised water.
- Calcium hydroxide: $Ca(OH)_2$, technical quality.
- Sodium chloride: NaCl, chemical quality.
- Sodium hydroxide: NaOH, chemical quality.
- Silver nitrate: $AgNO_3$, chemical quality.
- Chemicals for chloride analysis as required by the method employed (optional, see 6.4.6).

6.2.2 Apparatus

- Water-cooled diamond saw.
- Vacuum container: capable of containing at least th specimens.
- Vacuum pump: capable of maintaining a pressure of l than 50 mbar (5 kPa) in the container.

Published by NORDTEST P.O. Box 116 FIN–02151 ESPOO FINLAND Phone + 358 9 455 4600 Fax + 358 9 455 4
ISSN 0283–7153 Proj. 1388–98

- Migration set-up: One design (see Appendix 1) includes the following parts:
  - Silicone rubber sleeve: inner/outer diameter 100/115 mm, about 150 mm long.
  - Clamp: diameter range 105 – 115, 20 mm wide, stainless steel (see Figure 2 in Appendix 1).
  - Catholyte reservoir: plastic box, 370 x 270 x 280 mm (length x width x height).
  - Plastic support: (see Figure 3 in Appendix 1).
  - Cathode: stainless steel plate (see Figure 3 in Appendix 1), about 0.5 mm thick.
  - Anode: stainless steel mesh or plate with holes (see Figure 4 in Appendix 1), about 0.5 mm thick.

  Other designs are acceptable, provided that temperatures of the specimen and solutions during the test can be maintained in the range of 20 to 25 °C (see 6.4.2).
- Power supply: capable of supplying 0 - 60 V DC regulated voltage with an accuracy of ±0.1 V.
- Ammeter: capable of displaying current to ±1 mA.
- Thermometer or thermocouple with readout device capable of reading to ±1 °C.
- Any suitable device for splitting the specimen.
- Spray bottle.
- Slide calliper with a precision of ±0.1 mm.
- Ruler with a minimum scale of 1 mm.
- Equipment for chloride analysis as required by the test method employed (optional, see 6.4.6).

6.3 Preparation of the test specimen

6.3.1 Test specimen

If a drilled core is used, the outermost approximately 10 - 20 mm thick layer should be cut off (Note 1) and the next 50 ± 2 mm thick slice should be cut as the test specimen. The end surface that was nearer to the outermost layer is the one to be exposed to the chloride solution (catholyte).

If a ∅100 x 100 mm cast cylinder is used, cut a 50 ± 2 mm thick slice from the central portion of the cylinder as the test specimen. The end surface that was nearer to the as-cast surface is the one to be exposed to the chloride solution (catholyte).

If a ∅100 x 200 mm cast cylinder is used, prepare the test specimen by first cutting the cylinder into two halves (i.e. into two ∅100 x 100 mm cylinders), and then cutting a 50 ± 2 mm thick slice from one half. The end surface that was nearer to the first cut (the middle surface) is the one to be exposed to the chloride solution (catholyte).

Measure the thickness with a slide calliper and read to 0.1 mm.

Note 1. The term 'cut' here means to saw perpendicularly to the axis of a core or cylinder, using a water-cooled diamond saw.

6.3.2 Preconditioning

After sawing, brush and wash away any burrs from the surfaces of the specimen, and wipe off excess water from the surfaces of the specimen. When the specimens are surface-dry, place them in the vacuum container for vacuum treatment. Both end surfaces must be exposed. Reduce the absolute pressure in the vacuum container to a pressure in the range of 10–50 mbar (1–5 kPa) within a few minutes. Maintain the vacuum for three hours and then, with the vacuum pump still running, fill the container with the saturated $Ca(OH)_2$ solution (by dissolving an excess of calcium hydroxide in distilled or de-ionised water) so as to immerse all the specimens. Maintain the vacuum for a further hour before allowing air to re-enter the container. Keep the specimens in the solution for 18 ± 2 hours.

6.4 Procedure

6.4.1 Catholyte and anolyte

The catholyte solution is 10 % NaCl by mass in tap water (100 g NaCl in 900 g water, about 2 N) and the anolyte solution is 0.3 N NaOH in distilled or de-ionised water (approximately 12 g NaOH in 1 litre water). Store the solutions at a temperature of 20–25 °C.

6.4.2 Temperature

Maintain the temperatures of the specimen and solutions in the range of 20–25 °C during the test.

6.4.3 Preparation of the test

- Fill the catholyte reservoir with about 12 litres of 10 % NaCl solution.
- Fit the rubber sleeve on the specimen as shown in Figure 4 in Appendix 1 and secure it with two clamps. If the curved surface of the specimen is not smooth, or there are defects on the curved surface which could result in significant leakage, apply a line of silicone sealant to improve the tightness.
- Place the specimen on the plastic support in the catholyte reservoir (see Figure 1 in Appendix 1).
- Fill the sleeve above the specimen with 300 ml anolyte solution (0.3 M NaOH).
- Immerse the anode in the anolyte solution.
- Connect the cathode to the negative pole and the anode to the positive pole of the power supply.

6.4.4 Migration test

- Turn on the power, with the voltage preset at 30 V, and record the initial current through each specimen.
- Adjust the voltage if necessary (as shown in Table 1 in Appendix 2). After adjustment, note the value of the initial current again.

- Record the initial temperature in each anolyte solution, as shown by the thermometer or thermocouple.
- Choose an appropriate test duration according to the initial current (see Table 1 in Appendix 2).
- Record the final current and temperature before terminating the test.

6.4.5 Measurement of chloride penetration depth

- Disassemble the specimen by following the reverse of the procedure in 6.4.3. A wooden rod is often helpful in removing the rubber sleeve from the specimen.
- Rinse the specimen with tap water.
- Wipe off excess water from the surfaces of the specimen.
- Split the specimen axially into two pieces. Choose the piece having the split section more nearly perpendicular to the end surfaces for the penetration depth measurement, and keep the other piece for chloride content analysis (optional).
- Spray 0.1 M silver nitrate solution on to the freshly split section.
- When the white silver chloride precipitation on the split surface is clearly visible (after about 15 minutes), measure the penetration depth, with the help of the slide calliper and a suitable ruler, from the centre to both edges at intervals of 10 mm (see Figure 5 in Appendix 1) to obtain seven depths (notes 2, 3 and 4). Measure the depth to an accuracy of 0.1 mm.

Note 2: If the penetration front to be measured is obviously blocked by the aggregate, move the measurement to the nearest front where there is no significant blocking by aggregate or, alternatively, ignore this depth if there are more than five valid depths.

Note 3: If there is a significant defect in the specimen which results in a penetration front much larger than the average, ignore this front as indicative of the penetration depth, but note and report the condition.

Note 4: To obviate the edge effect due to a non-homogeneous degree of saturation or possible leakage, do not make any depth measurements in the zone within about 10 mm from the edge (see Figure 5 in Appendix 1).

6.4.6 Surface chloride content (optional, Note 5)

- From the other axially split specimen, cut an approximately 5 mm thick slice (Note 6) parallel to the end surface that was exposed to the chloride solution (catholyte).
- Determine the chloride content in the slice in accordance with NT BUILD 208 or by a similar method with the same or better accuracy.

Note 5: Information on chloride binding capacity of the tested material can be estimated from the surface chloride content.

Note 6: The thickness of the slice should always be less than the minimum penetration depth.

6.5 Expression of results

6.5.1 Test results

Calculate the non-steady-state migration coefficient from Equation (1):

$$D_{nssm} = \frac{RT}{zFE} \cdot \frac{x_d - \alpha\sqrt{x_d}}{t} \quad (1)$$

where:

$$E = \frac{U-2}{L} \quad (2)$$

$$\alpha = 2\sqrt{\frac{RT}{zFE}} \cdot \mathrm{erf}^{-1}\left(1 - \frac{2c_d}{c_0}\right) \quad (3)$$

D_{nssm}: non-steady-state migration coefficient, m^2/s;

z: absolute value of ion valence, for chloride, $z = 1$;

F: Faraday constant, $F = 9.648 \times 10^4$ J/(V·mol);

U: absolute value of the applied voltage, V;

R: gas constant, $R = 8.314$ J/(K·mol);

T: average value of the initial and final temperatures in the anolyte solution, K;

L: thickness of the specimen, m;

x_d: average value of the penetration depths, m;

t: test duration, seconds;

erf^{-1}: inverse of error function;

c_d: chloride concentration at which the colour changes, $c_d \approx 0.07$ N for OPC concrete;

c_0: chloride concentration in the catholyte solution, $c_0 = 2$ N.

Since $\mathrm{erf}^{-1}\left(1 - \frac{2 \times 0.07}{2}\right) = 1.28$, the following simplified equation can be used:

$$D_{nssm} = \frac{0.0239(273+T)L}{(U-2)t}\left(x_d - 0.0238\sqrt{\frac{(273+T)L\,x_d}{U-2}}\right) \quad (4)$$

where:

D_{nssm}: non-steady-state migration coefficient, $\times 10^{-12}$ m^2/s;

U: absolute value of the applied voltage, V;

T: average value of the initial and final temperatures in the anolyte solution, °C;

L: thickness of the specimen, mm;

x_d: average value of the penetration depths, mm;

t: test duration, hour.

6.6 Accuracy

6.6.1 Repeatability

The coefficient of variation of repeatability is 9 %, according to the results from the Nordic round-robin test between six laboratories /4/.

6.6.2 Reproducibility

The coefficient of variation of reproducibility is 13 % for Portland cement concrete or for concrete mixed with silica fume, and 24 % for concrete mixed with slag cement, according to the results from the Nordic round-robin test between six laboratories /4/.

6.7 Test report

The test report should, if known, include the following information:

a) Name and address of the test laboratory.

b) Date and identification number of the test report.

c) Name and address of the organisation or person who ordered the test.

d) Name and address of the manufacturer or supplier of the material or object tested.

e) Date of arrival of the material or object tested.

f) Description of the material or object tested, including sampling, composition, and curing age.

g) Purpose of the test.

h) Test method.

i) Any deviation from the test method.

j) Name and address of the person who performed the test.

k) Date of the test.

l) Test results, including the specimen dimensions, applied voltage, initial and final currents, initial and final temperatures, average and individual data of penetration depth and migration coefficient.

m) Any observation of an abnormal penetration front due to a defect in the specimen.

n) Optional information about surface chloride content.

o) Date and signature.

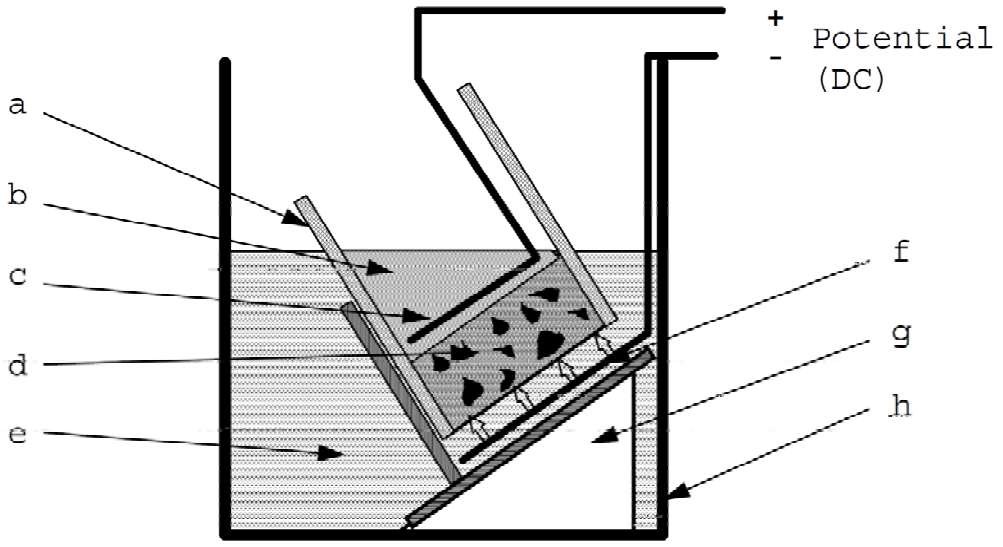

a. Rubber sleeve
b. Anolyte
c. Anode
d. Specimen
e. Catholyte
f. Cathode
g. Plastic support
h. Plastic box

Fig. 1. One arrangement of the migration set-up.

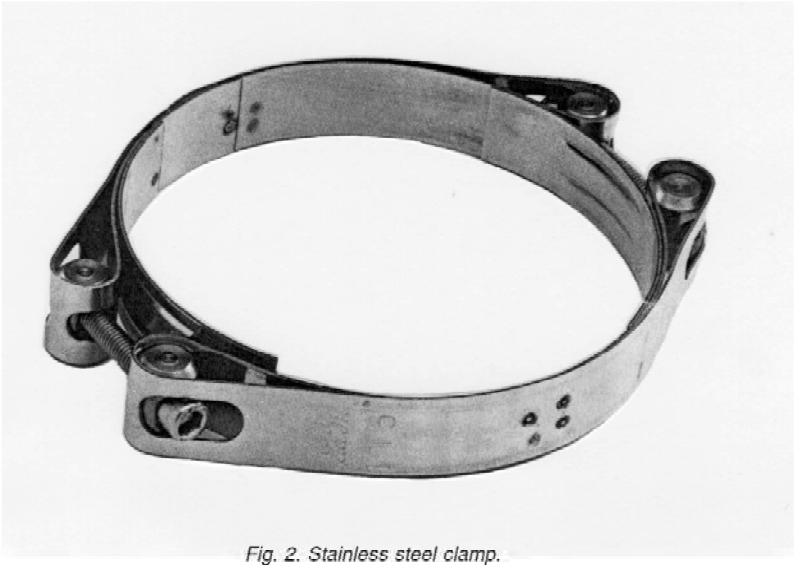

Fig. 2. Stainless steel clamp.

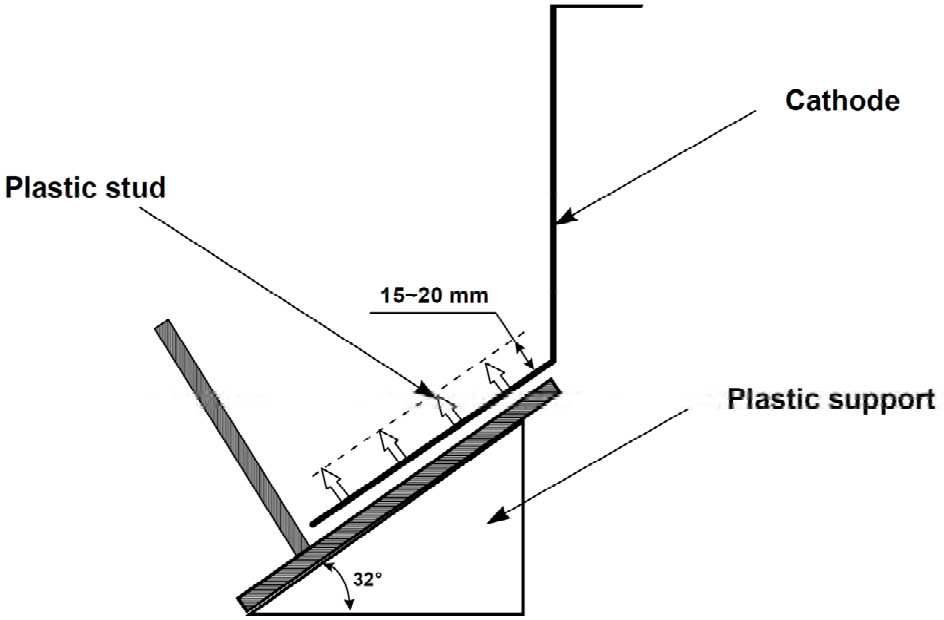

Fig. 3. Plastic support and cathode.

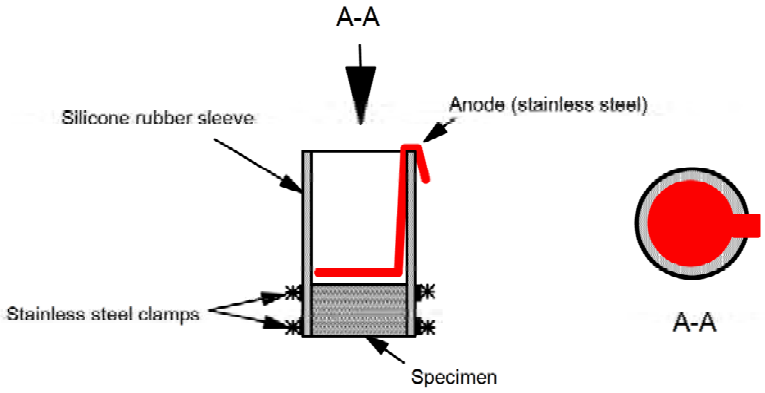

Fig. 4. Rubber sleeve assembled with specimen, clamps and anode.

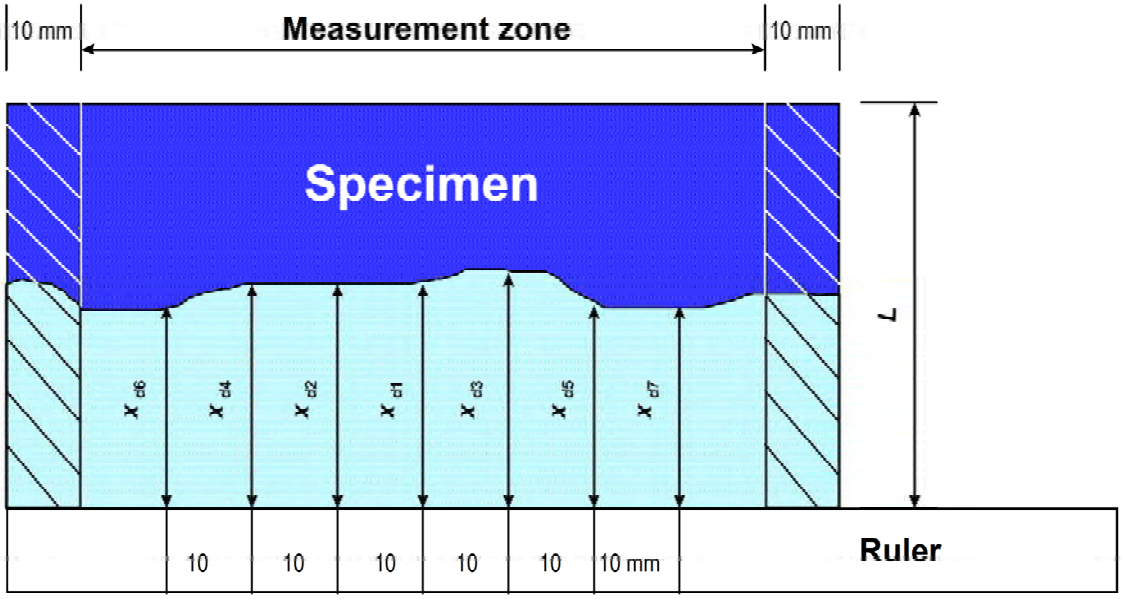

Fig. 5. Illustration of measurement for chloride penetration depths.

Table 1. Test voltage and duration for concrete specimen with normal binder content.

Initial current I_{30V} (with 30 V) (mA)	Applied voltage U (after adjustment) (V)	Possible new initial current I_0 (mA)	Test duration t (hour)
$I_0 < 5$	60	$I_0 < 10$	96
$5 \leq I_0 < 10$	60	$10 \leq I_0 < 20$	48
$10 \leq I_0 < 15$	60	$20 \leq I_0 < 30$	24
$15 \leq I_0 < 20$	50	$25 \leq I_0 < 35$	24
$20 \leq I_0 < 30$	40	$25 \leq I_0 < 40$	24
$30 \leq I_0 < 40$	35	$35 \leq I_0 < 50$	24
$40 \leq I_0 < 60$	30	$40 \leq I_0 < 60$	24
$60 \leq I_0 < 90$	25	$50 \leq I_0 < 75$	24
$90 \leq I_0 < 120$	20	$60 \leq I_0 < 80$	24
$120 \leq I_0 < 180$	15	$60 \leq I_0 < 90$	24
$180 \leq I_0 < 360$	10	$60 \leq I_0 < 120$	24
$I_0 \geq 360$	10	$I_0 \geq 120$	6

Note: For specimens with a special binder content, such as repair mortars or grouts, correct the measured current by multiplying by a factor (approximately equal to the ratio of normal binder content to actual binder content) in order to be able to use the above table.

Appendix B

Résumé de Thèse

DÉVELOPPEMENT ET COMBINAISON DE TECHNIQUES ÉLECTROMAGNÉTIQUES NON DESTRUCTIVES POUR L'ÉVALUATION DU BÉTON D'ENROBAGE AVANT CORROSION

Sachant que les techniques d'auscultation électromagnétiques non destructives (EM) sont sensibles à de nombreux paramètres d'état des bétons, l'objectif de ce projet de recherche est d'étudier le potentiel de ces méthodes d'investigation EM pour évaluer la durabilité des bétons et détecter la présence d'agents agressifs.

Dans un premier temps, une cellule de mesure EM coaxiale-cylindrique et une cellule de résistivité multi-anneaux (mise au point conçue dans cette thèse) ont été utilisées pour une étude paramétrique. Des modèles de régression multi-linéaires ont été développés pour chaque observable EM (résistivité électrique et permittivité diélectrique) en fonction du degré de saturation, de la teneur en chlorures, de la porosité et du coefficient de diffusion de différentes formulations de bétons et mortiers.

Dans un deuxième temps, des techniques de mesure EM in-situ ont été utilisées sur des corps d'épreuve homogènes pour évaluer leur état : un capteur de résistivité multi-électrodes, développé dans le cadre de cette thèse, un capteur capacitif et un système radar. Ces techniques ont été combinées pour donner une estimation quantitative du taux de saturation, de la teneur en chlorures et de la porosité des mélanges par optimisation non-linéaire des modèles de régression, développés dans la phase précédente.

Enfin, l'aptitude de ces techniques in-situ à détecter des gradients a également été étudiée. Il a été constaté que la tomographie de résistivité électrique (TRE), utilisant le nouveau système multi-électrodes était particulièrement adapté à la détermination de gradients dans le béton d'enrobage.

Mots clés : END, résistivité électrique, permittivité diélectrique, durabilité du béton, teneur en chlorure, teneur en eau, porosité, diffusivité.

1. Introduction

1.1. Contexte

Le béton est le matériaux fabriqué par l'homme le plus largement utilisé aujourd'hui [**1**]. Il est utilisé depuis des temps anciens pour la construction des structures, résistant souvent à l'épreuve du temps et prouvant ainsi sa durabilité inhérente. L'infrastructure de béton armé qui existe actuellement dans le monde représente un patrimoine économique et stratégique important, qui doit être géré avec beaucoup de diligence. Toutefois, de nombreuses structures en béton construites au 20^{e} siècle montrent des signes de détérioration, principalement due à des problèmes liés à la corrosion des armatures en acier. Dans le contexte de la prise de conscience mondiale vis-à-vis de l'environnement et de la durabilité, il est devenu primordial d'entretenir ces structures le plus efficacement possible et de concevoir de nouvelles infrastructures qui soient durables afin d'en garantir la longévité.

De nombreuses collectivités et propriétaires d'infrastructures ont ainsi introduit des mesures visant à traiter les problèmes de durabilité liés aux armatures en acier. Ces mesures associent généralement deux stratégies : tout d'abord, une approche fondée sur la performance pour la conception de nouvelles structures, en remplacement de l'approche prescriptive [**2**] [**3**]. Ceci implique que la vie en service de la structure est fondée sur des modèles prédictifs intégrant le critère de durabilité. Ces systèmes sont contrôlés au cours de la construction, et remplacent l'approche traditionnelle du « supposé satisfaisant », fondée sur la résistance du béton à la compression. Deuxièmement, la surveillance de l'état des structures permet d'évaluer l'état des structures existantes et des nouvelles structures de manière régulière ou continue, afin de réaliser des opérations de maintenance avant que la structure ne subisse des dommages importants. Ces approches devraient permettre d'améliorer la durabilité du réseau d'infrastructures en béton, mais en pratique, il est nécessaire de mettre au point des techniques efficaces permettant de garantir la réponse aux critères de durabilité au cours de la construction et d'effectuer un suivi de la performance des structures existantes tout au long de leur vie en service.

Les techniques traditionnelles d'essais destructifs prennent généralement beaucoup de temps et impliquent la réalisation de carottages dans les structures. Ainsi, ces essais ne sont ni optimums ni adaptés au suivi régulier ou continu. Plusieurs techniques d'évaluation non-destructives ont ainsi été élaborées dans le but de permettre une évaluation plus efficace des structures de béton. Le recours à ces techniques est particulièrement intéressant car elles sont plus rapides, plus économiques et peuvent être mises en œuvre sur site, n'impliquent pas d'actions de correction et peuvent être réalisées régulièrement sur une grande surface. Toutefois, étant donné que le béton est un matériau complexe et non-homogène, dont on ne comprend pas encore pleinement les

propriétés et les mécanismes de détérioration, il est nécessaire de réaliser un travail de grande envergure afin d'améliorer la fiabilité de ces techniques non-destructives.

1.2. Enoncé de la problématique

La corrosion est un problème important en ce qui concerne les bétons armés structurels. Elle est principalement causée par la présence d'eau et de chlorures dans l'environnement des armatures en acier. Dans les bétons de faible qualité, ou qui sont exposés à des environnements agressifs, le béton d'enrobage qui protège les aciers est pénétré, avec le temps, par des chlorures, qui finissent par provoquer la corrosion, la dégradation et la perte d'intégrité structurelle. Plusieurs indicateurs de durabilité ont ainsi été élaborés dans l'objectif d'évaluer la résistance du béton à ces dégradations. Cependant, ils sont généralement longs à obtenir en pratique.

Les techniques d'auscultation électromagnétique sont une alternative plus rapide et plus économique. Elles sont été introduites dans le contexte de l'ingénierie civile pour l'évaluation non destructive des structures en béton [**4**]. Ces techniques d'évaluation EM non destructives sont sensibles aux propriétés matérielles du béton. Ainsi, les éléments EM observables, tels que la résistivité électrique, ont été proposés comme indicateurs indirects de durabilité [**3**]. Les techniques électromagnétiques sont également sensibles à la présence d'eau et de chlorure et sont par conséquent étudiées afin d'évaluer l'état du béton dans le temps. Bien que l'application des techniques d'auscultation EM au béton ait été largement documentée, la plupart de ces études ne présentent pas les résultats de plusieurs études électromagnétiques sur la même série de bétons exposés à toute une variété de conditions. Il reste donc encore des incertitudes en ce qui concerne la nature précise des rapports entre les observables électromagnétiques et les paramètres décrivant l'état du béton, ainsi qu'en ce qui concerne l'influence des interactions entre ces paramètres sur la réponse électromagnétique du béton.

De même, lorsque le béton est évalué sur site, il existe de nombreuses variables qui exercent une influence sur la réponse électromagnétique et qui ne sont pas nécessairement liées à la durabilité du béton. Il existe également de nombreuses autres sources d'incertitudes, parmi lesquelles les influences de l'environnement extérieur telles que la température, les incertitudes dues à la variabilité inhérente au béton ainsi que le manque de précision et de répétitivité lié au processus de mesure [**5**]. Lorsqu'une seule technique d'auscultation est utilisée, il est très difficile d'évaluer de manière quantitative la durabilité du béton ou de caractériser son état. L'association de techniques EM et d'autres techniques non destructives a fait l'objet de récentes recherches visant à améliorer la fiabilité de l'évaluation sur site de la durabilité et de l'état du béton. [**6**].

1.3. Objectifs et vue d'ensemble

Le travail présenté ci-après vise à faire avancer l'évaluation de la durabilité des bétons de couverture par des techniques non destructives et à associer les techniques d'auscultation électromagnétique existantes présentant des sensibilités différentes aux paramètres liés à la dégradation du béton. Les objectifs principaux sont donc les suivants :

- Réaliser une étude paramétrique rigoureuse, afin d'évaluer la dépendance de certains observables EM à la sélection de paramètres importants liés à la durabilité et à l'état du béton ;
- Utiliser les résultats de cette étude afin d'associer la réponse des techniques non destructives EM afin de permettre une réalisation plus fiable de l'évaluation de l'état du béton d'enrobage ;
- Développer les techniques et équipements d'essais EM nécessaires à l'étude paramétrique et aux essais sur béton sur site, dans le cadre de la présente thèse.

Ce travail a plusieurs implications du point de vue pratique : tout d'abord, en améliorant la fiabilité de l'étude quantitative de l'état du béton sur site, la mise en œuvre de ces techniques pour le contrôle qualité, dans le cadre d'une approche fondée sur la performance au cours de la construction, devient une option envisageable. Deuxièmement, l'association de techniques EM peut améliorer le suivi non destructif de la dégradation du béton, dans le cadre de la stratégie de suivi de la santé structurelle, et être utilisé comme indication précoce de l'émergence de zones problématiques, avant l'apparition de la corrosion. Troisièmement, en permettant une quantification plus précise de l'infiltration d'agents agressifs dans le béton d'enrobage, il devient possible de mettre à jour plus facilement les modèles prédictifs de vie en service.

Le présent document est une traduction française résumée de la thèse complète en anglais. Il présente une vue d'ensemble concise des techniques électromagnétiques exploitées dans le cadre de la thèse, ainsi qu'une explication du travail expérimental le plus important réalisé. Pour de plus amples informations concernant la théorie de l'électromagnétique et la science des bétons, ainsi que pour les descriptifs détaillés de la procédure expérimentale, le lecteur pourra se référer au document principal.

2. Les fondamentaux de l'électromagnétique et les méthodes d'auscultation

Les observables électromagnétiques qui ont été étudiés pour l'auscultation non destructive du béton, dans le cadre de la présente thèse, sont la résistivité électrique et la permittivité

diélectrique du courant continu (CC). Le présent chapitre présente la théorie fondamentale des observables électromagnétiques utilisés et les méthodes ayant servi à les obtenir.

2.1. La résistivité électrique du courant continu (CC)

2.1.1. Contexte théorique

La résistivité électrique décrit la capacité d'un matériau à résister au mouvement de charges libres au sein d'un champ électrique appliqué. La résistivité électrique du béton peut ainsi être utilisée comme indicateur indirect de la durabilité du béton [**3**], étant donné qu'elle est liée à la facilité avec laquelle les ions de chlorure pénètrent dans le béton d'enrobage au cours du stade d'amorçage de la corrosion.

La résistivité d'un matériau homogène est déterminée par la mesure de la différence potentielle résultant d'un courant injecté puis par application d'un facteur de correction G qui normalise la résistance mesurée de l'espacement des électrodes et de la géométrie du spécimen.

$$\rho = G \cdot {}^{\Delta V}/_{I} \qquad \text{donc} \qquad \rho = G \cdot R \tag{1}$$

où $\boldsymbol{\rho}$ représente la résistivité [Ω.m], ΔV représente la différence potentielle [V], I est l'intensité de courant appliquée [A], R est la résistance [Ω] et G est le facteur géométrique [m].

L'application directe de la loi d'Ohm selon la Figure 1:(a) est souvent utilisée pour les mesures en laboratoire, car elle est applicable à des spécimens homogènes et isotropiques d'une surface transversale uniforme. La résistivité est déterminée en appliquant des électrodes à plaques des deux côtés du spécimen, avec un facteur géométrique défini sous la forme de $G=A/L$ (A étant la surface transversale du spécimen [m²] et L la longueur du spécimen entre les électrodes à plaque [m] ainsi que présenté à la Figure 1(a)).

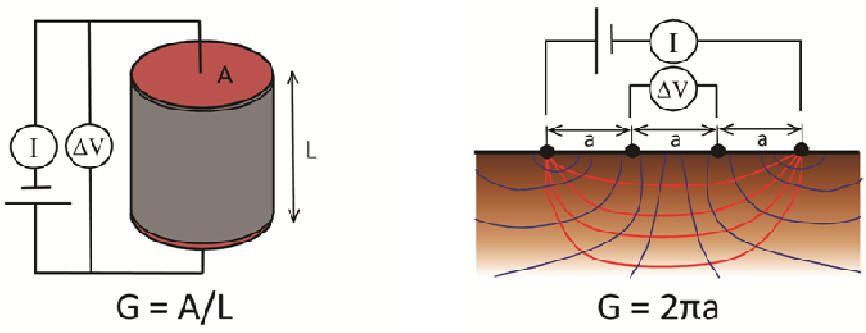

(a) (b)

Figure 1 : Détermination de la résistivité par (a) l'application directe de la Loi d'Ohm aux spécimens présentant une surface transversale uniforme et (b) la configuration Wenner pour les mi-espaces infinis où les lignes rouges représentent les lignes de courant et les lignes bleues les lignes équipotentielles.

Les techniques de surface faisant appel à des électrodes de point sont plus adaptées aux géométries complexes ou lorsqu'il n'est pas possible d'accéder aux côtés opposés d'un élément. La technique la plus répandue est la configuration en quatre points de Wenner [**7**] présentée à la Figure 1:(b) pour les applications sur béton [**8**] [**9**] [**10**], où le facteur géométrique peut être défini de manière analytique comme $G=2\pi a$ pour un mi-espace homogène infini.

Cependant, lorsque la configuration Wenner est appliquée à un élément de béton aux dimensions arbitraires et finies, les conditions de définition du facteur géométrique de Wenner ne sont plus valables. Il est donc nécessaire de déterminer un nouveau facteur géométrique afin de corriger les effets de limites. Ceci est possible soit par modélisation numérique [**11**] ou par calibrage d'un électrolyte dont la résistivité est connue [**12**] comme présenté plus en détail au Chapitre 2.1.2.

La sensibilité de la résistivité électrique aux paramètres liés aux conditions environnementales (notamment la teneur en eau et en chlorure) et la qualité du béton (ex : porosité) ont été bien documentées dans le cadre de recherches précédentes [**13**] [**14**] [**15**] [**16**]. La forme étendue de la loi d'Archie [**17**] lie la résistivité globale des roches à leur degré de porosité φ, degré de saturation S et à la résistivité de la solution poreuse ρ_w selon l'Eq. 2.

$$\rho = a\varphi^{-m}S^{-n}\rho_w \tag{2}$$

où a est le facteur de tortuosité, m l'exposant de cimentation et n l'exposant de saturation. Bien que la loi d'Archie soit habituellement considérée comme purement empirique [**16**] où a, m et n sont intégrés de manière expérimentale, elle a été éprouvée de manière analytique pour des cas simples [**18**] [**19**]. La loi d'Archie trouve son origine en géophysique, mais elle a également été appliquée à des pâtes et mortiers de béton (principalement dans des conditions de saturation) et a produit des résultats satisfaisants. [**20**] [**21**].

De nombreuses études empiriques ont été réalisées afin de relier la sensibilité du béton à la teneur en eau et en chlorure [**14**] [**22**] [**23**] [**24**]. La sensibilité de la résistivité à la teneur en eau et en chlorure pour les bétons ayant un ratio eau-ciment de 0,45 est démontrée par les résultats expérimentaux de la Figure 2 émanant d'une étude de Saleem et al. [**23**].

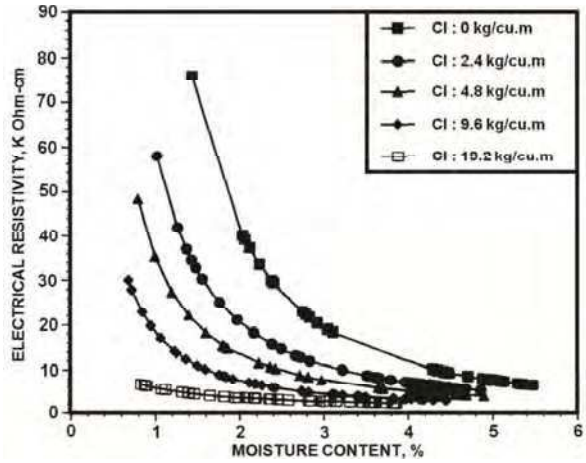

Figure 2 : Sensibilité d'une résistivité électrique à l'humidité et au chlorure (Saleem et al. [23]).

La sensibilité de la résistivité à plusieurs autres paramètres, par exemple la température, la tortuosité, la dimension des pores, mérite aussi d'être surveillée [**16**].

La résistivité du béton s'est révélée faiblement sensible aux fréquences de moins de 1000 Hz [**25**] [**14**]. Le courant alternatif de faible fréquence est donc normalement utilisé à la place du courant continu car il produit des résultats similaires, mais réduit de manière significative les effets négatifs dus à la polarisation des électrodes [**25**].

2.1.2. Techniques d'auscultation de la résistivité électrique

La mesure de la résistivité concrète est bien documentée dans la littérature et les techniques sur site sont communément appliquées en pratique, à l'aide des sondes de résistivité [**26**], cependant, des ports à électrode spécifiques ont dû être prévus pour l'auscultation du béton réalisée dans le cadre de la présente thèse, à la fois en laboratoire et in situ. Une cellule de résistivité a ainsi été développée afin de permettre la réalisation de mesures de résistivité sur des spécimens de carottages au cours de l'étude paramétrique, ainsi que deux versions d'une sonde de résistivité destinée aux mesures de résistivité de la surface au cours des autres programmes expérimentaux.

Ces dispositifs sont nouveaux, car ils ont été conçus spécifiquement pour cette thèse, et contiennent des caractéristiques originales qui n'ont pas été décrits précédemment dans la littérature. Notamment, la cellule et les sondes de résistivité sont conçues avec la capacité de détecter la présence de gradients de résistivité dans la profondeur du béton. Cette fonctionnalité était particulièrement importante au cours du travail expérimental, car il était crucial de vérifier l'homogénéité des spécimens pour l'étude paramétrique (Chapitre 3.1) afin d'obtenir des résultats fiables. De plus, la capacité de l'équipement à évaluer des gradients peut aussi être utilisée afin d'évaluer l'infiltration d'agents agressifs dans le béton, ce qui est une information de grande valeur pour l'étude des caractéristiques de diffusion et de la durabilité du béton d'enrobage. La géométrie était importante dans la conception de la cellule de résistivité, car elle devait pouvoir être utilisée sur des spécimens dont les dimensions sont équivalentes à la cellule EM cylindrique existante

(Chapitre 2.2.2.1) afin de permettre la mesure de permittivité et de résistivité sur les mêmes spécimens de carottages.

Les dispositifs de résistivité présentés dans ce chapitre sont utilisés en conjonction avec le résistivimètre Syscal Pro d'Iris Instruments, qui permet des mesures à basse fréquence (4 Hz) à l'aide de séquences pré-programmées contenant toutes les combinaisons possibles d'électrodes.

2.1.2.1. Développement d'une cellule de résistivité multianneaux

La cellule de résistivité multianneaux fonctionne selon le principe de l'application directe de la loi d'Ohm, tel que présenté au paragraphe 2.1.1. L'application directe de la loi d'Ohm est adaptée aux spécimens dont la géométrie est simple. Ainsi, la cellule a été conçue dans l'objectif d'ausculter des carottes de béton conditionnées dans le cadre de l'étude paramétrique présentée au chapitre 3.1.

La cellule de résistivité (Figure 3(a)) est composée de deux boîtiers semi-cylindriques fixés autour du spécimen de carottage de 75mm de diamètre par 70mm de hauteur. Cinq électrodes annulaires en éponge conductive (largeur 2 mm) sont placées à distance égale de part et d'autre de la cellule. La cellule multinanneaux met en œuvre une configuration de mesure à 4 électrodes, par laquelle le courant est injecté par deux électrodes à plaques et à disque en acier inoxydable placées en haut et en bas du spécimen. Les mesures potentielles sont prises indifféremment entre deux des électrodes annulaires (Figure 3(b)).

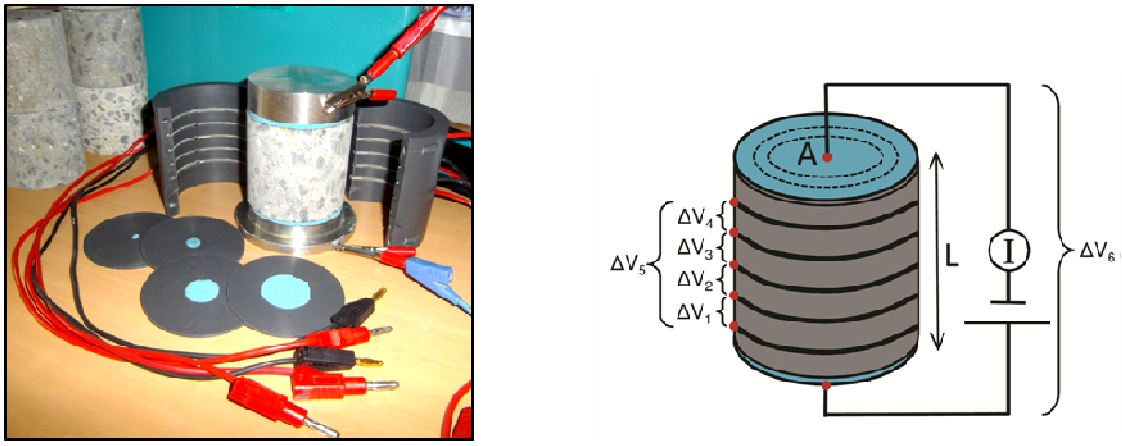

(a) (b)

Figure 3 : Cellule de résistivité multianneaux pour l'auscultation des carottages de béton où (a) présente la cellule avec différents types d'électrodes d'injection et (b) un diagramme indiquant les positions de mesure des différences de potentiel : ΔV_1 ΔV_2, ΔV_3, ΔV_4, ΔV_5 pour les mesures à 4 électrodes et ΔV_6 pour la méthode à 2 électrodes.

La littérature [**27**] décrit qu'une approche fondée sur 4 électrodes produit des résultats plus fiables que la méthode à 2 électrodes, en raison du fait qu'elle est moins sensible aux erreurs provoquées par la résistance au contact et à la polarisation des électrodes. Cette hypothèse a été de nouveau

testée dans le présent contexte, au regard de la cellule de résistivité multianneaux, par l'évaluation de la performance de la configuration à 4 électrodes et à 2 électrodes pour toute une gamme de conditions de contact. Afin de réaliser cela, différentes variations de la résistance au contact et de la polarisation des électrodes ont été testées en modifiant la zone de contact des électrodes d'injection de courant (à l'aide des diamètres de 4 mm, 10 mm, 20 mm, 30 mm et 75 mm) ainsi que présenté à la Figure 3(a).

Le facteur géométrique analytique défini par la loi d'Ohm (Equation (1)) n'est pas valable pour les électrodes à plaques de dimensions inférieures à la zone transverse du spécimen, à moins que la hauteur ne soit beaucoup plus grande que le diamètre. Les facteurs géométriques de chaque électrode à plaques et annulaire ont ainsi été déterminés à l'aide de la modélisation numérique (MATLAB et COMSOL Multiphysics) afin de compenser la taille des électrodes, l'espacement des électrodes ainsi que la géométrie du spécimen.

L'approche proposée par [**28**] selon les Equations (3) et (4) a été appliquée, où ρ_s [Ω.m], ΔV_s [V], I_s [A] et R_s [Ω] représentent la résistivité, la différence de potentiel mesurée, l'intensité de courant appliquée et la résistance des spécimens de béton et ρ_m [Ω.m] et I_m [A] sont la résistivité assignée et l'intensité de courant pour un modèle d'élément fini, avec une géométrie et une configuration d'électrodes identiques à celle du spécimen, ce qui produit une différence de potentiel modélisée de ΔV_m [V] et une résistance de R_m [Ω].

$$\rho_s = G\frac{\Delta V_s}{I_s} = GR_s \tag{3}$$

$$\rho_m = G\frac{\Delta V_M}{I_m} = GR_m \tag{4}$$

Le facteur géométrique approprié pour chaque combinaison de taille d'électrode à plaque et de configuration annulaire peut ainsi être exprimé comme suit :

$$G = \frac{\rho_m}{R_m} \tag{5}$$

Un modèle d'élément fini avec une géométrie et une configuration d'électrode identiques à celle de la cellule de résisitvité multianneaux a ainsi été généré, avec une résistivité assignée de ρ_m= 1 Ω.m et un courant assigné de I_m = 1 A, comme présenté à la Figure 4(a). La substitution des paramètres du modèle assignée à l'Equation (6) produit le facteur géométrique modélisé :

$$G = \frac{1}{\Delta V_m} \tag{6}$$

La Figure **4**(b) montre que le potentiel modélisé au « bord » du carottage est fortement influencé par le diamètre des électrodes (à plaques) d'injection du courant. Le champ électrique des électrodes à plaques inférieures à 75 mm n'est pas uniforme et mène à des facteurs géométriques modélisés différents du facteur géométrique analytique G=A/L.

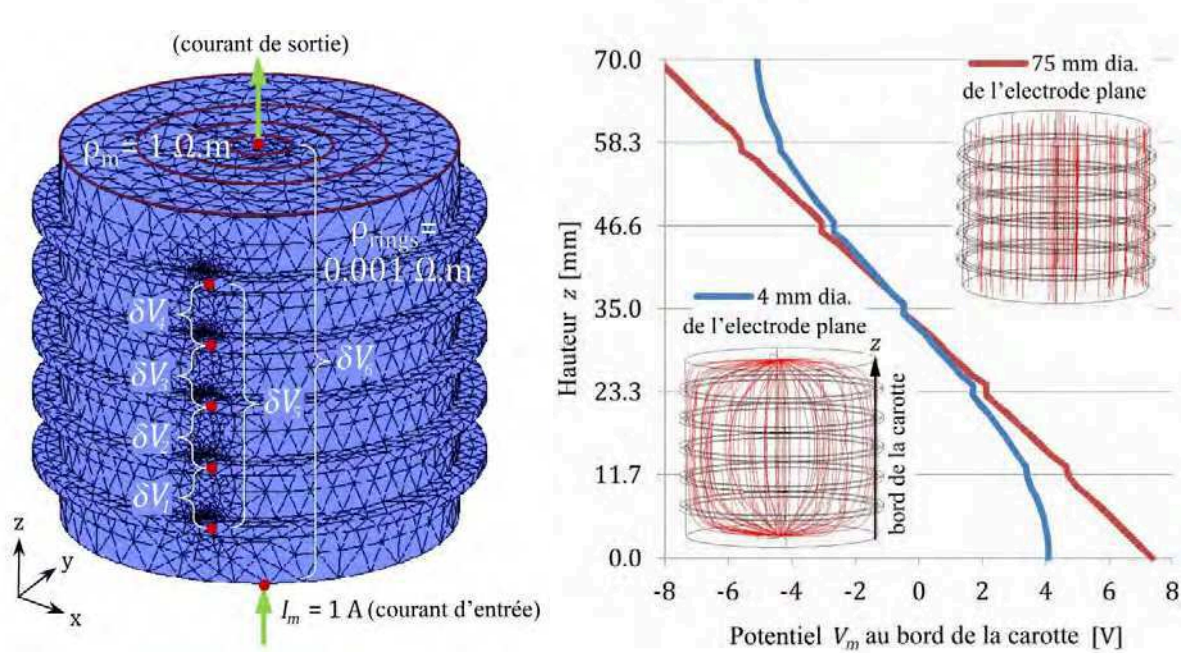

Figure 4 : Modélisation numérique de la cellule de résistivité multianneaux, (a) indiquant les propriétés du modèle d'élément fini et les positions des différences de potentiel modélisées et (b) présentant le potentiel modélisé sur la hauteur d'un spécimen (sur son « bord ») pour un diamètre d'électrode d'injection de courant de 4 mm et 75 mm. Les distributions linéaires du champ électrique modélisé du boîtier des électrodes à plaques de 4 mm et 75 mm sont également présentées (en rouge).

Le facteur géométrique final de chaque configuration d'électrode à plaques et d'électrode annulaire est présenté au Tableau 1.

Tableau 1: Facteurs géométriques modélisés de chaque taille d'électrode d'injection et de chaque position de mesure de potentiel.

Diamétre d'électrode d'injection	**Facteurs géometriques modelisés [m]**					
	$G_{\Delta V1}$	**$G_{\Delta V2}$**	**$G_{\Delta V3}$**	**$G_{\Delta V4}$**	**$G_{\Delta V5}$**	**$G_{\Delta V6}$**
4 mm	0.5740	0.4511	0.4511	0.5741	0.1263	0.0037
10 mm	0.5702	0.4493	0.4493	0.5701	0.1256	0.0095
20 mm	0.5564	0.4431	0.4431	0.5564	0.1233	0.0199
30 mm	0.5339	0.4335	0.4335	0.5340	0.1196	0.0305
75 mm	0.3807	0.3804	0.3804	0.3807	0.0951	0.0630
$G_{Analytique}$ $(A/L)_{75mm}$	0.3787	0.3787	0.3787	0.3787	0.0947	0.0631
% $Erreur_{75mm}$	0.5%	0.4%	0.4%	0.5%	0.4%	0.2%

Les facteurs géométriques modélisés ont été utilisés afin d'étudier la résistance au contact et les effets de polarisation sur la mesure des spécimens de carottes de béton. L'étude a confirmé qu'une configuration de mesure à 4 électrodes, où le courant est injecté par les électrodes à plaque et la différence de potentiel est mesurée entre deux des électrodes à anneaux, est supérieure à une configuration de mesure à 2 électrodes, où le courant est injecté et le potentiel est mesuré entre les deux mêmes électrodes. La Figure 5 montre l'influence de la polarisation et la résistance au contact des mesures à 4 électrodes et à 2 électrodes, car ces deux phénomènes sont liés à la taille des électrodes à plaques. Il apparaît clairement que la configuration en 2 points est beaucoup plus sensible aux effets de la polarisation et de résistance au contact que la configuration en 4 points.

De plus, les facteurs géométriques modélisés ont également été utilisés afin d'étudier l'influence des tailles d'agrégats sur les mesures de résistivité entre les électrodes annulaires. Les résultats sont présentés à la Figure 6, et montrent que le pourcentage moyen d'erreur a augmenté, passant de 0,04% pour les agrégats de 4 mm à 0,24% pour les agrégats de 20 mm. Ces erreurs sont considérées comme négligeables lorsqu'on les compare aux seuils acceptables pour des conditions de saturation contrôlées [**29**]. Ainsi, l'étude conclut que l'espacement des électrodes annulaires à 12 mm est suffisant pour étudier les bétons dans lesquels la taille des agrégats est inférieure à 20 mm.

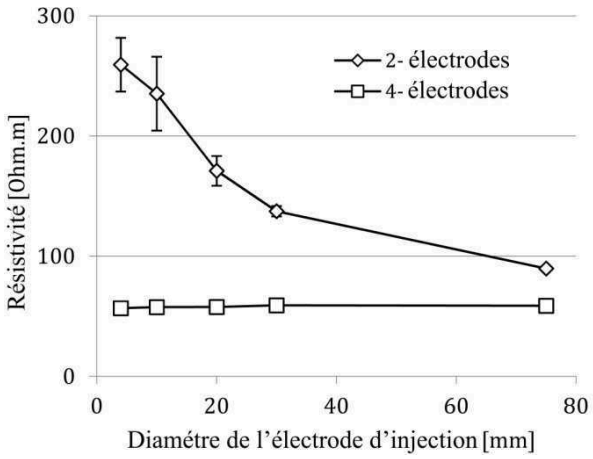

Figure 5 : résistivités mesurées déterminées à l'aide de la méthode en deux et en quatre points pour des électrodes d'injection de courant de diamètres différents.

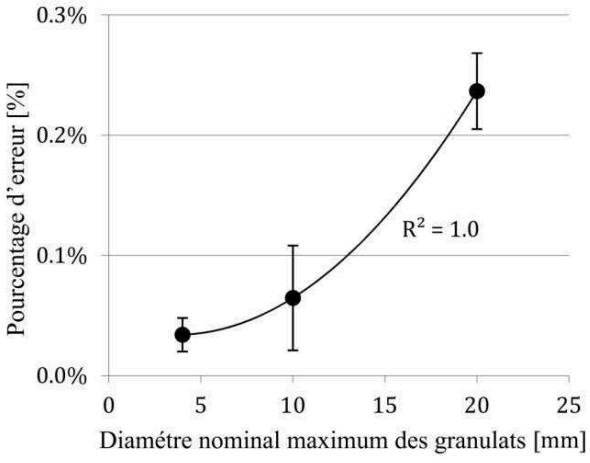

Figure 6 : Pourcentage d'erreur de différence de potentiel causé par la taille d'agrégat maximale nominale pour les mesures multianneaux.

2.1.2.2. Sonde de résistivité multi-électrodes

Les mesures de résistivité de surface de Wenner à l'aide d'un espacement fixe des électrodes sont habituellement utilisées pour l'auscultation du béton. Toutefois, dans les cas non-homogènes, ces mesures ne fournissent qu'une indication générale de la résistivité générale apparente d'un volume ausculté non connu. Etant donné que la profondeur d'auscultation de la surface des mesures de

résistivité est liée à la distance entre les électrodes d'injection de courant et les électrodes de mesure, l'augmentation de l'espacement des électrodes permet d'évaluer la variation de la résistivité en fonction de la profondeur. La profondeur médiane d'auscultation peut être liée analytiquement à l'espacement des électrodes et les résistivités apparentes mesurées peuvent ensuite être inversées à l'aide d'un protocole d'optimisation, afin de trouver un modèle représentatif de la subsurface. Le processus de cartographie des résistivités inversées en fonction de la profondeur et du décalage latéral est appelé Tomographie de Résistivité Electrique en 2D (ERT). Bien que l'ERT ait été largement utilisée pour les auscultations géophysiques, elle n'a été que rarement appliquée au béton [**30**] et lorsqu'elle l'a été, les auscultations se sont concentrées sur les sites de défauts mécaniques ou sur les armatures acier [**31**].

Une sonde de résistivité multi-électrodes a ainsi été développée dans le cadre de la présente thèse afin d'estimer la « véritable » subsurface à l'aide de l'ERT. Cette sonde a été utilisée dans le cadre d'un travail expérimental présenté aux Chapitres 4 et 5 et dans le but d'évaluer l'homogénéité des dalles de béton et d'étudier les gradients de propriétés. La sonde de résistivité est composée d'une série de 14 électrodes à points équipées d'embouts conducteurs en éponge (4 mm dia.) afin de minimiser la résistance au contact. Elles sont espacées de 20mm, suffisamment afin de permettre l'auscultation des mélanges de béton avec des tailles d'agrégats allant jusqu'à 13mm, conformément aux recommandations de Gowers et Millard [**27**]. Une configuration de Wenner a été utilisée en raison de sa bonne couverture verticale (environ 80 mm pour cette sonde) et de son bon ratio signal-bruit. 26 mesures de surface ont donc été possibles sur les quatre niveaux d'auscultation (c.-à-d. espacements d'électrodes a).

Etant donné que la constante géométrique de Wenner de $2\pi a$ est définie pour le mi-espace homogène et que les mesures devaient être réalisées sur des éléments béton de dimensions finies, les effets des limites sur les mesures devaient être pris en compte. La sensibilité des facteurs géométriques à la parallèle (direction x), à la perpendiculaire (direction y) et en dessous (direction z) de la sonde de résistivité a ensuite été étudiée par modélisation numérique. La Figure 7 présente le facteur géométrique modélisé G_m selon le facteur géométrique analytique G_a en fonction des décalages de seuils respectifs (d_x, d_y et d_z) normalisés au regard de l'espacement des électrodes a. Le décalage entre l'électrode la plus éloignée de la sonde et chaque limite a été respectivement augmenté, alors que les deux autres limites ont été conservées à une distance essentiellement infinie. Le décalage de la limite z s'est révélé être celui qui exerce la plus grande influence, suivi de y et ensuite x. En tout état de cause, les effets de limite semblent devenir négligeables au-delà des ratios d/a de 4.

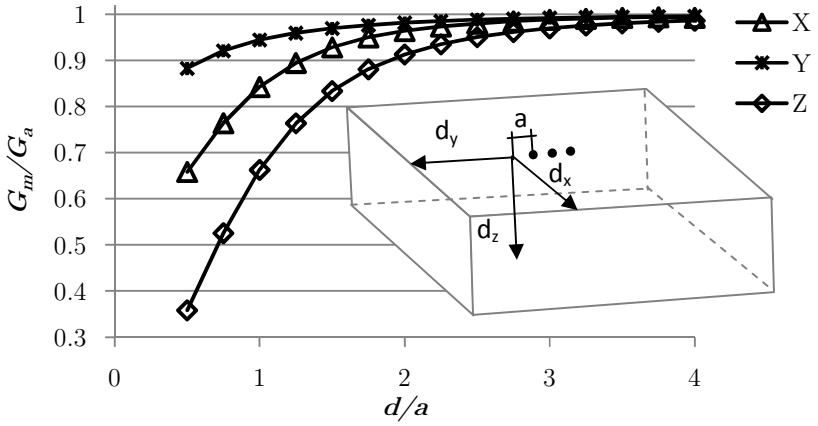

Figure 7 : impact des limites sur les facteurs géométriques analytiques de Wenner.

Avec l'espacement d'électrodes maximum de la sonde de résistivité multiélectrodes à 80mm, il était certain que les éléments de béton à tester seraient rarement conformes à un ratio *d/a* de plus de quatre. Ainsi, de nouveaux facteurs géométriques ont dû être calculés afin de compenser les effets de limites à l'aide de la modélisation numérique [10] similairement à ce qui est décrit au Chapitre 2.3. Un modèle FEM a été généré sous COMSOL Multiphysics, pouvant être facilement adapté aux dimensions pertinentes de l'élément ausculté afin de calculer les facteurs géométriques de chaque configuration d'électrode [18] (Figure 8(a) et (b)).

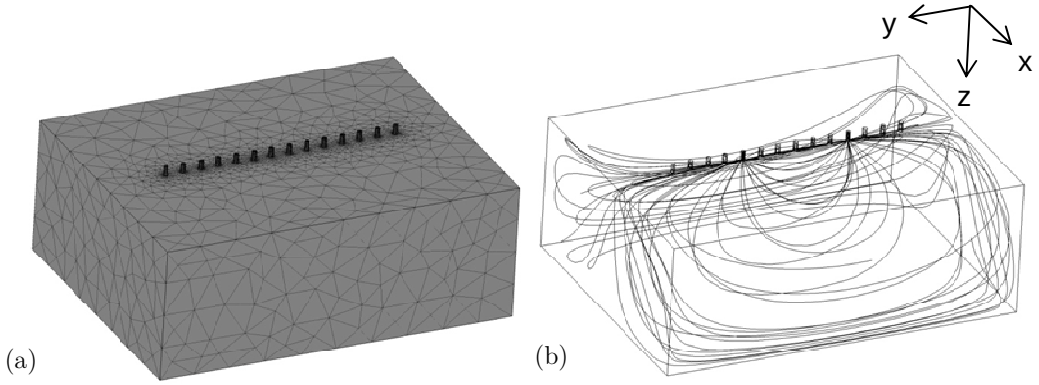

Figure 8 : Modélisation numérique pour déterminer les facteurs géométriques des géométries finies mesurées à l'aide de la sonde de résistivité multi-éléments avec (a) le treillis FEM pour une dalle et (b) l'influence des limites sur la distribution du champ électrique.

La procédure qu'il était envisagé de mettre en œuvre pour l'auscultation du béton à l'aide de la sonde est présentée à la Figure 9. Après la mesure des potentiels en surface Figure 9(i), les facteurs géométriques sont déterminés pour un modèle de géométrie similaire au médium ausculté (Figure 9(ii)). Les résistivités apparentes corrigées géométriquement peuvent ensuite être tracées ainsi qu'à la Figure 9(iii). Dans le cas d'un élément béton contenant des gradients de propriétés, le processus d'inversion de Loke et Barker [**32**] a été adopté afin d'estimer les « véritables » profils de résistivité en fonction de la profondeur (Figure 9(iv)). Le protocole d'inversion utilise comme

critères initiaux le dérivé de Fréchet [**33**] qui décrit les sensibilités des résistivités apparentes aux changements de la distribution de la résistivité de la subsurface. Les valeurs de résistivité de la subsurface sont ensuite optimisées de manière itérative afin de trouver un modèle représentatif qui produira des réponses prédites similaires aux réponses mesurées à la surface.

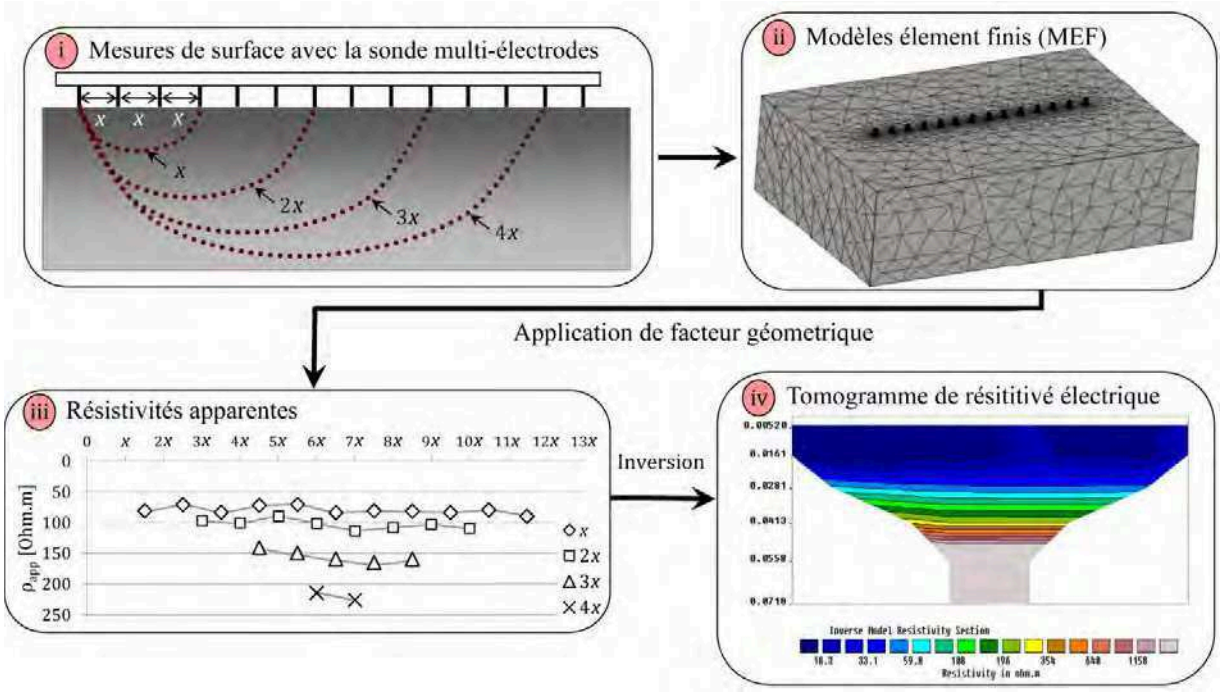

Figure 9 : étapes de traitement des données pour les mesures de résistivité où (i) indique les mesures de surface en quatre points à l'aide d'électrodes multiples, montrant l'augmentation de la profondeur d'auscultation au fur et à mesure que le décalage de l'électrode augmente, (ii) indique la correction géométrique par modélisation numérique, (iii) indique les résistivités apparentes calculées pour les configurations Wenner pour chaque niveau d'auscultation et (iv) indique les résistivités inversées en fonction de la profondeur à l'aide du logiciel d'inversion Res2Dinv [32].

2.1.2.3. Validation de la cellule et de la sonde de résistivité

L'étalonnage de la cellule et de la sonde de résistivité a été réalisé en testant différents électrolytes de résistivité connue afin de vérifier que les facteurs géométriques modélisés compensent effectivement correctement les effets de limites. La configuration expérimentale est illustrée à la Figure 10.

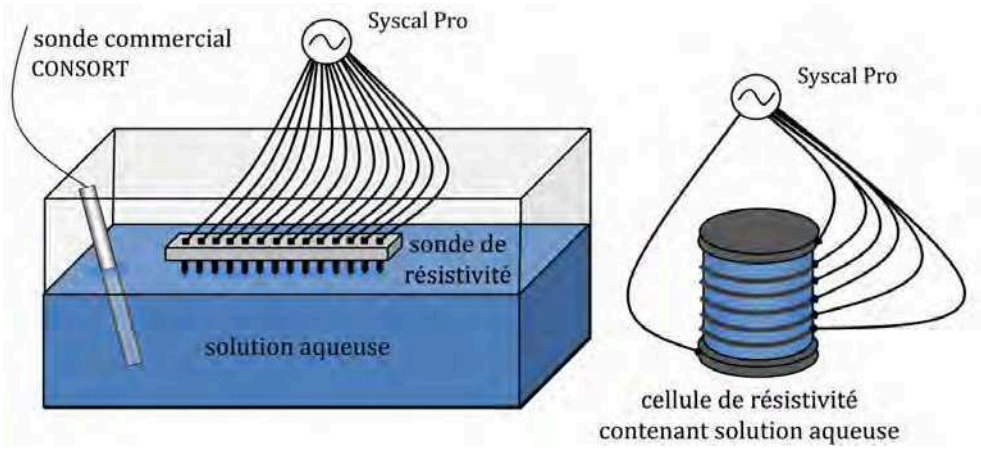

Figure 10 : configuration expérimentale pour le test de la sonde de surface et de la cellule de résistivité sur des solutions dont la résistivité est connue.

Premièrement, la résistivité d'une solution aqueuse par rapport à une série équivalente à celle du béton (10 à 1000 Ohm.m) a été déterminée à l'aide d'une sonde de conductivité du commerce (Consort C561), la résistivité étant l'inverse de la conductivité. La résistivité de la même solution a ensuite été déterminée dans la cellule de résistivité et à l'aide de la sonde de résistivité dans un conteneur de dimensions 400x300x200 mm. Les mesures ont été prises entre chaque électrode annulaire consécutive pour la cellule de résistivité (4 points de mesure) et pour toutes les combinaisons de paires d'électrodes de la sonde de résistivité (26 points de mesure). Chaque point de mesure a été corrigé à l'aide de facteurs géométriques modélisés sous COMSOL afin de tenir compte des effets limites de la cellule et du conteneur. La résistivité moyenne de chaque solution aqueuse a ensuite été calculée à partir des résistivités corrigées de la cellule et de la sonde, respectivement.

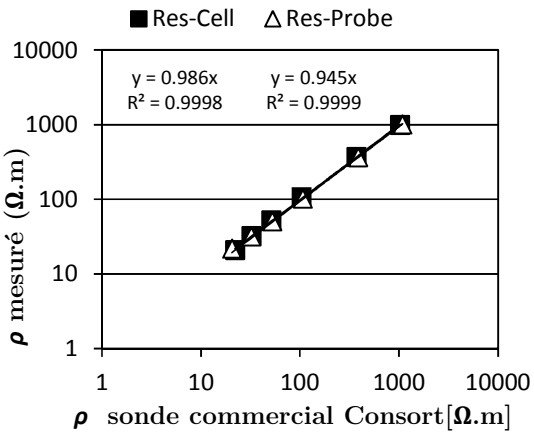

Figure 11 : Résultats de la cellule de résistivité et de la sonde de résistivité vis-à-vis de la résistivité calculée à l'aide des mesures de la sonde Consort.

	Résistivié mesuré (Ohm.m)		
Test	**Sonde commercial**	**Cellule de résistivité**	**Sonde de résistivité**
1	1020.4	1002.0	1081.6
2	370.4	374.6	386.7
3	103.4	108.2	106.5
4	51.3	53.0	52.3
5	32.3	32.5	32.1
6	22.1	21.1	20.5

Tableau 2 : Résultats d'étalonnage de la cellule de résistivité et de la sonde de résistivité pour les solutions salines de conductivité connue.

Les résultats ci-dessus (Tableau 2 et Figure 11) montrent que les valeurs de la cellule de résistivité et de la sonde de résistivité sont comparables aux résultats calculés à l'aide de la sonde de conductivité Consort. Il en a été conclu que l'application des facteurs géométriques modélisés produit des résultats fiables pour le cas idéal d'une solution saline, qui est totalement homogène et a une faible résistance de contact. Toutefois, la corrélation entre les résultats de la cellule de résistivité et la sonde doivent être validés plus avant pour pouvoir être utilisée pour de réelles applications de béton.

Les résultats de la cellule et de la sonde de résistivité ont donc été comparés entre trois mélanges de béton avec différentes teneurs en scories granulées des hauts fourneaux (0%, 50% et 70%) et un ratio w/b-ratio de 0,58 afin d'obtenir une série de valeurs de résistivité. Deux séries de dalles (0,3 m x 0,3 m x 0,15 m) ont été coulées pour chaque mélange – une dalle dans laquelle trois spécimens ont été carottés pour les mesures de la cellule de résistivité et un pour les mesures de surface à l'aide de la sonde de résistivité. Les essais ont été réalisés après 28 jours sur des spécimens saturés, considérés comme homogènes. Une bonne corrélation a été établie entre les mesures de la cellule et de la sonde, comme le montre la Figure 12.

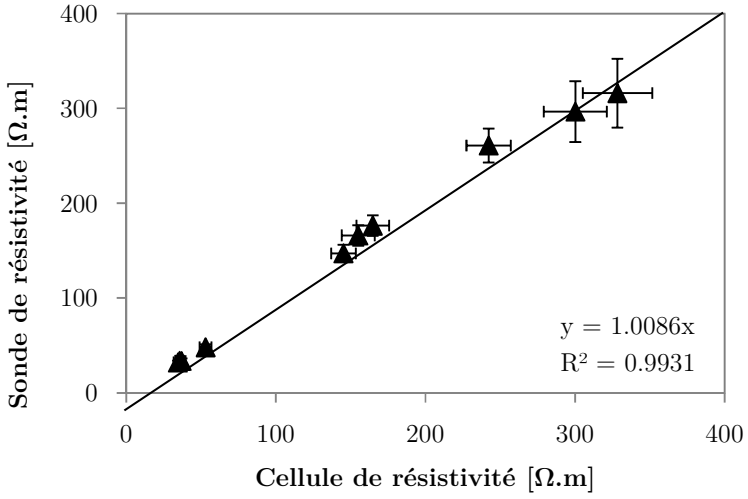

Figure 12 : Résultats de la sonde de résistivité par rapport à la cellule de résistivité pour un béton homogène.

Une étude de reproductibilité des mesures de la cellule de résistivité et de la sonde a été réalisée sur ces carottages et sur ces dalles. Le C_v représentant la reproductibilité de la cellule de résistivité varie de 0,8% à 10.5% et de 4% à 12% pour la sonde. Des résultats similaires ont été rapportés [**29**] pour une sonde portative Wenner dans des conditions contrôlées de laboratoire. Selon [**9**] un C_v de 10% est bon, 20% est acceptable et jusqu'à 40% est assez répandu pour les conditions in situ.

2.2. Permittivité diélectrique

2.2.1. Contexte théorique

Le second observable électromagnétique qui a été étudié dans le cadre de la présente thèse est la permittivité diélectrique. La permittivité diélectrique est une propriété matérielle liée à la capacité d'un matériau à stocker un champ électrique. La permittivité effective est une propriété complexe qui intègre les différentes manifestations de la polarisation qui se produisent au sein d'un matériau suite à l'application d'un champ électromagnétique. Elle est habituellement exprimée en fonction de la permittivité du vide (ε_0=8.854x10^{-12} Farad/m) comme dans l'Eq. 3.

$$\varepsilon_r^* = \frac{\varepsilon_e^*}{\varepsilon_0} = \varepsilon_r^{'} - j\varepsilon_r^{''} \tag{7}$$

où ε_e^* est la permittivité complexe effective, ε_r^* est la permittivité complexe relative, $\varepsilon_r^{'}$ est la constante diélectrique, $\varepsilon_r^{''}$ est le facteur de perte et $j^2 = -1$.

On peut dire qu'à une échelle macroscopique, la constante diélectrique représente la capacité du matériau à stocker l'énergie électromagnétique comme une polarisation électrique. Il s'agit d'un paramètre de valeur vraie et sans dimensions. Le facteur de perte représente les pertes d'énergie dues à la conduction et à l'absorption. Ces deux paramètres sont dépendants de la fréquence, particulièrement dans les supports dispersifs tels que le béton contenant de l'humidité et des chlorures.

Les modèles théoriques composites ont souvent été appliqués pour les bétons afin d'estimer leur permittivité, car le béton est essentiellement un composite composé d'une phase solide, d'une phase liquide et d'une phase gazeuse [**34**]. Le modèle de Lichtenecker-Rother [**35**] est un exemple de ce type de modèle, où la permittivité globale relative peut être exprimée en fonction des permittivités respectives de ses composants :

$$\varepsilon_r = \left[\sum V_i \left(\varepsilon_{ri}\right)^{\alpha}\right]^{1/\alpha} \tag{8}$$

où V_i est la fraction volumique et ε_{ri} est la constante diélectrique de la phase i et α est un paramètre d'ajustement lié aux couches de différents composants. α est souvent pris à 0,5, dans lequel le modèle est décrit comme le modèle d'index de réfraction (CRIM) ou modèle de propagation temporelle (TP) [**36**] [**31**], selon que les permittivités sont complexes ou réelles.

Les modèles théoriques composites ont été appliqués aux bétons avec un certain succès, confirmant ainsi la dépendance à l'eau de la permittivité du béton [**34**]. Toutefois, ces modèles ne tiennent pas compte du fait que la présence de solutions salines dans le béton provoquera une permittivité globale plus élevée que pour une eau non contaminée. Ceci est du à la polarisation inter faciale entre les phases liquide et solide du béton, connue sous le nom d'effet Maxwell-Wagner à de faibles

fréquences GPR [**37**], au vu du fait qu'il n'existe pas de différence significative entre les permittivités de l'eau et des solutions salines. Les modèles matériaux composites ne tiennent pas non plus compte de la dépendance de la permittivité à la fréquence dans un support dispersif, et sont plus adaptés à la prédiction de la constante diélectrique de matériaux à faibles pertes.

La fréquence de dispersion de la permittivité due à la teneur en eau et en chlorure a également fait l'objet d'études expérimentales, et les résultats obtenus à partir d'une ligne de transmission par Dérobert et al. [**38**] sont présentés à la Figure 13. Ils montrent que la permittivité globale d'un spécimen de béton est hautement sensible à la présence d'eau et d'ions. La nature dispersive des bétons contaminés par l'humidité et le chlorure est très prometteuse pour l'évaluation non destructive de l'état du béton.

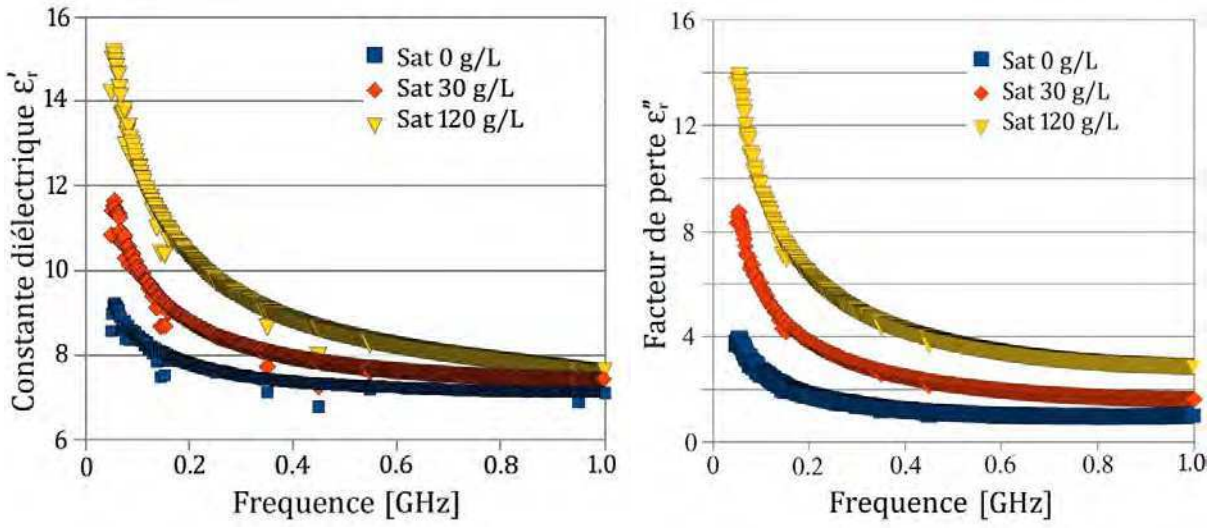

(a) (b)

Figure 13 : la sensibilité de la permittivité diélectrique du béton saturé à la teneur en chlorure pour (a) la constante diélectrique et (b) le facteur de perte pour trois concentrations en chlorure différentes (0 g/L, 30 g/L et 120 g/L) [38].

2.2.2. Techniques d'auscultation de la permittivité diélectrique.

Ce chapitre présente les techniques utilisées afin de déterminer la permittivité diélectrique du béton pour servir les objectifs de la présente thèse. Les techniques de laboratoire destinées à l'auscultation de spécimens de carottes de béton, à savoir la cellule électromagnétique cylindrique, et les techniques de surface adaptées à l'auscultation du béton in situ (capacimétrie et radar à pénétration de sol) sont abordées ici.

2.2.2.1. Cellule électromagnétique coaxiale cylindrique

La technique de ligne de transmission coaxiale est une méthode communément appliquée pour la détermination de la fréquence dépendante à la permittivité complexe des spécimens de béton[**39**] [**40**] [**41**]. Cette technique peut couvrir une gamme de fréquence large, jusqu'à plusieurs GHz, mais elle requiert habituellement une préparation et un usinage soigneux des spécimens et de ce fait, elle est uniquement adaptée à l'utilisation en laboratoire, dans des conditions contrôlées.

Une ligne de réflexion/transmission coaxiale fermée cylindrique, appelée cellule EM, a été utilisée dans le cadre de la présente thèse pour l'auscultation des spécimens de béton en laboratoire. Cette cellule EM a été développée par l'IFSTTAR dans le cadre d'un programme de recherche entre 2002 et 2005 par Adous et al. [**42**]. Le dispositif fonctionne sur le principe selon lequel le coefficient de réflexion de la vague de propagation due à l'interface entre la ligne coaxiale et le spécimen peut être liée à la permittivité complexe du matériau. Le système est présenté à la Figure 14. La cellule EM est adaptée à la détermination de la permittivité complexe des spécimens cylindriques et à des carottes de dimensions 75 mm dia. x 70 mm et une taille maximale d'agrégats de 20 mm, sur une bande de fréquence allant de 50 MHz à environ 1.6 GHz.

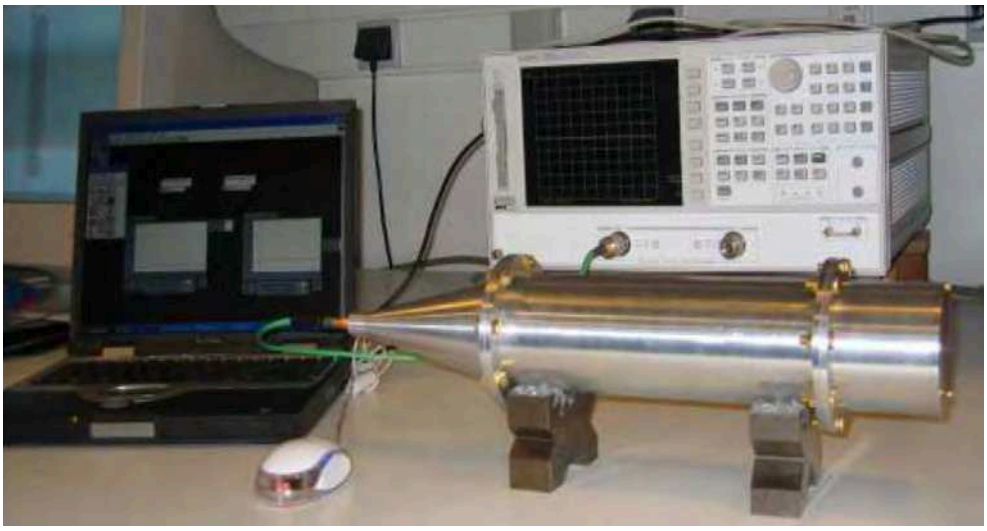

Figure 14 : Configuration complète de la cellule EM présentant l'analyseur de réseau vectoriel et les outils logiciels, selon Adous et al. [42].

2.2.2.2. Méthode capacitive

La capacimétrie [**43**] peut être utilisée afin de déterminer indirectement la constante diélectrique in situ du béton à de basses fréquences. La capacité est liée à la permittivité relative par l'équation analytique suivante, pour un compensateur appliqué en parallèle, de part et d'autre d'un spécimen de surface transverse constante :

$$C = {}^{A}/_{d}\,\varepsilon_0\varepsilon_r^{'} = \chi\varepsilon_0\varepsilon_r^{'} \tag{9}$$

où C [F] est la the capacité, A [m^2] est la zone surfacique des électrodes appliquées parallèlement sur le support, d [m] est la distance entre les électrodes et $\chi = A/d$ [m] est le facteur géométrique.

Pour les mesures de surface, où les électrodes sont positionnées côte-à-côte, le facteur géométrique ne peut pas être défini de manière analytique selon l'Equation (9). La capacité est donc obtenue par mesure de la variation de la fréquence de résonance Δf_{osc} [Hz] d'un courant oscillatoire entre l'air et le matériau étudié. Cela est réalisé à l'aide d'un capacimètre qui a été développé par le

LCP (*Laboratoire de Ponts et Chaussées*) en France dans les années soixante-dix pour l'auscultation du béton d'enrobage [**44**]. Le capacimètre fonctionne à environ 33 MHz, une fréquence à laquelle la permittivité est très sensible à la présence d'eau et de chlorure dans le béton [**45**] [**43**].

Le dispositif est composé de trois séries d'électrodes à plaques interchangeables de petite, moyenne et grande taille, comme présenté à la Figure 15, ce qui permet la mesure de surface pour les profondeurs d'auscultation croissantes. La profondeur d'influence de chaque série d'électrodes a été déterminée à l'aide de la modélisation numérique et d'un logiciel du commerce spécifique aux éléments finis (COMSOL Multiphysics). Elle est estimée à 9 mm, 20 mm et 80 mm respectivement, comme le montre la Figure 16(a).

Figure 15 : capacimètre avec des séries d'électrodes de petite à grande taille.

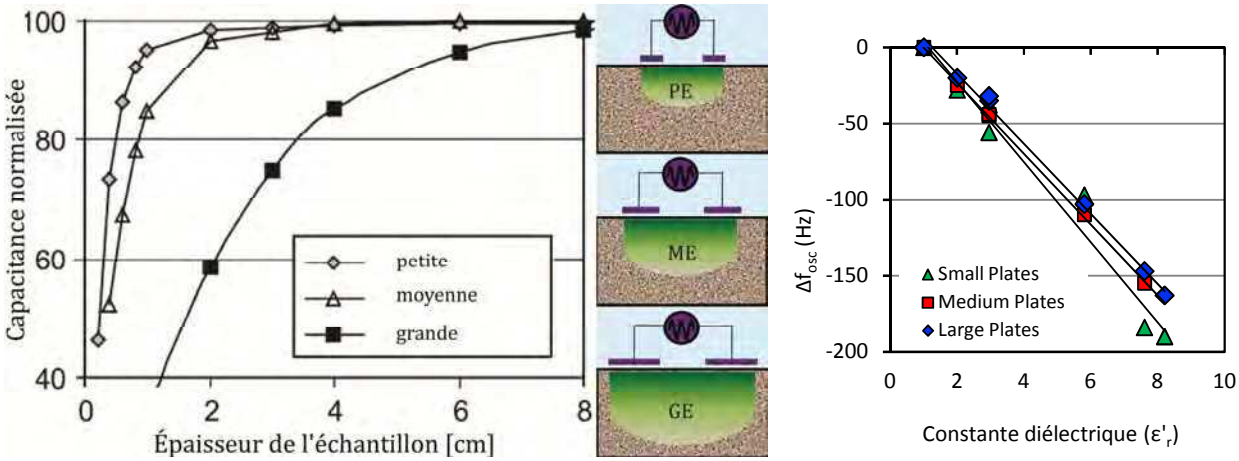

Figure 16 : séries d'électrodes à plaques de petite, moyenne et grande taille pour le capacimètre, présentant (a) leurs profondeurs d'influence respectives (Dérobert et al. 2008) et (b) leurs courbes d'étalonnage.

En pratique, la fréquence de résonance mesurée est directement liée à la permittivité relative à l'aide de l'étalonnage sur des matériaux dont la constante diélectrique est connue. Le rapport

entre Δf_{osc} et ε'_r est supposé être linéaire sur la gamme de permittivité du béton (Figure 16(b)) et les coefficients a et b sont donc positionnés de manière expérimentale selon l'Equation (10).

$$\Delta f_{osc} = a + b\varepsilon'_r \tag{10}$$

2.2.2.3. Radar à pénétration de sol

Le radar à pénétration de sol (RPS) fonctionne sur le principe de transmission des pulsation des ondes électromagnétiques au travers du support ausculté et les signaux reçus sont analysés (c.-à-d. en termes de temps de réponse ou d'amplitude) [**34**] [**31**] [**37**] [**46**].

La constante diélectrique d'un matériau a une influence significative sur la vélocité de l'onde électromagnétique qui se propage à l'intérieur de ce matériau. Pour les supports non dispersifs à faibles pertes, le rapport suivant est établi :

$$v \approx \frac{c}{\sqrt{\varepsilon'_r}} \tag{10}$$

où v représente la vélocité de l'onde (mm/ns) et c représente la vitesse de la lumière (300 mm/ns).

La constante diélectrique peut ainsi être calculée à partir des temps d'arrivée de l'onde électromagnétique, qui est habituellement liée à l'amplitude maximale du signal reçu. La fréquence centrale des antennes de radars pénétrants utilisées pour l'auscultation du béton est habituellement de 1500 MHz ou plus, ce qui donne une fréquence centrale de l'onde au sein du matériau atteignant approximativement 900 MHz ou plus. Les constantes diélectriques obtenues aux fréquences de fonctionnement du radar à pénétration de sol sont moins sensibles à la teneur en eau et en chlorure que la capacimétrie, comme le montre la Figure 13.

Deux configurations de radar bi-statiques ont été utilisées dans le cadre de la présente thèse. La première est une configuration classique, avec les antennes de transmission et de réception fixées à une distance constante et les temps d'arrivée des ondes réfléchies sont analysés afin d'estimer la profondeur de l'interface réflective, ainsi que présenté à la Figure 17(a). La permittivité du support peut aussi être déterminée à partir de la vélocité de groupe, calculée à partir de l'heure d'arrivée de l'amplitude la plus élevée du signal reçu.

Deuxièmement, la réflexion-réfraction grand angle a été utilisée pour les configurations où les antennes de transmission et de réception sont dissociées. Les mesures sont prises à décalages croissants, selon la Figure 17(b). Les informations de décalages multiples permettent d'obtenir la vélocité de la phase en fonction de la fréquence, à l'aide de la transformation du champ d'onde *f-β* [**47**] [**46**]. Au sein des supports dispersifs, la vélocité de propagation peut ainsi être déterminée plus précisément que lorsque la vélocité est calculée à partir du moment de l'arrivée du pic d'amplitude [**46**]. De plus, une méthode « d'intercouplage » a été élaborée par Ihamouten [**47**] et

peut être appliquée aux mesures RPS in situ pour l'estimation de la variation de fréquences de la permittivité complexe de divers bétons. Ihamouten [**47**] a également développé une procédure permettant la détermination d'une profondeur de couche de permittivité contrastée, sur la base de la théorie de guidage des ondes EM [**48**].

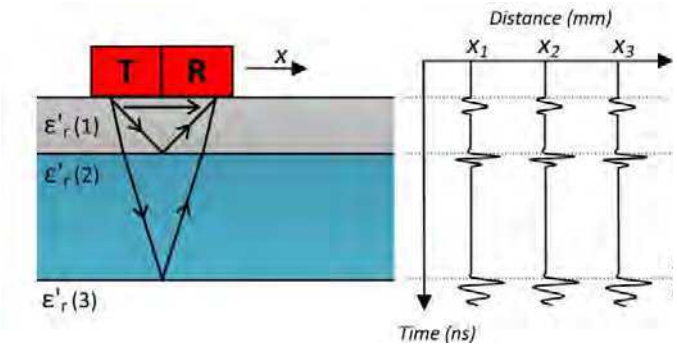

(a)

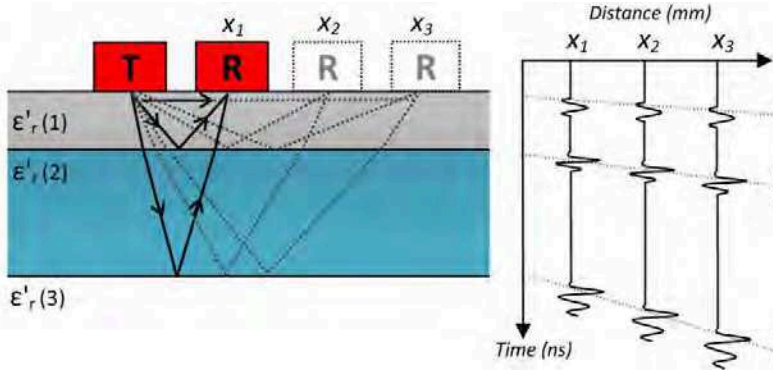

(b)

Figure 17 : schéma des configurations du radar à pénétration de sol et radargrammes typiques respectivement pour (a) la configuration classique, où le transmetteur et le récepteur sont maintenus à un décalage constant et (b) la réflexion-réfraction grand angle, où le récepteur est déplacé en fonction du transmetteur.

3. Principal programme expérimental

3.1. Etude paramétrique

3.1.1. Configuration expérimentale

La principale campagne expérimentale qui a été réalisée dans le cadre de la présente thèse se fonde sur une étude paramétrique rigoureuse, visant à évaluer la dépendance des observables EM aux propriétés inhérentes et à l'état du béton. Cette étude a été réalisée dans un environnement contrôlé, en laboratoire, en testant des carottes de béton conditionnées à l'aide de la cellule de

résistivité et de la cellule EM présentée précédemment. Les observables EM étudiés sont la résistivité électrique ρ, la constante diélectrique à 33 et 900 MHz (ε'_1 et ε'_2) ainsi que le facteur de perte à 33 et 900 MHz (ε''_1 et ε''_2). Ces observables ont été étudiés pour quatre formulations de mélanges différentes (deux bétons et deux mortiers, comme indiqué au Tableau 3) afin d'étudier l'effet des propriétés matérielles, telles que la porosité et la diffusivité du chlorure sur les observables. Le béton était mature et sélectionné conformément aux critères suivants :

- Gamme de propriétés du béton : le béton représente toute une gamme de porosités et de diffusivités, afin de permettre l'étude de l'influence de ces paramètres sur les observables EM. Les bétons sont également représentatifs des bétons habituellement mis en œuvres, afin de maîtriser les courbes à appliquer hors du cadre de la présente étude.
- Maturité du béton : il était important de réaliser l'étude sur un béton dont la structure poreuse resterait constante pour toute la durée du programme expérimental. Le béton mature, dont l'hydratation s'est stabilisée, a donc été sélectionné afin d'obtenir de bons résultats. Les spécimens de béton utilisés dans le cadre de l'étude ont été coulés en 2007, quatre ans avant le début de l'étude.
- Capacité à être facilement conditionné : étant donné que le béton a été testé à différents niveaux de saturation et de teneur en chlorure, les spécimens de béton devaient présenter une taille et un mélange pouvant être facilement saturé, homogénéisé et séché, afin de produire des résultats dans un espace-temps raisonnable. Les mélanges sélectionnés se sont révélés faciles à conditionner dans le cadre d'études précédentes [**47**].

Tableau 3 : formulation du mélange destiné à l'étude paramétrique de la sensibilité des observables EM à l'état du béton.

	B3 **E/C ≈ 0,35**	**B4** **E/C ≈ 0,65**	**B5** **E/C ≈ 0,35**	**B6** **E/C ≈ 0,65**
Constituant	Formule sèche au m3 (en kg)	Formule sèche au m3 (en kg)	Formule sèche au m3 (en kg)	Formule sèche au m3 (en kg)
Sable Pilier 0/4	417.18	445.21	596.7	648.68
Sable Pontreaux 0/2	428.28	449.23	601.0	651.78
Pontreaux 6/10	772.91	785.01	0.0	0.00
Pontreaux 10/20	0.00	0.00	0.0	0.00
Ciment 52,5 SPLC	518.92	341.36	757.2	492.10
SP Glénium 27	13.04	0.00	19.0	0.00
Eau d'ajout	187.57	235.03	261.8	331.90
Total (kg)	2338	2256	2236	2124
Porosité (2011) [%]	12.9	18.2	19.1	26.9
Diffusivité x 10^{-12} [m^2/s]	4.1	54.2	6.5	62.1

La résistivité et la permittivité des quatre mélanges ont été testées pour différentes concentrations de chlorure et degrés de saturations, comme l'indique la Figure 18. Un intérêt particulier a été porté à l'influence du degré de saturation sur les différents observables EM car cette variable est considérée comme particulièrement importante dans la littérature portant sur la réponse EM du béton [**16**]. Afin de conditionner les spécimens, un protocole de séchage a été appliqué, avec des points de mesure principaux pris à des niveaux de saturation de 100%, 80%, 60%, 40% et 0% pour trois états de conditionnement Cl (0, 15 et 30 g/L NaCl). Des points de mesure intermédiaires à des saturations de 90%, 70% et 50% ont également été pris pour l'état initial, non contaminé. Les paramètres de porosité, diffusivité du chlorure, degré de saturation et teneur en chlorure sont collectivement dénommés « paramètres d'état », dans le cadre de la présente thèse.

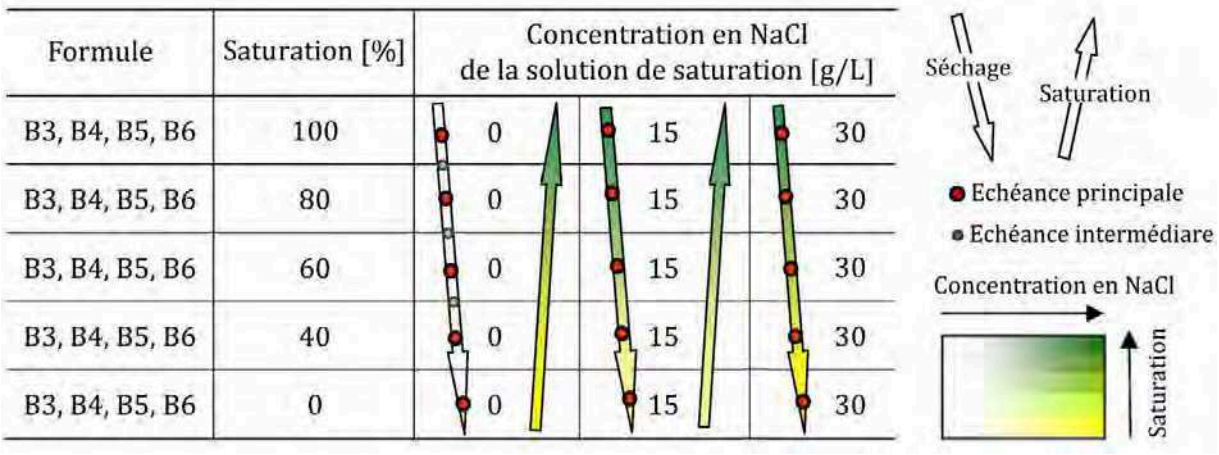

Figure 18 : programme de test, indiquant les points de tests pour chaque degré de saturation et de concentration en chlorure pour l'étude paramétrique.

3.1.2. Résultats de l'étude paramétrique

Les résultats de la dépendance des observables EM à la saturation et aux paramètres liés à la qualité du béton, c'est-à-dire la porosité et la diffusivité du chlorure sont présentés à la Figure 19. Les résultats des observables EM en fonction de la teneur totale en chlorure dans des conditions de saturation sont présentés à la Figure 20 et les observations les plus marquantes résultant de cette étude paramétrique sont présentées ci-dessous.

Le logarithme de résistivité s'est révélé particulièrement dépendant au degré de saturation du béton, comme le présente la Figure 19(a). Ce rapport est non-linéaire, avec une courbe quadratique qui correspond bien aux données expérimentales (valeurs r^2 de plus de 0,95 pour tous les mélanges). Il apparaît aussi clairement que le rapport entre $Log(\rho)$ et la porosité et la diffusivité est fortement influencé par le degré de saturation. En conséquence, on observe à la Figure 19(a_2) que $Log(\rho)$ est bien corrélé à la porosité, à de hauts degrés de saturation. En revanche, il est corrélé à la diffusivité du chlorure à de faibles degrés de saturation (Figure 19(a_1)). Un important rapport logarithmique entre $Log(\rho)$ et la teneur totale en chlorure a été observée, comme le montre la Figure 20(a).

Les constantes diélectriques, à la fois pour les hautes et les basses fréquences, présentent une dépendance linéaire au degré de saturation, ainsi que présenté à la Figure 19(b) et (c). Les résultats des différents mélanges montrent également qu'il existe un rapport linéaire avec la porosité, quel que soit le degré de saturation, avec l'exemple à 40% de saturation présenté à la Figure 19(c_l). Etant donné que cela implique que la permittivité n'est pas bien corrélée à la diffusivité du chlorure, la conclusion est que la constante diélectrique n'est pas influencée de manière significative par l'interconnexion des pores. Un rapport logarithmique des constantes diélectriques avec la teneur totale en chlorure est observée à la Figure 20(b) et (c). Les constantes diélectriques à 33 MHz se sont révélées plus sensibles au degré de saturation et de teneur en chlorure que les constantes diélectriques à 900 MHz.

Les facteurs de perte à haute et basse fréquence présentent un rapport quadratique à la saturation et au rapport logarithmique à la teneur en chlorure, comme le présente la Figure 19(d) et (e). Un rapport logarithmique est aussi observé entre le facteur de perte et la teneur totale en chlorure, à la Figure 20(d) et (e). La Figure 19 et la Figure 20 montrent clairement que les facteurs de perte sont particulièrement sensibles au degré de saturation et de teneur en chlorure, particulièrement à basse fréquence. Bien que les principales courbes développées pour les facteurs de perte peuvent avoir une application limitée en pratique avec les techniques actuellement disponibles, elles pourraient présenter un potentiel important une fois que les techniques permettant de déterminer in situ les facteurs de perte du béton seront arrivées à maturité. Cette sensibilité du facteur de perte à basse fréquence aux degrés de saturation et à la teneur en chlorure pourrait être particulièrement utile si les méthodes permettant de déterminer cet observable sont améliorées.

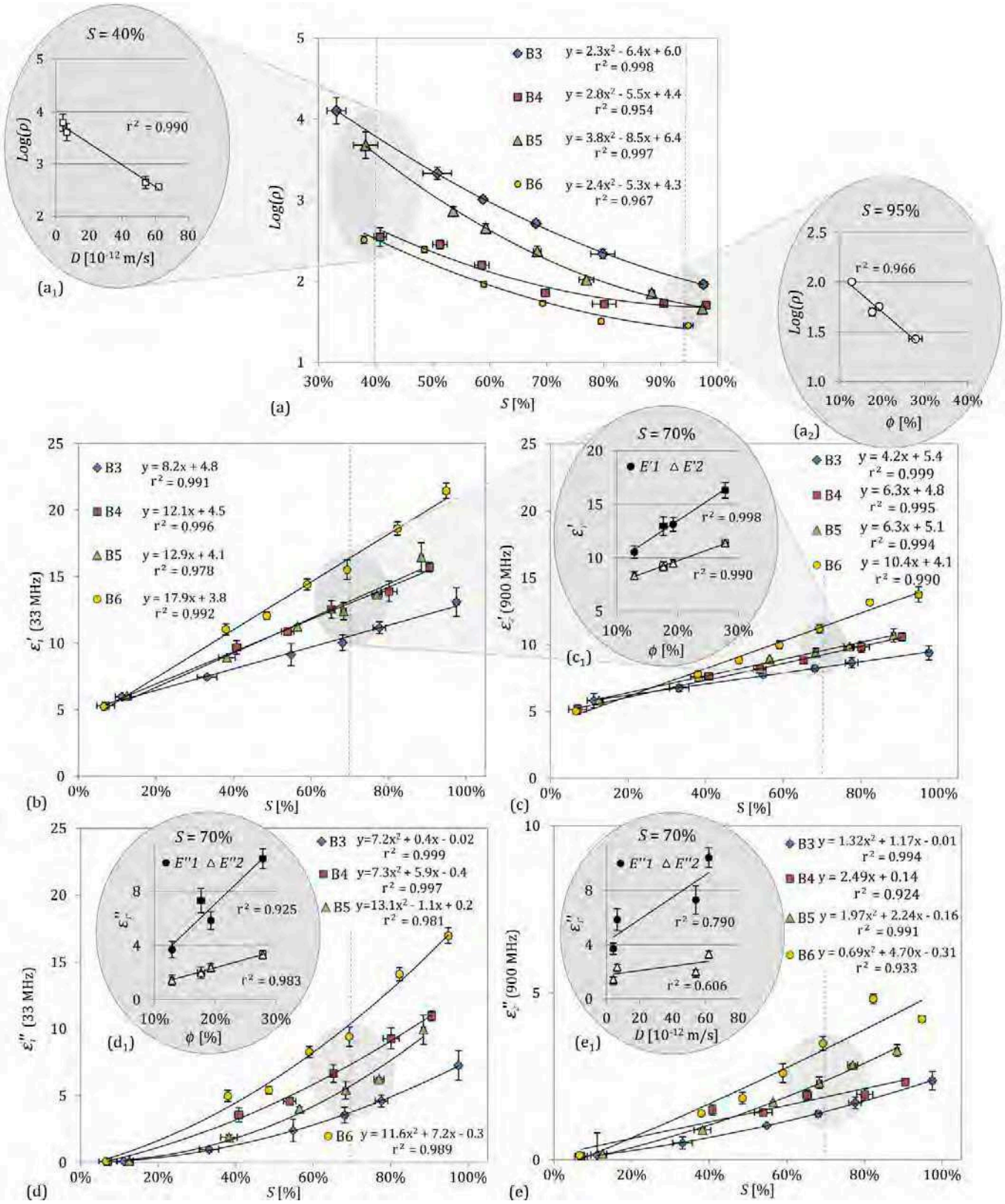

Figure 19 : **les observables EM en fonction du degré de saturation pour (a) le logarithme de résistivité *Log(ρ)* (b) la constante diélectrique à 33 MHz *ε'1*, (c) la constante diélectrique à 900 MHz *ε'2*, (d) le facteur de perte à 33 MHz *ε"1* et (e) le facteur de perte à 900 MHz *ε"2*.**

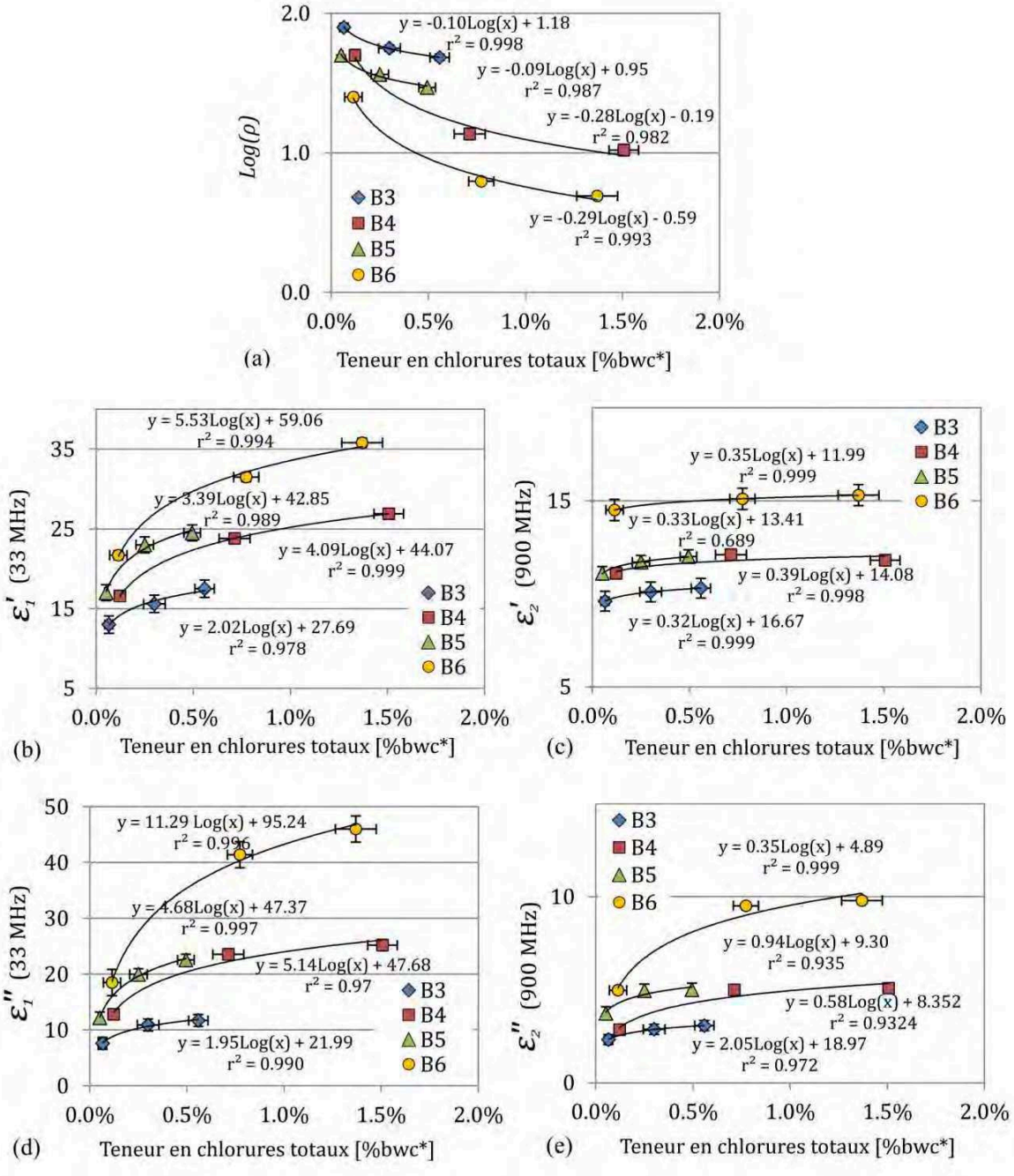

Figure 20 : observables EM en tant que fonctions de la teneur totale en chlorure par poids de ciment pour (a) le logarithme de résistivité *Log(ρ)* (b) la constante diélectrique à 33 MHz ε'_1, (c) la constante diélectrique à 900 MHz ε'_2, (d) le facteur de perte à 33 MHz ε''_1 et (e) le facteur de perte à 900 MHz ε''_2 (*g/100g de cement).

3.2. Application des modèles existants aux données mesurées

La performance des deux modèles théoriques composites les plus communément appliqués au béton en termes de résistivité et de permittivité, à savoir la loi d' Archie et le modèle Lichtenecker Rother (CRIM), a été évaluée au regard des résultats expérimentaux émanant de l'étude paramétrique. Ces modèles ont été présentés aux paragraphes 2.1.1 et 2.2.1. Les valeurs mesurées sur la base des valeurs modélisées à l'aide de la loi d'Archie sont présentées pour la

conductivité et la résistivité à la Figure 21(a) et (b). Bien que les résultats relatifs à la conductivité semblent être assez bon, avec une valeur r^2 de 0,95, la différence entre les résultats modélisés et les résultats mesurés apparaît lorsque les résultats sont convertis en termes de résistivité. La loi d'Archie fonctionne bien pour les conditions saturées, mais ses performances sont inadéquates pour les conditions non saturées et pour les mélanges dont les propriétés varient. Les résultats mesurés et modélisés pour la constante diélectrique, déterminée par le modèle CRIM, sont présentés à la Figure 22(a) pour 33 Hz et à la Figure 22(b) pour 900 Hz. Dans les deux cas, le modèle montre de bonnes performances à basse saturation, mais ne produit pas de résultats satisfaisants dans les conditions de haute saturation et de contamination aux chlorures.

Ainsi, la conclusion est que les modèles théoriques composites tels que la loi d'Archie et le modèle CRIM sont très limités lorsque les observables EM de différents bétons sont modélisés sur toute une gamme de saturations, de teneurs en chlorure et de fréquences. La littérature suggère [**34**] [**47**] [**49**] que des modèles phénoménologiques plus complexes peuvent produire de meilleurs résultats que les simples modèles théoriques composites. Toutefois, il est difficile de relier les paramètres utilisés par ces modèles aux paramètres liés à l'état du béton.

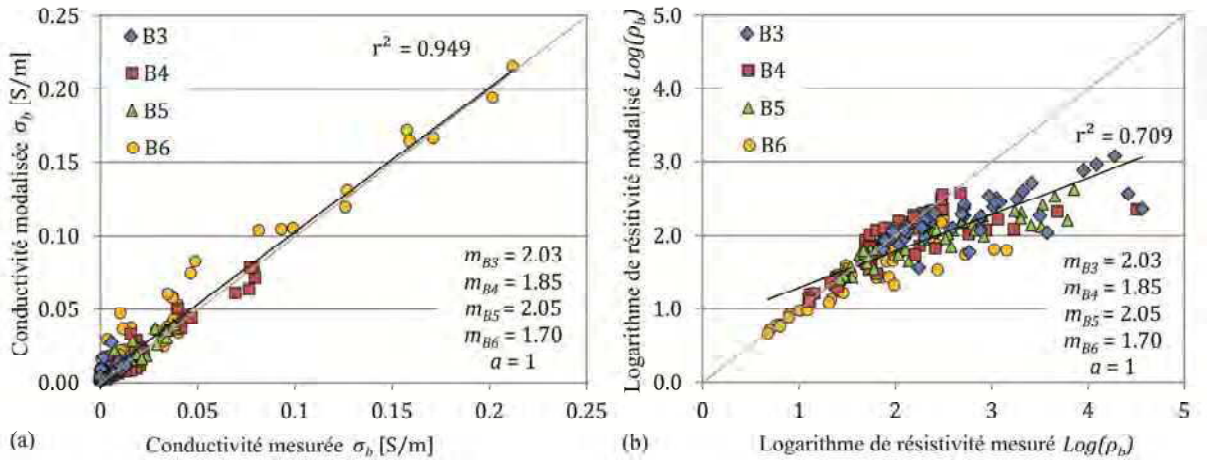

Figure 21 : **Application de la loi d'Archie par (a) conductivité modélisée vs conductivité modélisée σ_b pour des paramètres de mélange spécifiques m où $a = 1$ et (b) logarithme de résistivité modélisé $Log(\rho_b) = Log(1/\sigma_b)$ vs valeurs mesurées pour les paramètres spécifiques au mélange m où $a = 1$.**

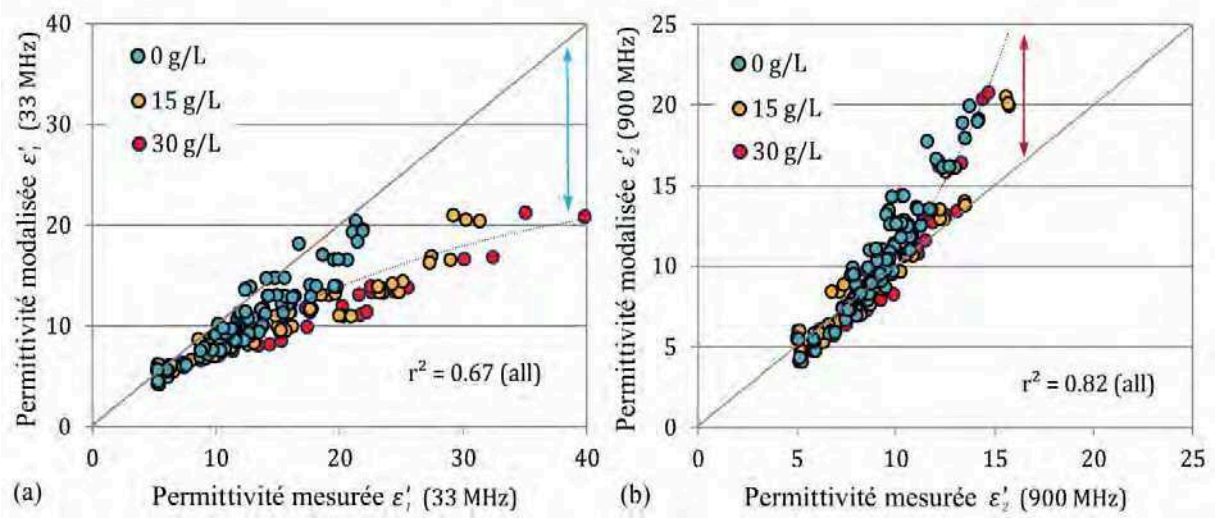

Figure 22 : Résultats du modèle CRIM model montrant (a) les constantes diélectriques modélisées par rapport aux constantes diélectriques mesurées ε'_1 à 33 MHz, (b) les constantes diélectriques modélisées par rapport aux constantes diélectriques mesurées ε'_2 à 900 MHz.

3.3. Analyse de régression linéaire multiple

3.3.1. Définition des modèles de régression multiples

Le chapitre précédent montre clairement qu'il n'est pas simple de définir un rapport général entre l'état du béton et ses réponses EM dans le large spectre d'états qui font partie intégrante de l'étude paramétrique. L'analyse de régression linéaire multiple a été choisie en tant qu'outil d'évaluation de l'influence combinée des paramètres d'état sur les observables EM, dans le cadre de la présente étude. La régression n'impose pas de connaître les paramètres physiques exacts du phénomène pour évaluer le rapport entre les variables dépendantes et indépendantes.

L'équation générale pour la régression linéaire multiple est présentée à Equation (12) :

$$y_i = \beta_0 + \beta_1 x_{i1} + \beta_2 x_{i2} + \ldots + \beta_p x_{ip} + e_i \quad (12)$$

$$i = 1, 2, \ldots, n$$

où y_i est la réponse pour l'observation i^{th} , x_{i1}, x_{i2},..., x_{ip} sont les variables, β_0, β_1,..., β_p sont les coefficients de régression et e_i est l'erreur estimée (résiduelle). Aussi : n est le nombre d'observations et p est le nombre de degrés de liberté (noter que bien qu'il n'existe aucune interaction entre les variables, elles sont présentées ici pour des raisons de simplicité, et peuvent aussi être inclues dans le modèle, comme la démonstration en sera faite ultérieurement).

L'objectif final de ce travail expérimental est l'estimation des paramètres d'état à partir de la réponse EM, en combinant les techniques in situ respectives, ainsi que présenté au Chapitre 4). Cet objectif a été atteint en résolvant le système d'équations multiples simultanées composé des

modèles de régression présentés au présent chapitre. Ainsi, afin de résoudre un problème défini de manière égale, le nombre d'équations relatives aux observables EM (« connues ») devait être égal au nombre de paramètres d'état (« inconnues »).

Dans le cadre de la présente thèse, sur la base des techniques EM disponibles, à savoir l'ERT, la capacimétrie et le RPS, les observables EM qui pouvaient être aisément mesurés de manière fiable in situ sont la résistivité du courant continu et les constantes diélectriques, respectivement à 33 et 900 MHz (ε'_1 t ε'_2). Le facteur de perte à 900 MHz (ε''_2) a également pu être déterminé, mais la procédure a pris plus de temps et les résultats obtenus sont moins fiables. La technique in situ permettant de déterminer le facteur de perte à 33 MHz (ε''_1) n'était pas encore disponible. Deux systèmes d'équations ont donc été élaborés. Ont été élaborés : premièrement, un système d'équations comprenant des modèles de régression pour *trois* observables EM, sur la base de *trois* paramètres d'état et deuxièmement, un système de modèles de *quatre* observables EM contenant *quatre* paramètres d'état. Le premier système était sensé être plus simple à mettre en œuvre en pratique, alors que le second était sensé produire de meilleurs résultats pour une large gamme de bétons. Les équations intégrées à chaque système d'équations (Système 1) et (Système 2) ont été basées sur les résultats des rapports obtenus dans le cadre de l'étude paramétrique.

Pour le premier système de modèles de régression, les trois paramètres d'état auxquels la résistivité et les constantes diélectriques ε'_1 et ε'_2 étaient le plus sensibles ont été sélectionnés. Le degré de saturation (S) et le logarithme de la teneur totale en chlorure ($C = Log(C\ell_t)$) ont été choisis comme variables liés à l'état du béton. La porosité (φ) a été choisie comme paramètre représentant les propriétés du béton étant donné que les trois observables EM sélectionnés présentaient une dépendance à la porosité au cours de l'étude paramétrique. Toutes les interactions entre les paramètres d'état ont été inclues afin de produire une fonction à douze termes pour chaque observable EM (appelé Système 1) :

$$Log(\rho)_i = a_o + a_1 S_{i1} + a_2 S^2_{i2} + a_3 C_{i3} + a_4 \varphi_{i4} + a_5 S_{i5} C_{i5} + \ldots + a_{11} S^2_{i11} C_{i11} \varphi_{i11} + e_{ai}$$

$$\varepsilon'_{1i} = b_o + b_1 S_{i1} + b_2 S^2_{i2} + b_3 C_{i3} + b_4 \varphi_{i4} + b_5 S_{i5} C_{i5} + \ldots + b_{11} S^2_{i11} C_{i11} \varphi_{i11} + e_{bi}$$

$$\varepsilon'_{2i} = c_o + c_1 S_{i1} + c_2 S^2_{i2} + c_3 C_{i3} + c_4 \varphi_{i4} + c_5 S_{i5} C_{i5} + \ldots + c_{11} S^2_{i11} C_{i11} \varphi_{i11} + e_{ci}$$

où a_o, …, a_j, …, a_{11}, b_o, …, b_j, …, b_{11}, c_o, …, c_j, …, c_{11},sont les coefficients de régression pour chaque terme des modèles de régression respectifs (j = 0, 1, …, 11) pour $Log(\rho)$, ε'_1 et ε'_2, S_{ij}, C_{ij} et φ_{ij} sont les paramètres d'état pour la $i^{ième}$ observation et le $(j+1)^{ième}$ terme du polynôme et e_{ai}, e_{bi} et e_{ci} sont les résidus pour la $i^{ième}$ observation de chaque modèle.

Les trois modèles de régression obtenus, y compris toutes les interactions, sont présentés à la Figure 23, avec les valeurs modélisées présentées face aux valeurs mesurées pour chaque observable EM.

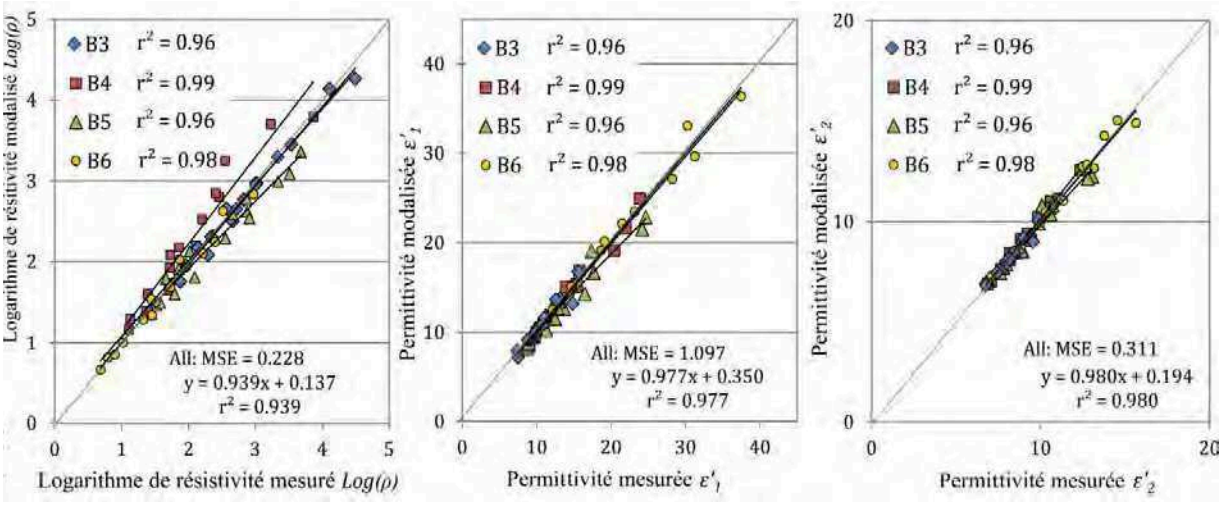

Figure 23 : résultats modélisés pour la régression multiple à 3 paramètres, y compris toutes les interactions, face aux valeurs mesurées pour (a) le logarithme de résistivité *Log(ρ)*, (b) la constante diélectrique à 33 MHz ε'_1 et (c) la constante diélectrique à 900 MHz ε'_2.

Comme anticipé, le modèle de régression de *Log(ρ)* ne produit pas d'aussi bons résultats que les deux autres modèles, avec la valeur r² de 0,939 qui est beaucoup plus faible que celle de ε'_1 et ε'_2. Ceci pourrait être du à l'influence des propriétés de diffusion sur la réponse de résistivité à des saturations plus basses. La Figure 23(a) montre clairement que les valeurs modélisées correspondant aux deux mélanges présentant des porosités similaires (B4 et B5) présentent le plus grand écart par rapport aux valeurs mesurées, ce qui augmente la résistivité. Les deux modèles relatifs aux constantes diélectriques à basse et haute fréquence produisent de meilleurs résultats, avec des valeurs r² proches de 0,98.

Le second système de modèles de régression inclut, en plus, la diffusivité du chlorure (D) en tant que paramètre d'état et le facteur de perte à 900 MHz (ε''_2) en tant qu'observable EM. Les équations du Système 1 ont été étendues et une quatrième équation a été ajoutée afin d'obtenir un système contenant un modèle de régression à 24 termes pour chaque observable EM, comme suit (appelé Système 2) :

$$Log(\rho)_i = a_o + a_1 S_{i1} + a_2 S^2_{i2} + a_3 C_{i3} + a_4 \varphi_{i4} + a_5 D_5 + \ldots + a_{23} S^2_{i23} C_{i23}\, \varphi_{i23} D_{i23} + e_{ai}$$

$$\varepsilon'_{1i} = b_o + b_1 S_{i1} + b_2 S^2_{i2} + b_3 C_{i3} + b_4 \varphi_{i4} + b_5 D_5 + \ldots + b_{23} S^2_{i23} C_{i23}\, \varphi_{i23} D_{i23} + e_{bi}$$

$$\varepsilon'_{2i} = c_o + c_1 S_{i1} + c_2 S^2_{i2} + c_3 C_{i3} + c_4 \varphi_{i4} + c_5 D_5 + \ldots + c_{23} S^2_{i23} C_{i23}\, \varphi_{i23} D_{i23} + e_{ci}$$

$$\varepsilon''_{2i} = d_o + d_1 S_{i1} + d_2 S^2_{i2} + d_3 D_{i3} + d_4 \varphi_{i4} + d_5 D_5 + \ldots + d_{23} S^2_{i23} C_{i23}\, \varphi_{i23} D_{i23} + e_{di}$$

où les symboles sont définis comme pour le système 1 avec l'addition de ε''_{2i} comme observable EM et la diffusivité D comme paramètres d'état ayant les coefficients de régression d_j avec $j = 0$, 1, …, 23.

Les résultats du modèle de régression à quatre paramètres pour chaque observable EM, ainsi que toutes les interactions, sont présentés à la Figure 24. La comparaison avec les résultats de la Figure 23(a), montrent que la valeur r^2 de *Log(ρ)* s'est considérablement améliorée, passant de 0,939 à 0,991 en raison de l'inclusion de la diffusivité comme paramètre d'état.

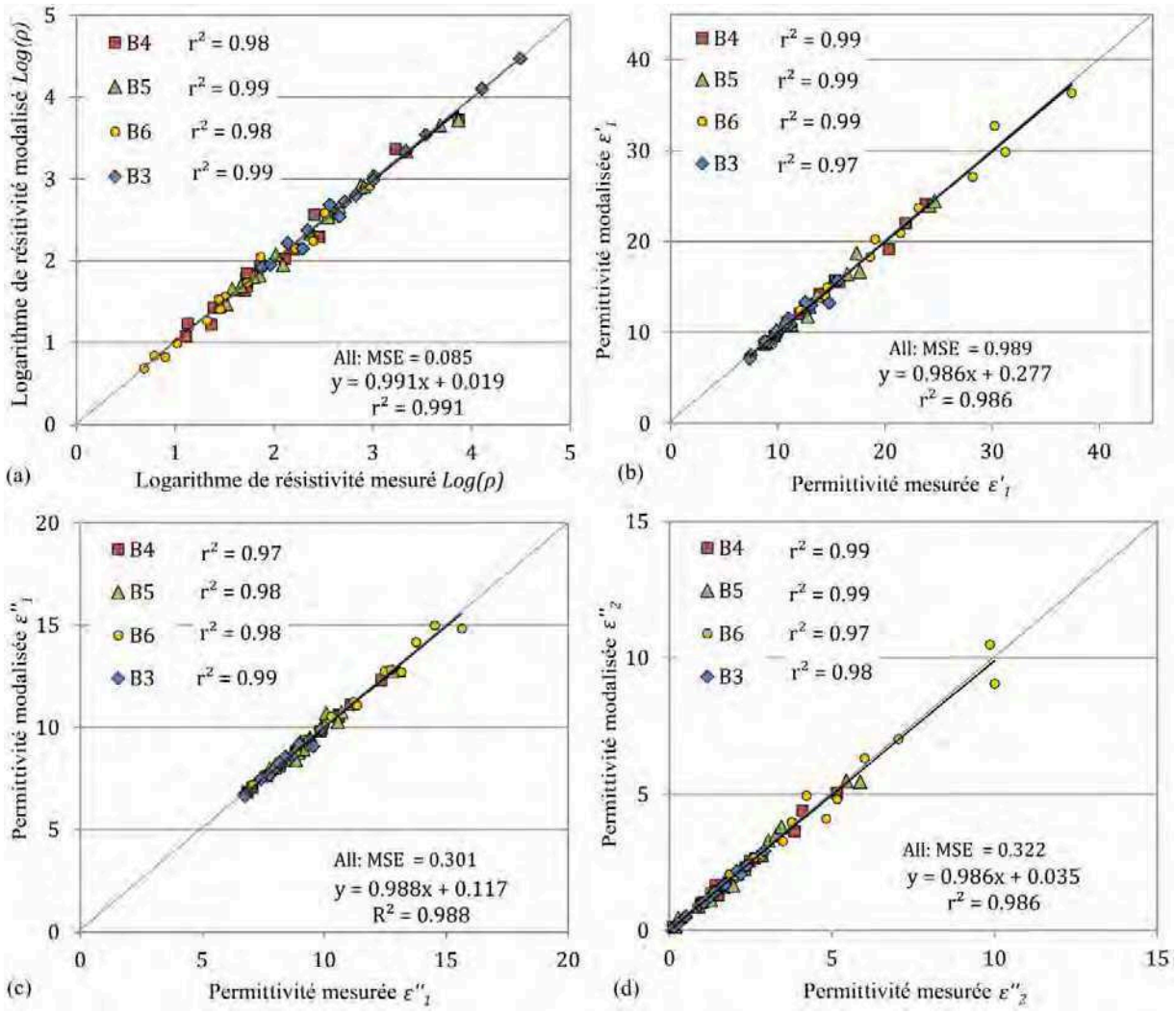

Figure 24 : résultats modélisés à partir de la régression multiple à 4 paramètres, y compris toutes les interactions, vis-à-vis des valeurs mesurées pour (a) le logarithme de résistivité *Log(ρ)*, (b) la constante diélectrique à 33 MHz ε'_1, (c) la constante diélectrique à 900 MHz ε'_2 et (d) le facteur de perte à 900 MHz ε''_2.

3.3.2. Vérification d'hypothèse

La vérification d'hypothèse [**50**] a été employée afin d'évaluer l'importance statistique de chaque paramètre d'état et les interactions entre eux. En testant chaque terme des modèles de régression

vis-à-vis d'une hypothèse zéro à l'aide du test F partiel, les termes pouvant être considérés comme importants et liés à un niveau de confiance choisi ont été établis. A l'aide de cette approche, les termes identifiés comme non significatifs ont pu être retirés afin de simplifier chaque modèle de régression sans compromettre sa capacité prédictive. Les gammes de paramètres d'état ont été normalisées afin d'être comprises entre -1 et 1 pour permettre la comparaison directe des amplitudes des coefficients, dans le but d'évaluer leur importance relative.

3.3.2.1. Evaluation des modèles de régression à 3 paramètres (Système 1)

Chaque coefficient de régression contenu dans les modèles de régression intégrés au Système 1 a été évalué, pour atteindre un niveau de confiance de 95% et dans le but de déterminer s'ils sont statistiquement importants. Le Tableau 4 présente les coefficients pour les paramètres normalisés et la probabilité que l'hypothèse zéro soit avérée (P > F). Les coefficients qui se sont révélés significatifs selon le test F, avec une confiance supérieure à 95%, sont surlignés en jaune. On observe que pour *Log(ρ)* aucun des termes d'interaction n'est significatif, alors que pour ε'_1 et ε'_2 certaines interactions entre la saturation, la teneur en chlorure et la porosité sont significatives. Egalement, pour *Log(ρ)* le terme lié au terme quadratique pour le degré de saturation S_1 est significatif, ce qui n'est pas le cas des deux autres observables EM (ce qui conforte les résultats de l'étude paramétrique).

Les modèles de régression ont été simplifiés afin de ne contenir que les termes significatifs et le Tableau 4 montre qu'il n'y a pas de baisse importante et présente les valeurs r^2 de l'ensemble des modèles de régression ainsi que les modèles simplifiés (r^2-ajusté).

Tableau 4 : Coefficients des paramètres normalisés du système à 3 paramètres, leurs importances telles que déterminées par le test F partiel et les coefficients ajustés pour le modèle simplifié (les coefficients dont la probabilité est supérieure à 95% sont non-zéro, surlignés en jaune).

EM obs. / Param.	*Log(ρ)*			ε'_1			ε'_2		
	$a_{(norm)}$	$\mathcal{P} > F$	$a_{adj(norm)}$	$b_{(norm)}$	$\mathcal{P} > F$	$b_{adj(norm)}$	$c_{(norm)}$	$\mathcal{P} > F$	$c_{adj(norm)}$
1	3.60		3.62	2.07		2.09	1.44		1.45
S_1	1.65	< 0.0001	1.71	1.02	< 0.0001	1.04	0.44	< 0.0001	0.43
S_2	-0.73	< 0.0001	-0.80	0.08	0.052	-	0.03	0.067	-
C	0.48	0.000	0.39	0.51	< 0.0001	0.49	0.06	0.001	0.05
ϕ	0.67	< 0.0001	0.71	0.49	< 0.0001	0.45	0.18	< 0.0001	0.18
$S_1 C$	0.22	0.072	-	0.44	< 0.0001	0.42	0.04	0.053	-
$S_2 C$	-0.22	0.292	-	-0.11	0.870	-	-0.03	0.260	-
$S_1 \phi$	-0.27	0.053	-	0.31	< 0.0001	0.33	0.16	< 0.0001	0.17
$S_2 \phi$	0.04	0.881	-	-0.08	0.552	-	0.00	0.751	-
ϕC	0.07	0.344	-	0.30	< 0.0001	0.42	-0.01	0.088	-
$S_1 C \phi$	0.08	0.646	-	0.21	0.027	-	-0.05	0.072	-
$S_2 C \phi$	0.01	0.971	-	-0.24	0.107	-	-0.05	0.287	-
r^2		0.939			0.979			0.986	
r^2(ajusté)		0.927			0.970			0.979	

3.3.2.2. Evaluation des modèles de régression à 4 paramètres (Système 2)

Afin d'évaluer la contribution des paramètres d'état et leurs interactions dans le cadre des modèles de régression à 4 paramètres (Système 2), un niveau de confiance de 99% était attendu car l'ajout de la diffusivité du chlorure était sensé améliorer la fiabilité des coefficients adaptés. Les coefficients de régression normalisés identifiés comme significatifs au regard du test F partiel sont surlignés en jaune au Tableau 5.

Les probabilités du test F partiel confirment ce qui a été observé au cours de l'étude paramétrique, à savoir que la diffusivité du chlorure D est significative en termes de $Log(\rho)$ comme le montre le Tableau 5. Bien que le modèle à 3 paramètres suggère qu'il n'existe pas d'interactions significatives pour $Log(\rho)$, le modèle à 4 paramètres montre l'existence d'interactions significatives qui étaient probablement masquées dans le modèle à 3 paramètres en raison d'une moindre adaptation des données.

Les termes significatifs pour ε'_1 et ε'_2 sont exactement les mêmes que ceux du modèle à 3 paramètres, ce qui indique que l'inclusion de la diffusivité n'améliore pas ces modèles et que la constante diélectrique ne dépend pas des propriétés diffusives du béton. Toutefois, l'étude des coefficients de ε''_2 montre que la diffusivité joue un rôle important en ce qui concerne le facteur de perte.

Les valeurs r^2 des modèles complets à 4 paramètres et des modèles simplifiés, ainsi que les r^2-ajustées sont présentées au Tableau 5. On observe qu'il n'existe pas de réduction majeure de l'adaptation, toutes les valeurs r^2 ajustées étant supérieures à 0,97. Les valeurs r^2 de $Log(\rho)$ montrent une amélioration importante par rapport aux valeurs du modèle à 3 paramètres, ce qui souligne l'avantage de l'ajout de la diffusivité du chlorure comme paramètre d'état supplémentaire.

Tableau 5 : les coefficients (après normalisation) des modèles factoriels complets à 4 paramètres, ainsi que l'importance de chaque coefficient telle que déterminée par le test F partiel, ces coefficients présentant une probabilité supérieure à 99% de ne pas être à zéro sont surlignés en jaune.

EM obs. / Param.	$Log(\rho)$			ε_1'			ε_2'			ε_2''		
	$a_{(norm)}$	$\mathcal{P}>F$	$a_{adj(norm)}$	$b_{(norm)}$	$\mathcal{P}>F$	$b_{adj(norm)}$	$c_{(norm)}$	$\mathcal{P}>F$	$c_{adj(norm)}$	$d_{(norm)}$	$\mathcal{P}>F$	$d_{adj(norm)}$
1	3.59			2.03		2.09	1.41		1.445	2.57		2.76
S_1	1.626	< 0.0001	1.732	1.048	< 0.0001	1.038	0.426	< 0.0001	0.433	2.153	< 0.0001	2.386
S_2	-0.658	< 0.0001	-0.845	0.230	0.014	-	0.117	0.041	-	0.788	< 0.0001	0.392
C	0.275	< 0.0001	0.297	0.438	< 0.0001	0.491	0.046	0.001	0.050	0.602	< 0.0001	0.925
ϕ	0.310	< 0.0001	0.394	0.431	< 0.0001	0.452	0.176	< 0.0001	0.184	1.009	< 0.0001	1.264
D	0.376	< 0.0001	0.349	0.048	0.014	-	0.058	0.029	-	0.113	0.000	-0.160
S_1C	0.413	0.000	-0.015	0.442	< 0.0001	0.415	0.072	0.035	-	0.905	< 0.0001	-0.617
S_2C	-0.217	0.029	-	0.032	0.717	-	0.058	0.243	-	0.643	0.051	-
$S_1\phi$	0.183	0.000	0.043	0.478	< 0.0001	0.328	0.190	< 0.0001	0.168	1.357	< 0.0001	0.547
$S_2\phi$	0.079	0.351	-	0.213	0.491	-	0.098	0.700	-	0.668	0.080	-
S_1D	-0.441	< 0.0001	-0.247	-0.166	0.015	-	-0.018	0.181	-	-0.481	< 0.0001	1.041
S_2D	0.059	0.655	-	-0.257	0.172	-	-0.088	0.341	-	-0.738	0.036	-
$C\phi$	-0.080	0.035	-	0.113	< 0.0001	0.415	-0.071	0.039	-	-0.031	< 0.0001	1.536
CD	0.156	0.228	-	0.179	0.025	-	0.057	0.334	-	0.482	0.042	-
ϕD	-0.029	0.013	-	0.031	0.141	-	0.042	0.778	-	0.227	0.938	-
$S_1C\phi$	-0.114	0.324	-	0.165	0.013	-	-0.016	0.034	-	0.215	0.028	-
$S_2C\phi$	0.470	-	-	0.013	-	-	0.135	0.193	-	0.963	-	-
$S_1\phi D$	0.259	0.331	-	-0.166	0.088	-	0.009	0.570	-	0.112	0.831	-
$S_2\phi D$	-0.166	-	-	-0.257	-	-	-0.137	0.043	-	-0.707	-	-
S_1CD	0.279	0.013	-	0.087	0.712	-	-0.018	0.812	-	0.378	0.137	-
S_2CD	-0.324	-	-	-0.158	-	-	-0.143	0.114	-	-0.574	-	-
$C\phi D$	0.470	0.015	-	0.133	0.265	-	-0.055	0.602	-	0.063	0.339	-
$S_1C\phi D$	-0.145	-	-	0.057	-	-	-0.055	0.275	-	0.063	-	-
$S_2C\phi D$	-0.285	-	-	-0.239	-	-	-0.091	0.281	-	-0.267	-	-
r^2		0.991			0.990			0.988			0.986	
r^2(ajusté)		0.972			0.970			0.974			0.972	

4. Association de techniques EM in situ afin d'estimer l'état du béton

Lorsque l'évaluation non destructive est réalisée in situ, il existe de nombreuses incertitudes qui peuvent influer sur la qualité de l'évaluation. Parmi ces incertitudes, les plus importantes sont liées à la méthode d'essai, l'influence de l'environnement, les incertitudes dues à la variabilité intrinsèque du béton, les facteurs humains et l'interprétation des données. Afin d'améliorer la fiabilité de l'évaluation in situ de l'état du béton, l'association de techniques d'évaluation non destructive a suscité beaucoup d'intérêt au cours des dernières années [**6**]. L'association de techniques peut être envisagée de différentes manières en fonction de l'objectif de l'évaluation non destructive [**6**].

Ce chapitre présente l'association de la réponse électromagnétique obtenue à partir de trois méthodes d'auscultation in situ afin d'évaluer l'état de dalles de béton du point de vue de la saturation et de la teneur en chlorure. Le système simplifié d'équation des modèles à trois paramètres (Système 1) présenté au chapitre précédent a été utilisé afin d'atteindre cet objectif.

4.1.1. Travail préparatoire et test du béton

Les mélanges de béton utilisés dans le cadre du travail présenté ici sont les mêmes que ceux utilisés pour l'étude paramétrique, comme présentés au Tableau 3. Ceci présente l'avantage de travailler sur un béton déjà mature, et de connaître les propriétés du mélange, ce qui réduit le nombre de tests destructifs supplémentaires nécessaires afin de déterminer l'état réel du béton. Les techniques d'auscultation expérimentale EM employées sont les mesures de la résistivité de surface, la méthode capacitive et le radar de pénétration de sol, tels que présentées au Chapitre 290. Les dalles de béton ont ensuite été évaluées à différents stades d'homogénéité en termes de saturation et de teneur en chlorures, en laboratoire, sous conditions contrôlées. Ceci a permis d'obtenir des conditions optimales d'auscultation afin de déterminer si les paramètres d'état pouvaient être évalués précisément à partir des observables EM. Le même protocole a donc été adopté que pour les spécimens de carottes de béton au Chapitre 1, à savoir saturation sous vide, étuvage et homogénéisation. Une dalle de dimensions 300x220x100 mm a été préparée pour chaque mélange, comme le montre la Figure 25 afin d'obtenir les états homogènes présentés au Tableau 6.

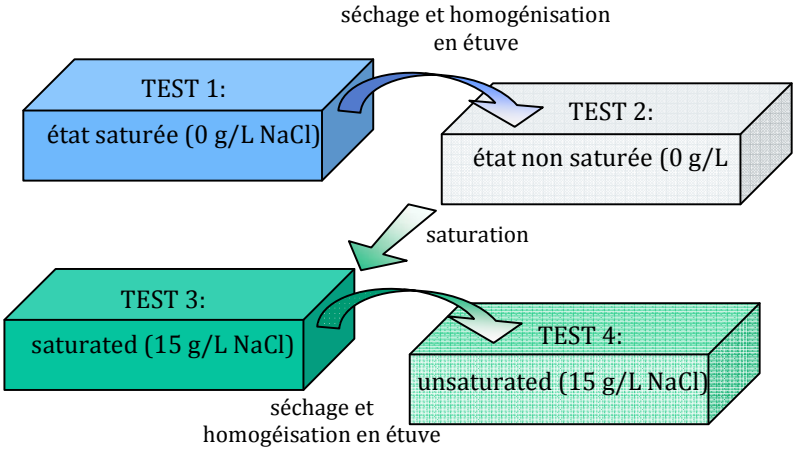

Figure 25 : schéma illustrant le protocole suivi afin de conditionner les dalles à quatre états différents (réalisé pour une dalle par mélange).

Tableau 6 : états conditionnés des dalles de béton visant à tester les techniques in situ. (* g/100 g de ciment)

Slab (mix)	Uncontaminated			NaCl contaminated		
	Degree of saturation [%]		Chloride	Degree of saturation [%]		Chloride
	Test 1	Test 2	[%bwc]	Test 3	Test 4	[%bwc]
B3	100	64.7	0.06	100	87.0	0.36
B4	100	51.4	0.12	100	78.7	0.79
B5	100	59.7	0.05	100	90.7	0.25
B6	100	42.5	0.11	100	75.2	0.67

4.1.2. Procédure d'auscultation EM

Ce chapitre présente la mise en œuvre des techniques d'auscultation in situ électromagnétiques présentée au Chapitre 2 pour l'auscultation du béton.

La sonde de résistivité multi-électrodes a été utilisée dans la configuration de Wenner et a permis de confirmer l'homogénéité des dalles grâce à sa capacité à mesurer la résistivité apparente à des profondeurs d'influence croissantes. Les dalles ont été placées sur une surface non-conductrice et la sonde a été placée proche du centre de la face supérieure, comme présenté à la Figure 26(a) et (b). Les mesures ont ensuite été corrigées pour tenir compte des effets limites en appliquant un facteur géométrique par le biais de la modélisation numérique. La sonde de résistivité multi-électrodes a également été utilisée afin d'évaluer l'homogénéité des dalles. L'homogénéité a pu être évaluée à l'horizontale et à la verticale par rapport à la profondeur et l'étude a confirmé que les dalles étaient suffisamment homogènes pour garantir l'obtention de bons résultats.

En ce qui concerne le capteur capacitif, la série d'électrodes à larges plaques a été utilisée afin d'obtenir des résultats pour la plus grande profondeur d'influence possible et avec le plus faible niveau de variabilité. Les mesures ont été prises proche du centre des dalles afin d'éviter l'influence des limites sur les côtés, comme le présente la Figure **26**(c) et (d). Les constantes diélectriques correspondantes ont ensuite été déterminées par application des courbes d'étalonnage pour la série d'électrodes présentée à la Figure 16(b).

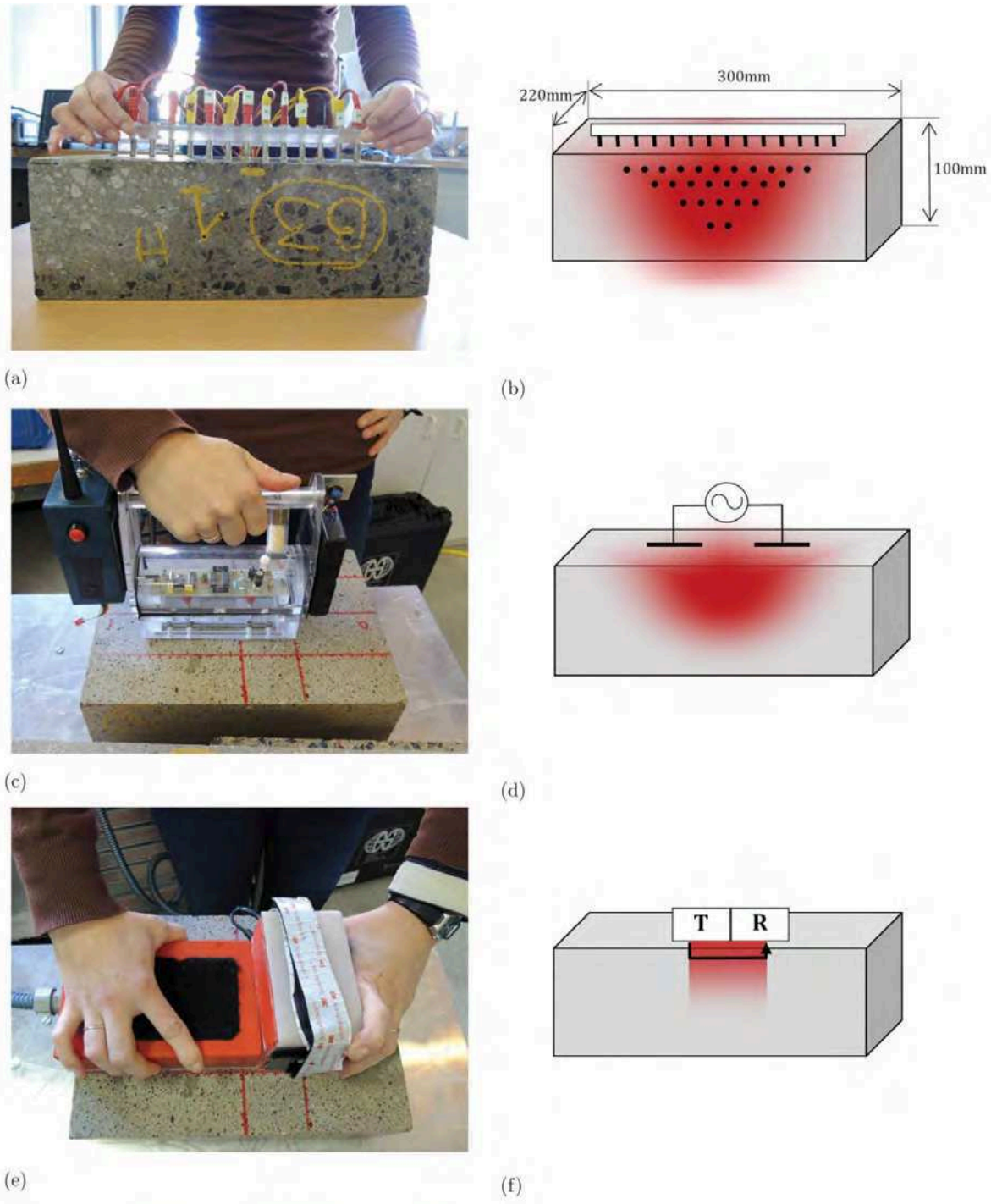

Figure 26 : Techniques EM in situ utilisées au cours de l'expérimentation et illustration de leur application avec (a) la sonde de résistivité (b) sa configuration (à des pseudoprofondeurs de 26 points de mesure), (c) la sonde capacitive avec (d) sa configuration et (e) le radar de pénétration de sol fixe, utilisant une onde directe avec (f) sa configuration.

La configuration RPS fixe, impliquant l'utilisation d'une antenne à une fréquence centrale de 1500 MHz a été utilisée, telle que décrite au Chapitre 2.2.2.3 et démontrée à la Figure **26**(e) et (f). La vitesse de propagation de l'onde directe a été déterminée à partir de l'heure d'arrivée du signal

pour chaque mesure et utilisée afin de déterminer la constante diélectrique en appliquant l'Equation (11).

4.1.3. Résultats expérimentaux

Les résultats finaux, ramenés à une moyenne, pour la sonde de résistivité, le capteur capacitif et le radar de pénétration de sol sont présentés à la Figure 27. Dans le cadre de la présente étude, il serait plus correct de faire référence à une résistivité *apparente* et à la permittivité diélectrique. Toutefois, il est possible d'accepter que ces valeurs approchent des véritables propriétés EM des dalles étant donné que celles-ci sont considérées comme homogènes.

La Figure 27(a), (c) and (e) présente les observables EM de chaque dalle vis-à-vis du degré de saturation et de la teneur totale en chlorures. Les données sont présentées comme une surface plane pour chaque dalle pour le but de la présentation, bien qu'il convienne de noter que cela n'est pas strictement correct car certains observables EM ont un rapport non linéaire avec le degré de saturation et la teneur totale en chlorures, ainsi que présenté au Chapitre 3.1. Toutefois, les tendances sont clairement observables, avec une forte baisse de $Log(\rho)$ et une augmentation des constantes diélectriques au fur et à mesure que le degré de saturation et la teneur en chlorure augmentent.

La Figure 27(b), (d) et (f) présente les résultats mesurés des techniques de vérification in situ face aux valeurs prédites par le calcul à l'aide des modèles de régression à 3 paramètres présenté au Chapitre 3.3.1. Les barres d'erreurs indiquent l'écart standard pour chaque mesure finale. Les résultats obtenus à partir des dalles correspondent relativement bien aux valeurs estimées, avec des valeurs respectives r^2 de 0,943, 0,945 et 0,972 pour la résistivité, la capacimétrie et le RPS. Ceci est acceptable si l'ont tient compte du fait qu'il existe de multiples incertitudes qui ont joué un rôle au cours du test des dalles et du développement des modèles de régression. La variation aléatoire inhérente aux observables, aux paramètres d'état, aux incertitudes liées à l'homogénéisation, aux techniques de test, aux opérateurs de test etc. mènent à une accumulation d'erreurs, même en conditions contrôlées. Un coefficient de détermination de l'ordre de 0,95 est donc considéré comme correct dans le cadre de la présente étude.

4.2. Analyse des données : Estimation des paramètres d'état

4.2.1. Méthodologie

L'objectif du travail expérimental présenté ici était d'estimer les paramètres d'état des dalles pour chaque condition de test, à partir des modèles de régression linéaires élaborés et présentés au Chapitre 3.3. Les trois observables obtenus à partir du travail expérimental ont permis de résoudre le système d'équations simultanées à 3 paramètres. Le système d'équations à 3

paramètres (Système 1) a été simplifié sur la base des résultats de l'analyse de régression et réorganisé, comme le montrent les équations suivantes :

$$\mathbf{0} = \boldsymbol{Log(\rho)} - (\mathbf{a_o} + \mathbf{a_s}\boldsymbol{S} + \mathbf{a_{s2}}\boldsymbol{S^2} + \mathbf{a_c}\boldsymbol{C} + \mathbf{a_\varphi}\boldsymbol{\varphi} + \mathbf{a_{s\varphi}}\boldsymbol{S\varphi} + \mathbf{a_{sc}}\boldsymbol{SC} + \boldsymbol{e_{Log(\rho)}})$$

$$0 = \varepsilon'_{1i} - (b_o + b_s S + b_c C + b_\varphi \varphi + b_{s\varphi} S\varphi + b_{sc} SC + b_{c\varphi} C\varphi + e_{\varepsilon'1i})$$

$$0 = \varepsilon'_{12} - (c_o + c_s S + c_c C + c_\varphi \varphi + c_{s\varphi} S\varphi + e_{\varepsilon'12})$$

où $Log(\rho)$, ε'_1 and ε'_2 sont les valeurs moyennes mesurées pour le logarithme de la résistivité, les constantes diélectriques à 33 MHz and at 900 MHz, a…, b… and c… sont les coefficients de régression pour chaque paramètre d'état telle que calculée dans le cadre de l'analyse de régression pour les modèles simplifiés.

Les observables EM sont devenus les « connus » et les paramètres d'état les « inconnus », par contraste avec le problème de régression linéaire présenté au Chapitre 3.3. Le problème est donc devenu un problème d'inversion non linéaire. Pour les systèmes non linéaires, l'utilisation de l'optimisation des moindres carrés ne fournit pas nécessairement une solution fermée. Cela implique qu'il peut exister des minima locaux, et qu'il peut être très difficile de trouver le minimum global ou approprié. Pour cette raison, les méthodes dites « ouvertes » sont utilisées lorsque les valeurs initiales sont choisies pour les paramètres qui doivent être résolus. Puis elles sont affinées à l'aide d'approximations successives afin d'obtenir la solution. Parmi ces méthodes, la méthode de Newton-Raphson est probablement la plus communément employée, et plusieurs manuels sont disponibles sur le sujet [**51**] [**52**] [**53**].

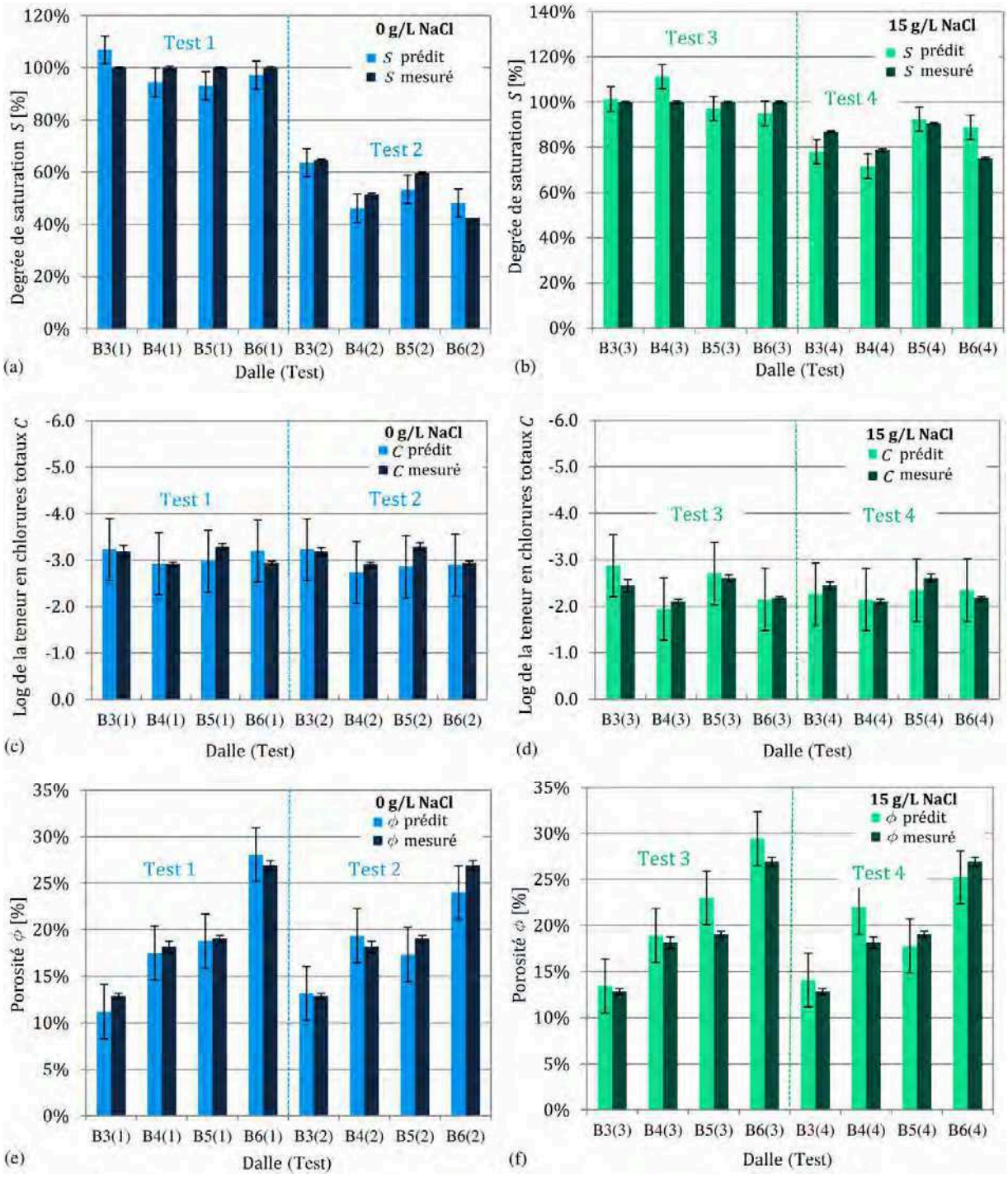

Figure 27 : Les observables EM pour les techniques in situ sur des dalles conditionnées présentés (à gauche) comme fonction de la saturation et de la teneur en chlorure et (à droite) face aux valeurs modélisées pour le logarithme de résistivité (a)-(b), la constante diélectrique (c)-(d) à) environ 33 MHz et la constante diélectrique (e)-(f) à environ 900 MHz.

Les méthodes numériques et la théorie de l'optimisation n'étant pas le thème central de la présente étude, des outils logiciels d'optimisation ont été utilisés afin d'établir la solution optimisée de chaque paramètre d'état (Microsoft Excel Solver utilisant la méthode simplex, de

gradient réduit généralisée et les méthodes de branche, sur la base de la méthode de Newton-Raphson). Il est important de souligner que l'optimisation d'un problème non linéaire ne convergeait pas nécessairement vers la solution correcte. En raison des incertitudes liées aux modèles et aux mesures utilisées ici, la solution tendait à être un minimum local plutôt qu'un minimum global. De ce fait, il était important de définir des contraintes appropriées et de fournir une hypothèse réaliste à partir de laquelle le processus itératif a été initié. Afin d'obtenir des résultats avec des limites réalistes, la gamme de chaque paramètre d'état a aussi été contrainte. Ces gammes correspondent à celles pour lesquelles les modèles ont été élaborés, étant appropriées pour le béton. Elles ont été élargies afin de compenser les erreurs de régression de chaque paramètre d'état obtenu au cours de la modélisation de régression présentée au Chapitre 3.3. L'hypothèse initiale de chaque paramètre d'état a été prise en tant que médiane des gammes définies précédemment. Toutefois, en pratique, ces hypothèses pourraient être améliorées si des informations *a priori* concernant l'état du béton étaient connues (dans le cadre de la présente étude, l'hypothèse est que cela n'était pas le cas).

4.2.2. Résultats et argumentation

Les résultats des paramètres d'état respectifs sont présentés pour chaque dalle et chaque test à la Figure 28. Les *valeurs prédites* font référence aux paramètres d'état tels que déterminés à partir des observables EM mesurés à l'aide de l'optimisation décrite précédemment, alors que les *valeurs mesurées* sont les valeurs qui ont été déterminées directement, ainsi que présentées au Tableau 6. Les barres d'erreur pour les valeurs prédites sont les erreurs au moindre carré pour chaque paramètre d'état déterminé au cours de l'analyse de régression présentée au Chapitre 3.3. Les barres d'erreurs correspondant aux valeurs mesurées sont les écarts standard communément acceptés et documentés pour la saturation et la porosité, et l'erreur de mesure pour le logarithme de la teneur en chlorure, tel que déterminé à partir de 3 tests. L'étude de la Figure 28 montre que les résultats obtenus à partir du processus d'optimisation sont assez bons, avec des valeurs prédites relatives aux paramètres d'état qui sont assez proches des valeurs réelles.

Les erreurs de pourcentage absolu des valeurs prédites par rapport aux valeurs mesurées sont présentées au Tableau 7 et à la Figure 29. On observe que les erreurs de pourcentage absolu relatives aux paramètres d'état pour le cas du 0 g/L NaCl (Tests 1 et 2) sont bonnes, à savoir inférieures à 15%. Toutefois, il semble que la variabilité est plus élevée pour le cas du ,15 g/L NaCl (Tests 3 et 4) avec des erreurs de pourcentage absolu seulement inférieures à 20%. Cette diminution de fiabilité en fonction de la teneur en chlorure pourrait être due au fait que la teneur en chlorure est le paramètre d'état auquel $Log(\rho)$ et ε'_1 sont le moins sensibles et auquel ε'_2 n'est pas du tout sensible.

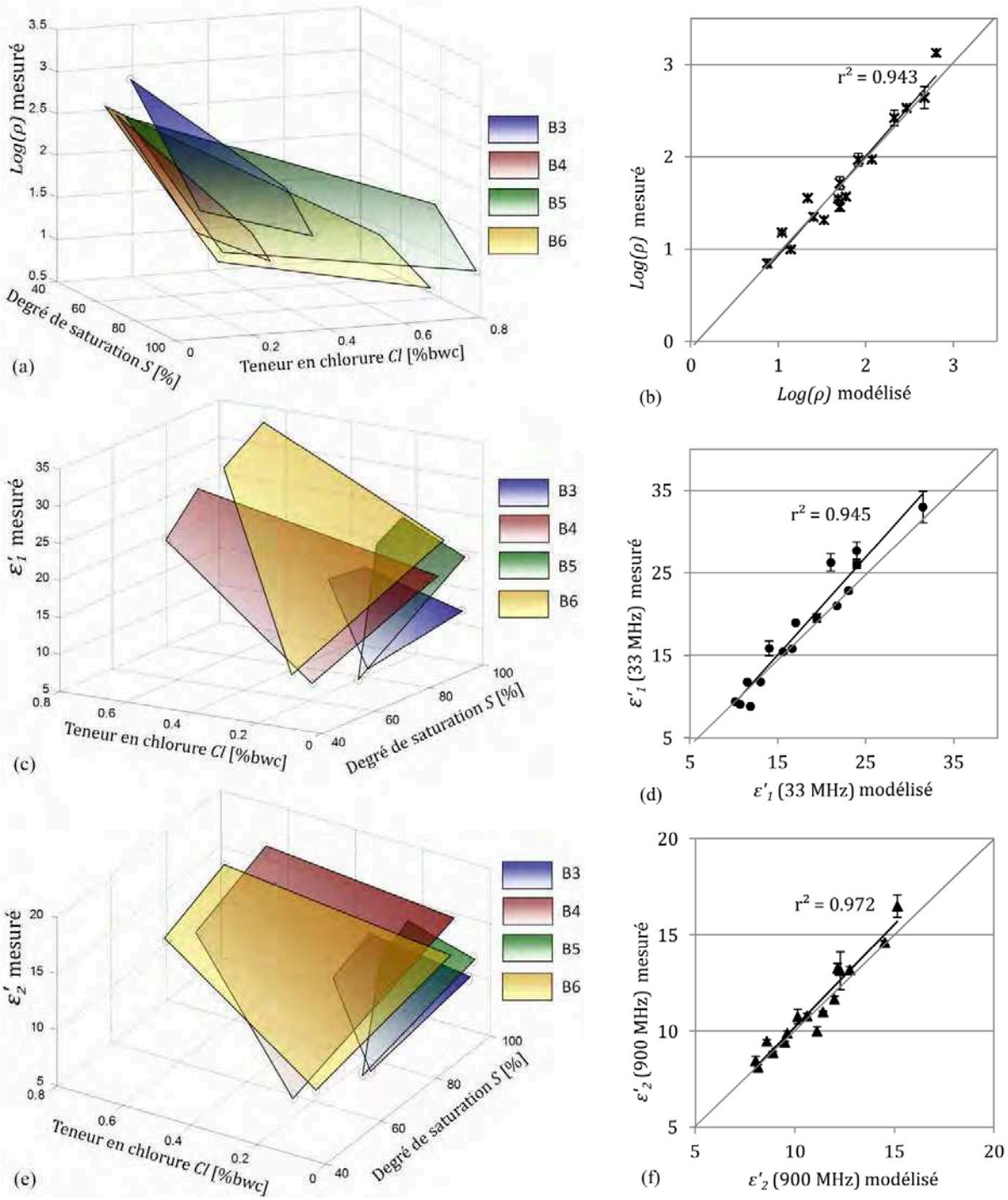

Figure 28 : valeurs prédites et mesurées pour (a) le degré de saturation à 0 g/L NaCl (Tests 1 et 2) et (b) à 15 g/L NaCl (Tests 3 et 4), (c) le logarithme de la teneur total en chlorures à 0 g/L NaCl (Tests 1 et 2) et (c) à 15 g/L NaCl (Tests 3 et 4) et (e) la porosité à 0 g/L NaCl (Tests 1 et 2) t (f) à 15 g/L NaCl (Tests 3 et 4).

Tableau 7 : erreurs de pourcentage absolu des valeurs prédites pour les paramètres d'état en fonction du degré de saturation, du logarithme de la teneur totale en chlorures et de la porosité, par rapport aux valeurs mesurées.

Erreur absolue [%] $\lvert pred./mes. - 1 \rvert$						
0 g/L	**Test 1**			**Test 2**		
	S	$C = Log(C\ell_t)$	ϕ	S	$C = Log(C\ell_t)$	ϕ
B3	6.9%	1.3%	12.9%	1.7%	1.2%	2.3%
B4	5.6%	0.4%	3.7%	10.1%	6.1%	6.5%
B5	6.9%	9.4%	1.5%	10.6%	13.0%	9.0%
B6	2.8%	8.8%	4.3%	13.4%	1.4%	10.9%
15 g/L	**Test 3**			**Test 4**		
	S	$C = Log(C\ell_t)$	ϕ	S	$C = Log(C\ell_t)$	ϕ
B3	1.4%	17.5%	4.5%	10.4%	7.5%	9.5%
B4	11.3%	7.9%	4.1%	9.0%	2.0%	20.8%
B5	2.8%	3.5%	20.6%	2.0%	10.1%	6.6%
B6	5.0%	1.3%	9.3%	18.3%	7.8%	6.3%

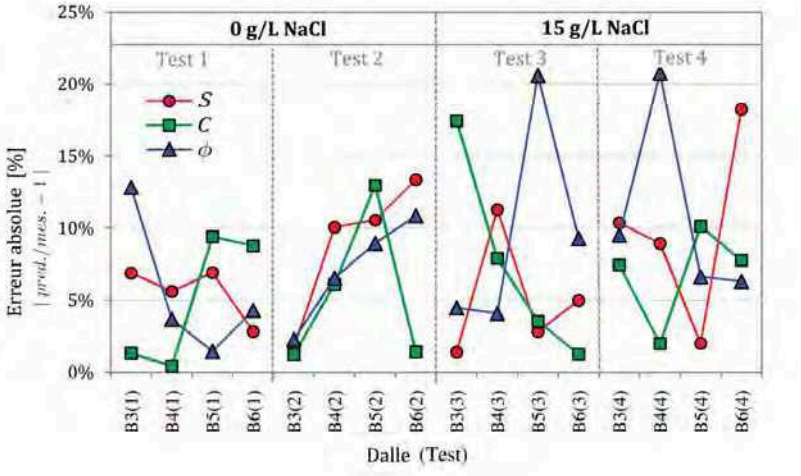

Figure 29 : erreurs de pourcentage absolu des valeurs prédites pour les paramètres d'état en fonction du degré de saturation, du logarithme de la teneur totale en chlorure et de la porosité par rapport aux valeurs mesurées.

Les résultats des observables EM respectifs obtenus à partir des dalles pour quatre conditionnements sont comparables aux mesures de cellules présentées au chapitre précédent. Ces résultats ont été associés afin d'estimer les paramètres d'état (degré de saturation, teneur en chlore et porosité) des dalles à différents états. Les paramètres d'état ont été assez bien estimés pour les états de contamination par l'eau (pourcentage d'erreur inférieur à 15%) et un peu moins bien estimés pour les contaminations au chlorure (inférieur à 20%). L'inclusion d'une quatrième technique, sensible à la teneur en chlorure, pourrait améliorer les résultats et permettre d'estimer la diffusivité en tant que paramètre d'état. En conclusion, l'association des modèles de régression par la résolution d'un système d'équations génère des résultats acceptables pour les mesures en laboratoire, dans un environnement contrôlé. Etant donné qu'en pratique, certaines informations sont souvent disponibles concernant le support ausculté, il serait possible d'améliorer la fiabilité

avec laquelle les paramètres d'état sont estimés pour le béton in situ, où la variabilité du béton est souvent plus importante.

5. Techniques EM in situ pour l'auscultation des gradients de béton

Enfin, une étude expérimentale a été réalisée afin de comparer la capacité de tomographie de résistivité électrique (TRE), la capacimétrie et le radar de pénétration des sols (RPS) (configurations fixe et avec décalages multiples) afin d'évaluer l'état du béton d'enrobage en présence de gradients d'eau et de chlorure. Chacune de ces techniques est sensible aux modifications des propriétés électromagnétiques en fonction de la profondeur du support ausculté dans une certaine mesure. L'objectif principal de cette étude était de comparer la capacité des méthodes respectives afin de détecter la pénétration des électrolytes dans le béton, ainsi que de discerner les électrolytes de différentes teneurs en chlorures. Plusieurs tests semi-destructifs et destructifs ont aussi été réalisés dans un but de comparaison.

5.1. Paramètres et conditionnement du mélange de béton

Le mélange utilisé pour le programme expérimental est présenté au Tableau 8 avec un ratio ciment-eau effectif (en tenant compte de l'absorption des agrégats respectifs) calculé à 0,58.

Tableau 8 : mélange tel qu'utilisé pour le programme expérimental sur les gradients du béton d'enrobage.

Constituents	**Origine**	**Densité sèche (kg/m³)**	**Coefficient d'absorption (%)**
Granulats (10/20)	Croix Gibat	621	1.0%
Granulats (6.3/16)	Croix Gibat	425	1.6%
Sable (0/4)	Fréhel	567	8.1%
Sable (0/4)	Mauron	332	5.2%
Ciment (CEMII/A LL 42.5 R)	Lafarge (Saint Pierre La Cour)	267	-
Eau		169	-
Adjutant	CHRYSO 760 (SPHRE)	1.6	-

Trois dalles de béton identiques de 450 x 350 x130 mm ont été coulées pour l'évaluation de la pénétration de l'eau et du chlorure dans le temps. De nombreux échantillons cylindriques de plus petite taille ont également été fabriqués comme carottes témoin et pour les tests destructifs. Le

mélange a été caractérisé en termes de durabilité au moyen de tests de carotte, présentés au Tableau 9 :

Tableau 9 : caractérisation du mélange en termes de durabilité.

Indicateurs de durabilité mesuré selon les protocols de l'AFPC AFREM [1997]		Resultat	Classe de durabilité selon Baroghel-Bouny et al. 2007
Coefficient de diffusion apparent (10^{-12} $m^2.s^{-1}$)	D_{app}	25.4	Faible
Résistivité électrique charactéristique (Ω.m)	ρ_{char}	54	Faible
Permeability à l'eau ($kg.m^{-2}.h^{-0,5}$)	K_{liq}	2.2	-
Porosité accessible à l'eau (%)	P_w	15.7	Faible
Perméabilité aux gaz (10^{-18} m^2)	K_{gas}	509	Faible

Après un temps de durcissement de 28 jours, les dalles ont été séchées pendant deux mois à 60°C et un mois à 85°C jusqu'à obtention d'une masse constante. Chaque dalle a ensuite été partiellement submergée jusqu'à 20mm dans une solution contenant différents niveaux de chlorure (Dalle 1 : 0 g/L, Dalle 2 : 15 g/L et Dalle 3 : 30 g/L NaCl). Les coins des dalles ont été placés sur des cales en bois afin de permettre la pénétration à partir du bas, alors que les côtés ont été revêtus d'une résine époxy afin d'empêcher l'infiltration latérale. Les propriétés EM des dalles ont ensuite été testées sur une période de trois jours (T0 à T5) afin de suivre la pénétration des électrolytes, à 6 jours (T6) et enfin à 23 jours (T7) lorsque les dalles étaient présumées saturées, comme l'indique le Tableau 10. Les dalles ont été conservées en conditions contrôlées à 20°C et dans une humidité relative de 80% pour toute la durée du programme expérimental.

Tableau 10 : Tableau des temps de test pour les techniques d'auscultation non destructive et destructives.

Test	Temps d'immersion* (jours)	Essais non destructifs sur les dalles				Essais semi-destructifs et destructifs en carottes		
		Résisti-vité	Sondes capacitives	RPS (1) offset constant	RPS (2) WARR	Gamma-densimétrie	Colori-métrie	Profiles de chlorures
T0	0	-	×	×	×	×	-	-
T1	0.1	×	×	×	×	×	×	×
T2	0.3 (0.4)	×	×	×	×	×	×	×
T3	0.9 (1.1)	×	×	×	×	×	×	×
T4	1.1 (1.4)	×	×	×	×	×	×	-
T5	1.6 (2.1)	×	×	×	×	×	×	-
T6	6.2	-	-	-	-	×	×	-
T7	23.2	×	×	-	×	×	-	×

*les temps d'immersion pour les essais semi-destructifs et destructifs entre parenthesis étaient différents

5.2. Procédure d'auscultation EM

Les techniques EM ont été mises en œuvre comme suit (voir Figure 30) pour chaque dalle de béton :

a) Résistivité au courant continu : déterminée à partir des mesures multi-électrodes à 4 Hz sur la face humide du béton. Une constante géométrique modélisée numériquement a ensuite été appliquée à chaque point de mesure afin de corriger l'espacement des électrodes et les effets de limite pour produire les résistivités apparentes. Les résistivités apparentes mesurées ont été inversées à l'aide du progiciel commercial d'inversion Res2DInv [**32**] à l'aide d'une contrainte de modèle robuste afin d'optimiser les résultats pour les transitions brusques.

b) Les constantes diélectriques ont été déterminées à environ 33 MHz au moyen de la méthode capacitive pour les électrodes à grandes, moyennes et petites plaques et les tests ont été réalisés sur la face humide du béton.

c) Méthode RPS 1 : Mesures RPS à décalage constant en mode réflexion, utilisé pour estimer la profondeur d'infiltration des solutions dans le temps. Les mesures, à une fréquence centrale de 2600 MHz, ont été prises sur la face sèche des dalles, en partant de l'hypothèse que la partie sèche du béton était non dispersive. La vélocité de groupe de l'onde EM a pu être déterminée pour l'état à sec (T0) étant donné que la profondeur de la surface de réflexion était connue (en bas de la dalle). La profondeur du front de saturation a ensuite été calculée à l'aide des heures d'arrivée de l'onde réfléchie à partir du front de saturation et de la vélocité connue pour l'état à sec.

   L'amplitude de l'onde directe a également été évaluée en fonction du temps et de la concentration en chlorure.

d) Méthode RPS 2 – réflexion/réfraction grand angle : la configuration RPS réflexion-réfraction grand angle a été appliquée à une fréquence centrale de 1500 MHz sur la face sèche des dalles de béton. Ceci a permis de déterminer les constantes diélectriques des états homogènes sec (ε'_{r1}) et saturés (ε'_{r2}) à l'aide de la procédure d'inversion du guide d'onde [**47**]. De plus, cela permet d'estimer la profondeur d'infiltration des solutions dans le temps. Les courbes de dispersion pour tous les modes électriques transverses (TE) de

l'onde de propagation ont ensuite été déterminées à l'aide du f-β de transformation du champ d'onde des données réelles observées. Une permittivité pondérée a été calculée à partir des valeurs connues de ε'_{r1}, ε'_{r2} et une profondeur d'infiltration choisie h_1 (h_2 = *130mm* - h_1) a ensuite été assignée à un modèle numérique afin de produire des courbes de dispersion synthétiques pour chaque mode. En optimisant manuellement h_1 jusqu'à ce qu'il épouse les courbes de dispersion obtenues pour les données réelles, la profondeur d'infiltration de la solution pour chaque temps de test a été déterminée. Pour de plus amples informations concernant cette technique, merci de consulter [**47**].

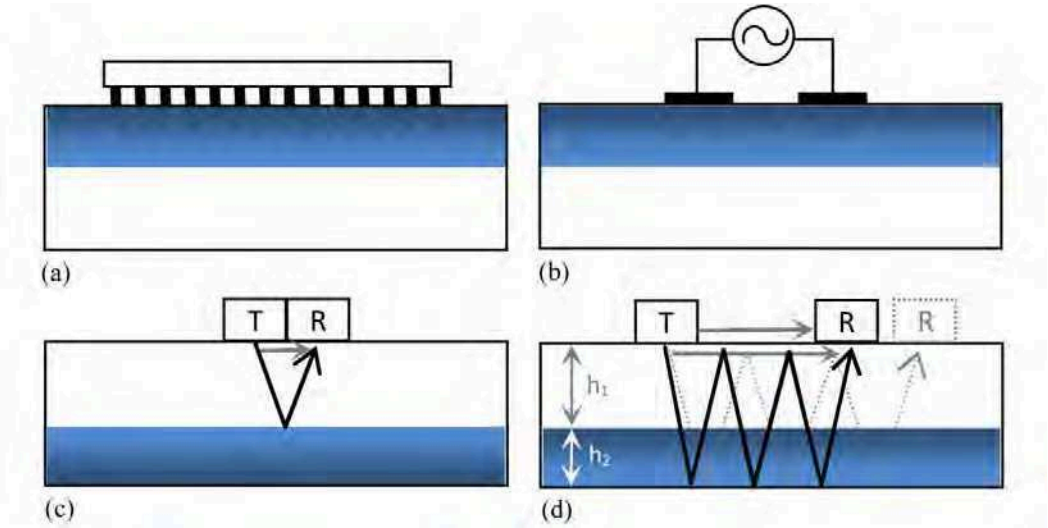

Figure 30 : Représentation schématique des quatre configuration EM utilisées afin de suivre l'infiltration des solutions dans les dalles de béton avec (a) représentant la méthode ERT, (b) la méthode capacitive, (c) la méthode RPS 1 à l'aide de l'onde réfléchie et la méthode RPS 2 à l'aide de l'approche de guidage de l'onde.

Les tests destructifs et semi-destructifs ont également été réalisés sur des spécimens témoins placés dans les solutions respectives afin de vérifier les résultats non-destructifs :

- La Gammadensimétrie a été réalisée afin d'évaluer la profondeur du front d'infiltration de l'eau pour les temps de test T0 à T7. Cette méthode mesure l'absorption des rayons gamma du spécimen en fonction des incréments de hauteur de 5mm et s'avère particulièrement efficace pour déterminer la teneur en eau en fonction de l'état sec ou saturé en raison du coefficient élevé d'absorption élevée des rayons gamma de l'eau. La technique n'est pas sensible à la présence de chlorures car les coefficients d'absorption de l'eau et du chlorure sont similaires. La technique est entièrement présentée ici in [**54**].

- L'infiltration du chlorure a été évaluée à l'aide de la colorimétrie (Baroghel-Bouny et al. 2007b) en pulvérisant du nitrate d'argent sur des spécimens témoins coupés en deux verticalement afin de détecter les solutions contaminées par le chlorure pour chaque temps de test.
- Les concentrations de chlorure ont été déterminées à l'aide du profilage du chlorure [**55**] pour les temps de test T1, T2, T3 et T7.

Un résumé des temps de test et des tests réalisés est présenté au Tableau 10.

5.3. Résultats et argumentation

5.3.1. **Résistivité au courant continu**

La Figure 31(a) présente les résultats des tomogrammes de chaque dalle pour les temps de test T1 à T5 et T7, obtenus à partir de l'inversion réalisée par le progiciel Res2Dinv [**32**]. Une transition brutale d'une résistivité faible (région contaminée par l'humidité/le chlorure) à une résistivité forte (région sèche) a été observée pour chaque état. Cette transition représente la profondeur de pénétration des solutions respectives et la profondeur augmente avec le temps jusqu'à ce que la dalle atteigne un état homogène, saturé à T7 (23 jours).

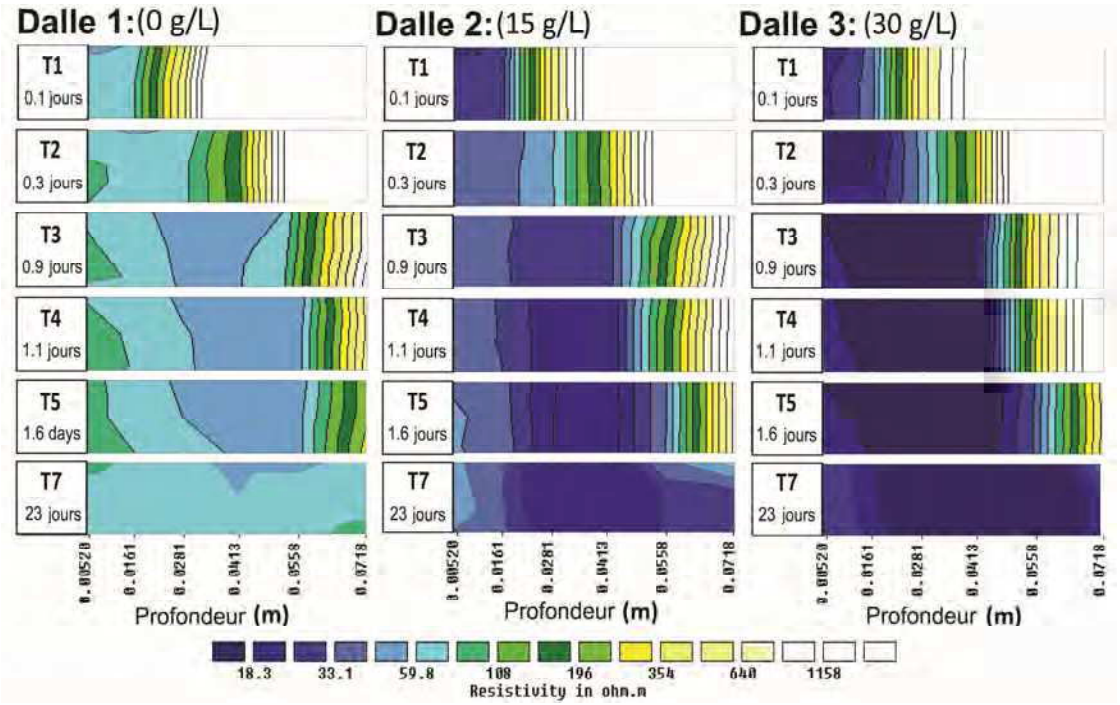

(a)

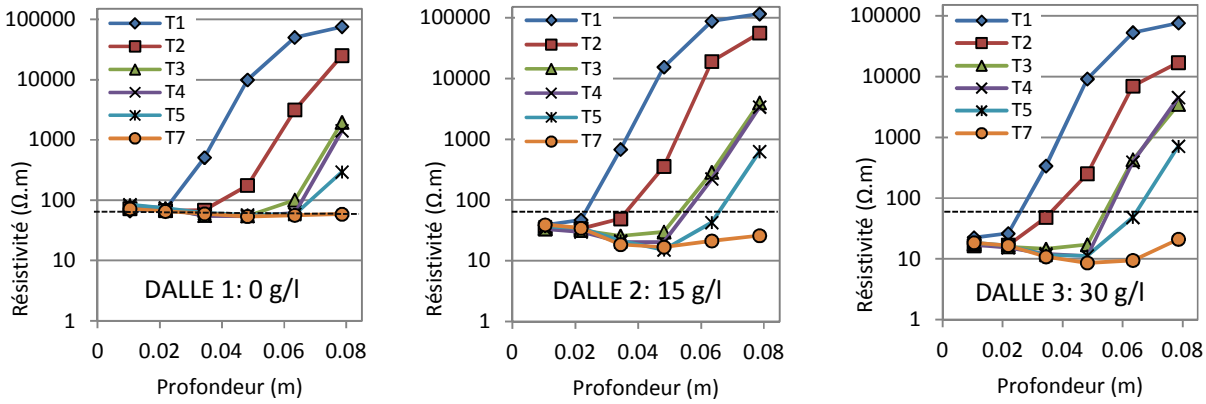

(b)

Figure 31 : résultats de résistivité pour la Dalle 1 (0 g/L NaCl), Dalle 2 (15 g/L NaCl) et Dalle 3 (30 g/L NaCl) pour les temps de test de T1 à T5 et T7 présentant (a) des extraits de résistivité électrique (b) la résistivité moyenne calculée à partir de l'ERT sur la profondeur.

Les valeurs de résistivité moyenne pour chaque incrément de profondeur ont été calculées à partir des résultats d'inversion et sont présentées à la in Figure 31(b). Pour la dalle ne contenant pas de chlorure (Dalle 1), la résistivité pour l'état saturé était d'environ 60 Ohm.m (indiquée par la ligne en pointillés). La profondeur du front de saturation pour la Dalle 1 aux temps de test T1 à T5 est estimée se situer au point de rupture entre les courbes respectives et la courbe saturée (T7). Pour les dalles 2 et 3 la profondeur du front d'infiltration de la saturation pour chaque temps de test est mesurée au point où leurs courbes respectives croisent la ligne de 60 Ohm.m. L'hypothèse consiste donc à dire que l'eau pénètre plus rapidement que les ions de chlorure et qu'une résistivité égale à celle d'un béton saturé en eau marque le front d'infiltration même pour les dalles contaminées par le chlorure. Suite à cette procédure, le taux d'infiltration dans les trois dalles s'est révélé très similaire. La profondeur du front d'infiltration passe d'environ 20mm pour l'état initial à T1 à un état totalement saturé à T7.

La résistivité moyenne obtenue après 23 jours varie de manière importante pour les trois dalles, ce qui démontre la capacité de la résistivité à discerner entre les différentes concentrations en chlorure : environ 60 Ohm.m pour la dalle 1, 26 Ohm.m pour la dalle 2 et 18 Ohm.m pour la dalle 3. La valeur saturée de la dalle 1 est comparable avec la valeur de résistivité caractéristique présentée au Tableau 9 avec un pourcentage d'erreur de of 11,1% correspondant à celui qui est indiqué dans la littérature [**29**].

La limite de la technique de résistivité multi-électrodes est que l'espacement minimum entre les électrodes (20mm dans le cas présent) détermine la résolution des résultats obtenus par l'inversion (c.-à-d. les incréments de profondeur inversés). En raison de la résolution liée à cette

configuration d'électrode particulière, la position du front de saturation peut uniquement être déterminée approximativement à 10mm près.

5.3.2. Capacimétrie

Les constantes diélectriques calculées à l'aide de la méthode capacitive pour les séries d'électrodes de petite, moyenne et grande taille sont présentées à la Figure 32(a), (b) et (c). Les électrodes respectives auscultent les volumes croissants de la subsurface du béton correspondant à leur taille. L'état constant est atteint lorsque les courbes s'aplatissent et représente un état homogène, saturé, atteint au-delà du volume de subsurface auquel le capteur est sensible.

L'aplatissement de la courbe intervient lorsque la profondeur d'influence des séries d'électrodes augmente et peut donc être associé à l'infiltration des électrolytes. En regardant de près, on peut voir que la dalle 1 non contaminée atteint l'état constant plus rapidement que les dalles contaminées. Ceci correspond à l'observation, en ce qui concerne la résistivité, selon laquelle il existe un gradient de chlorure au-delà du front de saturation.

La sensibilité de la méthode capacitive à la teneur en chlorure peut être observée car la permittivité relative augmente de manière importante lorsque la teneur en chlorure augmente. Les valeurs atteintes pour un état homogène sont approximativement 13,3 pour la dalle 1, 18,1 pour la dalle 2 et 21,5 pour la dalle 3.

Il est prévu, dans un avenir proche, de mettre en place un protocole d'inversion pour cette technique afin de permettre la cartographie de la permittivité sur la profondeur, de manière similaire à la résistivité.

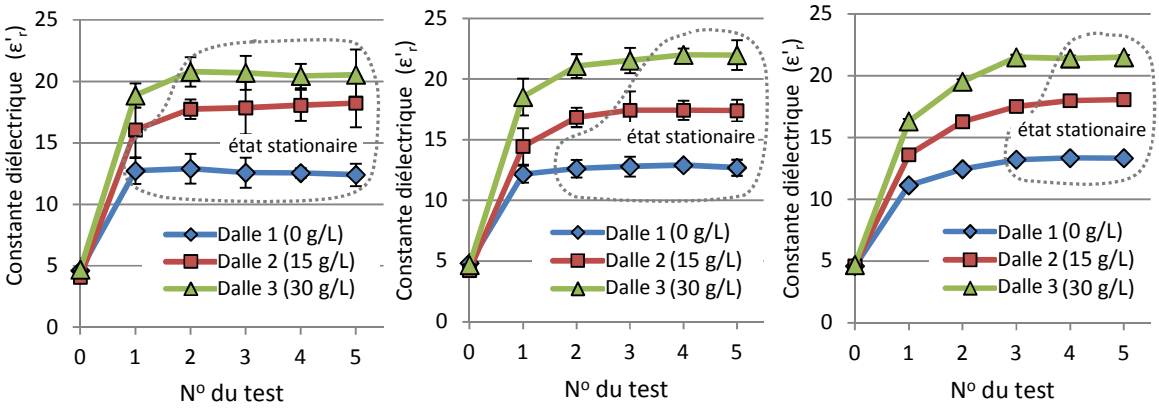

(a) Petites électrodes (b) Moyennes électrodes (c) Grandes électrodes

Figure 32 : constantes diélectriques pour chaque dalle par temps de test, ainsi que déterminé par les différentes tailles d'électrodes capacitives (a) petites électrodes, avec une profondeur d'influence de 9mm, (b) électrodes moyennes, avec une profondeur d'influence de 20 mm et grandes électrodes, avec une profondeur d'influence de 80mm.

5.3.3. Radar de pénétration des sols (RPS)

5.3.3.1. Méthode 1

La Figure 33(a) présente les résultats des radargrammes pour la configuration RPS décalée constante en mode réflexion (fréquence centrale de l'antenne à 2600 MHz). Etant donné que les tests ont été réalisés du côté sec de la dalle de béton (voir Fig. 8), la pénétration va dans le sens de bas en haut. L'onde réfléchie à partir du front de saturation peut être clairement discernée et est indiquée par une flèche pour chaque temps de test.

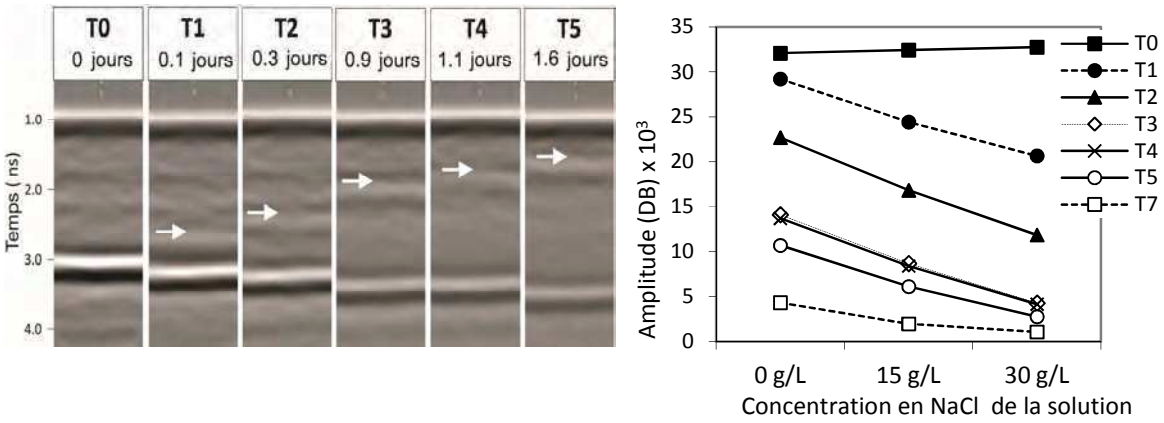

(a) (b)

Figure 33 : méthode RPS 1 : mesures de décalage constant en mode réflexion (a) extraits de radargrammes pour la dalle 1 indiquant l'onde réfléchie à partir du front de pénétration, (b) difference d'amplitude de l'onde directe pour les solutions respectives.

Le taux de pénétration du front de saturation pour les trois dalles s'est révélé similaire, ce qui conforte les résultats des mesures de résistivité. Toutefois, l'amplitude de l'onde directe est très différente, ce qui démontre l'influence de la salinité des solutions respectives sur la forme de l'onde, comme le présente la Figure 33(b). L'amplitude de l'onde directe a aussi diminué de manière significative au fur et à mesure de la progression de l'infiltration et de l'augmentation du taux de chlorure.

5.3.3.2. Méthode 2

Les mesures RPS avec la configuration de réflexion/réfraction grand angle (fréquence centrale de l'antenne à 1500 MHz) ont généré les constantes diélectriques des dalles 1, 2 et 3 déterminées à partir de l'onde directe à environ 4,7 pour l'état à sec (ε'_{r1}) et 8,7, 9,4 et 9,8 pour les états saturés (ε'_{r2}).

L'étude a vérifié que les signaux obtenus pour les modes TE avaient pénétré le front d'infiltration, ce principalement à partir du bas de la dalle, contrairement à la méthode 1, où les signaux étaient clairement réfléchis à partir du front d'infiltration. Les profondeurs d'infiltration ont ainsi été

déterminées à l'aide de l'approche d'Ihamouten [**47**], selon laquelle la dalle est traitée comme un guide d'onde. Les courbes de dispersion de la vélocité de phase en fonction de la fréquence obtenue à partir des données mesurées pour chaque temps de test ont été ajustées afin d'optimiser manuellement les données synthétiques présentées à la Figure 34. Les résultats étaient comparables à ceux obtenus à partir des résultats RPS fixes (Figure 33). Ils permettent de démontrer l'approche de guide d'onde pour l'estimation des profondeurs d'infiltration des solutions dans le béton. Ils indiquent aussi que l'évolution du front d'infiltration peut être estimée à l'aide de l'onde réfléchie à partir du bas de l'élément béton lorsque la limite d'infiltration n'est pas suffisamment solide pour produire une réflexion.

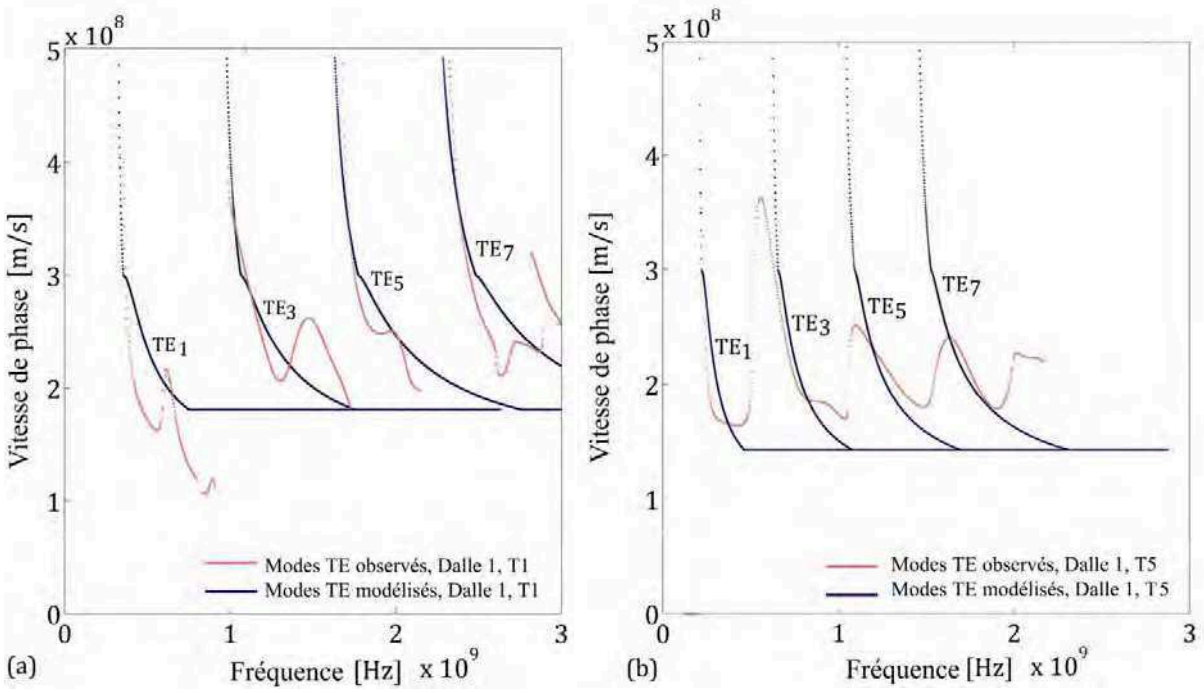

Figure 34 : RPS Méthode 2 : Modes TE réels (observés) et synthétisés (modélisés) pour la dalle 1 selon les temps de test (a) T1 (profondeur d'infiltration optimisée de 20 mm) et (b) T5 (profondeur d'infiltration optimisée de 80 mm). L'axe de la vélocité de phase s'étend à la valeur physiquement impossible de 5x108 afin de mieux observer les asymptotes.

5.4. Comparaison des résultats destructifs et non destructifs

5.4.1. Evaluation de l'infiltration du front de saturation

Toutes les méthodes non destructives employées dans le cadre de la campagne expérimentale ont réussi, dans une certaine mesure, à suivre le progrès du front de saturation dans le temps pour les différentes dalles. Les résultats de résistivité et RPS ont démontré que le taux d'infiltration pour les dalles respectives était très similaire. L'étude a confirmé de manière destructive, par le biais de la gammadensimétrie sur des carottes témoin, qu'il n'y avait en effet que peu de différence entre les taux d'infiltration de l'eau dans les différentes dalles. En termes de gammadensimétrie, le front d'infiltration de l'eau est défini comme situé entre les limites « à sec » et de « saturation » définies

par les intercepts indiqués à la Figure 35(a). L'intercept gamma 1 sera nommé ici « front d'infiltration à saturation » et l'intercept gamma 2 sera nommé front d'infiltration de l'eau.

La Figure 35(b) présente les teneurs en eau moyennes calculés à partir des résultats de gammadensimétrie, les carottes témoin montrent la variation de l'eau par rapport à la profondeur des carottes pour chaque temps de test. La Figure 35(c) présente la saturation et le front d'infiltration de l'eau liés au front d'infiltration du chlorure tel qu'obtenu grâce à la colorimétrie. L'étude montre que la pénétration des ions de chlorure se produit plus lentement que la pénétration de l'eau. La Figure 35(d) montre les résultats de profilage du chlorure des carottes témoin contenant 30 g/L de chlorure testé à T1, T2 et T3 et T7. Un gradient significatif de la concentration totale en chlorure apparaît entre la surface et le front d'infiltration du chlorure.

Ainsi, l'étude conclut à la validité de l'hypothèse, exprimée en termes de mesures de résistivité, selon laquelle le front d'infiltration de la saturation peut être associé à une résistivité proche de celle du béton saturé en eau, même pour les dalles contaminées.

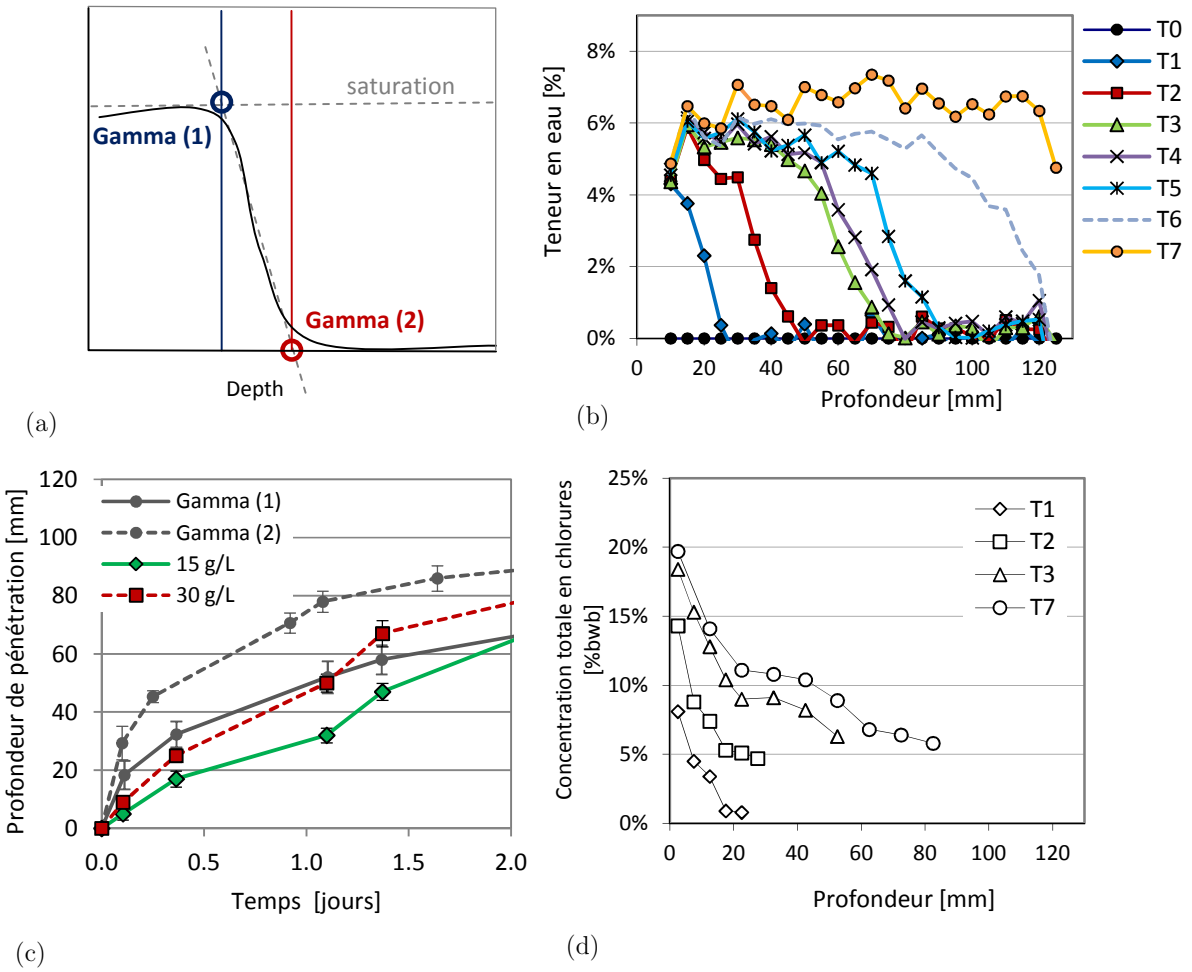

Figure 35 : résultats des tests destructifs sur les spécimens témoins (a) schéma montrant l'intercept 1 et l'intercept 2 utilisés afin de définir les limites du front d'infiltration de l'eau en termes de gammadensimétrie, (b) résultats de

gammadensimétrie des carottes témoin montrant la pénétration de l'infiltration d'eau pour chaque temps de test (c) pénétration du front d'infiltration de l'eau (gammadensimétrie) et du front de chlorure (colorimétrie) pour des échantillons témoins de 15 g/L et 30 g/L dans le temps et (d) concentration totale en chlorure mesurée par profilage par poids de béton.

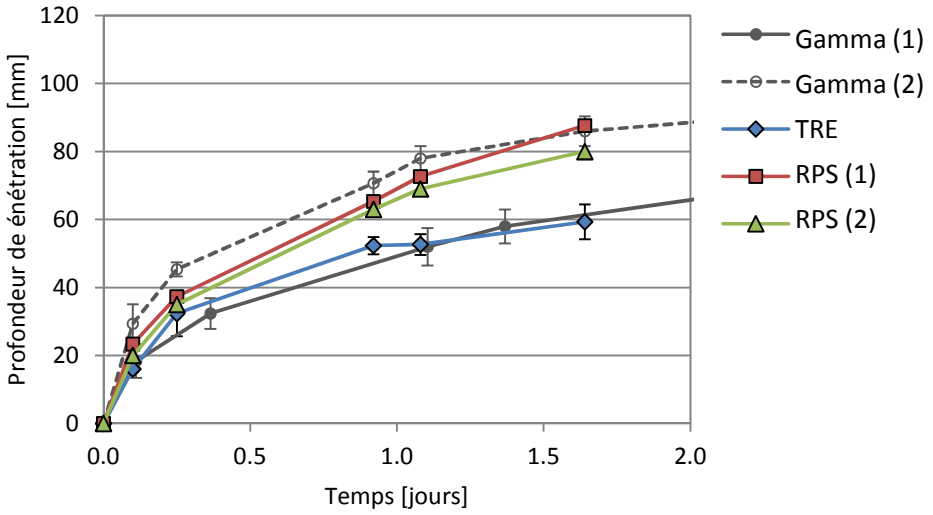

Figure 36 : Estimation de la pénétration de l'eau telle que déterminée de manière non destructive par la résistivité, les mesures du radar à décalage constant (RPS 1) et du radar multi-décalage (RPS 2) ainsi que les résultats de gammadensimétrie pour le front d'infiltration de la saturation (Gamma 1) et le front d'infiltration de l'eau (Gamma 2).

Il existe une très bonne corrélation entre le taux de pénétration de l'eau, tel qu'estimé à partir des mesures non destructives et des résultats de gammadensimétrie semi-destructive. La Figure 36 présente la profondeur d'infiltration dans le temps, déterminée par résistivité (TRE), les données du radar à décalage constant (RPS 1) et multi-décalage (RPS 2) et par la gammadensimétrie.

Une différence apparaît entre les résultats TRE et les données du RPS. Elle est probablement due au protocole expérimental appliqué, où les mesures de résistivité ont été effectuées à partir de la face humide des dalles et le front d'infiltration a été déterminé à la position correspondant à la résistivité du béton saturé. Le front d'infiltration estimée par TRE correspond donc à celui du front d'infiltration de la saturation (Gamma 1). Il est présenté à la Figure 36. Les mesures RPS ont été prises à partir de la face sèche des dalles et les profondeurs d'infiltration estimées sont plus proches du front d'infiltration de l'eau (Gamma 2). La propagation des ondes électromagnétiques a donc été en premier lieu influencée par la position du front d'infiltration de l'eau.

Etant donné que le processus d'inversion pour la capacimétrie est toujours en cours de développement, il n'est pas possible de définir la position du front d'infiltration en fonction de la profondeur estimée par la capacimétrie.

5.4.2. Sensibilité à la teneur en chlorure

Les valeurs de résistivité (TRE), de permittivité basse fréquence (capacimétrie), d'amplitudes des ondes directes (RPS 1) et de permittivité haute fréquence (RPS 2) ont montré des sensibilités très différentes à la présence du chlorure dans les échantillons. Les résultats des trois méthodes ont été normalisés pour ce qui est de la dalle 1, qui ne contient pas de NaCl, afin d'évaluer la sensibilité des différentes méthodes au chlorure. La différence relative entre chacune des méthodes et la dalle 1 est présentée à la Fig. 15 pour l'état saturé (T7).

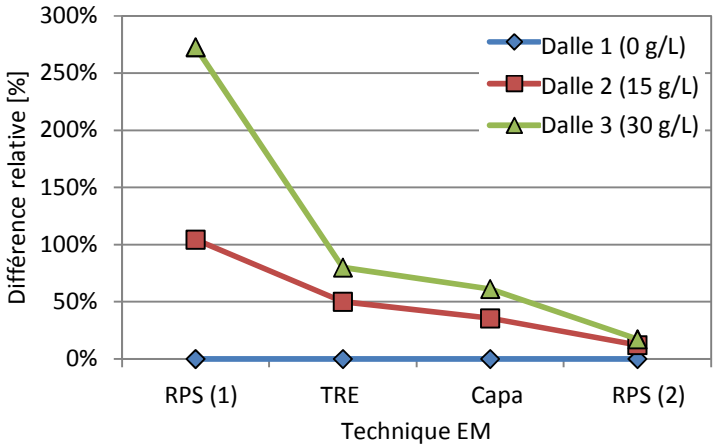

Figure 37 : sensibilité des méthodes EM à la teneur en chlorure.

La Figure 37 montre que l'amplitude de l'onde directe à 2600 MHz est la plus sensible à la teneur en chlorure. Ceci est du à l'atténuation significative de l'onde causée par la présence de chlorures. Les résultats TRE sont sensibles à la présence de chlorure, mais dans une moindre mesure, suivis par la permittivité déterminée à partir de la capacimétrie à 33 MHz et la permittivité déterminée à 1500 MHz. Cette différence de sensibilité des différentes méthodes montre un grand potentiel en termes de futurs travaux sur la base d'une association de méthodes électromagnétiques afin d'évaluer la teneur en eau et en chlorure dans le béton.

5.5. Résumé

Les conclusions de l'étude sont les suivantes :

1. La tomographie de résistivité électrique est un outil utile pour suivre l'infiltration des électrolytes dans le béton. Les profils sont bien corrélés avec les profils de teneur en eau déterminés par les tests de gammadensimétrie réalisés sur des carottes au conditionnement identiques. La technique indique aussi clairement une baisse de la résistivité au fur et à mesure de l'augmentation de la teneur en NaCl dans le béton.

2. La capacimétrie est prometteuse pour le suivi des gradients de propriétés dans le béton, étant donné qu'il est possible de mesurer en fonction des différentes profondeurs d'influence à l'aide de différentes configurations d'électrodes. Toutefois, il reste nécessaire d'utiliser un protocole d'inversion afin d'obtenir la permittivité en fonction de la profondeur.
3. Les résultats du RPS à décalage constant en mode réflexion (2600 MHz) montrent une bonne capacité à suivre le front d'infiltration de l'eau. Toutefois, la méthode est limitée par le fait qu'il est nécessaire de disposer d'une limite claire de contraste de permittivité pour que cette technique fonctionne bien.
4. L'utilisation de la configuration multi-décalage (réflexion-réfraction grand angle) (1500 MHz) a permis d'estimer le front d'infiltration de l'eau en traitant les dalles comme un guide d'onde. Cette méthode est particulièrement utile si l'onde électromagnétique n'est pas réfléchie à partir du front d'infiltration, mais pénètre cette barrière et est réfléchie à partir du bas de l'élément en béton.

Les techniques in situ montrent diverses capacités à fournir des informations quantitatives et qualitatives concernant l'état du béton et pour identifier la présence de gradients de propriété. Toutes les techniques sont prometteuses pour la future caractérisation non destructive du béton et la recherche sur l'association de ces méthodes afin d'évaluer quantitativement la teneur en eau et en chlorure est en cours.

6. Conclusion et perspectives

L'infrastructure de béton armé fait partie intégrante de la société moderne, elle est indispensable. Afin de garantir la construction de structures en béton durables et de les entretenir le mieux possible tout au long de leur vie en service, le suivi de l'état du béton est essentiel. Nombreuses sont procédures de tests destructives et traditionnelles permettant d'évaluer la durabilité du béton qui sont onéreuses et prennent beaucoup de temps. L'évaluation non destructive des structures de béton est donc adoptée par de plus en plus d'autorités afin de compléter ou même de remplacer ces techniques destructives.

Les techniques d'auscultation non destructive électromagnétiques (EM) sont particulièrement bien adaptées à l'évaluation de l'état du béton, car elles sont sensibles aux paramètres liés à la corrosion, qui est l'un des problèmes les plus importants au regard du vieillissement des structures de béton armé. Cependant, la variabilité inhérente au béton, ainsi que d'autres facteurs d'influence

sur ces techniques liées aux tests in situ, sont telles que l'utilisation d'une seule technique ne permet souvent pas de produire des résultats fiables. L'association de plusieurs techniques non destructives est donc devenue le centre d'intérêt de la communauté de recherche autour des NDE au cours des dernières années. L'objectif est d'améliorer la fiabilité et l'interprétation des résultats.

La présente thèse s'est concentrée sur l'association des techniques d'évaluation EM comme moyen d'évaluer la durabilité et l'état du béton d'enrobage au cours du stade d'apparition de la corrosion. Bien que de nombreuses recherches soient disponibles sur le sujet de la dépendance des observables EM à différents aspects de l'état du béton et de sa durabilité, la plupart des études ne documentent pas la réponse de plusieurs techniques EM pour le même béton. Afin de réaliser cela, deux nouveaux dispositifs de mesure de la résistivité électrique ont été développés afin d'évaluer à la fois la résistivité et la permittivité diélectrique des mêmes spécimens. Une étude paramétrique a ensuite été menée afin d'évaluer la réponse EM de toute une gamme de mélanges et d'états de béton dans un environnement contrôlé, en laboratoire. En conséquence de l'étude paramétrique, un modèle de régression a été élaboré pour chaque observable EM, qui a pu être déterminé à l'aide des techniques in situ disponibles (résistivité, capacimétrie et RPS). Ces techniques ont été associées afin d'estimer le degré de saturation, la teneur en chlorure et la porosité des dalles de béton en solutionnant un système d'équations comprenant les modèles de régression.

La capacité des techniques d'auscultation EM à détecter la présence de gradients dans le béton est également très précieuse en pratique, particulièrement pour le suivi en continu de l'état du béton d'enrobage. La capacité des trois techniques in situ à suivre l'infiltration de l'eau et des chlorures dans le béton a donc également fait l'objet d'une étude dans le cadre d'une campagne expérimentale collaborative.

Les résultats de ces études démontrent le potentiel des techniques EM non destructives à estimer l'état du béton de manière non destructive et à suivre l'évolution des paramètres liés à la corrosion dans le temps. L'association de ces techniques est un outil indispensable pour réduire les incertitudes liées aux résultats in situ. Il est donc faisable d'employer des techniques d'évaluation électromagnétiques non destructives dans le cadre d'une stratégie de gestion des infrastructures en béton armé afin de garantir la durabilité de ces ouvrages sur le long terme.

7. Travaux en perspective

Les sujets importants qui n'ont pas été totalement traités dans le cadre de la présente thèse et qui font actuellement l'objet de recherches sont les suivants :

- Bien que le béton utilisé dans le cadre de la présente thèse présente de grandes variations de durabilité, il n'était pas du tout représentatif de tous les types de béton rencontrés en

pratique. Bien que les modèles développés ici devraient être applicables aux mélanges les plus courants, des travaux supplémentaires devront être menés afin d'évaluer la sensibilité des observables EM aux additifs minéraux et chimiques.

- Les modèles développés pour la permittivité diélectrique ne tiennent pas compte de l'influence du type d'agrégat utilisé dans le béton, qui est connue pour être significative. Une différence de type d'agrégat va seulement provoquer une « modification » du modèle qui pourrait être corrigée par étalonnage, mais cette méthode appelle à la réalisation de travaux supplémentaires.
- Etant donné que le travail expérimental a été en majeure partie réalisé sur du béton non armé, il sera nécessaire de poursuivre la recherche autour de l'influence de la présence d'acier sur les réponses électromagnétiques.
- L'inversion des résultats pour les bétons non homogènes afin d'estimer les véritables propriétés EM en fonction de la profondeur a uniquement été réalisée pour la résistivité. Etant donné que ces algorithmes d'inversion sont techniquement composés pour un mi-espace infini, il reste encore à valider que l'application d'un facteur géométrique avant l'inversion (comme cela a été fait dans le cadre de la présente thèse) permettra toujours de générer des résultats exacts. Un processus d'inversion peut également être utilisé pour les résultats émanant de la sonde capacitive et le développement de cette procédure est actuellement étudié au sein de l'IFSTTAR.
- La variabilité des mesures réalisées in situ est beaucoup plus importante que pour les spécimens utilisés dans le cadre de la présente thèse. En pratique, il est beaucoup plus complexe d'optimiser les résultats afin de caractériser le béton in situ de manière qualitative. De nouvelles recherches adoptent des approches plus sophistiquées, telles que la théorie de la possibilité ou le « fuzzy neural » qui pourrait améliorer la fiabilité des résultats de manière significative.
- Le travail présenté ici sera poursuivi par l'association de techniques EM visant à évaluer les gradients de teneur en eau et en chlorure dans le béton de manière indépendante.

Références

[1] J.M. Crow, "The concrete conundrum," *Chemistry World*, vol. 62, 2008.

[2] M.G Alexander and H. Beushausen, "Performance-based durability testing, design and specification in South Africa: latest developments," *Proceedings of The International Conference on Concrete Construction, Kingston University, London, UK, 9–10 September 2008*, 2009.

[3] V. Baroghel-Bouny and et al., *Concrete for a given structure service life*. Paris: Association Française de Génie Civil (AFGC), 2007.

[4] V.M. and Carino, N.J. Malhotra, *Handbook on Nondestructive Testing of Concrete.*: CRC Press, 2004.

[5] Z.-M. and Breysse, D. and Larget, M. and Balayssac, J.-P. Sbartaï, "Combining NDT techniques for improved

evaluation of concrete properties," *Cement & Concrete Composites*, vol. 34, pp. 725-733, 2012.

[6] D. Breysse, Ed., *Non-Destructive Assessment of Concrete Structures: Reliability and Limits of Single and Combined Techniques: State-Of-the-Art Report of the RILEM Technical Committee 207-INR.*: Springer, Technology & Engineering, 2012.

[7] F. Wenner, "A method for measuring earth resistivity," *Bureau of Standards*, pp. 469-478, 1915.

[8] R. B. Polder, "Test methods for on site measurement of resistivity of concrete - a RILEM TC-154 technical recommendation," *Construction and Building Materials*, vol. 15, pp. 125-131, 2001.

[9] C. Andrade, R. Polder, and M. Basheer, "Chapter 5. Non-Destructive Methods to Measure Ion Migration, RILEM Report 040, Non-Destructive Evaluation of the Penetrability and Thickness of Concrete Cover," RILEM TC 189-NEC: State of the Art Report, 2007.

[10] Y. Liu, A. Suarez, and F.J. Presuel-Moreno, "Characterization of New and Old Concrete Structures Using Surface Resistivity Measurements," *Final Report, Contact Number BD546, RPWO #08, Florida Department of Transportation Research Center*, 2010.

[11] R. and Palma Lopes, S. and Villain, G and Dérobert, X. Du Plooy, "Development of a multi-ring resistivity cell and multielectrode resistivity probe for investigation of cover concrete condition," *NDT & E International*, vol. 54, pp. 27-36, 2013.

[12] S. Feliu, C. Andrade, J. Gonzalez, and C. Alonso, "A new method for In-situ measurement of electrical resistivity of reinforced concrete," *Materials and Structures*, vol. 29 p.362-365, 1996.

[13] G. E. Monfore, "The Electrical Resisitivity of Concrete," *Journal of the PCA Research and Development Laboratories*, vol. 10, pp. 35-48, 1968.

[14] Ø.E. Gjørv, Ø. Vennesland, and A.H.S. El-Busaudy, "Electrical resistivity of concrete in the oceans," *9th Annual Offshore Technology Conference, Houston, Texas*, pp. 581-588, 1977.

[15] F. Hunkeler, "The resistivity of pore water solution - a decisive parameter of rebar corrosion and repair methods," *Construction and Building Materials*, vol. 10, pp. 381-389, 1996.

[16] D.A. Whiting and M.A. Nagi, "Electrical resistivity of concrete—literature review," vol. Portland Cement Association, R \& D Serial no. 2457, p. 57, 2003.

[17] G.E. Archie, "The Electrical Resistivity Log as an Aid in Determining Some Reservoir Characteristics," *Transactions of the American Institute of Mining and Metallurgical Engineers*, vol. 146, p. 54 to 62, 1942.

[18] P.N. Sen, C. Scala, and M.H. Cohen, "A self-similar model for sedimentary rocks with application to the dielectric constant of fused glass beads," *Geophysics*, vol. 46, pp. 781–795, 1981.

[19] P. W. J. Glover, "A generalized Archie's law for n phases," *Geophysics*, vol. 75, pp. 247–265, 2010.

[20] H.W. Whittington, J. McCarter, and M.C. Forde, "The conduction of electricity through concrete," *Magazine of Concrete Research, Vol 33, No. 114*, pp. 48-60, 1981.

[21] P.J. Tumidajski, A.S. Schumacher, S. Perron, P. Gu, and J.J. Beaudoin, "On the relationship between porosity and electrical resistivity in cementitious systems," *Cement and Concrete Research*, vol. 26, no. 4, pp. 539-544, 1996.

[22] W. Lopez and J.A. Gonzalez, "of the degree of pore saturation on the resistivity of concrete and the corrosion rate of steel reinforcement," *Cement and Concrete Research*, vol. 23, pp. 368-376, 1993.

[23] M. Saleem, M. Shameem, S.E. Hussain, and M. Maslehuddin, "Effect of moisture, chloride and sulphate contamination on the electrical resistivity of Portland cement concrete," *Construction and Building Materials, Vol 10*, pp. 209-214, 1996.

[24] Z.M. Sbartaï, S. Laurens, J. Rhazi, J-P. Balayssac, and G. Arliguie, "Using radar direct wave for concrete condition assessment: Correlation with electrical resistivity," *Journal of Applied Geophysics*, vol. 62, pp. 361-374, 2007.

[25] E. Hammond and T.D. Robson, "Comparison of electrical resistivity for various cements and concretes," *The*

Engineer , vol. 199, no. 5156 p.78-80, 1955.

[26] R.N. Cox, R. Cigna, O. Vennesland, and T. Valente, "Corrosion and protection of metals in contact with concrete, Final Report," Brussels, EUR 17608 EN, ISBN 92-828-0252-3,1997:148 1997.

[27] T. and Icenogle, P. Rupnow, "Surface Resistivity Measurements for Quality Assurance Pave the Way to Savings in Louisiana," *TR NEWS*, vol. 279, pp. 46-47, 2012.

[28] K.R. Gowers and S.G. Millard, "Measurement of concrete resistivity for assessment of corrosion severity of steel using Wenner technique," *ACI Materials Journal*, vol. 96, pp. 536-542, 1999.

[29] L. Marescot, S. Rigobert, S. Palma Lopes, R. Lagabrielle, and D. Chapellier, "A general approach for DC apparent resistivity evaluation on arbitrarily shaped 3D structures," *Journal of Applied Geophysics*, vol. 60, no. 55-67, 2006.

[30] W. Morris, E.I. Moren, and A.A. Sagüés, "Practical Evaluation of resistivity of concrete in test cylinders using a Wenner array probe," *Cement and Concrete Research*, vol. 26, no. 12, pp. 1779-1787, 1996.

[31] A. Seppanen, "Electrical Resistance Tomography Imaging of Concrete," *Concrete Repair, Rehabilitation and Retrofitting II – Alexander et al (eds) , Taylor & Francis Group, London*, 2009.

[32] W. Daily, A. Ramirez, A. Binley, and S. Henry-Poulter, "Electrical resistance tomography of concrete structures," in *ECAPT94: 3rd European concerted action meeting on process tomography, Lisbon (Portugal), 24–27 Mar* , 1994.

[33] M. H. Loke and R. D. Barker, "Rapid least-squares inversion of apparent resistivity pseudosections by a quasi-Newton method. ," *Geophysical Prospecting*, vol. 44, no. 1, pp. 131–152, 1996.

[34] P.R. McGillivray and D.W. Oldenburg, "Methods for calculating Fréchet derivatives and sensitivities for the non-linear inverse problem: a comparitive study," *Geophysical Prospecting*, vol. 38, pp. 499-524, 1990.

[35] A. Robert, "Dielectric permittivity of concrete between 50 MHz and 1 GHz and GPR measurements for building materials evaluation," *Journal of Applied Geophysics*, vol. 40, pp. 89-94, 1998.

[36] K. Lichtenecker and K. Rother, "Die Herleitung des logarithmischen Mischungsgesetz es aus allgemeinen Prinzipien der stationären Strömung," *Physikalische Zeitschrift*, vol. 30, pp. 255-260.

[37] M.D. Knoll, "A petrophysical basis for ground penetrating radar and early time electromagnetics: Electrical properties of sand-clay mixtures," *University of British Columbia*, 1996.

[38] D.J. Daniels, *Ground-penetrating radar*, 2nd ed. London, UK: Institute of Electrical Engineers, 2004.

[39] J. Hugenschmidt and R. Loser, "Detection of chlorides and moisture in concrete structures with GPR," *Materials and Structures*, vol. 41, pp. 785-792, 2008.

[40] X. Dérobert, G. Villain, R. Cortas, and J-L. Chazelas, "EM characterization of hydraulic concretes in the GPR frequency band using a quadratic experimental design," *NDTCE'09, Non-Destructive Testing in Civil Engineering, Nantes, France, June 30 - July 3*, 2009.

[41] G. Villain, Z.M. Sbartaï, X. Dérobert, V. Garnier, and J.-P. Balayssac, "Durability diagnosis of a concrete structure in a tidal zone by combining NDT methods: laboratory tests and case study," *Construction and Building Materials*, vol. 37, pp. 893–903, 2012.

[42] S. Laurens, J. Balayssac, J. Rhazi, and G. Arliguie, "Influence of concrete relative humidity on the amplitude of Ground-Penetrating radar (GPR) signal," *Materials and Structures*, vol. 35, pp. 198-203, 2002.

[43] W.C. Chew, "Design and calibration of a large broadband dielectric measurement cell," *Geoscience and Remote Sensing, IEEE Transactions on*, vol. 29, pp. 42-47, 1991.

[44] O. Büyükoztürk, T-Y. Yu, and J.A. Ortega, "A methodology for determining complex permittivity of construction materials based on transmission-only coherent, wide-bandwidth free-space measurements," *Cement & Concrete Composites, Vol 28*, pp. 349–359, 2006.

[45] I.L. and Riad, S.M. and Mostaf, R. and Su, W. Al-Qadi, "Design and evaluation of a coaxial transmission line fixture to characterize portland cement concrete," *Construction and Building Materials*, vol. 11, pp. 163 - 173, 1997.

[46] M. Adous, P. Quéffélec, and L. Laguerre, "Coaxial-cylindrical transition line for broadband permittivity measurement of civil engineering materials," *Measurement Science and Technology*, vol. 17, no. 8, pp. 2241-2246, 2006.

[47] X. Dérobert, J. Iaquinta, G. Klysz, and J.P Balayssac, "Use of capacitive and GPR techniques for non-destructive evaluation of cover concrete," *NDT&E Int.*, vol. 41, no. 1, pp. 44-52, 2008.

[48] N.L. Tran and R. Ambrosino, "Mesure de la teneur en eau des sols et des matériaux par une méthode capacitive: 3-applications de la méthode capacitive de mesure de la teneur en eau," *Bulletin des Ponts et Chaussées*, vol. 60, pp. 173-175, 1972.

[49] A. Khelidj, G. Bastian, V. Baroghel-Bouny, and Villain G., "Experimental study of the evolution of heat and moisture transfer parameters of a concrete slab," *Magazine of Concrete Research*, vol. 59, no. 5, pp. 377-386, 2007.

[50] A. Ihamouten, G. Villain, and X. Dérobert, "Complex permittivity frequency variations from multi-offset GPR data: Hydraulic concrete characterization," *IEEE Transactions on Instrumentation and Measurement*, vol. 61, no. 6, pp. 1636-1648., 2012.

[51] A. Ihamouten, *Caractérisation physique et hydrique de bétons d'ouvrage par propagation d'ondes électromagnetique.* Université de Nantes, Ecole Doctorale Science et Technologies de I'information et Mathématiques., 2011.

[52] J. and Streich, R. and Green, A. Van der Kruk, "Properties of surface waveguides derived from separate and joint inversion of dispersive TE and TM GPR data," *Geophysics*, vol. 71, pp. K19-K29, 2006.

[53] A. Revil, "Effective conductivity and permittivity of unsaturated porous materials in the frequency range 1 mHz - 1GHz," *Water Resources Research*, vol. 49, pp. 1-22, 2013.

[54] D.C. Montgomery, *Design and Analysis of Experiments*, 5th ed. New York: Wiley, 2000.

[55] C.T. Kelley, *Iterative Methods for Linear and Nonlinear Equations.* Philadelphia: Society for Industrial and Applied Mathematics, 1995.

[56] S.C. and Canale, R.P. Chapra, *Numerical Methods for Engineers*, 4th ed.: McGraw-Hill, 2001.

[57] J. Kiusalaas, *Numerical Methods in Engineering with Matlab.*: Cambridge University Press, 2005.

[58] G. Villain and M. Thiery, "Gammadensimetry: A method to determine drying," *NDT&E International*, vol. 39, pp. 328–337, 2006.

[59] G. et al. Arliguie, *GranDuBé - Grandeurs associées à la Durabilité des Bétons, AFGC-RGCU*, Presses de l'ENPC, Ed. Paris, 2007.

[60] J.-M. Østvik, C.K. Larsen, Ø. Vennesland, E.J. Sellevold, and M.C. Andrade, "Electrical resistivity of concrete Part I: Frequency dependence at various moisture contents and temperatures," *2nd International Symposium on Advances in Concrete through Science and Engineering, Quebec City, Canada, September 11-13*, 2006.

UNIVERSITÉ DE NANTES
membre de l'unam
L'Université Nantes Angers Le Mans

Division de la recherche et des écoles doctorales
Bureau des études doctorales & Coordination des écoles doctorales

ABSTRACT

THE DEVELOPMENT AND COMBINATION OF ELECTROMAGNETIC NON-DESTRUCTIVE EVALUATION TECHNIQUES FOR THE ASSESSMENT OF COVER CONCRETE CONDITION PRIOR TO CORROSION

Electromagnetic (EM) non-destructive evaluation techniques are sensitive to parameters related to the durability of concrete. This research project investigated the potential of electromagnetic investigation techniques to assess concrete durability and detect the presence of harmful agents (i.e. moisture and chloride). The combination of three in situ electromagnetic techniques to assess concrete condition was also shown to have great potential.

The first phase in this research project comprised a parametric study to assess the sensitivity of the different electromagnetic observables to concrete condition. Custom electromagnetic test equipment (an existing co-axial electromagnetic cell) and a multi-ring dc-resistivity cell (developed as part of this thesis) were employed. Multiple linear regression models were then developed for each EM observable (dc-resistivity and dielectric permittivity) as a function of degree of saturation, chloride content, porosity and diffusion coefficient.

During the second phase EM evaluation techniques suitable for in situ measurements were used to assess the condition of homogeneous (unreinforced) concrete slabs. A multi-electrode dc-resistivity probe developed during this thesis, capacitive probe and ground penetrating radar (GPR) were employed. The techniques were combined to estimate the condition of each slab by non-linear optimization of the regression models developed in the previous phase. It was found that electrical resistivity tomography (ERT) using the newly developed multi-electrode resistivity probe was especially useful to assess gradients within concrete.

Keywords : NDT, electrical resistivity, dielectric permittivity, concrete durability, chloride content, water content, porosity, chloride diffusivity.

RÉSUMÉ

DÉVELOPPEMENT ET COMBINAISON DE TECHNIQUES ÉLECTROMAGNÉTIQUES NON DESTRUCTIVES POUR L'ÉVALUATION DU BÉTON D'ENROBAGE AVANT CORROSION

Sachant que les techniques d'auscultation électromagnétiques non destructives (EM) sont sensibles a de nombreux paramètres d'état des bétons, l'objectif de ce projet de recherche est d'étudier le potentiel de ces méthodes d'investigation EM pour évaluer la durabilité des bétons et détecter la présence d'agents agressifs.

Dans un premier temps, une cellule de mesure EM coaxiale-cylindrique et une cellule de résistivité multi-anneaux (mise au point conçue dans cette thèse) ont été utilisées pour une étude paramétrique. Des modèles de régression multi-linéaires ont été développés pour chaque observable EM (résistivité électrique et permittivité diélectrique) en fonction du degré de saturation, de la teneur en chlorures, de la porosité et du coefficient de diffusion de différentes formulations de bétons et mortiers.

Dans un deuxième temps, des techniques de mesure EM in-situ ont été utilisées sur des corps d'épreuve homogènes pour évaluer leur état : un capteur de résistivité multi-électrodes, développé dans le cadre de cette thèse, un capteur capacitif et un système radar. Ces techniques ont été combinées pour donner une estimation quantitative du taux de saturation, de la teneur en chlorures et de la porosité des mélanges par optimisation non-linéaire des modèles de régression, développés dans la phase précédente.

Enfin, l'aptitude de ces techniques in-situ a détecter des gradients a également été étudiée. Il a été constaté que la tomographie de résistivité électrique (TRE), utilisant le nouveau système multi-électrodes était particulièrement adapté a la détermination de gradients dans le béton d'enrobage.

Mots clés : END, résistivité électrique, permittivité diélectrique, durabilité du béton, teneur en chlorure, teneur en eau, porosité, diffusivité.